Acoustic excitation of nuclear spin waves in the easy-plane antiferromagnetic material $KMnF_3$

Kh. G. Bogdanova, V. A. Golenishchev-Kutuzov, V. E. Leont'ev, M. R. Nazipov,
and M. M. Shakirzyanov

Kazan Physicotechnical Institute, Russian Academy of Sciences, 420029 Kazan, Russia

M. I. Kurkin and V. V. Nikolaev

Institute of Metal Physics, Urals Branch of the Russian Academy of Sciences, 620239 Ekaterinburg, Russia

(Submitted 17 April 1997)
Zh. Éksp. Teor. Fiz. **112**, 1830–1840 (November 1997)

Ultrasound damping at $T=4.2$ K in single crystal easy-plane antiferromagnetic $KMnF_3$ is studied experimentally as a function of the magnitude and direction of a constant magnetic field **H** at frequencies of 640–670 MHz, corresponding to the frequencies of nuclear spin waves. Two experimental situations are examined: in the first, the vector **H** lies in the easy magnetization plane (001), and in the second, **H** forms an angle with (001). For longitudinal ultrasound waves propagating along the hard magnetization axis [001], it is found that the damping depends resonantly on the magnitude of the field **H**. In the first case a single damping maximum is observed, and in the second, two damping peaks that are well resolved with respect to the field. The angular dependence of the resonance damping signals on the direction of the constant magnetic field is found to have a 90° periodicity in all cases. The observed effects are explained by resonant ultrasonic excitation of nuclear spin waves. On the basis of an analysis of the magnetoacoustic interaction energy, it is shown that in the first case, nonzero oscillations of the antiferromagnetism vector **L** occur only in the basal plane, while in the second, oscillations of **L** occur both in the basal and a vertical plane, which are associated, respectively, with two branches of the nuclear spin waves. It is also shown that the 90° periodicity in the angular dependence of the damping signals is associated with a fourth order [001] axis. © *1997 American Institute of Physics.* [S1063-7761(97)02211-7]

1. INTRODUCTION

The principal characteristic of nuclear spin waves,[1] as of electronic spin waves (magnons),[2] is that their frequencies $\omega_n(\mathbf{q})$ depend on the wave vector $\mathbf{q}$, which varies within the limits of the Brillouin zone over $0\leqslant\mathbf{q}\leqslant\mathbf{Q}$, where $\mathbf{Q}$ is the reciprocal lattice vector. The range of variation in the frequencies of the nuclear spin waves (the width of the spin wave band),

$$\omega_p=\omega_n(\mathbf{Q})-\omega_n(0), \tag{1}$$

is determined by an indirect interaction of the nuclear magnetic moments **m** through magnons[3] and therefore depends strongly on the shape of the magnon spectrum $\omega_e(\mathbf{q})$.

In two-sublattice antiferromagnets, which include $KMnF_3$, the magnon spectrum has two branches $\omega_{e1}(\mathbf{q})$ and $\omega_{e2}(\mathbf{q})$ (in accordance with the number of magnetic sublattices), whose spectral widths are determined by the exchange interaction $(\omega_{ei}(\mathbf{Q})-\omega_{ei}(0)=\omega_E\sim10^{13}-10^{14}\ \mathrm{s}^{-1},\ i=1,2)$. The $\omega_{ei}(0)$ are related to weaker magnetic interactions (with external magnetic fields, magnetic anisotropy fields, etc.), so that $\omega_{ei}\ll\omega_E$. In easy-plane antiferromagnets, the ratio $\omega_{e1}(0)/\omega_{e2}(0)\approx10^{-2}-10^{-3}$ because of the large difference in the magnitudes of the anisotropy fields in the basal plane, $\mathbf{H}_a$, and along the hard magnetization axis, $\mathbf{H}_A$.[4] In the weakly anisotropic ferromagnetic materials, cubic $RbMnF_3$ and almost cubic $KMnF_3$, this ratio is typically

$$\omega_{e1}(0)/\omega_{e2}(0)\simeq1. \tag{2}$$

The relationship between the exchange frequency ω_E and $\omega_{ei}(0)$ determines the radius of the indirect interaction of the nuclear magnetic moments $\mathbf{m}_j$ and $\mathbf{m}_j'$ through the magnons:[3]

$$r_0(i)=a\omega_E/\omega_{ei}(0), \tag{3}$$

where a is the interatomic separation in the crystal. $r_0(i)$ depends on the magnon branch number i because the interactions of the various components of the vectors $\mathbf{m}_j$ and $\mathbf{m}_j'$ are different. In easy-plane and cubic antiferromagnetic materials in constant magnetic fields $H<10^4$ Oe, $r_0(i)$ can attain macroscopic sizes $(r_0\sim(10^3-10^4)a\approx(10^{-5}-10^{-4})$ cm), which ensures formation of nuclear spin waves at liquid helium temperatures, when the nuclear spins are in a disordered paramagnetic state.[3]

Nuclear spin waves have been studied in most detail in easy-plane antiferromagnets based on manganese atoms ($MnCO_3$, $CsMnF_3$ etc.).[5–9] These compounds are the most convenient objects for such research for the following reasons: first, as do other antiferromagnetic materials, they have a large radius $r_0\approx10^{-5}-10^{-4}$ cm (3); second, ^{55}Mn nuclei have a large magnetic moment ($\approx$3.5 nuclear magnetons); third, strong hyperfine fields $H_n=650$ kOe act on them; and fourth, the natural abundance of the magnetic isotope ^{55}Mn is close to 100%.

The easy-plane antiferromagnetic materials are distinguished by the fact that only the indirect interaction through low frequency magnons, $\omega_{e1}(\mathbf{q})$, is significant because

1063-7761/97/111001-06$10.00

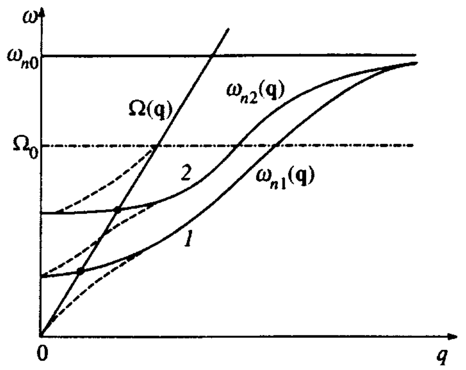

FIG. 1. Dispersion curves for sound waves $\Omega(\mathbf{q})$ and for the two branches of nuclear spin waves $\omega_{n1}(\mathbf{q})$ and $\omega_{n2}(\mathbf{q})$.

$r_0(2) \ll r_0(1)$, so only one branch of the nuclear spin waves, $\omega_{n1}(\mathbf{q})$ develops. For the other branch, $\omega_{n2}(\mathbf{q})$, the nuclear spin wave band is narrower than the NMR line.

In the past, mostly the nonlinear effects produced by nuclear spin waves have been studied: the production of echo signals by frequency modulation;[9] parametric excitation of nuclear spin waves;[5–8] hysteresis in stationary NMR signals.[10,11] In these papers, nuclear spin waves were excited by a varying magnetic field. In the present paper, we report studies of nuclear magnetoacoustic resonances in which nuclear spin waves are excited by the elastic field of an acoustic wave, as in the case of the electron magnetoacoustic resonance with magnons.[2] Although magnetoelastic interactions can play an important role even in ordinary NMR,[12] in the case of NMR their role can only be evaluated indirectly. In the case of the nuclear magnetoacoustic resonance, it is possible to intervene actively in the magnetoelastic dynamics, by varying the amplitude, frequency, and polarization of the sound. In addition, magnetic and magnetoacoustic fields differ in symmetry and this shows up in the selection rules for excitation of the different branches of nuclear spin waves.

Nuclear spin waves were excited and their properties studied in the antiferromagnetic compound $\mathrm{KMnF_3}$ which has a cubic structure with a weak tetragonal distortion. In this sort of antiferromagnet, because of Eq. (2) the indirect interaction through both magnon branches is significant and this causes both nuclear spin wave branches, $\omega_{n1}(\mathbf{q})$ and $\omega_{n2}(\mathbf{q})$ to develop.[13–15] The dispersion curves for the nuclear spin waves $\omega_{n1}(\mathbf{q})$ and $\omega_{n2}(\mathbf{q})$ and the acoustic wave $\Omega(\mathbf{q})$ are shown schematically in Fig. 1. The intersection points of the curves

$$\Omega(\mathbf{q}) = \omega_{n1}(\mathbf{q}) \quad \text{and} \quad \Omega(\mathbf{q}) = \omega_{n2}(\mathbf{q}) \tag{4}$$

correspond to resonance conditions in the first and second nuclear spin wave branches. The dashed curves in Fig. 1 represent the distortion in the nuclear spin and sound waves in the neighborhood of these resonances, which shows up, in particular, as a change in the sound speed V_S that is well known from the electron magnetoacoustic resonance.[2] The behavior of V_S in the nuclear magnetoacoustic resonance region was not studied there, however. The main purpose of that study was to observe and study the nuclear magnetoacoustic resonance signal from both nuclear spin wave branches.

The nuclear magnetoacoustic resonance signals were observed using the fact that the width of the nuclear spin wave bands, $\omega_{pi}(\mathbf{q})$, which represent a dynamic frequency shift,[3,9] has a strong dependence on the magnitude of the constant magnetic field **H**. Thus, the points where the branches of the nuclear spin waves intersect can be displaced along the $\Omega(\mathbf{q})$ curves using the magnetic field **H** to make them coincide with the frequency Ω_0 of the acoustic oscillations excited in the sample. The fields **H** at which these coincidences occur can be determined experimentally from the absorption peak for the input acoustic power.

2. SAMPLES AND MEASUREMENT TECHNIQUE

$\mathrm{KMnF_3}$ has a cubic structure at room temperature which undergoes a weak tetragonal distortion as a result of two structural phase transitions at $T_1 = 188.6\,\mathrm{K}$ and $T_2 = 91.5\,\mathrm{K}$.[16,17] Antiferromagnetic ordering occurs at $T_N = 88.3\,\mathrm{K}$. The corresponding collinear two-sublattice antiferromagnetic structure is determined by the antiferromagnetism vector $\mathbf{L} = (\mathbf{M}_1 - \mathbf{M}_2) \| [001]$, where [001] is a fourth-order axis. At $T_M = 81.5\,\mathrm{K}$ there is a magnetic orientational phase transition in which **L** tilts into the basal plane and a weak ferromagnetism $\mathbf{M} = \mathbf{M}_1 + \mathbf{M}_2$ develops.[16–19] The symmetry of all these transitions has been analyzed elsewhere.[20]

The presence of a weak ferromagnetism in the tetragonal antiferromagnetic materials has been shown[3,20] to lead to the formation of a domain structure with four directions of **L** and **M**, which makes experiments more complicated. This can be avoided, however, by cooling the sample to below 100 K in a field $H \simeq 8\,\mathrm{kOe}$, as has been done in the present work.

The single crystals of $\mathrm{KMnF_3}$ on which the measurements were made were prepared in the form of parallelepipeds from a single piece with dimensions of $4 \times 4 \times 4.7\,\mathrm{mm}^3$ and $3 \times 3 \times 4\,\mathrm{mm}^3$, whose edges coincided with the principal crystallographic axes [100], [010], and [001]. The end surfaces of the crystals were made flat and mutually parallel to within 1/5 wavelength of the acoustic wave. Ultrasonic waves were excited in a pulsed regime at one of the end surfaces, (001), of the sample and detected at the opposite end. They were polarized longitudinally and had a frequency in the range 600–700 MHz. The acoustic wave vector **q** was always oriented along the [001] axis.

The measurements were taken at $T = 4.2\,\mathrm{K}$. The helium cryostat with the sample was rotated about the R axis, always perpendicular to **H** (Fig. 2a and b). The angle between the R axis and the wave vector **q** was set equal to 0° (direct orientation, Fig. 2a) or 20° (oblique orientation, Fig. 2b). The constant magnetic field was varied from 0 to 8 kOe.

To simplify the observations and calculations we used a single pass of the acoustic pulse through the sample. The ratio of its amplitude U to the amplitude U_0 of the incident sound determines the measured absorption coefficient.

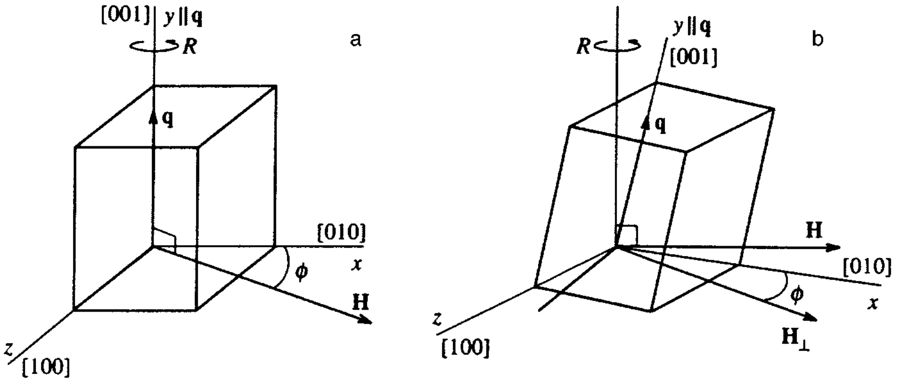

FIG. 2. Experimental geometry: (a) direct orientation (**H** lying in the easy magnetization plane), (b) oblique orientation (**H** directed at an angle to the easy magnetization plane).

3. MEASUREMENT RESULTS

Resonant damping in a constant magnetic field of ultrasonic pulses at frequencies of 630–670 MHz propagating along the [001] direction of the crystal was observed for the two orientations of the sample relative to R.

In the first case the vectors **H** and **q** were perpendicular to one another and **H** lay in the easy magnetization plane (001) of the sample (direct orientation) (Fig. 2a). In the second case, the angle between **H** and **q** was varied from 70° to 110° (oblique orientation) (Fig. 2b). In the plots of U/U_0 as a function of H for fixed values of ϕ (where ϕ is the angle between the x axis and the direction of $\mathbf{H}_\perp$) the following features were observed: a single intense peak for direct orientation (Figs. 3a and 4a) and two intense peaks for oblique orientations (Fig. 3b and 4b).

Plots of the ratios U/U_0 as functions of the orientation of the constant magnetic field with respect to the crystallographic axes (i.e., of the angle ϕ) are shown in Figs. 5 and 6. The constant magnetic fields $H=H_1$ (direct orientation, Figs. 5a and 6a) and $H=H_1'$ and $H=H_2'$ (oblique orientation, Figs. 5b and 6b) correspond to the acoustic absorption peaks. As can be seen from Figs. 5 and 6, the angular dependence of U/U_0 has a 90° periodicity in the direction of **H** in both cases, consistent with the fact that the [001] direction is a fourth-order axis.

The curves in Figs. 3–6 correspond to two frequencies, 644 and 655 MHz. Similar curves were obtained for other frequencies in the range 630–670 MHz. These anomalies vanish outside this range. Since the 630–670 MHz band corresponds to NMR frequencies for $\mathrm{KMnF_3}$,[13–15] we have at-

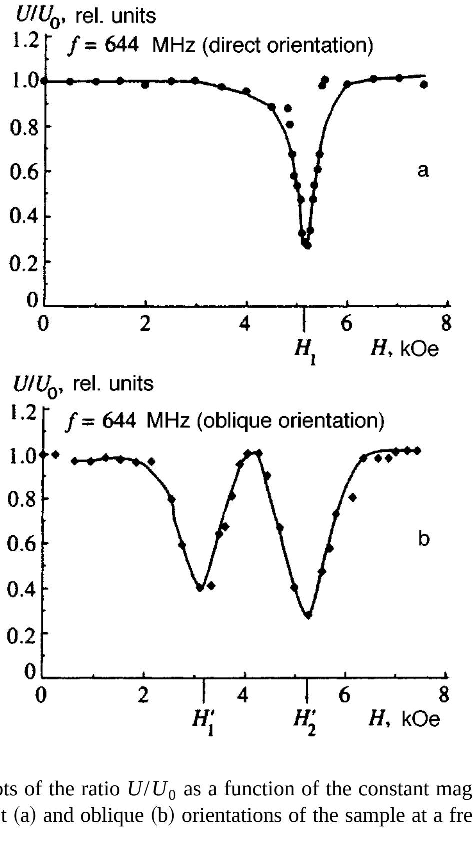

FIG. 3. Plots of the ratio U/U_0 as a function of the constant magnetic field H for direct (a) and oblique (b) orientations of the sample at a frequency of 644 MHz.

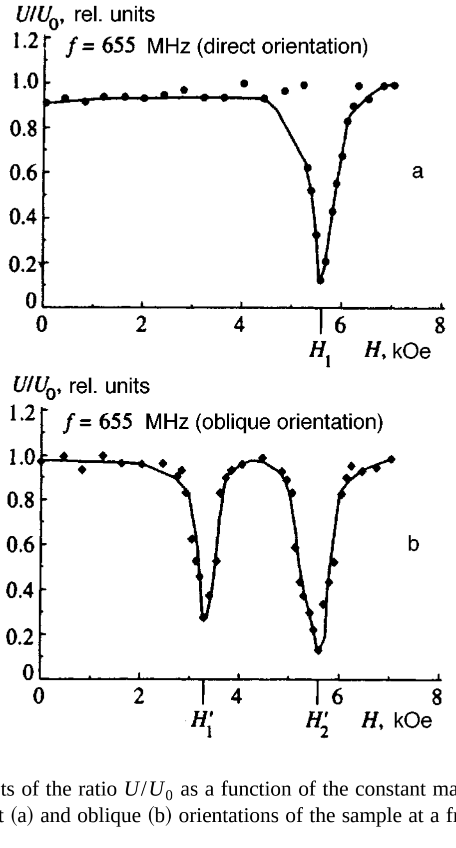

FIG. 4. Plots of the ratio U/U_0 as a function of the constant magnetic field H for direct (a) and oblique (b) orientations of the sample at a frequency of 655 MHz.

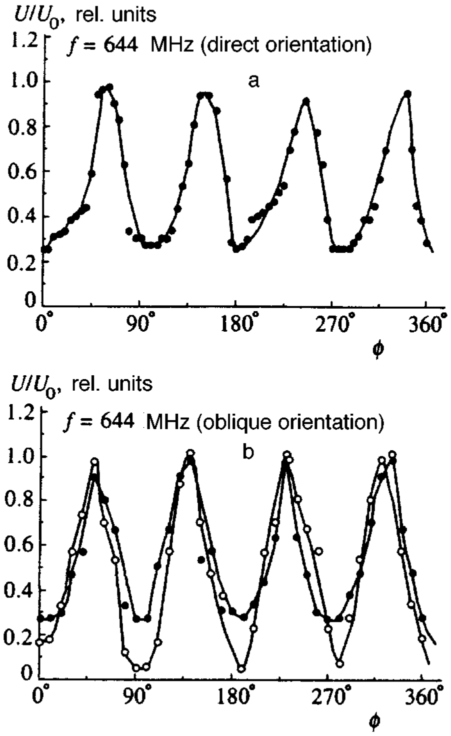

FIG. 5. Angular dependences of the ratio U/U_0 for direct (a) and oblique (b) orientations of the sample at a frequency of 644 MHz.

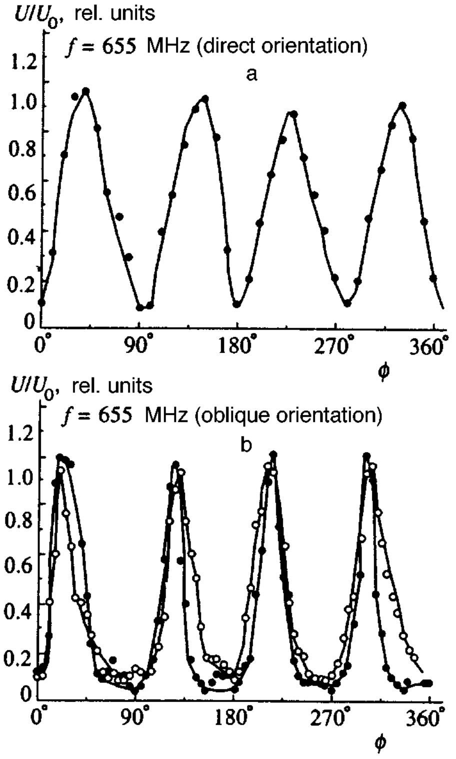

FIG. 6. Angular dependences of the ratio U/U_0 for direct (a) and oblique (b) orientations of the sample at a frequency of 655 MHz.

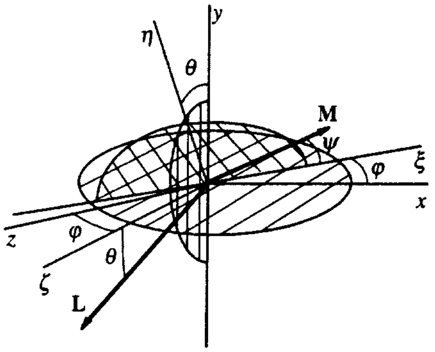

FIG. 7. Euler angles θ, φ, and ψ which define the orientation of the vectors **L** and **M**, where θ is the angle between **L** and ζ (or y and η) in the $y\zeta$ plane; φ is the angle between z and ζ (or x and ξ) in the zx plane; ψ is the angle between **M** and ξ in the $\eta\xi$ plane.

tempted to relate the observed minima of U/U_0 in Figs. 3 and 4 to a resonant interaction of sound with the two nuclear spin wave branches near the points where $\Omega(\mathbf{q})$ intersects $\omega_{n1}(\mathbf{q})$ and $\omega_{n2}(\mathbf{q})$ (Fig. 1). This is discussed in the next section of this article, where expressions are derived for the magnetoelastic energy corresponding to the interaction of the first, V_1, and second, V_2, branches of the nuclear spin waves with longitudinal sound in the propagation geometry being examined here ($\mathbf{q}\|[001]$) (see Eq. (26):

$$V_1 \sim \sin\psi \sin 2\varphi, \quad V_2 \sim \cos\psi \sin 2\varphi, \tag{5}$$

where φ is the angle between **L** and z ($z\|[100]$) and ψ is the angle between **M** and the basal plane (001) (the zx plane in Fig. 7). Equations (5) have been derived for **L** oriented in the basal plane ($\mathbf{L}\perp[001]$) and correspond to the magnetoelastic part of the interaction responsible for the weak ferromagnetism in $\mathrm{KMnF_3}$.[20]

It can be seen from Eq. (5) that for $\psi = 0$, $V_1 = 0$, so that one minimum should remain in the $U(H)/U_0$ curve. Measurements with direct orientation (Figs. 3a and 4a) were made specially as a control experiment to verify Eq. (5). The second characteristic feature of V_1 and V_2 is that they go to zero for $\varphi = 0, \pm\pi/2, \pi$. At these values of φ we should have $U(H)/U_0 \approx 1$, in agreement with Figs. 3 and 4.

4. DISCUSSION OF RESULTS

To describe the phenomena owing to the nuclear magnetoacoustic resonance which have been observed in the experiment, we can begin with the equations of motion of the nuclear magnetizations $\mathbf{m}_i$ of the sublattices,[1]

$$\frac{d\mathbf{m}_i}{dt} = \gamma_n(\mathbf{m}_i \times \mathbf{H}_{ni}), \quad i = 1,\ 2, \tag{6}$$

where γ_n is the nuclear gyromagnetic ratio and the $\mathbf{H}_{ni}$ are the effective magnetic fields, determined by the interactions in which the nuclear spins participate. The strongest interaction, which greatly exceeds all the others, is the hyperfine interaction:[1]

$$\mathscr{H}_N = -\sum_{i=1}^{2} A_i \int d\mathbf{r}\mathbf{M}_i(\mathbf{r})\mathbf{m}_i(\mathbf{r}), \tag{7}$$

where A_i is the hyperfine interaction constant for the ith sublattice. In the case of crystallographically equivalent sublattices (as in $\mathrm{KMnF_3}$), the constants $A_1 = A_2 = A$. The interaction $\mathscr{H}_N$ is equivalent to the effect of an effective magnetic field

$$\mathbf{H}_{ni}(\mathbf{r},t)=A\mathbf{M}_i(\mathbf{r},t) \tag{8}$$

originating in the electronic magnetization $\mathbf{M}_i$ on the nuclear magnetization $\mathbf{m}_i$ which appears in Eq. (6). Given these remarks, in the following we restrict ourselves to considering just this effective field (8) in Eqs. (6).

In coordinate systems (x_i, y_i, z_i) attached to the equilibrium directions of the sublattice magnetizations $\mathbf{M}_{0i}$ $(\mathbf{M}_{0i}\|z_i)$, Eq. (6) take their simplest form. For small oscillations in $\mathbf{m}_i$, when we can neglect the changes in the z-component ($m_i^{z_i}=m_0$) as second order quantities compared to the variations in $m_i^{x_i}$ and $m_i^{y_i}$, Eq. (6) can be written in the form

$$\frac{dm_i^{x_i}}{dt}=\omega_{n0}m_i^{y_i}-\gamma_n\Delta H_{ni}^{y_i}(\mathbf{r},t)m_0,$$

$$\frac{dm_i^{y_i}}{dt}=-\omega_{n0}m_i^{x_i}+\gamma_n\Delta H_{ni}^{x_i}(\mathbf{r},t)m_0 \quad (i=1,2), \tag{9}$$

where m_0 is the equilibrium value of $m_i^{z_i}$, $\omega_{n0}=\gamma_n AM_0$ is the unshifted NMR frequency determined by the static part of the hyperfine field $H_{ni}=AM_0$ ($M_0=M_{01}=M_{02}$ is the equilibrium magnetization of the electronic sublattices), and

$$\Delta\mathbf{H}_{ni}(\mathbf{r},t)=A\Delta\mathbf{M}_i(\mathbf{r},t)=A(\mathbf{M}_i(\mathbf{r},t)-\mathbf{M}_{0i}) \tag{10}$$

is the dynamic part of $\mathbf{H}_{ni}$ owing to oscillations of the $\mathbf{M}_i(\mathbf{r},t)$ near their equilibrium values. In this case, these oscillations have the form

$$\Delta\mathbf{M}_i(\mathbf{r},t)=\Delta\mathbf{M}_{im}(\mathbf{r},t)\Delta\mathbf{M}_{iu}(\mathbf{r},t), \tag{11}$$

where the oscillations $\Delta\mathbf{M}_{im}(\mathbf{r},t)$, given by

$$\Delta\mathbf{M}_{im}(\mathbf{r},t)=\sum_{j=1}^{2}\int dr'\chi_{ij}(\mathbf{r}-\mathbf{r}')A\mathbf{m}_j(\mathbf{r}'), \tag{12}$$

are caused by the hyperfine fields

$$\mathbf{H}'_{ei}(\mathbf{r},t)=A\mathbf{m}_i(\mathbf{r},t), \tag{13}$$

acting on the electron spins from the part of the nuclei. These oscillations ensure the generation of nuclear spin waves.[3] Equation (12) includes the quantities $\chi_{ij}(\mathbf{r},t)$, which determine the response of the magnetization $\mathbf{M}_i(\mathbf{r})$ at the point $\mathbf{r}$ to the $\mathbf{h}_j(\mathbf{r}')$ applied to the j-sublattice at the point $\mathbf{r}'$. The second term in Eq. (11), which is the principal term in the magnetoacoustic resonance, is caused by the magnetoelastic fields $\mathbf{h}_{ju}$ associated with the elastic deformations by the acoustic wave:

$$\Delta\mathbf{M}_{iu}(\mathbf{r},t)=\sum_{j=1}^{2}\int dr'\chi_{ij}(\mathbf{r}-\mathbf{r}')\mathbf{h}_{ju}(\mathbf{r}',t). \tag{14}$$

The fields $\mathbf{h}_{ju}$ are defined as the variational derivatives of the magnetoelastic energy V_{ME},[3,21]

$$\mathbf{h}_{ju}(\mathbf{r}',t)=\delta V_{ME}/\delta\mathbf{M}_i(\mathbf{r}',t), \tag{15}$$

where

$$V_{ME}=\sum_{i,j=1}^{2}\sum_{\alpha,\beta,\gamma,\delta}\int dr\, B_{ij}^{\alpha\beta\gamma\delta}M_i^{\alpha}(\mathbf{r})M_j^{\beta}(\mathbf{r})U_{\gamma\delta}(\mathbf{r},t), \tag{16}$$

and

$$U_{\gamma\delta}(\mathbf{r},t)=\frac{1}{2}\{\partial U_{\gamma}(\mathbf{r},t)/\partial r_{\delta}+\partial U_{\delta}(\mathbf{r},t)/\partial \mathbf{r}_{\gamma}\}, \tag{17}$$

while $\mathbf{U}$ is the elastic displacement vector and the $B_{ij}^{\alpha\beta\gamma\delta}$ are the magnetoelastic interaction constants.

By solving Eq. (9) in conjunction with Eqs. (10)–(17), it is possible to calculate the spectrum and amplitudes of the nuclear spin waves excited by the elastic field $U(\mathbf{r},t)$. But in order to do this, it is necessary to know the components of the susceptibilities $\chi_{ij}(\mathbf{r}-\mathbf{r}')$, which depend on the orientation of the vectors $\mathbf{M}_{0i}$ that are determined by the magnitude and direction of the field $\mathbf{H}$. Unfortunately, this kind of calculation can be done in analytic form completely only for a few orientations of $\mathbf{H}$ along the most symmetric directions in the crystal. Although they are free of this restriction, numerical calculations require knowledge of all the necessary parameters of the substance. In addition, it would be desirable to confirm in advance that the model is applicable to solving our problem. Such proofs have been successfully obtained by analyzing the selection rules for excitation of nuclear spin waves by longitudinally polarized acoustic waves. To do this we used a property of the solutions of Eq. (9) which can be established without solving the equations themselves. It turned out that one branch of the nuclear spin waves interacts only with oscillations of $\mathbf{L}=\mathbf{M}_1-\mathbf{M}_2$ in the basal plane, during which only the angle φ varies. (See Fig. 7.) The other branch of the nuclear spin waves interacts only with oscillations of $\mathbf{L}$ in a vertical plane which are described by the single angle θ. Perturbations which affect the angle ψ do not excite either branch of the nuclear spin waves.

This property of nuclear spin waves allows us to find the conditions under which the interaction of sound with each of the nuclear spin wave branches goes to zero by analyzing the interaction V_{ME} (16) and without calculating $\chi_{ij}(\mathbf{r}-\mathbf{r}')$.

The procedure for this analysis reduces to the following: the expression for the magnetoelastic energy (16) can be conveniently rewritten to account for the specific symmetry of crystalline KMnF$_3$ by shifting from the magnetizations $\mathbf{M}_i$ to the vectors $\mathbf{L}$ and $\mathbf{M}$. For tetragonal crystals, such as KMnF$_3$, Eq. (16) takes the form

$$V_{ME}=V_{LL}+V_{LM}+V_{MM}, \tag{18}$$

where V_{LL} only contains components of the vector $\mathbf{L}$, V_{LM} depends on products of components of both vectors $\mathbf{L}$ and $\mathbf{M}$, and V_{MM} is a term quadratic in components of $\mathbf{M}$. Since the ratio $M/L\simeq\omega_{ei}(0)/\omega_E\approx10^{-3}$, V_{LM} has a significant effect only when the corresponding terms in V_{LL} equal zero. Similarly, it makes sense to include V_{MM} only if V_{LM} has no effect. For longitudinal sound propagating along the $y\|[001]$ axis, the effect of V_{MM} can be neglected and the expressions for V_{LL} and V_{LM} can be written in the form

$$V_{LL}=B_1L_y^2U_{yy}+B_2(L_z^2+L_x^2)U_{yy},$$

$$V_{LM}=B_3(M_xL_z+M_zL_x)U_{yy}, \tag{19}$$

where $B_1=b_{33}$, $B_2=b_{23}$, and $B_3=b_{63}$.[22] Subsequently, the components of $\mathbf{L}$ and $\mathbf{M}$ must be expressed in terms of the angles θ, φ, and ψ (Fig. 7):

$$L_x = L_0 \cos\theta \sin\varphi, \quad L_y = -L_0 \sin\theta,$$

$$L_z = L_0 \cos\theta \cos\varphi,$$

$$M_x = M_0 \cos\psi \cos\varphi + M \sin\psi \sin\theta \sin\varphi,$$

$$M_y = M_0 \sin\psi \cos\theta,$$

$$M_z = -M_0 \cos\psi \sin\varphi + M_0 \sin\psi \cos\varphi \sin\theta, \tag{20}$$

where L_0 and M_0 are the equilibrium values of **L** and **M**, while the angles θ and ψ describe the emergence of **L** and **M**, respectively, from the basal plane. The small oscillations in **L** and **M** owing to the deformation field $U(\mathbf{r},t)$ are determined by small changes in the angles θ and φ ($\delta\theta$ and $\delta\varphi$, respectively):

$$\theta = \theta_0 + \delta\theta, \quad \varphi = \varphi_0 + \delta\varphi, \tag{21}$$

where θ_0 and φ_0 are the equilibrium values of θ and φ. Expanding Eq. (19) in powers of $\delta\theta$ and $\delta\varphi$, we obtain

$$V_{LL} = V_0^{LL} + V_1^{LL}\delta\theta + V_2^{LL}\delta\varphi,$$

$$V_{LM} = V_0^{LM} + V_1^{LM}\delta\theta + V_2^{LM}\delta\varphi, \tag{22}$$

where

$$V_1^{LL}(\psi,\theta_0,\varphi_0) = (B_1 - B_2)L_0^2 U_{yy} \sin 2\theta_0,$$

$$V_2^{LL}(\psi,\theta_0,\varphi_0) = 0, \tag{23}$$

$$\begin{aligned} V_1^{LM}(\psi,\theta_0,\varphi_0) = B_3 L_0 M_0 U_{yy} & \\ \times(-2\cos\psi\cos\theta_0 \sin 2\varphi_0 & \\ + \sin\psi \sin 2\theta_0 \cos 2\varphi_0), & \end{aligned} \tag{24}$$

and

$$\begin{aligned} V_2^{LM}(\psi,\theta_0,\varphi_0) = B_3 L_0 M_0 U_{yy} & \\ \times(-2\cos\psi\sin\theta_0 \cos 2\varphi_0 & \\ + \sin\psi \cos 2\theta_0 \sin 2\varphi_0). & \end{aligned} \tag{25}$$

Equations (23)–(25) imply that when the vector **L** lies in the basal plane ($\theta_0 = 0$), only V_1^{LM} and V_2^{LM} are nonzero, with

$$V_1^{LM}(\psi,0,\varphi_0) = B_3 L_0 M_0 U_{yy} \sin\psi \sin 2\varphi_0,$$

$$V_2^{LM}(\psi,0,\varphi_0) = -2B_3 L_0 M_0 U_{yy} \cos\psi \sin 2\varphi_0, \tag{26}$$

which characterize the magnetoelastic interaction and are coupled to oscillations of the vector **L** in, respectively, the basal plane for V_2^{LM} and a vertical plane for V_1^{LM}. The corresponding components of the magnetoelastic field, $h_1(V_1^{LM})$ and $h_2(V_2^{LM})$, obtained with the aid of Eqs. (15)–(22) and (26), in accordance with the above remarks, excite different branches of the nuclear spin waves, thereby determining the experimentally observed angular dependences of the nuclear magnetoacoustic resonance signals. Since Eq. (26) have been obtained for $\theta_0 = 0$, we may assume that in the low temperature phase ($T < 81.5$ K), the antiferromagnetism vector **L** lies in the basal plane. This conclusion is consistent with some earlier papers[20,23,24] and contradicts another[25] in which it is assumed that $\theta_0 \neq 0$.

We thank E. A. Turov, V. V. Men'shchenin, and I. F. Mirsaev for valuable comments during the writing of this paper.

This work was supported by the Russian Fund for Fundamental Research (project 96-02-16489).

[1] P. G. de Gennes, P. Pincus, F. Hartman-Boutron *et al.*, Phys. Rev. **129**, 1105 (1963).
[2] A. I. Akhiezer, V. G. Bar'yakhtar, and S. V. Peletminskii, *Spin Waves*, North-Holland, Amsterdam (1968).
[3] M. I. Kurkin and A. E. Turov, *NMR* in *Magnetically Ordered Materials and its Applications* [in Russian], Nauka, Moscow (1990), p. 244.
[4] A. S. Borovik-Romanov, *Antiferromagnetism. Papers on antiferromagnetism and ferrites* [in Russian], Fizmatgiz, Moscow (1962).
[5] A. J. Heeger, A. M. Portis, D. T. Traney *et al.*, Phys. Rev. Lett. **7**, 307 (1961).
[6] L. W. Hinderks and P. M. Richards, J. Appl. Phys. **41**, 931 (1970).
[7] V. I. Ozhogin and A. Yu. Yakubovskiĭ, Zh. Éksp. Teor. Fiz. **67**, 287 (1974) [Sov. Phys. JETP **40**, 144 (1975)].
[8] S. A. Govorkov and V. A. Tulin, Zh. Éksp. Teor. Fiz. **70**, 1876 (1976) [Sov. Phys. JETP **43**, 977 (1976)].
[9] A. S. Borovik-Romanov, Yu. M. Bun'kov, B. S. Dumesh *et al.*, Usp. Fiz. Nauk **142**, 537 (1984) [Sov. Phys. Usp. **27**, 235 (1984)].
[10] V. A. Tulin, Zh. Éksp. Teor. Fiz. **55**, 831 (1968) [Sov. Phys. JETP **28**, 431 (1969)]; **78**, 149 (1980) [**51**, 73 (1980)].
[11] M. I. Kurkin, Fiz. Tverd. Tela **33**, 1805 (1991) [Sov. Phys. Solid State **33**, 1014 (1991)].
[12] Kh. G. Bogdanova, V. A. Golenishchev-Kutuzov, M. I. Kurkin *et al.*, Zh. Éksp. Teor. Fiz. **103**, 163 (1993) [JETP **76**, 89 (1993)].
[13] A. M. Protis, G. L. Witt, and A. J. Higer, J. Appl. Phys. **34**, 1052 (1963).
[14] G. L. Witt and A. M. Portis, Phys. Rev. **136**, 1316 (1964).
[15] W. J. Ince, Phys. Rev. **184**, 574 (1969).
[16] G. Shirane, V. Minkiewicz, and A. Linz, Solid State Commun. **8**, 1941 (1970).
[17] K. Gezi, J. D. Axe, G. Shirane, and A. Linz, Phys. Rev. B **5**, 1933 (1972).
[18] O. Beckman and K. Knox, Phys. Rev. **121**, 376 (1961).
[19] A. J. Higer, O. Beckman, and A. M. Portis, Phys. Rev. **123**, 1652 (1961).
[20] Yu. A. Izyumov, F. A. Kassam-Ogly, and V. E. Naĭsh, FMM **51**, 500 (1981).
[21] V. I. Ozhogin and V. L. Preobrazhenskiĭ, Usp. Fiz. Nauk **155**, 593 (1988) [Sov. Phys. Usp. **31**, 713 (1988)].
[22] G. A. Smolenskiĭ, V. V. Lemanov, G. M. Nedlin, M. P. Petrov, and R. V. Pisarev, *Physics of Magnetic Dielectrics* [in Russian], Nauka, Leningrad (1974), Ch. 4.
[23] M. Hidaka, J. Phys. Soc. Jpn. **39**, 103 (1975); **39**, 180 (1975).
[24] M. Hidaka, N. Ohama, A. Okazaki *et al.*, Solid State Commun. **16**, 1121 (1975).
[25] K. Saiki, K. Horai, and H. Yoshioka, J. Phys. Soc. Jpn. **35**, 1016 (1973).

Translated by D. H. McNeill

Nonlinear magnetohydrodynamic waves in compensated metals

V. G. Peschanskiĭ*) and D. I. Stepanenko

Kharkov State University, 310077 Kharkov, Ukraine

(Submitted 29 May 1997)
Zh. Éksp. Teor. Fiz. **112**, 1841–1846 (November 1997)

We show that if a conductor is placed in a quantizing magnetic field $\mathbf{H}_0$, nonlinear small-amplitude electromagnetic waves can propagate in the conductor. For compensated metals we find the solution of the Maxwell equations when the field $\mathbf{H}_0$ is perpendicular to the direction in which the waves propagate. © *1997 American Institute of Physics.* [S1063-7761(97)02311-1]

As established by Konstantinov and Perel'[1] and Kaner and Skobov,[2] when a conductor is placed in a strong uniform magnetic field $\mathbf{H}_0$, slowly decaying electromagnetic waves can propagate in it, whose frequency is much lower than the cyclotron frequency of the conduction electrons. Because of the high density of charge carriers in metals, the nonlinear effects in metals are weak and have only a small influence on the wave processes. The spectrum of these waves can easily be found from the Maxwell equations linearized with respect to the weak electric and magnetic fields of the wave. The situation changes when a quantizing magnetic field is applied to the system: the nonlinearity may become strong enough to have an effect even if the wave amplitude is small. If the distance between the Landau levels is much larger than the level width and the temperature spread β^{-1} of the equilibrium Fermi charge-carrier distribution function, the amplitude of the quantum oscillating part of the magnetic susceptibility χ may reach values of order unity.[3] Here one must bear in mind that quantization of the energy levels of the charge carriers is caused not by an exact microscopic field but by the average macroscopic value of the field, so that the magnetization $\mathbf{M}(\mathbf{B})$ and the magnetic field $\mathbf{H}=\mathbf{B}-4\pi\mathbf{M}(\mathbf{B})$ are complicated functions of the magnetic induction $\mathbf{B}=\mathbf{B}_0+\tilde{\mathbf{B}}$, with $\mathbf{B}_0$ the uniform part of the induction and $\tilde{\mathbf{B}}$ the field of the wave. When the values of B_0 satisfy $|1-4\pi\chi(B_0)|\ll 1$, the term in the Maxwell equation that is linear in the amplitude of the magnetic field of the wave, $[1-4\pi\chi(B_0)]\partial\tilde{\mathbf{B}}(x,t)/\partial x$, may prove to be of the same order as the nonlinear terms, with the result that the wave process becomes decidedly nonlinear.

In compensated conductors, with equal electron and hole densities $(n_e=n_h=n)$, there can be magnetohydrodynamic waves of two types: one similar to an Alfvén wave, and the other similar to a rapidly propagating magnetoacoustic wave in a gaseous plasma. In this paper we examine the propagation of waves along the x axis perpendicular to the vector $\mathbf{B}_0=(0,0,B_0)$ on the assumption that the z axis coincides with the crystal symmetry axis higher than the second order. In this case there is no Alfvén wave, while the electromagnetic field of the rapidly propagating magnetoacoustic wave has the form $\mathbf{E}=(0,E(x,t),0)$ and $\tilde{\mathbf{B}}_0=(0,0,\tilde{B}(x,t))$ and can be found by solving the system of equations

$$\frac{\partial\tilde{B}}{\partial t}=-c\frac{\partial E}{\partial x},\quad \frac{\partial\tilde{B}}{\partial x}=-\frac{4\pi J_y}{c},\tag{1}$$

where c is the speed of light in vacuum, and $\mathbf{J}=\mathbf{j}+c$ curl $\mathbf{M}$ is the total current density, which consists of the conductivity current density $\mathbf{j}$ generated by the electric field $\mathbf{E}$ and the current density $\mathbf{j}'=c$ curl $\mathbf{M}$ induced by the magnetic field.

The first order in the wave electromagnetic field, the components of $\mathbf{J}$ are given by the following expressions:[4]

$$j_i(\mathbf{r},t)=\int_{-\infty}^{t}dt'\int d^3r'\,Q_{ik}(\mathbf{r},\mathbf{r}',t-t')E_k(\mathbf{r}',t'),\tag{2}$$

$$\begin{aligned}j_1'(\mathbf{r},t)=\frac{1}{c}\int d^3r'\,Q_{ik}(\mathbf{r},\mathbf{r}',0)\tilde{A}_k(\mathbf{r}',t)\\ -\frac{e^2}{2c}\tilde{A}_k(\mathbf{r},t)\mathrm{Tr}\Bigg\{\hat{\rho}_0\sum_n\Bigg[\frac{\partial\hat{v}_i}{\partial\hat{p}_{nk}}\delta(\mathbf{r}-\mathbf{r}_n)\\ +\delta(\mathbf{r}-\mathbf{r}_n)\frac{\partial\hat{v}_i}{\partial\hat{p}_{nk}}\Bigg]\Bigg\},\end{aligned}\tag{3}$$

where $\hat{\rho}_0$ is the equilibrium statistical operator of the system of the conduction electrons with a dispersion $\varepsilon(\mathbf{p})$ and hence a velocity $\mathbf{v}=\partial\varepsilon/\partial\mathbf{p}$, $\mathbf{p}_n=-i\hbar\,\partial/\partial\mathbf{r}_n-\mathbf{A}_0(\mathbf{r}_n)e/c$ is the kinematic momentum, $\mathbf{A}_0(\mathbf{r})$ and $\tilde{\mathbf{A}}(\mathbf{r},t)$ are the vector potentials of the field $\mathbf{B}_0$ and the wave magnetic field, and the summation with respect to n is over all particles with charge e.

The kernel of the integral operator in (2) and (3) for a homogeneous medium depends only on $r-r'$:

$$\begin{aligned}Q_{ik}(\mathbf{r},\mathbf{r}',t-t')=Q_{ik}(\mathbf{r}-\mathbf{r}',t-t')\\ =\int_0^{\beta}d\zeta\,\mathrm{Tr}[\hat{\rho}_0\hat{I}_k(\mathbf{r}',t'-i\hbar\zeta)\hat{I}_i(\mathbf{r},t)],\end{aligned}\tag{4}$$

where $\hat{\mathbf{I}}(\mathbf{r},t)$ is the current density operator of an unperturbed system of charge carriers in the interaction representation.

If the wavelength λ is much larger than the radius r_0 of the orbit of the charge carriers in the magnetic field and the wave frequency is much lower than the cyclotron frequency ω_B, the integral expression for the current density $\mathbf{J}$ can be reduced to a local one, i.e., it can be represented by a series expansion in powers of $\tilde{\mathbf{B}}$ and $\mathbf{E}$ and their derivatives with respect to x and t. In the expression for the conduction current we can ignore the gradient terms, proportional to powers of the small parameter r_0/λ, and the quantum oscillating correction proportional to $\sqrt{\hbar\omega_B/\varepsilon_F}$, where ε_F is the Fermi energy. As a result, in the expression for the current density we can limit ourselves to two terms,

$$j_y=\frac{\sigma_0}{(\Omega\tau)^2}\left(1+\tau\frac{\partial}{\partial t}\right)E(x,t). \tag{5}$$

Here σ_0 is the static conductivity in the absence of a magnetic field, τ is the mean free time, and Ω is equal (to within a dimensionless factor of order unity) to $\omega_B=eB_0/mc$, where m is the characteristic cyclotron mass of a conduction electron.

On the other hand, if we wish to calculate the induced current density $\mathbf{j}'$, we must take into account the quantization of the energy levels of the charge carriers, since the part of the magnetic susceptibility that oscillates with the reciprocal value of the magnetic field is significantly larger than the smoothly varying part.

To find $\mathbf{j}'$ we write (3) as

$$j_1'(\mathbf{r},t)=\frac{1}{c}\int d^3r'\,Q_{ik}(\mathbf{r}',0)[\widetilde{A}_k(\mathbf{r}-\mathbf{r}',t)-\widetilde{A}_k(\mathbf{r},t)]. \tag{6}$$

Expanding the function $\widetilde{A}_k(\mathbf{r}-\mathbf{r}',t)$ in a power series in $\mathbf{r}'$ and using the symmetry property $Q_{ik}(\mathbf{r},0)=Q_{ki}(-\mathbf{r},0)$, we arrive at an expression for the linear part of the magnetization current:

$$j_y'=-c\chi(B_0)\,\frac{\partial\widetilde{B}}{\partial x}-c\gamma(B_0)r_0^2\frac{\partial^3\widetilde{B}}{\partial x^3}, \tag{7}$$

where

$$\chi(B_0)=\chi_{zz}=-\frac{1}{2c^2}\int d^3r\,Q_{yy}(\mathbf{r},0)x^2, \tag{8}$$

$$\gamma(B_0)=-\frac{1}{24c^2r_0^2}\int d^3r\,Q_{yy}(\mathbf{r},0)x^4. \tag{9}$$

Clearly, χ and γ are of the same order of magnitude.

The nonlinear correction to the magnetization is proportional only to the third power of the wave magnetic field, since the value B_0 at which $\chi(B_0)=1/4\pi$ holds is the point of inflection of the $H=H(B)$ curve, i.e. $\partial^2M(B)/\partial B^2=0$. The terms that contain a nonlinearity and derivatives with respect to x in the asymptotic expansion of the magnetization can be ignored, since they are proportional to powers of the product of two small parameters, r_0/λ and $\widetilde{B}/B_0$. This leads us to an expression for the current density induced by the magnetic field:

$$j_y'=-c\chi(B_0)\,\frac{\partial\widetilde{B}}{\partial x}+\frac{c\xi}{B_0^2}\,\frac{\partial\widetilde{B}^3}{\partial x}-c\gamma(B_0)r_0^2\frac{\partial^3\widetilde{B}}{\partial x^3}, \tag{10}$$

where $\xi=\alpha(\varepsilon_F/\hbar\Omega)^2\chi(B_0)$, with α a dimensionless factor of order unity that depends on the specific form of the dispersion law of the charge carriers.

Substitution of (5) and (10) in the Maxwell equations yields an equation for $\widetilde{B}$:

$$\frac{\partial^2}{\partial x^2}\left\{[1-4\pi\chi(B_0)]\widetilde{B}+\frac{4\pi\xi}{B_0^2}\,\widetilde{B}^3-4\pi\gamma(B_0)r_0^2\frac{\partial^2\widetilde{B}}{\partial x^2}\right\}=\frac{4\pi\sigma_0}{(c\Omega\tau)^2}\left(1+\tau\frac{\partial}{\partial t}\right)\frac{\partial\widetilde{B}}{\partial t}. \tag{11}$$

In dimensionless variables this equation becomes

$$\frac{\partial^2}{\partial x_1^2}\left(\pm u+2u^3-\frac{\partial^2u}{\partial x_1^2}\right)=\frac{\partial^2u}{\partial t_1^2}+\frac{1}{\omega_0\tau}\,\frac{\partial u}{\partial t_1}, \tag{12}$$

where

$$x_1=\frac{x}{\delta},\quad t_1=\omega_0t,\quad \delta=\frac{\sqrt{4\pi\gamma}r_0}{\kappa},\quad \kappa^2=|1-4\pi\chi(B_0)|,$$

$$\omega_0=\frac{\Omega c\kappa}{\omega_p\delta},\quad \omega_p^2=\frac{4\pi\sigma_0}{\tau},\quad u=\frac{\widetilde{B}}{b},\quad b=B_0\sqrt{\frac{\kappa^2}{2\pi\xi}}.$$

The "plus" in Eq. (12) corresponds to the case $\chi(B_0)<1/4\pi$; the "minus" to the case $\chi(B_0)>1/4\pi$. The physical meaning of the parameters δ, b, ω_0, and ω_p is obvious: $\delta\simeq r_0/\kappa\gg r_0$ is the distance on which the electromagnetic field changes significantly, b and ω_0 are equal (in order of magnitude) to the amplitude and frequency of the wave, and ω_p is the plasma frequency.

Two conditions must be met if we want weakly decaying waves to exist: $\varepsilon_F/\hbar\Omega\geqslant10^3$ and $\omega_0\tau\simeq\Omega\tau(\Omega c/\omega_pv_F)\kappa^2\gg1$, where v_F is the velocity of charge carriers whose energy is equal to the Fermi energy. The first condition guarantees that at low temperatures the magnetic susceptibility is of order unity and the second, that the dissipation term in Eq. (12) is small. In metals where the number of charge carriers is of order one per atom the conditions are met for sufficiently pure specimens, where the collision time of the charge carriers is greater than, or of the order of, 10^{-9} s in magnetic fields of order 10 T.

In the zeroth approximation in the small parameter $\eta=(\omega_0\tau)^{-1}$, Eq. (12) has a wave solution dependent on the variable $\theta(x_1,t_1)=x_1-Vt_1$:

$$u(\theta(x_1,t_1))=a\sqrt{k}\,\mathrm{sn}\left[\frac{a}{\sqrt{k}}(x_1-Vt_1),k\right]. \tag{13}$$

Here $a=\sqrt{\partial u(\theta)/\partial\theta}$ at $\theta=0$, k is the modulus of the elliptic function sn, and the wave velocity V is related to k by

$$V^2=\frac{1}{k}[a^2(1+k^2)+sk], \tag{14}$$

where $s=\mathrm{sgn}[1-4\pi\chi(B_0)]$.

The effect of weak dissipation can easily be taken into account by writing the solution of Eq. (12) in the form of a series in powers of η:

$$u(x_1,t_1)=u^{(0)}(x_1,t_1)+\eta u^{(1)}(x_1,t_1)+\cdots, \tag{15}$$

where

$$u^{(0)}(x_1,t_1)=a(T)\sqrt{k}\,\mathrm{sn}\left[\frac{a(T)}{\sqrt{k}}\,\theta(x_1,t_1),k\right], \tag{16}$$

$T=\eta t_1$ is the "slow time," and

$$\frac{\partial\theta(x_1,t_1)}{\partial x_1}=1,$$

$$\frac{\partial\theta(x_1,t_1)}{\partial t_1}=-V(T)=-\sqrt{\frac{a^2(T)(1+k^2)+sk}{k}}.$$

The wave amplitude $a(T)$ and velocity of propagation $V(T)$ are slowly varying functions of time. Inserting the series (15) for u into Eq. (12) and collecting terms of equal orders in the parameter η, we see that the function (16) satisfies the zeroth-approximation equation, while the first-approximation equation is

$$\frac{\partial}{\partial\theta}\left[(-V^2+s)u^{(1)}+6u^{(0)2}u^{(1)}-\frac{\partial^2 u^{(1)}}{\partial\theta^2}\right]=-u^{(0)}\left(V+\frac{\partial V}{\partial T}\right)$$
$$-2\left(u^{(0)}+\theta\frac{\partial u^{(0)}}{\partial\theta}\right)V\frac{\partial\ \ln a}{\partial T}\equiv F(\theta). \tag{17}$$

The time dependence of the amplitude and velocity of propagation of the wave can be found from the fact that the right-hand side of Eq. (17) is orthogonal to the solution u^* of the conjugate equation

$$\left[(V^2-s)\frac{\partial u^*}{\partial\theta}-6u^{(0)2}\frac{\partial u^*}{\partial\theta}+\frac{\partial^3 u^*}{\partial\theta^3}\right]=0. \tag{18}$$

For a particular solution of Eq. (18) we take $u^{(0)}$. Then the orthogonality condition

$$\int_0^K d\theta\ u^{(0)}(\theta)F(\theta)=0 \tag{19}$$

leads to

$$a(T)V(T)=a(0)V(0)e^{-T}, \tag{20}$$

where K is the period of $u^{(0)}(\theta)$.

Doing simple calculations, we find that

$$a^2(T)=\frac{[f(k,T)-s]k}{2(1+k^2)},\quad V^2(T)=\frac{f(k,T)+s}{2}, \tag{21}$$

where

$$f(k,T)=\sqrt{1+4k^{-1}(1+k^2)a^2(0)V^2(0)e^{-2T}}.$$

The Maxwell equations (1) and the condition (20) can be used to find the electric field of the wave:

$$E(x_1,t_1)=b\frac{\Omega\kappa}{\omega_p}\sqrt{k}a(0)V(0)\exp(-\eta t_1)$$
$$\times\mathrm{sn}\left[\frac{a(T)}{\sqrt{k}}\theta(x_1,t_1,k)\right]. \tag{22}$$

The asymptotic behavior of the time-dependent magnetic field as $t\rightarrow\infty$ depends on the sign of s. At $s=-1$ dissipation leads to the onset of a stationary domain structure.[3] If in (21) we let t go to ∞, we get

$$V(\infty)=0,\quad a^2(\infty)=\frac{k}{1+k^2}.$$

This implies

$$u(x_1,\infty)=a(\infty)\sqrt{k}\ \mathrm{sn}\left[\frac{a(\infty)}{\sqrt{k}}(x_1-\varphi),k\right],$$

$$\varphi=\int_0^\infty V(t_1)dt_1,$$

so that the distribution of magnetic induction is a system of periodically alternating layers. The time-dependence of $u(x_1,t_1)$ for the case where dissipation is not weak can easily be established. For $\eta\geqslant 1$ the system passes aperiodically to an inhomogeneous stationary state. If $s=+1$ holds, in the limit $t\rightarrow\infty$ we get

$$a(\infty)=0,\quad u(x_1,\infty)=0,$$

and with the passage of time the distribution of magnetic induction within the specimen becomes uniform.

We are grateful to the Ukrainian Government and the International Science Foundation for partial financial support of our work (Grant No. K5X100).

*)Also at B. I. Verkin Low-Temperature Physicotechnical Institute, Ukrainian National Academy of Sciences, 310164 Kharkov, Ukraine.

---

[1] O. V. Konstantinov and V. I. Perel', Zh. Éksp. Teor. Fiz. **38**, 161 (1960) [Sov. Phys. JETP **11**, 117 (1960)].
[2] E. A. Kaner and V. G. Skobov, Adv. Phys. **17**, 605 (1968).
[3] J. Condon, Phys. Rev. **145**, 526 (1965).
[4] O. V. Konstantinov and V. I. Perel', Zh. Éksp. Teor. Fiz. **37**, 786 (1959) [Sov. Phys. JETP **10**, 560 (1960)].

Translated by Eugene Yankovsky

Melting of the condensed inert gases

B. M. Smirnov

Institute of High Temperatures, Russian Academy of Sciences, 127412 Moscow, Russia

(Submitted 20 May 1997)
Zh. Éksp. Teor. Fiz. **112**, 1847–1862 (November 1997)

The melting of a macroscopic system of bound atoms with a pairwise interaction is examined as a vacancy formation process. It is found that the existence of a liquid state is related to a double-humped dependence of the partition function on the number of vacancies, where the peaks correspond to the solid and liquid states and the heights of the peaks are equal at the melting point. In order for the liquid state to form, the derivative of the vacancy interaction with respect to energy must have a maximum. The vacancies are compressed as a result of the interaction. In the condensed inert gases, the specific energy of vacancy formation is proportional to the resulting empty space per atom. *© 1997 American Institute of Physics.* [S1063-7761(97)02411-6]

1. INTRODUCTION

Melting is a first order phase transition which occurs at a fixed temperature in macroscopic systems and is characterized by a certain energy expenditure per unit volume. This kind of phenomenological description of the phenomenon is sufficient for analyzing its thermodynamics.[1–4] The microscopic description is much more complicated. For the simplest macroscopic systems consisting of atoms with a pairwise interaction that are examined below, melting is accompanied by the formation of vacancies within the material,[1–4] and this leads to an increase in the volume of the system during the transition from the solid to the liquid state, as well as to the expenditure of energy in vacancy formation. Nevertheless, the liquid state is an excited state of a system of bound atoms and, since melting takes place when the thermal energies of the atoms are low compared to the specific energy of formation of the vacancies, the liquid state should have a large statistical weight compared to the solid state.

Recently, interesting information has been obtained on the melting of clusters, or systems consisting of a finite number of bound atoms.[5–15] The basis of the analysis is the molecular dynamics method, in which clusters are modeled as a system of interacting classical atoms so that it is possible to account correctly for the collective processes which play a fundamental role in phase transitions.

Experience in studying clusters with pairwise, usually Lenard–Jones, interactions among the atoms has been useful for understanding the microscopic picture of phase transitions. First, the cluster analysis uses clearcut criteria for the liquid state of a system of bound atoms that are based on the correlation between the coordinates of atoms in time. For clusters with closed shells this kind of analysis reveals the existence of one or more distinct excited states, which constitute the liquid state of the cluster. Second, in clusters the liquid and solid phases coexist over a range of parameters, as opposed to macroscopic systems of bound atoms, in which there is no coexistence of the phases and the transition between them is discontinuous. These are all features of systems with finite and infinite numbers of bound atoms. Third, for clusters with closed shells, the transition to the liquid state corresponds to the transport of atoms to the cluster surface and the formation of vacancies in the inner shells. These transitions are dynamic, so that at a certain time atoms are ejected toward the cluster surface and the resulting vacancies are filled in, but surface atoms can then return to the inner shells.

The molecular dynamics method is optimal for the analysis of a phase transition, since this phenomenon is determined by collective interactions of the atoms, which are taken into account in this model. Nevertheless, the results obtained for clusters have not made it possible to produce an instructive model for their melting that takes the microscopic character of the transition into account. In particular, spectral analysis of atomic motion cannot be used to extract the simple aspects of the behavior of the phase transition.

Thus, from a microscopic standpoint, the liquid state of a system of bound atoms with pairwise interactions is an excited state of a system with vacancies inside it. This leads to a number of fundamental questions, such as why the liquid state of a system of bound atoms stands out as one of its many excited states. Likewise, what is a vacancy in the liquid state of such a system? The subject of this paper is a microscopic analysis of models for melting in systems consisting of finite and infinite numbers of bound atoms with pairwise interactions. The basis of this analysis is data for the condensed inert gases and molecular dynamics calculations for clusters with pairwise atomic interactions.

2. TWO-LEVEL APPROXIMATION

We begin by examining the nature of melting in a large cluster with a closed structure and consisting of atoms with a pairwise interaction. A cluster of this sort is made up of a certain number of shells or layers of atoms. Obviously, a phase transition for the surface and inner layers will take place at different temperatures. However, if we consider a large cluster for which the number of atoms in the surface and near-surface layers is relatively low, then melting involving the bulk of the atoms will be unrelated to surface effects. Therefore, in the following discussion of macroscopic systems of bound atoms, we only deal with clusters of this type.

From a microscopic standpoint, this phenomenon corresponds to a transition of atoms from the inner layers to the cluster surface. The existence of a distinct excited state of the cluster, which we assume to be a liquid, obviously means that the excitation probability as a function of the number of excited atoms is characterized by a sharp maximum. In other words, the partition function of the cluster as a function of the number of excited atoms in the surface layer has a sharp maximum, so that the width of this maximum encloses few atoms compared to the average number of excited atoms. Note that this conclusion follows logically from the condition for the existence of a liquid state as the most probable excited state of the cluster.

We base the mathematical description of this aspect of the excitation of the system of bound atoms on a two-level approximation.[16] Let us introduce the partition functions of the ground (solid) $Z_{\rm sol}$ and excited (liquid) $Z_{\rm liq}$ states of the system of bound atoms. Clearly,

$$Z_{\rm liq}=Z_{\rm sol}\, g\, \exp(-\Delta E/T), \tag{1}$$

where g is the ratio of the statistical weights of the liquid and solid states, ΔE is the excitation energy of the liquid state, and T is the temperature of the cluster. We assume that the probability of finding the cluster in other states makes a small contribution to the total partition function of the cluster, so that the probabilities of finding it in the solid and liquid states are given, respectively, by

$$w_{\rm sol}=\left[1+g\,\exp\left(-\frac{\Delta E}{T}\right)\right]^{-1},$$

$$w_{\rm liq}=g\,\exp\left(-\frac{\Delta E}{T}\right)\left[1+g\,\exp\left(-\frac{\Delta E}{T}\right)\right]^{-1}. \tag{2}$$

These equations apply equally well to a cluster and to a macroscopic system of atoms as an infinite cluster.

We define the melting temperature T_m in accordance with the formula $w_{\rm sol}(T_m)=w_{\rm liq}(T_m)$, i.e.,

$$g\,\exp(-\Delta E/T_m)=1. \tag{3}$$

Let ε be the energy of formation for a single vacancy, h the statistical weight of an isolated vacancy, and v the total number of vacancies. Taking $v \ll n$, where n is the number of atoms in the cluster, we obtain $g \sim h^n$, and since $\Delta E=v\varepsilon$, for the width of the phase transition region we have

$$\Delta T \sim T_m^2/(\varepsilon v). \tag{4}$$

One of the fundamental differences between a cluster and a macroscopic system of bound atoms follows from this equation. In a cluster, which contains a finite number of vacancies, the solid and liquid phases can coexist over a certain temperature range,[5–15] while the phase transition region for a macroscopic system contracts to a point, i.e., the phase transition takes place at fixed temperature.

Let us turn our attention to yet another feature of this transition, which shows up most distinctly during surface melting, when an atom from the surface layer is carried to the cluster surface, so that a vacancy is formed in the surface layer. A stable site on the cluster surface corresponds to finding an atom in one of the troughs between surface atoms, and to carry an atom into this state requires the breaking of more bonds than the atom has in its final state. This means that for the atom to be transferred to its final state, it must overcome a barrier whose height is of the same order of magnitude as the bond strength of a few simple bonds, and which exceeds the thermal energy of the atom undergoing the transition. The barrier nature of atomic excitation in a cluster (see Refs. 10 and 11, for example) is of fundamental significance for transitions between the solid and liquid states of a cluster. It implies that the characteristic time for the cluster to be found in the liquid or solid states greatly exceeds the characteristic transition time from one state to the other. Thus, the coexistence of the solid and liquid phases in a cluster means that there is a definite probability of coming upon the cluster in the solid or liquid state, but that there is no intermediate state.

This two-level cluster model, which forms the basis of the phenomenological theory of phase transitions in systems with finite and infinite numbers of bound atoms, imposes certain requirements on the excited state of the system, which in the case of a pairwise atomic interaction we shall treat as the formation of a set of vacancies. Let us state these requirements. We denote the partition function of a cluster consisting of n atoms with $v \gg 1$ vacancies by Z_v. In the two-level system we make implicit use of the fact that Z_v has a sharp, narrow maximum for some number of vacancies $v_{\rm max}$. Expanding $\ln Z_v$ near the maximum and assuming that the normalization of the partition function is determined by a narrow region of vacancy numbers near $v_{\rm max}$, we obtain an expression for the partition function Z_v in this region in the form of the Gaussian function

$$Z_v=Z_{\rm max}\,\exp[-(v-v_{\rm max})^2/\Delta], \tag{5}$$

where $Z_{\rm max}$ is the partition function for $v_{\rm max}$ vacancies and the parameter Δ follows from the equation

$$\frac{2}{\Delta}=-\frac{d^2}{dv^2}\ln Z_v(v_{\rm max}). \tag{6}$$

By definition,

$$v_{\rm max} \gg \Delta \gg 1. \tag{7}$$

Integrating Eq. (5), we find

$$Z_{\rm liq}=(\pi\Delta)^{1/2} Z_{\rm max}, \tag{8}$$

and, according to Eq. (7), in the phase transition region we find

$$Z_{\rm max} \ll Z_{\rm sol}. \tag{9}$$

Thus, Eqs. (5)–(9) follow from the two-level model for a cluster phase transition and are a consequence of representing the states of a system of bound atoms in the form of two states, the liquid and solid.

We now illustrate the convenience of this two-level model using a calculation of the specific heat of the cluster in the phase transition region as an example. Let E_{ex} be the cluster excitation energy, and η, the part of the excitation

TABLE I. Parameters of the condensed inert gases.

Parameter	Ne	Ar	Kr	Xe	Average
R_e, Å	3.09	3.76	4.01	4.36	–
D, meV	3.64	12.3	17.3	24.4	–
a, Å	3.156	3.755	3.992	4.335	–
$\rho(0)/\rho_0$	1.06	1.00	0.99	0.98	1.01 ± 0.04
$\rho_{\mathrm{sol}}/\rho_0$	0.899	0.920	0.926	0.952	0.92 ± 0.02
$\rho_{\mathrm{liq}}/\rho_0$	0.776	0.804	0.800	0.827	0.80 ± 0.02
$\rho_{\mathrm{sol}}/\rho_{\mathrm{liq}}-1$	0.159	0.144	0.157	0.151	0.153 ± 0.006
T_m/D	0.583	0.585	0.576	0.570	0.578 ± 0.006
$\Delta H_{\mathrm{fus}}/D$	0.955	0.990	0.980	0.977	0.98 ± 0.01
ε_0/D	5.1	5.5	5.5	5.4	5.4 ± 0.2

Note. Here D and R_e are the depth of the potential well for a pairwise atomic interaction and the distance corresponding to the minimum of the pairwise interaction potential[19–22]; the other parameters are taken from handbooks.[23,24] a is the crystal lattice constant; $\rho_0=\sqrt{2}/a^3$; $\rho(0)$ and ρ_{sol} are the densities of the solid state at absolute zero and at the melting point; ρ_{liq} is the density of the liquid state at the melting point; T_m is the melting temperature in energy units; ΔH_{fus} is the specific energy of fusion; and ε_0 is the energy of vaporization of an atom from the liquid state at the melting point.

energy contained in the kinetic energy of the atoms. For the case of atoms executing harmonic oscillations in a cluster, $\eta=0.5$, and η is close to this value in the excitation region being considered here. For the total kinetic energy of the cluster atoms we have

$$E_{\mathrm{kin}}=\eta E_{ex} w_{\mathrm{sol}}+\eta(E_{ex}-\Delta E) w_{\mathrm{liq}}. \tag{10}$$

This yields the specific heat of the cluster:

$$C_v=\frac{dE_{\mathrm{kin}}}{dT}=\eta\,\frac{dE_{ex}}{dT}-\eta\Delta E\,\frac{dw_{\mathrm{liq}}}{dT}=C_V^0+\frac{\Delta E^2}{T^2}\,g \times\exp\left(-\frac{\Delta E}{T}\right)\left[1+g\,\exp\left(-\frac{\Delta E}{T}\right)\right]^{-2}, \tag{11}$$

where C_V^0 is that part of the specific heat not related to the phase transition, which therefore varies smoothly over the temperature range of the phase transition. The cluster specific heat (11) has a maximum at the melting temperature (3) given by

$$C_V^{\max}=C_V^0+\frac{\Delta E^2}{4T_m^2}. \tag{12}$$

Since the specific heat C_V^0 is proportional to the number n of atoms in the cluster, ΔE is proportional to the number v of vacancies in the cluster and $v\sim n$, which implies that the contribution of the phase transition to the cluster specific heat increases as the cluster becomes larger. This implies, in particular, that the specific heat of a macroscopic system of atoms goes to infinity at the melting point. The equations obtained above for the specific heat of a cluster in the phase transition region are convenient for analyzing numerical simulations of the behavior of clusters by the molecular dynamics method, and they reflect the capabilities of the two-level scheme.

Treating the liquid state of a condensed system of bound atoms as the excited state of a system requires that it also be described under conditions such that the system is in the solid state. This consideration is used in describing the aggregate state of condensed gas atoms or molecules over a wide range of parameters.[17,18]

3. FIXED-SITE MODEL

The fixed-site model is the simplest model for describing the liquid state of a cluster or macroscopic atomic system. In terms of this model it is assumed that the formation of a vacancy, as through removal of an atom from a site in the crystal lattice, does not change the positions of the neighboring atoms. In this way, a vacancy in this model represents an empty space that develops at the site of the lost atom. We use this model to analyze the excitation of condensed inert gases, noting that it is applicable on the average, i.e., it is not suitable for analyzing the interaction among the vacancies, which is of fundamental importance for the development of the liquid state.

Here we note that the parameters of various condensed inert gases obey a scaling law in which the pairwise interaction of the atoms serves as the basis units. Some parameters of the condensed inert gases relevant to melting are listed in Table I. The interaction potential for two inert gas atoms is known fairly well based on a number of their parameters that depend on the pairwise atomic interaction. These parameters include the differential and total atomic scattering cross sections and the thermal conductivity and viscosity, as well as the self diffusion coefficients of the atoms in the gases, the second virial coefficient of the gases, the spectroscopic parameters of the diatomic molecules, the geometric and energy parameters of the corresponding crystals, parameters near the critical point, etc. In this way the pairwise interaction potential of the inert gas atoms are known to high accuracy.[19–22]

Note, in addition, the short-range character of the interaction of the inert gas atoms in the condensed systems, so that the energy of a condensed inert gas is determined by the interaction of atoms that are nearest neighbors in the system. In fact, for the actual inert gases Ne, Ar, Kr, and Xe, the statistical averages are $a/R_e=1.004\pm0.014$ and $\varepsilon_{sub}/D=6.4\pm0.2$, where a is the distance between nearest neighbors of the crystal lattice at absolute zero, R_e is the equilibrium distance between the atoms of the corresponding diatomic molecule, ε_{sub} is the binding energy per atom of the atoms in the crystal, and D is the depth of the well in the interaction potential for two atoms of the given inert gas. In

TABLE II. Parameters of the condensed inert gases related to the formation of vacancies.

Parameter	Ne	Ar	Kr	Xe	Average
$v_{\max}/(nh)$, 10^{-5}	3.1	1.5	1.3	1.4	1.9 ±0.8
q	10.10	10.27	10.11	10.19	10.2 ±0.1
n/v_0	6.3	6.9	6.4	6.6	6.6 ±0.3
ξ	0.96	0.93	1.02	0.96	0.96±0.04
$n/v_{\rm liq}$	4.3	4.2	4.1	4.1	4.2 ±0.1
$V(v_{\rm liq})/D$	2.0	2.3	2.5	2.4	2.3 ±0.3
A/D	2.5	2.9	3.0	3.0	2.8 ±0.2
$Z_{\rm rot}$, 10^4	0.24	2.3	8.0	21	–

the case of a short-range interaction potential for the atoms in a condensed system, these ratios are $a/R_e=1$ and $\varepsilon_{sub}/D=6$, while for a Lenard–Jones potential, $a/R_e=0.97$ and $\varepsilon_{sub}/D=8.61$. It can be seen that the short-range potential, which only accounts for the interaction among nearest neighbors, provides the better fit for a condensed inert gas system. It is precisely for a short-range atomic interaction that the fixed-site model, in which the removal of an atom from a lattice site does not change the positions of the neighboring atoms, can be correct. Naturally, when this model is valid, an excited state of the system corresponding to the removal of an atom from a lattice site will be characterized by a higher statistical weight than the system ground state.

We use the fixed-site model to find the partition function when vacancies are present in a macroscopic system of bound atoms with a pairwise interaction. We determine the partition function of the system as a function of the number of vacancies, neglecting the interaction among vacancies. Let us isolate a large cluster containing n atoms ($n\gg 1$), for which surface effects are negligible compared to volume effects, from a macroscopic system. In this case, all the atoms in the cluster, like all the vacancies, are in an equivalent position. In the fixed-site model, the formation of vacancies leads to expansion of the cluster, so that this cluster includes $n+v$ sites, of which n are occupied by atoms. Given this, the partition function of the cluster is

$$Z_v=C_{n+v}^{v}h^v\exp(-v\varepsilon/T)Z_0. \tag{13}$$

Here Z_0 is the partition function of the cluster without vacancies, the number of combinations C_{n+v}^{v} is the number of ways of placing the atoms and vacancies inside the cluster, allowing for the indistinguishability of the atoms and of the vacancies, h is an additional statistical weight owing to vacancy formation, and ε is the vacancy formation energy. In the following we consider the parameter range

$$n\gg v\gg 1 \tag{14}$$

and neglect the interaction of the vacancies in the first stage of the analysis. Using Eq. (14) in Eq. (13) and expanding the exponent in the partition function in powers of $1/v$, we obtain

$$Z_v=Z_0\exp S,\quad S=v(1+\ln h-\varepsilon/T+\ln n-\ln v). \tag{15}$$

This yields Eq. (5) with the following parameters

$$v_{\max}=nh\exp(-\varepsilon/T),\quad \Delta=2v_{\max}. \tag{16}$$

According to Eq. (15), the partition function increases as the number of vacancies is raised, as long as the number of vacancies is small, and the maximum value of the exponent in the partition function is

$$S_{\max}=v_{\max}=nh\exp(-\varepsilon/T)\gg 1. \tag{17}$$

The values of $v_{\max}/(nh)$ for the condensed inert gases are listed in Table II. This macroscopic limit $v_{\max}\gg 1$ applies to systems with a large number of bound atoms. Here the maximum in the partition function, when the number of vacancies in the system is relatively small, corresponds to the solid state of the system. When the number of vacancies is increased further, $S(v)$ falls off monotonically in this approximation. The liquid state of the system of bound atoms corresponds to the next maximum of $S(v)$; the dependence of this function on the number of vacancies is shown in Fig. 1.

To describe the liquid state of a system of bound atoms, it is necessary to include the interaction of vacancies in the analysis. Then the fixed-site model is no longer applicable, so that we must define the vacancies. Let us imagine a monovacancy as the empty closed space inside a system of bound atoms which is formed as a result of removing an internal atom from the system. If the number of vacancies is high enough that their interaction becomes significant, then the volume of a vacancy differs from the volume per atom in the solid state of the system. Here the shape of the vacancy changes with time in accordance with the motion of the surrounding atoms. Since near ordering is preserved in the liquid, i.e., the distances between nearest neighbors in the solid and liquid states at the melting point are the same, it is convenient to turn to the fixed-site model for comparison, if the shape of a monovacancy can correspond to a unit cell of the

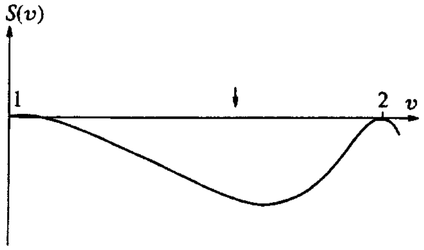

FIG. 1. The logarithm of the partition function of a system of bound atoms with a pairwise interaction as a function of the number of vacancies. The maximum 1 corresponds to the solid state and the maximum 2, to the liquid state. The interaction of the vacancies is significant to the right of the arrow.

crystal lattice. In the following we use this comparison to determine the number of nearest neighbors in the liquid state. Here the vacancy itself as an empty space of definite shape loses its significance, and the dependence of the partition function on the number of vacancies must be understood as a dependence on the volume occupied by the given system of bound atoms under specified external conditions.

Let us isolate a cluster containing n atoms in the solid state, so that each atom has 12 nearest neighbors. In the liquid state, this cluster contains v_0 vacancies and each atom has q nearest neighbors on the average. Relating the change in volume of the cluster during the transition to the liquid state to the change in density, we have

$$\frac{n+v_0}{n}=\frac{\rho_{\text{sol}}}{\rho_{\text{liq}}},$$

where ρ_{sol} and ρ_{liq} are the densities of the macroscopic system in the solid and liquid states at the melting point. Assuming that the number of vacancies is relatively small, we find that the formation of a single vacancy leads to the breaking of 12 bonds. The total number of bonds in a system containing $n+v_0$ atoms is $6(n+v_0)$. If v_0 atoms are then removed from the system, then the total number of bonds in it becomes $qn/2=6(n+v_0)-12v_0=6(n-v_0)$. Hence

$$q=12-12v_0/n=24-12\rho_{\text{sol}}/\rho_{\text{liq}}. \tag{18}$$

The number of nearest neighbors for the liquid state in the inert gases found using Eq. (18) and the relative number of vacancies are given in Table II. It can be seen that the transition from the solid to the liquid state takes place as a result of an expansion of the system of bound atoms. Then the bonds between the atoms are weakened, and this is compensated by a rise in the statistical weight owing to an increase in the volume of the system. The liquid state corresponds to an optimal increase in the system volume.

We now determine the specific energy of the phase transition under consideration. Let ε be the binding energy per atom in the solid state at the melting point. We define it as the sum of the specific energy ε_0 expended in evaporating a single atom at the melting temperature and the specific energy of fusion, ΔH_{fus}:

$$\varepsilon=\varepsilon_0+\Delta H_{\text{fus}}. \tag{19}$$

Therefore, the total binding energy of the atoms in a solid cluster containing n atoms is given by $E_{\text{sol}}=\varepsilon n$ by definition. Let us determine it for the liquid state. Take a cluster containing $n+v_0$ atoms in the solid state, so that the binding energy of the atoms is $\varepsilon(n+v_0)$. Remove v_0 atoms from this cluster, assuming that this number is relatively small, i.e., neglecting the interaction of the vacancies. Given that each bond involves two atoms, we find that removing a single atom requires energy 2ε, i.e, the binding energy of the atoms in the liquid state obtained by removing v_0 atoms from the cluster is $\varepsilon(n-v_0)=\varepsilon_0 n$. Then, using Eq. (19), we obtain

$$v_0/n=\Delta H_{\text{fus}}/\varepsilon. \tag{20}$$

Note the relationship between the energy of vacancy formation in Eq. (13) and the specific energy of fusion, ΔH_{fus}. This relationship is given by $\varepsilon v_0=\Delta H_{\text{fus}} n$, and the parameter ε in Eq. (13) equals the vacancy formation energy in the solid state of the system.

Equation (20) can be used to determine the specific energy of fusion, based on Eq. (18) for the relative number of vacancies. Let us introduce the parameter

$$\xi=\frac{\varepsilon}{\Delta H_{\text{fus}}}\frac{v_0}{n}=\frac{\varepsilon}{\Delta H_{\text{fus}}}\frac{\rho_{\text{sol}}-\rho_{\text{liq}}}{\rho_{\text{liq}}}. \tag{21}$$

If the assumptions used in determining the number of vacancies in terms of the change in density and energy are valid, then this parameter equals unity. The values of ξ calculated using Eq. (21) and listed in Table II show that these assumptions can be used to determine the effective number of vacancies in the actual inert gases with the corresponding accuracy.

Although the equation $\xi=1$, which establishes the relationship between the specific energy of vacancy formation and the change in the density of a system of bound atoms, has been obtained neglecting the interaction of the vacancies, it can be satisfied even when this condition is violated. Essentially, this reflects the fact that the average energy per atom is proportional to the average number of nearest neighbors which, in turn, can be expressed in terms of the density of the system. Given this connection, we can obtain the following relationship between the excitation energy ΔH of a system of bound atoms in a state with a given volume occupied by vacancies and the density ρ of the system of bound atoms:

$$\Delta H=\varepsilon(\rho_{\text{sol}}/\rho-1). \tag{22}$$

This equation transforms to $\xi=1$ for the liquid state of the system.

4. INTERACTION OF VACANCIES IN CONDENSED ATOMIC SYSTEMS

It follows from an analysis of the partition function of the excited state of a system of bound atoms that the interaction of vacancies is of fundamental importance to the liquid state of that system. Thus, in the liquid state a certain density of vacancies is realized. In particular, we show that a more rigorous criterion is required than Eq. (14) for the weakness of the vacancy interaction, which is violated in the condensed inert gases. In fact, in the fixed-site model, the probability that a given vacancy abuts another vacancy equals $12v/n$ in the limit of a small ratio of the number v of vacancies to the number of atoms, i.e., instead of Eq. (14) in this model the criterion for weakness of the vacancy interaction has the form

$$n\gg 12v. \tag{23}$$

Clearly, this criterion is not satisfied for the liquid state of the real inert gases; that is, the interaction of the vacancies is important for the liquid state of the inert gases.

An analysis shows that the fixed-site model leads to inconsistencies as soon as the vacancy interaction is taken into account. Let us begin with the Stillinger–Weber model,[25] in which the vacancies are treated as quasiparticles and their pairwise interaction is considered. Then the number of vacancies in the liquid state of the system follows from the minimum condition for the Hamiltonian. It would seem that this model provides a good match to the fixed-site model, in which the quasiparticles are the empty spaces produced by removal of atoms from lattice sites. Then the interaction of the quasiparticles corresponds to the interaction of the nearest neighbors in the system. If we use this interaction in the fixed-site model, then to obtain the observed melting parameters of the actual condensed inert gases, it is necessary to assume the formation of cavities encompassing dozens of monovacancies inside the condensed inert gas.[26]

This inconsistency suggests that it is the fixed-site model which is not valid, rather than the Stillinger–Weber model, which includes a quadratic interaction for the vacancies. Despite its logical consistency, however, the Stillinger–Weber model is not suitable for the actual inert gases, because it does not yield the liquid state of a system of bound atoms as a maximum in the partition function (see below).

We now analyze the general character of the vacancy interaction. We specify it in the form $vV(v/n)$, so that the binding energy of the atoms in the excited state of this system of bound atoms has the form

$$E=\varepsilon(n-v)+vV(v/n). \tag{24}$$

For large v such that $v \gg n$, the interaction function for the vacancies obviously has the asymptotic form $V(x)=1-1/x$, $x \gg 1$, but in analyzing the phase transition we shall be interested in this function for small values of the argument. To analyze its form we construct the partition function (13) including the vacancy interaction, so that instead of Eq. (15) for the partition function and its derivatives we have

$$S=\ln\frac{Z_v}{Z_0}=v\left(1+\ln h+\ln\frac{n}{v}-\frac{\varepsilon}{T_m}\right)+\frac{W}{T_m}, \tag{25a}$$

$$\frac{dS}{dv}=\ln h+\ln\frac{n}{v}-\frac{\varepsilon}{T_m}+\frac{W'}{T_m}, \tag{25b}$$

$$\frac{d^2S}{dv^2}=-\frac{1}{v}+\frac{W''}{T_m}, \tag{25c}$$

where $W=vV(v/n)$.

The general form of the exponent in the partition function as a function of the number of vacancies is shown in Fig. 1. The first maximum corresponds to the solid state of the system and is attained for a very small number of vacancies, when vacancy interaction can certainly be neglected. This maximum corresponds to a relative number of vacancies consistent with Eq. (16): $v_{\max}/n=\exp(-\varepsilon/T)$. The value of this quantity for the condensed inert gases at the melting point is shown in Table II, where the smallness of this ratio is evident. After the peak, $S(v)$ decreases as the vacancy number is increased until the vacancy interaction turns on. This vacancy interaction energy and the energy of vacancy formation in the solid state have opposite signs, so that as the vacancy number increases further, the vacancy interaction brings the function $S(v)$ to a minimum and then makes it increase. A situation of this type occurs, for example, with a power law dependence $V(v)$ which, in particular, corresponds to the Stillinger–Weber model.

Formation of the second maximum in $S(v)$, which corresponds to the liquid state, requires a special form of W, so that the equation $W'=A$ (where $A=\varepsilon-T\ln(hn/v)$) or

$$V\left(\frac{v}{n}\right)+\frac{v}{n}V'\left(\frac{v}{n}\right)-A=0, \tag{26}$$

has two solutions. For this form of the vacancy interaction energy, the solid and liquid states of the system of bound atoms, which correspond to the maxima in the figure, exist and are separated from one another. We have assumed that A depends weakly on the number of vacancies. In Table II we list the value of this function for the inert gases at the melting point; its average value is 2.8.

Let us analyze Eq. (25) in the region of the liquid state of the system of bound atoms. Since $S(v)$ is proportional to the number of vacancies or the number of atoms in the system, this quantity approaches infinity in macroscopic systems of bound atoms. The width of the maximum in the partition function is of order $v^{1/2}$, i.e., in the limit of a large number of atoms in a macroscopic system, the relative width of the maximum approaches zero. For this reason, the width of the maximum in $S(v)$ is of no fundamental significance. Accordingly, at the melting point, the maxima of $S(v)$ for the solid and liquid states must be equal. This leads to the following equation relating the optimal number of vacancies v_{liq} in the liquid state to the melting temperature T_m:

$$\frac{nh}{v_{\mathrm{liq}}}\exp\left(-\frac{\varepsilon}{T_m}\right)=1+\ln\frac{hn}{v_{\mathrm{liq}}}-\frac{\varepsilon}{T_m}-\frac{V(v_{\mathrm{liq}})}{T_m}. \tag{27}$$

Hence, in particular, it is possible to obtain the vacancy interaction energy $V(v_{\mathrm{liq}})$ for the liquid state at the melting point, i.e., the reduction in the specific energy of vacancy formation in the liquid state compared to that in the solid. To do this we use the equation $\Delta H_{\mathrm{fus}}n=(E-V)v_{\mathrm{liq}}$ for the specific energy of formation of the liquid state; then Eq. (27) reduces to

$$\frac{nh}{v_{\mathrm{liq}}}\exp\left(-\frac{\varepsilon}{T_m}\right)=1+\ln\frac{hn}{v_{\mathrm{liq}}}+\frac{\Delta H_{\mathrm{fus}}}{T_m}\frac{n}{v_{\mathrm{liq}}}, \tag{28}$$

where the right-hand side is small. In addition, this yields

$$V(v_{\mathrm{liq}})=\varepsilon-\Delta H_{\mathrm{fus}}n/v_{\mathrm{liq}}. \tag{29}$$

Equation (28) makes clear the importance of the parameter h, which characterizes the enhancement in the partition function of an individual atom when an empty space develops inside a system of bound atoms. When only the measured parameters for the melting of the condensed inert gases are available, we cannot find the corresponding value of h. We merely note that Eq. (28) has a solution for $\ln h > \Delta H_{\mathrm{fus}}/T_m-1$.

For concreteness we set $h=100$ in the following. The corresponding solutions of Eqs. (28) and (29) for the condensed inert gases are listed in Table II. In this case, vacancy interactions lead to their contraction and to a drop in the energy expended in the formation of a single vacancy. The energy expended in the formation of an empty space inside a system of bound atoms remains proportional to its volume; that is, the two effects (the contraction of vacancies and the reduction in their energy of formation) cancel one another.

Equation (26) is not an equation for the function $V(v/n)$, but gives its value at the melting point. That is, the behavior of this function cannot be clarified by analyzing this equation. The general requirement for the function $V(v/n)$ is that Eq. (26) be satisfied for two values of v. Then the smaller value $v_{\min}/n$ corresponds to the minimum of $S(v)$, while the value of S for the liquid state corresponds to the larger value of v_{liq}/n that satisfies Eq. (26). In the following we consider, as an example, the simplest form of $V(v)$ that satisfies these requirements,

$$V(x)=C[\exp(-\alpha n/v)-\exp(-k\alpha n/v)]. \tag{30}$$

With this dependence on the number of vacancies, the specific energy of the vacancy interaction rapidly goes to zero for a small number of vacancies and approaches the order of magnitude of the energy of vacancy formation in the solid state when the number of vacancies and the number of atoms in the system are of the same order. Under the conditions (14), this limit is of no interest to us. For this form of the vacancy interaction energy, Eq. (26) takes the form

$$(1+x)\exp(-x)-(1+kx)\exp(-kx)=A/C,$$

$$x=\alpha n/v. \tag{31}$$

Next we find the parameters in the function (30) for $k=2$ and $k=10$. Given that the left-hand side of Eq. (27) is close to zero, Eqs. (26) and (27) yield the following equation for the argument of Eq. (30):

$$1+x-\frac{(k-1)x}{\exp[(k-1)x]-1}=\frac{A}{A-T_m}. \tag{32}$$

To obtain numerical solutions of this equation, we take the average values of the parameters characterizing the melting of the condensed inert gases: $A=2.8$, $T_m=0.58$, and $n/v_{\text{liq}}=4.2$. (We have used the parameter values taken from Tables I and II). Note that the function on the left-hand side of Eq. (31) has a maximum at $x_{\max}=\ln k^2/(k-1)$, where it equals $1+kx_{\max}/(k+1)$. The larger value of v (or smaller x) satisfying Eq. (32) applies to the liquid state, while the smaller value, which is a solution of Eq. (26), corresponds to the minimum of $S(v)$. For the liquid state of the condensed inert gases, these equations yield $x=0.89$, $\alpha=0.22$, and $C=9.1$ for $k=2$ and $x=0.38$, $\alpha=0.093$, and $C=3.3$ for $k=10$. Continuing the function $V(v/n)$ with these parameters into the region with a smaller number of vacancies and correcting the value of $A(v)$ for the reduced number of vacancies, for the minimum of the function $S(v)$ we find $x=2.6$, $n/v_{\min}=12$, and $A(v_{\min})=2.2$ when $k=2$, and $x=1.25$, $n/v_{\min}=13$, and $A(v_{\min})=2.1$ when $k=10$, where $v_{\min}$ corresponds to the minimum of $S(v)$. Here $S(v)/n$ is close to zero for the solid and liquid states, while its minimum is -1.6 for $k=2$ and -1.0 for $k=10$. These numerical values of the parameters show that the criterion (23) fails at the minimum of $S(v)$, i.e., vacancy interactions become important.

Let us summarize this analysis. We found that the logarithm of the partition function as a function of the number of vacancies must have a double-humped shape, with the first peak corresponding to the solid and the second, to the liquid state of a system of bound atoms with pairwise interactions. This shape corresponds to the two states of aggregation of the macroscopic atomic system and requires a certain type of interaction of the vacancies which, in particular, does not include a power-law dependence of the vacancy interaction energy on the relative number of vacancies. The interaction leads to contraction of the vacancies as their number increases, as well as a reduction in the energy of formation of individual vacancies if they are regarded as voids left after removal of internal atoms to the outside. At the same time, in the condensed inert gases the specific energy of formation of an empty space inside the system of bound atoms is conserved during the transition from the solid to the liquid state. Moreover, the formation of the liquid state imposes certain requirements on the parameter h, which characterizes the increase in the partition function for an atom owing to vacancy formation.

Thus, the liquid state of a system of bound atoms can be realized only under certain conditions. Relying on the parameters of the condensed inert gases at the melting temperature, we have been able to obtain only a qualitative picture of the solid-to-liquid phase transition as the number of vacancies within that system increases. A computer simulation of a system of bound atoms using the molecular dynamics method makes it possible to understand the details of this picture, including the type of interaction among the bound atoms that is required to permit formation of the liquid state of the system.

5. INTERACTION OF STRUCTURES DURING A PHASE TRANSITION

The transition of a system of bound atoms to the liquid state is accompanied by the formation of vacancies inside it, which leads to an increase in the volume of the system of bound atoms and creates new possibilities for the movement of atoms. Since each atom in the system interacts with a large number of atoms, the formation of vacancies and their existence are determined by collective effects. Clearly, it is difficult to separate the different collective effects because of the disordered motion of a large number of atoms. One exception is the case of structures interacting during a phase transition,[27] which we examine below.

Let us isolate from an atomic crystal lattice with close-packed structure a cluster of 13 atoms consisting of a central atom and its 12 nearest neighbors with the structure of a cube–octahedron whose surface contains 8 equilateral triangles and 6 squares. This cluster is characterized by 36 bonds between nearest neighbors inside the cluster and 84 bonds between cluster atoms and atoms surrounding them in the crystal lattice. The isolated cluster of 13 atoms can have an icosahedral structure whose surface consists of 20 equilateral triangles. This sort of cluster has 42 bonds between nearest neighbors and, although the bond lengths of the cluster, including the central atom, are 5% shorter than the bond lengths for the nearest surface atoms, the icosahedral structure for this cluster with pairwise atomic interactions is energetically more favorable than the cube–octahedron structure. The interaction with the surrounding neighbors makes this transition unfavorable in the crystal lattice, but as the density of the system is reduced, the energy of the transition decreases. A virtual transition of an arbitrary cluster inside a system of bound atoms to an icosahedral structure and its return to the initial state can lead to a rotation of the cluster and, thereby, to a change in the positions of the atoms within the crystal lattice. This represents a different type of movement of atoms within the system than hole diffusion inside a crystal lattice. In this way, this transition mechanism corresponds to a liquid state whose nature differs from that in the fixed-site model.

Let us estimate the energy parameters for this transition as a function of the density of the system. For simplicity we assume that the parameters of the isolated cluster do not depend on the lattice density, and that the distance from the central atom to the surrounding clusters of atoms is determined by the average atomic density. Then the binding energy E of the system, in which we include the binding energy of the atoms in the cluster and the interaction energy of the cluster atoms with the surrounding atoms, is

$$E=120-90(a-R_e)^2U'', \tag{33a}$$

where the energy unit is taken to be the depth D of the well in the pairwise atomic interaction potential, a is the lattice constant, R_e is the equilibrium distance between the atoms in a diatomic molecule, and U is the potential for the pairwise interaction of the atoms and its second derivative is taken at the equilibrium separation between the atoms. Equation (33a) corresponds to the case $a-R_e \ll R_e$, and the density ρ of atoms is related to the lattice constant by $\rho=\sqrt{2}/a^3$. In calculating the binding energy E' of the atoms when the cluster forms an icosahedral structure, we use a short-range potential for the atomic interaction that includes attraction only, and take the average over the position of the surrounding atoms on the sphere where it lies. This yields[27]

$$E'=42+34/(R_e\sqrt{U''}). \tag{33b}$$

If we use a truncated Lenard–Jones potential for the pairwise interaction potential, so that only interactions between nearest neighbors take place in the lattice (i.e., $U''=72/R_e^2$), then the energy levels (33) cross for $a/R_e=1.11$ or for a system density of $0.74\rho_0$, where $\rho_0=\sqrt{2}/R_e^3$, while the density of the condensed inert gases in the liquid state is typically $0.8\rho_0$, roughly in agreement with this estimate.

We now calculate the partition function Z_{rot} corresponding to the rotation of a cluster inside a system of bound atoms. If the rotation is free, then $Z_{\mathrm{rot}}=T/B$, where T is the temperature of the system in energy units, $B=\hbar^2/(2I)$ is the rotational constant of the cluster, and I is its moment of inertia. The rotational constant of the cluster can be related to the rotational constant of a diatomic molecule, B_{mol}, by taking into account the equality of the equilibrium separation in the molecule and the distances between the surface atoms and the central atom of the cluster. This yields $B=B_{\mathrm{mol}}/24$, so that at the melting temperature T_m we have

$$Z_{\mathrm{rot}}=24T_m/B_{\mathrm{mol}}. \tag{34}$$

Table II lists the values of the partition function owing to cluster rotation within the condensed inert gases at the melting point.

If we treat melting of the condensed inert gases as the result of a structural transition, so that the increased density in the solid state creates the possibility of free rotation of these clusters within the system, then the melting condition has the form

$$Z_{\mathrm{rot}}\exp(-\Delta E/T_m)=1. \tag{35}$$

Here ΔE is the specific energy of the transition. If it applies to 13 atoms, i.e., $\Delta E=13\Delta H_{\mathrm{fus}}$, then we find that condition (35) is not satisfied at the melting temperature for the condensed inert gases. This means that a structural transition as a collective phenomenon within a system of bound atoms with pairwise interactions does not form a basis for the melting of the condensed inert gases, although it may show up in the properties of the liquid state, including critical phenomena.

6. CONCLUSION

This analysis has shown that the liquid state of a system of bound atoms with a pairwise interaction can be realized under certain conditions, including when the vacancies within the system have a certain type of interaction. The analysis is based on the melting parameters of the condensed inert gases, which yields two points on the partition function of the system as a function of the number of vacancies. A more complete picture of this phenomenon might be provided by a computer simulation of the system by the molecular dynamics method which, in principle, can give the partition function as a function of the system volume. Perhaps in the first stage it would be simpler to study surface melting, where a system of bound atoms forms a layer of atoms on a substrate.

[1] Ya. I. Frenkel', *The Kinetic Theory of Liquids* [in Russian], Nauka, Moscow (1975).

[2] I. Z. Fisher, *Statistical Theory of Liquids*, Univ. of Chicago Press, Chicago (1966).

[3] H. E. Stanley, *Introduction to Phase Transitions and Critical Phenomena*, Clarendon Press, Oxford (1971).

[4] A. R. Ubbelohde, *The Molten State of Matter*, Wiley, Chichester (1978).

[5] R. S. Berry, J. Jellinek, and G. Natanson, Phys. Rev. A **30**, 919 (1984).

[6] J. Jellinek, T. L. Beck, and R. S. Berry, J. Chem. Phys. **84**, 2783 (1986).

[7] T. L. Beck, J. Jellinek, and R. S. Berry, J. Chem. Phys. **87**, 545 (1987).

[8] T. L. Beck and R. S. Berry, J. Chem. Phys. **88**, 3910 (1988).

[9] R. S. Berry, T. L. Beck, H. L. Davis, and J. Jellinek, Adv. Chem. Phys. **90**, 75 (1988).

[10] D. J. Wales and R. S. Berry, J. Chem. Phys. **92**, 4283 (1990).

[11] D. J. Wales, Chem. Phys. Lett. **166**, 419 (1990).

[12] H. P. Cheng and R. S. Berry, Phys. Rev. A **45**, 7969 (1992).

[13] R. E. Kunz and R. S. Berry, Phys. Rev. Lett. **71**, 3987 (1993).

[14] R. S. Berry, Chem. Phys. **93**, 1895 (1993).

[15] R. E. Kunz and R. S. Berry, Phys. Rev. B **49**, 1895 (1994).

[16] B. M. Smirnov, Usp. Fiz. Nauk **164**, 1165 (1994).

[17] V. S. Vorob'ev, JETP Lett. **62**, 574 (1995).

[18] V. S. Vorob'ev and A. V. Eletskiĭ, Teplofiz. Vyssh. Temp. **33**, 862 (1995).

[19] R. A. Aziz and M. J. Slaman, Chem. Phys. **130**, 187 (1989).

[20] R. A. Aziz and M. J. Slaman, J. Chem. Phys. **92**, 1030 (1990).

[21] A. K. Dham, A. R. Allnatt, W. J. Meath, and R. A. Aziz, Mol. Phys. **67**, 1291 (1989).

[22] A. K. Dham, W. J. Meath, A. R. Allnatt, R. A. Aziz, and M. J. Slaman, Chem. Phys. **142**, 173 (1990).

[23] D. R. Lide (ed.), *Handbook of Chemistry and Physics*, CRC Press, London (1993–1994).

[24] I. K. Kikoin (ed.), *Handbook of Physical Quantities* [in Russian], Énergoatomizdat, Moscow (1994).

[25] F. H. Stillinger and T. A. Weber, J. Chem. Phys. **81**, 5095 (1984).

[26] B. M. Smirnov, Usp. Fiz. Nauk **162**(12), 97 (1992).

[27] B. M. Smirnov, Phys. Scr. **48**, 483 (1993); **50**, 427 (1994).

Translated by D. H. McNeill

Isotope effect in ferromagnets

V. M. Zverev

P. N. Lebedev Physics Institute, Russian Academy of Sciences, 117924 Moscow, Russia

(Submitted 22 May 1997)
Zh. Éksp. Teor. Fiz. **112**, 1863–1872 (November 1997)

A phenomenological approach to the theory of the isotope effect in ferromagnets is developed on the basis of the phenomenon of magnetoelasticity. Parameters whose experimental measurement permits a quantitative calculation of the contribution of acoustic phonons to the isotope shift of the Curie temperature are identified. An estimate of the isotope shift of the Curie temperature in the Invar alloy $Fe_{0.75}Pt_{0.25}$ is given. © *1997 American Institute of Physics.* [S1063-7761(97)02511-0]

1. INTRODUCTION

Although the question of the influence of the interaction of electrons with lattice vibrations on magnetism has been addressed in the literature (see, for example, Ref. 1), the traditional view has been that the contribution of this interaction to magnetic properties is relatively small. Support for this notion was provided by the relatively small contribution of the electron–phonon interaction at zero temperature to the expression for the reciprocal of the spin magnetic susceptibility, which was evaluated because of the condition of adiabaticity as a small parameter of order the ratio of the Debye energy $k_B\Theta$ to the Fermi energy ε_F, where Θ is the Debye temperature and k_B is the Boltzmann constant.[1] We note that the change in the lattice properties caused by ferromagnetism was not taken into account in this evaluation. This evaluation corresponds, in particular, to the fact that a change of the same order appears in the Stoner exchange-enhancement factor

$$S=[1+2\nu(\psi+\psi_{\text{el-ph}})]^{-1}, \tag{1.1}$$

which specifies the increase in the magnetic susceptibility of real metals in comparison with the result from the theory of a noninteracting electron gas. Here ν is the electron density of states at the Fermi level for an assigned electron spin projection, ψ is the interelectronic exchange coupling constant, and $\psi_{\text{el-ph}}$ is the contribution resulting from consideration of the dependence of the energy of the zero-point lattice vibrations on the electron spin polarization. Despite the relative smallness of this contribution,[2]

$$\psi_{\text{el-ph}}/\psi\sim k_B\Theta/\varepsilon_F\sim\sqrt{m_e/M_i}, \tag{1.2}$$

where m_e is the electron mass and M_i is the atomic mass of the atoms in the crystal lattice, Hopfield[3] expressed an expectation that the electron–phonon interaction can play an important role in the case of weakly ferromagnetic metals with strong exchange enhancement:

$$|S|\gg 1. \tag{1.3}$$

The prediction made in Ref. 3 regarding the very large isotope effect in the dependence of the Curie temperature on the atomic mass of the atoms in the crystal lattice of a weak ferromagnet such as $ZrZn_2$ was related specifically to this condition. The assertion in Ref. 3 becomes obvious on the basis of (1.1)–(1.3), if we take into account the following relation for the Curie temperature: $T_C\propto|S|^{-\gamma}$, where $\gamma=1/2$ in the Stoner model[4] and $\gamma=3/4$ in the paramagnetic model of a ferromagnetic metal (see, for example, Refs. 5 and 6). We then obtain (compare with Ref. 3)

$$I=\frac{d\ \ln T_C}{d\ \ln M_i}=\gamma S\,\frac{\psi_{\text{el-ph}}}{2\psi}. \tag{1.4}$$

Hopfield[3] suggested using the following values of the parameters appearing in Eq. (1.4) for $ZrZn_2$: $\gamma=1/2$, $S\simeq-238$, and $\psi_{\text{el-ph}}/\psi\sim 0.1$. This leads to an estimate of the isotope coefficient $|I|\gg 1$. However, the experiment in Ref. 7 did not confirm this prediction, but gave the value $I=-0.1\pm 0.3$ for the Zn isotopes and $I=-0.2\pm 0.2$ for the Zr isotopes in $ZrZn_2$. This disparity between theory and experiment can be attributed, in particular, to the fact that the use of the value $\psi_{\text{el-ph}}/\psi\sim 0.1$ to estimate the isotope coefficient I in reference to $ZrZn_2$ was not seriously substantiated in Ref. 3. Moreover, according to the claims of Fay and Appel[2] and of Pickett,[8] attempts to theoretically calculate $\psi_{\text{el-ph}}$ lead only to a rough estimate and do not allow us to consider the contribution made by the electron-phonon interaction to the Stoner factor (1.1) fully established. We can extricate ourselves from this situation by devising a phenomenological approach to the theory of the isotope effect in ferromagnets, in which the parameters of the theory can be related to experimentally measured quantities and can thereby be estimated in reference to real ferromagnets. The usefulness of such an approach becomes especially clear in connection with the recent experimental discovery of a giant isotope shift $\Delta T_C>20$ K of the Curie temperature in $La_{0.8}Ca_{0.2}MnO_{3+y}$ when the ^{16}O oxygen isotope is replaced by ^{18}O, for which the isotope coefficient is $I\simeq-0.85$.[9] This discovery is a direct indication of the existence of ferromagnets having magnetic properties in which the electron–phonon interaction plays an important role.

A phenomenological approach to the theory of the influence of thermal acoustic phonons on the magnetic properties of ferromagnets was proposed in Refs. 10 and 11 on the basis of the well-known phenomenon of magnetoelasticity. This phenomenon is manifested as a dependence of the elastic moduli of a ferromagnet on the magnetization, which leads to an analogous dependence of the Debye temperature of acoustic phonons on the magnetization; therefore, the contribution of acoustic phonons to the free energy of a ferromagnet depends on the magnetization. The latter is the reason why acoustic phonons are manifested in the magnetic properties of ferromagnets. Within such an approach it was possible to uncover a comparatively small set of experimentally measurable parameters, which enable us to quantitatively calculate the contribution of thermal acoustic phonons to various magnetic properties of ferromagnets. These parameters were determined in Ref. 11 for the pure metals iron and nickel and for Fe–Ni, Fe–Ni–Mn, and Fe–Pt Invar alloys on the basis of an analysis of the available experimental data in the literature, enabling the formulation of quantitative statements regarding the role of thermal phonons in the magnetic properties of these ferromagnets. In particular, an anomalously large contribution of the thermal phonons to the Curie constant of Fe–Pt Invar alloys was discovered. It is therefore natural to pose the question of the magnitude of the isotope effect in these alloys.

In this communication the isotope shift of the Curie temperature caused by magnetoelasticity is studied on the basis of a generalization of the approach described in Refs. 10 and 11, and the conditions for observing this effect in ferromagnets with high and low Curie temperatures are analyzed. The parameters whose experimental measurement enables us to quantitatively calculate the contribution of acoustic phonons to the isotope shift of the Curie temperature in real ferromagnets are identified. An estimate of the isotope shift of the Curie temperature in the Invar alloy $Fe_{0.75}Pt_{0.25}$ based on experimental data is given.

2. GENERAL RELATIONS

Magnetoelasticity plays a fundamental role below. For numerous ferromagnets (see, for example, Ref. 12) the dependence of the elastic moduli on the magnetization has a very simple form. The model of an isotropic elastic medium, which is characterized by a bulk modulus K and a shear modulus G, is frequently used to describe ferromagnets. To avoid confusion, we must follow the rules of thermodynamics, which require the exact determination of the thermodynamic variables on which the elastic moduli, in particular, depend. Under the conditions of a constant magnetization M, for the elastic moduli we can write[12]

$$K_M(T,M)=K(T)+K'M^2, \quad G_M(T,M)=G(T)+G'M^2, \tag{2.1}$$

where $K(T)$ and $G(T)$ are the elastic moduli of the paramagnetic state, which depend on the temperature owing to the usual anharmonicity of phonons. The values of the elastic moduli $K(T)$ and $G(T)$ are found in the ferromagnetic region by extrapolation with neglect of the phase transition from the paramagnetic region, where they exhibit a normal temperature dependence (see, for example, Ref. 13). It is important to stress that, according to Ref. 12, the magnetoelastic coefficients K' and G' for numerous ferromagnets are independent of temperature over a fairly broad range of variation of the magnetization.

In experimental investigations of the elasticity of ferromagnets the elastic moduli are usually measured at a constant magnetic induction (or at a constant magnetic field H). The bulk modulus at a constant magnetic field K_H is related to K_M by the well-known thermodynamic relation[13]

$$\frac{1}{K_H(P,T,H)}-\frac{1}{K_M(P,T,M)}=\frac{1}{\chi_P}\left(\frac{\partial\omega}{\partial H}\right)^2_{P,T}. \tag{2.2}$$

Here $\chi_P=(\partial M/\partial H)_{P,T}$ is the isothermal paraprocess magnetic susceptibility at a constant pressure P, and $(\partial\omega/\partial H)_{P,T}=V^{-1}(\partial V/\partial H)_{P,T}$ is the induced magnetostriction, where V is the volume of the ferromagnet. Equation (2.2) is presented here because of the need to distinguish between the experimentally measured bulk modulus K_H and the bulk modulus K_M needed for the theoretical model described below. Within the phenomenological approach relations (2.1) and (2.2) can be used to determine the dependence of the bulk modulus K_M on the magnetization and to find the bulk magnetoelastic coefficient K' (see, for example, Refs. 11 and 13). Experimental data for the remaining quantities appearing in (2.1) and (2.2) are used for this purpose. We stress that the shear modulus at a constant magnetic field G_H does not differ from the shear modulus at a constant magnetization G_M. This simplifies the determination of the shear magnetoelastic coefficient G' on the basis of experimental data.[11]

It should also be noted that microscopic theories of the elasticity of ferromagnetic metals are sometimes devised without an understanding of which bulk modulus is being used. As was shown in Ref. 14, such a lack of understanding is the reason for Kim's paradoxical statements in Ref. 15, where, instead of the estimates (1.2) and (1.4), quantities $|S|$ times larger appear in the conditions (1.3) in the approach used. On the other hand, we cite Ref. 16, in which it shown how not only the bulk moduli at a constant magnetic field and a constant magnetization can be distinguished, but also explicit expressions for them can be obtained within a microscopic treatment. We also note that since the elasticity of a lattice is associated with Debye screening of the Coulomb field in the itinerant-electron model, the Debye screening radius at a constant magnetic field r_H and the analogous radius at a constant magnetization r_M are different.

Magnetoelasticity makes the contribution of acoustic phonons to the free energy of a ferromagnet depend on the magnetization. In the Grüneisen corresponding-states model we write the following expression for this contribution:[17]

$$F_{\mathrm{ph}}(V,T,M)=\Theta^l_M f_l\left(\frac{T}{\Theta^l_M}\right)+2\Theta^t_M f_t\left(\frac{T}{\Theta^t_M}\right). \tag{2.3}$$

Here we have introduced the partial Debye temperatures for the longitudinal modes

$$\Theta^l_M=\frac{\hbar}{k_B\sqrt{\rho}}\left(\frac{6\pi^2}{v}\right)^{1/3}\sqrt{K_M+\frac{4}{3}G_M} \tag{2.4}$$

and the transverse modes

$$\Theta^t_M=\frac{\hbar}{k_B\sqrt{\rho}}\left(\frac{6\pi^2}{v}\right)^{1/3}\sqrt{G_M} \tag{2.5}$$

of the acoustic phonons, where ρ is the mass density and v is the unit-cell volume of the crystal. In our treatment we shall neglect the possible dependence of Θ_M^l and Θ_M^t on the temperature, i.e., we shall neglect the usual anharmonicity of the phonons. At the same time, according to (2.1), we shall take into account the dependence of the Debye temperatures (2.4) and (2.5) on the magnetization caused by magnetoelasticity. Bearing in mind the smallness of the magnetoelasticity contribution to the moduli in (2.1), we can write Eqs. (2.4) and (2.5) in the form

$$\Theta_M^l = \Theta_l + \Theta_l' M^2, \quad \Theta_M^t = \Theta_t + \Theta_t' M^2, \tag{2.6}$$

where

$$\frac{\Theta_l'}{\Theta_l} = \frac{3K' + 4G'}{2(3K+4G)}, \quad \frac{\Theta_t'}{\Theta_t} = \frac{G'}{2G}. \tag{2.7}$$

The magnetization-dependent phonon contribution to the free energy (2.3) of a ferromagnet can be written in accordance with expressions (2.6) in the form

$$\Delta F_{\mathrm{ph}}(V,T,M) = \sum_{s=l,t} (1+\delta_{s,t}) \Theta_s' \varphi_s\left(\frac{T}{\Theta_s}\right) M^2, \tag{2.8}$$

where

$$\varphi_s(x) = f_s(x) - x f_s'(x), \tag{2.9}$$

and $\delta_{s,t} = 1$ for $s = t$ and $\delta_{s,t} = 0$ for $s \neq t$.

Let us now consider the temperature range near the ferromagnetic transition. Then for (2.8) we can write the following expansion with respect to the temperature:

$$\Delta F_{\mathrm{ph}}(V,T,M) = V \sum_{s=l,t} (1+\delta_{s,t}) \frac{\Theta_s'}{\Theta_s} \left[\frac{1}{V} \Theta_s \varphi_s\left(\frac{T_C}{\Theta_s}\right) + C_{\mathrm{ph}}^s(T_C)(T - T_C) \right] M^2, \tag{2.10}$$

where $C_{\mathrm{ph}}^s(T) = -(T/V\Theta_s) f_s''(T/\Theta_s)$ is the partial contribution of the longitudinal ($s = l$) and transverse ($s = t$) modes of the acoustic phonons to the lattice specific heat at the temperature T.[18] We note here that a linear temperature dependence appears in (2.10) not only near T_C, but also over the broad temperature range $T \geqslant T_C$ for ferromagnets with high Curie temperatures ($T_C \gg \Theta_{l,t}/4$), where the phonon specific heat C_{ph}^s can be considered constant.[18]

Of course, apart from the phonon contribution to the free energy (2.10) of a ferromagnet, the theory should take into account the magnetism of electrons caused by their exchange interaction as a primary factor. For the magnetization-dependent electronic contribution to the free energy of a ferromagnet above the Curie temperature in the paramagnetic state, as well as in the ferromagnetic state, but not very far from the Curie temperature, where the magnetization is small, we can use the expansion

$$\Delta F_{\mathrm{el}}(V,T,M) = V \left\{ \frac{1}{2} [a_1(T_C) + \alpha(T - T_C)] M^2 + \frac{1}{4} a_3 M^4 \right\}. \tag{2.11}$$

Formulas (2.10) and (2.11) enable us to write an expression for the magnetic part of the free energy of a ferromagnet in a general form that corresponds to the Landau theory of second-order phase transitions:[18]

$$\Delta F_M(V,T,M) = V \left[\frac{1}{2C}(T - T_C) M^2 + \frac{1}{4} a_3 M^4 \right], \tag{2.12}$$

where the Curie temperature is specified by the following equation

$$a_1(T_C) + \frac{2}{V} \sum_{s=l,t} (1+\delta_{s,t}) \Theta_s' \varphi_s\left(\frac{T_C}{\Theta_s}\right) = 0, \tag{2.13}$$

and the Curie constant C is given by the relation

$$\frac{1}{C} = \alpha + 2 \sum_{s=l,t} (1+\delta_{s,t}) C_{\mathrm{ph}}^s(T_C) \frac{\Theta_s'}{\Theta_s}. \tag{2.14}$$

According to Eq. (2.13), the influence of the acoustic phonons is manifested in the determination of the Curie temperature, and according to (2.14) it is manifested in the phonon renormalization of the Curie constant. It is convenient to rewrite Eq. (2.14) in the following manner:

$$C = \frac{1 - X(T_C)}{\alpha}, \tag{2.15}$$

where the magnitude of the dimensionless parameter (compare with Refs. 10 and 11)

$$X(T_C) = X_l(T_C) + 2X_t(T_C) \tag{2.16}$$

in comparison with unity will quantitatively determine the contribution of the acoustic phonons to the Curie constant, and the parameters

$$X_s(T_C) = 2CC_{\mathrm{ph}}^s(T_C) \frac{\Theta_s'}{\Theta_s}, \quad s = l,\ t, \tag{2.17}$$

will characterize the partial contributions of the respective acoustic modes. Clearly, only thermal phonons make a contribution to the Curie constant (2.15). Now, in the limit of high Curie temperatures ($T_C \gg \Theta_{l,t}/4$) the parameters

$$X_s = \frac{2k_B C}{v} \frac{\Theta_s'}{\Theta_s}, \quad s = l,\ t, \tag{2.18}$$

do not depend on the Curie temperature, and at low Curie temperatures ($T_C \ll \Theta_{l,t}/4$) they decrease as

$$X_s(T_C) \sim C_{\mathrm{ph}}^s(T_C) \sim (T_C/\Theta_s)^3, \quad s = l,\ t. \tag{2.19}$$

Therefore, metals and alloys which have comparatively high Curie temperatures were selected as examples for the quantitative determination of $X(T_C)$ in real ferromagnets in Ref. 11.

Relations (2.12)–(2.14) enable us to study the manifestations of acoustic phonons in various thermodynamic properties of ferromagnets. Here we shall examine the consequences of Eq. (2.13) as applied to the determination of the dependence of the Curie temperature on the atomic mass of the atoms in the crystal lattice, i.e., the isotope effect in ferromagnets. Differentiating (2.13) with respect to the atomic mass M_i and using Eqs. (2.14) and (2.17), we find the following expression for the isotope coefficient:

$$\frac{d\ln T_C}{d\ln M_i}=-\frac{1}{2}\sum_{s=l,t}(1+\delta_{s,t})X_s(T_C)\times\left[1-\frac{\Theta_s\varphi_s(T_C/\Theta_s)}{VT_C C_{\rm ph}^s(T_C)}\right].\tag{2.20}$$

In deriving Eq. (2.20) it was assumed that, according to (2.7), the ratio Θ_s'/Θ_s does not depend on the atomic mass. The main difference between (2.20) and the result in Ref. 19 is the presence of the factors $X_{l,t}(T_C)$ in (2.20), which determine the magnitude of the isotope effect to a significant extent. This difference is attributed to the model used in Ref. 19, according to which it was assumed during the treatment of the isotope effect on the basis of an equation similar to Eq. (2.13) that $a_1=\text{const}$ and does not depend on T_C, i.e., the Curie temperature is determined completely by the contribution of the thermal phonons in such a model. In addition, Eq. (2.20), unlike the results in Ref. 19, takes into account the contribution of both the longitudinal and transverse modes of the acoustic phonons, as well as the contribution of the zero-point lattice vibrations.

Let us present the expressions for Eq. (2.20) that correspond to ferromagnets with high and low Curie temperatures, as well as the special case of the Debye model. For high Curie temperatures ($T_C\gg\Theta_{l,t}/4$), using an expansion of the functions

$$\varphi_s(x)=f_s(0)+k_BNx\left(1-\frac{\alpha_s}{x}+\frac{\beta_s}{x^2}\right),\quad s=l,\ t,\tag{2.21}$$

where N is the number of unit cells in the crystal, from (2.20) we find the following expression for the isotope coefficient:

$$\frac{d\ln T_C}{d\ln M_i}=\frac{1}{2}\sum_{s=l,t}(1+\delta_{s,t})X_s\ \frac{\Theta_s}{T_C}\left(\frac{f_s(0)}{k_BN}-\alpha_s+2\beta_s\frac{\Theta_s}{T_C}\right).\tag{2.22}$$

Here the parameters X_s do not depend on T_C and are given by Eq. (2.18). In the special case of the Debye model, in which $f_s(0)=3k_BN/8$, $\alpha_s=3/8$, and $\beta_s=1/20$, from (2.22) we obtain

$$\frac{d\ln T_C}{d\ln M_i}=\frac{1}{20}\left[X_l\left(\frac{\Theta_l}{T_C}\right)^2+2X_t\left(\frac{\Theta_t}{T_C}\right)^2\right].\tag{2.23}$$

In the other limiting case of low Curie temperatures ($T_C\ll\Theta_{l,t}/4$), in which

$$\varphi_s(x)=f_s(0)+O(x^4),\quad s=l,\ t.\tag{2.24}$$

Formula (2.20) leads to an isotope effect which is completely determined by the zero-order lattice vibrations:

$$\frac{d\ln T_C}{d\ln M_i}=\frac{1}{2}\sum_{s=l,t}(1+\delta_{s,t})X_s\frac{\Theta_s}{T_C}\left(\frac{f_s(0)}{k_BN}\right).\tag{2.25}$$

For the Debye model Eq. (2.25) takes the form

$$\frac{d\ln T_C}{d\ln M_i}=\frac{3}{16}\left(X_l\frac{\Theta_l}{T_C}+2X_t\frac{\Theta_t}{T_C}\right).\tag{2.26}$$

Comparing (2.22) and (2.23) with (2.25) and (2.26) for assigned values of $X_{l,t}$, we can conclude that the absolute value of the isotope effect is greater in ferromagnets with low Curie temperatures ($T_C\ll\Theta_{l,t}/4$). This conclusion differs qualitatively from the result obtained above, according to which the contribution of the acoustic phonons to the Curie constant (2.15) is greater in absolute value, the higher is the Curie temperature in comparison with the Debye temperatures of the acoustic phonons.

3. DISCUSSION OF RESULTS AND CONCLUSIONS

The treatment performed shows that the quantitative determination of the contribution of acoustic phonons to the isotope shift of the Curie temperature in real ferromagnets first calls for finding the dimensionless parameters $X_{l,t}(T_C)$ or, in the case of the limiting expressions (2.22) and (2.23) or (2.25) and (2.26), the parameters $X_{l,t}$ (2.18) on the basis of experimental data. This requires knowledge of experimental values for the Curie constant C, the phonon specific heat $C_{\rm ph}^s(T_C)$, the elastic moduli K and G, and the magnetoelastic coefficients K' and G'. Such a set of parameters was determined in Ref. 11 (see Tables I and II therein) on the basis of experimental data for the pure metals Fe and Ni, the iron-nickel Invar alloys $\mathrm{Fe}_{1-x}\mathrm{Ni}_x$ ($0.30<x\leqslant0.45$), the ternary alloys $\mathrm{Fe}_{0.65}(\mathrm{Ni}_{1-x}\mathrm{Mn}_x)_{0.35}$ ($0\leqslant x\leqslant0.13$), and the iron-platinum Invar alloys $\mathrm{Fe}_{1-x}\mathrm{Pt}_x$ ($x=0.28,\ 0.25$) with various degrees of order S of the atoms in the crystal-lattice sites. An anomalously large value was found for the dimensionless parameter $X\simeq-0.51$ to -0.54 in the Invar alloy $\mathrm{Fe}_{0.75}\mathrm{Pt}_{0.25}$ with a degree of order $S=0.70$ (see Table II in Ref. 11). It is natural to utilize the data in Ref. 11 in reference to this alloy in estimating the contribution of acoustic phonons to the isotope shift of the Curie temperature caused by magnetoelasticity on the basis of the phenomenological approach developed in Sec. 2.

According to Table I in Ref. 11, for the Invar alloy $\mathrm{Fe}_{0.75}\mathrm{Pt}_{0.25}$ with a degree of order $S=0.70$ we have the experimental values $K=12.6\times10^2-14.1\times10^2$ kbar and $G=6.9\times10^2-7.0\times10^2$ kbar for the elastic moduli and $K'=1.0\times10^5-1.3\times10^5$ and $G'=-2.11\times10^5$ for the magnetoelastic coefficients. This enables us to use formulas (2.7) to find that Θ_l'/Θ_l varies from -3.2×10^{-8} to $4.2\times10^{-8}\ \mathrm{G}^{-2}$ and Θ_t'/Θ_t varies from -15.1×10^{-8} to $15.3\times10^{-8}\ \mathrm{G}^{-2}$. These parameters determine the dependence of the Debye temperatures (2.6) on the magnetization. The data for the Curie constant $C=0.29$ K and the high-temperature limit of the specific heat of the s acoustic mode $C_{\rm ph}^s=k_B/v=0.27\times10^7\ \mathrm{erg/cm^3\cdot K}$ are taken from Table II in Ref. 11. Then Eq. (2.18) enables us to estimate the dimensionless parameters $X_l\simeq-0.04$ to -0.07 and $2X_t\simeq-0.47$, which characterize the partial contributions of the longitudinal-acoustic mode and two transverse-acoustic modes to the isotope effect. Next, we determine the Debye temperatures of the acoustic phonons $\Theta_{l,t}$ from formulas (2.4) and (2.5) using the data presented above for the elastic moduli K and G, the mass density $\rho=11.7\ \mathrm{g/cm^3}$, and the unit-cell volume of the cubic crystal $v=51.9\ \text{Å}^3$ in accordance with Table III in Ref. 20. This gives $\Theta_l\simeq350$ K and

$\Theta_t \simeq 194$ K. Since the condition $T_s \gg \Theta_{l,t}/4$ holds for the Curie temperature $T_C \simeq 386$ K of this alloy, as determined from Table III in Ref. 20, Eq. (2.22) can be used for numerical estimates of the isotope effect in this alloy. Setting the coefficients $f_l(0)=f_t(0)=f(0)$, $\alpha_l=\alpha_t=\alpha$, and $\beta_l=\beta_t=\beta$ in (2.22), which do not depend on the mode index, we find

$$\frac{d\ln T_C}{d\ln M_i} \simeq -(0.14-0.15)\left(\frac{f(0)}{k_B N}-\alpha\right)-(0.16-0.17)\beta. \tag{3.1}$$

We next consider the possibility in which $|f(0)/k_B N-\alpha| \sim \alpha < 1$ and $\beta \ll \alpha$. From (3.1) we obtain the estimate

$$\left|\frac{d\ln T_C}{d\ln M_i}\right| \simeq 0.14\alpha, \tag{3.2}$$

or for the absolute value of the isotope shift of the Curie temperature we have

$$|\Lambda T_C| \simeq (54\ \mathrm{K})\left(\alpha\frac{\Delta M_i}{M_i}\right), \tag{3.3}$$

where ΔM_i is the isotope change in the atomic mass. For the replacement of the ^{54}Fe isotope by ^{56}Fe or by ^{58}Fe we find $\Delta M_i/M_i \simeq 3.7-7.4\%$. Then, formula (3.3) gives $|\Delta T_C| \simeq (2-4)\alpha$ K. Since $\alpha < 1$, for an upper estimate of the isotope shift of the Curie temperature in the Invar alloy $Fe_{0.75}Pt_{0.25}$ we obtain $|\Delta T_C| < 2$–4 K. Finally, we present an estimate of the isotope shift of the Curie temperature for this alloy according to the Debye model when $f(0)/k_B N=\alpha=3/8$ and $\beta=1/20$. From (3.1) we obtain

$$\Delta T_C \simeq -(0.1-0.2)\mathrm{K}. \tag{3.4}$$

Thus, in contrast to the anomalously large phonon renormalization of the Curie constant for this alloy discovered in Ref. 11, the contribution of the acoustic phonons to the isotope shift of the Curie temperature is comparatively small. This finding is not unexpected, since, according to the phenomenological approach developed in Sec. 2, the Invar alloy $Fe_{0.75}Pt_{0.25}$ is a ferromagnet with a comparatively high Curie temperature ($T_s \gg \Theta_{l,t}/4$). On the other hand, the estimates of the dimensionless parameters X_l and $2X_t$ presented above allow us to advance the argument that acoustic phonons can cause a large isotope shift of the Curie temperature when $|d\ln T_C/d\ln M_i| \sim 1$ holds in ferromagnets which have magnetoelastic coefficients of comparatively large absolute values, as, for example, the Invar alloy $Fe_{0.75}Pt_{0.25}$ and simultaneously have Curie temperatures that are low compared with the Debye temperatures. Mention should also be made of the work of Karchevskii *et al.*,[21] who first observed the isotope shift in the Curie temperature $T_C=4.0\pm0.5$ K in going from uranium hydride, UH_3, to uranium deuteride, UD_3, for which the isotopic coefficient is relatively small, $I \simeq -2\times10^{-2}$. We stress that the phenomenological approach developed here to the theory of the isotope effect in ferromagnets indicates the set of parameters whose experimental measurement permits a quantitative calculation of the contribution of acoustic phonons to the isotope shift of the Curie temperature in real ferromagnets caused by magnetoelasticity.

In conclusion, we express our thanks to V. P. Silin and R. Z. Levitin for a useful discussion of the question considered here. This work was performed as part of project 96-02-17318-a of the Russian Fund for Fundamental Research.

[1] C. Herring, *Magnetism*, G. T. Rado and H. Suhl (eds.), Academic Press, New York and London (1966), Vol. 4, p. 290.
[2] D. Fay and J. Appel, Phys. Rev. B **20**, 3705 (1979); **22**, 1461 (1980).
[3] J. J. Hopfield, Phys. Lett. A **27**, 397 (1968).
[4] D. M. Edwards and E. P. Wohlfarth, Proc. R. Soc. London, Ser. A **303**, 127 (1968).
[5] I. E. Dzyaloshinskiĭ and P. S. Kondratenko, Zh. Éksp. Teor. Fiz. **70**, 1987 (1976) [Sov. Phys. JETP **43**, 1036 (1976)].
[6] T. Moriya, *Spin Fluctuations in Itinerant Electron Magnetism*, Springer-Verlag, Berlin (1985) [Russ. transl., Mir, Moscow (1988)].
[7] G. S. Knapp, E. Corenzwit, and C. W. Chu, Solid State Commun. **8**, 639 (1970).
[8] W. E. Pickett, Phys. Rev. Lett. **48**, 1548 (1982); Phys. Rev. B **26**, 1186 (1982).
[9] G. M. Zhao, K. Conder, H. Keller, and K. A. Müller, Nature (London) **381**, 676 (1996).
[10] V. P. Silin and V. M. Zverev, Phys. Lett. A **184**, 315 (1994).
[11] V. M. Zverev and V. P. Silin, JETP Lett. **64**, 37 (1996).
[12] G. Hausch, Phys. Status Solidi A **15**, 501 (1973).
[13] M. Shiga, K. Makita, K. Uematsu, Y. Muraoka, and Y. Nakamura, J. Phys.: Condens. Matter **2**, 1239 (1990).
[14] V. M. Zverev and V. P. Silin, Fiz. Met. Metalloved. **65**, 895 (1988).
[15] D. J. Kim, Phys. Rep. **171**, 129 (1988).
[16] V. M. Zverev and V. P. Silin, Fiz. Tverd. Tela (Leningrad) **31**(5), 123 (1989) [Sov. Phys. Solid State **31**, 788 (1989)].
[17] V. M. Zverev and V. P. Silin, Fiz. Tverd. Tela (Leningrad) **30**, 1989 (1988) [Sov. Phys. Solid State **30**, 1148 (1988)].
[18] L. D. Landau and E. M. Lifshitz, *Statistical Physics, Vol. 1*, 3rd. ed., Pergamon Press, Oxford–New York (1980).
[19] V. M. Zverev and V. P. Silin, Zh. Éksp. Teor. Fiz. **93**, 709 (1987) [Sov. Phys. JETP **66**, 401 (1987)].
[20] H. C. Ling and W. S. Owen, Acta Metall. **31**, 1343 (1983).
[21] A. I. Karchevskiĭ, E. V. Artyushkov, and L. I. Kikoin, Zh. Éksp. Teor. Fiz. **36**, 636 (1959) [Sov. Phys. JETP **9**, 442 (1959)].

Translated by P. Shelnitz

de Haas–van Alphen effect in superconductors

M. G. Vavilov and V. P. Mineev

L. D. Landau Institute of Theoretical Physics, 142432 Chernogolovka, Moscow Region, Russia

(Submitted 1 June 1997)
Zh. Éksp. Teor. Fiz. **112**, 1873–1892 (November 1997)

A theory of the de Haas–van Alphen effect in type-II superconductors is proposed. The effect of the electron scattering by nonmagnetic impurities in a magnetic field in the potential produced by a nonuniform distribution of the order parameter in a mixed state is investigated. The magnitude of the order parameter and quasiparticle density of states are determined from the solution of the system of Gor'kov equations. It is shown that in the presence of even a small amount of impurities, the superconducting state near the upper critical field is gapless. In this region, the oscillatory (in the magnetic field) contribution to the density of states and the characteristic damping of the amplitude of the magnetization oscillations in the superconducting state are found. [S1063-7761(97)02611-5]

1. INTRODUCTION

Quantum oscillations of the magnetization—the de Haas–van Alphen effect—are a well-studied phenomenon in the physics of normal metals. In superconductors, the magnetic fields in which it is possible to observe the dHvA effect in practice are ordinarily much higher than the critical field of the phase transition from the superconducting into the normal state.

According to the standard Lifshitz–Kosevich theory,[1] each extremal cross section of the Fermi surface makes a contribution to the oscillatory part of the magnetization

$$M_{\rm osc} \propto \sqrt{H}\,\frac{2\pi^2 T/\omega_c}{\sinh(2\pi^2 T/\omega_c)}\exp\left(-\frac{\pi}{\omega_c\tau}\right)\times\sin\left(\frac{2\pi F}{H}+\Phi\right). \tag{1}$$

Here $\omega_c = eH/m^*c$ is the cyclotron frequency, $F=(c/2\pi e)S$, S is the area of the extremal section of the Fermi surface, and τ is the electron scattering time of the impurities. The Planck constant $\hbar$ is everywhere set equal to 1. The quantity $1/2\pi\tau$ is the Dingle temperature. Both the temperature and impurity factors in Eq. (1) decrease rapidly with decreasing magnetic field, which should not exceed the upper critical field H_{c2} of the superconductor. Appreciable oscillations of the magnetization can therefore be expected to appear only at very low temperatures

$$T < \frac{eH_{c2}}{2\pi^2 m^* c} \sim \frac{T_c^2}{\mu}. \tag{2}$$

Here T_c is the temperature of the transition to the superconducting state in zero field and μ is the Fermi energy. On the other hand, on account of impurity scattering,[2] dHvA oscillations are appreciable only in sufficiently pure metals, i.e. when $\omega_c\tau \gg 1$, which can be rewritten as $l_{\rm imp} \gg R_c$. Here $l_{\rm imp}=v_F\tau$ is the mean free path length, $R_c = k_F\lambda^2$ is the cyclotron radius, k_F is the Fermi wave vector, and $\lambda=\sqrt{c/eH}$ is the magnetic length, which in a field of the order of H_{c2} is equal to the coherence length $\xi(T)$. Therefore the requirement that the purity of the sample be high enough to observe dHvA oscillations in fields of the order of H_{c2},

$$l_{\rm imp} \gg k_F\xi^2, \tag{3}$$

is much stronger than the standard condition on the purity of a superconductor, $l_{\rm imp} \gg \xi_0$.

Thus, the dHvA effect in the range of fields and temperatures typical of type-II superconductors can be observed only in quite rarely encountered ultrapure superconductors with a high upper critical field. Examples of such superconductors are compounds with the structure A-15 (V_3Si, Nb_3Sn),[3,4] borocarbides ($YNiB_2C$),[5] and some organic and layered superconductors (see the reviews in Refs. 6 and 7). Thus, in V_3Si,[3] where $H_{c2}=18.5$ T, $T_c=17$ K, $\xi_0=6.3$ nm, and $l_{\rm imp}>R_c=130$ nm, dHvA oscillations in fields of the order of H_{c2} can be observed at temperatures of the order of 1 K.

The dHvA effect in the materials indicated above remains even in a transition to a mixed state ($H<H_{c2}$). The frequency of the oscillations remains the same, and the amplitude decreases with decreasing field more rapidly than in the normal state.

The damping of the amplitude of the magnetization oscillations in type-II superconductors has been calculated theoretically.[8,9] It was shown that in the mixed state of the material, the quasiparticle scattering by a spatially nonuniform distribution of the order parameter $\Delta(\mathbf{R})$ leads to additional broadening of the Landau levels

$$\frac{1}{\tau_s} \sim \sqrt{\mu\omega_c}\,\frac{H_{c2}-H}{H_{c2}}. \tag{4}$$

As a result, besides the Dingle factor, the amplitude of the dHvA effect acquires another, temperature-independent, factor $\exp(-\pi/\omega_c\tau_s)$ and decreases fairly rapidly away from the phase transition line H_{c2}.

The derivation of the expression (4) is unsatisfactory from a theoretical standpoint. The problem is that in Ref. 8 the electron spectrum and the level broadening are obtained by formally replacing the spectrum found in Ref. 10 in the momentum representation by a corresponding quantum expression. The description in terms of the continuous variables $\xi = k^2/2m - \mu$ and the polar angle θ is a good one when the spacing between the Landau levels is small compared with the temperature T or the width $\Gamma = 1/2\tau$ of the levels. In studying the dHvA effect we are dealing with precisely the opposite situation $\omega_c > 2\pi^2 T$ and $\omega_c > \pi\Gamma$, so that the momentum representation cannot be used to calculate the spectrum. Moreover, the mean-square modulus of the order parameter appears in Ref. 8 as a phenomenological parameter, whereas it should be determined from the self-consistency equation.

The quantum approach developed by Stephen[9] nonetheless confirmed Maki's results.[8] In Ref. 9, however, in a calculation of the quasiparticle self-energy, a summation over the principal quantum number was replaced by an integral, which is admissible only if the level widths are greater than the spacing between the levels. This is why the same results are obtained in Refs. 8 and 9.

Descriptions of the dHvA effect in superconductors are also proposed in Refs. 11–13. For all the difference in the approaches, the authors used in one way or another a BCS-type spectrum

$$E = \sqrt{E_n^2(k_z) + \Delta^2}, \tag{5}$$

where

$$E_n(k_z) = \omega_c(n + 1/2) + k_z^2/2m - \mu. \tag{6}$$

Stephen[9] showed that the spectrum (5) is realized only in sufficiently weak fields $\sqrt{\mu\omega_c} \ll T$. By virtue of (2), it is therefore impossible to observe magnetization oscillations in this region.

The spectrum (5) likewise can also formally be obtained in the ultraquantum limit $\omega_c \sim \mu$.[14] It is well known, however, that in the theory of superconductivity, the mean-field approximation is inapplicable in the ultraquantum limit (see Ref. 15). The mathematical model employed in Ref. 14 thereby does not yield a faithful description of superconductivity in strong fields.

In the present paper a self-consistent quantum theory of the effect in a mixed state is developed. It is shown that for a finite impurity concentration, despite the requirement of high purity $\omega_c > \pi\Gamma$, which is necessary in order to observe the dHvA effect, in the mixed state near the upper critical field H_{c2} there is a region of gapless superconductivity where the density of states at the Fermi surface remains finite:

$$N(E=0) = N_0\left(1 - \frac{2\sqrt{\pi^3 n_F}}{L \ln n_F}\,\frac{H_{c2} - H}{H_{c2}}\right). \tag{7}$$

Here N_0 is the density of states in the normal metal, $n_F = \mu/\omega_c$ is the number of Landau levels below the Fermi level, and L is a numerical constant ≈ 2.

The oscillatory part of the density of states, and consequently the oscillatory part M_{osc}^s of the magnetization in the mixed state, is also depressed compared with its value M_{osc}^n (1) in the normal state

$$\frac{M_{\text{osc}}^s}{M_{\text{osc}}^n} = 1 - \frac{2\sqrt{\pi n_F}}{L \ln n_F}\,\frac{H_{c2} - H}{H_{c2}}. \tag{8}$$

The results (7) and (8) were obtained in the linear approximation in the squared order parameter $\Delta^2 \sim (H_{c2} - H)/H_{c2}$ under the conditions $T < \Gamma < \omega_c$. Any attempt to go beyond the linear approximation encounters substantial mathematical difficulties due to the nondiagonal nature of the self-energy matrix, which is unavoidable as a result of the spatially nonuniform distribution of the order parameter.

Our presentation is organized as follows. In the next section, the Gor'kov equations for the electron Green's function in the mixed state of a superconductor are written out. Next, the wave functions that define the magnetic-sublattice representation—the best representation for solving the problem of Landau quantization in the field of the periodic potential of the order parameter—are determined in explicit form. In the next two sections, the order parameter of the superconductor and the solutions of the self-consistency equations for the impurity self-energy part are presented. In Sec. 6 the electron density of states near the Fermi surface is calculated and the thermodynamic potential and magnetic moment of the superconductor are calculated according to the known density of states.

2. ELECTRON GREEN'S FUNCTION IN AN IMPURE SUPERCONDUCTOR

The Gor'kov equations for an impure superconductor are

$$(i\omega - \hat{H}_0(\mathbf{r}) - \hat{\Delta}(\mathbf{r}) - \hat{u}(\mathbf{r}))\hat{G}(\mathbf{r},\mathbf{r}',\omega) = \hat{1}\delta(\mathbf{r} - \mathbf{r}'), \tag{9}$$

where

$$\hat{H}_0(\mathbf{r}) = \begin{pmatrix} H_0(\mathbf{r}) & 0 \\ 0 & -H_0^*(\mathbf{r}) \end{pmatrix},$$

$$\hat{\Delta}(\mathbf{r}) = \begin{pmatrix} 0 & \Delta(\mathbf{r}) \\ \Delta^*(\mathbf{r}) & 0 \end{pmatrix},$$

$$\hat{u}(\mathbf{r}) = u(\mathbf{r})\hat{\tau}_3 = \begin{pmatrix} u(\mathbf{r}) & 0 \\ 0 & -u(\mathbf{r}) \end{pmatrix},$$

$u(\mathbf{r})$ is the impurity scattering potential,

$$H_0(\mathbf{r}) = \frac{1}{2m}\left(-i\frac{\partial}{\partial \mathbf{r}} + \frac{e}{c}\mathbf{A}(\mathbf{r})\right)^2 - \mu \tag{10}$$

is the single-particle Hamiltonian of electrons in a magnetic field, and μ is the chemical potential. The magnetic field is assumed to be uniform and oriented along the external field, which is certainly justified for $H \sim H_{c2}$ in superconductors with a large Ginzburg–Landau parameter κ in which the dHvA effect is observed ($\kappa \approx 17$ in V_3Si). To simplify the calculations we neglect the effect of the magnetic field on the electron spins.

The eigenfunctions $\phi_l(\mathbf{r})$ of the operator $H_0(\mathbf{r})$ are Landau wave functions, written in an appropriate gauge, or any linear combinations of these functions satisfying the orthonormality condition. The explicit form of the functions $\phi_l(\mathbf{r})$ and the gauge for the magnetic field will be given in the next section. The matrix $\hat{G}(\mathbf{r},\mathbf{r}',\omega)$, containing both the normal and anomalous Green's functions $G(\mathbf{r},\mathbf{r}',\omega)$ and $F(\mathbf{r},\mathbf{r}',\omega)$, can be written in both the coordinate representation and the $\phi_l(\mathbf{r})$ representation:

$$\hat{G}(\mathbf{r},\mathbf{r}',\omega)$$
$$=\begin{pmatrix} G(\mathbf{r},\mathbf{r}',\omega) & F(\mathbf{r},\mathbf{r}',\omega) \\ F^{+}(\mathbf{r},\mathbf{r}',\omega) & -G(\mathbf{r}',\mathbf{r},-\omega) \end{pmatrix}$$
$$=\sum_{ll'}\begin{pmatrix} \phi_l(\mathbf{r})G_{ll'}(\omega)\phi^*_{l'}(\mathbf{r}') & \phi_l(\mathbf{r})F_{ll'}(\omega)\phi_{l'}(\mathbf{r}') \\ \phi^*_l(\mathbf{r})F^{+}_{ll'}(\omega)\phi^*_{l'}(\mathbf{r}') & -\phi_{l'}(\mathbf{r}')G_{l'l}(-\omega)\phi^*_l(\mathbf{r}) \end{pmatrix}. \tag{11}$$

The order parameter $\Delta(\mathbf{r})$ can be determined from the self-consistency equation

$$\Delta^*(\mathbf{r})=|g|T\sum_{\omega} F^{+}(\mathbf{r},\mathbf{r},\omega), \tag{12}$$

where g is the attractive potential between electrons near the Fermi surface.

For isotropic impurity scattering in the approximation of low impurity density ($l_{\mathrm{imp}}\gg k_F^{-1}$), we assume that the average of the product $u(\mathbf{r}_1)u(\mathbf{r}_2)$ over all possible impurity configurations is

$$\overline{u(\mathbf{r}_1)u(\mathbf{r}_2)}=n_{\mathrm{imp}}u^2\delta(\mathbf{r}_1-\mathbf{r}_2). \tag{13}$$

Here u is the characteristic strength of the impurity scattering potential and n_{imp} is the impurity density. Furthermore, we neglect multiple scattering by a single impurity (Born approximation). Under these assumptions, retaining the notation (11) for the Green's function averaged over the positions of the impurities, we obtain[16]

$$\hat{G}(\mathbf{r},\mathbf{r}',\omega)=\hat{g}(\mathbf{r},\mathbf{r}',\omega)$$
$$+\int d\mathbf{r}_1\hat{g}(\mathbf{r},\mathbf{r}_1,\omega)\hat{\Delta}(\mathbf{r}_1)\hat{G}(\mathbf{r}_1,\mathbf{r}',\omega)$$
$$+\int d\mathbf{r}_1\hat{g}(\mathbf{r},\mathbf{r}_1,\omega)\hat{\Sigma}_{\mathrm{imp}}(\mathbf{r}_1)\hat{G}(\mathbf{r}_1,\mathbf{r}',\omega). \tag{14}$$

The impurity self-energy part satisfies the self-consistency equation

$$\hat{\Sigma}_{\mathrm{imp}}(\mathbf{r},\omega)=\begin{pmatrix} \overline{G}(\mathbf{r},\omega) & \overline{F}(\mathbf{r},\omega) \\ \overline{F^{+}}(\mathbf{r},\omega) & -\overline{G}(\mathbf{r},-\omega) \end{pmatrix}$$
$$=n_{\mathrm{imp}}u^2\hat{\tau}_3\hat{G}(\mathbf{r},\mathbf{r},\omega)\hat{\tau}_3. \tag{15}$$

The matrix Green's function of a pure normal metal in a magnetic field has the form

$$\hat{g}(\mathbf{r},\mathbf{r}',\omega)=\begin{pmatrix} g(\mathbf{r},\mathbf{r}',\omega) & 0 \\ 0 & -g(\mathbf{r}',\mathbf{r},-\omega) \end{pmatrix}. \tag{16}$$

The Green's function $g(\mathbf{r},\mathbf{r}',\omega)$ can be expressed in tems of the eigenfunctions of the operator H_0 as

$$g(\mathbf{r},\mathbf{r}',\omega)=\sum_{l}\phi_l(\mathbf{r})g_l(\omega)\phi^*_l(\mathbf{r}'), \tag{17}$$

where

$$g_l(\omega)=(i\omega-\xi_l)^{-1}. \tag{18}$$

We shall also rewrite Eq. (14) in the $\phi_l(\mathbf{r})$ representation:

$$\begin{pmatrix} G_{ll'}(\omega) & F_{ll'}(\omega) \\ F^{+}_{ll'}(\omega) & -G_{l'l}(-\omega) \end{pmatrix}=\begin{pmatrix} g_l(\omega)\delta_{ll'} & 0 \\ 0 & -g_l(-\omega)\delta_{ll'} \end{pmatrix}$$
$$+\sum_{l_1}\begin{pmatrix} g_l(\omega)(\overline{G}_{l_1l}(\omega)G_{l_1l'}(\omega)+\tilde{\Delta}_{ll_1}F^{+}_{l_1l'}(\omega)) & g_l(\omega)(\overline{G}_{l_1l}(\omega)F_{l_1l'}(\omega)-\tilde{\Delta}_{ll_1}G_{l'l_1}(-\omega)) \\ -g_l(-\omega)(\tilde{\Delta}^*_{ll_1}(\omega)G_{l_1l'}(\omega)+\overline{G}_{ll_1}(\omega)F^{+}_{l_1l'}(\omega)) & -g_l(\omega)(\tilde{\Delta}^*_{ll_1}(\omega)F_{l_1l'}(\omega)-\overline{G}_{ll_1}(\omega)G_{l'l_1}(-\omega)) \end{pmatrix}. \tag{19}$$

Here we have introduced the notation

$$\overline{G}_{ll'}=\int d\mathbf{r}\;\phi_l(\mathbf{r})\phi_{l'}(\mathbf{r})\overline{G}(\mathbf{r},\omega). \tag{20}$$

$$\overline{F}_{ll'}(\omega)=\int d\mathbf{r}\;\phi^*_l(\mathbf{r})\phi^*_{l'}(\mathbf{r})\overline{F}(\mathbf{r},\omega), \tag{21}$$

$$\Delta_{ll'}=\int d\mathbf{r}\;\phi^*_l(\mathbf{r})\phi^*_{l'}(\mathbf{r})\Delta(\mathbf{r}), \tag{22}$$

$$\tilde{\Delta}(\mathbf{r},\omega)=\Delta(\mathbf{r})+\overline{F}(\mathbf{r},\omega). \tag{23}$$

The quantities $\overline{G}(\mathbf{r},\omega)$ and $\overline{F}(\mathbf{r},\omega)$ are determined by Eq. (15).

Our goal is to calculate the density of states and to solve the self-consistency equation for Δ to second order in Δ. To do so, we represent all functions in Eq. (19) as a sum of two terms, the first of which contains the lowest power of Δ, while the second is the next term in the expansion in powers of Δ. Denoting the power of Δ by a corresponding index, we have

$$G_{ll'}(\omega)=G^{(0)}_{ll'}(\omega)+G^{(2)}_{ll'}(\omega), \tag{24}$$

$$F_{ll'}(\omega)=F^{(1)}_{ll'}(\omega)+F^{(3)}_{ll'}(\omega), \tag{25}$$

$$\overline{G}_{ll'}(\omega)=\overline{G}^{(0)}_{ll'}(\omega)+\overline{G}^{(2)}_{ll'}(\omega). \tag{26}$$

We note that $\overline{G}^{(0)}_{ll'}(\omega)$ is simply the self-energy part of the Green's function of an impure normal metal. The magnitude of $\overline{G^{(0)}}(\mathbf{r})$ does not depend on the coordinate $\mathbf{r}$, and since the wave functions $\phi_l(\mathbf{r})$ are orthonormal, we have $\overline{G}^{(0)}_{ll'}(\omega)=\delta_{ll'}\overline{G}^{(0)}(\omega)$.

The following relations can be obtained from Eq. (19):

$$G^{(0)}_{ll'}(\omega)=\delta_{ll'}G^{(0)}_{l}(\omega)=\frac{\delta_{ll'}}{g_l^{-1}(\omega)-\overline{G^{(0)}_l}},\tag{27}$$

$$G^{(2)}_{ll'}(\omega)=G^{(0)}_{l}(\omega)\overline{G^{(2)}_{l'l}}(\omega)G^{(0)}_{l'}(\omega)+\sum_{l_1}G^{(0)}_{l}(\omega)\tilde{\Delta}_{ll_1}(\omega)F^{+(1)}_{l_1l'}(\omega),\tag{28}$$

and for the anomalous Green's function

$$F^{+(1)}_{ll'}(\omega)=-G^{(0)}_{l}(-\omega)\tilde{\Delta}^{*}_{ll'}(\omega)G^{(0)}_{l'}(\omega),\tag{29}$$

$$F^{+(3)}_{ll'}(\omega)=-\sum_{l_1}G^{(0)}_{l}(-\omega)\tilde{\Delta}^{*}_{ll_1}(\omega)G^{(2)}_{l_1l'}(\omega)-\sum_{l_1}G^{(0)}_{l}(-\omega)\overline{G^{(2)}_{ll_1}}(\omega)F^{+(1)}_{l_1l'}(\omega).\tag{30}$$

The solution of the self-consistency equation for the impurity self-energy part for a normal metal is $\overline{G^{(0)}_l}(\omega)=-i\Gamma_{\text{imp}}\,\text{sign}\,\omega$, where $\Gamma_{\text{imp}}=\pi n_{\text{imp}}u^2N_0$. The second-order correction in Δ is given by

$$\overline{G^{(2)}_{ll'}}(\omega)=n_{\text{imp}}u^2\sum_{pp'}\int d\mathbf{r}\,\phi_l(\mathbf{r})\phi_p(\mathbf{r})\times\phi^{*}_{p'}(\mathbf{r})\phi^{*}_{l'}(\mathbf{r})G^{(2)}_{pp'}(\omega).\tag{31}$$

In the next section we present the functions $\phi_l(\mathbf{r})$ and the matrix elements $\Delta_{ll'}$ in explicit form.

3. MAGNETIC-SUBLATTICE REPRESENTATION

The mixed state in type-II superconductors consists of an Abrikosov vortex lattice with one flux quantum $\phi_0=\pi c/e$ per unit cell. To simplify the calculations, we choose a square vortex lattice with edge length a such that $a^2=\pi\lambda^2$. The form of the lattice can influence the dependence of the amplitude of the order parameter Δ on the strength of the field and the temperature. All other results are independent of the type of lattice.

The solution of the linearized equation for the order parameter is the function

$$\Delta(\mathbf{r})=\Delta f_0(\mathbf{r}),\tag{32}$$

where

$$f_0(\mathbf{r})=\sqrt[4]{2}\sum_{\nu}\exp\left(i\,\frac{2\pi\nu}{a}\,y\right)\exp\left[-\left(\frac{x}{\lambda}+\frac{\pi\nu}{a}\,\lambda\right)^2\right]\tag{33}$$

in the Landau gauge $\mathbf{A}(\mathbf{r})=(0,Hx,0)$.

To calculate the matrix elements of the order parameter $\Delta(\mathbf{r})$, it is convenient to choose a complete set of eigenfunctions of the Hamiltonian H_0 in the form of the following linear combinations of Landau functions (magnetic-sublattice representation[17]):

$$\phi_l(\mathbf{r})=\sqrt{\frac{a}{\lambda}}\exp(ik_zz)\sum_{m}\exp(-iq_xam)\times\exp\left[i\left(q_y+\frac{\pi m}{a}\right)y\right]\varphi_n\left(\frac{x}{\lambda}+\left(q_y+\frac{\pi m}{a}\right)\lambda\right),\tag{34}$$

where

$$\varphi_n(s)=\frac{1}{\sqrt{2^nn!\sqrt{\pi}}}\exp\left(-\frac{s^2}{2}\right)H_n(s),\tag{35}$$

and

$$H_n(s)=(-1)^ne^{s^2}\frac{d^n}{ds^n}\,e^{-s^2}\tag{36}$$

are Hermite polynomials. In the magnetic-translation lattice there are two flux quanta ϕ_0 per unit cell (the charge of a Cooper pair is twice the electron charge). For this reason we choose a lattice in the form of a rectangle with edges $a_x=a$ and $a_y=2a$. Then $l=\{n,k_z,\vec{q}\}$ and the vector $\vec{q}$ lies in the first Brillouin zone: $-\pi/a<q_x<\pi/a$ and $-\pi/2a<q_y<\pi/2a$. The summation over the quantum numbers in the preceding section is to be interpreted as

$$\sum_{l}=\sum_{n=0}^{\infty}\int\frac{dk_z}{2\pi}\int_{-\pi/a}^{\pi/a}\frac{dq_x}{2\pi}\int_{-\pi/2a}^{\pi/2a}\frac{dq_y}{2\pi}.\tag{37}$$

The energy levels of the single-particle Hamiltonian (10) are

$$\xi_l=\xi_n(k_z)=\omega_c(n+1/2)+k_z^2/2m^{*}-\mu.\tag{38}$$

The functions $g_l(\omega)$ and $G^{(0)}_l(\omega)$, defined by Eqs. (18) and (27), do not depend on the wave vector $\vec{q}$.

The matrix element $\Delta_{ll'}$ in the magnetic-sublattice representation has the form (see Appendix A)

$$\Delta_{ll'}=(2\pi)^3\delta(k_z+k_z')\,\delta(\vec{q}+\vec{q}\,')\Delta_{nn'}(\vec{q}),\tag{39}$$

$$\Delta_{nn'}(\vec{q})=(-1)^{n'}\Delta\sqrt{\sqrt{2\pi}\,\frac{(n+n')!}{2^{n+n'+1}n!n'!}}\times\sum_{\nu}\exp(2i\nu q_xa)\times\varphi_{n+n'}\left(\sqrt{2}\left(q_y\lambda+\frac{\pi\lambda\nu}{a}\right)\right).\tag{40}$$

4. SOLUTION OF THE EQUATIONS FOR THE IMPURITY SELF-ENERGY PART

We seek the function $\tilde{\Delta}(\mathbf{r},\omega)$, defined in Eq. (23), in the form $\tilde{\Delta}(\mathbf{r},\omega)=\Delta(\mathbf{r})[1+\alpha(\omega)]$. Substituting the expression for $\Delta_{ll'}$ into (29) and transforming back to the coordinate representation (see Appendix B), we obtain

$$F^{+(1)}(\mathbf{r},\mathbf{r},\omega)=-\Delta^*(\mathbf{r})[1+\alpha(\omega)]\,\frac{1}{\sqrt{2}\pi\lambda^2}\int\frac{dk_z}{2\pi}\times\sum_{nn'}\left[\frac{(n+n')!}{2^{n+n'+1}n!n'!}\times G_n^{(0)}(-\omega,k_z)G_{n'}^{(0)}(\omega,k_z)\right]. \tag{41}$$

Comparing this expression with Eq. (23), we obtain

$$\alpha(\omega)=\frac{\beta(\omega)}{1-\beta(\omega)}, \tag{42}$$

where

$$\beta(\omega)=n_{\mathrm{imp}}u^2\,\frac{1}{\sqrt{2}\pi\lambda^2}\int\frac{dk_z}{2\pi}\sum_{nn'}\left[\frac{(n+n')!}{2^{n+n'+1}n!n'!}\,G_n^{(0)}\times(-\omega,k_z)G_{n'}^{(0)}(\omega,k_z)\right]. \tag{43}$$

Stirling's formula gives the estimate

$$\frac{(n+n')!}{2^{n+n'+1}n!n'!}\approx\frac{1}{\sqrt{4\pi n}}\exp\left(-\frac{(n-n')^2}{4n}\right). \tag{44}$$

Let $m=n'-n$, and let us replace, according to the Poisson formula, the summation over n by the corresponding integration

$$\beta(\omega)=-n_{\mathrm{imp}}u^2\,\frac{1}{\sqrt{2}\pi\lambda^2}\times\int\frac{dk_z}{2\pi}\sum_m\int dn\,\frac{1}{\sqrt{4\pi n}}\times\exp\left(-\frac{m^2}{4n}\right)\sum_r e^{2i\pi rn}\times\frac{1}{i\omega+\xi_n(k_z)+i\Gamma_{\mathrm{imp}}\mathrm{sign}\;\omega}\times\frac{1}{i\omega-\xi_n(k_z)-\omega_c m+i\Gamma_{\mathrm{imp}}\mathrm{sign}\;\omega}. \tag{45}$$

Then in the sum over r we can neglect oscillatory terms with $r\neq0$, which contain an additional small factor $\sqrt{\omega_c/r\mu}\,\exp(-2\pi r\Gamma_{\mathrm{imp}}/\omega_c)$. This factor arises because for $r\neq0$, only the region near the extremal section of the Fermi surface makes a significant contribution to the integral over k_z, while for $r=0$ the entire Fermi surface contributes. We do not present here the calculations for terms with $r\neq0$, since they are entirely analogous to the calculations made in Sec. 6 for the oscillatory density of states.

In the remaining term with $r=0$, we transform from integration over n to integration over the coordinates of the two-dimensional vector $\vec{k}_\perp$, so that $\omega_c(n+1/2)=k_\perp^2/2m^*$, and then we integrate over the components of the three-dimensional vector $\mathbf{k}$, treating $\mathbf{k}$ as a vector comprised of $\vec{k}_\perp$ and k_z:

$$\int_0^\infty\frac{dn}{2\pi\lambda^2}\int\frac{dk_z}{2\pi}=\int\frac{2\pi k_\perp dk_\perp}{(2\pi)^2}\int\frac{dk_z}{2\pi}=\int\frac{d\mathbf{k}}{(2\pi)^3}=N_0\int d\xi\int_0^{\pi/2}\sin\,\theta\,d\theta. \tag{46}$$

For $\omega\ll\Gamma_{\mathrm{imp}}\ll\omega_c$ it is sufficient to retain the $m=0$ term in the sum over m. The integration yields

$$\beta(\omega)=\sqrt{\frac{\pi\omega_c}{8\mu}}. \tag{47}$$

The semiclassical approximation is applicable in the limit $\omega>\omega_c$. Therefore the summation over the quantum number $n'=n+m$ can be replaced by integration. To estimate the integral we set $\exp(-m^2/4n)\approx1$. As a result, we find that for large ω the quantity $\beta(\omega)$ does not exceed

$$\sqrt{\frac{\pi^3\omega_c}{8\mu}\frac{\Gamma_{\mathrm{imp}}}{\omega_c}}. \tag{48}$$

Therefore, when $n_F=\mu/\omega_c\gg1$, $\beta(\omega)$ is small. In the following calculations we ignore the difference between $\widetilde{\Delta}(\mathbf{r},\omega)$ and $\Delta(\mathbf{r})$.

It will be seen from the calculations below (see Sec. 6) that to find the density of states to order Δ^2 it is sufficient to know the impurity self-energy part integrated over the quasimomentum $\vec{q}$:

$$\overline{G^{(2)}}_{nn'}(\omega)=\int\frac{d\vec{q}}{(2\pi)^2}\,\overline{G^{(2)}_{nn'}}(k_z,\vec{q},\omega).$$

We integrate the right- and left-hand sides of Eq. (31) over the quasimomentum $\vec{q}$ and, using Eqs. (28) and (29), obtain (see Appendix B)

$$\overline{G^{(2)}}_{nn'}(\omega)=\frac{\delta_{nn'}n_{\mathrm{imp}}u^2}{2\pi\lambda^2}\sum_m\int\frac{dk_z}{2\pi}\times\left\{[G_m^{(0)}(k_z,\omega)]^2\overline{G^{(2)}}_{mm}(\omega)-\frac{\Delta^2}{2\pi\lambda^2}[G_m^{(0)}(k_z,\omega)]^2\sum_{m_1}\left[\frac{(m+m_1)!}{2^{m+m_1+1}m!m_1!}\times G_{m_1}^{(0)}(k_z,-\omega)\right]\right\}. \tag{49}$$

In deriving Eq. (49) we employed the fact that

$$\int\frac{d\vec{q}}{(2\pi)^2}\,\phi_{n\vec{q}k_z}(\mathbf{r})\phi^*_{n'\vec{q}k_z}(\mathbf{r})=\frac{1}{2\pi\lambda^2}\,\delta_{nn'}, \tag{50}$$

where the integral extends over the first Brillouin zone.

Subsequent calculations are similar to the calculation of $\beta(\omega)$. Specifically, we employ the relation (44), transform from summation over m to integration, and drop small oscillatory terms. In the nonoscillatory term, we use the relations (46) to transform from integration over m and k_z to integration over $\xi=\xi_m(k_z)$. Since $\overline{\overline{G}^{(2)}}_{mm}(\omega)$ does not depend on m, the integral of the first term in Eq. (49) over ξ equals zero. Therefore the quantity $\overline{\overline{G}^{(2)}}_{nn'}(\omega)$ is determined by the second term in Eq. (49). In the case $\omega \ll \Gamma_{\text{imp}} \ll \omega_c$, retaining only the $m_1=m$ term in the sum over m_1, we obtain

$$\overline{\overline{G}^{(2)}}_{mm}(\omega) \approx \frac{i}{16\pi\lambda^2}\sqrt{\frac{\pi\omega_c}{\mu}}\frac{\tilde{\Delta}^2}{\Gamma_{\text{imp}}}. \tag{51}$$

If $\omega>\omega_c$, the nonoscillatory part of $\overline{\overline{G}^{(2)}}$ equals zero, since in this limit the summation over m_1 in the second term in Eq. (49) can be replaced by integration, and the subsequent integration over m yields zero.

5. SOLUTION OF THE SELF-CONSISTENCY EQUATION FOR THE ORDER PARAMETER

The order parameter of a superconductor is the solution of the self-consistency equation (12). Equation (12), linearized with respect to $\Delta(\mathbf{r})$,

$$\Delta(\mathbf{r}) = -|g|T\sum_{\omega}\int d\mathbf{r}' \times G^{(0)}(\mathbf{r},\mathbf{r}',\omega)G^{(0)}(\mathbf{r},\mathbf{r}',-\omega)\Delta(\mathbf{r}'), \tag{52}$$

determines the metal–superconductor phase transition curve as a function of temperature and magnetic field. It possesses an infinite number of solutions $f_N(\mathbf{r})$, which are eigenfunctions of the Schrödinger equation for a particle with charge $2e$ in a magnetic field H.[18] Substituting $\Delta(\mathbf{r})=f_N(\mathbf{r})$ into Eq. (52) yields an equation for the upper critical field H_N in which superconductivity might appear with a spatial dependence of the order parameter given by $f_N(\mathbf{r})$. The highest value of the upper critical field H_{c2} is reached for $N=0$ in the function $f_0(\mathbf{r})$ given by Eq. (33).

Any solution of the self-consistency equation (12) can be represented as a linear combination of the functions $f_N(\mathbf{r})$:

$$\Delta(\mathbf{r}) = \Delta\sum_{N=0}^{\infty} a_N f_N(\mathbf{r}). \tag{53}$$

To find the dependence of the amplitude of the order parameter on the deviation of the magnetic field from the upper critical field, we multiply both sides of Eq. (12) by $\Delta f_N(\mathbf{r})$ and integrate over $\mathbf{r}$. The result is an algebraic system of equations for the coefficients a_N. Let $a_0=1$. It is easy to verify, from the structure of the system of equations for the coefficients a_N, that all a_N with $N\neq 0$ are small as $(H_{c2}-H)/H_{c2}$. It is therefore sufficient to retain only the equation with $N=0$, which to terms of order Δ^4 has the form

$$\Delta^2 = |g|T\sum_{\omega}\sum_{nn'}\int\frac{d\vec{q}}{(2\pi)^2}\int\frac{dk_z}{2\pi}\Delta_{nn'}(\vec{q}) \times[F^{(1)+}_{nn'}(k_z,\vec{q},\omega)+F^{(3)+}_{nn'}(k_z,\vec{q},\omega)]. \tag{54}$$

Let us calculate the first term in (54), which contains $F^{(1)+}_{nn'}(k_z,\vec{q},\omega)$, for fields H less than the upper critical field H_{c2}. Using the result of Appendix B and Eq. (44), we write it in the explicit form

$$-|g|T\Delta^2\sum_{\omega}\frac{1}{2\pi\lambda^2}\sum_{nn'}\frac{\exp[-(n'-n)^2/4n]}{\sqrt{4\pi n}} \times\int\frac{dk_z}{2\pi}G^{(0)}_n(k_z,-\omega)G^{(0)}_{n'}(k_z,\omega). \tag{55}$$

In this expression, the divergent sum over frequencies must be cut off at a frequency of order ϵ_c—the characteristic thickness of the layer where electrons attract one another near the Fermi surface. The divergence actually means that large values $\omega\sim\epsilon_c$ make the main contribution in Eq. (55). Therefore, to calculate the first term in Eq. (54) we can replace summation over the quantum numbers n and m by integration over $k_\perp^2=2m^*\omega_c n$ and $p_\perp^2=2m^*\omega_c n'$, respectively. We perform the integration as follows: we replace the integral over $p_\perp$ by an integral over $\tilde{p}_\perp=p_\perp-k_\perp$ and transform from integrals over k_z and $\vec{k}_\perp$ to an integral over the components of the three-dimensional vector $\mathbf{k}=(\vec{k}_\perp,\, k_z)$ (compare with Eq. (46)). We obtain

$$2\pi i\frac{\Delta^2|g|N_0}{\sqrt{2\pi}}\lambda T\sum_{\omega}\int_0^{\pi/2}\sin\,\theta d\theta \times\int\frac{1}{\tilde{p}_\perp v_F\sin\,\theta-2i(|\omega|+\Gamma_{\text{imp}})}\exp\left(-\frac{\tilde{p}_\perp^2\lambda^2}{2}\right)d\tilde{p}_\perp. \tag{56}$$

Substituting the Fourier transforms for both factors in the integral over $\tilde{p}_\perp$, we find

$$|g|N_0\Delta^2 2\pi T\sum_{\omega}\int_0^{\pi/2}\sin\,\theta d\theta\int\frac{\lambda d\rho}{v_F} \times\exp\left[-\frac{(\rho\,\sin\,\theta)^2}{2}\right]\exp\left[-\frac{2(|\omega|+\Gamma_{\text{imp}})\lambda\rho}{v_F}\right]. \tag{57}$$

As expected, the resulting expression is identical to the semiclassical result. Next, following a standard procedure,[19] we arrive at an expression for the amplitude of the order parameter Δ^2 in the limit $T\to 0$:

$$N_0\Delta^2\ln\sqrt{\frac{H_{c2}}{H}} = T\sum_{\omega}\sum_{\substack{nn\\ mm'}}\int\frac{dk_z}{2\pi}G^{(0)}_n(k_z,-\omega) \times G^{(0)}_m(k_z,\omega)G^{(0)}_{n'}(k_z,-\omega) \times G^{(0)}_{m'}(k_z,\omega)Y^{nn'}_{mm'}, \tag{58}$$

where

$$Y^{nn'}_{mm'} = \int\frac{d\vec{q}}{(2\pi)^2}\Delta_{nm}(\vec{q})\Delta^*_{nm'}(\vec{q})\Delta_{n'm}(\vec{q})\Delta^*_{n'm'}(\vec{q}).$$

We took account of the fact that the two terms containing $\overline{G}^{(2)}_{ll'}$ that appear in $F^{(3)+}_{nn'}(k_z,\vec{q},\omega)$ cancel one another after summation over frequency ω. In the limit $\Gamma_{\text{imp}}\ll\omega_c$, we retain the term corresponding to $n=m=n'=m'$ and neglect the remaining terms, which are small to the degree that the ratio $\Gamma_{\mathrm{imp}}/\omega_c$ is small. Hence,

$$N_0\Delta^2 \ln\left(\frac{H_{c2}}{H}\right)^{1/2} = T\sum_\omega \sum_n \int \frac{dk_z}{2\pi} \frac{1}{[(\omega+\Gamma_{\mathrm{imp}})^2+\xi_n^2(k_z)]^2} Y_{nn}^{nn}. \tag{59}$$

We rewrite the integral Y_{nn}^{nn} in the form

$$Y_{nn}^{nn}=\frac{1}{2\pi\lambda^2}\sum_{\vec{Q}} \sigma_n(\vec{Q})\sigma_n(-\vec{Q}), \tag{60}$$

and the Fourier transforms $\sigma_n(\vec{Q})$ are

$$\sigma_n(\vec{Q})=2\pi\lambda^2\int \frac{d\vec{q}}{(2\pi)^2} e^{i\vec{q}\vec{Q}}\Delta_{nn}(\vec{q})\Delta_{nn}^*(\vec{q}). \tag{61}$$

The vectors $\vec{Q}=(2aN_x, 2aN_y)$. The quantity (61) is calculated in Appendix D. Substituting the expression for $\sigma_n(\vec{Q})$ into Eq. (60), we find

$$Y_{nn}^{nn}=\frac{\Delta^4}{2\pi\lambda^2}\Sigma_n, \tag{62}$$

where

$$\Sigma_n=\left(\frac{(2n)!}{2^{2n+1}n!n!}\right)^2 \sum_{N_x,N_y} \exp[-\pi(N_x^2+N_y^2)] \times L_{2n}^2(\pi(N_x^2+N_y^2)). \tag{63}$$

Here the $L_n(s)$ are Laguerre polynomials.

If in Eq. (63) the summations over N_x and N_y are replaced by integration, then the value of the integral will be 1 for all n. The sum, however, depends on n and assumes values approximately equal to 2 with a variance of some 10%. For subsequent calculations, we neglect the dependence of the sum on n and set the value of the sum equal to some number $L\approx 2$. Dropping, as usual, the oscillating terms in the Poisson series, we perform the integration in Eq. (59) over $\xi_n(k_z)$. In the low-temperature limit the sum over ω can be replaced by an integral. The integral over the angle θ diverges near $\theta=0$. Since the expressions above are valid for $n_F \gg 1$, we have the natural cutoff $\theta_c\approx 1/k_F\lambda$. Finally, we obtain

$$\Delta^2(H)\approx\frac{16\pi n_F}{L\ln n_F}\Gamma_{\mathrm{imp}}^2\frac{H_{c2}-H}{H_{c2}}, \tag{64}$$

where $n_F=\mu/\omega_c$. Here $\ln(H_{c2}/H)$ is replaced by its series expansion in powers of $H_{c2}-H$.

We emphasize that the result (63) is valid when $T<\Gamma_{\mathrm{imp}}\ll\omega_c$.

6. DENSITY OF STATES

The density of states $N(E)$ can be expressed in the standard manner in terms of the Green's function

$$N(E)=-\frac{1}{\pi}\operatorname{Im}\sum_l G_{ll}(E),$$

$$G_{ll'}(E)=G_l^{(0)}\delta_{ll'}+G_{ll'}^{(2)}. \tag{65}$$

We write an explicit expression for the density of states per unit volume to first order in Δ^2:

$$\begin{aligned}N(E)=&-\frac{1}{\pi}\operatorname{Im}\frac{1}{2\pi\lambda^2}\sum_n\int\frac{dk_z}{2\pi}G_n^{(0)}(k_z,E)\\&-\frac{1}{\pi}\operatorname{Im}\sum_n\int\frac{dk_z}{2\pi}G_n^{(0)2}(k_z,E)\left(\overline{\overline{G^{(2)}}}_{nn}(E)\right.\\&\left.-\frac{1}{2\pi\lambda^2}\Delta^2\sum_{n'}\frac{(n+n')!}{2^{n+n'+1}n!n'!}G_{n'}^{(0)}(k_z,-E)\right).\end{aligned} \tag{66}$$

The first term is the density of states of the normal metal. One can see that the correction to the density of states can be expressed in terms of the quantity $\overline{\overline{G^2}}(T)$ found in Sec. 4.

We use the Poisson formula

$$\sum_n \cdots = \sum_r \int dn\, e^{2\pi irn}\cdots$$

to perform the summation over the Landau level numbers, and we obtain for the density of states an expression of the form

$$N(E)=\sum_r N^{(r)}(E).$$

The $r=0$ term corresponds to the nonoscillatory ''average'' value of the density of states $N^{(0)}(E)$. To calculate this term it is convenient to transform from integration over n to integration over the coordinates of a two-dimensional vector $\vec{k}_\perp$ such that $\vec{k}_\perp^2=2m\omega_c n$. Treating $\vec{k}$ and k_z as components of a three-dimensional vector **k** we arrive at a semiclassical integral, which can be computed by making the substitution (46). The first term, containing $\overline{\overline{G^{(2)}}}$, on the right-hand side of Eq. (66) vanishes after an integration over ξ. We perform the integration over ξ and θ in the last term in Eq. (66), just as in the calculations of Eqs. (47) and (51) for $E<\Gamma_{\mathrm{imp}}\ll\omega_c$, using the relation (44) and retaining only the $n'=n$ term in the sum over n'.[1)] The result is

$$N^{(0)}(E)=N_0\left(1-\frac{\sqrt{\pi}}{8\sqrt{n_F}}\frac{\Delta^2}{\Gamma_{\mathrm{imp}}^2}\right). \tag{67}$$

We substitute the value of Δ determined in Eq. (64)

$$N^{(0)}(E)=N_0\left(1-\frac{2\sqrt{\pi^3 n_F}}{L\ln n_F}\frac{H_{c2}-H}{H_{c2}}\right). \tag{68}$$

From this expression we find the region of existence of gapless superconductivity:[2)]

$$\frac{H_{c2}-H}{H_{c2}}<\frac{L\ln n_F}{2\pi^{3/2}\sqrt{n_F}}. \tag{69}$$

We now examine the oscillatory corrections to the density of states. We transform from integration over n to integration over $\xi_n(k_z)=\xi$. The integrations over ξ and k_z are performed independently. Then

$$\int \frac{dk_z}{2\pi}\exp\left(-2\pi i\,\frac{k_z^2}{2m\omega_c}\,r\right)=\frac{1}{2\pi\lambda\sqrt{r}}\exp\left(-i\,\frac{\pi}{4}\right).$$

For the rth term of the Poisson series $(r\neq 0)$ we obtain the expression

$$N^{(r)}(E)=\frac{\sqrt{m^3\omega_c}}{2\pi^2}\,\frac{(-1)^r}{\sqrt{r}}\,A_r(\Delta)\,\mathrm{Im}\,\exp\left[i\,\frac{2\pi r}{\omega_c}\,(E+\mu)-i\,\frac{\pi}{4}\right]\exp\left(-\frac{2\pi r\Gamma_{\mathrm{imp}}}{\omega_c}\right), \tag{70}$$

where

$$A_r(\Delta)=\left(1-\frac{\Delta^2}{\sqrt{4\pi n_F}}\,\frac{1}{4\Gamma_{\mathrm{imp}}^2}\right). \tag{71}$$

In the derivation of Eq. (70) we dropped terms that are small to the degree that $\Gamma_{\mathrm{imp}}/\omega_c$ is small. Then the oscillatory correction to the density of states is damped at the transition to the superconducting state compared with its value in the normal state.

7. MAGNETIZATION OSCILLATIONS

The thermodynamic potential is

$$\Omega=-2T\int dE\;N(E)\ln(1+e^{-E/T}).$$

Integrating by parts, we have for the rth oscillating harmonic $\Omega^{(r)}$

$$\Omega^{(r)}=\frac{\sqrt{m^{*3}\omega_c^5}}{(2\pi^2)^2}\,\frac{(-1)^r}{r^{3/2}}\,A_r(\Delta)\cos\left(\frac{2\pi\mu}{\omega_c}\,r-\frac{\pi}{4}\right)\times\frac{2\pi^2T/\omega_c}{\sinh(2\pi^2Tr/\omega_c)}\exp\left(-\frac{2\pi r\Gamma_{\mathrm{imp}}}{\omega_c}\right), \tag{72}$$

where the factor $A_r(\Delta)$ is defined in Eq. (71). Hence the oscillatory part of the magnetization is

$$M^{(r)}=-\frac{\partial\Omega^{(r)}}{\partial H}=\frac{1}{2\pi^3}\left(\frac{e}{c}\right)^{3/2}\sqrt{H}\mu\,\frac{(-1)^r}{r^{1/2}}\,A_r(\Delta)\sin\left(\frac{2\pi r\mu}{\omega_c}+\frac{\pi}{4}\right)\times\frac{2\pi^2T/\omega_c}{\sinh(2\pi^2Tr/\omega_c)}\exp\left(-\frac{2\pi r\Gamma_{\mathrm{imp}}}{\omega_c}\right). \tag{73}$$

To calculate $\partial\Omega^{(r)}(E)/\partial H$ it is sufficient to differentiate only the factor $\exp(2i\pi r\mu/\omega_c)$. We note that the density of states can be determined in terms of the quantities such as $\overline{G^{(2)}}_{nn}(E)$ and Δ^2, which in turn likewise contain rapidly oscillating corrections. Nonetheless, when differentiating the density of states with respect to the magnetic field they can be neglected, since their contribution to the derivative of the density of states compared with the contribution indicated above is an infinitesimal of the same order as the oscillatory corrections to $\overline{G^{(2)}}$ and Δ^2 compared with their average values.

In contrast to a normal metal (see Eq. (1)), the answer has an additional factor $A_r(\Delta)$, corresponding to the damping that quasiparticles acquire as a result of scattering by the nonuniform distribution of the order parameter. Substituting the expression (64) into Eq. (71), we obtain

$$A_r(H)=1-\frac{2\sqrt{\pi n_F}}{L\ \ln n_F}\,\frac{H_{c2}-H}{H_{c2}}. \tag{74}$$

8. CONCLUSIONS

The results of this work are reminiscent of the results obtained in Refs. 8 and 9. Indeed, to first order in Δ^2, the suppression of the magnetization oscillations that was found in Refs. 8 and 9 is proportional to

$$1-\frac{\pi^{3/2}\Delta^2}{\sqrt{\mu\omega_c^3}}=1-\alpha\sqrt{\frac{\mu}{\omega_c}}\frac{H_{c2}-H}{H_{c2}}, \tag{75}$$

where α is of the order of 1, which qualitatively agrees with Eq. (74). We note, however, that in Refs. 8 and 9, Eq. (75) was derived under the implicit assumption that the width of the levels in the normal state is greater than the spacing between Landau levels. We now discuss this question in greater detail.

We first examine the expression for the order parameter obtained with various relationships among the quantities T, Γ_{imp}, and ω_c. Stephen[9] showed that in the weak-field limit $\sqrt{\mu\omega_c}<T$ the amplitude of the order parameter has the form

$$\Delta^2(H)\propto T_c^2\left(1-\frac{H}{H_{c2}}\right). \tag{76}$$

Since scattering by impurities broadens the levels similarly to the temperature, fields for which $\sqrt{\mu\omega_c}<\Gamma_{\mathrm{imp}}$ can likewise be treated as weak. In such fields, Eq. (76) determines the amplitude of the order parameter. In intermediate fields, where $\sqrt{\mu\omega_c}>T$, Γ_{imp} but nevertheless $\omega_c<T$, Γ_{imp}, the discrete structure of the spectrum is inconsequential and the magnitude of the order parameter assumes the form

$$\Delta^2(H)\propto\mu\omega_c\left(1-\frac{H}{H_{c2}}\right). \tag{77}$$

In Ref. 9 it is assumed that the result (77) is also valid in the strong-field limit, where magnetization oscillations are observed. In the present paper it is shown (see Eq. (64)) that in the region of strong fields $(\omega_c\gg\Gamma_{\mathrm{imp}}>T)$, the order parameter is determined by the expression

$$\Delta^2\propto\mu\omega_cF\left(\frac{\Gamma_{\mathrm{imp}}}{\omega_c}\right)\left(1-\frac{H}{H_{c2}}\right),$$

where, according to Eq. (64), $F(x)=x^2$ for $x\ll 1$. The form of the function $F(x)$ for arbitrary x can be determined from Eq. (58). The function $F(x)$ increases with x and reaches a constant value of the order of 1 at $x\sim 1$. This leads to Stephen's result Eq. (77). Similar characteristic ranges of magnetic fields also occur in calculations of the electron Green's function in the superconducting states (see footnote 1).

We also note that the exponential damping of the densities of states indicated in Refs. 8 and 9 falls outside the limits of accuracy of the theory. The problem is that the calculations in Refs. 8 and 9 neglected the detailed spatial structure of the order parameter, which is a valid procedure only when terms no higher than the first power of Δ^2 are studied. For arbitrary Δ^2, the indicated simplification is achieved by averaging over a random arrangement of vortices,[9] and a number of unconvincing arguments are presented as justification. Moreover, in calculations of higher orders in Δ^2, the self-consistency equation must be solved to the same degree of accuracy.

We now summarize the main results. The condition

$$T<\Gamma_{\mathrm{imp}}\ll\omega_c\,, \tag{78}$$

under which the results of the present work were obtained means that, specifically, the superconductor is highly pure:

$$l_{\mathrm{imp}}\gg k_F\lambda^2.$$

Nonetheless, the presence of even such a small quantity of impurity results in the formation of a gapless superconducting state near H_{c2}. The region (69) of existence of this state in ordinary type-II superconductors, where the number of Landau levels $n_F=\mu/\omega_c$ fitting below the Fermi level is enormous, reduces to a vanishingly small neighborhood of the upper critical field. However, n_F is not so large in superconductors with low Fermi energy and high H_{c2}. For example, in V_3Si (Ref. 3) n_F only ranges into the dozens, and the magnetic field interval $H_{c2}-H$ where gapless superconductivity exists can equal some tenths of H_{c2}. In this region Landau quantization is preserved, and therefore in a magnetic field there is an oscillatory contribution to the magnetization of the sample; its amplitude (73) rapidly decays as the field decreases.

We thank A. I. Larkin for a discussion of the results obtained in this work, and also M. I. Kagan and L. A. Fal'kovskiĭ, who read the manuscript and made a number of useful remarks.

This work was supported in part by the Ministry of Science of the Russian Federation (''Statistical Physics'' program) and the Russian Fund for Fundamental Research (Grant No. 96-0216041).

APPENDIX A

We calculate an element of the order parameter $\Delta_{ll'}$ determined by the expression (32) in the magnetic-sublattice representation (34). We write the explicit expression for $\Delta_{ll'}$:

$$\Delta_{ll'}=\Delta\,\frac{a}{\lambda}\int d\mathbf{r}e^{-i(k_z+k_z')z}\sum_{\nu,\nu',\mu}\exp(iq_xa\nu)\exp(iq_x'a\nu')$$
$$\times\exp\left[-i\left(q_y+\frac{\pi\nu}{a}y\right)\right]\exp\left[-i\left(q_y'+\frac{\pi\nu'}{a}\right)y\right]$$
$$\times\exp\left(\frac{2\pi i\mu y}{a}\right)\varphi_n\left(\frac{x}{\lambda}+\left(q_y+\frac{\pi\nu}{a}\right)\lambda\right)$$
$$\times\varphi_{n'}\left(\frac{x}{\lambda}+\left(q_y'+\frac{\pi\nu'}{a}\right)\lambda\right)\exp\left(-\left(\frac{x}{\lambda}+\frac{\pi\mu}{a}\,\lambda\right)^2\right). \tag{79}$$

The integration is performed over each coordinate separately:

$$\int dz\,\exp[-i(k_z+k_z')z]=2\pi\delta(k_z+k_z'). \tag{80}$$

$$\int dy\,\exp\left[-i\left(q_y+\frac{\pi\nu}{a}\right)y\right]\exp\left[-i\left(q_y'+\frac{\pi\nu'}{a}\right)y\right]$$
$$\times\exp\left(\frac{2\pi i\mu y}{a}\right)=2\pi\delta(q_y+q_y')\,\delta_{\nu+\nu',2\mu}\,. \tag{81}$$

Here we took account of the fact that $\vec{q}$ and $\vec{q}\,'$ are vectors in the first Brillouin zone. Since the sum $\nu+\nu'=\mu$ is an even number, the difference $\nu-\nu'$ is also an even number.

In the integral over the coordinate x we replace the integration variable by

$$\frac{\tilde{x}}{\lambda}=\frac{x}{\lambda}+\frac{\pi\mu}{a}\,\lambda.$$

Using the fact that $\nu+\nu'=2\mu$, the integrand can be rewritten in a form containing only the difference $\nu-\nu'$, which we denote by 2κ, where κ is an integer. Using the Kronecker delta symbol, we now transform from summation over ν, ν', and μ to summation over μ and κ and perform the summation over μ. Since

$$\exp(iq_xa\nu)\exp(iq_x'a\nu')=\exp\left[\frac{i(q_x+q_x')(\nu+\nu')a}{2}\right]$$
$$\times\exp\left[\frac{i(q_x-q_x')(\nu-\nu')a}{2}\right],$$

and the integral over x does not depend on μ, we have

$$\sum_{\mu}\exp[i(q_x+q_x')\mu a]=\frac{2\pi}{a}\,\delta(q_x+q_x'), \tag{82}$$

where q_x and q_x' are components of a vector in the first Brillouin zone.

It remains to perform the integration over the coordinate x. We introduce the variable $p=(q_y+\pi\kappa/a)\lambda$. The integral has the form

$$\lambda\int ds\;e^{-s^2}\varphi_n(s+p)\varphi_{n'}(s-p).$$

Using the explicit form of the function $\varphi_n(s)$ (35) we arrive at the integral

$$(-1)^{n+n'}e^{p^2}\int ds\left(\frac{d^n}{ds^n}\,e^{-(s+p)^2}\right)\left(\frac{d^{n'}}{ds^{n'}}\,e^{-(s-p)^2}\right).$$

Here we have dropped the normalization coefficients of the functions $\varphi_n(s)$. The equality

$$e^{-s^2}=\sqrt{\pi}\int \frac{d\xi}{2\pi}\, e^{i\xi s}e^{-\xi^2/4},$$

makes it possible to rewrite the integral as

$$(-1)^n \pi e^{-p^2}\int \frac{d\xi}{2\pi}\,(i\xi)^{n+n'}e^{2i\xi p}e^{-\xi^2/2}.$$

Calculating the inverse Fourier transform we arrive at

$$(-1)^{n'}\sqrt{\frac{\pi}{2^{n+n'+1}}}\,e^{-p^2}H_{n+n'}(\sqrt{2}p). \tag{83}$$

The expressions (80), (81), and (82) make it possible to represent the matrix element of the order parameter in the form (39). Collecting all factors together and using the expression (83), we arrive at Eq. (40).

APPENDIX B

To derive the expression (41) it is necessary to calculate the integral

$$\begin{aligned}&\int \frac{d\vec{q}}{(2\pi)^2}\,\phi^*_{nk_z\vec{q}}(\mathbf{r})\phi^*_{n',-k_z,-\vec{q}}(\mathbf{r})\Delta^*_{nn'}(\vec{q})\\ &\quad=\sqrt{\sqrt{2\pi}\,\frac{(n+n')!}{2^{n+n'+1}n!n'!}}\,\Delta\,\frac{a}{\lambda}\int\frac{d\vec{q}}{(2\pi)^2}\\ &\qquad\times\sum_{\nu,\nu',\kappa}\exp[iq_xa(\nu-\nu')]\exp\left[-i\left(q_y+\frac{\pi\nu}{a}\right)y\right]\\ &\qquad\times\exp\left[-i\left(-q_y+\frac{\pi\nu'}{a}\right)y\right]\exp(-2i\kappa q_xa)\\ &\qquad\times\varphi_n\left(\frac{x}{\lambda}+\left(q_y+\frac{\pi\nu}{a}\right)\lambda\right)\varphi_{n'}\left(\frac{x}{\lambda}+\left(-q_y+\frac{\pi\nu'}{a}\right)\lambda\right)\\ &\qquad\times\varphi_{n+n'}\left(\sqrt{2}\left(q_y\lambda+\frac{\pi\kappa\lambda}{a}\right)\right).\end{aligned} \tag{84}$$

The integration over q_x is trivial

$$\int_{-\pi/a}^{\pi/a}\frac{dq_x}{2\pi}\exp[iq_xa(\nu-\nu'-2\kappa)]=\frac{1}{a}\,\delta_{\nu-\nu',2\kappa}.$$

To calculate the integral over q_y we employ the equality $\nu-\nu'=2\kappa$, transform from summation over ν, ν', and κ to summation over $\nu-\nu'=2\kappa$ and $\nu+\nu'=2\mu$, and regroup terms in the arguments of the functions $\varphi_n(s)$ so as to obtain

$$\begin{aligned}&(-1)^{n'}\sqrt{\sqrt{2\pi}\,\frac{(n+n')!}{2^{n+n'+1}n!n'!}}\frac{1}{\lambda}\sum_{\kappa}\int_{-\pi/2a}^{\pi/2a}\frac{dq_y}{2\pi}\\ &\quad\times\sum_{\mu}\exp\left(-\frac{2\pi i\mu y}{a}\right)\varphi_{n+n'}\left(\sqrt{2}q_y\lambda+\frac{\pi\kappa\lambda}{a}\right)\\ &\quad\times\varphi_n\left(q_y\lambda+\frac{\pi\kappa\lambda}{a}+\xi\right)\varphi_{n'}\left(q_y\lambda+\frac{\pi\kappa\lambda}{a}-\xi\right),\end{aligned}$$

where $\xi=x/\lambda+\pi\mu\lambda/a$. We note that

$$\sum_{\kappa}\int_{-\pi/2a}^{\pi/2a}\frac{dq_y}{2\pi}\,f\left(q_y\lambda+\frac{\pi\kappa\lambda}{a}\right)=\int_{-\infty}^{\infty}\frac{dq_y}{2\pi}\,f(q_y\lambda), \tag{85}$$

and we substitute the functions $\varphi_n(s)$ from Eq. (35) into the integrand. Furthermore, we employ the explicit expression for the Hermite polynomial $H_{n+n'}(\sqrt{2}s)$ (see Eq. (36)). Dropping the factors, we present the form of the resulting integral:

$$\int ds\; H_n(s+\xi)H_{n'}(s-\xi)\,\frac{d^{n+n'}}{ds^{n+n'}}\,e^{-s^2}.$$

Integrating by parts $n+n'$ times and using the fact that

$$\frac{d^{n+n'}}{ds^{n+n'}}\,H_n(s+\xi)H_{n'}(s-\xi)=2^{n+n'}(n+n')!,$$

we arrive at the integral $\int ds\ \exp(-s^2)=\sqrt{2}$. Finally, we find

$$\begin{aligned}&\int\frac{d\vec{q}}{(2\pi)^2}\,\phi^*_{nk_z\vec{q}}(\mathbf{r})\phi^*_{n',-k_z,-\vec{q}}(\mathbf{r})\Delta^*_{nn'}(\vec{q})\\ &\quad=\frac{1}{\sqrt{2}\pi\lambda^2}\,\frac{(n+n')!}{2^{n+n'+1}n!n'!}\,\Delta^*(\mathbf{r}),\end{aligned} \tag{86}$$

where $\Delta(\mathbf{r})$ is given by Eq. (32).

APPENDIX C

The derivation of Eq. (49) requires the integral

$$I=\int\frac{d\vec{q}}{(2\pi)^2}\,\Delta_{nn'}(\vec{q})\Delta^*_{nn'}(\vec{q}).$$

We substitute the matrix element of the order parameter in the form (40)

$$\begin{aligned}I&=\sqrt{2\pi}\Delta^2\,\frac{(n+n')!}{2^{n+n'+1}n!n'!}\sum_{\nu,\nu'}\int_{-\pi/a}^{\pi/a}\frac{dq_x}{2\pi}\\ &\quad\times\exp[2iq_x(\nu-\nu')a]\int_{-\pi/2a}^{\pi/2a}\frac{dq_y}{2\pi}\\ &\quad\times\varphi_{n+n'}\left(\sqrt{2}\left(q_y\lambda+\frac{\pi\lambda\nu}{a}\right)\right)\varphi_{n+n'}\left(\sqrt{2}\left(q_y\lambda+\frac{\pi\lambda\nu'}{a}\right)\right).\end{aligned}$$

Carrying out the integration over q_x, we find that $\nu'=\nu$, and

$$\begin{aligned}I&=\sqrt{2\pi}\Delta^2\,\frac{(n+n')!}{2^{n+n'+1}n!n'!}\sum_{\nu}\int_{-\pi/2a}^{\pi/2a}\frac{dq_y}{2\pi a}\\ &\quad\times\varphi_{2n}\left(\sqrt{2}\left(q_y\lambda+\frac{\pi\lambda\nu}{2a}\right)\right)\varphi_{2n}\left(\sqrt{2}\left(q_y\lambda+\frac{\pi\lambda\nu}{a}\right)\right).\end{aligned}$$

Using Eq. (85), we find

$$I=\frac{\Delta^2}{2\pi\lambda^2}\,\frac{(n+n')!}{2^{n+n'+1}n!n'!}. \tag{87}$$

APPENDIX D

We now calculate the Fourier transform in the expression (61). We substitute into Eq. (61) the matrix element of the order parameter in the form (40):

$$\sigma_n(\vec{Q})=\sqrt{2\pi}\,\frac{(2n)!}{2^{2n+1}n!^2}\sum_{\nu,\nu'}\int_{-\pi/a}^{\pi/a}\frac{dq_x}{2\pi}$$

$$\times\exp[2iq_x(N_x+\nu-\nu')a]$$

$$\times\int_{-\pi/2a}^{\pi/2a}\frac{dq_y}{2\pi}\exp(2iN_yq_ya)$$

$$\times\varphi_{2n}\left(\sqrt{2}\left(q_y\lambda+\frac{\pi\lambda\nu}{a}\right)\right)\varphi_{2n}\left(\sqrt{2}\left(q_y\lambda+\frac{\pi\lambda\nu'}{a}\right)\right). \tag{88}$$

Here we set $\vec{Q}=(2aN_x, 2aN_y)$. Carrying out the integration over q_x, we find that $\nu'-\nu=N_x$, and

$$\sigma_n(\vec{Q})=\sqrt{2\pi}\,\frac{(2n)!}{2^{2n+1}n!^2}\sum_{\nu}\int_{-\pi/2a}^{\pi/2a}\frac{dq_y}{2\pi a}$$

$$\times\exp(2iN_yq_ya)\varphi_{2n}\left(\sqrt{2}\left(q_y\lambda+\frac{\pi\lambda\nu}{2a}\right)\right)$$

$$\times\varphi_{2n}\left(\sqrt{2}\left(q_y\lambda+\frac{\pi\lambda\nu}{a}+\frac{\pi\lambda N_x}{a}\right)\right).$$

We now use Eq. (85) and replace the integration variable in the integral over q_y by

$$\tilde{q}_y\lambda=q_y\lambda+\frac{\pi\lambda N_x}{2a}.$$

We arrive at

$$\sigma_n(\vec{Q})=\frac{\sqrt{2}}{2^{4n}n!^2}\,\frac{1}{2a\lambda}\exp(-i\pi N_xN_y)\exp\left(-\frac{\pi N_x^2}{2}\right)$$

$$\times\int\frac{dq_y}{2\pi a}\exp(2iN_yq_ya)\exp(-2q_y^2\lambda^2)$$

$$\times H_{2n}\left(\sqrt{2}\left(q_y\lambda-\frac{\pi\lambda N_x}{2a}\right)\right)$$

$$\times H_{2n}\left(\sqrt{2}\left(q_y\lambda+\frac{\pi\lambda N_x}{2a}\right)\right).$$

The integral on the right-hand side of this expression is calculated in Ref. 17. Finally, we find

$$\sigma_n(\vec{Q})=\frac{(2n)!}{2^{2n+1}n!^2}\,\frac{\exp(-i\pi N_xN_y)}{2\pi\lambda^2}$$

$$\times\exp\left[-\frac{\pi}{2}(N_x^2+N_y^2)\right]L_{2n}(\pi(N_x^2+N_y^2)), \tag{89}$$

where the $L_n(s)$ are Laguerre polynomials.

[1] This is the point where Stephen[9] performs the integration over n', which is admissible only for $\Gamma_{\rm imp}>\omega_c$, i.e. outside the region where the dHvA effect is observable.

[2] The damping of the density of states can be observed experimentally. To do so, it is necessary to measure the dependence of the specific heat on the magnetic field intensity at sufficiently low temperatures.

---

[1] I. M. Lifshitz and A. M. Kosevich, Zh. Éksp. Teor. Fiz. **29**, 730 (1955).

[2] Yu. A. Bychkov, Zh. Éksp. Teor. Fiz. **39**, 1401 (1961) [Sov. Phys. JETP **12**, 977 (1961)].

[3] R. Corcoran, N. Harrison, S. M. Hayden, P. Meeson, M. Springfield, and P. J. van der Wel, Phys. Rev. Lett. **72**, 701 (1994).

[4] N. Harrison, S. M. Hayden, P. Meeson, M. Springfield, P. J. van der Wel, and A. A. Menovsky, Phys. Rev. B **50**, 4208 (1994).

[5] G. Goll, M. Heinecke, A. J. M. Jansen, W. Jess, L. Nguyen, E. Steep, K. Winzer, and P. Wyber, Phys. Rev. B **53**, 8871 (1996).

[6] R. Corcoran, N. Harrison, C. J. Haworth *et al.*, Physica B **206-207**, 534 (1995).

[7] M. Springford and A. Wasserman, J. Low Temp. Phys. **105**, 273 (1996).

[8] K. Maki, Phys. Rev. B **44**, 2861 (1991).

[9] M. J. Stephen, Phys. Rev. B **45**, 5481 (1992).

[10] U. Brandt, W. Pesch, and L. Tewordt, Z. Physik **201**, 209 (1967).

[11] S. Dukan and Z. Tesanovic, Phys. Rev. Lett. **74**, 2311 (1995).

[12] P. Miller and B. L. Gyorffy, J. Phys.: Condens. Matter **7**, 5579 (1995).

[13] K. Miyake, Physica B **186-188**, 115 (1993).

[14] M. Rasolt and Z. Tesanovich, Rev. Mod. Phys. **64**, 709 (1992).

[15] V. M. Yakovenko, Phys. Rev. B **47**, 8851 (1993).

[16] A. A. Abrikosov, L. P. Gor'kov, and I. E. Dzyaloshinskiĭ, *Methods of Quantum Field Theory in Statistical Physics* [in Russian], Fizmatgiz, Moscow (1962) [Prentice-Hall, Englewood Cliffs, N. J. (1963)].

[17] Yu. A. Bychkov and E. I. Rashba, Zh. Éksp. Teor. Fiz. **85**, 1826 (1983) [Sov. Phys. JETP **58**, 1062 (1983)].

[18] I. W. Gruenberg and L. Günther, Phys. Rev. **176**, 606 (1968).

[19] E. Helfand and N. R. Werthamer, Phys. Rev. **147**, 288 (1966).

Translated by M. E. Alferieff

Investigation of the hyperfine interaction in the antiferromagnetic $CsMnI_3$

L. A. Prozorova, S. S. Sosin, D. V. Efremov, and S. V. Petrov

P. L. Kapitsa Institute of Physical Problems, Russian Academy of Sciences, 117334 Moscow, Russia

(Submitted 17 June 1997)
Zh. Éksp. Teor. Fiz. **112**, 1893–1898 (November 1997)

The lower branch of the resonance spectrum of the quasi-one-dimensional triangular antiferromagnetic $CsMnI_3$ has been investigated experimentally. This branch possesses a gap due to the dynamic hyperfine interaction. The temperature dependence of the energy gap was studied in detail at several frequencies. A theoretical calculation of the corresponding spectrum of coupled electron-nuclear spin oscillations was performed in the ''hydrodynamic approximation'' with an empirical correction for thermal fluctuations of the antiferromagnetic system. The good agreement between the calculation and experimental data makes it possible to determine the zero-point spin reduction in the antiferromagnetic. [S1063-7761(97)02711-X]

1. INTRODUCTION

The dynamical properties of antiferromagnetics are strongly affected by the interaction of the electronic and nuclear magnetic subsystems. Specifically, the NMR spectrum of the magnetic ions depends strongly on the type of exchange ordering of the electronic spins. It was noted first in Ref. 1 that the nuclear spins associated with the triangular exchange structure occupy inequivalent positions with respect to an external magnetic field so that their resonance spectrum should consist of three branches. Later, such a spectrum of coupled electronic–nuclear oscillations was studied experimentally for the easy-plane antiferromagnetic $CsMnBr_3$.[2,3] Three branches with different magnetic-field dependences were indeed observed in the NMR spectrum, and a temperature-dependent gap due to the dynamical interaction with the nuclear spins appeared in one of the acoustic branches of the AFMR spectrum. Thus, the results were basically in agreement with the theoretical prediction mentioned above and with calculations[3] performed on the basis of the phenomenological approach of Ref. 4.

However, a more detailed analysis of the experimental data reveals large deviations from the theory. There can be several reasons for these deviations. Above all, the exchange structure of $CsMnBr_3$ is strongly influenced by quantum fluctuations and is strongly distorted by a magnetic field applied in the easy-plane of the crystal. These circumstances make the approach used to describe the spectrum of oscillations less accurate. Finally, the analysis of the temperature dependences of the magnetic-resonance spectrum is probably complicated by the characteristic behavior, the nature of which remains unknown,[5] of this antiferromagnetic above $T\sim 3$ K.

The properties of the easy-axis antiferromagnetic $CsMnI_3$ investigated in the present work make it possible to eliminate most of the difficulties listed above. Furthermore, similar AFMR spectrum and its temperature dependence have been investigated in detail in nickel compounds (for example, in $RbNiCl_3$ (Ref. 6)), where there is essentially no hyperfine interaction with the nuclear subsystem. This makes it easier to distinguish the antiferromagneticic and paramagnetic contributions to the temperature evolution of the spectrum of coupled oscillations.

2. EXPERIMENTAL RESULTS

In the present work, the low-frequency part of the resonance spectrum of the antiferromagnetic $CsMnI_3$ in a magnetic field oriented perpendicular to the six-fold axis of the crystal was investigated at different temperatures. The experiments were performed in the frequency range 3.3–18 GHz with a direct-amplification spectrometer. Quasitoroidal resonators with $Q=500-800$ were employed as the absorbing cell in the lower part of this range and high-Q square resonators ($Q>1500$) were used at frequencies of 9 GHz and higher. A superconducting solenoid generated the external magnetic field, which could be continuously varied up to 10 kOe. The experimental cell was located inside a helium dewar, whose temperature (from 4.2 to 1.3 K) was measured to within 0.02 K according to the saturated vapor pressure. The experimental crystal was glued to a binary plane, making it possible to orient the six-fold axis C_6 perpendicular to the field to within $\pm 0.5°$.

A single 0.5–1 kOe wide absorption line was observed at all frequencies. The line shifted in the direction of lower fields with decreasing temperature (see Fig. 1) and the relative shift increased strongly with decreasing frequency. At the frequencies 5.7, 4.3, and 3.3 GHz there existed a range of temperatures (below 1.7 K, 2.5 K, and 3.9 K, respectively) at which the resonance line shifted to zero field and then vanished. These data attest to the presence of a gap, which increases with temperature, in the resonance spectrum.

The characteristic features listed above are illustrated in Fig. 2, which displays the temperature dependence of the resonance field at different frequencies. Here it is clearly seen that the change in the resonance field with decreasing temperature becomes sharper at low frequencies; this corresponds to the gap gradually approaching the given frequency. A series of curves of the lower ''AFMR branch'' as a function of the field was constructed from the results of the measurements for several temperatures. Two of these curves (at the beginning and end of the interval) are presented in

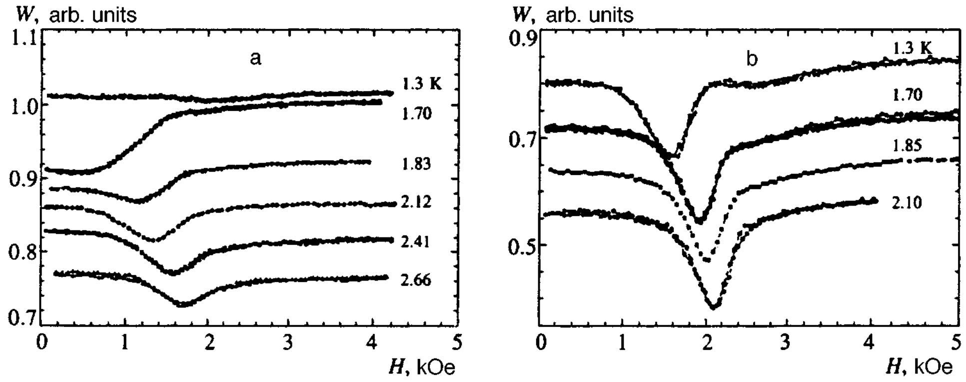

FIG. 1. Variation of the resonance absorption lines with temperature at frequencies 5.7 GHz (a) and 7.2 GHz (b).

Fig. 3. A theoretical description of the data obtained and a discussion of the agreement between theory and experiment are given in the next section.

3. DISCUSSION AND MAIN CONCLUSIONS

The resonance properties of the electronic spin system are most easily studied in a phenomenological approach,[4] which is the most convenient method for describing the long-wavelength dynamics of antiferromagnetics with a complicated exchange structure and weak relativistic interactions. The exchange symmetry of a triangular antiferromagnetic is given by the transformation of two orthogonal unit vectors according to the same irreducible representation:

$$\mathbf{S}(\mathbf{r})=\langle S\rangle[\mathbf{l}_1\cos(\mathbf{k}\cdot\mathbf{r})+\mathbf{l}_2\sin(\mathbf{k}\cdot\mathbf{r})], \tag{1}$$

where $\mathbf{k}=(1/3,1/3,1)$ in reciprocal lattice units. The susceptibility tensor of such an antiferromagnetic has two principal values $\chi_\perp$ and $\chi_\parallel$ with respect to the vector $\mathbf{n}=\mathbf{l}_1\times\mathbf{l}_2$ perpendicular to the plane of the spins. The macroscopic dynamics of the system is determined by a Lagrangian with density

$$\mathscr{L}_e=\frac{\chi_\perp}{2\gamma^2}(\mathbf{\Omega}+\gamma\mathbf{H})^2+\frac{\eta\chi_\perp}{2\gamma^2}(\mathbf{n}\cdot(\mathbf{\Omega}+\gamma\mathbf{H}))^2-U_a, \tag{2}$$

where $\eta=(\chi_\parallel-\chi_\perp)/\chi_\perp$, $\mathbf{\Omega}$ is the angular rotation velocity in spin space, and U_a is the anisotropy energy, whose form is discussed in detail in Ref. 7. The parameterization of the rotation of the spin system for obtaining linearized equations of motion is determined by expanding any spin vector σ and angular velocity vector $\mathbf{\Omega}$ up to second-order in the rotation angle $\boldsymbol{\theta}$:

$$\boldsymbol{\sigma}=\boldsymbol{\sigma}_0+\boldsymbol{\theta}\times\boldsymbol{\sigma}_0+\frac{1}{2}\boldsymbol{\theta}\times(\boldsymbol{\theta}\times\boldsymbol{\sigma}_0),\quad \mathbf{\Omega}=\dot{\boldsymbol{\theta}}+\frac{1}{2}\boldsymbol{\theta}\times\dot{\boldsymbol{\theta}}, \tag{3}$$

where the equilibrium values of the vectors $\boldsymbol{\sigma}_0$ are determined from the condition that the Lagrangian has a maximum at $\mathbf{\Omega}\equiv 0$. Specifically, in the case at hand, when the field $\mathbf{H}$ is perpendicular to C_6, the vector $\mathbf{n}_0$ is directed along the field.

The paramagnetic nuclear system is treated as a collection of free magnetic moments at finite temperature which are located in different effective fields $\mathbf{H}^{\rm eff}(\mathbf{r}_i)=A\mathbf{S}(\mathbf{r}_i)+\mathbf{H}$ (A is the hyperfine interaction constant).

Since the characteristic relaxation times of the nuclear spins of Mn^{2+} are much longer than the period of the microwave oscillations ($\omega\tau\gg 1$), we can neglect the thermodynamic coupling of the magnetization of the paramagnet in fields $\mathbf{H}_i^{\rm eff}$ with the rest of the system and describe the magnetization in the form of conserved spontaneous magnetic moments. This description is similar to the model of ferromagnetic sublattices. For this reason the corresponding Lagrangian can be represented as a sum for $N=6$ independent ferromagnets (see Ref. 4):

$$\mathscr{L}_n=\frac{1}{N}\sum_{r=1}^{N}\frac{1}{\gamma_n}(\mathbf{M}_i\cdot(\mathbf{\Omega}_i+\gamma_n\mathbf{H}_i^{\rm eff}(\theta))). \tag{4}$$

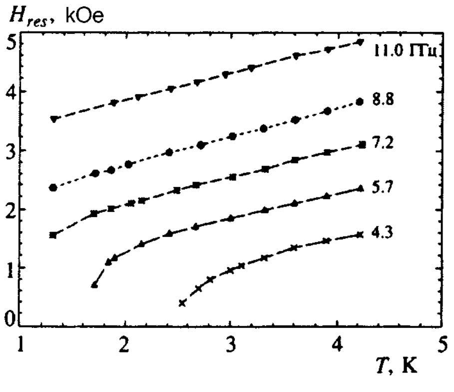

FIG. 2. Resonance field of the experimental branch versus temperature at different frequencies.

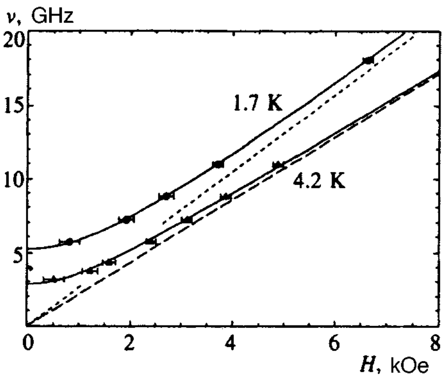

FIG. 3. Field dependence of the ν_2 branch at two temperatures. Solid lines—fit of the expression (7); dashed lines—AFMR spectrum without the hyperfine interaction.

The magnetic moments and angular frequencies of the motion of each sublattice near equilibrium can be parametrized in terms of small rotation angles φ_i similarly to Eq. (3), the total magnetization of the sublattices being determined from the conditions of equilibrium $\mathbf{M}_{0i}=\chi_n\mathbf{H}_i^{\mathrm{eff}}$. This approach is obviously different from the one used in Ref. 3, since it does not assume that the conditions of thermodynamic equilibrium of the nuclear subsystem are satisfied while the subsystem is in motion.

The complete Lagrangian of the system of electronic and nuclear spins can be written as

$$\mathscr{L}=\mathscr{L}_e+\mathscr{L}_n. \tag{5}$$

Varying the Lagrangian with respect to $\theta,\dot{\theta}$ and $\varphi_i,\dot{\varphi}_i$ we obtain a system of 21 equations describing the coupled spin oscillations. Eliminating from this system the components of the nuclear-spin angles, we obtain the following characteristic equation for the frequencies:

$$\begin{vmatrix} \left(\dfrac{\nu}{\gamma}\right)^2-\eta(H^2+H_c^2)-\dfrac{\Delta^2(\nu^2-\gamma_n^2H^2)}{2\gamma^2(\nu^2-\nu_n^2)} & \dfrac{i\nu H}{\gamma}(1+\eta) \\ -\dfrac{i\nu H}{\gamma}(1-\eta) & \left(\dfrac{\nu}{\gamma}\right)^2-\eta H^2-\dfrac{\Delta^2(\nu^2-\gamma_n^2H^2)}{2\gamma^2(\nu^2-\nu_n^2)} \end{vmatrix}=0,\quad \nu^2-\nu_{e_3}^2-\frac{1}{1+\eta}\,\frac{\Delta^2\nu^2}{\nu^2-\nu_n^2}=0, \tag{6}$$

where $\nu_n=\gamma_n\sqrt{A^2\langle S\rangle^2+\overline{H^2}}$ is the unshifted nuclear frequency, $\Delta=\gamma A\langle S\rangle\sqrt{\chi_n/\chi_\perp}$ is the width of the dynamical gap in the mixed spectrum, and ν_{e_3} is the field-independent branch of the initial AFMR spectrum. Assuming $\nu^2\gg\nu_n^2$ and neglecting in weak fields the off-diagonal elements of the characteristic equation (6), we obtain simple expressions for the ''antiferromagneticic'' modes:

$$\nu_1^2=\nu_{e_1}^2+\frac{\Delta^2}{2},\quad \nu_2^2=\nu_{e_2}^2+\frac{\Delta^2}{2},\quad \text{and}\quad \nu_3^2=\nu_{e_3}^2+\frac{\Delta^2}{1+\eta}, \tag{7}$$

where $\nu_{e_1}=\gamma\sqrt{\eta(H^2+H_c^2)}$ and $\nu_{e_2}=\gamma\sqrt{\eta}H$ are approximate expressions for the initial antiferromagneticic branches.

As one can see from Fig. 3, Eq. (7) for ν_2 describes the experimental data well at low temperature. The two other branches were not investigated, since in the case $H\perp C_6$ the ν_3 branch is unobservable because of the absence of dispersion with respect to the field and the branch ν_1 lies at frequencies above 100 GHz and is essentially insensitive to the hyperfine interaction.

The mean value $\langle S\rangle$ of the electronic spins, which is lower than the classical value $S=5/2$ on account of fluctuations of the ground state of the quasi-one-dimensional antiferromagnetic, can be determined from the value of Δ. The hyperfine interaction constant $A=215\pm5$ kOe can be taken from the investigation of the EPR spectrum of the solid solution of CsMnI$_3$ in CsMgI$_3$,[8] and the antiferromagneticic susceptibility $\chi_\perp$ at $T\ll T_N$ was measured in Ref. 9 and equals $7.5\cdot10^{-3}$ emu/mole. The nuclear spin of Mn^{2+} is $I=5/2$ and the nuclear magnetic moment $\mu-\gamma_n\hbar I=3.47\mu_n$ (μ_n is the nuclear magneton). Substituting all available values into the equation for Δ^2, we obtain

$$\Delta^2=\frac{(\gamma_n\hbar)^2I(I+1)N_A}{3kT\chi_\perp}(\gamma A\langle S\rangle)^2\simeq\frac{30\langle S\rangle^2}{T}\ \mathrm{GHz}^2$$

($\chi_\perp/N_A$ is the antiferromagneticic susceptibility per spin).

The value of Δ at temperatures $T\ll T_N$ can be determined quite accurately from existing experimental data. For example, the second of the equations (7) with $\eta=0.88$ and $\Delta=7.6\pm0.3$ GHz describes well the measured resonance spectrum at $T=1.7$ K (see Fig. 3). The value $\langle S\rangle=1.8\pm0.1$ calculated hence is essentially identical to the neutron-diffraction value $\langle S\rangle=1.85\pm0.05$.[9]

Thus, despite strong quantum fluctuations in the antiferromagneticic system CsMnI$_3$, a calculation of the spectrum of coupled oscillations in the hydrodynamic approximation

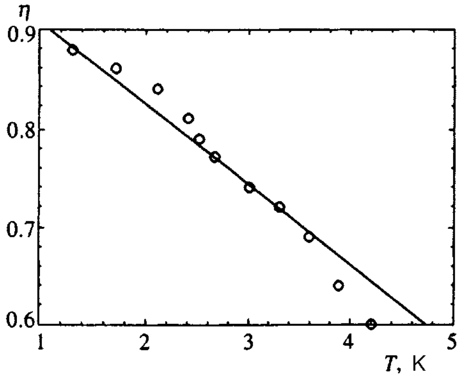

FIG. 4. η versus temperature. Solid line—calculation of $(\chi_\parallel-\chi_\perp)/\chi_\perp$ from the results of magnetostatic measurements.[9]

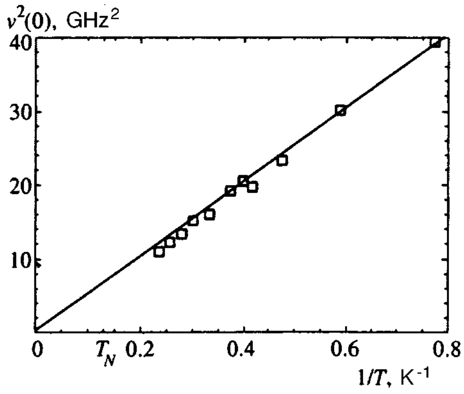

FIG. 5. Gap $\nu_2(0)$ versus temperature plotted as the function $\nu^2(1/T)$.

shows excellent agreement with experiment. This can be explained by the fact that the contribution of zero-point vibrations to the resonance spectrum at low frequencies $\nu \ll \nu_{ex}$ is determined mainly by their effect on the ground state of the antiferromagnetic, i.e. it reduces to the same renormalization of the order parameter and static susceptibility as in the static case. Since they are phenomenological constants in this approach, they need not be calculated starting from the classical model, but rather they can be replaced by their experimental values, as shown above.

The lower magnetic-resonance branch can be described in exactly the same way in the entire experimental temperature range $T \leqslant T_N/2$. This requires taking account of the temperature dependences of not only the nuclear susceptibility χ_n but also the static parameters $\chi_\parallel$, $\chi_\perp$, and $\langle S \rangle$ of the electronic system which appear in the second of the equations (7). The self-consistency of this approach is easily checked by comparing the values of the parameters determined by fitting the spectrum at different temperatures (see Fig. 3) and the corresponding data from magnetostatic and neutron experiments.[9] The results of such a comparison for the parameter η are presented in Fig. 4. Figure 5 shows the temperature dependence of the gap in the ν_2 branch. In addition, all characteristics of the antiferromagnetic which appear in the gap are renormalized in such a manner as to eliminate their temperature contribution in Δ. The function so obtained and plotted as $\nu^2(1/T)$ reflects the Curie law for the paramagnetic susceptibility of the nuclei, confirming the fact that this branch can be described in the mean-field approximation, which was used above, in the entire temperature interval. It also follows from Fig. 5 that the contribution of the magnetoelastic interaction to the dynamic gap in the spectrum falls within the experimental error.

We thank A. F. Andreev and V. I. Marchenko for valuable suggestions concerning the theoretical part of this work, and also the late A. S. Borovik-Romanov, A. I. Smirnov, I. A. Zaliznyak, and A. M. Tikhonov for useful discussions. This work was supported in part by the Russian Fund for Fundamental Research (Grant No. 95-02-04555-a) and CRDI (Grant RP1-207). Two of us (D. V. E. and S. S. S.) are also grateful to Förschungszentrum Jülich GmbH and ISSEP (''Soros Graduate Student'' subprogram).

[1] A. V. Chubukov, J. Phys. C: Sol. St. Phys. **21**, L441 (1988).
[2] A. S. Borovik-Romanov, B. S. Dumesh, A. M. Tikhonov, and S. V. Petrov, JETP Lett. **64**, 225 (1996).
[3] I. A. Zaliznyak, N. N. Zorin, and S. V. Petrov, JETP Lett. **64**, 473 (1996).
[4] A. F. Andreev and V. I. Marchenko, Usp. Fiz. Nauk **130**, 39 (198) [Sov. Phys. Usp. **23**, 21 (1980)].
[5] X. Xu. K. Okada, M. Fuji *et al.*, J. Phys.: Condens. Matter **8**, L371 (1996).
[6] O. A. Petrenko, S. V. Petrov, and L. A. Prozorova, Zh. Éksp. Teor. Fiz. **98**, 727 (1990) [Sov. Phys. JETP **71**, 406 (1990)].
[7] S. I. Abarzhi, M. E. Zhitomirskiĭ, O. A. Petrenko *et al.*, Zh. Éksp. Teor. Fiz. **104**, 3232 (1993) [JETP **77**, 521 (1993)].
[8] G. L. McPherson, R. C. Koch, and G. D. Stucky, J. Chem. Phys. **60**, 1424 (1974).
[9] H. W. Zandbergen, J. Solid State Chem. **35**, 367 (1980).

Translated by M. E. Alferieff

Nonsingular skyrmions for Landau levels with odd occupation number in a two-dimensional system

S. V. Iordanskiĭ and S. G. Plyasunov

L. D. Landau Institute of Theoretical Physics, Russian Academy of Sciences, 142432 Chernogolovka, Moscow Region, Russia

(Submitted 19 June 1997)
Zh. Éksp. Teor. Fiz. **112**, 1899–1914 (November 1997)

The number of particles, energy and other physical parameters in the presence of a skyrmion vortex have been calculated using the gradient expansion technique. Unlike other researchers, we have not used the approximation of functions projected on a single Landau level. If other Landau levels are included in the scheme, we have a simple physical model and a substantially modified expression for the skyrmion energy. Generation of one skyrmion is thermodynamically favorable, so they should emerge spontaneously near odd-integer filling factors. © *1997 American Institute of Physics.* [S1063-7761(97)02811-4]

1. INTRODUCTION

The theory of macroscopic skyrmion-type spin excitations in the neighborhood Landau levels with odd occupation number in two-dimensional systems under quantum Hall effect conditions has been developed in a number of theoretical treatments. Sondhi *et al.*[1] employed the Chern–Simons phenomenological approach, showed that such excitations should exist, and calculated the energy. Then Fertig *et al.*[2] numerically calculated the energy and wave function using the Hartree–Fock technique and approximation of functions projected on a single Landau level. Moon *et al.*[3] operated within the framework of the same model and applied the gradient expansion technique to a skyrmion of large dimensions so that to derive analytically expressions for the energy and number of particles. Their results were revised by Bychkov *et al.*,[4] who developed a technique for calculations in any order of the gradient expansion. This model was also used in calculating the effective action[5] with a topological term (see also the discussion in Ref. 6). Experimental observation of such excitations has remained a pressing problem, because the first report that skyrmions had been detected using NMR techniques[7] were questioned in a later publication.[8]

The approximation of functions projected on a single Landau level is usually justified by the large cyclotron energy $\hbar\omega_c$ in comparison with the Coulomb energy, which is of the order of $e^2/kl_{\mathscr{H}}$, where $l_{\mathscr{H}}^2=c\hbar/e\mathscr{H}$ and k is the dielectric constant. Calculations published to date are very involved and based on assumptions that are difficult to prove. The final expressions for the energy and density are obtained after lengthy calculations and do not permit a clear physical interpretation of the results. In this paper we show that the approximation of projected functions is insufficient for an adequate description of a skyrmion. The inclusion of adjacent Landau levels gives rise to a substantial change in the energy and allows us to present an easily understandable physical model for interpretation of basic results. Our preliminary results were published earlier,[9] and this paper presents a more detailed report containing results based on an appropriate gradient expansion.

Skyrmions correspond to a nonuniform rotation of spinors, i.e., second-quantization operators for electrons, using a nonuniform rotation matrix $U(\mathbf{r})$. The initial spinors ψ are expressed in terms of new spinors χ through the expression $\psi(\mathbf{r})=U(\mathbf{r})\chi(\mathbf{r})$. The matrix $U(\mathbf{r})$ is parametrized using the three Euler angles:

$$U(\mathbf{r})=U_z(\gamma(\mathbf{r}))U_y(\beta(\mathbf{r}))U_z(\alpha(\mathbf{r})),$$

where

$$U_z(\alpha)=\cos\frac{\alpha}{2}+i\sin\frac{\alpha}{2}\sigma_z,$$

$$U_y(\beta)=\cos\frac{\beta}{2}+i\sin\frac{\beta}{2}\sigma_y,$$

and σ_x, σ_y, σ_z are the Pauli matrices. At large distances from the core and with a finite g-factor for the electrons, the average spin should be aligned with the applied magnetic field. Therefore the angle β, which is measured with respect to the magnetic field vector, should rapidly (as can be shown, exponentially) drop to zero as $r\to\infty$. The matrix $U(\mathbf{r})$ is assumed to have no singularities for all $\mathbf{r}$, which is equivalent to the absence of singularities of the matrix

$$A_k=-iU^+\frac{\partial U}{\partial x_k}=\Omega_k^l(\mathbf{r})\sigma_l,$$

where $k=x,y$ and $l=x,y,z$, and the Pauli matrices are

$$\sigma_x=\begin{pmatrix}0&1\\1&0\end{pmatrix},\quad \sigma_y=\begin{pmatrix}0&-i\\i&0\end{pmatrix},\quad \sigma_z=\begin{pmatrix}1&0\\0&-1\end{pmatrix}.$$

The expressions for Ω_k^l can be easily derived by directly differentiating $U(\mathbf{r})$:

$$\Omega_k^z=\frac{1}{2}(\partial_k\alpha+\cos\beta\,\partial_k\varphi)$$

$$\Omega_k^x=\frac{1}{2}(\sin\beta\cos\alpha\,\partial_k\varphi-\sin\alpha\,\partial_k\beta),\tag{1}$$

$$\Omega_k^y=\frac{1}{2}(\cos\alpha\,\partial_k\beta+\sin\beta\sin\alpha\,\partial_k\varphi).$$

The nontrivial topology generated by the matrix $U(\mathbf{r})$ is related to properties of the mappings $\alpha(\mathbf{r})$ and $\varphi(\mathbf{r})$, where $\mathbf{r}$ traverses a circle of large radius. The degree of the mapping of a plane to a sphere and parametrized by angles φ and β equals the degree of the circle-to-circle mapping, i.e., the winding number, which is a characteristic of a vortex singularity in $\varphi(\mathbf{r})$. In order to make $\Omega_k^l(\mathbf{r})$ nonsingular, the pointlike singularity in $\varphi(\mathbf{r})$ should coincide with the singularity in $\alpha(\mathbf{r})$ and be located at a point where $\cos\beta=-1$. Thus, the matrix U should contain all three Euler angles, and the corresponding spinor $\psi(\mathbf{r})$ has a vortex singularity at large distances with an integer quantum number because the wave functions are single-valued. Therefore a more appropriate term is nonsingular vortices whose core is defined by a skyrmion, analogous to ^{3}He,[10] although, in contrast to the case of ^{3}He, winding numbers are arbitrary integers, not only even numbers. The integral

$$\frac{1}{2\pi}\int \operatorname{curl}\,\mathbf{\Omega}^z d^2r=Q$$

is a topological invariant and can be expressed in terms of the phase change in the spinor ψ on a contour of large radius.

In a transformation defined by the matrix U, the original Lagrangian of electrons with a pair interaction in a magnetic field, i.e.,

$$L=\int\left[i\psi^+\frac{\partial\psi}{\partial t}-\frac{1}{2m}\psi^+(-i\partial_k-A_{0k})^2\psi\right]d^2r\,dt+\frac{1}{2}\int V(\mathbf{r}-\mathbf{r}')\psi^+(\mathbf{r})\psi^+(\mathbf{r}')\psi(\mathbf{r}')\psi(\mathbf{r})d^2r'\,d^2r\,dt-gH\int\psi^+\sigma_z\psi d^2r\,dt, \tag{2}$$

goes over to a Lagrangian for the spinors χ:

$$L'=\int i\chi^+\left[\frac{\partial\chi}{\partial t}-\Omega_t^l\sigma_l\chi-\frac{1}{2m}(i\partial_k-A_{0k}+\Omega_k^l\sigma_l)^2\chi\right]d^2r\,dt-\frac{1}{2}\int V(\mathbf{r}-\mathbf{r}')\chi^+(\mathbf{r})\chi^+(\mathbf{r}')\chi(\mathbf{r}')\chi(\mathbf{r})d^2r'\,d^2r\,dt+g\mathcal{H}\int U^+\sigma_zU\chi d^2r\,dt. \tag{3}$$

We assume that the matrix U is also a function of time, Ω_t^l is a variable similar to that defined by Eq. (1) but contains differentiation with respect to time, and A_0 is the vector potential of a constant magnetic field. The Lagrangian (3) can be readily derived through direct differentiation using derivatives of the identity $U^+U=1$.

The dimensions of the skyrmion core are determined by the competition between the Coulomb interaction, which tends to enlarge the region with a variable charge density and large derivatives of U, and the Zeeman energy, which, on the contrary, tends to contract the region containing spins with the unfavorable orientation. Almost all of the Coulomb energy is the contribution from the region within the range at which the change in the Zeeman energy is comparable to the Coulomb energy, and beyond this range it does not change. At larger distances the only contribution is the Zeeman energy and the energy due to the nonuniformity of the spin alignment, and the competition between them causes the departure of the spin direction from its optimum value to go to zero exponentially. If the g-factor is small, the core region is fairly large, so derivatives of U are small, which allows us to use the gradient expansion in calculating the physical parameters. In this paper, we discuss such a situation, and our attention is focused on the topologically invariant terms, whose contribution is not changed when the matrix U is deformed. This allows us to ignore the Zeeman energy or take it into account in first-order perturbation theory.

The effective action, which depends on U, is calculated by integrating over the fermions the corresponding expression for the partition function and is expressed by the formula[11] $S=i\,\mathrm{Tr}\,\ln G$, where G is the electron Green's function, and the trace is calculated by summing over both spin and space-time variables. This action will be calculated using an expansion in terms of the gradients of U and the Hartree–Fock approximation, whose applicability will be justified below.

2. GREEN'S FUNCTION IN THE HARTREE–FOCK APPROXIMATION

In calculating the Green's function, we use the Hartree–Fock approximation, which is accurate when the occupation number of the Landau levels is odd within an error of order $V_{\mathrm{int}}/\hbar\omega_c$, which is assumed to be small. This approach allows us to express the Hamiltonian in the Hartree–Fock approximation:

$$H=\int\chi^+\left[\Omega_t^l\sigma_l+\frac{1}{2m}(-i\partial_k-A_{0k}+\Omega_k^l\sigma_l)^2\right]\chi d^2r+\int V(\mathbf{r}-\mathbf{r}')\langle\chi^+(\mathbf{r}')\chi(\mathbf{r}')\rangle\chi^+(\mathbf{r})\chi(\mathbf{r})d^2r'\,d^2r-\int V(\mathbf{r}-\mathbf{r}')\langle\chi^+(\mathbf{r}')\sigma_l\chi(\mathbf{r})\rangle\chi^+(\mathbf{r})\sigma_l\chi(\mathbf{r}')\times d^2r\,d^2r' \tag{4}$$

(the term responsible for the interaction is transformed to the sum of the exchange and direct interactions, and the small Zeeman energy is neglected). In the direct interaction, the Fourier component of zero momentum corresponding to a neutralizing background charge can be omitted (see, for example, Ref. 11).

We will assume that all mean values are close to the uniform values of parameters for a filled Landau level. Our analysis is limited to the case of uniform exchange, when the difference $\mathbf{r}-\mathbf{r}'$ can be neglected, which formally corresponds to a range of $V(\mathbf{r})$ smaller than the magnetic length. The exclusion of nonlocal exchange is probably not important and does not affect topological terms, but it makes all calculation significantly easier. The final results can be easily generalized to the case of nonlocal exchange. Note also that a model with a similar Hamiltonian arises in calculations of the energy of electrons which belong to one Landau level. As a result, we obtain a model with the Hamiltonian

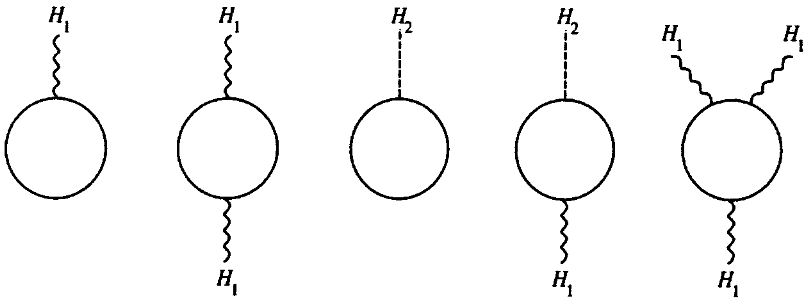

FIG. 1.

$$H=\int\left[\chi^{+}\Omega_{t}^{l}\sigma_{l}\chi^{+}+\frac{1}{2m}\chi^{+}(-i\partial_{k}-A_{0k}+\Omega_{k}^{l}\sigma_{l})^{2}\chi-\gamma\rho\chi^{+}\sigma_{l}n_{l}\chi^{+}+V_{0}\rho\chi^{+}\chi\right]d^{2}r, \tag{5}$$

where γ and V_0 are the constants of the exchange interaction and direct interaction, respectively, $\mathbf{n}$ is the unit vector aligned with the average spin direction, and ρ is the mean density. Assuming that the rotation velocities Ω^l_μ and their derivatives $\partial\Omega\sim\Omega^2$ are small, we calculate the Green's function using perturbation theory. The Hamiltonian can be expressed in the form $H=H_0+H_1+H_2$, where

$$H_{0}=\int\chi^{+}\left[\frac{1}{2m}(-i\partial_{k}-A_{0k})^{2}-\gamma\rho\sigma_{l}n_{l}-\mu\right]\chi d^{2}r, \tag{6}$$

$$H_{1}=\frac{1}{m}\int\chi^{+}[\Omega_{k}^{l}\sigma_{l}(-i\partial_{k}-A_{0k})+\Omega_{t}^{l}\sigma_{l}]\chi d^{2}r, \tag{7}$$

$$H_{2}=\frac{1}{2m}\int\chi^{+}\left[(\Omega_{k}^{l}\sigma_{l})^{2}-i\frac{\partial\Omega_{k}^{l}}{\partial r_{k}}\sigma_{l}\right]\chi d^{2}r. \tag{8}$$

We employ the grand canonical ensemble and introduce a chemical potential μ. The unimportant constant of direct interaction is set to zero, as in the case of Coulomb interaction.

The Green's function for the bare Hamiltonian is the Green's function for noninteracting electrons in a constant magnetic field, where, we assume that in the highest occupied Landau level s only the lower-spin sublevel is filled. In what follows, we consider for simplicity the case when the lowest level with $s=0$ is occupied, so that the Green's function has the form

$$G_{0}(\mathbf{r},\mathbf{r}',t,t')=-i\langle T\chi(\mathbf{r},t)\chi^{+}(\mathbf{r}',t')\rangle=\sum_{p,s}\int g_{s}(\omega)e^{i\omega(t'-t)}\Phi_{sp}(\mathbf{r})\Phi_{sp}^{*}(\mathbf{r}')\frac{d\omega}{2\pi}. \tag{9}$$

Here T is the time-ordering operator for fermion operators, summation is performed over all s and p, and the spin matrices $g_s(\omega)$ correspond to the filling of the sublevel $s=0$ with spins directed along the average spin aligned with the z-axis. All the other states are vacant. The normalized functions $\Phi_{sp}(\mathbf{r})$ correspond to eigenfunctions of Landau levels. Here we use the Landau gauge. We select a system of units in which the applied magnetic field is $\mathscr{H}=1$, the magnetic length is $l_{\mathscr{H}}=1$, and $\hbar=1$.

For the Hamiltonian (6) the matrices $g_s(\omega)$ can be easily calculated:

$$g_{0}(\omega)=\frac{1}{\omega+(\gamma\rho-i\delta)\sigma_{z}+\mu}, \tag{10}$$

$$g_{s}(\omega)=\frac{1}{\omega+\gamma\rho\sigma_{z}-s/m+\mu+i\delta}, \tag{11}$$

where $\delta\to 0$ and the chemical potential includes the energy $1/2m$ of the lowest level.

Expression (9) allows us to develop a perturbation theory for the full Green's function $G=G_0+G_1+G_2+\dots$ The corresponding graphs for the action S are shown in Fig. 1. In calculations it is convenient to express the operator in Eq. (7) in the form

$$\frac{1}{m}\Omega_{k}^{l}\sigma_{l}(-i\partial_{k}-A_{0k})=\frac{1}{m}(\Omega_{+}^{l}\pi^{-}+\Omega_{+}^{l}\pi^{+})\sigma_{l}. \tag{12}$$

The operator $\pi^{+}\Phi_{sp}=\sqrt{2(s+1)}\Phi_{(s+1)p}$ raises the Landau index, and the operator $\pi^{-}\Phi_{sp}=\sqrt{2}\Phi_{(s-1)p}$ lowers the Landau index, which is a direct consequence of properties of oscillator functions, for which

$$\Omega_{+}^{l}=-\frac{i\Omega_{x}^{l}+\Omega_{y}^{l}}{2},\quad \Omega_{-}^{l}=\frac{i\Omega_{x}^{l}-\Omega_{y}^{l}}{2}. \tag{13}$$

Let us calculate the correction to the first order in Ω to the Green's function:

$$G_{1}(\mathbf{r},\mathbf{r}',t,t')=\int e^{-i\omega(t-t')}g_{s}(\omega)\Phi_{s,p}(\mathbf{r})\Phi_{s,p}^{*}(\mathbf{r}_{1})\times\left\{\frac{1}{m}[\Omega_{+}^{l}(\mathbf{r}_{1})\pi^{-}+\Omega_{-}^{l}(\mathbf{r}_{1})\pi^{+}]+\Omega_{t}^{l}(\mathbf{r}_{1})\right\}\sigma_{l}g_{s'}(\omega')e^{-i\omega'(t_{1}-t')}\times\Phi_{s'p'}(\mathbf{r}_{1})\Phi_{s'p'}^{*}(\mathbf{r}')\frac{d\omega}{2\pi}\frac{d\omega_{1}}{2\pi}d^{2}r_{1}dt_{1}. \tag{14}$$

We are interested in the Green's function $G(\mathbf{r},\mathbf{r};t,t+\delta)$, which determines the density. In this case only terms with $s=0$, $s'=1$, $s=1$, $s'=0$, and $s=s'=0$ are nonzero, the rest vanish because of analytical properties of g_s for $s>0$. In addition, the difference between t and t' can be neglected to within terms of order m owing to the fast oscillations of one of the Green's functions. In the initial stage, we also neglect the term with Ω_t^l, which can be easily calculated. The integrand in Eq. (14) decays rapidly as a function of $|\mathbf{r}-\mathbf{r}_1|$ larger then the magnetic length, so we can expand $\Omega(\mathbf{r}_1)$ in powers of the difference $\mathbf{r}-\mathbf{r}_1$ and retain only linear terms. Summation over p yields the following expression:

$$\begin{aligned} &G_1(\mathbf{r},\mathbf{r},t,t+\delta)\\ &\quad=\frac{\sqrt{2}}{m}\int g_0\sigma_l g_0 e^{i\omega\delta}\frac{\partial\Omega_-^l}{\partial r_k}R_{00}(\mathbf{r},\mathbf{r}_1)R_{10}(\mathbf{r}_1,\mathbf{r})d^2r_1\frac{d\omega}{2\pi}\\ &\quad+\frac{\sqrt{2}}{m}\int g_0(\omega)\sigma_l g_1 e^{i\omega\delta}\frac{d\omega}{2\pi}\int R_{00}(\mathbf{r},\mathbf{r}_1)R_{01}(\mathbf{r}_1,\mathbf{r})\\ &\quad\times(r_1-r)_k\frac{\partial\Omega_-^l}{\partial r_k}d^2r_1+\frac{1}{m}\int g_1(\omega)\sigma_l g_0(\omega)e^{i\omega\delta}\frac{d\omega}{2\pi}\\ &\quad\times\int R_{11}(\mathbf{r},\mathbf{r}_1)R_{10}(\mathbf{r}_1,\mathbf{r})(r_1-r)_k\frac{\partial\Omega_+^l}{\partial r_k}d^2r_1. \end{aligned}\tag{15}$$

We have introduced the functions

$$R_{00}(\mathbf{r},\mathbf{r}_1)=\frac{1}{2\pi}\exp\left[-\frac{(\mathbf{r}-\mathbf{r}_1)^2}{4}\right],\tag{16}$$

$$R_{11}(\mathbf{r},\mathbf{r}_1)=\frac{1}{2\pi}\left[1-\frac{(\mathbf{r}-\mathbf{r}_1)^2}{2}\right]\exp\left[-\frac{(\mathbf{r}-\mathbf{r}_1)^2}{4}\right],\tag{17}$$

$$R_{10}(\mathbf{r}_1,\mathbf{r})=\frac{1}{2\pi}\frac{x_1-x-i(y_1-y)}{\sqrt{2}}\exp\left[-\frac{(\mathbf{r}-\mathbf{r}_1)^2}{4}\right],\tag{18}$$

$$R_{01}(\mathbf{r}_1,\mathbf{r})=\frac{1}{2\pi}\frac{x-x_1-i(y_1-y)}{\sqrt{2}}\exp\left[-\frac{(\mathbf{r}-\mathbf{r}_1)^2}{4}\right].\tag{19}$$

When we integrate with respect to $\mathbf{r}_1$, the term that does not contain derivatives of Ω vanishes because its integrand is an odd function. The integrals in Eq. (15) are easily calculated, and we obtain, using Eqs. (13), (11), and (10),

$$\begin{aligned} G_1'(\mathbf{r},\mathbf{r},t,t+\delta)&=\frac{1}{4m\gamma}\frac{\sigma_l-\sigma_z\sigma_l\sigma_z}{2}(\operatorname{div}\mathbf{\Omega}^l-i\operatorname{curl}\mathbf{\Omega}^l)\\ &+\frac{1}{2\pi}\left[\frac{\sigma_z\sigma_l-\sigma_l\sigma_z}{4}\operatorname{div}\mathbf{\Omega}^l\right.\\ &\left.-i\frac{(1+\sigma_z)\sigma_l+\sigma_l(1+\sigma_z)}{4}\operatorname{curl}\mathbf{\Omega}^l\right], \end{aligned}$$

which includes only the main, spin-independent part $g_1\sim m$. In Eq. (14) for G_1 the term containing Ω_t^l should take into account only the case $s=s'=0$, since all other combinations yield values of order m, which can be neglected. Only the terms with poles of first order in ω contribute, and this contribution is easy to calculate:

$$G_1''=-\frac{i}{2\pi}\Omega_t^l\frac{\sigma_l-\sigma_z\sigma_l\sigma_l}{4\gamma\rho}.$$

The final expression has the form

$$\begin{aligned} G_1(\mathbf{r},\mathbf{r}',t,t+\delta)=\frac{1}{2\pi}&\left[\frac{\sigma_z\sigma_l-\sigma_l\sigma_z}{4}\operatorname{div}\mathbf{\Omega}^l\right.\\ &\left.-i\frac{(1+\sigma_z)\sigma_l+\sigma_l(1+\sigma_z)}{4}\operatorname{curl}\mathbf{\Omega}^l\right]\\ &-i\Omega_t^l\frac{\sigma_l-\sigma_z\sigma_l\sigma_z}{8\pi\gamma\rho}\\ &+\frac{1}{4m\gamma}\frac{\sigma_l-\sigma_z\sigma_l\sigma_z}{2}\\ &\times(\operatorname{div}\mathbf{\Omega}^l-i\operatorname{curl}\mathbf{\Omega}^l). \end{aligned}\tag{20}$$

For the density $\rho=-i\operatorname{Tr}G(\mathbf{r},\mathbf{r},t,t+\delta)$ we obtain

$$\rho(\mathbf{r},t)=\frac{1}{2\pi}(1-\operatorname{curl}\mathbf{\Omega}^z).\tag{21}$$

This result was first obtained from phenomenological considerations.[1] In the case of nonprojected functions, this result has a clear physical interpretation: the lowest Landau level is fully occupied in the effective local magnetic field $\mathcal{H}_{\text{eff}}=1-\operatorname{curl}\mathbf{\Omega}^z$, which corresponds to the density $\rho=1/2\pi l^2(\mathcal{H}_{\text{eff}})$, where $l(\mathcal{H}_{\text{eff}})$ is the magnetic length in the effective field.

Although the calculations have been performed in the first order in Ω, the result, however, contains derivatives, which means that second-order terms are present. Therefore we should calculate a second-order correction to the Green's function expressed in the symbolic notation as

$$\begin{aligned} G_2(\mathbf{r},\mathbf{r},t,t+\delta)=\frac{1}{m^2}&G_0(\Omega_+^l\pi^-+\Omega_-^l\pi^+)\sigma_l G_0(\Omega_+^{l'}\pi^-\\ &+\Omega_-^{l'}\pi^+)\sigma_{l'}G_0+G_0H_2G_0. \end{aligned}$$

Since it is a second-order correction, derivatives of Ω can be neglected. The contribution due to the last term is zero because in this approximation only states with $s=0$ should be taken into account in the expression for G_2, as a result, we have a second-order pole in the density, and integration over ω yields zero. The first term contains contributions proportional to $g_0g_1g_0$ and $g_1g_0g_1$, where g corresponds to one of the three Green's functions in this expression. The integrals over the spatial variables and p are easily calculated, and we obtain

$$\begin{aligned} G_2=\frac{1}{m^2 2\pi}\int&[g_0\sigma_l g_1\sigma_{l'}g_0\Omega_+^l\Omega_-^{l'}\\ &+g_1\sigma_l g_0\sigma_{l'}g_1\Omega_-^l\Omega_+^{l'}]e^{i\omega\delta}\frac{d\omega}{2\pi}d^2r\,dt. \end{aligned}$$

The second-order correction to the density includes the trace of this expression. Transposing the matrices under the trace, we get in the first term in brackets the square of the diagonal matrix $g_0^2(\omega)$, which has a second-order pole. Using the usual rule for calculating a residue due to a pole in the upper half-plane, we obtain

$$\operatorname{Tr}G_2=\frac{1}{2\pi m^2}\int[-2g_1^2\Omega_+^l\Omega_-^l+2g_1^2\Omega_+^l\Omega_-^l]d^2r\,dt=0.$$

Thus, including terms of up to the second order, the density is expressed by Eq. (21), which is identical to the result obtained in Ref. 3.

3. CALCULATION OF ACTION, ENERGY, AND NUMBER OF PARTICLES

We shall calculate the action by the formula $S=i\mathrm{Tr}\ \ln G$ using the perturbation theory for G and retaining only the part which depends on the rotation operator:

$$S=i\ \mathrm{Tr}\bigg[H_1G_0+\frac{1}{2}H_1G_0H_1G_0+H_2G_0+\frac{1}{2}(H_2G_0H_1G_0 +H_1G_0H_2G_0)+\frac{1}{3}H_1G_0H_1G_0H_1G_0+\dots\bigg].$$

In this section, we limit our calculations to the second order of the perturbation theory. The calculations are similar to the calculation of the Green's function. The action in the first order has the form

$$S_1=i\ \mathrm{Tr}\int\Omega_t^l\sigma_lg_0(\omega)e^{i\omega\delta}\frac{d^2rdt}{2\pi}\frac{d\omega}{2\pi} +i\ \mathrm{Tr}\int\sigma_lg_0(\omega)e^{i\omega\delta}\frac{d\omega}{2\pi}(\Omega_+^l\pi^- +\Omega_-^l\pi^+)\Phi_{0p}(r)\Phi_{0p}^*(r)d^2rdt.$$

The second integral is evaluated using integration by parts, and we finally have

$$S_1=-\frac{1}{2\pi}\int\Omega_t^zdrdt-\frac{1}{2\pi}\frac{1}{2m} \times\int(i\ \mathrm{div}\ \mathbf{\Omega}^z-\mathrm{curl}\ \mathbf{\Omega}^z)d^2rdt. \tag{22}$$

The action in the second order is composed of two terms, one of which contains a product of two H_1:

$$S_2'=\frac{i}{2m^2}\mathrm{Tr}\int(\Omega_-^l\pi^++\Omega_+^l\pi^-)\sigma_lg_s(\omega)\Phi_{sp}(\mathbf{r})\Phi_{sp}^*(\mathbf{r}') \times(\Omega_-^{l'}\pi^++\Omega_+^{l'}\pi^+)\sigma_{l'}g_{s'}(\omega)\Phi_{s'p'}(\mathbf{r}')\Phi_{s'p'}^* \times(\mathbf{r})e^{i\omega\delta}d^2r'd^2rdt\frac{d\omega}{2\pi}.$$

In this expression, we neglect derivatives of Ω. Only terms with $s=0$, $s'=1$ and $s=1$, $s'=0$ are nonvanishing. Using the properties of the operators π^+ and π^- and calculating the integral, one can easily obtain an expression for the full second-order action (the contribution of the term with H_2 is calculated similarly):

$$S_2=\frac{1}{4\pi}\int\mathrm{Tr}[\sigma_{l'}\sigma_l(1+\sigma_z)+\sigma_l\sigma_{l'}] \times(1+\sigma_z)\Omega_-^l\Omega_+^{l'}d^2rdt-\frac{1}{2\pi} \times\int\bigg[\frac{(\mathbf{\Omega}^l)^2}{2m}-\frac{i}{2m}\frac{\partial\Omega_k^z}{\partial r_k}\bigg]d^2rdt.$$

The first integral contains a symmetrical part corresponding to the case $l=l'$ and is cancelled out by the second integral. The remaining asymmetrical part contains only $l,l'=x,y$ and can be rewritten using the identity $\mathrm{curl}\ \mathbf{\Omega}^z =2(\Omega_x^x\Omega_y^y-\Omega_y^x\Omega_x^y)$, which can be derived by differentiating the identity $U^+U=1$. As a result, we have an expression for the action in second order:

$$S_2=\frac{1}{2m}\int\mathrm{curl}\ \mathbf{\Omega}^z\frac{d^2rdt}{2\pi}+i\int\mathrm{div}\ \mathbf{\Omega}^z\frac{d^2rdt}{2\pi}. \tag{23}$$

The full expression for the action including terms up to second order with due account of Eq. (22) has the form

$$S=\int\Omega_t^z\frac{d^2rdt}{2\pi}+\frac{1}{m}\int\mathrm{curl}\ \mathbf{\Omega}^z\frac{d^2rdt}{2\pi} -\mu\int\mathrm{curl}\ \mathbf{\Omega}^z\frac{d^2rdt}{2\pi}, \tag{24}$$

where we have added the term with the chemical potential.

These results are in full agreement with those reported in our preliminary publication[9] and have a simple physical interpretation. The electrons locally fully occupy the lowest spin sublevel in the local effective magnetic field $\mathscr{H}_{\mathrm{eff}}=1-\mathrm{curl}\ \mathbf{\Omega}^z$, and the electron density equals the local density of states. This circumstance justifies the use of the Hartree–Fock approximation with an accuracy of order $V_{\mathrm{int}}/\hbar\omega_c$ in the same manner as it does for the fully filled Landau level. The effective magnetic field is lower than the applied field for skyrmions with positive Q. Note that the gap between local spin levels is determined by the exchange energy. Electrons with spins aligned in the direction opposite to the mean spin "see" the effective magnetic field $\mathscr{H}_{\mathrm{eff}}=1+\mathrm{curl}\ \mathbf{\Omega}^z$.

Let us analyze in detail the expression for energy in a steady state with due account of the interaction terms. In the case of Coulomb interaction, one must take account of the neutralizing positively charged background, which eliminates the zeroth Fourier component, so the expression for the direct interaction does not contain a term linear in density, but only the quadratic expression

$$E_{\mathrm{pot}}=\frac{1}{2}\int\frac{e^2}{|\mathbf{r}-\mathbf{r}'|}\mathrm{curl}\ \mathbf{\Omega}^z(\mathbf{r})\mathrm{curl}\ \mathbf{\Omega}^z(\mathbf{r}')\frac{d^2rd^2r'}{(2\pi)^2}.$$

The leading term in the exchange energy is linear in the density perturbation. In order to calculate this term, we should obtain the exchange energy density as a function of magnetic field for the density of a fully occupied Landau level, $-(e^2/2\pi l_{\mathscr{H}}^3)\sqrt{\pi/2}$, differentiate it with respect to magnetic field, and multiply by the correction to the effective magnetic field, which yields the perturbation of the exchange energy

$$E_{\mathrm{ex}}=\int\frac{3e^2}{4\sqrt{2\pi}l_{\mathscr{H}}}\mathrm{curl}\ \mathbf{\Omega}^zd^2r.$$

Moreover, we must take into account the correction due to nonuniformity of the mean spin direction, $(1/2)J\int(\partial n^i/\partial r_k)^2d^2r$, where $J=(1/16\sqrt{2\pi})e^2/l_{\mathscr{H}}$.[3,4] We must also include the Zeeman energy. The resulting equation yields the change in the thermodynamic energy due to formation of a vortex:

$$F=\delta\langle H-\mu N\rangle=-\frac{\hbar\omega_c}{2}Q+\frac{3e^2}{2l_{\mathcal{H}}}\sqrt{\frac{\pi}{2}}\,Q$$
$$+\frac{e^2}{2}\int\frac{\operatorname{curl}\boldsymbol{\Omega}^z(\mathbf{r})\operatorname{curl}\boldsymbol{\Omega}^z(\mathbf{r}')}{(2\pi)^2|\mathbf{r}-\mathbf{r}'|}d^2r\,d^2r'$$
$$+\int\left[\frac{1}{2}J\left(\frac{\partial n_i}{\partial r_k}\right)^2+g\mathcal{H}\cdot\mathbf{n}\,\frac{1}{2\pi l^2_{\mathcal{H}}}\right]d^2r. \qquad (25)$$

The chemical potential in this equation is set to $\mu=\hbar\omega_c/2$, which corresponds to filling of the lower spin sublevel at a large distance from the vortex core. As we assumed at the beginning, the cyclotron energy is much larger than the interaction energy. For this reason F is negative at positive topological number Q, which determines the change in the electron number, $\delta N=-Q$, due to vortex formation. Thus, generation of nonsingular vortices is thermodynamically advantageous at the chemical potential corresponding to full occupation of the lower Landau spin sublevel, and vortices should be generated spontaneously. The gain in the thermodynamic potential increases with Q.

One can also calculate the energy of a one-particle excitation in the presence of a vortex. This can be done by studying the poles of the Green's function $G(\mathbf{r},\mathbf{r},\omega)$, but a more convenient approach is based on the fact that this energy corresponds to a variational derivative of the full energy with respect to the local density of electrons with different spin orientations. By presenting F in the form of a functional of the densities ρ_+ and ρ_-, where the signs correspond to the spin alignments parallel and opposite to the local mean spin, we obtain

$$F=\int\left\{\frac{\hbar\omega_c(\mathcal{H}^+_{\text{eff}})\rho_+ +\hbar\omega_c(\mathcal{H}^-_{\text{eff}})\rho_-}{2}-\mu(\rho_+ +\rho_-)\right.$$
$$\left.-\frac{1}{2}(\rho_+ -\rho_-)^2\left[\gamma'-J'\left(\frac{\partial n^l}{\partial r_k}\right)^2\right]\right\}d^2r$$
$$+\int\frac{e^2}{2|\mathbf{r}-\mathbf{r}'|}\Big[\delta\rho_+(\mathbf{r}+\delta\rho_-(\mathbf{r})][\delta\rho_+(\mathbf{r}')$$
$$+\delta\rho_-(\mathbf{r}')]d^2r\,d^2r'+\int g\mathcal{H}\cdot\mathbf{n}(\rho_+ -\rho_-)d^2r. \qquad (26)$$

In this expression

$$\gamma'\rho_+^2=\frac{e^2}{2\pi l^3_{\mathcal{H}}}\sqrt{\frac{\pi}{2}}-\frac{3e^2}{4\pi l_{\mathcal{H}}}\sqrt{\frac{\pi}{2}}\operatorname{curl}\boldsymbol{\Omega}^z,\qquad J'\rho_+^2=J.$$

By varying with respect to ρ_+ and ρ_-, we obtain the hole energy in the fully occupied state:

$$\epsilon_h=-\frac{\delta F}{\delta\rho_+}=\frac{2e^2}{l_{\mathcal{H}}}\sqrt{\frac{\pi}{2}}\left(1-\frac{3}{2}l^2_{\mathcal{H}}\operatorname{curl}\boldsymbol{\Omega}^z\right)$$
$$+\frac{\hbar\omega_c}{2}\operatorname{curl}\boldsymbol{\Omega}^z+\int\frac{e^2}{|\mathbf{r}-\mathbf{r}'|}\operatorname{curl}\boldsymbol{\Omega}^z(\mathbf{r}')\,\frac{d^2r'}{2\pi}$$
$$-2\pi Jl^2_{\mathcal{H}}\left(\frac{\partial n^l}{\partial r_k}\right)^2-g\mathcal{H}\cdot\mathbf{n}. \qquad (27)$$

Similarly, the energy of an electron with reversed spin is

$$\epsilon_e=\frac{2e^2}{l_{\mathcal{H}}}\sqrt{\frac{\pi}{2}}\left(1-\frac{3l^2_{\mathcal{H}}}{2}\operatorname{curl}\boldsymbol{\Omega}^z\right)+\frac{\hbar\omega_c}{2}\operatorname{curl}\boldsymbol{\Omega}^z$$
$$-\int\frac{e^2}{|\mathbf{r}-\mathbf{r}'|}\operatorname{curl}\boldsymbol{\Omega}^z(\mathbf{r}')\,\frac{d^2r'}{2\pi}+2\pi Jl^2_{\mathcal{H}}\left(\frac{\partial n^l}{\partial r_k}\right)^2$$
$$-g\mathcal{H}\cdot\mathbf{n}. \qquad (28)$$

These results are valid when the perturbation theory in Ω applies, which means that the energy correction for one-particle excitations are small in comparison with the initial energy gap separating the lower spin sublevel from the upper one. Thus, the perturbation theory applies only if the small additional term in the expression for the one-particle energy, $(\hbar\omega_c/2)l^2_{\mathcal{H}}\operatorname{curl}\boldsymbol{\Omega}^z\sim(\hbar\omega_c/2)l^2_{\mathcal{H}}/L_c^2$ is small in comparison to the leading term, namely, the exchange energy $\sim e^2/l_{\mathcal{H}}$. Hence the vortex core dimension should be sufficiently large, $L_c\gg l_{\mathcal{H}}\sqrt{\hbar\omega_c/e^2}$. This condition requires that the g-factor should be sufficiently small, since the core dimension is determined by the competition between the Zeeman and Coulomb energies, $g\mathcal{H}\rho L_c^2\sim e^2/L_c$. It follows that the condition

$$L_c^3\sim e^2l^2_{\mathcal{H}}/g\mathcal{H}\gg l^3_{\mathcal{H}}(\hbar\omega_c l_H/e^2)^{3/2}$$

should hold.

Note that addition of an electron with inverted spin adds the exchange energy to the thermodynamic energy and subtracts the energy of Coulomb interaction with the skyrmion charge (if Q is positive), while all other terms are much smaller because the gradients are small. In this case, the Coulomb energy increases with the total core charge, while the exchange energy is determined locally, and its leading term is independent of the vortex charge. This permits formation of both metastable and bound states below the chemical potential level. In this case the total number of electrons with ''wrong'' spin orientations in magnetic field is a unit less than for a vortex without a bound electron. The formation of a vortex still lowers the thermodynamic potential. In real experimental conditions the ratio between the cyclotron and Coulomb energies is not very high, and the g-factor is not too small, so the statements above should be confirmed by numerical calculations.

4. HOPF'S INVARIANT IN THE ACTION

In addition to the topological number Q, which is the degree of the mapping, there is the Hopf topological invariant corresponding to the degree of linking of lines of constant $\mathbf{n}(\mathbf{r},t)$ for the time-dependent matrix U (see, for example, Ref. 12). This invariant should be included in the expression for the action, and the coefficient in front of it should determine the skyrmion statistics or, to be exact, the phase change due to interchange of two skyrmions.[13] This coefficient was calculated by Apel and Bychkov[5] in the approximation where functions are projected on a single Landau level. This calculation, however, is based on several assumptions that are difficult to check, and the result was questioned in the discussion in Ref. 6. The authors of the latter publication refer to their earlier quasiclassical calculation of the Green's function, which uses the frequency and momentum as "good" quantum numbers, and quote their result. In this section, we present a direct calculation of this factor in the limit of a high magnetic field without any additional assumptions. To do this, one needs to find the action in third order in Ω, retaining only the terms linear in Ω_t^l, which are included in the Hopf invariant.

Using the perturbation theory for Green's function, one can easily obtain an expression for the action in the third order of the perturbation theory:

$$S=i\ \mathrm{Tr}\left[H_1G_0+\frac{1}{2}H_1G_0H_1G_0+H_2G_0+\frac{1}{2}(H_1G_0H_2G_0 +H_2G_0H_1G_0)+\frac{1}{3}H_1G_0H_1G_0H_1G_0\right]. \tag{29}$$

The terms of up to second order were calculated in the previous section, but one should keep in mind that in the terms formally of second order the time derivatives were not taken into account; they should be included in the third-order expression for the action. We will calculate systematically the various third-order terms.

Consider the term of second order in H_1 containing Ω_t^l, which was neglected in the previous section since we assumed $\Omega_t\sim\Omega^2$. After simple calculations, we have

$$\begin{aligned}S_2^1=\frac{i}{m}\int \mathrm{Tr}\ &\sigma_l g_s(\omega)\sigma_{l'}g_s'(\omega)e^{i\omega\delta}\Omega_t^l(r,t)\\ &\times\Phi_{sp}(\mathbf{r})\Phi_{sp}^*(\mathbf{r}_1)[\Omega_+^{l'}(\mathbf{r}_1,t)\pi^-\\ &+\Omega_-^{l'}(\mathbf{r}_1,t)\pi^+]\Phi_{s'p'}(\mathbf{r}_1)\\ &\times\Phi_{s'p'}^*(\mathbf{r})d^2rd^2r'dt\frac{d\omega}{2\pi}.\end{aligned} \tag{30}$$

Given the required accuracy prescribed above, there is only one term with $s=s'=0$ and terms with $s=1$, $s'=0$; $s=0$, $s'=1$. By introducing the variables $\mathbf{R}=(\mathbf{r}+\mathbf{r}_1)/2$ and $\boldsymbol{\rho}=\mathbf{r}_1-\mathbf{r}$, and expanding $\Omega_t(\mathbf{r})$ and $\boldsymbol{\Omega}(\mathbf{r}_1)$ in powers of $\boldsymbol{\rho}$ through first order, we obtain

$$\begin{aligned}S_{200}^1=\frac{i\sqrt{2}}{2m}\int \mathrm{Tr}\ &\sigma_l g_0(\omega)\sigma_{l'}g_0(\omega)e^{i\omega\delta}\left[\Omega_t^l(\mathbf{R})\frac{\partial\Omega_-^{l'}}{\partial R_k}\right.\\ &\left.-\Omega_-^{l'}(\mathbf{R})\frac{\partial\Omega_t^l}{\partial R_k}\right]R_{00}(-\boldsymbol{\rho})R_{10}(\boldsymbol{\rho})\rho_k d^2\rho d^2Rdt\frac{d\omega}{2\pi}.\end{aligned}$$

After taking into account Eqs. (10) and (11) and integrating with respect to ω and $\boldsymbol{\rho}$, we have

$$\begin{aligned}S_{200}^1=&\frac{1}{4m\gamma}\\ &\times\int [i\Omega_t^l\ \mathrm{div}\ \boldsymbol{\Omega}^l-i(\boldsymbol{\Omega}_l\nabla)\Omega_t^l\\ &-\Omega_t^l\nabla\times\boldsymbol{\Omega}^l-\boldsymbol{\Omega}^l\nabla\Omega_t^l]\ \frac{d^2rdt}{2\pi}.\end{aligned} \tag{31}$$

Similarly we calculate the terms with $s=0$, $s'=1$; $s=1$, $s'=0$, where it is only necessary to retain one pole corresponding to filled states in the expression for g_0:

$$\begin{aligned}S_{201}^1=\frac{1}{2}\int &[\Omega_t^l\nabla\times\boldsymbol{\Omega}^l+\boldsymbol{\Omega}^l\times\nabla\Omega_t^l]\ \frac{d^2rdt}{2\pi}\\ &+\frac{1}{4}\ \mathrm{Tr}\ \sigma_l\sigma_{l'}\sigma_z\int[-i\Omega_t^l\ \mathrm{div}\ \boldsymbol{\Omega}^{l'}\\ &+i\boldsymbol{\Omega}^{l'}\nabla\Omega_t^l]\ \frac{d^2rdt}{2\pi}.\end{aligned} \tag{32}$$

In addition to these terms, there is a second-order contribution with two $\boldsymbol{\Omega}^l$ discussed in the previous section, but without time derivatives. We calculate these derivatives similarly to the space derivatives by introducing the variables $T=(t+t')/2$ and $\tau=t'-t$, noting that for our purposes only terms with $s=1$, $s'=0$ and $s=0$, $s'=1$ are important since all the rest contain too many derivatives. After omitting the term without time derivatives, we have

$$\begin{aligned}S_2^2=\frac{i}{m^2}\int \mathrm{Tr}\ &\sigma_l g_0(\omega)\sigma_{l'}g_1(\omega')e^{i\omega\delta}\tau\ \exp[i(\omega\\ &-\omega')\tau]\left[\Omega_-^l\frac{\partial\Omega_+^{l'}}{\partial T}\right.\\ &\left.-\Omega_+^{l'}\frac{\partial\Omega_-^l}{\partial T}\right]\frac{d\omega\ d\omega'}{(2\pi)^2}d\tau\frac{dTd^2r}{2\pi}.\end{aligned}$$

By replacing τ with the derivative of the corresponding exponential function and integrating by parts, we obtain, using Eq. (16),

$$\begin{aligned}S_2^2=-\frac{1}{2}\int &\boldsymbol{\Omega}^l\times\frac{\partial\boldsymbol{\Omega}^l}{\partial t}\ \frac{d^2rdt}{2\pi}-\frac{i}{4}\ \mathrm{Tr}\ \sigma_{l'}\sigma_l\sigma_z\\ &\times\int\left(\boldsymbol{\Omega}^l\frac{\partial\Omega^{l'}}{\partial t}-\boldsymbol{\Omega}^{l'}\frac{\partial\boldsymbol{\Omega}^l}{\partial t}\right)\ \frac{d^2rdt}{2\pi}.\end{aligned}$$

In the calculation of the third-order terms, all terms should be expressed similarly through the derivatives of $\boldsymbol{\Omega}^l$. Using the identity $\partial_t\Omega_k^l-\partial_k\Omega_k^l=2e^{ljm}\Omega_t^j\Omega_k^m$, where e^{ljm} is the absolutely antisymmetrical unit tensor of the third rank, one can easily transform this expression to

$$\begin{aligned}S_2^2=-\frac{1}{2}\int &(\boldsymbol{\Omega}^l\times\nabla\Omega_t^l+e^{ljm}\boldsymbol{\Omega}^l\times\boldsymbol{\Omega}^m\Omega_t^j)\ \frac{d^2rdt}{2\pi}\\ &-\frac{i}{2}\ \mathrm{Tr}\ \sigma_{l'}\sigma_l\sigma_z\int(\boldsymbol{\Omega}_l\nabla\Omega_t^{l'}\\ &+2e^{l'jm}\boldsymbol{\Omega}^l\boldsymbol{\Omega}^m\Omega_t^j)\ \frac{d^2rdt}{2\pi}.\end{aligned} \tag{33}$$

Among the terms of the third order properly, the simplest is that containing H_2 and H_1:

$$\begin{aligned}S_{21}=\frac{i}{2m}\ \mathrm{Tr}\int &[(\boldsymbol{\Omega}^l)^2\\ &-i\sigma_l\ \mathrm{div}\ \boldsymbol{\Omega}^l]\Omega_t^{l'}g_0(\omega)\sigma_{l'}g_0(\omega)e^{i\omega\delta}\frac{d\omega}{2\pi}\ \frac{d^2rdt}{2\pi}.\end{aligned} \tag{34}$$

The rest contain additional derivatives. Only the term with the divergence contributes to the action:

$$S_{21}=-\frac{i}{2m\gamma}\sum_{l\neq z}\int\Omega_t^l\,\mathrm{div}\,\boldsymbol{\Omega}^l\frac{d^2rdt}{2\pi}. \tag{35}$$

The remaining terms of third order contain only H_1 with two spatial components Ω_k^l and one time component Ω_t^l:

$$\begin{aligned}S_3=\frac{i}{m^2}\int&\Omega_t^l\Phi_{sp}(\mathbf{r})\Phi_{sp}^*(\mathbf{r}_1)(\Omega_+^{l_1}\pi^-\\&+\Omega_-^{l_1}\pi^+)\Phi_{s_1p_1}(\mathbf{r}_1)\Phi_{s_1p_1}^*(\mathbf{r}_2)(\Omega_+^{l_2}\pi^-\\&+\Omega_-^{l_2}\pi^+)\Phi_{s_2p_2}(\mathbf{r}_2)\Phi_{s_2p_2}^*(\mathbf{r})d^2rd^2r_1d^2r_2dt\\&\times\int\mathrm{Tr}\,\sigma_lg_s\sigma_{l_1}g_{s_1}\sigma_{l_2}g_{s_2}e^{i\omega\delta}\frac{d\omega}{2\pi}.\end{aligned}$$

Contributions of the required order come only from terms with $s=s_2=0$, $s_1=1$ and $s=s_2=1$, $s_1=0$, and derivatives of $\boldsymbol{\Omega}$ can be omitted.

The calculation in the first case is similar to that of Eqs. (31) and (35). Using the standard formula and expressing all summands in terms of Ω_t^l and Ω^l, we obtain

$$\begin{aligned}S_3^0=-\frac{i}{m\gamma}\sum_{l\neq z}\mathrm{Tr}\,\sigma_l\sigma_{l_1}\sigma_{l_2}\int&\Omega_t^l\boldsymbol{\Omega}^{l_1}\\&\times\boldsymbol{\Omega}^{l_2}\frac{d^2rdt}{2\pi}+\frac{i}{4}\mathrm{Tr}\,\sigma_z\sigma_{l_1}\sigma_{l_2}\int\Omega_t^z\boldsymbol{\Omega}^{l_1}\boldsymbol{\Omega}^{l_2}\frac{d^2rdt}{2\pi}\\&+\frac{1}{2}\sum_{l\neq z}\int\Omega_t^z(\boldsymbol{\Omega}^l)^2\frac{d^2rdt}{2\pi}.\end{aligned} \tag{36}$$

The result for the case $s=s_2=1$, $s_1=0$ is derived in the standard manner using the expressions for traces of products of Pauli matrices:

$$\begin{aligned}S_3^1=-\frac{1}{2}\int\Omega_t^z(\boldsymbol{\Omega}^z)^2\frac{d^2rdt}{2\pi}+\frac{1}{2}\sum_{l\neq z}\int&[\Omega_t^z(\boldsymbol{\Omega}^l)^2\\&-\Omega_t^l\boldsymbol{\Omega}^z\boldsymbol{\Omega}^l]\frac{d^2rdt}{2\pi}+\frac{i}{4}\mathrm{Tr}\,\sigma_l\sigma_{l_1}\sigma_{l_2}\int\Omega_t^l\boldsymbol{\Omega}^{l_1}\\&\times\boldsymbol{\Omega}^{l_2}\frac{d^2rdt}{2\pi}.\end{aligned} \tag{37}$$

The final expression for the part of the action containing the Hopf invariant is obtained by adding the calculated terms of Eqs. (31)–(33) and (35)–(37). Let us explain this sum. The terms with $1/\gamma$ in the expressions for S_3^0, S_2^0, and S_{21} reduce to an integral of a total derivative:

$$\frac{1}{4m\gamma}\sum_{l\neq z}\int[-i\,\mathrm{div}(\Omega_t^l\boldsymbol{\Omega}^l)-\nabla\times(\Omega_t^l\boldsymbol{\Omega}^l)]\frac{d^2rdt}{2\pi}=0$$

since $\boldsymbol{\Omega}^l$ decays exponentially at large distances when $l\neq z$. Similarly, the term containing

$$-\frac{i}{4}\mathrm{Tr}\sigma_l\sigma_m\sigma_z\int\{\Omega_t^l\,\mathrm{div}\,\boldsymbol{\Omega}^m+(\boldsymbol{\Omega}^m\nabla)\Omega_t^l\}\frac{d^2rdt}{2\pi},$$

reduces to a vanishing integral over an infinitely distant surface.

The terms with $\Omega_t^z(\boldsymbol{\Omega}^l)^2$ and $\Omega_t^l(\Omega^z\boldsymbol{\Omega}^l)$ also cancel out, which can be proved using the algebraic identities for S_2^2. As a result, only skew-symmetric terms remain in the action S_3:

$$\begin{aligned}S_3=\frac{i}{4}\mathrm{Tr}\,\sigma_l\sigma_{l_1}\sigma_{l_2}\int\Omega_t^l\boldsymbol{\Omega}^{l_1}\times\boldsymbol{\Omega}^{l_2}\frac{d^2rdt}{2\pi}+\frac{1}{2}\int\Omega_t^l\nabla\\\times\boldsymbol{\Omega}^l\frac{d^2rdt}{2\pi}-\int e^{ljm}\Omega_t^j\boldsymbol{\Omega}^l\times\boldsymbol{\Omega}^m\frac{d^2rdt}{2\pi}.\end{aligned}$$

After calculating the trace and using the formula for $\nabla\times\boldsymbol{\Omega}^l$, we finally have

$$S_3=e^{ljm}\int\Omega_t^l\boldsymbol{\Omega}^j\times\boldsymbol{\Omega}^m\frac{d^2rdt}{2\pi}. \tag{38}$$

According to Refs. 12 and 13, the Hopf integer-valued invariant can be expressed in terms of $\boldsymbol{\Omega}$:

$$h=\frac{1}{2\pi^2}\int e^{ljm}\Omega_t^l\boldsymbol{\Omega}^j\times\boldsymbol{\Omega}^md^2rdt.$$

Thus, the Hopf term in the expression for action has the form

$$S^h=\pi h. \tag{39}$$

This result coincides with that given in Ref. 6 and is different from that of Ref. 5. Thus, skyrmions, in the accepted terminology,[12] are fermions.

One should keep in mind, however, that the Hopf integer-valued invariant h corresponds to a mapping of the sphere S_3 onto the sphere S_2, which requires in our case that Ω should go to zero at large $\mathbf{r}$ and t, i.e., $Q=0$. If skyrmions exist for all t, the integer-valued topological invariant characterizing the linking of curves $\mathbf{n}=\mathrm{const}$ is slightly modified.[14,15] Nonetheless, the relation between S_3 and h given above still holds, as well as the statement about the ''fermion'' nature of skyrmions.

5. CONCLUSIONS

In this paper we have presented a theory of nonsingular skyrmions for two-dimensional electron systems in a strong magnetic field. In our calculations, we have not used any assumptions except the small value of the Coulomb energy $e^2/l_{\mathscr{H}}$ in comparison with the cyclotron energy $\hbar\omega_c$ and the smallness of the g-factor. We have shown that the widely used approximation of wave functions projected on a single Landau level is not sufficient for an adequate description. The effect of adjacent Landau levels is important and leads to a modification of the expression for the thermodynamic energy of a skyrmion, namely, it reduces it by $\hbar\omega_c/2$, which is assumed to be a large value. This should lead to spontaneous formation of skyrmions with positive degree of mapping at occupation numbers close to odd integers. If the g-factor is small, and the skyrmion core dimension is accordingly large, the process has a simple physical interpretation:[9] the vortex core contains an additional effective magnetic field, whose total magnetic flux contains a number of flux quanta equal to the topological invariant, namely the degree of the mapping. Locally the Landau level is fully occupied in the total magnetic field (external plus effective magnetic fields) and separated by a gap from states with higher energies. The total number of particles is different owing to the variation in the density, which is equal to the local density of states. As a result, an electric charge develops due to elimination of a number of electrons equal to the number of effective magnetic flux quanta for positive degree of the mapping. This positive local charge can create bound electron states. Their energy with respect to the chemical potential is determined by the negative energy of interaction with the core charge and the positive exchange energy, since all local spin states with the lower energy are already occupied. Since the exchange energy is of order $e^2/l_{\mathcal{H}}$ and independent of the core dimension, unlike the direct Coulomb energy e^2/L_c, where $L_c \sim l_{\mathcal{H}}(e^2/l_{\mathcal{H}} g\mathcal{H})^{1/3}$, which decreases with the core dimension, the bound state level in our approximation should be higher than the chemical potential. In real experiments, L_c is not very different from $l_{\mathcal{H}}$, and numerical calculations are required for clarifying this situation. Note that the appearance of bound states reduces the total spin due to vortex formation. The Hopf topological term in the expression for action has also been calculated. The value of the coefficient of the Hopf invariant is identical to the quasiclassical result given in Ref. 6. Thus, skyrmions should behave like fermions. All this makes skyrmions very like the ‘‘composite’’ fermions introduced phenomenologically in Ref. 16.

The authors express their gratitude to G. E. Volovik for helpful discussions. The research reported in the paper was supported by grant RPI-273 of the US Civilian Research and Development Foundation for Independent States of the Former Soviet Union. The work was also supported by grant No. 95-05883 of the Russian Fund for Fundamental Research and by the Statistical Physics program sponsored by the Ministry of Science and Technology of Russia.

[1] S. Sondhi, A. Kahlrede, S. Kivelson, and E. Rezai, Phys. Rev. B **47**, 16418 (1993).

[2] H. Fertig, L. Brey, R. Cote, and A. MacDonald, Phys. Rev. B **50**, 11018 (1994).

[3] K. Moon, H. Mori, Kun Yang, S. Girvin, and A. MacDonald, Phys. Rev. B **51**, 5138 (1995).

[4] Yu. Bychkov, T. Maniv, and I. Vagner, Phys. Rev. B **53**, 10148 (1995).

[5] W. Apel and Yu. Bychkov, Phys. Rev. Lett. **78**, 2188 (1997).

[6] G. Volovik and V. Yakovenko, E-prints Archive Cond-Mat/9703228, 26 March, 1997.

[7] S. Barret, G. Dabbagh, L. Pfeiffer, K. West, and R. Tycko, Phys. Rev. Lett. **74**, 5112 (1995).

[8] I. Kukushkin, K. von Klitzing, and K. Eberl, Phys. Rev. B **55(16)**, (1997).

[9] S. Iordanskii and S. Plyasunov, JETP Lett. **65**, 259 (1997).

[10] M. Salomaa and G. Volovik, Rev. Mod. Phys. **59**, 533 (1987).

[11] A. Abrikosov, L. Gor'kov, and I. Dzyaloshinskiĭ, *Methods of Quantum Field Theory in Statistical Physics*, Prentice-Hall, Englewood Cliffs, NJ (1963).

[12] F. Wilczek and A. Zee, Phys. Rev. Lett. **51**, 2250 (1983).

[13] G. Volovik and V. Yakovenko, J. Phys.: Condens. Matter **1**, 5263 (1989).

[14] V. Ruutu, U. Parts, J. Koivuniemi, M. Krusius, E. Thunenberg, and G. Volovik, JETP Lett. **60**, 671 (1994).

[15] Yu. Makhlin and T. Misirpashaev, JETP Lett. **61**, 49 (1995).

[16] K. Jain, Phys. Rev. Lett. **63**, 199 (1989).

Translation provided by the Russian Editorial offic.

ERRATA

Erratum: Magnetic and structural correlations in EuMnO and BiMnO crystals in the paramagnetic temperature range [JETP 85, 156–162 (July 1997)]

E. I. Golovenchits, V. A. Sanin, and A. V. Babinskiĭ

A. F. Ioffe Physicotechnical Institute, Russian Academy of Sciences, 194021 St. Petersburg, Russia

[S1063-7761(97)02911-9]

In the title of the article, the subscripts were omitted from the formulas of the materials being studied. The correct title is ''Magnetic and structural correlations in $EuMn_2O_5$ and $BiMn_2O_5$ crystals in the paramagnetic temperature range.'' The correct name of the second author is V. A. Sanina. On page 160, in the right-hand column, in the first sentence of the second paragraph from the bottom, M^{3+} should be Mn^{3+}.

Erratum: Kinetic theory of semiconductor cascade laser based on quantum wells and wires [JETP 84, 375–382 (February 1997)]

V. F. Elesin and A. V. Krasheninnikov

Moscow State Institute of Engineering Physics, 115409 Moscow, Russia

[S1063-7761(97)03011-4]

The correct list of References should read as follows:

[1] A. F. Kazarinov and R. A. Suris, Fiz. Tekh. Poluprovod. **5**, 797 (1971) [Sov. Phys. Semicond. **5**, 707 (1971)]; Fiz. Tekh. Poluprovod. **6**, 148 (1972) [Sov. Phys. Semicond. **6**, 120 (1972)]; Fiz. Tekh. Poluprovod. **7**, 488 (1973) [Sov. Phys. Semicond. **7**, 347 (1973)].

[2] J. Faist, F. Capasso, D. Sivco *et al.*, Science **264**, 553 (1994); Appl. Phys. Lett. **65**, 2901 (1994).

[3] J. Faist, F. Capasso, C. Sirtori *et al.*, Appl. Phys. Lett. **66**, 538 (1995); J. Faist, F. Capasso, C. Sirtori *et al.*, Appl. Phys. Lett. **67**, 3057 (1995).

[4] C. Sirtori, J. Faist, F. Capasso *et al.*, Appl. Phys. Lett. **68**, 1745 (1996).

[5] V. F. Elesin and Yu. V. Kopaev, Zh. Éksp. Teor. Fiz. **108**, 2186 (1995) [JETP **81**, 1192 (1995)].

[6] V. F. Elesin and Yu. V. Kopaev, Solid State Commun. **96**, 897 (1995).

[7] J. Faist, F. Capasso, C. Sirtori *et al.*, Phys. Rev. Lett. **76**, 411 (1996).

[8] A. S. Aleksandrov and V. F. Elesin, Zh. Éksp. Teor. Fiz. **58**, 1062 (1970) [Sov. Phys. JETP **31**, 571 (1970)].

[9] E. O. Kane, J. Phys. Chem. Solids **1**, 249 (1957).

[10] B. Gelmont, V. Gorfinkel, and S. Luryi, Appl. Phys. Lett. **68**, 2171 (1996).

[11] R. Mickevicius, R. Gaska, V. Mitin *et al.*, Semicond. Sci. Technol. **9**, 886 (1994).

1063-7761/97/111048-01$10.00

Theoretical study of β-decay of a negative tritium ion

F. F. Goryaev and L. P. Sukhanov

Russian Research Center ''Kurchatov Institute,'' 123182 Moscow, Russia

(Submitted 26 May 1997)
Zh. Éksp. Teor. Fiz. **112**, 1537–1542 (November 1997)

A calculation of the probability of the main β-decay channel of a negative tritium ion is described as one of the processes that can affect the β-spectrum of a tritium source near the end point. The appropriate energy parameters have been calculated. This process should be taken into account in interpreting measured β-spectra near the end point in connection with determining the neutrino rest mass.
[S1063-7761(97)00111-X]

1. INTRODUCTION

The first theoretical studies of the effect of β-decay in a nucleus on the electron shell of an atom were undertaken by Migdal and Fainberg.[1,2] Later restructuring of electron shells caused by β-decay was theoretically investigated by many authors (see, for example, the review in Ref. 3). In the case of β-decay of a nucleus within a molecule, the physical process is complicated since β-decay may generate both electron and vibration–rotation excitations, and even lead to dissociation of a molecule. Only β-decay of the simplest HT molecule was investigated in detail.[4–7] The most accurate calculation was performed by Wolniewicz.[7] The effect of tritium β-decay on excitation of electron shells of OHT, NH_2T, and CH_3T molecules was studied by Ikuta *et al.*[8]

Restructuring of electron shells of molecules due to β-decay of one of their nuclei attracted researchers' attention in connection with the problem of determining the neutrino rest mass. This is because measurement of the β-spectrum shape near its high-energy edge is the most accurate technique for determination of the neutrino rest mass. Such experiments have been carried out using tritium sources because tritium has the lowest β-electron cut-off energy, $E_{\beta,\max}=18.6$ keV, which provides the best energy resolution.

In the first publication by Hanna and Pontecorvo[9] the upper limit on the neutrino mass was set at about 1 keV, which corresponded to the energy resolution of their technique. All further progress in experimental studies was connected with improvements in the resolution of measuring devices. A degree of success in this field was achieved by Bergkvist,[10,11] who obtained an upper limit on the neutrino mass of about 55 eV at the 90% level of confidence using a magnetic β-spectrometer with a resolution of about 50 eV at the tritium β-spectrum edge. Bergkvist was the first to achieve an energy resolution comparable to the excitation energy of helium ions produced as a result of β-decay and indicated the importance of these excitations for the β-spectrum shape description and hence for estimates of the neutrino mass.

In 1980 a lower limit of the neutrino rest mass was determined for the first time by processing results of a set of experiments done at the Institute of Theoretical and Experimental Physics (ITEP).[12,13] The doubly tritiated aminio acid ($C_5H_{11}NO_2$) was used as a source of β-electrons. Measurements were performed on a unique iron-free spectrometer[14] with an energy resolution of about 45 eV and a background intensity fifteen times as low as in Bergkvist's spectrometer. Since the excitation spectrum of the β-source was unknown, the authors suggested processing the data in two limiting cases:

(a) a spectrum with one final state, which is equivalent to the absence of excitations in the source; the estimated interval for the neutrino mass with 99% confidence is

$$14\leqslant m_\nu\leqslant 26 \text{ eV};$$

(b) atomic tritium in Bergkvist's two-level approximation;[10] the resulting mass interval is

$$24\leqslant m_\nu\leqslant 46 \text{ eV}.$$

These results indicate that the neutrino mass obtained by processing the experimental data essentially depends on how the β-decay energy is redistributed among electron degrees of freedom of the β-source. Thus the issue of the effect of the source chemical structure on the β-spectrum was put on the agenda.

After the publications of the ITEP group,[12,13] some authors[15–18] attempted to take into account the effect of the β-decay energy lost to the electronic channel in neutrino mass measurements. In particular, Kaplan *et al.*[18] consistently took account of the effect of the source molecular structure on the β-spectrum shape and calculated probabilities of excitations in different molecules containing a tritium nucleus. The multiplicity of β-decay channels and their effect on the reliability interval for the neutrino rest mass were discussed.

In the experiment performed by the INR RAS–INP KI (Institute for Nuclear Research, Russian Academy of Sciences, and Institute of Nuclear Physics at Kurchatov Institute) collaboration (Troitsk) in 1994 the β-spectrum of tritium was measured near the end point.[19] The experimental facility was an integrating electrostatic spectrometer with adiabatic magnetic collimation and a gaseous tritium source of electrons. After processing the experimental data, they obtained

$$m_\nu^2=-18\pm 6 \quad (\text{eV})^2.$$

An investigation of the β-spectrum in the region 7–15 eV below the end point indicated that the resulting negative

TABLE I. Probability of the main channel of β-decay of T^- tritium ion and energy characteristics of decay reaction.

Set of basis functions	T^-			He				
	E_{tot}, a.u.	ε, a.u.	E_{ion}, eV	E_{tot}, a.u.	ε, a.u.	E_{ion}, eV	ΔE, eV	W_{00}
3-21G	-0.4004	0.0774	-2.11	-2.8357	-0.9036	24.59	66.3	0.55
$4s/2s$	-0.4481	0.0232	-0.63	-2.8552	-0.9141	24.87	65.5	0.46
$5s/3s$	-0.4868	-0.0450	1.22	-2.8599	-0.9169	24.95	64.6	0.33
$6s/4s$	-0.4876	-0.0455	1.24	-2.8611	-0.9177	24.97	64.6	0.33
Experimental data	-	-	0.75	-		24.59	64.6	

mass squared could be ascribed to a peak in the differential spectrum corresponding to a total decay probability of $6\cdot 10^{-11}$. The upper limit for m_ν was set to 4.5 eV with a 95% level of confidence.

These experimental results attract attention to the nature of the peak in the tritium β-spectrum. One of noise sources distorting the β-spectrum shape can be negative tritium ions in the gas target. This paper reports on a calculation of the probability of the main β-decay channel of a negative tritium ion and its energy characteristics.

2. CALCULATIONS OF PROBABILITY OF β-DECAY OF A NEGATIVE TRITIUM ION AND ENERGY CHARACTERISTICS OF THE PROCESS

The β-decay of a negative tritium ion is described by the equation

$$T^- \to {}^3\mathrm{He} + e_\beta^- + \widetilde{\nu}_e, \tag{1}$$

in which a β-electron, antineutrino $\widetilde{\nu}_e$, and a helium atom ^{3}He are created. The helium atom can be created in various electronic states, i.e., Eq. (1) describes a mutlichannel process. Here we consider the case when the helium atom is in the ground state, i.e., the $0\to 0$ channel of reaction (1).

In this calculation, one can assume with reasonable accuracy that the probability of obtaining the final ^{3}He atom in the ground state of its electron shell is described by the Migdal theory of sudden perturbations[20] and equals

$$W_{00}=|\langle \Psi_0(\mathrm{He})|\Psi_0(T^-)\rangle|^2, \tag{2}$$

where $\Psi_0(T^-)$ and $\Psi_0(\mathrm{He})$ are the wave functions of the T^- ion and ^{3}He atom in their ground states, respectively.

It is well known that wave functions of systems with many electrons can be calculated only approximately. We have used the Hartree–Fock–Roothaan (HFR) method.[21,22] Note that this method does not take account of electron correlation effects. In this connection, the most reliable results were obtained by Kaplan *et al.*,[18,23] who consistently took into account the effect of an electron correlation in some molecules containing a tritium atom. It was shown that, in the simplest case of the diatomic HT molecule, the probability of obtaining the electron shell of the $(\mathrm{HHe})^+$ complex in the ground state after the tritium β-decay is overestimated within 7% if an electron correlation is neglected. The calculations reported in these papers indicated a small contribution from the electron correlation to the probability of producing the final molecule in the ground electron state, thus justifying the application of the HFR method.

The probability of the T^- ion β-decay via the main channel of reaction (1) in the HFR approximation is determined by the formula

$$W_{00}=|\langle \varphi_{1s}^{T^-}(\mathbf{r})|\varphi_{1s}^{\mathrm{He}}(\mathbf{r})\rangle|^4, \tag{3}$$

where $\varphi_{1s}^{T^-}(\mathbf{r})$ and $\varphi_{1s}^{\mathrm{He}}(\mathbf{r})$ are $1s$-orbitals of the T^- ion and ^{3}He atom, respectively. We calculated the matrix element in Eq. (3) using various basis sets of Cartesian functions of Gaussian form.[22] The exponents and contraction coefficients for s-functions of He and T atoms were taken from Refs. 24 and 25. The exponents of diffuse s-functions for the T^- ion were calculated by minimizing its total energy. The variational coefficients and energy characteristics of the T^- ion and ^{3}He atom were computed using the MICROMOL code[26] adapted to AT 386/486 personal computers.[27]

The energy characteristics under consideration are the following: E_{tot} is the total energy of the ground state of the two-electron system, ε is the orbital energy (Hartree–Fock one-electron energy), E_{ion} is the ionization potential of the two-electron system, and ΔE is the chemical shift for the main channel of β-decay. The ionization potential was calculated using the Koopmans theorem,[22] according to which $E_{ion}=-\varepsilon$. The chemical shift ΔE is determined by the expression

$$\Delta E = E_0(T^-) - E_0({}^3\mathrm{He}), \tag{4}$$

where $E_0(T^-)$ is the total energy of the T^- ion ground state and $E_0({}^3\mathrm{He})$ is the total energy of the ^{3}He ground state.

3. RESULTS AND DISCUSSION

We have calculated the probability of the main channel of process (1), in which a tritium ion undergoes β-decay, and the corresponding energy characteristics. The results of these calculations are summarized in Table I.

In calculations by the Roothaan method, we used various sets of basis functions. Our calculations indicate a tendency to obtain a lower probability of the process under investigation when the set of basis functions is enhanced and yield an asymptotic value $W_{00}=0.33$. As was noted above, the HFR method does not take into account the electron correlation, whose contribution to the probability is small. Therefore an improved value of this probability is not the main goal of our study. Table I indicates that the ionization potential of the tritium ion tends to a positive value as the set of basis functions is enhanced, but it is slightly different from the experimental value due to the electron correlation neglected in our model. At the same time, the results for the more compact ^{3}He atom and for the chemical shift of reaction (1) are in fair agreement with experimental data.

It is noteworthy that the $0\rightarrow 1$ channel, in which the ^{3}He atom is produced in the first excited state, is not essential for interpretation of the β-spectrum of the HT molecular source in the INR RAS–INP KI experiment, which can be justified as follows.

The chemical shift in the $0\rightarrow 1$ channel equals

$$\Delta E_{0\rightarrow 1}=E_0(\mathrm{T}^-)-E_1(^3\mathrm{He})=44.0\ \mathrm{eV}.$$

Kaplan *et al.*[23] obtained the following chemical shift for the process $\mathrm{HT}\rightarrow(\mathrm{HHe})^+$:

$$\Delta E=E_0(\mathrm{HT})-E_0(\mathrm{HHe}^+)=49.1\ \mathrm{eV}.$$

This means that the energies produced in these reactions are close and differ substantially from the chemical shift calculated by us for the main channel $0\rightarrow 0$:

$$\Delta E=E_0(\mathrm{T}^-)-E_0(^3\mathrm{He})=64.6\ \mathrm{eV}.$$

Thus, the calculations of probability reported in the paper indicate the necessity of taking into account the process under investigation in interpretation of β-spectrum curves near the end point in the experiment.[19]

4. CONCLUSIONS

In this paper we have discussed β-decay of a negative tritium ion T^- and calculated the probability of creating the resulting He atom in the ground state. This process is of interest in connection with experiments currently being performed by the INR RAS–INP KI collaboration with a view to determining the neutrino rest mass through precise measurements of the high-energy region of the spectrum of β-electrons generated in decay of tritium in a gaseous source. The error in the limits on the neutrino mass obtained in such experiments is a few electronvolts. For this reason, all processes that can change the cut-off energy of β-electrons by a value of this order should be taken into account in processing the experimental data. One source of such errors can be negative tritium ions in the gas target. Specifically, when the tritium electron shell transitions to the ground state (GS) of a positive helium ion, an energy of about 41 eV is emitted, whereas in a similar transition of a T^- ion to the ground state of a He atom an energy of about 65 eV is released. Thus, the probability of the $\mathrm{T}^-\rightarrow\mathrm{He(GS)}$ transition in β-decay of a tritium nucleus is important for an estimate of a possible effect of negative tritium ions on measurements of the neutrino rest mass.

The authors are grateful to S. S. Gershtein for stimulating our interest in this research, and to S. P. Alliluev and A. L. Barabanov for valuable critical remarks.

[1] A. Migdal, J. Phys. (USSR) **4**, 449 (1941).
[2] E. Fainberg, J. Phys. (USSR) **4**, 423 (1941).
[3] I. S. Batkin and Yu. G. Smirnov, Élement. Chast. Atom. Yadra **11**, 1421 (1980).
[4] H. M. Schwartz, J. Chem. Phys. **23**, 400 (1955).
[5] M. Cantwell, Phys. Rev. **101**, 1747 (1956).
[6] M. Wolfsberg, J. Chem. Phys. **24**, 24 (1956).
[7] L. Wolniewicz, J. Chem. Phys. **43**, 1087 (1965).
[8] S. Ikuta, S. Iwata, and M. Imamura, J. Chem. Phys. **66**, 4671 (1977).
[9] G. C. Hanna and B. Pontecorvo, Phys. Rev. **75**, 933 (1949).
[10] K. E. Bergkvist, Nucl. Phys. B **39**, 317 (1972).
[11] K. E. Bergkvist, Phys. Scr. **4**, 23 (1971).
[12] V. S. Kozik, V. A. Lyubimov, E. G. Novikov *et al.*, Yad. Fiz. **32**, 301 (1980) [Sov. J. Nucl. Phys. **32**, 154 (1980)].
[13] V. A. Lyubimov, E. G. Novikov, V. Z. Nozik *et al.*, Zh. Éksp. Teor. Fiz. **81**, 1158 (1981) [Sov. Phys. JETP **54**, 616 (1981)].
[14] E. F. Tret'yakov, Izv. Akad. Nauk SSSR, Ser. Fiz. **39**, 583 (1975).
[15] M. Fukugita and R. Kubodeva, Z. Phys. C **9**, 365 (1981).
[16] J. Law, Phys. Lett. B **102**, 371 (1981).
[17] C. Chengrui, H. Tschsin, and C. Shaolin, Preprint AS-ITP-81-22 (1981).
[18] I. G. Kaplan, V. N. Smutnyi, G. V. Smelov, Zh. Éksp. Teor. Fiz. **84**, 833 (1983) [Sov. Phys. JETP **57**, 483 (1983)].
[19] A. I. Belesev, A. I. Bleile, E. V. Geraskin *et al.*, Preprint INR–862/94 (1994).
[20] A. B. Migdal, *Qualitative Methods in Quantum Theory*, Benjamin, Reading, MA (1977).
[21] M. Dewar, *The Molecular Orbitals Theory in Organic Chemistry*, McGraw Hill, New York (1972).
[22] S. Huzinaga, *Method of Molecular Orbitals*, Iwanami Shoten (1983).
[23] I. G. Kaplan, G. V. Smelov, and V. N. Smutnyi, Dokl. Akad. Nauk SSSR **279**, 1110 (1984).
[24] S. Huzinaga, J. Chem. Phys. **42**, 1293 (1965).
[25] T. H. Dunning Jr. and P. J. Hay, in *Methods of Electronic Structure Theory*, ed. by H. F. Schaefer III, Plenum Publishing Corporation, N. Y. (1977), Vol. 1, p. 1.
[26] S. M. Colwell, *MICROMOL Tutor*, Cambridge University (1987).
[27] L. P. Sukhanov and Sh. Sh. Nabiev, Zh. Fiz. Khim. **70**, 848 (1996).

Translation provided by the Russian Editorial office.

Quantum-electrodynamic processes in a strong nonclassical electromagnetic field

O. B. Prepelitsa

Institute of Applied Physics, Academy of Sciences of Moldova, 277028 Kishinev, Moldova

(Submitted 9 January 1997)
Zh. Éksp. Teor. Fiz. **112**, 1543–1556 (November 1997)

Quantum-electrodynamic processes that take place in the presence of a squeezed electromagnetic field are discussed. Integral formulas are derived that make it possible to express the probability of any process in a squeezed electromagnetic field in terms of the probability of the same process in a classical electromagnetic field. The main laws that govern processes of first order in the fine-structure constant as functions of the number of photons involved and the quantum fluctuations are examined. Tunneling formulas for the probability of a photon producing an electron–positron pair in a strong squeezed field are derived. Also, resonant electron–electron scattering is examined and the scattering cross section as a function of the statistical properties of the field (the way the field has been squeezed) is investigated. It is found that the quantum fluctuations of the squeezed electromagnetic field give rise to an increase in the scattering cross section, with the probability of the process in a phase-squeezed electromagnetic field always being higher than the probability of the process in an amplitude-squeezed electromagnetic field.
[S1063-7761(97)00211-4]

1. INTRODUCTION

For a long time the quantum electrodynamics of phenomena that occur in the presence of a strong electromagnetic field has been the object of intense theoretical study.[1–18] These studies produced a number of interesting results. In particular, it was found that electron and photon states in the field of a wave cease to be stationary (if one allows for the electromagnetic-field vacuum). As result, processes of first order in the fine-structure constant α_0 become possible,[1–4] such as the emission of a photon by an electron and the creation by a photon and annihilation (followed by emission of radiation) of an electron–positron pair. Another important theoretical result is the possibility of resonant processes of higher order in α_0, e.g., scattering of a photon by an electron,[5] electron–electron scattering,[6] and generation of harmonics when an electron is decelerated by a Coulomb center.[8] The resonant behavior of the cross section is due to the emergence of the intermediate particle on the mass shell. In this case we are dealing with a chain of successively coupled processes that are first-order in α_0.

Note that in all the above papers it is assumed that the external electromagnetic field is classical or coherent (which actually means classical if we ignore radiative corrections). It would be interesting to study quantum-electrodynamic processes in the presence of a nonclassical electromagnetic field, which is essentially quantum in nature and possesses nontrivial statistical properties.

This paper is a study of the effect of quantum fluctuations of the applied electromagnetic field on quantum-electrodynamic processes. For the external quantized electromagnetic field we take a squeezed electromagnetic field. The explanation of this choice lies in the unusual statistical properties of such a field,[19] which are known to vary within broad limits: from bunching to antibunching of photons. This makes it possible to study how pair correlations of photons belonging to the external electromagnetic field affect the cross sections of quantum mechanical reactions. What is important is that a squeezed electromagnetic field exhibits its nonclassical properties in its interaction with matter. This happens in the strong fields,[20] which are usually needed in quantum-electrodynamic processes. If there is the possibility of building high-power sources of squeezed light (with a photon concentration of 10^{20} cm^{-3}; see Ref. 21), it would seem interesting to study the effect of the photons of such light on processes studied by quantum electrodynamics.

Here is a possible definition of a squeezed state of an electromagnetic field:[19]

$$|s\rangle_{\mathbf{k}}=T_{\mathbf{k}}(\alpha)D_{\mathbf{k}}(\eta)|0\rangle_{\mathbf{k}}, \tag{1}$$

where $|0\rangle_{\mathbf{k}}$ is the vacuum state of mode $\mathbf{k}$,

$$T_{\mathbf{k}}(\alpha)=\exp(\alpha a_{\mathbf{k}}^{\dagger}-\alpha^* a_{\mathbf{k}}),$$

$$D_{\mathbf{k}}(\eta)=\exp[\tfrac{1}{2}\eta^*(a_{\mathbf{k}})^2-\tfrac{1}{2}\eta(a_{\mathbf{k}}^{\dagger})^2]$$

are the translation and contracting operators, and

$$\alpha=|\alpha|\exp(i\varphi_\alpha), \qquad \eta=r\,\exp(i\varphi_r)$$

are complex-valued parameters, with $0\leqslant|\alpha|$, $r<\infty$, $0\leqslant\varphi_\alpha$, and $\varphi_r<2\pi$; $a_{\mathbf{k}}^{\dagger}$ and $a_{\mathbf{k}}$ are the electromagnetic field creation and annihilation operators, which satisfy the ordinary commutation relations for bosonic operators.

If we apply the translation and contracting operators to the electromagnetic field operator, the latter are transformed in the following manner:[19]

$$T_{\mathbf{k}'}^{\dagger}(\alpha)a_{\mathbf{k}}^{\dagger}T_{\mathbf{k}'}(\alpha)=a_{\mathbf{k}}^{\dagger}+\delta_{\mathbf{kk}'}\alpha^*, \tag{2}$$

$$D_{\mathbf{k}'}^{\dagger}(\eta)a_{\mathbf{k}}^{\dagger}D_{\mathbf{k}'}(\eta)=a_{\mathbf{k}}^{\dagger}[1+\delta_{\mathbf{kk}'}(\cosh r-1)] - \delta_{\mathbf{kk}'}a_{\mathbf{k}}\sinh r\,\exp(-i\varphi_r). \tag{3}$$

In this paper we will derive general formulas that will allow us to express the probability of any quantum-

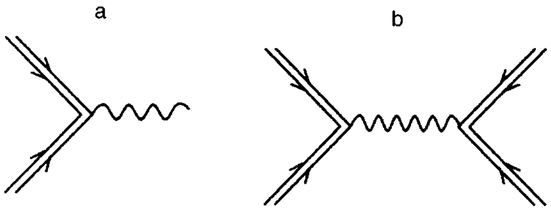

FIG. 1.

electrodynamic process in the presence of a squeezed electromagnetic field in terms of the probability of the same process in a classical electromagnetic field. We use them to examine processes of first order in α_0 in a squeezed electromagnetic field (Fig. 1a). The general properties of such processes are studied for the region where perturbation theory in the external field is applicable. We find that the dependence of the probability of a process on the statistical properties of the applied field begins to manifest itself when the number of photons involved in the process is greater than one. Here the probability of processes in a phase-squeezed electromagnetic field is higher than the probability of processes in an amplitude-squeezed electromagnetic field, which in turn is always higher than the probability of processes in a classical field. We study in detail the production of an electron–positron pair in the presence of a squeezed electromagnetic field of high intensity, i.e., when tunneling is the main mechanism. We also show that in this case the functional dependence of the probability of a process on the average intensity of the field in a squeezed electromagnetic field is quite different than it is in a classical field. Electron–electron scattering in the presence of a squeezed electromagnetic field is examined (Fig. 1b). In the nonresonance region, the electron–electron scattering cross section in a field is much smaller than when the colliding electrons are free. In the resonance region, the probability of scattering in an external field may exceed the probability of scattering without a field by several orders of magnitude. We study by numerical methods the dependence of the reaction cross section on the statistical properties (the way squeezing was achieved) of the squeezed electromagnetic field. A general feature here is that the probability of quantum-electrodynamic processes grows with the intensity of field strength fluctuations and with the intensity of the squeezed electromagnetic field.

2. PROBABILITY OF QUANTUM-ELECTRODYNAMIC PROCESSES IN THE PRESENCE OF A SQUEEZED ELECTROMAGNETIC FIELD

Let us examine the behavior of an electron interacting with a single-mode squeezed electromagnetic field. The field is assumed fixed, i.e., we ignore the effect produced by the photons re-emitted into an excited mode.

The external electromagnetic field is described by a potential of the form

$$A_{\mathrm{ext}}=\sqrt{\frac{1}{2\omega_{\mathbf{k}}}}\,[e_\lambda a_{\mathbf{k}}^\dagger \exp(ikx)+e_\lambda^* a_{\mathbf{k}}\exp(-ikx)], \tag{4}$$

where $\omega_{\mathbf{k}}$ and e_λ are, respectively, the frequency and polarization of a photon with a wave vector $\mathbf{k}$. Here and in what follows we use a system of units with $c=\hbar=1$, a notation $x=(t,\mathbf{r})$, $k=(\omega_{\mathbf{k}},\mathbf{k})$, and define $ab=a_0b_0-\mathbf{a}\cdot\mathbf{b}$ as the scalar product of the four-vectors $a=(a_0,\mathbf{a})$ and $b=(b_0,\mathbf{b})$.

Note that formula (4) has been used to separate the mode $\mathbf{k}$, while the fact that at the time when the interaction of this mode with an electron was switched on the mode was precisely in the squeezed state (1) will be taken into account later, when we calculate the matrix elements of the evolution operator. What is important here is that the mode $\mathbf{k}$ is highly excited, so that it is convenient to go over to the Furry representation. This will make it possible to account for the interaction of the electron and the external field exactly, while the interaction of the electron and the other modes $\mathbf{k}'$ $(\mathbf{k}'\neq\mathbf{k})$ will be taken into account perturbatively.

In the Furry representation the scattering matrix is

$$S=T\,\exp\left[-i\int d^4x\,j(x,a_{\mathbf{k}}^\dagger,a_{\mathbf{k}})A(x)\right], \tag{5}$$

$$j(x,a_{\mathbf{k}}^\dagger,a_{\mathbf{k}})=eN(\overline{\psi}(x,a_{\mathbf{k}}^\dagger,a_{\mathbf{k}})\gamma\psi(x,a_{\mathbf{k}}^\dagger,a_{\mathbf{k}})),$$

$$\psi(x,a_{\mathbf{k}}^\dagger,a_{\mathbf{k}})=\sum_{\mathbf{p}}\,[b_{\mathbf{p}}\theta(\varepsilon_{\mathbf{p}})+d_{\mathbf{p}}^\dagger\theta(-\varepsilon_{\mathbf{p}})]\varphi_{\mathbf{p}}(x,a_{\mathbf{k}}^\dagger,a_{\mathbf{k}}),$$

$$A(x)=\sum_{\mathbf{k}'\neq\mathbf{k}}\sqrt{\frac{1}{2\omega_{\mathbf{k}'}}}\,[e_{\lambda'}a_{\mathbf{k}'}^\dagger\,\exp(ik'x)$$

$$+e_{\lambda'}^*a_{\mathbf{k}'}\,\exp(-ik'x)], \tag{6}$$

where e is the electron charge, γ stands for the Dirac matrices, $b_{\mathbf{p}}$ and $d_{\mathbf{p}}$ are the electron–positron field operators, which satisfy the anticommutation relations for fermion operators,

$$\theta(\varepsilon_{\mathbf{p}})=\begin{cases}1, & \varepsilon_{\mathbf{p}}\geqslant 0,\\ 0, & \varepsilon_{\mathbf{p}}<0\end{cases}$$

is the Heaviside function, and $\varepsilon_{\mathbf{p}}=|\mathbf{p}_0|$ is the absolute value of the particle energy.

The function $\varphi_{\mathbf{p}}(x,a_{\mathbf{k}}^\dagger,a_{\mathbf{k}})$ is a solution of the Dirac equation with potential (4):

$$\left(i\gamma\frac{\partial}{\partial x}-eA_{\mathrm{ext}}-m\right)\varphi_{\mathbf{p}}(x,a_{\mathbf{k}}^\dagger,a_{\mathbf{k}})=0 \tag{7}$$

(the function $\varphi_{\mathbf{p}}(x,a_{\mathbf{k}}^\dagger,a_{\mathbf{k}})$ is known explicitly,[7] but we will not write it because it is extremely cumbersome).

Note that the sign of the normal ordering in (6) refers only to the operators of the electron–positron system and does not involve the electromagnetic field operators, which are present in $\varphi_{\mathbf{p}}(x,a_{\mathbf{k}}^\dagger,a_{\mathbf{k}})$.

Let us examine the amplitude of the transition from the initial state $|i\rangle$ of the photon and electron–positron system to the final state $|f\rangle$:

$$A_{fi}={}_{\mathbf{k}}\langle l|\langle f|S|i\rangle|s\rangle_{\mathbf{k}}$$

(the photon subsystem consists of all the modes $\mathbf{k}'\neq\mathbf{k}$). Here we have allowed for the fact that initially the mode $\mathbf{k}$ was in the squeezed state $|s\rangle_{\mathbf{k}}$ (Eq. (1)), and then evolved into the state $|l\rangle_{\mathbf{k}}$. At this point we must mention the difference in the concept of ‘‘prescribed field’’ for a classical electromagnetic field and for a quantized electromagnetic field. The function $\varphi_{\mathbf{p}}(x,a^{\dagger}_{\mathbf{k}},a_{\mathbf{k}})$ is a solution of Eq. (7) (see Ref. 7), which has been considered separately from the corresponding Maxwell equation for the field, i.e., we have ignored the interaction with photons re-emitted by charged particles into the mode **k**. In this sense the field of the mode **k** is fixed, but the quantum-statistical state of the mode **k** is not. Indeed, in the process of quantum transitions an electron draws energy (photons) from an excited mode, with the result that the quantum state of the mode changes. Hence, in the formula for the transition amplitude A_{fi}, the state $|l\rangle_{\mathbf{k}}$ is generally not identical to the state $|s\rangle_{\mathbf{k}}$.

Let us square the absolute value of the amplitude A_{fi} and sum over all possible states $|l_{\mathbf{k}}\rangle$. Using the partition of unity

$$\sum_{l} |l\rangle_{\mathbf{k}\mathbf{k}}\langle l| = 1,$$

and Eqs. (5) and (6), we can write the transition probability as follows:

$$W_{\mathrm{sq}} = {}_{\mathbf{k}}\langle s|\hat{W}(a^{\dagger}_{\mathbf{k}},a_{\mathbf{k}})|s\rangle_{\mathbf{k}}, \tag{8}$$

$$\hat{W}(a^{\dagger}_{\mathbf{k}},a_{\mathbf{k}}) = \left\langle i\left| T\,\exp\left[i\int d^4x\, j(x,a^{\dagger}_{\mathbf{k}},a_{\mathbf{k}})A(x)\right]\right| f\right\rangle \times \left\langle f\left| T\,\exp\left[-i\int d^4x\, j(x,a^{\dagger}_{\mathbf{k}},a_{\mathbf{k}})A(x)\right]\right| i\right\rangle. \tag{9}$$

Since $\hat{W}(a^{\dagger}_{\mathbf{k}},a_{\mathbf{k}})$, like any function of operators, is a symbolic notation for a power series, we can use the generating function

$$G(z,z^*) = \exp(z a^{\dagger}_{\mathbf{k}})\exp(z^* a_{\mathbf{k}}) \tag{10}$$

to write Eq. (9) in the form

$$\hat{W}(a^{\dagger}_{\mathbf{k}},a_{\mathbf{k}}) = \hat{W}_N\left(\frac{\partial}{\partial z},\frac{\partial}{\partial z^*}\right) G(z,z^*)|_{z=z^*=0}.$$

Here by $\hat{W}_N(\partial/\partial z,\partial/\partial z^*)$ we denote the normal image of the function $\hat{W}(a^{\dagger}_{\mathbf{k}},a_{\mathbf{k}})$, in which we have replaced $a^{\dagger}_{\mathbf{k}}\to\partial/\partial z$ and $a_{\mathbf{k}}\to\partial/\partial z^*$. (Here we do not discuss the problem of the convergence of series, e.g., the perturbation series in α_0, and interpret series as formal quantities.)

Bearing in mind the last expression, we can write the probability (8) as

$$\hat{W}_{\mathrm{sq}} = \hat{W}_N\left(\frac{\partial}{\partial z},\frac{\partial}{\partial z^*}\right) G_{\mathrm{sq}}(z,z^*)|_{z=z^*=0}, \tag{11}$$

where $G_{\mathrm{sq}}(z,z^*) = {}_{\mathbf{k}}\langle s|G(z,z^*)|s\rangle_{\mathbf{k}}$.

Thus, all the information about the dependence of the probability of the process on the quantum-statistical properties of the external electromagnetic field is contained in the average value of the generating function.

Using Eqs. (1)–(3) and performing simple transformations, we find the average value of the generating function:

$$G_{\mathrm{sq}}(z,z^*) = \exp(z\alpha^* + z^*\alpha)\exp\left\{ -\frac{1}{2}\sinh^2 r \times\left[z\,\exp\left(-\frac{i\varphi_r}{2}\right) - z^*\,\exp\left(\frac{i\varphi_r}{2}\right)\right]^2\right\}. \tag{12}$$

Equation (12) was derived in the approximation $\overline{n}\gg 1$, where $\overline{n}$ is the average number of photons in the mode **k**, and we also assume that $\sinh r\cosh r \approx \sinh^2 r$, which is true in two cases: when the external electromagnetic field is in a coherent state $(r=0)$, and when it is strongly squeezed $(r\gg 1)$.

We transform the above expression to a more convenient form. To this end we use the Poisson integral:

$$\int_{-\infty}^{\infty} d\xi\,\exp(-a\xi^2 + ib\xi) = \sqrt{\frac{\pi}{a}}\,\exp\left(-\frac{b^2}{4a}\right),$$

$$\mathrm{Re}\,a > 0.$$

After performing obvious transformations, we arrive at the final expression for the generating function averaged over the state of the squeezed electromagnetic field:

$$G_{\mathrm{sq}}(z,z^*) = \frac{1}{\sqrt{2\pi\sinh^2 r}}\int_{-\infty}^{\infty} d\xi\,\exp\left(-\frac{\xi^2}{2\sinh^2 r}\right) \times\exp\left\{ z\,\exp(-i\varphi_\alpha)\left[|\alpha| + i\xi \times\exp\left[i\left(\varphi_\alpha - \frac{\varphi_r}{2}\right)\right]\right] + z^*\,\exp(i\varphi_\alpha) \times\left[|\alpha| - i\xi\,\exp\left[-i\left(\varphi_\alpha - \frac{\varphi_r}{2}\right)\right]\right]\right\}. \tag{13}$$

Note that Eq. (13) contains the phase parameters φ_α and φ_r, which determine the dependence of the function $G_{\mathrm{sq}}(z,z^*)$ on the way in which the applied electromagnetic field was squeezed and hence on the quantum-statistical properties of the field.[19] Below we discuss the two most interesting cases: amplitude squeezing $(2\varphi_\alpha - \varphi_r = 0)$, and phase squeezing $(2\varphi_\alpha - \varphi_r = \pi)$.

Returning to formula (11) and allowing for (13), we can write the probability of the process as

$$W_{\mathrm{sq}} = \frac{2}{\sqrt{2\pi\sinh^2 r}}\int_{|\alpha|}^{\infty}\frac{d\xi\,\xi}{\sqrt{\xi^2 - |\alpha|^2}} \times\exp\left(-\frac{\xi^2 - |\alpha|^2}{2\sinh^2 r}\right) W_{\mathrm{cl}}(\xi), \quad 2\varphi_\alpha - \varphi_r = 0,$$

$$W_{\mathrm{sq}} = \frac{2}{\sqrt{2\pi\sinh^2 r}}\,\frac{1}{2}\int_{-\infty}^{\infty} d\xi \times\exp\left(-\frac{(\xi - |\alpha|)^2}{2\sinh^2 r}\right) W_{\mathrm{cl}}(|\xi|), \quad 2\varphi_\alpha - \varphi_r = \pi, \tag{14}$$

where

$$G_{\mathrm{cl}}(z,z^*) = \exp(z\xi e^{-i\varphi} + z^*\xi e^{i\varphi}),$$

$$W_{\mathrm{cl}}(\xi)=\hat{W}_N\left(\frac{\partial}{\partial z},\frac{\partial}{\partial z^*}\right)G_{\mathrm{cl}}(z,z^*)|_{z=z^*=0}.$$

Note that the expression for $G_{\mathrm{cl}}(z,z^*)$ differs from the general formula (10) in that the operators $a_{\mathbf{k}}^\dagger$ and $a_{\mathbf{k}}$ are replaced by c-numbers ξ, which means that $G_{\mathrm{cl}}(z,z^*)$ is a generating function for the case of a classical electromagnetic field with an amplitude ξ (here φ is the initial phase of the classical electromagnetic field). Hence $W_{\mathrm{cl}}(\xi)$ is the corresponding probability of a transition in the presence of a classical electromagnetic field.

We have developed a general method for calculating the probability of any quantum-electrodynamic process in the presence of a squeezed electromagnetic field via the expression for the probability of the same process in a classical field. This makes it possible to divide the problem of calculating the cross section of a reaction in a squeezed electromagnetic field into two stages: the calculation of the cross section in a classical electromagnetic field, and the averaging of the result via (14).

The form of Eqs. (14) and the condition of their applicability, $\overline{n}\gg 1$, or more precisely $\overline{n+1}\approx\overline{n}$, suggest that the derived expressions for the probability are, in a certain sense, of quasiclassical nature. Note that the quasiclassicality of (14) does not mean that we must completely ignore the quantum fluctuations of the squeezed electromagnetic field—if this were so, further research in this area would lose all meaning. Indeed, consider the relationship

$$\Lambda_n={}_{\mathbf{k}}\langle s|(a_{\mathbf{k}}^\dagger)^{2n}(a_{\mathbf{k}})^{2n}|s\rangle_{\mathbf{k}}-{}_{\mathbf{k}}\langle s|(a_{\mathbf{k}}^\dagger)^{n}(a_{\mathbf{k}})^{n}|s\rangle_{\mathbf{k}}^2,$$

which describes n-photon correlations in an electromagnetic field. We can show that the approximation $\overline{n+1}\approx\overline{n}$ takes into account the quantum fluctuations resulting from correlations between photons of the squeezed electromagnetic field but, in the process, the contribution from correlations between the photons of the applied field and the zero-point vacuum oscillations in Λ_n gets lost. Thus, the approximation is true at least in two cases: when the photons of the squeezed electromagnetic field are strongly correlated $(r\gg 1)$, and when the state (1) degenerates into a coherent state, whose quasiclassicality is well-known.

Note that expressions similar to (14) were obtained in Refs. 20 and 22, where the interaction of a hydrogenlike system and a strong squeezed electromagnetic field was investigated, and also in Ref. 23. Now it is clear that Eqs. (14) are of a general nature and reflect the objective quantum-statistical properties of a squeezed electromagnetic field. Note that they can be applied to a much broader class of problems than this paper examines. Clearly, the probability of transitions, initiated by a squeezed electromagnetic field, of a bound electron, an electron in an external magnetic field, etc., can be expressed in terms of the probabilities of transitions in a classical electromagnetic field, in accordance with Eqs. (14). To prove this statement we must include the terms that describe the corresponding interactions in the zeroth-approximation Hamiltonian and repeat the line of reasoning that brought us to (14).

From (14) we can easily arrive at the limit $r=0$, i.e., when the external field can be assumed classical, and at the limit $\alpha=0$, when the electromagnetic field in in the squeezed vacuum state:

$$W_{\mathrm{sq},v}=\frac{1}{\sqrt{2\pi\sinh^2 r}}\int_{-\infty}^{\infty}d\xi\times\exp\left(-\frac{\xi^2}{2\sinh^2 r}\right)W_{\mathrm{cl}}(|\xi|). \tag{15}$$

The results we arrived at in this section are of a general nature. Below we will use them to study specific quantum-electrodynamic processes that take place in a squeezed electromagnetic field, which for the sake of simplicity is assumed to be circularly polarized.

3. QUANTUM VACUUM EFFECTS IN AN EXTERNAL SQUEEZED ELECTROMAGNETIC FIELD

Below we examine processes of first order in the fine-structure constant, represented by the diagram in Fig. 1a. Such process are known to be energetically forbidden (for free particles) and can occur only in the presence of an external field.

According to Ref. 4, the probabilities of quantum-electrodynamic processes in the field of a classical electromagnetic wave with a strength $\mathbf{E}_{cl}=\mathbf{E}_0\sin(\omega_{\mathbf{k}}t)$ depend on the invariant parameter

$$\chi_{\mathrm{cl}}^2=\frac{2e^2\overline{\mathbf{E}_{\mathrm{cl}}^2}}{m^2\omega_{\mathbf{k}}^2}, \tag{16}$$

where m is the electron rest mass, and the bar denotes an average over the period of the wave.

The region $\chi_{\mathrm{cl}}\ll 1$ corresponds to a weak electromagnetic field, for which perturbation theory is valid. In this case the probability of a process calculated per unit volume per unit time can be written as follows:[4]

$$w_{\mathrm{cl}}(n)=P(n)\chi_{\mathrm{cl}}^{2n}. \tag{17}$$

Here n is the number of photon involved in the process, and $P(n)$ is a function of the momenta of the initial and final particles.

Using the correspondence principle, we can easily show that when the applied electromagnetic field is a squeezed field, the analog of the parameter (16) is the quantity

$$\chi_{\mathrm{sq}}^2=\frac{2e^2\overline{{}_{\mathbf{k}}\langle s|\mathbf{E}^2|s\rangle_{\mathbf{k}}}}{m^2\omega_{\mathbf{k}}^2}, \tag{18}$$

where

$$\mathbf{E}=i\sqrt{\frac{\omega_{\mathbf{k}}}{2}}\,[\mathbf{e}_\lambda a_{\mathbf{k}}^\dagger\exp(ikx)-\mathbf{e}_\lambda^* a_{\mathbf{k}}\exp(-ikx)]$$

is the electromagnetic field operator.

Consider the case of a weak squeezed electromagnetic field, $\chi_{\mathrm{sq}}\ll 1$. Plugging (17) into (14) and (15) and performing elementary integration, we obtain

$$w_{\mathrm{sq}}(n)=\frac{w_{\mathrm{cl}}(n)}{(1+\mu)^{n}}\begin{cases}\displaystyle\sum_{m=0}^{n}\frac{n!(2m-1)!!}{m!(n-m)!}\mu^{m}, \\ 2\varphi_{\alpha}-\varphi_{r}=0, \\ \displaystyle\sum_{m=0}^{n}\frac{(2n)!(2m-1)!!}{(2m)!(2n-2m)!}\mu^{m}, \\ 2\varphi_{\alpha}-\varphi_{r}=\pi,\end{cases} \tag{19}$$

$$w_{\mathrm{sq},v}(n)=(2n-1)!!\,w_{\mathrm{cl}}(n).$$

The parameter

$$\mu=\frac{\overline{{}_{\mathbf{k}}\langle s|\mathbf{E}^{2}|s\rangle_{\mathbf{k}}}-\overline{{}_{\mathbf{k}}\langle s|\mathbf{E}|s\rangle_{\mathbf{k}}^{2}}}{\overline{{}_{\mathbf{k}}\langle s|\mathbf{E}|s\rangle_{\mathbf{k}}^{2}}}=\frac{\sinh^{2}r}{|\alpha|^{2}} \tag{20}$$

describes the quantum fluctuations of the strength of the squeezed electromagnetic field and can be interpreted as the measure of the field's nonclassical behavior.

Equations (19) are the general expressions for the probability of various processes, described by the diagram in Fig. 1a, in a weak squeezed electromagnetic field ($\chi_{\mathrm{sq}}\ll 1$), where the processes involving the smallest possible number of quanta of the external electromagnetic field have the highest probability of occurring. Note that the condition $\chi_{\mathrm{sq}}\ll 1$ corresponds to a real experimental situation, since it encompasses the intensity of all optical-frequency fields.

Equations (19) imply that the probabilities of processes involving a single quantum of the external electromagnetic field are the same for classical and squeezed electromagnetic fields: $w_{\mathrm{sq}}(1)=w_{\mathrm{sq},v}(1)=w_{\mathrm{cl}}(1)$. Differences emerge when the process involves more than one photon, $n>1$, with the probabilities being nonlinear functions of the strength of the applied field. For instance, the probability of a transition with $n>1$ becomes highest when the field is the squeezed-vacuum state. Equations (19) also imply that the dependence on the way in which the field was squeezed (amplitude-squeezed or phase-squeezed) manifests itself most vividly when the fluctuations in the strength of the applied electromagnetic field are of the same order as the average strength value, $\mu\approx 1/2$. Here the probability of a process in a phase-squeezed electromagnetic field ($2\varphi_{\alpha}-\varphi_{r}=\pi$) is always higher than in an amplitude-squeezed field ($2\varphi_{\alpha}-\varphi_{r}=0$). This is a reflection of the well-known fact that the probabilities of multiphoton processes strongly depend on the statistical properties of the applied electromagnetic field. In particular, more heavily bunched light (phase-squeezed) is absorbed more strongly than less heavily bunched light (amplitude-squeezed), a fact that results in an increase in the probability of the process in the presence of the corresponding type of electromagnetic field.

So far we have studied the general laws governing processes of first order in α_0. Let us now investigate in greater detail the process of electron–positron pair production initiated by a gamma quantum in the presence of a squeezed electromagnetic field. Pair production requires an energy of order $2m$. Hence there exists a threshold in the number of photons absorbed from the applied electromagnetic field:

$$n_{\min}=\frac{m^{2}(1+\chi^{2})}{kk'},$$

where χ is determined by Eq. (16) or (18), depending on the type of applied field, and k and k' are, respectively, the wave four-vector of the photon of the external field and the incident gamma quantum. Pair formation is possible only if $n\geqslant n_{\min}$. For an electromagnetic field in the optical range the parameter $n_{\min}$ proves to be very large within a broad energy range of the incident quantum, with the result that pair production is accompanied by absorption of an extremely large number of photons from the wave. Let us assume that the squeezed electromagnetic field is strong, so that $\chi_{\mathrm{sq}}\kappa_{\mathrm{sq}}\gtrsim 1$ and $\kappa_{\mathrm{sq}}\ll 1$, where $\kappa_{\mathrm{sq}}=(kk'/m^{2})\chi_{\mathrm{sq}}$. For our calculations we use the formula for the differential probability of pair production in a classical electromagnetic field:[4]

$$w_{\mathrm{cl}}^{\gamma\to e^{-}e^{+}}=Z(k_0')\,\kappa_{\mathrm{cl}}\exp\left(-\frac{8}{3\kappa_{\mathrm{cl}}}\right),$$

$$\kappa_{\mathrm{cl}}\ll 1,\quad \chi_{\mathrm{cl}}^{2}\kappa_{\mathrm{cl}}\gtrsim 1,\quad \kappa_{\mathrm{cl}}=\frac{kk'}{m^{2}}\chi_{\mathrm{cl}}. \tag{21}$$

We substitute (21) in (14). Bearing in mind (20), we obtain

$$w_{\mathrm{sq}}^{\gamma\to e^{-}e^{+}}=Z(k_0')\sqrt{\frac{1+\mu}{2\pi\mu\kappa_{\mathrm{sq}}^{2}}}\int_{-\infty}^{\infty}dz\sqrt{z^{2}+\frac{\kappa_{\mathrm{sq}}^{2}}{1+\mu}}$$
$$\times\exp\left[-\frac{(1+\mu)z^{2}}{2\mu\kappa_{\mathrm{sq}}^{2}}-\frac{8}{3\sqrt{z^{2}+\kappa_{\mathrm{sq}}^{2}/(1+\mu)}}\right],$$

$$2\varphi_{\alpha}-\varphi_{r}=0,$$

$$w_{\mathrm{sq}}^{\gamma\to e^{-}e^{+}}=Z(k_0')\sqrt{\frac{1+\mu}{2\pi\mu\kappa_{\mathrm{sq}}^{2}}}\int_{-\infty}^{\infty}dz|z|$$
$$\times\exp\left[-\frac{1+\mu}{2\mu\kappa_{\mathrm{sq}}^{2}}\left(z-\frac{\kappa_{\mathrm{sq}}}{\sqrt{1+\mu}}\right)^{2}-\frac{8}{3|z|}\right],$$

$$2\varphi_{\alpha}-\varphi_{r}=\pi.$$

If we allow for the fact that $\kappa_{\mathrm{sq}}\ll 1$, we can use the Laplace method[24] to calculate the integrals. Establishing the points of maxima of the expressions in the square brackets and performing elementary transformations, we find the asymptotic expressions for the probability of photon pair production in the presence of a squeezed electromagnetic field:

$$w_{\mathrm{sq}}^{\gamma\to e^{-}e^{+}}=Z(k_0')\,\frac{\kappa_{\mathrm{sq}}}{\sqrt{1+\mu}}\left(1+\frac{4}{3}\,\frac{\mu\sqrt{1+\mu}}{\kappa_{\mathrm{sq}}}\right)$$
$$\times\exp\left(-\frac{8}{3}\,\frac{1+\mu}{\kappa_{\mathrm{sq}}}\right),$$

$$2\varphi_{\alpha}-\varphi_{r}=0,$$

$$w_{\mathrm{sq}}^{\gamma\to e^{-}e^{+}}=Z(k_0')\,\kappa_{\mathrm{sq}}\left(1+\frac{16\mu}{\kappa_{\mathrm{sq}}}\right)$$

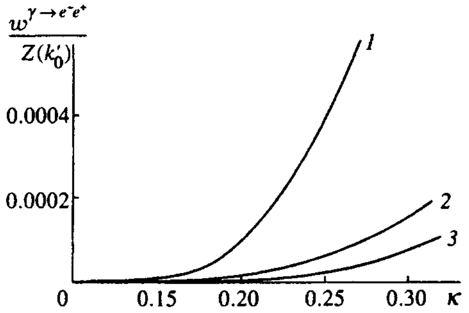

FIG. 2. Differential probability of a photon producing an electron–positron pair in the presence of a phase-squeezed (curve *1*), amplitude-squeezed (curve *2*), and classical (curve *3*) electromagnetic field; $\kappa=\kappa_{\text{sq}}$ or κ_{cl} depending on type of field, and $\mu=3/2$.

$$\times\exp\left[-\frac{8}{3\kappa_{\text{sq}}}\left(1+\frac{4\mu}{\kappa_{\text{sq}}}\right)\right],$$

$$2\varphi_\alpha-\varphi_r=\pi, \tag{22}$$

if $\kappa_{\text{sq}}\geqslant(8/3)\mu\sqrt{1+\mu}$, and

$$w_{\text{sq}}^{\gamma\to e^-e^+}=\frac{4}{3}Z(k_0')\left[\frac{\mu\kappa_{\text{sq}}^2}{3(1+\mu)}\right]^{1/3}\left\{1+\frac{1}{8}\left[\frac{9\kappa_{\text{sq}}^2}{\mu^2(1+\mu)}\right]^{1/3}\right\}$$
$$\times\exp\left[-\frac{1}{2\mu}-6\left(\frac{1+\mu}{9\mu\kappa_{\text{sq}}^2}\right)^{1/3}\right],$$

$$2\varphi_\alpha-\varphi_r=0,$$

$$w_{\text{sq}}^{\gamma\to e^-e^+}=\frac{4}{3}Z(k_0')\left[\frac{\mu\kappa_{\text{sq}}^2}{3(1+\mu)}\right]^{1/3}\left\{1+\frac{1}{4}\left[\frac{\kappa_{\text{sq}}^2}{81\mu^2(1+\mu)}\right]^{1/3}\right\}$$
$$\times\exp\left\{-6\left(\frac{1+\mu}{9\mu\kappa_{\text{sq}}^2}\right)^{1/3}\left[1-\left(\frac{\kappa_{\text{sq}}}{9\mu\sqrt{1+\mu}}\right)^{1/2}\right]\right\},$$

$$2\varphi_\alpha-\varphi_r=\pi, \tag{23}$$

if $\kappa_{\text{sq}}\leqslant(8/3)\mu\sqrt{1+\mu}$.

These expressions (and Eq. (21)) describe electron–positron pair production due to the tunneling effect. Equations (22) are true for a weak squeezed field, which differs little from a coherent (classical) electromagnetic field. Accordingly, the expressions (22) constitute a correction to (21). Equations (23) are true for a strongly squeezed field. Here, obviously, the probability of a process has a quite different dependence on the average intensity of the applied field than in the case of a classical field (Eq. (21)), which is a consequence of the fact that the squeezed electromagnetic field is nonclassical.

Equations (23) lead to the limit $\alpha\to0$ $(\mu\to\infty)$, i.e., to the case where the electromagnetic field is in a squeezed-vacuum state:

$$w_{\text{sq},v}^{\gamma\to e^-e^+}=\frac{4}{3}Z(k_0')\left(\frac{\kappa_{\text{sq}}^2}{3}\right)^{1/3}\exp\left[-6\left(\frac{1}{9\kappa_{\text{sq}}^2}\right)^{1/3}\right].$$

An analysis of (22) and (23) shows that as the intensity of the squeezed electromagnetic field increases, the dependence of the probability of a process on the way the field was squeezed becomes stronger (Fig. 2), and so does the dependence on the quantum fluctuations of the applied field. Here, if we compare (21), (22), and (23), we see that an increase in the fluctuations of the external electromagnetic field is accompanied by an increase in the probability of the process. In other words, pair correlations between photons, which are responsible for fluctuations in the intensity of the squeezed electromagnetic field, facilitate electron–positron pair production.

4. ELECTRON–ELECTRON SCATTERING IN THE PRESENCE OF A SQUEEZED ELECTROMAGNETIC FIELD

To manifest processes that are first-order in the fine-structure constant, the electromagnetic field must be extremely strong. Hence, from the viewpoint of the possibility of experimental verification, the most interesting processes are those of higher orders in α_0, which in certain condition are of a resonant nature.[5,6,8–13]

According to (14), the differential cross section of electron–electron scattering in a squeezed electromagnetic field can be written as

$$\frac{d\sigma_{\text{sq}}(n)}{d\Omega}=\sqrt{\frac{2(1+\mu)}{\pi\mu\chi_{\text{sq}}^2}}\int_{\chi_{\text{sq}}/\sqrt{1+\mu}}^{\infty}\frac{dz\ z}{\sqrt{z^2-\chi_{\text{sq}}^2/(1+\mu)}}$$
$$\times\exp\left[-\frac{1+\mu}{2\mu\chi_{\text{sq}}^2}\left(z^2-\frac{\chi_{\text{sq}}^2}{1+\mu}\right)\right]\frac{d\sigma_{\text{cl}}(n)}{d\Omega},$$

$$2\varphi_\alpha-\varphi_r=0, \tag{24}$$

$$\frac{d\sigma_{\text{sq}}(n)}{d\Omega}=\sqrt{\frac{1+\mu}{2\pi\mu\chi_{\text{sq}}^2}}\int_{-\infty}^{\infty}dz\ \exp\left[-\frac{1+\mu}{2\mu\chi_{\text{sq}}^2}\right.$$
$$\left.\times\left(z-\frac{\chi_{\text{sq}}}{\sqrt{1+\mu}}\right)^2\right]\frac{d\sigma_{\text{cl}}(n)}{d\Omega},$$

$$2\varphi_\alpha-\varphi_r=\pi. \tag{25}$$

We limit ourselves to the nonrelativistic approximation $|\mathbf{p}|/m\ll1$ and $\chi_{\text{sq}}\ll1$. Then, using the results of Refs. 6, 11, and 13, we can express $d\sigma_{\text{cl}}(n)/d\Omega$ as follows:

$$\frac{d\sigma_{\text{cl}}(n)}{d\Omega}=\left(\frac{4e^2}{m|\mathbf{n}_{fi}|v^2}\right)^2[|M_\theta(n)|^2+|M_{\theta-\pi}(n)|^2$$
$$-\text{Re}(M_\theta(n)M_{\theta-\pi}(n))], \tag{26}$$

$$M_\theta(n)=\frac{\mathbf{p}^2}{\omega_{\mathbf{k}}^2}\sum_{s=-\infty}^{\infty}\frac{J_s(A_1z)J_{n-s}(A_2z)}{(2s-n-b)^2+a^2}, \tag{27}$$

$$A_1=A+B,\quad A_2=A-B,\quad A=-\frac{|\mathbf{p}|}{\omega_{\mathbf{k}}}|\mathbf{n}_{fi}|\sin\vartheta,$$

$$B=\frac{|\mathbf{p}|v}{\omega_{\mathbf{k}}}(\mathbf{n}_i(\mathbf{n}_i\cdot\mathbf{n}_{\text{ext}})-\mathbf{n}_f(\mathbf{n}_f\cdot\mathbf{n}_{\text{ext}}))_\perp,$$

$$b=\frac{|\mathbf{p}|}{\omega_{\mathbf{k}}}|\mathbf{n}_{fi}|\cos\vartheta,$$

$$a^2=\frac{\mathbf{p}^2}{\omega_{\mathbf{k}}^2}|\mathbf{n}_{fi}|^2\sin^2\vartheta+4i\frac{|\mathbf{p}|\Gamma}{\omega_{\mathbf{k}}^2}|\mathbf{n}_{fi}|\cos\vartheta,$$

where $\mathbf{p}$ is the particle momentum prior to scattering in the center-of-mass system, $v=|\mathbf{p}|/m$, $\mathbf{n}_{fi}=\mathbf{n}_f-\mathbf{n}_i$, with $\mathbf{n}_i$ and $\mathbf{n}_f$ the unit vectors pointing in the direction of particle motion in the center-of-mass system before and after scattering, $\mathbf{n}_{\text{ext}}=\mathbf{k}/|\mathbf{k}|$, and θ is the angle between $\mathbf{n}_f$ and $\mathbf{n}_i$, $\Gamma=(e^2\omega^2/6)\chi_{\text{sq}}^2$ is the width of electron states in the field (the probability of electron emission per unit time), and the subscript $\perp$ indicates the projection of the respective vector on the polarization plane of the applied electromagnetic field. Using the integral representation of the Bessel functions,[25] we transform $M_\theta(n)$ into

$$M_\theta(n)=\frac{\mathbf{p}^2}{4\pi^2 a\omega_{\mathbf{k}}^2}\int_{-\pi}^{\pi}d\varphi\int_0^\infty dt\,\exp[iA_1 z\sin(\varphi+2t)+iA_2 z\sin\varphi+in(\varphi+t)-ibt-at]+\text{c.c.}\qquad(28)$$

If we now allow for (24), (25), and (28), we can easily see that in weak fields, for which $A_{1,2}\chi_{\text{sq}}\leqslant 1$, the scattering cross sections in squeezed and classical electromagnetic fields are related through formulas similar to (19). In the general case the expressions (24), (25), and (28) can be studied only numerically (see below).

Let us examine the nonresonant case $\operatorname{Re} a\gg 1$ ($A_{1,2}\approx A$ and $\vartheta\neq 0,\pi$). Approximate integration of Eq. (28) yields

$$M_\theta^{\text{nonres}}(n)\approx\frac{J_n(2Az)}{|\mathbf{n}_{fi}|^2}.$$

Since $|J_n(x)|\leqslant 1$, we can show that in the nonresonant scattering region at a fixed n the cross section is always smaller than the cross section of free-electron scattering, both in a classical electromagnetic field and in a quantized electromagnetic field. Bearing in mind that there exists a certain analogy between multilevel optical systems and the energy spectrum of an electron in a field,[4] we can assume that the effect is of the same origin as in atomic systems, in which a strong electromagnetic field is capable of completely suppressing processes occurring in the presence of such a field (absorption of probing radiation,[26] spontaneous decay of an excited level,[27] and the like).

We now turn to the case of resonant scattering. Formula (27) shows that resonance occurs when $\vartheta=0$, π and the difference $n-b$ is an even number. Here $|A_{1,2}|\approx B$ and the expression for $M_\theta(n)$ becomes

$$M_\theta^{\text{res}}(n)=\frac{|\mathbf{p}|}{2i\Gamma|\mathbf{n}_{fi}|}J_{(n+b)/2}(Bz)J_{(n-b)/2}(-Bz).$$

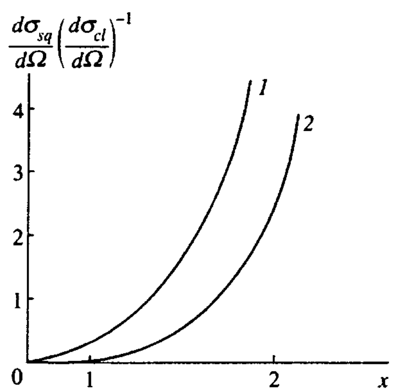

FIG. 3. Ratio of the differential electron–electron scattering cross sections in squeezed and classical electromagnetic field. Curve *1* refers to the nonresonant scattering region and to the case where the squeezed field is in the squeezed-vacuum state, $n=0$, $\vartheta=45°$, $\theta=30°$, and $x=2A\chi$. Curve *2* refers to the resonant scattering region and the case of an amplitude-squeezed electromagnetic field, $n=1$, $b=1$, $\mu=1$, and $x=B\chi$.

Note that, the conditions for resonance that are met for a given scattering angle θ are not met for the angle $\theta-\pi$ (except for particular spatial arrangements of the vectors $\mathbf{n}_i$, $\mathbf{n}_{\text{ext}}$, and $\mathbf{n}_f$). Hence $|M_\theta^{\text{res}}(n)|\gg|M_{\theta-\pi}(n)|$, and the contribution of the exchange interaction to (26) can be ignored. Thus, nonrelativistic electrons in the resonance region are scattered as spinless particles. A numerical analysis of (24) and (25) shows that the differential scattering cross section near a resonance exceeds by many orders of magnitude the differential scattering cross section of free electrons (here we do not consider forward scattering, $\theta=0$, where there is a singularity due to the properties of the Coulomb potential). There is a common feature of scattering in the nonresonant and resonant regions (Fig. 3): the probability of the process in a strongly fluctuating electromagnetic field is always higher than the probability in a coherent field.

In conclusion several remarks are in order. The approximation of quasistationary states (with width Γ) adopted in this section is equivalent to the idea that the interaction of an electron an the external electromagnetic field is switched on adiabatically. This leads to the requirement $\tau\gg 1/\Gamma$, where τ is the switch-on to switch-off time of the pulse, or the time that the electron spends in the field of the wave. Moreover, Γ imposes the following restriction on the spectral width, $\Delta\omega_{\mathbf{k}}$, of the source of the squeezed electromagnetic field: $\Gamma\gg\Delta\omega_{\mathbf{k}}$. Otherwise, in conditions of the present problem, we cannot assume that the external electromagnetic is single-mode.

[1] A. I. Nikishov and V. I. Ritus, Zh. Éksp. Teor. Fiz. **46**, 776 (1964) [Sov. Phys. JETP **19**, 529 (1964)].
[2] I. I. Gol'dman, Zh. Éksp. Teor. Fiz. **46**, 1412 (1964) [Sov. Phys. JETP **19**, 954 (1964)].
[3] L. S. Brown and T. W. Kibble, Phys. Rev. **133**, 705 (1964).
[4] V. I. Ritus, in *Quantum Electrodynamics of Phenomena in an Intense Field* [in Russian], Nauka, Moscow (1979) (Vol. 111 of Trudy Fiz. Inst. Akad. Nauk SSSR).
[5] V. P. Oleĭnik, Zh. Éksp. Teor. Fiz. **53**, 1997 (1967) [Sov. Phys. JETP **26**, 1132 (1968)].
[6] V. P. Oleĭnik, Zh. Éksp. Teor. Fiz. **52**, 1049 (1967) [Sov. Phys. JETP **25**, 697 (1967)].
[7] I. Berson, Zh. Éksp. Teor. Fiz. **56**, 1627 (1969) [Sov. Phys. JETP **29**, 871 (1969)].
[8] I. V. Lebedev, Opt. Spektrosk. **32**, 120 (1972) [Opt. Spectrosc. **32**, 59 (1972)].
[9] M. V. Fedorov, Zh. Éksp. Teor. Fiz. **68**, 1209 (1975) [Sov. Phys. JETP **41**, 601 (1975)].
[10] A. V. Borisov, V. I. Zhukovskiĭ, and P. A. Éminov, Zh. Éksp. Teor. Fiz. **78**, 530 (1980) [Sov. Phys. JETP **51**, 267 (1980)].
[11] J. Bergou, S. Varro, and M. V. Fedorov, J. Phys. A **14**, 2305 (1981).
[12] J. Bergou and S. Varro, J. Phys. A **14**, 22281 (1981).
[13] V. P. Kraĭnov and S. P. Roshchupkin, in *Interaction of Laser Light and Resonant Media* [in Russian], Énergoizdat, Moscow (1982).
[14] I. F. Ginzburg, G. L. Kotkin, and S. I. Polityko, Yad. Fiz. **40**, 1495 (1984) [Sov. J. Nucl. Phys. **40**, 949 (1984)].
[15] M. V. Galynskiĭ and S. M. Sikach, Zh. Éksp. Teor. Fiz. **101**, 828 (1992) [Sov. Phys. JETP **74**, 441 (1992)].

[16] S. P. Goreslavsky, N. B. Narozhny, O. V. Shcherbachev, and V. P. Yakovlev, Laser Phys. **3**, 418 (1993).
[17] S. P. Goreslavskiĭ, N. B. Narozhnyĭ, and O. V. Shcherbachev, JETP Lett. **61**, 261 (1996).
[18] N. B. Narozhnyĭ and M. S. Fofanov, Zh. Éksp. Teor. Fiz. **110**, 26 (1996) [JETP **83**, 14 (1996)].
[19] R. Loudon and P. Knight, J. Mod. Phys. **34**, 709 (1987).
[20] A. V. Belousov, V. A. Kovarskiĭ, and O. B. Prepelitsa, Zh. Éksp. Teor. Fiz. **108**, 447 (1995) [JETP **81**, 241 (1995)].
[21] V. P. Bykov, Ups. Fiz. Nauk **161**, No. 10, 145 (1991) [Sov. Phys. Usp. **33**, 253 (1991)].
[22] O. B. Prepelitsa, Teor. Mat. Fiz. **105**, 471 (1995).
[23] V. A. Kovarsky, Phys. Lett. A **221**, 195 (1996).
[24] M. V. Fedoryuk, *The Saddle-Point Method* [in Russian], Nauka, Moscow (1987), p. 28.
[25] I. S. Gradshteyn and I. M. Ryzhik, *Tables of Integrals, Sums, Series and Products*, Fizmatgiz, Moscow (1962), p. 966 [English transl.: Academic Press, New York (1980)].
[26] V. A. Kovarskiĭ, Zh. Éksp. Teor. Fiz. **57**, 1217 (1969) [Sov. Phys. JETP **30**, 663 (1969)].
[27] O. B. Prepelitsa, Opt. Spektrosk. **81**, 337 (1996) [Opt. Spectrosc. **81**, 340 (1996)].

Translated by Eugene Yankovsky

Radiation of slow electromagnetic waves in an isotropic medium with spatial dispersion

M. V. Marmazeev and M. I. Ryazanov

Moscow State Institute of Engineering Physics, 115409 Moscow, Russia

(Submitted 14 February 1997)
Zh. Éksp. Teor. Fiz. **112**, 1557–1562 (November 1997)

This paper discusses the distinctive features of radiation of electromagnetic waves with anomalously large values of the wave vector and small phase velocity that exist near narrow absorption lines. The distribution of radiated energy with respect to angle and frequency is calculated for Čerenkov radiation and bremsstrahlung of the slow waves. It is shown that the angular distribution of the slow-wave bremsstrahlung exhibits a characteristic maximum in the direction perpendicular to the plane of motion of the particles.

1. INTRODUCTION

It is well known that in many physical situations the effects of spatial dispersion lead only to small quantitative corrections; however, near a narrow absorption line spatial dispersion can give rise to large changes and even alter the physical picture qualitatively.[1] Addition of terms with powers of the wave vector to the dielectric permittivity increases the order of the dispersion equation, leading to the appearance of new roots of this equation. Far from the absorption line these roots lie outside the region of applicability of the theory and are fictitious. However, near the absorption additional roots can appear that have real physical meaning, i.e., new auxiliary waves appear.[2,3] In particular, experimental study of the reflection of light from crystals of CdS and ZnTe confirms that the dielectric permittivity near the exciton absorption line has the form[4–8]

$$\varepsilon(\omega,\mathbf{k})=\varepsilon_0+\frac{4\pi\alpha_0\omega_0^2}{\omega_0^2-\omega^2+(hk^2\omega_0/M)-2i\Gamma\omega}, \tag{1}$$

where M is the exciton mass and Γ is the line width. It is not difficult to see that the real part of this dielectric permittivity reaches its largest value when ω and k satisfy the relation

$$|\omega_0^2-\omega^2+(hk^2\omega_0/M)|\sim\Gamma\omega, \tag{2}$$

which allows values of k that are large compared to ω/c but small compared to an inverse interatomic distance. In the frequency range where the dielectric permittivity has the form Eq. (1), the dispersion equation for small absorption can be written in the form

$$\begin{gathered}(ck/\omega)^4+G(ck/\omega)^2+F=0,\\ F=4\pi\alpha_0(Mc^2/h\omega_0)(\omega_0/\omega)^2-\varepsilon_0[(\omega_0/\omega)^2-1],\\ G=(Mc^2/h\omega_0)[(\omega_0/\omega)^2-1]-\varepsilon_0.\end{gathered} \tag{3}$$

The existence of a second solution to the dispersion equation implied by Eq. (3), i.e., the existence of auxiliary waves, is also confirmed by experiment. Thus, whereas the measurements of the reflection of light from CdS cannot be explained even qualitatively if it is assumed that the dispersion equation has only one solution, by postulating that auxiliary waves exist it becomes possible to obtain a complete quantitative explanation for the experimental data.[4–8] It is convenient to transform Eq. (3) to the form

$$\{(ck/\omega)^2-K_1^2\}\{(ck/\omega)^2-K_2^2\}=0, \tag{4}$$

where

$$K_{1,2}^2=(1/2)\{-G+(-)[G^2+4F]^{1/2}\}. \tag{5}$$

It follows from Eq. (5) that large values of the wave vector are possible when G and F are large, i.e., when the inequalities

$$Mc^2|(\omega_0/\omega)^2-1|\gg h\omega,\quad Mc^2 4\pi\alpha_0(\omega_0/\omega)^2\gg h\omega_0 \tag{6}$$

are satisfied.

In many materials the exciton mass is comparable in order of magnitude to the mass of an electron[4–8]; therefore, $Mc^2\sim10^5$ eV, and for $\hbar\omega_0$ of order of a few eV these inequalities can be satisfied. This implies that electromagnetic waves can really exist whose wave vector k is large compared to ω/c but small compared to inverse interatomic distances. Such waves have low phase velocity, but phenomenological macroscopic electrodynamics remains a useful way to describe them. Thus, for example, for CdS,[7] with $\omega_0=2.55$ eV, $4\pi\alpha_0=10^{-2}$, $\Gamma=2\cdot10^{-4}$ eV, $\varepsilon_0=8$, and $M=0.9m$ (here m is the mass of a free electron), $ck/\omega\gg1$ over a rather narrow frequency range (for frequencies $\omega\sim1.01\omega_0$ the ratio $ck/\omega\sim15$).

2. SLOW ELECTROMAGNETIC WAVES NEAR AN ABSORPTION LINE

Let us consider electromagnetic waves in the frequency range near a narrow absorption line where the dielectric permittivity can be written in the form Eq. (1) and dispersion equations (3), (4) are valid. In the region of interest to us, i.e., large ck/ω, the pole term is large and the constant term can be dropped, and because $\omega-\omega_0\gg\Gamma$ we can neglect the imaginary part of $\varepsilon(\omega,k)$. Then in this frequency range the Maxwell equations connect the Fourier transforms of the magnetic field $\mathbf{H}(\mathbf{q},\omega)$ and current density $\mathbf{j}(\mathbf{q},\omega)$ by the relation $(Q_{1(2)}=(\omega/c)K_{1(2)})$

$$(q^2-Q_1^2)(q^2-Q_2^2)\mathbf{H}(\mathbf{q},\omega)$$
$$=(4\pi i/c)(g+q^2)(\mathbf{q}\times\mathbf{j}(\mathbf{q},\omega)), \qquad (7)$$

where $g=2M(\omega-\omega_0)/h$. From Eq. (7) it is not difficult to obtain

$$\mathbf{H}(\mathbf{q},\omega)=\mathbf{H}_1(\mathbf{q},\omega)+\mathbf{H}_2(\mathbf{q},\omega),$$
$$\mathbf{H}_{1(2)}(\mathbf{q},\omega)=\frac{(4\pi i/c)(g+q^2)(\mathbf{q}\times\mathbf{j}(\mathbf{q},\omega))}{\{Q_{1(2)}^2-Q_{2(1)}^2\}(q^2-Q_{1(2)}^2+i0)}. \qquad (8)$$

If Q_1 is a real quantity and Q_2 is complex, then at large distances $\mathbf{H}_2$ disappears and we need only consider $\mathbf{H}_1$. In this case the dependence of the field on coordinates at large distances has the form

$$\mathbf{H}_1(\mathbf{r},\omega)$$
$$=\frac{(4\pi i/c)}{\{Q_1^2-Q_2^2\}}\int d^3q\,\frac{(g+q^2)(\mathbf{q}\times\mathbf{j}(\mathbf{q},\omega))\exp(i\mathbf{q}\cdot\mathbf{r})}{(q^2-Q_1^2+i0)}. \qquad (9)$$

Using the well-known relation

$$\int d^3p\Phi(\mathbf{p})\exp(i\mathbf{p}\cdot\mathbf{r})(p^2-k^2+i0)^{-1}$$
$$=(2\pi^2/r)\Phi(k\mathbf{r}/r)\exp(ikr), \qquad (10)$$

which is correct for $kr\gg1$ to within small corrections of order $1/kr$, it is not difficult to obtain an expression for the field at large distances when $Q_1r\gg1$:

$$\mathbf{H}(\mathbf{r},\omega)=(2\pi)^3(i/cr)$$
$$\times\exp(ikr)(\mathbf{k}\times\mathbf{j}(\mathbf{k},\omega))(g+k^2)/(Q_2^2-Q_1^2)^{-1}, \qquad (11)$$

where $\mathbf{k}=Q_1(\mathbf{r}/r)=Q_1\mathbf{n}$.

3. RADIATION OF SLOW ELECTROMAGNETIC WAVES

Using Eq. (11) it is not difficult to obtain the following relation for the distribution of radiated energy with respect to angle and frequency at large distances from the source:

$$d^2E(\mathbf{n},\omega)/d\omega\ d\Omega$$
$$=(2\pi)^6(\varepsilon(k,\omega))^{-1/2}|(\mathbf{k}\times\mathbf{j}(\mathbf{k},\omega))|^2Y(k,\omega)/c, \qquad (12)$$

in which $Y(k,\omega)$ contains all the deviations from the usual expression caused by inclusion of spatial dispersion:

$$Y(k,\omega)=(g+k^2)^2/(g^2+4f\ ), \qquad (13)$$

where

$$f=2\pi\alpha_0\omega_0(M/h)(\omega/c)^2. \qquad (14)$$

The reason why an additional solution for the field appears when spatial dispersion is included can ultimately be traced to the presence of this factor. If the equation of motion of a charged particle $\mathbf{r}=\mathbf{R}_0(t)$ is known, then the angular and frequency distribution of the energy it radiates can be written in the form ($\mathbf{V}=d\mathbf{R}/dt$)

$$d^2E/d\omega\ d\Omega=(e^2\omega^2/4\pi^2c^3)\varepsilon^{1/2}(k,\omega)$$
$$\times\int\int dT\ dt[\mathbf{n}\cdot\mathbf{V}(T+t/2)]$$
$$\times[\mathbf{n}\cdot\mathbf{V}(T-t/2)]\exp\{i\omega t-i\mathbf{k}\cdot\mathbf{b}(T,t)\}, \qquad (15)$$

where $\mathbf{b}(T,t)=\mathbf{R}(T+t/2)-\mathbf{R}(T-t/2)$. It follows from Eq. (13) that the factor $Y(k,\omega)$ does not depend on the angles. Then the angular integration can be carried out in the usual way, which leads to a spectrum of the radiation that can be written in the form

$$dE/d\omega=(e^2\omega^2/\pi c^3)\varepsilon^{1/2}(k,\omega)Y(k,\omega)\int\int dT\ dt$$
$$\times\{c^2-\mathbf{V}(T+t/2)\cdot\mathbf{V}(T-t/2)\varepsilon(\omega,k)\}$$
$$\times(1/k|b(T,t)|)\{\sin[\omega t-k|b(T,t)|]$$
$$-\sin[\omega t+k|b(T,t)|]\}. \qquad (16)$$

4. ČERENKOV RADIATION OF SLOW WAVES

Let us consider Čerenkov radiation of slow waves by a charge e moving uniformly with velocity $\mathbf{v}$ in a material. Substituting the law of motion in the form $\mathbf{R}=\mathbf{v}t$ into Eq. (15) gives the distribution of radiated energy with respect to angle and frequency:

$$d^2E/d\omega\ d\Omega=T(e^2\omega^2/2\pi c^3)\varepsilon^{1/2}(k,\omega)(\mathbf{n}\times\mathbf{v})^2Y(k,\omega)$$
$$\times\delta(\omega-\mathbf{k}\cdot\mathbf{v}), \qquad (17)$$

where T is the total time of flight. The delta function entering into Eq. (17) rigorously connects the angle of emission of the radiation θ with its frequency and the velocity of the particle through the relation

$$2c^2=v^2\cos^2\theta\{[G^2+4F]^{1/2}-G\}. \qquad (18)$$

Energy and momentum conservation permit the existence of this radiation only if the velocity of a particle is larger than a threshold value v_0 determined by the equation

$$v_0^2=2c^2/\{[G^2+4F]^{1/2}-G\}. \qquad (19)$$

5. RADIATION OF SLOW WAVES BY A CHARGE MOVING IN ARBITRARY FASHION WITH VELOCITY BELOW THE THRESHOLD FOR ČERENKOV RADIATION

Radiation of slow waves by a particle moving in an arbitrary fashion at velocity $v<v_0$ can be treated as ordinary radiation in a medium, with the sole difference that the additional factor $Y(k,\omega)$ appears. An interesting case is when the velocity $v\gg v_0-v>0$. Here the situation is analogous to radiation of ultrarelativistic particles in vacuum. The length of that segment of the particle's path from which radiated waves arrive at the detector with phases that are close in value (i.e., the generation length of the radiation or the coherence length) is in this case much larger than the wavelength of the wave field, and the distinctive features that arise in the process of radiating slow waves here are analogous to well-known features of the radiation of ordinary waves by ultrarelativistic particles.[9–12] This allows us to simulate the radiation of ordinary waves at high energies by using radiation of slow waves by nonrelativistic particles. For example, if the coherence length, i.e., the length of particle path along which radiation is generated, is much larger than the scattering amplitude of the particle by an atom of the material, then we can use the approximation that the particle velocity changes suddenly during the collision. In the case of radiation of ordinary waves whose frequency is not too high, this approximation is applicable for ultrarelativistic particles, while for radiation of slow waves this approximation can also be used for nonrelativistic particles. The law of motion of a particle in this approximation has the form

$$\mathbf{r}(t)=\mathbf{v}t, \quad t<0, \quad \mathbf{r}(t)=\mathbf{u}t, \quad t>0,$$

and substituting this into Eq. (15) yields

$$d^2E/d\omega\, d\Omega = (e^2\omega^2/4\pi^2c^3)\varepsilon^{1/2}(k,\omega)Y(k,\omega)\left|(\mathbf{n}\times\mathbf{v})/(\omega-\mathbf{k}\cdot\mathbf{v}) - (\mathbf{n}\times\mathbf{u})/(\omega-\mathbf{k}\cdot\mathbf{u})\right|^2. \tag{20}$$

6. RADIATION OF SLOW WAVES DURING THE COLLISION OF A RELATIVISTIC CHARGE PARTICLE WITH AN ATOM

For a relativistic particle, Čerenkov radiation of slow waves always takes place; however, when the particle collides with an atom its velocity changes, so that bremsstrahlung appears as well. Taking into account that the approximation of a sudden change in the velocity is valid in this case as well, and substituting the corresponding law of motion of the particle into Eq. (15), we can find the distribution of radiated energy in the form

$$d^2E/d\omega\, d\Omega=(d^2E/d\omega\, d\Omega)_{Ch}+(d^2E/d\omega\, d\Omega)_{br}, \tag{21}$$

$$(d^2E/d\omega\, d\Omega)_{Ch}=(T/2)(e^2\omega^2/2\pi c^3)\varepsilon^{1/2}(k,\omega)Y(k,\omega)\times\{(\mathbf{n}\times\mathbf{v})^2\delta(\omega-\mathbf{k}\cdot\mathbf{v})+(\mathbf{n}\times\mathbf{u})^2\delta(\omega-\mathbf{k}\cdot\mathbf{u})\}, \tag{22}$$

$$(d^2E/d\omega\, d\Omega)_{br}=(e^2\omega^2/4\pi^2c^3)\varepsilon^{1/2}(k,\omega)Y(k,\omega)\times\left\{\frac{(\mathbf{n}\times\mathbf{v})(\omega-\mathbf{k}\cdot\mathbf{v})}{(\omega-\mathbf{k}'\cdot\mathbf{v})^2+(\mathbf{k}''\cdot\mathbf{v})^2}-\frac{(\mathbf{n}\times\mathbf{u})(\omega-\mathbf{k}\cdot\mathbf{u})}{(\omega-\mathbf{k}'\cdot\mathbf{u})^2+(\mathbf{k}''\cdot\mathbf{u})^2}\right\}. \tag{23}$$

Here T is the total observation time, and $\mathbf{k}=\mathbf{k}'+i\mathbf{k}''$; absorption in the medium is assumed to be small, and is taken into account only when necessary for integration. Comparing Eqs. (22) and (17), it is not difficult to verify that Eq. (22) consists of the sum of the energy of the Čerenkov radiation emitted by the particle before and after the sudden change in its velocity. The energy radiated as a result of the velocity change of the particle is determined by Eq. (23). An important difference, which is connected with the existence of Čerenkov radiation, is the fact that $\omega-\mathbf{k}\cdot\mathbf{v}$ and $\omega-\mathbf{k}\cdot\mathbf{u}$ can have any values. In particular, in those regions of frequency and angle where these quantities have opposite signs, the difference of the two fractions in Eq. (23) is replaced by their sum, so that the contribution of these regions of frequency and angle to the total energy radiated is considerably increased.

Let us discuss under what conditions it is possible for this increase in the intensity of the radiation to occur. Let the z axis of a spherical system of coordinates be directed along $\mathbf{v}$, the direction of the vector $\mathbf{k}$ be given by angles θ and ϕ, and the angle ϕ be measured from the plane of the vectors $\mathbf{v}$ and $\mathbf{u}$. Then

$$\mathbf{k}\cdot\mathbf{v}=kv\cos\theta,$$

$$\mathbf{k}\cdot\mathbf{u}=ku\{\sin\alpha\sin\theta\cos\phi+\cos\alpha\cos\theta\},$$

where α is the angle between $\mathbf{v}$ and $\mathbf{u}$, so that $\mathbf{u}\cdot\mathbf{v}=uv\cos\alpha$. The range of angles in which the increase in intensity takes place is determined by the inequalities

$$\cos\theta<\omega/kv,$$

$$\cos\alpha\cos\theta+\sin\alpha\sin\theta\cos\phi>\omega/kv \tag{24}$$

or

$$\cos\theta>\omega/kv,$$

$$\cos\alpha\cos\theta+\sin\alpha\sin\theta\cos\phi<\omega/kv. \tag{25}$$

Then the characteristic maximum in the angular distribution of slow waves lies near the direction perpendicular to the plane of the vectors $\mathbf{v}$ and $\mathbf{u}$, i.e., near the normal to the plane of motion of the particle. Let us consider as a qualitative example radiation in the direction for which $\cos\phi=0$. Then the increase in intensity occurs in that range of angles determined by the inequalities

$$\cos\theta>\omega/kv>\cos\alpha\cos\theta. \tag{26}$$

Because the characteristic angles of deviation are small during the collision of a relativistic particle with an atom, we have $\alpha\ll 1$ and the increase in intensity of the radiation takes place in a rather narrow region of angles, while the contribution of this region to the spectrum of the radiation is small. The radiated energy in the angular region Eq. (26) takes the form

$$(d^2E/d\omega\, d\Omega)_{br}=(e^2\omega^2/4\pi^2c^3)\varepsilon^{1/2}(k,\omega)Y(k,\omega)v^2\alpha^2(\omega-kv)^2. \tag{27}$$

7. DISCUSSION OF RESULTS

The distinctive features of the radiation of waves with anomalously small phase velocity demonstrated above can be of interest in connection with the possibility of simulating radiation by ultrarelativistic particles in vacuum using the radiation of slow waves by nonrelativistic particles in a medium. In addition, this constitutes a new type of electromagnetic interaction in matter. Anomalously slow electromagnetic waves can exist not only near narrow absorption lines in an isotropic medium with spatial dispersion but also in noncubic crystals for frequencies close to zeroes of the principal values of the dielectric permittivity tensor[13] within rather narrow ranges of frequency and directions of propagation. In the latter case, the radiation of slow waves turns out to be a more complicated process due to the narrowness of the region in which they exist.

In discussing anomalous slow waves we must also keep in mind that their short wavelengths make them more sensitive to the presence of small nonuniformities in the medium. This sensitivity is manifested in an enhancement of scattering and hence an increase in the extinction coefficient. This somewhat limits the applicability of the ordinary approximation of a uniform medium to these waves, i.e., as macroscopic disturbances.

[1] L. D. Landau and E. M Lifshitz, *Electrodynamics of Continuous Media*, 2nd Engl. ed. (Pergamon Press, Oxford (1984).

[2] S. I. Pekar, Zh. Éksp. Teor. Fiz. **33**, 1022 (1957) [Sov. Phys. JETP **6**, 785 (1958)].

[3] V. L. Ginzburg, Zh. Éksp. Teor. Fiz. **34**, 1593 (1958) [Sov. Phys. JETP **7**, 1096 (1958)].

[4] J. J. Hopfield and D. G. Thomas, Phys. Rev. **132**, 563 (1963).

[5] I. V. Makarenko, I. N. Uraltsev, and V. A. Kiselev, Phys. Stat. Solidi **98**, 773 (1980).

[6] L. E. Solov'ev and A. B. Babinskiĭ, JETP Lett. **23**, 263 (1976).

[7] S. I. Pekar and M. I. Strashnikova, Zh. Éksp. Teor. Fiz. **68**, 2047 (1975) [Sov. Phys. JETP **41**, 1024 (1975)].

[8] S. I. Pekar, *Crystal Optics and Auxiliary Light Waves* [in Russian], Naukova Dumka, Kiev (1982).

[9] M. L. Ter-Mikaelyan, *The Influence of a Medium on Electrodynamic Processes at High Energies* [in Russian], Armenian Acad. Sci. Publ., Yerevan (1969).

[10] V. N. Vaĭner V. M. Katkov, and V. S. Fadin, *Radiation by Nonrelativistic Electrons* [in Russian], Atomizdat, Moscow (1973).

[11] G. M. Garibyan and Yam Shi, *X-Ray Transition Radiation* [in Russian], Armenian Acad. Sci. Publ., Yerevan (1983).

[12] A. I. Akhiezer and N. F. Shul'ga, *High- Energy Electrodynamics in Matter* [in Russian], Nauka, Moscow (1993).

[13] M. I. Ryazanov, Zh. Éksp. Teor. Fiz. **103**, 1840 (1993) [JETP **76**, 910 (1993)].

Translated by Frank J. Crowne

Spectral properties of backward stimulated scattering in liquid carbon disulfide

Guang S. He, Yiping Cui, and Paras N. Prasad

Photonics Research Laboratory, State University of New York at Buffalo, Buffalo, New York 14260-3000, USA

(Submitted 13 March 1997)
Zh. Éksp. Teor. Fiz. **112**, 1563–1573 (November 1997)

The spectral structure of backward stimulated scattering from a 10 cm-long CS_2-liquid cell is investigated by using Q-switched 10-ns and 532-nm laser pulses with different spectral linewidths. Under a narrow spectral line ($\sim 0.1\ \mathrm{cm}^{-1}$) pump condition, very strong sharp lines near the pump wavelength (λ_0) position and the first-order stimulated Raman scattering (λ_{s1}) position can be observed. However, under a wide line ($\approx 1\ \mathrm{cm}^{-1}$) pump condition, only a strong and superbroadening spectral band can be observed mainly in the red-shift side of the pump wavelength. The different spectral features under these two conditions can be explained by a competition between stimulated Brillouin, Raman, and Rayleigh–Kerr scattering. Under both pump conditions, the broadening spectral distributions are not consistent with the predictions given by stimulated Rayleigh-wing scattering theories, but can be interpreted well utilizing the theoretical model of stimulated Rayleigh–Kerr scattering. *© 1997 American Institute of Physics.* [S1063-7761(97)00411-3]

I. INTRODUCTION

Early observations of spectral broadening (up to $\sim 15\ \mathrm{cm}^{-1}$) of the backward stimulated scattering from a Kerr liquid cell were reported in the mid-1960s and interpreted phenomenologically as stimulated Rayleigh-wing scattering (SRWS).[1–3] According to SRWS theories,[1–4] the normalized exponential gain profile is given by

$$g_{\mathrm{SRWS}}(\Delta\nu=\nu_0-\nu)\propto|E_0|^2(2\pi\Delta\nu\tau)/[1+(2\pi\Delta\nu\tau)^2], \tag{1}$$

where ν_0 and ν are the frequency of the pump line and the frequency of SRWS respectively; τ is the molecular reorientational relaxation time of a given Kerr liquid comprised of anisotropic molecules, and E_0 is the amplitude of a monochromatic incident optical electric field. For the same optical intensity level (in units of $\mathrm{W/cm}^2$), a smaller spectral linewidth will yield a greater E_0 value and a higher gain value. According to Eq. (1) one can find that there will be attenuation on the anti-Stokes side of the pump line, and gain on the Stokes side, respectively. In particular, the location of the gain maximum on the Stokes side will be determined by

$$\Delta\nu_{\max}=1/2\pi\tau. \tag{2}$$

For CS_2 the measured value of τ is about 1.5–2 ps, so that the value of $\Delta\nu_{\max}$ should be $\sim 3\ \mathrm{cm}^{-1}$. During the early SRWS studies, it was difficult to accomplish a reliable quantitative comparison between experimental measurements and theoretical predictions due to the influence from strong stimulated Brillouin scattering, poor spectral resolution, and the overexposure effect of the photographic films or plates employed.[1,2]

Since the mid-1980s, superbroadening ($>400\ \mathrm{cm}^{-1}$) forward stimulated scattering from a Kerr-liquid-filled hollow fiber system has been reported and systematically investigated.[5–10] The main features of this kind of spectral broadening behavior can not be simply interpreted by either SRWS theories,[1,3,11] stimulated thermal Rayleigh scattering,[12,13] or self/cross-phase modulation mechanisms.[14] However, they can be explained well based on the theoretical model of stimulated Rayleigh–Kerr scattering (SRKS).[5–9] According to this model a much broader gain curve on the Stokes side of the pump line should be observed, and can be expressed as[5,6]

$$g(\Delta\nu\geqslant 0)=\lambda_0^2N\sigma(\Delta\nu)I_0/[4\pi h\nu_0(\delta\nu_0)]. \tag{3}$$

Here λ_0 is the pump wavelength, N is the molecular density of the scattering medium, I_0 is the pump intensity, h is Planck's constant, and $\delta\nu_0=1/2\pi\tau$ is the spectral linewidth of the elementary Rayleigh–Kerr scattering process. Finally, the scattering cross section $\sigma(\Delta\nu)$ is given by

$$\sigma(\Delta\nu)=(2\pi/c)^4\nu_0^4(\alpha_\parallel^2-\alpha_\perp^2)\cos^2[f(\Delta\nu)], \tag{4}$$

where c is the speed of light, $\alpha_\parallel$ and $\alpha_\perp$ are the maximum and minimum molecular polarizabilities of a given Kerr liquid, and $f(\Delta\nu)$ is an increasing function of $\Delta\nu$ which can be experimentally determined for a given scattering medium. A trial function such as

$$f(\Delta\nu)=(a\Delta\nu)^b \tag{5}$$

can be used to fit the experimental data of the forward stimulated scattering spectra from a CS_2-liquid-filled fiber system. Here, $\Delta\nu$ is in units of cm^{-1}, and $f(\Delta\nu)$ is in units of angular degrees. The best fitting parameters for CS_2 liquid were $a=7.5\cdot 10^9$ and $b=0.148$.[5]

It is different from the SRWS theory that on the anti-Stokes side of the pump line, an observable spectral broadening is also predicted by the SRKS theory. In this case, the gain curve on the anti-Stokes side of the pump wavelength can be expressed as[5,6]

$$g(\Delta\nu\leqslant 0)=g(0)[1/(2\pi\tau)^2]/[(\Delta\nu)^2+1/(2\pi\tau)^2], \tag{6}$$

where $g(0)$ is the maximum stimulated scattering gain value at $\Delta\nu=0$, and τ is still the molecular reorientational relaxation time. The experimental results for forward superbroad-

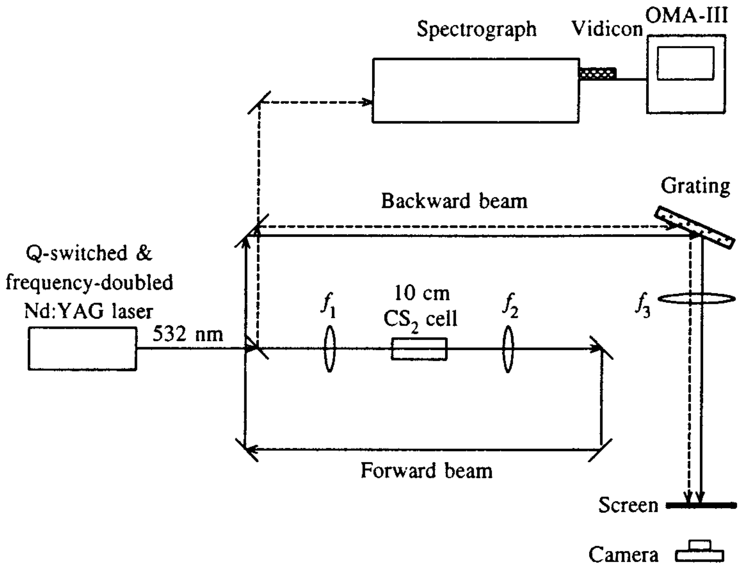

FIG. 1. The experimental setup for spectral measurements of forward and backward stimulated scattering from a 10 cm-long CS_2-liquid cell.

ening stimulated scattering from a CS_2 liquid-filled hollow-fiber system were basically in agreement with the above theoretical description.[5–10] In these cases, however, someone might not be entirely convinced by thinking that the intensity of the transmitted pump beam is so high, that the possible small-red-shifted SRWS may be covered by the transmitted pump signal, and, also, a cascade effect may take place for a long hollow-fiber sample. For these reasons, it seems necessary to pursue a thorough study of the spectral properties of backward stimulated scattering in a shorter CS_2-liquid cell, in which case the intense pump beam background and the spatial cascade effect can be eliminated.

2. EXPERIMENTAL SETUP

In this work, we report the spectral-broadening measurements of backward stimulated scattering from a 10 cm-long CS_2-liquid cell pumped with either a narrow ($\sim 0.1\ \mathrm{cm}^{-1}$) 532-nm laser line or a wide ($\sim 1\ \mathrm{cm}^{-1}$) 532-nm laser line. The experimental setup is schematically shown in Fig. 1. The pump source was a frequency-doubled and Q-switched Nd:YAG laser with a ~ 10 ns pulsewidth, ~ 1-mrad beam divergence, ~ 3-mm beam size, and 10-Hz repetition rate. The spectral width of the output laser pulses was $\sim 1\ \mathrm{cm}^{-1}$ when a Pockels cell was used as a Q-switching element. When a BDN dye-doped acetate sheet was employed as the Q-switching element, the output spectral linewidth was $\sim 0.1\ \mathrm{cm}^{-1}$, measured by a Fabry–Perot etalon. Exchanging the Q-switching element did not cause any considerable change of the output pulse duration and profile.[7]

The incident 532-nm pump laser beam was focused through a $f_1 = 30$ cm lens into a 10 cm-long quartz liquid cell filled with CS_2. The liquid sample was specially purified, i.e., glass-distilled twice and then filtered through a 0.2 μm filter. Therefore, linear absorption due to residual impurities in the liquid and possible stimulated thermal scattering can be neglected. A special feature of the setup shown in Fig. 1 is that the forward beam and the backward beam from the CS_2 liquid-cell can be measured simultaneously by a spectrographic device. The spectral distributions of the backward and forward stimulated emission from the liquid-cell sample could be measured by three different systems: (i) a low-spectral-resolution ($\sim 9\ \mathrm{cm}^{-1}$) system consisting of a single grating (1800 lines/mm), a $f_3 = 60$ cm focusing lens, and an ordinary camera; (ii) a medium-resolution ($-1.8\ \mathrm{cm}^{-1}$) system consisting of a grating spectrograph (Triplemate from SPEX) in conjunction with a vidicon-OMA (optical multichannel analyzer) III device (from EG&G Princeton Applied Research); and (iii) a high-resolution ($\sim 0.48\ \mathrm{cm}^{-1}$) system consisting of a double-monochromator (Jobin–Yvon) in conjunction with the same vidicon-OMA III device.

The temporal profiles of the pump laser pulse and the backward stimulated scattering pulse can be easily measured using a 350-MHz oscilloscope (Tektronix 2467 with C1001 video camera).[7] At pump intensity levels 150–400 $\mathrm{MW/cm}^2$, the pulse width of backward stimulated scattering from the 10-cm long CS_2-liquid-filled cell measured 4–6 ns.

3. RESULTS AND DISCUSSION

Typical spectral photographs of backward stimulated scattering from the 10 cm-long CS_2-liquid-filled cell are shown in Fig. 2 by using the spectral measurement system (i) with a spectral resolution of $\sim 9\ \mathrm{cm}^{-1}$ at a pump intensity $I_0 \approx 150\ \mathrm{MW/cm}^2$. The photograph shown in Fig. 2a is obtained using the wide ($\sim 1\ \mathrm{cm}^{-1}$) pump line, which shows a smoothly decreasing and superbroadening spectrum mainly on the Stokes side of the pump wavelength and is obviously broader than the previously reported SRWS by more than one order of magnitude.[1,2]

In contrast, the photograph shown in Fig. 2b is obtained using a narrow ($\sim 0.1\ \mathrm{cm}^{-1}$) pump line, and exhibits two strong sharp spectral lines accompanied by a much weaker broadening component. In Fig. 2b the first sharp line was nearly located at the pump line (λ_0) position, and the second line was located at the first-order Stokes stimulated Raman scattering line (λ_{s1}) position with a Raman shift of $\sim 656\ \mathrm{cm}^{-1}$. A Fabry–Perot etalon measurement showed that the first sharp line in Fig. 2b is the backward stimulated

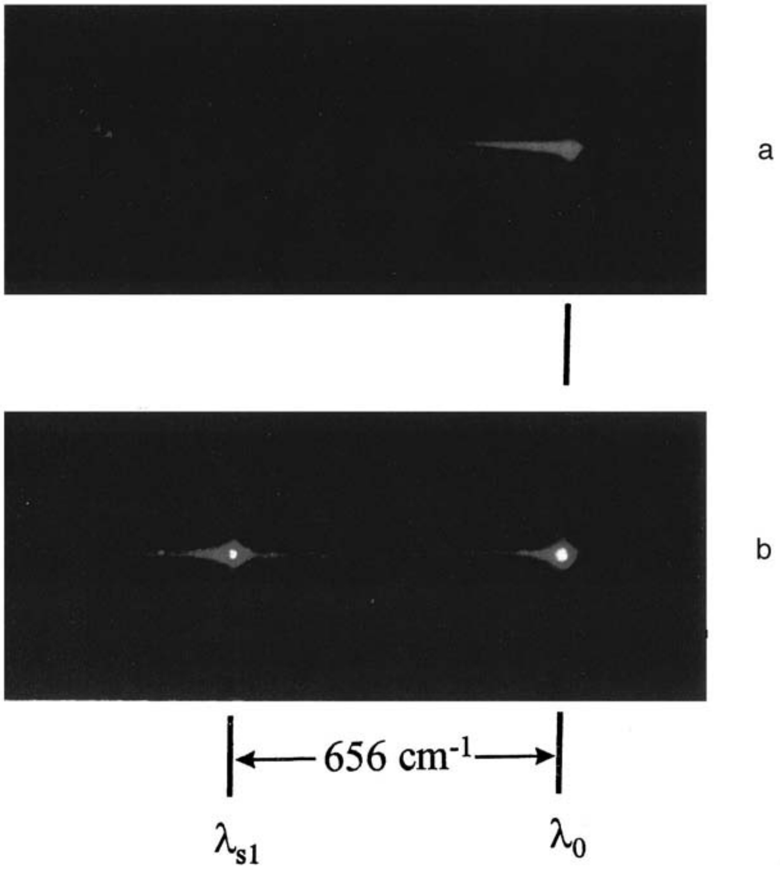

FIG. 2. Spectral photographs of backward stimulated scattering from the CS_2-liquid sample pumped by *a* $\sim 1\ \mathrm{cm}^{-1}$-wide 532-nm line (a) and $\sim 0.1\ \mathrm{cm}^{-1}$-wide 532-nm line (b), respectively. The pump intensity is $I_0 \approx 150\ \mathrm{MW/cm}^2$ and the spectral resolution is $\sim 9\ \mathrm{cm}^{-1}$.

Brillouin scattering line accompanied by a weaker broad wing mainly on the red side.

The substantial difference between Fig. 2a and Fig. 2b can be explained by a competition effect among three major stimulated scattering processes in a CS_2-type transparent liquid: stimulated Brillouin scattering (SBS), stimulated Raman scattering (SRS), and stimulated Rayleigh–Kerr scattering (SRKS) (or possible SRWS scattering?). For different pump conditions, the relative threshold requirements for various stimulated scattering processes may be considerably different, even for a given sample. Under the same pump pulse duration and intensity level, the threshold requirements for SBS and SRS quite sensitively depend on the spectral width of the pump line. For instance, the reported experimental results show that the SBS threshold increases following an increase in the pump linewidth.[15–17] In fact, the threshold increase (or efficiency decrease) of SBS becomes more severe if the pump linewidth is much greater than the frequency shift of the backward SBS.[18,19] For liquid CS_2, this shift is about $\sim 0.25\ \mathrm{cm}^{-1}$, so the pump condition in Fig. 2a is an example of the latter case.

It is reasonable to assume that in the case of Fig. 2a, the backward SBS and SRS were suppressed due to their higher threshold requirements under wide line excitation. Therefore, the backward SRKS process became the dominant mechanism contributing to the observed superbroadband spectral distribution. In contrast, in the case of Fig. 2b, the SBS and SRS were the dominant processes contributing to the two strong sharp lines, due to their relatively lower threshold requirements under narrow line excitation.

Figure 3 shows photographs of the spectra for both the forward and backward stimulated emission from the same 10-cm long CS_2-liquid cell sample pumped with the 532-nm line of $\sim 1\ \mathrm{cm}^{-1}$ width at three different pump intensity levels. In Fig. 3 for each photograph the upper spectrum corresponds to forward emission, comprising the transmitted pump line and the forward stimulated scattering, while the lower spectrum corresponds to backward stimulated scattering only. It can be seen in Fig. 3 that at lower pump intensity (Fig. 3a), the forward emission is mainly composed of a transmitted pump line (λ_0) and the first-order Stokes stimulated Raman scattering line (λ_{s1}); whereas at higher pump intensity (Fig. 3c), there is also a considerable red-shifted broadening component added to the λ_0 line. This is understandable because at a lower pump level, forward broadening stimulated scattering takes only a very small percentage of the total forward beam. As the pump intensity is increased, the ratio between forward broadening scattering and transmitted λ_0 emission becomes greater, and the red-spread wing looks broader and stronger. This behavior is essentially the same as that of the forward SRKS observed in a CS_2-liquid cell sample.[5,9]

In addition, it should be noted that the spectral structure of the forward emission shown in Fig. 3 is quite similar to that of the backward stimulated emission shown in Fig. 2b. This similarity is understandable because in the latter case,

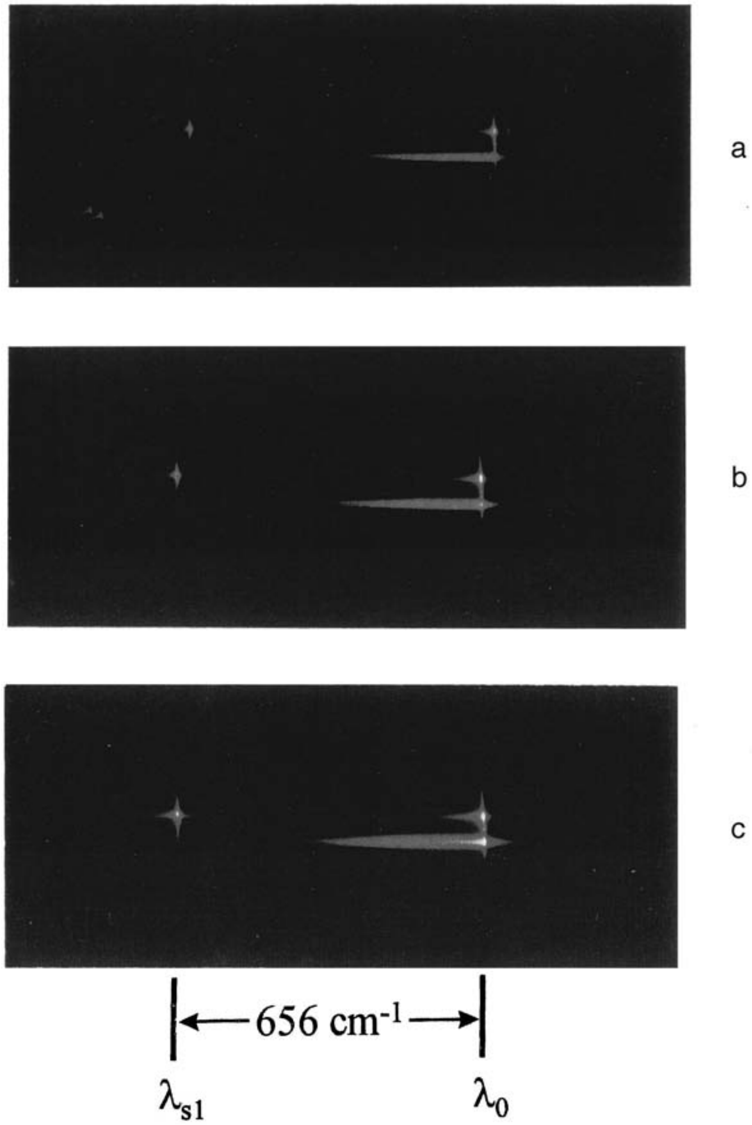

FIG. 3. Spectral photographs of the forward stimulated emission (upper track) and backward stimulated scattering (lower track) pumped by the $\sim 1\ \mathrm{cm}^{-1}$-wide 532-nm line at various pump intensity levels: $I_0 \approx 170$ (a), 250 (b), 400 (c) MW/cm^2.

instead of the pump line, backward SBS is the predominant component excited by the narrow ($\sim 0.1\ \mathrm{cm}^{-1}$) pump line, so that the entire backward SRKS feature is partially covered by the intense SBS line, as shown in Fig. 2b. On the other hand, in Fig. 3 one can see that the spectral feature of backward stimulated scattering remains basically unchanged at the three different pump intensity levels. This fact can easily be understood because there is no competition with the other predominant sharp line.

We should now further clarify which mechanism, SRKS or SRWS, is mainly responsible for the observed spectral broadening of backward emission pumped with either the $\sim 0.1\ \mathrm{cm}^{-1}$ line or the $\sim 1\ \mathrm{cm}^{-1}$ line. For this purpose, quantitative spectral measurements with higher spectral resolution are needed. To observe the detailed spectral distribution pumped with a narrow line ($\sim 0.1\ \mathrm{cm}^{-1}$), spectral measurement system (iii), with much higher resolution ($\sim 0.48\ \mathrm{cm}^{-1}$), was employed to record the incident pump line profile, as well as the backward stimulated scattering line profile near λ_0.

The measured results are shown in Figs. 4 and 5. To ensure a reliable linear display of the spectral intensity distribution near the base of the sharp line, the incident beam in the double monochromator was attenuated by neutral density filters with various attenuation ratios. For the incident pump beam alone (with the sample removed), Fig. 4 shows a nearly symmetric spectral distribution at the base of the pump line under different attenuation ratios. In contrast, for the backward stimulated scattering beam, Fig. 5 shows a strong sharp line attributed to the backward SBS (its wavelength shift was less than the apparatus resolution), as well as asymmetrically broadened components in the two wings.

One can see two features in Fig. 5: 1) although the spectral distribution on the Stokes side is stronger and broader, there is still a measurable spectral broadening component on the anti-Stokes side; and 2) no spectral maximum was observed at a red-shifted position of $\sim 3\ \mathrm{cm}^{-1}$ (predicted by the SRWS theories[1–4]). These two features cannot be interpreted by the SRWS theories; however, they might well be explained by the superposition of a strong SBS sharp line and a relatively weak SRKS band.

This assumption can be further supported by spectral measurements of backward stimulated scattering pumped with a wide ($\sim 1\ \mathrm{cm}^{-1}$) laser line using the spectral mea-

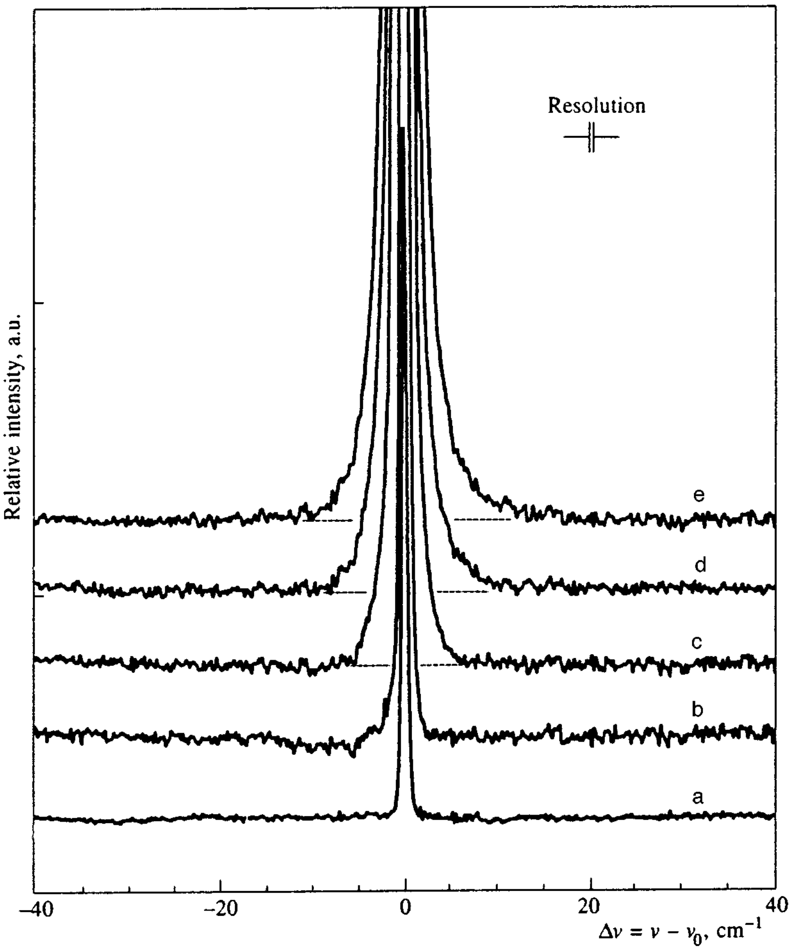

FIG. 4. Detailed spectral distribution of the ~0.1 cm^{-1}-wide 532-nm pump line at various attenuation ratios: 1/80 (a), 1/90 (b), 1/30 (c), 1/6 (d), 1/1 (e). The spectral resolution is ~0.48 cm^{-1}.

surement system (ii). In this case, no SBS component is expected and the backward SRKS process becomes dominant; the measured spectral distribution at various pump intensity levels is shown in Fig. 6 with a spectral resolution of ~1.8 cm^{-1}. It can be seen in Fig. 6 that once the pump intensity is high enough ($\geqslant$200 MW/cm^2), the relative spectral distribution does not change much, which means that the full-scale spectral distribution characteristic of SRKS has been established. These results are basically consistent with that shown in Fig. 3 for backward stimulated scattering. Another feature shown in Fig. 6 is that still there are detectable spectral components on the anti-Stokes side of λ_0.

Based on the measured spectral distribution data for backward stimulated scattering, the corresponding spectral exponential gain curve can be obtained by taking appropriate logarithms.[5] As a result, the normalized spectral gain curve for backward stimulated scattering obtained with 0.48 cm^{-1} resolution is given in Figs. 7 and 8 by the solid line; the small random negative spikes were due to a poorer signal/noise ratio near the zero-point. The pump linewidth was ~1 cm^{-1} and the pump intensity ~500 MW/cm^2.

In Fig. 7 the Stokes gain curve predicted by the SRKS theory is given by a dash-dotted line, using Eqs. (3), (4), and (5) with the same fit parameters used in Ref. 5, while the anti-Stokes gain curve predicted by Eq. (6) is shown by a dashed line using a fit parameter of $\tau = 1.77$ ps.[5] One can see that the agreement between our experimental results and the theoretical fit is quite good. In contrast, the normalized gain curve predicted by the SRWS theory is shown in Fig. 8 by a dashed line, using Eq. (1) with a fit parameter of $\tau = 1.5$ ps. In this case, the negative section of the theoretical curve implies an attenuation of the anti-Stokes components, so no anti-Stokes component would be observed. One can see clearly in Fig. 8 that the predictions of SRWS theory are not consistent with our experimental results.

Finally, one might consider the possibility of spectral broadening due to self phase modulation of possible subpulse structure within the ~10 ns pulse envelope, which would not be resolved by our 350-Mz oscilloscope system with ~1-ns resolution. However, this possibility is not likely to be true, based on the following considerations.

First, according to the uncertainty principle ($\Delta\nu\Delta t \approx 1$), the duration of possible subpulses would not be less than 300 ps and 30 ps, limited by spectral linewidths 0.1 cm^{-1} and 1 cm^{-1}, respectively. If the self phase modulation plays an essential role, spectral broadening behavior should strongly depend on pump pulse duration. Under similar experimental conditions, we did use a ~100 ps laser pulse and a ~0.5 ps laser pulse to pump a liquid CS$_2$ sample separately, and observed no evidence of self phase modulation in the forward emission, except for spectral broadening behavior similar to that shown in Fig. 2a or Fig. 6.[7–10] Thus,

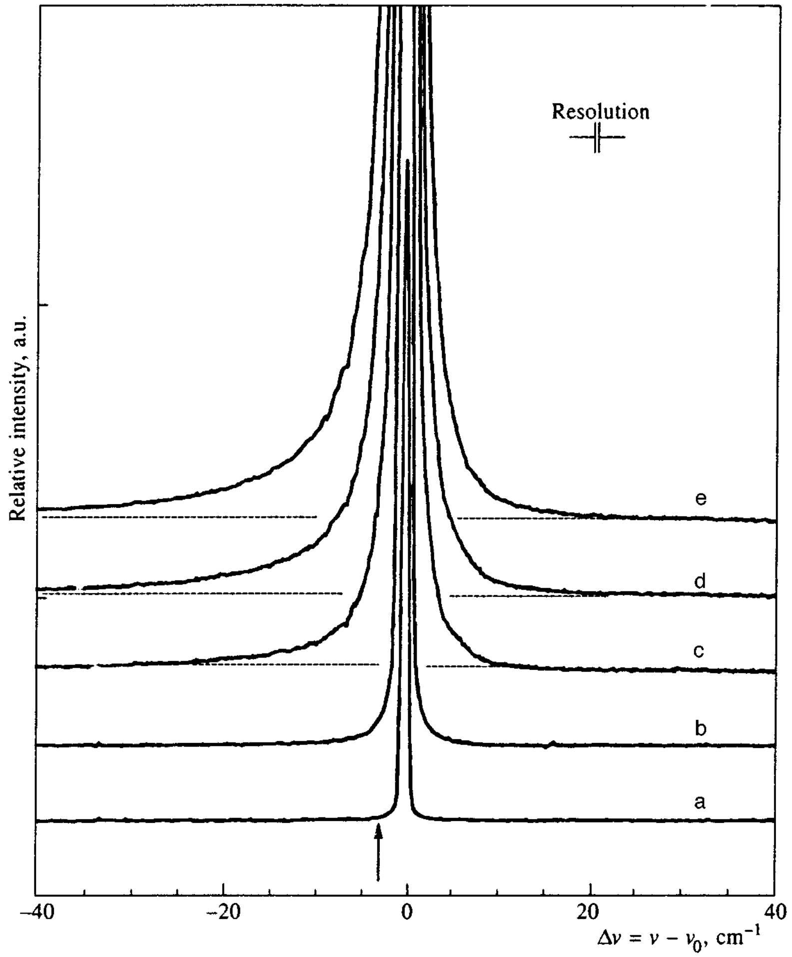

FIG. 5. Detailed spectral distributions of backward stimulated scattering from the CS_2-sample pumped by the $\sim 1\ \mathrm{cm}^{-1}$-wide 532-nm line with various attenuation ratios: 1/180 (a), 1/90 (b), 1/30 (c), 1/6 (d), 1/1 (e). The pump intensity is $I_0 \approx 150\ \mathrm{MW/cm}^2$, and the arrow indicates the maximum gain position predicted by the stimulated Rayleigh-wing scattering theory with an assumed value of $\tau = 1.5$ ps.

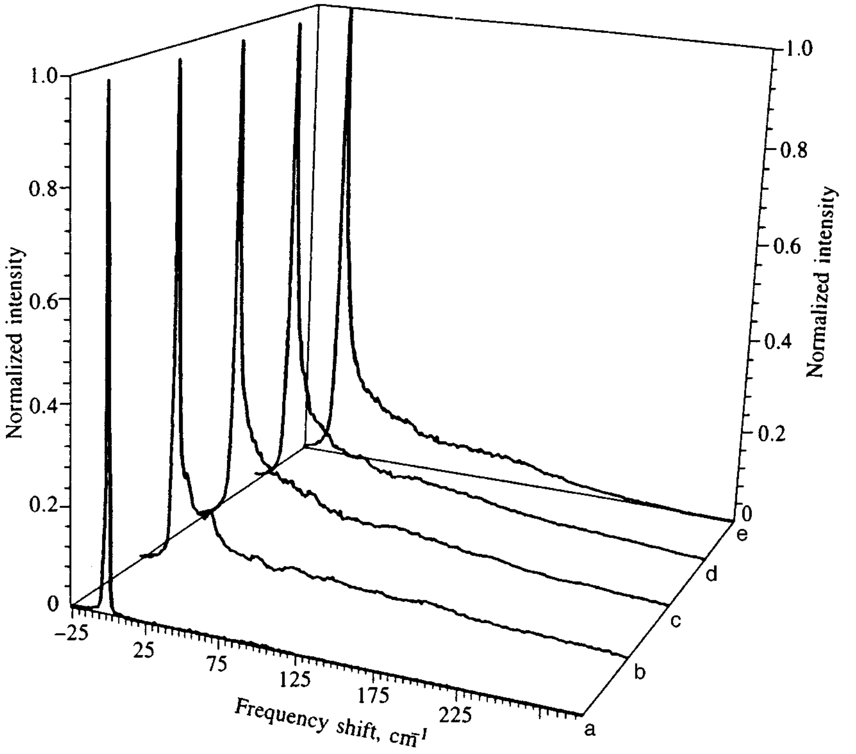

FIG. 6. Normalized spectral distributions of the backward stimulated scattering from the CS_2-sample pumped with the $\sim 1\ \mathrm{cm}^{-1}$-wide 532-nm line at various intensity levels: $I_0 \approx 30$ (b), 75 (c), 150 (d), 475 (e) $\mathrm{MW/cm}^2$. The spectrum of the incident pump line is shown in (a), and the spectral resolution is $\sim 1.8\ \mathrm{cm}^{-1}$.

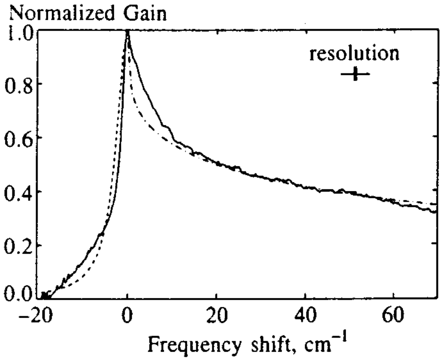

FIG. 7. Normalized gain curves for backward stimulated scattering based on measured data (solid line) and fits (dashed line and dash-dotted line) given by stimulated Rayleigh–Kerr scattering theory. The pump intensity is $I_0 \approx 500$ MW/cm^2, the pump linewidth ~ 1 cm^{-1}, and the spectral resolution ~ 0.48 cm^{-1}.

the spectral broadening behavior of CS_2 is not sensitively dependent on pump pulse duration under our experimental conditions.

Second, if self phase modulation is the major mechanism causing the observed spectral broadening, there should be a periodically modulated spectral structure, as demonstrated by early self-focusing experiments.[20–23] Our spectral measurements with various resolutions (~ 9 cm^{-1}, ~ 1.8 cm^{-1}, and ~ 0.48 cm^{-1}) reveal no discrete or modulated spectral structure.

Lastly, if self phase modulation is the predominant mechanism, the same spectral broadening should occur in the transmitted pump line that takes the highest percentage of the forward emission. However, as shown in Fig. 3, spectral broadening in the backward direction is much greater than in the forward direction. All these considerations are unfavorable for the self phase modulation assumption.

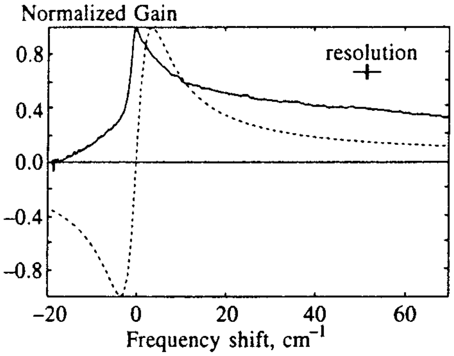

FIG. 8. Normalized gain curves for backward stimulated scattering based on measured data (solid line) and fits (dashed line) predicted by the stimulated Rayleigh-wing scattering theory with an assumed value of $\tau = 1.5$ ps. The pump intensity is $I_0 \approx 500$ MW/cm^2, the pump linewidth ~ 1 cm^{-1}, and the spectral resolution ~ 0.48 cm^{-1}.

4. CONCLUSION

We have accomplished a thorough measurement of the spectral structure of backward stimulated scattering from a 10 cm-long CS_2-liquid cell pumped by ~ 10-ns and 532-nm laser pulses with linewidths of ~ 1 cm^{-1} and ~ 0.1 cm^{-1}. Under the ~ 1 cm^{-1} line pump condition, only a strong superbroadening spectral band is observed in the backward stimulated scattering. However, under the ~ 0.1 cm^{-1} line pump condition, a strong SBS sharp line and a relatively weak broadening component can be observed together. The differing spectral structure of backward stimulated scattering under different pump linewidths can be explained by considering the threshold dependence of SBS on pump linewidth. Under both pump line conditions, spectral broadening behavior cannot be interpreted by either the SRWS theory or the self-modulation assumption, but can be explained well by the SRKS theory.

This work was supported by the US Air Force Office of Scientific Research through contract No F4962093C0017.

[1] D. I. Mash, V. V. Morozov, V. S. Starunov, and I. L. Fabelinskiĭ, JETP Lett. **2**, 25 (1965).
[2] G. I. Zaitsev, Y. I. Kyzylasov, V. S. Serarunov, and I. L. Fabelinskiĭ, JETP Lett. **6**, 35 (1967).
[3] N. Bloembergen and P. Lallemant, Phys. Rev. Lett. **16**, 81 (1966).
[4] Y. R. Shen, *The Principles of Nonlinear Optics*, Wiley, New York (1984), pp. 195, 275, 294.
[5] G. S. He and P. N. Prasad, Phys. Rev. A **41**, 2687 (1990).
[6] G. S. He, R. Burzynski, and P. N. Prasad, J. Chem. Phys. **93**, 7647 (1990).
[7] G. S. He, G. C. Xu, Y. Pang, and P. N. Prasad, J. Opt. Soc. Am. B **8**, 1907 (1991).
[8] G. S. He and G. C. Xu, IEEE J. Quantum Electron. **28**, 323 (1992).
[9] G. S. He, Y. P. Cui, G. C. Xu, and P. N. Prasad, Appl. Opt. **32**, 4507 (1993).
[10] G. S. He, M. Casstevens, R. Burzynski, and X. Li, Appl. Opt. **34**, 444 (1995).
[11] E. J. Miller and R. W. Boyd, Int. J. Heat Mass Transf. **4**, 765 (1992).
[12] G. I. Zaitsev, Yu. I. Kyzylasov, V. S. Starunov, and I. L. Fabelinskiĭ, JETP Lett. **6**, 255 (1967).
[13] W. Rother, H. Meyer, and W. Kaiser, Z. Naturforsch. A **25A**, 1136 (1970).
[14] R. R. Alfano (ed.), *The Supercontinuum Laser Source*, Springer-Verlag, New York (1989).
[15] I. G. Zubarev and S. I. Mikhailov, Kvant. Elektron. (Moscow) **1**, 385 (1974) [Sov. J. Quantum Electron. **4**, 683 (1974)].
[16] Y. S. Kuo, K. Choi, and J. K. McIver, Opt. Commun. **80**, 233 (1991).
[17] A. A. Filippo and M. R. Perrone, IEEE J. Quantum Electron. **28**, 1859 (1992).
[18] G. Cook, in *Conference on Laser and Electro-Optics, 1994 OSA Technical Digest Series*, Optical Society of America, Washington, D.C. (1994), Vol. 8, p. 12.
[19] P. Narum, M. D. Skeldon, and R. W. Boyd, IEEE J. Quantum Electron. **22**, 2161 (1986).
[20] Fujio Shimizu, Phys. Rev. Lett. **19**, 1097 (1967).
[21] T. K. Gustafson, J. P. Taran, H. A. Haus, J. R. Lifsitz, and P. L. Kelly, Phys. Rev. **177**, 306 (1969).
[22] R. Polloni, C. A. Sacchi, and O. Svelto, Phys. Rev. Lett. **23**, 690 (1969).
[23] Y. R. Shen and M. M. T. Loy, Phys. Rev. A **3**, 2099 (1971).

Published in English in the original Russian journal. Reproduced here with stylistic changes by the Translation Editor.

Interference in the photodecomposition of negative atomic hydrogen ions in an electric field

P. A. Golovinskiĭ

Voronezh State Architecture and Construction Academy, 394680 Voronezh, Russia

(Submitted 27 March 1997)
Zh. Éksp. Teor. Fiz. **112**, 1574–1583 (November 1997)

The quantum interference of electron waves in the photodecomposition of negative hydrogen ions in an external uniform electric field is examined. The structure of the photodetachment amplitudes is discussed. A simple analytic expression for the electron flux distribution is derived. Finally, it is shown that the structure of the electron flux is affected by the angular dependence of the wave function. © *1997 American Institute of Physics.* [S1063-7761(97)00511-8]

1. INTRODUCTION

Photodecomposition of atoms and negative ions in the presence of a constant uniform electric field has been studied by many theoreticians and experimenters. Attention has usually been focused on finding the total cross section of the process as a function of the field strength and photon frequency. A remarkable feature of photoionization of neutral atoms is the presence of singularities in the above-threshold region.[1–7] In contrast, photodecomposition of negative ions in the presence of a constant electric field does not lead to the formation of resonance structures; instead the cross section is characterized by a slowly modulated dependence on the electric field strength.[8–13]

The total cross section of the photodecomposition of negative ions in the *s* state has been thoroughly studied in the approximation in which the electron in the final state is assumed free.[8–13] The approximation is based on the fact that without an external electric field the detachment of a single electron that was initially bound in the *s* state results in the electron passing into a final *p* state, which is only weakly distorted by the atomic potential.

The situation is different when we are dealing with negative ions of halogens, where the ground state is a *p* state. Here one of the main photodetachment channels is the *p*-*s* transition. Hence the zero-potential approximation cannot be applied even in the absence of an electric field,[14–19] and the free-electron approximation[20] is unsatisfactory.[21,22] The common approach to solving the problem in this case is to re-expand the transition amplitude in cylindrical coordinates,[5,6,23,24] which allows for a transition from the intratomic region to the region of free motion in a constant uniform electric field and allows one to calculate the cross section of the process.

Photodecomposition of a negative ion in the presence of a constant electric field makes it possible to monitor the wave properties of an electron in the final state. Classical electron trajectories in such a field become two-valued, which leads to interference of the corresponding quantum amplitudes. Demkov *et al.*[25] were the first to formulate the important idea of a ''photoionization microscope.'' Recent experiments have shown that for Br^- a ring structure does indeed exist.[26]

Earlier the theory of the effect was developed in a number of papers.[1–4,25,27–29] It allows, at least in principle, calculation of the electron distribution and hence the interference pattern. At the same time, it must be noted that the approximations discussed in Refs. 25, 28, and 29 were of a semiclassical nature and can be used only in the classically accessible region. A quantum mechanical calculation for a negatively charged ion of atomic hydrogen was done by Fabrikant.[30] The result was an expression for the wave function in the form of an integral of a rapidly oscillating function, which, however, is of little use when numerical calculations in the range of the experimental parameters are done and makes the problem less perspicuous. Earlier an analytic formula applicable for all distances from the center of the interference pattern was derived by Kondratovich and Ostrovsky,[4] but it can be used only near the threshold of the process for negative ions of halogens with an initial *p*-electron.

The present paper derives a simple analytic formula applicable at all distances from the center of the interference pattern for the case where a negative ion of the hydrogen atom is the source.

2. THE PHOTODECOMPOSITION AMPLITUDE

The formation of the interference pattern by photoelectrons in an electric field is a result of two physically distinct processes: photodecomposition and the propagation of the electron wave in the presence of an external field. We begin by studying the photodecomposition amplitude, following the method developed by Du and Delos.[8]

We will assume that the laser field that causes photodecomposition is weak, so that the interaction of an electron with the light can be considered a perturbation. To allow for the effect of a static electric field we will use Airy functions to build a complete orthogonal set of the final states.

The interaction of an electron and the light can be written as (here we use the atomic system of units $e=m_e=\hbar=1$)

$$W=-\frac{iA}{c}\exp(i\mathbf{k}_{\mathrm{ph}}\cdot\mathbf{r})(\mathbf{e}\cdot\boldsymbol{\nabla}),\tag{1}$$

where A is the amplitude of the vector potential of the laser field, c is the speed of light in vacuum, $\mathbf{k}_{\mathrm{ph}}$ is the photon momentum, $\mathbf{e}$ is the polarization vector, and ω is the photon frequency. The expression for the cross section is[20]

$$\sigma=\frac{4\pi^2}{c\omega}\int|M_{fi}|^2\delta(E_i+\omega-E)\,dq_x dq_y d\eta, \tag{2}$$

where $E=(q_x^2+q_y^2)+\eta$ is the electron energy in the final state, and η is the energy of the z-component of electron motion in the continuum. The matrix element between the initial state $|i\rangle$ and the final state $|f\rangle$ in the continuous spectrum can be written as follows:

$$M_{fi}=\langle\psi_f(\eta)|-i\,\exp(i\mathbf{k}_{\mathrm{ph}}\cdot\mathbf{r})(\mathbf{e}\cdot\boldsymbol{\nabla})|\psi_i\rangle. \tag{3}$$

The final state ψ_f can be expressed in terms of Airy functions:

$$\psi_f=\frac{\exp(iq_x x)}{\sqrt{2\pi}}\,\frac{\exp(iq_y y)}{\sqrt{2\pi}}\left(\frac{4}{F}\right)^{1/6}\mathrm{Ai}(\xi), \tag{4}$$

where

$$\xi=-(a+z)b,\quad a=\frac{\eta}{F},\quad b=(2F)^{1/3}, \tag{5}$$

with F the strength of a constant uniform field pointing in the direction opposite to that of the z axis.

The initial state of the negative ion of the hydrogen atom can be represented to good accuracy by the following expression:[31,32]

$$\psi_i(\mathbf{r})=B\,\frac{e^{-\kappa r}-e^{-\beta r}}{r},$$

$$\kappa=0.236,\quad \beta=0.75,\quad B=0.325. \tag{6}$$

A useful approach to calculating the matrix element M_{fi} is to introduce in Eq. (3) the Fourier transforms of the initial wave function (6) and the wave function of the final state (4):

$$\psi_i(\mathbf{p})=B\left(\frac{2}{\pi}\right)^{1/2}\alpha(p),\quad \alpha(p)=\frac{1}{\kappa^2+p^2}-\frac{1}{\beta^2+p^2}, \tag{7}$$

$$\psi_f(\mathbf{p})=\frac{\delta(q_x-p_x)\,\delta(q_y-p_y)}{\sqrt{2\pi F}}\exp\left[\frac{i}{F}\left(\frac{p_z^3}{6}-\eta p_z\right)\right]. \tag{8}$$

We write the expression (3) for the matrix element M_{fi} in integral form:

$$M_{fi}=M(\kappa)-M(\beta),$$

$$M(\kappa)=\frac{B}{\pi F^{1/2}}$$

$$\times\int_{-\infty}^{\infty}dp_z\,\frac{\mathbf{q}\cdot\mathbf{e}+e_z p_z}{\kappa^2+(q_x-k_{\mathrm{ph},x})^2+(q_y-k_{\mathrm{ph},y})^2+(p_z-k_{\mathrm{ph},z})^2}$$

$$\times\exp\left[\frac{i}{F}\left(\frac{p_z^2}{6}-\eta p_z\right)\right],\quad \mathbf{q}=(q_x,q_y). \tag{9}$$

The region near the point p_z of stationary phase, which satisfies the equation[8]

$$\frac{p_z^2}{2}=\eta, \tag{10}$$

provides the greatest contribution to the integral in (9). Since the initial state is described by the function $\psi_i(\mathbf{p})$, which slowly varies in the vicinity of the point of stationary phase, the value of the function at this point can be taken outside the integral sign. This yields the following expression:

$$M(\kappa)=iB\times 2^{4/3}F^{5/6}$$

$$\times\frac{-i(\mathbf{q}\cdot\mathbf{e})/F+e_z\partial/\partial\eta}{\kappa^2+(q_x-k_{\mathrm{ph},x})^2+(q_y-k_{\mathrm{ph},y})^2+(p_z-k_{\mathrm{ph},z})^2}$$

$$\times\mathrm{Ai}\left[-\left(\frac{2}{F^2}\right)^{1/3}\eta\right], \tag{11}$$

which determines the value of the differential scattering cross section.

To estimate the retardation correction to the total scattering cross section near the threshold, we point the polarization vector $\mathbf{e}$ parallel to the constant field $\mathbf{F}$ $(\mathbf{q}\cdot\mathbf{e}=0)$ and employ the asymptotic behavior of (6) in the form $B\exp(-\kappa r)/r$. Then

$$M(\kappa)=\frac{C}{\kappa^2+(\mathbf{q}-\mathbf{k}_{\mathrm{ph}})^2+2\eta}\,\frac{\partial}{\partial\eta}\,\mathrm{Ai}\left[-\left(\frac{2}{F^2}\right)^{1/3}\eta\right], \tag{12}$$

where $C=iB2^{1/3}F^{5/6}$.

Plugging (12) into (2), we get

$$\sigma=\frac{4\pi^2|C|^2}{c\omega(p^2+k_{\mathrm{ph}}^2+\kappa^2)^2}\int_{-\infty}^{F}d\eta\int_0^{2\pi}d\varphi$$

$$\times\left|\frac{\partial}{\partial\eta}\,\mathrm{Ai}\left[-\left(\frac{2}{F^2}\right)^{1/3}\eta\right]\right|^2\left(1-\frac{2k_{\mathrm{ph}}\,q\cos\varphi}{p^2+k_{\mathrm{ph}}^2+\kappa^2}\right)^{-2}. \tag{13}$$

Now we use the relation

$$\int_0^{2\pi}\frac{d\varphi}{(1-\varepsilon\cos\varphi)^2}=\frac{2\pi}{(1-\varepsilon^2)^{3/2}} \tag{14}$$

and write (13) as

$$\sigma=\frac{64\pi^3}{c\omega}\,\frac{B^2F}{(p^2+k_{\mathrm{ph}}^2+\kappa^2)^2}D^r\left(\frac{2^{1/3}E}{F^{2/3}}\right), \tag{15}$$

where

$$D^r(u)=\int_{-\infty}^{u}\frac{1}{(1-\varepsilon^2)^{3/2}}\left|\frac{d}{dv}\,\mathrm{Ai}(-v)\right|^2dv,$$

$$\varepsilon=\frac{2k_{\mathrm{ph}}q}{p^2+k_{\mathrm{ph}}^2+\kappa^2},\quad q^2=2\left[E-\left(\frac{F^2}{2}\right)^{1/3}v\right]. \tag{16}$$

At $\varepsilon=0$, i.e., ignoring all retardation effects, we arrive at the result in the dipole approximation.[8]

Using only the first two terms in the expansion of $(1-\varepsilon^2)^{-3/2}$ in a Taylor series, i.e., $(1-\varepsilon^2)^{-3/2}\approx 1+3\varepsilon^2/2$, makes it possible to separate the contribution of retardation effects. An estimate yields $\varepsilon^2\approx\omega/c^2\approx 10^{-5}$ for processes near the threshold. Figure 1 depicts the function

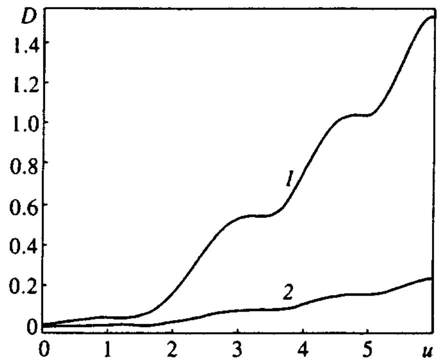

FIG. 1. The modulating factor $D(u)$ (curve *1*) and the correction to it (multiplied by 10^5) due to the retardation effect (curve *2*).

$D(u)=D^r(u)|_{\varepsilon=0}$ without allowance for retardation,[8] and the correction $D^r(u)-D(u)$. The correction is small, which agrees with the above estimate.

When the direction of the electric field coincides with the direction of the polarization vector and we take into account the more exact wave function (6), the total cross section becomes

$$\sigma=\frac{64\pi^3}{c\omega}\alpha^2(p)B^2D\left(\frac{2^{1/3}E}{F^{2/3}}\right). \tag{17}$$

Near the threshold the correction to the result obtained in Ref. 8 roughly amounts to $(\kappa/\beta)^4\approx 0.01$, but increases with the photon energy.[21]

3. THE INTERFERENCE PATTERN

Consider the problem of the interference of electron waves in the final state in the photodecomposition of a negative ion of the hydrogen atom. We will ignore retardation effects and use the asymptotic expression for the initial wave function. We start with the equation for the wave function in the final state:

$$(\nabla^2/2+Fz+E)\psi=W\psi_i. \tag{18}$$

Here the operator W was taken in the dipole approximation, i.e., $W\approx -i(A/c)(\mathbf{e}\cdot\nabla)$ ($k_{\text{ph}}\to 0$ and $\exp(i\mathbf{k}_{\text{ph}}\cdot\mathbf{r})\approx 1$).

To solve the inhomogeneous equation (18), we use the Green's function which is the solution of the equation

$$(\nabla^2/2+Fz+E)G_E(\mathbf{r},\mathbf{r}')=\delta(z-z')\delta(x-x')\delta(y-y'). \tag{19}$$

We look for the solution of (19) in the form

$$G_E(\mathbf{r},\mathbf{r}')=\frac{1}{(2\pi)^2}\int \exp(i\mathbf{q}\cdot(\mathbf{r}_\perp-\mathbf{r}'_\perp))g_E(\mathbf{q},z,z')d^2q, \tag{20}$$

where $\mathbf{r}_\perp=(x,y)$ is the component of $\mathbf{r}$ perpendicular to the z axis. The arrangement of the vectors $\mathbf{e}$, $\mathbf{q}$, $\mathbf{r}_\perp$ is shown in Fig. 2.

The function $g_E(\mathbf{q},z,z')$ satisfies the equation

$$\left(\frac{1}{2}\frac{d^2}{dz^2}+Fz+\eta\right)g_E(\mathbf{q},z,z')=\delta(z-z'). \tag{21}$$

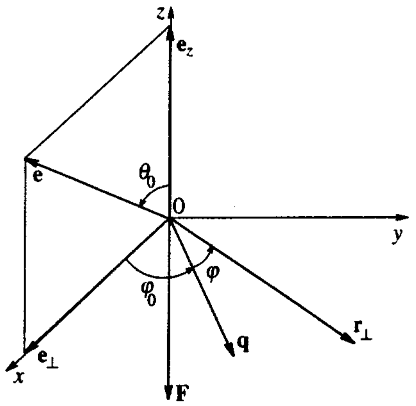

FIG. 2. Arrangement of the electric field vector $\mathbf{F}$, the polarization vector $\mathbf{e}$, the transverse projection $\mathbf{r}_\perp$ of the radius vector, and the transverse projection $\mathbf{q}$ of the electron momentum.

Using the linear change of variables (5), we can write the Green's function in terms of the Airy functions:[33–35]

$$g_E(\mathbf{q},z,z')=-\frac{2\pi}{b}\,\text{Ci}(\xi_<)\text{Ai}(\xi_>), \tag{22}$$

where $\xi_{><}=(\xi+\xi'\pm|\xi-\xi'|)/2$, $\text{Ci}(\xi)=\text{Bi}(\xi)+i\,\text{Ai}(\xi)$, and the asymptotic behavior (as $\xi\to-\infty$) of the functions Ai and Bi is[36]

$$\text{Ai}(\xi)\simeq\pi^{-1/2}|\xi|^{-1/4}\sin\left(\phi+\frac{\pi}{4}\right),$$

$$\text{Bi}(\xi)\simeq\pi^{-1/2}|\xi|^{-1/4}\cos\left(\phi+\frac{\pi}{4}\right),\quad \phi=\frac{2|\xi|^{3/2}}{3}. \tag{23}$$

This asymptotic behavior holds when the distance to the classical turning point $z=-\eta/F$ is large.

When calculating the electron flux, we are interested in regions far from the ion, in which the large and small arguments of the Green's function in (22) are essentially separated and Eq. (18) becomes

$$\psi\simeq-\frac{2iABF\alpha(p)}{bc}\times\int_0^\infty\int_0^{2\pi}d\varphi\; q\,dq\;\text{Ci}(-(a+z)b)\times\exp(i\mathbf{q}\cdot\mathbf{r}_\perp)\left(e_z\frac{\partial}{\partial\eta}-i\frac{\mathbf{q}\cdot\mathbf{e}}{F}\right)\text{Ai}\left[-\left(\frac{2}{F^2}\right)^{1/3}\eta\right], \tag{24}$$

where the matrix element M_{fi} is taken from (9) and (11) at $k_{\text{ph}}=0$.

In (24) we first integrate with respect to φ in the plane perpendicular to the direction of the electric field. Here $\mathbf{q}\cdot\mathbf{e}=\sin\theta_0(\cos\varphi\cos\varphi_0-\sin\varphi\sin\varphi_0)$ and $e_z=\cos\theta_0$, where φ and φ_0 are the angles in the xy plane, and θ_0 is the angle between the z axis and the polarization vector $\mathbf{e}$. Integrating with respect to φ in Eq. (24) amounts to calculating integrals of the form

$$I_n=\int_{-\pi}^{\pi}\exp(iqr\cos\varphi)s_n(\varphi)d\varphi, \tag{25}$$

where $s_0=1$, $s_1=\cos\varphi$, and $s_2=\sin\varphi$. For $n=0$ and 1 the integral (25) yields Bessel functions of order zero and their derivatives:[36]

$$I_0=2\pi J_0(qr),\quad I_1=-2i\pi J_0'(qr). \tag{26}$$

For $n=2$ the integral vanishes because the integrand is an odd function. Bearing all this in mind, we can write

$$\begin{aligned}\psi\simeq&-\frac{4i\pi ABF\alpha(p)}{bc}\int_0^\infty qdq\ \mathrm{Ci}(-(a+z)b)\\&\times\left[\mu_0 J_0(q\rho)\frac{\partial}{\partial\eta}-\frac{\mu_1}{F}\frac{\partial J_0(\rho r)}{\partial\rho}\right]\\&\times\mathrm{Ai}\left[-\left(\frac{2}{F^2}\right)^{1/3}\eta\right],\end{aligned}\tag{27}$$

where $\mu_0=\cos\theta_0$, $\mu_1=\sin\theta_0\cos\varphi_0$, and $\rho=|\mathbf{r}_\perp|$.

Let us evaluate the integral with respect to q by employing the asymptotic expression for Ci at large positive values of z. According to (23), we can write

$$\begin{aligned}\psi\simeq&Q\int_0^\infty qdq\ \exp\left(-i\frac{tq^2}{2}\right)\\&\times\left(\mu_0 J_0(q\rho)\frac{\partial}{\partial\eta}-\frac{\mu_1}{F}\frac{\partial J_0(\rho r)}{\partial\rho}\right)\\&\times\mathrm{Ai}\left[-\left(\frac{2}{F^2}\right)^{1/3}\eta\right],\end{aligned}\tag{28}$$

where

$$Q=-\frac{4i\pi^{1/2}ABF\alpha(p)}{bc(zb)^{1/4}}\exp(i\tilde{\phi}),$$

$$\tilde{\phi}=t\left(\frac{2z}{3}+\frac{E}{F}\right)+\frac{\pi}{4},$$

and $t=(2z/F)^{1/2}$ is the classical time of electron motion from source to screen.

When the argument of the Bessel functions is large, the asymptotic behavior of the functions is given by the following expression:

$$J_n(u)\simeq\left(\frac{2}{\pi u}\right)^{-1/2}\cos\left(u-\frac{n\pi}{2}-\frac{\pi}{4}\right)$$

(see Ref. 36), and the integrand in (28) has a stationary point corresponding to the classical value of the transverse component of momentum, $q_c=\rho/t$. Hence we can plug in the value of the Airy function at the stationary point. The resulting integral can now be easily calculated. At $n=0$ we have[37]

$$\mathscr{I}(\rho)=\int_0^\infty\exp\left(-i\frac{tq^2}{2}\right)J_0(\rho q)qdq=\frac{1}{t}\exp\frac{i\rho^2}{2t}. \tag{29}$$

The derivative of this expression yields the term with $n=1$:

$$\frac{\partial}{\partial\rho}\int_0^\infty\exp\left(-i\frac{tq^2}{2}\right)J_0(\rho q)qdq=\frac{i\rho}{t}\mathscr{I}(\rho). \tag{30}$$

Thus, at the point on the screen where an electron is detected we have

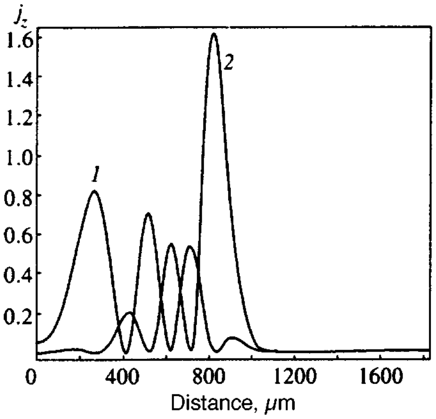

FIG. 3. Quantum interference pattern for H^-: curve *1* corresponds to the case $\mathbf{e}\|\mathbf{F}$, and curve *2* to the case of $\mathbf{e}\perp\mathbf{F}$ and $\varphi_0=0$. The electron energy in the continuous spectrum is 0.4 cm^{-1}, the electric field strength is 100 V m^{-1}, and the distance is $z=0.5$ m (Ref. 26).

$$\psi\simeq Q\mathscr{I}(\rho)\left[\mu_0\frac{\partial}{\partial\eta}-\mu_1\frac{i\rho}{tF}\right]\mathrm{Ai}\left[-\left(\frac{2}{F^2}\right)^{1/3}\eta\right]\Bigg|_{q=q_c}. \tag{31}$$

The analytic expression (31) for the wave function of the final state contains all the information needed for calculating the electron current density along the z axis, $j_z\simeq-i(\psi^*\partial\psi/\partial z-\mathrm{c.c.})$, and determines the details of the interference pattern. We see that to calculate the electron current we need to know the z-derivative of ψ. However, for a screen that is far from the source the motion of an electron in a uniform electric field becomes semiclassical. Then we can put $\psi\simeq\exp(iS)$ (see Ref. 38), where S is the classical action. Hence $j_z\simeq p_z(z,\rho)|\psi|^2$ within the accuracy of the semiclassical approximation, which is determined by the parameter $d(p^{-1}(z,\rho))/dz\ll1$ for $F^2t^3\gg1$. Actually, the semiclassical formula for the electron flux proves to be highly accurate.

This makes it possible to write the final expression for the two characteristic polarizations. For the polarization along the external field we have

$$j_z^l(\rho)\simeq j_0\left(\frac{2}{tF^2}\right)^{2/3}\left|\frac{d}{dx}\mathrm{Ai}(-x)\right|^2, \tag{32}$$

and for the transverse polarization we have

$$j_z^\perp(\rho)\simeq j_0\left(\frac{\cos\varphi_0}{tF}\right)^2\left|\frac{\rho\mathrm{Ai}(-x)}{t}\right|^2, \tag{33}$$

where $j_0=p_z|Q|^2$, and $x=(\nu/2)^{2/3}(1-\rho^2/\rho_{\max}^2)$, with $\nu=p^3/F$ and $\rho_{\max}=pt$ the classical size of the pattern. For an arbitrary orientation of the polarization vector we have

$$j_z(\rho)=j_z^l(\rho)\cos^2\theta_0+j_z^\perp(\rho)\sin^2\theta_0. \tag{34}$$

Figure 3 depicts the results of calculating the interference pattern for H^- for two different polarizations. The normalized value of the flux is chosen at $j_0=1$. The pattern is cylindrically symmetric when the polarization is along **F**, while for transverse polarization the angular structure of the electron current corresponds to the angular structure of the wave function of the electron in the continuum immediately after the electron leaves the ion. We see that in contrast to what was said in Ref. 29, the flux minima reach zero, exactly just as they did in Refs. 25, 28, and 30. This can be attributed to the fact that Du[29] matched the solutions in different spatial regions semiclassically but did not allow for the phase of the quantum amplitude.

The study of the interference patterns that emerge in the photodecomposition of negative halogen ions, for which experimental data are only now appearing,[26] means taking into account the finiteness of the scattering length of the s-wave and the hyperfine structure of the atom. This problem lies considerably outside the scope of the paper and will be the topic of a future study.

4. CONCLUSION

The interference pattern that emerges when photoelectrons move in a uniform electric field reflects both the intensity and the phase structure of the wave. The central part of the pattern can be obtained in the semiclassical approximation. However, near the classical turning point this approximation has a nonphysical singularity. The proposed quantum description makes it possible to obtain an analytic solution at large distances from a negative ion of the hydrogen atom in the entire transverse distribution region, including the region beyond the classical turning point. Thus it becomes possible to investigate quantum mechanically the effect of the microscopic wave function of a photoelectron on the macroscopic interference pattern. This supports the main conclusion of Demkov *et al.*[25] concerning the possibility of building a ‘‘photoionization microscope.’’ It also makes it possible to directly observe the penetration of a barrier by the wave function.

The work was done in association with C. Blondel and C. Delsart of the Aimé Cotton Laboratory of Atomic and Molecular Physics at the Center d'Orsay (France). I am grateful to Yu. N. Demkov for his assistance in the statement of the problem and to I. Yu. Kiyan for fruitful discussions.

[1] V. D. Kondratovich and V. N. Ostrovsky, J. Phys. B **17**, 1981 (1984).
[2] V. D. Kondratovich and V. N. Ostrovsky, J. Phys. B **17**, 2011 (1984).
[3] V. D. Kondratovich and V. N. Ostrovsky, J. Phys. B **23**, 21 (1990).
[4] V. D. Kondratovich and V. N. Ostrovsky, J. Phys. B **23**, 3785 (1990).
[5] D. A. Harmin, Phys. Rev. A **26**, 2656 (1982).
[6] D. A. Harmin, in *Atoms in Strong Fields*, C. A. Nicolaides, Ch. W. Clark, and M. H. Nayfeh (eds.), Plenum Press, New York (1990), p. 61.
[7] V. V. Kolosov, JETP Lett. **44**, 588 (1986).
[8] M. L. Du and J. B. Delos, Phys. Rev. A **38**, 5609 (1988).
[9] Du Ning-Yi, I. J. Fabrikant, and A. F. Starace, Phys. Rev. A **48**, 2968 (1993).
[10] Gao Bo and A. Starace, Phys. Rev. A **42**, 5580 (1990).
[11] Q. Wang and A. Starace, Phys. Rev. A **51**, 1260 (1995).
[12] N. D. Gibson, B. J. Davies, and D. J. Larson, Phys. Rev. A **48**, 1948 (1993).
[13] M. L. Du, Phys. Rev. A **51**, 1955 (1995).
[14] T. J. Robinson and S. Geltman, Phys. Rev. **153**, 4 (1967).
[15] J. Cooper and R. N. Zare, J. Chem. Phys. **48**, 942 (1968).
[16] J. Cooper and J. B. Martin, Phys. Rev. **126**, 1482 (1962).
[17] D. H. Lee, C. Y. Tang, J. S. Thompson, W. D. Brandon, U. Ljungblad, D. Hanstorp, D. J. Pegg, J. Dellwo, and G. D. Alton, Phys. Rev. A **51**, 4284 (1995).
[18] H. Hanstorp, C. Bengston, and D. J. Larson, Phys. Rev. A **40**, 670 (1989).
[19] V. Radojevič, H. P. Kelly, and W. R. Jonson, Phys. Rev. A **35**, 2117 (1987).
[20] N. D. Gibson, B. J. Davies, and D. J. Larson, Phys. Rev. A **48**, 310 (1993).
[21] P. A. Golovinskiĭ and I. Yu. Kiyan, Usp. Fiz. Nauk **160**, No. 6, 97 (1990) [Sov. Phys. Usp. **33**, 453 (1990)].
[22] P. A. Golovinski, I. Yu. Kiyan, and V. S. Rostovtsev, J. Phys. B **23**, 2743 (1990).
[23] Wong Hin-Yiu, A. R. P. Rau, and C. H. Green, Phys. Rev. A **33**, 2393 (1988).
[24] I. I. Fabrikant, J. Phys. B **27**, 4545 (1994).
[25] Yu. N. Demkov, V. D. Kondratovich, and V. N. Ostrovskiĭ, JETP Lett. **34**, 403 (1981).
[26] F. Dulieu, *Photodétachment d'ion négatif d'halogènes, Thèse*, Université de Paris-Sud, Centre d'Orsay (1996).
[27] V. D. Kondratovich and V. N. Ostrovskiĭ, Zh. Ėksp. Teor. Fiz. **79**, 395 (1980) [Sov. Phys. JETP **52**, 198 (1980)].
[28] I. I. Fabrikant, Zh. Ėksp. Teor. Fiz. **79**, 2070 (1980) [Sov. Phys. JETP **52**, 1045 (1980)].
[29] M. L. Du, Phys. Rev. A **40**, 4983 (1989).
[30] I. I. Fabrikant, J. Phys. B **23**, 1139 (1990).
[31] B. M. Smirnov, *Atomic Collisions and Elementary Processes in Plasma* [in Russian], Atomizdat, Moscow (1968), p. 211.
[32] P. A. Golovinskiĭ and B. A. Zon, Izv. Akad. Nauk SSSR, Ser. Fiz. **41**, 2305 (1991).
[33] Yu. N. Demkov and G. F. Drukarev, Zh. Ėksp. Teor. Fiz. **47**, 918 (1964) [Sov. Phys. JETP **20**, 614 (1965)].
[34] I. I. Fabrikant, Phys. Rev. A **40**, 2373 (1989).
[35] M. Kleber, Phys. Rep. **236**, 331 (1994).
[36] *Handbook of Mathematical Functions*, M. Abramovitz and I. A. Stegun (eds.), National Bureau of Standards Applied Mathematics Series 55, Washington, D.C. (1964).
[37] V. A. Ditkin and A. P. Prudnikov, *Integral Transforms and Operational Calculus*, Pergamon Press, Oxford (1965).
[38] L. D. Landau and E. M. Lifshitz, *Quantum Mechanics: Non-relativistic Theory*, 3rd ed., Pergamon Press, Oxford (1977).

Translated by Eugene Yankovsky

Structure of a collisionless shock front with relativistically accelerated particles

I. N. Toptygin

St. Petersburg State Technical University, 195251 St. Petersburg, Russia

(Submitted 24 February 1997)
Zh. Éksp. Teor. Fiz. **112**, 1584–1602 (November 1997)

A nonlinear self-consistent analytic theory is developed to describe the front structure of a strong magnetohydrodynamic (MHD) collisionless shock wave that generates accelerated particles (including ultrarelativistic particles). The theory is used to predict the degree of compression of matter at the plane front of such a wave, which can greatly exceed compression at an ordinary gas-dynamic front, and also the velocity, density, and pressure profiles. The energy spectrum of the accelerated particles, which is produced by the complex velocity profile at the shock transition, is determined self-consistently. New nonlinear effects are predicted that have not been discussed previously in the literature: a strong dependence of the particle acceleration regimes on the rate of injection; the existence of several regimes within a certain range of injected powers with differing spectra of accelerated particles, shapes of the shock transition profile, and magnitudes of compression of the medium; and the possibility of spontaneous jumps between different states of the shock transition. The question of stability of these states is discussed. For the values of the system parameters used here, the nonlinear regimes correspond to extremely low injection rates, of order $10^{-2}-10^{-10}$ of the plasma flux density advancing into the front, and to exponents of the power-law spectra of accelerated particles between 5 and 3. © *1997 American Institute of Physics.* [S1063-7761(97)00611-2]

1. INTRODUCTION AND STATEMENT OF THE PROBLEM

The structure of collisionless shock fronts in a rarefied plasma has long attracted the attention of investigators.[1–3] This problem has acquired a new facet ever since the discovery[4,5] that magnetohydrodynamic (MHD) collisionless shock waves in a turbulent medium efficiently transform the energy of mechanical motion of the plasma into energy of accelerated particles. The primary mechanism for this acceleration is provided by first-order Fermi acceleration. When a magnetic field is present with a component that is longitudinal with respect to the front, there is also a certain contribution from the drift acceleration of the particles by the electric field.[6]

An estimate of the efficiency of this conversion shows that for strong shock waves (with Mach number $M \gg 1$) the energy of the accelerated particles is of the same order as the energy of the advancing hydrodynamic flux, which suggests that accelerated particles have a strong effect on the structure of the shock front. This implies that the problem of particle acceleration by a strong shock front must be solved self-consistently, because the profile of the transition layer will in turn affect the efficiency of acceleration and the rate of particle injection from the ambient thermal plasma into the acceleration regime.

The complexity of this problem comes not only from its nonlinear character, but also from the need to combine macroscopic and kinetic approaches to solve it. Whereas local properties of a shock wave can be investigated using conservation laws for macroscopic quantities, the computation of the basic macroscopic parameters of the accelerated particles—their pressure and energy density—requires a kinetic approach. This is because the pressure of the accelerated particles depends strongly on the shape of their energy spectrum, the maximum energy they are accelerated to, and the injection power. In fact, a computation of the energy spectrum of accelerated particles is of interest in its own right. For these reasons, researchers have primarily emphasized numerical methods in solving the problem as posed.[7–9] However, numerical calculations cannot always clarify the physical picture to a sufficient degree, nor do they yield overall dependences on key physical parameters, which can lead to erroneous conclusions. Furthermore, numerical methods require further development before they can deal with situations more complicated than an isolated shock wave—for example, involving an ensemble of strong shock fronts.[10]

In this paper we use a combination of the hydrodynamic and kinetic approaches. In Sec. 2 we derive the basic parameters of the shock transition (the magnitude of the thermal velocity jump, the shape of the precursor, and the spatial pressure distribution of the accelerated particles) from the conservation laws in terms of two global parameters—the degree of compression σ of the thermal plasma in the shock wave and the conversion coefficient η of the plasma flux energy into energy of relativistic particles. Our second step (Sec. 3) is to calculate the distribution function of accelerated particles at the distorted shock front, which allows us to close the system of equations for a given injection rate and determine self-consistently both the structure of the shock transition and the spectrum, and also the total energy of the accelerated particles. In the last section we present results of a numerical solution of the resulting transcendental equations and a summary of the basic features of the nonlinear distortion of the shock front by accelerated particles.

We use an isotropic distribution function $N(z,p)$ to describe the energetic particles, which in the one-dimensional stationary case satisfies the equation[6]

$$\frac{\partial}{\partial z}\left[\kappa(z,p)\,\frac{\partial N}{\partial z}\right]-u(z)\,\frac{\partial N}{\partial z}+\frac{p}{3}\,\frac{\partial N}{\partial p}\,\frac{du}{dz}=-Q(p,z) \quad (1)$$

and the normalization condition

$$\int_0^\infty N(p,z)p^2dp=n_c(z).$$

Here $n_c(z)$ is the number density of accelerated particles, $Q(p,z)$ is the density of the source of accelerated particles, $u(z)$ is the hydrodynamic velocity of the medium, and $\kappa(z,p)$ is the diffusion coefficient for energetic particles, arising from the fine-scale electromagnetic fields of the plasma. Note that Eq. (1) holds at the surface $z=z_0$ as well, where there is an abrupt velocity jump Δu. In this case

$$\frac{du}{dz}=-\Delta u\,\delta(z-z_0) \quad (2)$$

and Eq. (1) can be used to derive boundary conditions for the distribution function and flux density of accelerated particles.

By using Eq. (1), we postulate that the plasma is turbulent and that the energetic particles undergo frequent scattering that gives rise to the diffusive character of their motion. This scattering of the energetic particles also ensures that their motion couples to the background plasma. However, with increasing energy this interaction with the plasma will in general become weaker, and there is a certain energy at which it becomes negligible. These particles become free and leave the system, taking their energy with them and thereby giving rise to the phenomenon of ''de-excitation,''[7] analogous to de-excitation of excited atoms in strong gas-dynamic shock waves. The escape of particles with these energies can be taken into account by including a ''sink'' of particles with appropriate energies on the right side of Eq. (1) along with the source.

The turbulence can be generated both by external energy sources and by the accelerated particles themselves, which can generate, for example, Alfvén waves due to flow instability. In the latter case, the turbulence can derive from the energy of the shock wave, and turbulent pulsations will be one of the dynamic factors that affect the structure of the shock transition.[11] However, in a strong shock wave, most of the energy is energy of hydrodynamic motion and accelerated particles, so that the dynamic role of turbulence is small. For this reason, here we consider turbulence in the vicinity of the shock transition to be specified by an external factor. We will also not take into account the dynamic role of large-scale magnetic fields. This is entirely legitimate when the shock wave propagates along the magnetic field (longitudinal shock wave). However, even for an arbitrary direction of the field its effect on the energetics of a strong shock wave is not large, because only a small portion of the total energy of the system is allotted to it.

Written in hydrodynamic form, Eq. (1) becomes the equation of energy balance of the accelerated particles[6]

$$\frac{dq_c}{qz}=u\,\frac{dP_c}{dz}+\int_0^\infty Q(p,z)T(p)p^2dp. \quad (3)$$

Here

$$P_c(z)=\frac{1}{3}\int_0^\infty pvN(p,z)p^2dp \quad (4)$$

is the pressure of the energetic particles, and q_c is their energy flux, which can be expressed in terms of the pressure and kinetic energy density

$$w(z)=\int_0^\infty T(p)N(p,z)p^2dp \quad (5)$$

by means of the relation

$$q_c(z)=-\overline{\kappa(z)}\,\frac{dw}{dz}+u(w+P_c), \quad (6)$$

where $\overline{\kappa(z)}$ is the diffusion coefficient averaged over the particle spectrum. We use the well-known relation between pressure and energy density of noninteracting particles

$$P_c=(\gamma_c-1)w, \quad (7)$$

where $\gamma_c=5/3$ and 4/3 in the nonrelativistic and relativistic cases, respectively. Simple expressions for γ_c at intermediate semirelativistic energies will be presented below.

The use of the hydrodynamic equations (3)–(6) to describe the energetic particles implies a description of the plasma at this stage based on a two-fluid model, in which the two ion species (thermal-gas ions and accelerated particles) differ significantly both in their average energies and energy distributions (spectra), and also in their mean free paths Λ ($\Lambda_c \gg \Lambda_g$, where the label g is used for the thermal component) and the character of their interaction with the discontinuity. Energetic particles, in contrast to thermal particles, can cross the shock discontinuity many times, acquiring considerable energy as a result.

2. CALCULATION OF SHOCK TRANSITION PARAMETERS FROM CONSERVATION LAWS

At low pressures of the accelerated particles (weak injection), the structure of a collisionless MHD shock front is determined by the properties of its thermal component and depends considerably on the orientation of the large-scale magnetic field in front of it. In sufficiently strong (supercritical) quasilongitudinal shock waves with an Alfvén Mach number somewhat greater than unity, the thermal front consists of a transition region whose thickness is some dozens of ion inertial lengths c/ω_{pi}, occupied by fluctuations of the magnetic field with $\delta B/B\approx 1$ and frequencies below the gyrofrequency of an ion.[12,13] The origin of these oscillations is related to ion kinetic instability. In this paper we do not attempt to describe this region, which we refer to as the thermal discontinuity, although its structure and properties are very relevant to the problem of injection of ions and electrons into the acceleration regime by the shock wave.[9,14]

As the pressure of accelerated particles increases, apart from an upstream thermal jump, a region appears in which the plasma is smoothly decelerated. This region, known as the precursor,[7,9] owes its existence to the effects of accelerated particles. The extent of this region can greatly exceed the thickness of the thermal discontinuity (by several orders of magnitude) and is determined by a parameter $L\approx v\Lambda_c/u$.

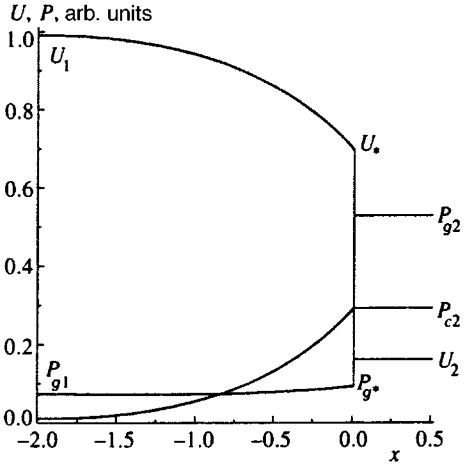

FIG. 1. Schematic illustration of the behavior of plasma parameters at a shock transition.

As the pressure of energetic particles increases, the magnitude of the thermal jump decreases, and the hydrodynamic theory allows it to disappear completely.

In Fig. 1, we illustrate schematically the variation in macroparameters within the shock transition. We set the thickness of the thermal jump equal to zero, and assume that the pressure of accelerated particles is continuous across it because their range between scattering events exceeds its thickness, so that they can freely pass through the front. We also assume that the shock wave is nonrelativistic and that the mechanism under discussion for the acceleration leaves the particle injection energies nonrelativistic. It is natural to assume that the injected particles are drawn from the ambient plasma, and that their source is located in the region of primary acceleration, i.e., at the thermal jump. On the right side of Eq. (1) we also include a sink that describes the escape of particles from the system:

$$Q(p,z)=Q_0 p_0^{-2}\delta(p-p_0)\delta(z)-Q_m(p)f(z). \tag{8}$$

The quantities p_0 and Q_0 should be determined by the injection mechanism. The choice of p_0 and an estimate of Q_0 are given in Sec. 4. The choice of the sink function $Q_m(p)$ will be made in Sec. 3 when we compute the distribution function of the accelerated particles.

The function $f(z)$ describes the spatial distribution of sources of escaping particles. We normalize this function by the condition $\int_{-\infty}^{0} f(z)dz=1$. Escaping particles are generated throughout the region in which acceleration takes place, i.e., at $z\leqslant 0$. Since the maximum of $f(z)$, like the injection maximum, is located in the region of strongest acceleration, we replace $f(z)$ by $\delta(z)$ whenever this does not lead to significant error.

Conservation of mass flux j, momentum flux P_{zz}, and energy flux q can be written in the form

$$j=\rho(z)u(z)=\rho_1 u_1,\quad \rho=\rho_g+\rho_c, \tag{9}$$

$$P_{zz}=ju(z)+P_g(z)+P_c(z)=ju_1+P_{g1}, \tag{10}$$

$$q=\frac{ju^2(z)}{2}+\frac{\gamma_g}{\gamma_g-1}u(z)P_g(z)+\frac{\gamma_c}{\gamma_c-1}u(z)P_c(z)$$
$$-\frac{\overline{\kappa(z)}}{\gamma_c-1}\frac{dP_c}{dz}+q_m\Theta(z)=\frac{ju_1^2}{2}+\frac{\gamma_g}{\gamma_g-1}u_1P_{g1}. \tag{11}$$

Here we have used the well-known expression for the energy flux of a nonrelativistic monatomic gas ($\gamma_g=5/3$) of noninteracting particles, and Eqs. (6) and (7) for the flux of kinetic energy of the gas of accelerated particles. The viscosity and thermal conduction of the primary plasma are not taken into account over the region in which the parameters vary smoothly. The quantity

$$q_m=\int_0^\infty Q_m(p)K(p)p^2dp \tag{12}$$

is the energy flux carried by particles departing the system; the function

$$\Theta(z)=\begin{cases}\int_{-\infty}^{z} f(z)dz & \text{for } z\leqslant 0,\\ 1 & \text{for } z>0\end{cases}$$

describes the increase in the flux of escaping particles in the acceleration region. In all the cases discussed here, escaping particles make a negligible contribution to the mass and momentum balance, and will not be included in Eqs. (9) and (10).

In the absence of accelerated particles, the velocity varies only within the thin thermal front, and the conservation laws (9)–(11) enable us to express ρ_2,u_2,P_{g2} behind the front in terms of the parameters of the advancing flux j,u_1,P_{g1}. In the presence of acceleration, these equations are not enough to find the unknown quantities behind the front, u_2,P_{g2},P_{c2} (as well as γ_c and q_m). This is because the conservation laws do not contain information about the fraction of particles shunted into the accelerated component from the advancing flux, nor about the energy they acquire during acceleration. These parameters themselves depend on the global structure of the shock front, including its smooth part. We therefore solve the problem self-consistently, choosing as the self-consistency parameters the quantities

$$\sigma=\frac{\rho_2}{\rho_1}=\frac{u_1}{u_2},\quad \eta=\frac{P_{c2}}{ju_1}. \tag{13}$$

The first is the global compression of the material at the shock front, while the second is that fraction of the dynamic pressure at the system input that is converted into pressure of the accelerated particles. We express the profile of the shock transition and the velocity at the thermal jump u_* in terms of these quantities; then, after calculating the distribution function of accelerated particles, we close the system of equations, which enables us to find all the system parameters for a given injection power.

Applying Eqs. (10) and (11) to the region $z>0$ and eliminating P_{g2} from them, and also using the notation (13), we find the relation

$$\eta=\frac{\gamma_c-1}{\gamma_g-\gamma_c+k\sigma(\gamma_g-1)(\gamma_c-1)}\left[\frac{(\gamma_g-1)\sigma}{2}+\frac{\gamma_g+1}{2\sigma}\right.$$
$$\left.-\gamma_g+\frac{\sigma-1}{M^2}\right]\geqslant 0. \qquad (14)$$

Here we have introduced the dimensionless parameters $k=q_m/u_1P_{c2}$ for the energy flux of escaping particles and $M^2=ju_1/\gamma_gP_{g1}>1$ for the square of the Mach number of the advancing nonrelativistic plasma flux.

When $\gamma_c=\gamma_g$ (acceleration up to nonrelativistic energies) there cannot be any escaping particles, i.e., $k=0$. Therefore, the expression in square brackets reduces to zero, which yields the well-known compression for gas-dynamic waves:

$$\sigma_{\min}^{-1}=\frac{\gamma_g-1}{\gamma_g+1}+\frac{2}{M^2(\gamma_g+1)}. \qquad (15)$$

The degree of compression $\sigma_{\min}$ does not exceed 4 for any Mach number in nonrelativistic plasma with $\gamma_g=5/3$. However, for $\gamma_c<\gamma_g$ the compression increases.

We can obtain a bound on the pressure of the accelerated particles with the help of Eq. (10). Applying it to the region behind the front $z>0$, we have

$$P_{c2}=j(u_1-u_2)+P_{g1}-P_{g2}. \qquad (16)$$

The ratio P_{g2}/P_{g1} cannot be less than that value which corresponds to pressure variations that conform to the Poisson adiabat $P_g\sim\rho_g^{\gamma_g}$, for a given compression σ, i.e., $P_{g2}/P_{g1}\geqslant\sigma^{\gamma_g}$. Equality corresponds to the absence of a thermal jump, in which case the entropy of the thermal component (per particle) does not change. That is, the total entropy increases at the shock transition exclusively because of particle acceleration. Note, however, that the latter possibility can only be realized when no sources of additional plasma heating are present in the precursor region. One candidate for such a source, in particular, is the aforementioned turbulence generated by accelerated particles and dissipated in the thermal plasma. We do not include processes of this kind here. From Eq. (16) we obtain

$$0\leqslant\eta\leqslant\eta_m=1-\sigma^{-1}+\frac{1-\sigma^{\gamma_g}}{\gamma_gM^2}, \qquad (17)$$

which, combined with Eq. (14), bounds the possible values of parameters of the problem. The equality on the right side of Eq. (17) defines the dimensionless pressure η_m of accelerated particles over the front.

Equation (14) and inequality (17) can be used to find the maximum changes in the compression within the shock wave and the energy flux of the escaping particles for a given Mach number. By using the left-hand inequality (17) and the fact that for $\eta=0$, we must also necessarily have $k=0$, we find a lower bound on the compression $\sigma\geqslant\sigma_{\min}$, where $\sigma_{\min}$ is given by Eq. (15). The right-hand inequality (17) bounds the compression from above. As already noted, equality corresponds the case in which all the excess energy of the incident flux is transmitted to accelerated particles. In this case there is no thermal jump, and the energy of the accelerated particles is highest for a given M. For this limiting case, denoting the corresponding compression by σ_m, we obtain

$$\frac{1}{2}\left(1-\frac{1}{\sigma_m^2}\right)+\frac{1-\sigma_m^{\gamma_g}}{(\gamma_g-1)M^2}$$
$$=\left[k+\frac{\gamma_c}{\sigma_m(\gamma_c)-1}\right]\left[1-\frac{1}{\sigma_m}+\frac{1-\sigma_m^{\gamma_g}}{\gamma_gM^2}\right]. \qquad (18)$$

We can regard this equation as a generalization of the Hugoniot adiabat to the case of a shock wave with accelerated particles and a degraded front without a thermal jump. It connects four quantities—the Mach number, the energy flux of escaping particles, the compression, and the adiabatic exponent for accelerated particles. Of these four quantities, the Mach number must be specified as an external parameter of the problem. The energy flux k is primarily (but not completely—see below) determined by the injection power, which is also an independent quantity. The quantities γ_c and k can be calculated self-consistently at the kinetic stage of solution (see Eqs. (38) and (65)). The last parameter—the maximum compression σ_m—can be expressed in terms of the other three using Eq. (18). Depending on their relative magnitude, it can vary over wide limits.

Let us consider the most important case of strong shock waves, i.e., $M\gg 1$. We can obtain consistent consequences from Eq. (18) if $\sigma^{\gamma_g}/M^2\to 0$ as $M\to\infty$. The compression is easily determined:

$$\sigma_m=\frac{\gamma_c+1}{(\gamma_c-1)(1-2k)}. \qquad (19)$$

If nonrelativistic particles predominate among the accelerated particles and the escape effect is small, then $\gamma_c\approx\gamma_g$ and $k\to 0$. We then have $\sigma_m\approx 4$, which coincides with Eq. (15) as $M\to\infty$. Note that although we have assumed that the acceleration leads primarily to nonrelativistic energies, this does not rule out the possibility of the front spreading. Accelerated nonrelativistic particles must inevitably have large transport lengths compared to thermal particles, which also determines the width of the front if the pressure of accelerated particles exceeds the pressure of thermal plasma.

Another limiting case is where relativistic particles dominate the spectrum. Here $\gamma_c\to 4/3$, and the escape effect has its maximum possible magnitude. This extreme situation corresponds to $k\to 1/2$, for which $\sigma_m\to\infty$ and $\eta_m\to 1$. In this limit, which cannot be realized in nature, the gas behind the front would be motionless and infinitely compressed, and all the energy of the incident plasma flux would be transferred to escaping particles:

$$q_m=ku_1P_{c2}=k\eta_mju_1^2=ju_1^2/2.$$

Thus, depending on the injection power and acceleration efficiency, and also the particle escape conditions, the following values are possible for a shock wave with a spread-out front:

$$0\leqslant k\leqslant 1/2, \quad 4<\sigma_m<\infty. \qquad (20)$$

These parameters vary within the same limits for waves with a finite thermal jump as well.

Note that the authors of Ref. 8 derive a dependence $\sigma \propto M^{3/4}$ for a strong shock wave with accelerated particles. From our discussion it is clear that a dependence of this kind cannot be universal in character, and at best can correspond only to a certain specific choice of injection power and other parameters of this system. In our case this value of the compression corresponds to maximum pressure of the accelerated particles for a given finite Mach number.

In light of these results, as $M \to \infty$ we have the following theoretical bounds on the compression, encompassing both shock waves with finite thermal jumps and shock waves with degraded fronts:

$$\frac{\gamma_g+1}{\gamma_g-1} \leqslant \sigma \leqslant \sigma_m = \frac{\gamma_c+1}{(\gamma_c-1)(1-2k)}. \tag{21}$$

For finite values of M the interval (21) can be narrowed. It can be found numerically.

Let us now find the velocity jump in the plasma across the thermal front by invoking conservation of momentum flux to the thermal jump. Taking into account that the accelerated particles pass freely through the thermal front, so that their pressure is the same on both sides of it, we find $P_{g2} = P_{g*} + j(u_* - u_2)$. In the region $z<0$ the velocity of the plasma varies smoothly, and the pressure of the thermal component must follow the Poisson adiabat $P_{g*} = P_{g1} y_*^{-\gamma_g}$, where $y_* = u_*/u_1$. Substituting these relations into Eq. (16) and using Eq. (14), we find

$$y_* + \frac{1}{\gamma_g M^2 y_*^{\gamma_g}} = 1 + \frac{1}{\gamma_g M^2} - \eta. \tag{22}$$

These equations enable us to write the compression of the plasma at the thermal front in terms of the Mach number and other parameters introduced previously. Recall that all equations from Eq. (14) onward are meaningful only for relativistic accelerated particles, i.e., for $\gamma_c < \gamma_g$. However, when $\gamma_c = \gamma_g$ the global compression is given by (15), and the right side of Eq. (22) becomes ambiguous. This ambiguity arises from the fact that the compression at the thermal discontinuity can acquire different values $1 \leqslant \sigma_* \leqslant 4$, depending on the relation between the thermal and accelerated components.

In solving Eq. (22) we must take the root for which $y_* \geqslant \sigma^{-1}$. In the strong shock wave limit $M \to \infty$, the range of values Eq. (21) for the global compression corresponds to $1 \leqslant \sigma_* \leqslant \sigma_m$. At the right-hand end of the interval, σ_* coincides with σ, and consequently there is no thermal jump in this (unique) case. For $\sigma < \sigma_m$ we always have $\sigma_* \leqslant \sigma$, i.e., the thermal jump is nonzero, although it can be extremely small for large M.

An equation that describes the velocity profile $u(z)$ over the smooth segment $-\infty < z \leqslant 0$ can be obtained using the conservation laws (10) and (11). We first obtain this equation for the case in which the number of escaping particles is negligible, i.e., $k \approx 0$. Using Eq. (10), we eliminate $P_c(z)$ from Eq. (11) and express $P_g(z)$ in terms of the velocity using the Poisson adiabat

$$P_g(z) = P_{g1} \left(\frac{u_1}{u(z)} \right)^{\gamma_g}. \tag{23}$$

As a result we find a first-order nonlinear differential equation for $u(z)$. In the dimensionless variables $x(z)$ and $y(x) = u(x)/u_1$, where $dx = u_1 dz / 2\overline{\kappa(z)}$, this equation takes the form

$$\frac{dy}{dx} = -\frac{(\gamma_c+1)(1-y)}{1-M^{-2}y^{-\gamma_g-1}} \left[y - \frac{\gamma_c-1}{\gamma_c+1} - \frac{2\gamma_c}{\gamma_g(\gamma_c+1)M^2} - \frac{2(\gamma_g-\gamma_c)(y^{1-\gamma_g}-1)}{\gamma_g(\gamma_g-1)(\gamma_c+1)(1-y)M^2} \right], \tag{24}$$

and must be integrated with the boundary condition $y(0) = y_*$. The latter quantity (and also the exponent γ_c for the adiabat of the accelerated particles) can take on different values for a given M, as follows from Eqs. (14), (21), and (22). Note that in our treatment the velocity discontinuity is isolated and localized; therefore, Eq. (24) has no singular points in the domain of our variables, in contrast to Refs. 15 and 7.

If we neglect terms of order M^{-2}, the equation simplifies and admits an analytic solution. Introducing the notation $y_0 = y_m|_{k=0} = (\gamma_c-1)/(\gamma_c+1)$, we write it in the form

$$\frac{dy}{dx} = -\frac{2}{1-y_0}(1-y)(y-y_0). \tag{25}$$

We now include escaping particles. A particle can escape only when accelerated by a strong shock wave; therefore, in what follows we neglect terms of order M^{-2}. We again use the conservation laws (9)–(11). Since the exact form of the function $\Theta(z)$ in the region $z<0$ is unknown *a priori*, we resort to interpolation. When $z \to -\infty$ the function $\Theta(z) \to 0$, while when $z \to 0$ we have $\Theta(z) \to 1$. Withn these two limits, it follows from Eqs. (10) and (11) that the derivative dy/dz takes the corresponding values

$$\frac{dy}{dz} = -\frac{2u_1}{2\overline{\kappa}(z)}(1-y)$$

and

$$\frac{dy}{dz} = -\frac{(\gamma_c+1)u_1}{2\overline{\kappa}(z)}(1-y_*)(y-y_m).$$

It is natural to use an interpolation equation similar to Eq. (25) over the entire domain of the variable $0 \geqslant z > -\infty$:

$$\frac{dy}{dx} = -\frac{2}{1-y_m}(1-y)(y-y_m), \tag{26}$$

in which the constant y_0 is replaced by y_m, which takes into account escaping particles, and a new independent variable has been introduced:

$$dx = \frac{(1-y_m)u_1}{2\overline{\kappa}(z)} \left\{ 1 + \frac{\gamma_c-1}{2} \times \exp\left[-\int_z^0 \frac{u_1 dz'}{2\overline{\kappa}(z')} \right] \right\} dz, \quad x(0)=0. \tag{27}$$

Equations (25) and (26) have a solution that satisfies the boundary condition $y(0) = y_*$. The solution for $y_* > y_m$ can be written in various forms:

$$y(x)=\frac{1}{2}(1+y_m)-\frac{1}{2}(1-y_m)\tanh\left[x+\frac{1}{2}\ln\frac{1-y_*}{y_*-y_m}\right]$$
$$=\frac{y_*(\sigma_m-1)+[2-y_*(1+\sigma_m)]\tanh x}{\sigma_m-1+(\sigma_m+1-2\sigma_m y_*)\tanh x},\quad x\leqslant 0. \tag{28}$$

In the region behind the shock transition the velocity of the plasma, like that of an ordinary shock wave, is a constant: $y(x)=u_2/u_1$ for $x>0$. The solution (28) generalizes the result of Axford *et al.*[15] to the case of a shock wave with a thermal jump.

For $y_*=y_m$ there is no thermal jump and the shock transition is completely washed out. The solution (28) is no longer valid in this case, because the region in which the change in velocity takes place (the degraded front) is carried off to $-\infty$. Equation (26) must be solved again, changing the boundary conditions to $y|_{x\to\infty}\to 1$, $y|_{x\to-\infty}\to y_m$, which leads to the usual solution

$$y(x)=\frac{1}{2}(1+y_m)-\frac{1}{2}(1-y_m)\tanh x, \tag{29}$$

for a smooth transition between two stationary states.[15,16] For shock waves of intermediate strength with a finite value of M, it is not difficult to solve Eq. (24) numerically.

3. SELF-CONSISTENT DETERMINATION OF THE SHAPE OF THE SPECTRUM AND PRESSURE OF ACCELERATED PARTICLES

In the macroscopic theory developed above, the four parameters σ, η, k, and γ_c are still unknown. They must be calculated from the kinetic equation (1), which enables us to find the shape of the spectrum of accelerated particles. This in turn determines the exponent of the Poisson adiabat γ_c, as well as the total energy and energy flux of the accelerated particles for a given injection power Q_0, which will be determined by the global structure of the shock transition.

Under reasonable assumptions about the diffusion coefficient (see below), Eq. (1) yields power-law solutions in p. Therefore, it is useful to first find the relation between the adiabatic exponent γ_c and the spectral index α of the distribution function:

$$N(p)=(\alpha-3)n_c p_0^{-3}(p_0/p)^{\alpha},\quad \alpha>3,\quad p\geqslant p_0, \tag{30}$$

where n_c is the number density of accelerated particles and $p_0\leqslant mc$ is the injection momentum. Calculating the pressure P_c and energy density w according to Eqs. (4) and (5) and determining the adiabatic exponent according to Eq. (7), we find

$$\alpha>5,\ P_c\approx\frac{2(\alpha-3)}{3(\alpha-5)}\frac{p_0^2}{2m}n_c,\quad \gamma_c=\frac{5}{3}; \tag{31}$$

$$\alpha\leqslant 5,\quad P_c=C(\alpha)cp_0n_c, \tag{32}$$

where

$$C(\alpha)\approx\begin{cases}(2p_0/3mc)\ln(2mc/p_0), & \alpha=5,\\ ((\alpha-3)/6\sqrt{\pi})\Gamma(\alpha/2-2) & \\ \quad\times\Gamma(5/2-\alpha/2)(p_0/mc)^{\alpha-4}, & 5>\alpha>4\end{cases}, \tag{33}$$

$$C(\alpha)\approx\begin{cases}(1/3)\ln(2p_m/mc), & \alpha=4,\\ ((\alpha-3)/3(4-\alpha))(p_0/p_m)^{\alpha-4}, & 4>\alpha>3\end{cases}. \tag{34}$$

We also find that

$$\gamma_c=\begin{cases}5/3-g(5) & \text{for }\ \alpha=5,\\ 4/3+g(\alpha) & \text{for }\ \alpha<4,\\ \alpha/3+g(\alpha) & \text{for }\ 5>\alpha\geqslant 4\end{cases}, \tag{35}$$

where

$$g(\alpha)\approx\begin{cases}((\alpha-3)^2/9C(a))[(p_0/p_m)^{\alpha-4}-p_0/2mc],\\ 5\geqslant\alpha\geqslant 4\\ ((4-\alpha)/3\sqrt{\pi}(\alpha-3))(mc/p_m)^{4-\alpha}\\ \quad\times\Gamma(\alpha/2-1)\Gamma(5/2-\alpha/2),\\ 4>\alpha>3\end{cases}. \tag{36}$$

Here we denote the cutoff momentum by p_m ($p_m\geqslant mc$), which bounds the energy of the accelerated particles from above. Under real conditions this bound stems from the finite extent of the shock wave front, its finite lifetime, and the increase in the diffusion coefficient with particle energy, which leads to escape of high-energy particles from the front and an end to acceleration. In order that Eq. (1) automatically yield solutions with bounded energy, we take the following steplike energy dependence of the diffusion coefficient:

$$\kappa(z,p)=\begin{cases}\kappa(z), & p<p_m;\\ \infty, & p>p_m.\end{cases} \tag{37}$$

This dependence corresponds to the assumption that a particle becomes free once it has achieved a momentum p_m and departs the system, i.e., the distribution function satisfies the condition

$$N(z,p)=0\quad\text{for }\ p>p_m \tag{38}$$

for any z.

The diffusion coefficient (37) corresponds to a sink function

$$Q_m(p)=Q_m p_m^{-2}\delta(p-p_m) \tag{39}$$

in Eq. (8), which we localize at $z=0$, i.e., we assume $f(z)=\delta(z)$. The strength of the sink Q_m must be chosen in such a way that (38) is satisfied. We consider the limiting momentum p_m to be an external parameter of the problem determined from other considerations (the real extent of the front, intensity of turbulence and magnetic field).

We can solve Eq. (1) with the diffusion coefficient (37) in analytic form if the velocity profile $u(z)$ is given by the solutions (28) and (29). Taking the right side of Eq. (1) in the form Eqs. (8) and (39) and carrying out a Mellin transform with respect to the variable p,

$$\overline{N(s,z)}=\int_0^\infty N(p,z)p^{s-1}dp, \tag{40}$$

we obtain

$$\frac{d}{dz}\,\kappa(z)\,\frac{d\overline{N}}{dz}-u(z)\,\frac{d\overline{N}}{dz}-\frac{s\,du}{3dz}\,\overline{N}=\left(Q_m p_m^{s-3}-Q_0 p_0^{s-3}-\frac{s}{3}(u_*-u_2)\overline{N}\right)\delta(z), \tag{41}$$

where we have extracted the singular part at the thermal discontinuity from the derivative du/dz.

We next transform to the independent variable $\zeta=(y-y_m)/(1-y_m)$, using a simplified relation (compared to Eq. (27)) between dx and dz of the form $dx/dz=(\gamma_c+1)(1-y_m)u_1/4\kappa(z)$, which yields the correct result in the region of highest acceleration near the thermal jumps, and somewhat overestimates the derivative dx/dz for $z\gg 2\kappa/u_1$, where the acceleration is very small. This leads to a hypergeometric equation in the standard form[17]:

$$\zeta(1-\zeta)\,\frac{d^2\overline{N}}{d\zeta^2}+[c-(a+b+1)\zeta]\,\frac{d\overline{N}}{d\zeta}-ab\overline{N}=0. \tag{42}$$

Here

$$a+b+1=\frac{2\gamma_c}{\gamma_c+1},\quad ab=-\frac{2s}{3(\gamma_c+1)},$$
$$c=1+\frac{2y_m}{(\gamma_c+1)(1-y_m)}. \tag{43}$$

The function $\overline{N}(s,\zeta)$ satisfies the boundary conditions

$$\overline{N}|_{\zeta=1}=0, \tag{44}$$

$$\left(\frac{d\overline{N}}{d\zeta}+\frac{2s(y_*-\sigma^{-1})(1-y_m)}{3(\gamma_c+1)(1-y_*)(y_*-y_m)}\,\overline{N}\right)_{\zeta=\zeta_*}=\frac{2(1-y_m)(Q_m p_m^{s-3}-Q_0 p_0^{s-3})}{(\gamma_c+1)(y_*-y_m)(1-y_*)u_1}. \tag{45}$$

The second condition incorporates the right side of Eq. (41) (equality of flux on the two sides of the thermal discontinuity). Despite the fact that the quantities a and b contain radicals, the symmetry of the coefficients of Eq. (42) results in a solution in the form of a rational function of the variable s.

The solution of the equation that satisfies the boundary conditions (44) and (45) can be expressed in terms of hypergeometric functions[16] as

$$\overline{N}(s,\zeta)=\frac{4(Q_0 p_0^{s-3}-Q_m p_m^{s-3})}{u_1(\gamma_c+1)^2(\gamma_*-y_m)(1-y_*)\Phi(s)}\times(1-\zeta)^{c-a-b}F(c-a,c-b;c-a-b+1;1-\zeta), \tag{46}$$

when $1\geqslant\zeta\geqslant\zeta_*>0$, and

$$\Phi(s)=(1-\zeta_*)^{c-a-b+1}\times\left[c-a-b-\frac{2s(y_*-\sigma^{-1})}{3(\gamma_c+1)(y_*-y_m)}\right]\times F(c-a,c-b;c-a-b+1;1-\zeta_*)+(1-\zeta_*)^{c-a-b}\frac{(c-a)(c-b)}{c-a-b+1}\times F(c-a+1,c-b+1;c-a-b+2;1-\zeta_*). \tag{47}$$

The solution (46) refers to the precursor region $x\leqslant 0$. Behind the thermal front $x>0$, the distribution function does not depend on position, and by virtue of continuity at the boundary $x=0$ ($\zeta=\zeta_*$) its value $\overline{N_2}(s)$ is determined by Eq. (46) evaluated at $\zeta=\zeta_*$: $\overline{N_2}(s)=\overline{N}(s,\zeta_*)$.

When $\zeta_*\to 0$ ($y_*\to y_m$), the hypergeometric series diverges and solution (46), (47) is no longer meaningful. In this case, which corresponds to the absence of a thermal jump, solution (28) also becomes meaningless, as noted above. It should be replaced by the solution (29).

To determine the spectrum of accelerated particles in this limit, we must solve Eq. (42) again for the region $1\geqslant\zeta\geqslant 0$ with boundary conditions

$$\overline{N}|_{\zeta=1}=0,\quad \overline{N}|_{\zeta=0}\ \text{bounded},$$
$$\overline{N}|_{\zeta=1/2+0}=\overline{N}|_{\zeta=1/2-0},$$
$$\left.\frac{\partial\overline{N}}{\partial\zeta}\right|_{\zeta=1/2+0}-\left.\frac{\partial\overline{N}}{\partial\zeta}\right|_{\zeta=1/2-0}=\frac{4(Q_m p_m^{s-3}-Q_0 p_0^{s-3})}{u_1}. \tag{48}$$

These boundary conditions correspond to injection and escape of particles with the highest energies for $\zeta=1/2$ ($x=0$), i.e., at the point of largest curvature of the shock transition profile.

The solution of Eq. (42) with boundary conditions (48) has the form

$$\overline{N}(s,\zeta)=\frac{2^{c-a-b+2}(Q_0 p_0^{s-3}-Q_m p_m^{s-3})F(a,b;c;1/2)}{u_1\Phi(s)F(c-a,c-b;c-a-b+1;1/2)}\times(1-\zeta)^{c-a-b}F(c-a,c-b;c-a-b+1;1-\zeta) \tag{49}$$

for $1\geqslant\zeta\geqslant 1/2$, and

$$\overline{N}(s,\zeta)=\frac{4(Q_0 p_0^{s-3}-Q_m p_m^{s-3})}{u_1\Phi(s)}\,F(a,b;c;\zeta) \tag{50}$$

for $1/2\geqslant\zeta\geqslant 0$, where now

$$\Phi(s)=\frac{ab}{c}\,F(a+1,b+1;c+1;1/2)+(c-a-b)F(a,b;c;1/2)\times\left[2+\frac{(c-a)(c-b)F(c-a+1,c-b+1;c-a-b+2;1/2)}{(c-a-b)(c-a-b+1)F(c-a,c-b;c-a-b+1;1/2)}\right]. \tag{51}$$

The spectrum of accelerated particles can be calculated by inverting the Mellin transform,

$$N(p,\zeta)=\frac{1}{2\pi i}\int_{-i\infty}^{+i\infty}\overline{N}(s,\zeta)p^{-s}ds. \tag{52}$$

For $p>p_m\gg p_0$, the contour of integration can be closed on an arc of infinite radius in the right-hand half-plane, and the value of the integral will be determined by the residues of the expression under the integral sign at the poles α whose positions are given by the equation

$$\Phi(\alpha)=0, \tag{53}$$

where the values of α are the exponents of individual power-law terms. In the problem under discussion (see below), Eq. (53) always has exactly one real root.

We now return to determining the intensity Q_m of the flux of escaping particles. Since the solutions (46) and (49), (50) are proportional to the difference $Q_0p_0^{s-3}-Q_mp_m^{s-3}$, the corresponding distribution function $N(p,\zeta)$ for $p>p_m$ and in the presence of exactly one root α will be proportional to the difference $Q_0(p_0/p)^{\alpha-3}-Q_m(p_m/p)^{\alpha-3}$, and (38) enables us to relate the flux of escaping particles to the injection power:

$$Q_m=Q_0(p_0/p_m)^{\alpha-3}. \tag{54}$$

Another useful relation can be obtained from the balance equation for the number of accelerated particles. Under steady-state conditions, the particles injected into the acceleration regime generate a flux of accelerated particles $n_{c2}u_2$, which is carried off by the turbulent plasma behind the shock transition, and a flux of escaping particles Q_m. Using Eqs. (54) and (13), we find

$$Q_0=\frac{n_{c2}u_1}{\sigma[1-(p_0/p_m)^{\alpha-3}]}. \tag{55}$$

For the dimensionless energy flux of escaping particles $k=q_m/u_1P_{c2}$, we find, using Eqs. (54), (39), and (12), that

$$k=\frac{cp_0Q_0}{u_1P_{c2}}\left(\frac{p_0}{p_m}\right)^{\alpha-4}. \tag{56}$$

Combining Eqs. (55), (56), and (14), we can relate the dimensionless injection parameter $Q=Q_0/n_{g1}u_1$ and the energy flux k to the spectral index and the global compression:

$$Q=\frac{u_1^2(\gamma_c-1)(1+4/\sigma^2-5/\sigma)}{cv_0\{(5-3\gamma_c)C(\alpha)[1-(p_0/p_m)^{\alpha-3}]+2(\gamma_c-1)(p_0/p_m)^{\alpha-4}\}}, \tag{57}$$

$$k=\frac{(p_0/p_m)^{\alpha-4}}{\sigma C(\alpha)[1-(p_0/p_m)^{\alpha-3}]}. \tag{58}$$

Here γ_c and $C(\alpha)$ depend on the spectral index through Eqs. (33)–(36), and v_0 is the velocity of the injected particles. Relations (55)–(58) are valid for any finite value of the thermal jump. If, however, there is no jump and the shock transition is washed out, the compression $\sigma=\sigma_m$ is given by Eq. (21), and Eqs. (57), and (58) simplify:

$$Q=\frac{u_1^2}{cv_0}\left(\frac{p_m}{p_0}\right)^{\alpha-4}\left(1-\frac{1}{\sigma_m}\right)k_m, \tag{59}$$

$$k_m=\left\{2+(\gamma_c+1)C(\alpha)\left(\frac{p_m}{p_0}\right)^{\alpha-4}\right.$$
$$\left.\times\left[1-\left(\frac{p_0}{p_m}\right)^{\alpha-3}\right](\gamma_c-1)^{-1}\right\}^{-1}. \tag{60}$$

An estimate of the parameter k using Eqs. (58), (60) and (33)–(36) shows that for spectra with $\alpha\geqslant 4$ and $p_m\gg mc$, the escape effect is small, and will be only important for mildly sloping spectra with $\alpha<4$.

We now calculate the spectral index and other parameters of the shock transition. We begin with the simplest situation, where there is no thermal jump and the velocity profile is given by Eq. (29), while the distribution function is specified by Eqs. (49)–(52). For $p_m>p>p_0$ the term with Q_m can be integrated along a contour that is closed in the left half-plane, where there are no poles. This is because the mechanism that acts at the shock transition is first-order Fermi acceleration, for which the injected particles can only increase in energy. The term with Q_0 is integrated along the right half-circle and yields a power-law contribution with the previous index α determined from Eq. (53).

In this case the index α and dimensionless pressure η_m of accelerated particles Eq. (17) depend only on σ_m. Therefore, it is convenient to specify the compression σ_m as an independent parameter and express the remaining quantities in terms of it, including the injection power necessary to sustain a given compression according to Eq. (59). In this case the distribution function can also be simplified:

$$N_2(p)=(\alpha-3)\left(1-\frac{1}{\sigma_m}\right)\frac{u_1^2n_{g1}}{cv_0p_0^3}\left(\frac{p_0}{p}\right)^{\alpha},\quad p\leqslant p_m. \tag{61}$$

Values of the spectral index α can be calculated by numerically finding roots of the function (51) for various values of the global compression σ_m. The injection power is determined from Eqs. (59) and (60).

In a situation where the thermal jump has a finite value, it is necessary to determine the spectral index by requiring that the function (47) vanish. As an independent variable we can use either the global compression σ again, expressing the

TABLE I. Spectral indices of accelerated particles and required injection power for various values of the global compression.

1	σ	4.05	4.25	4.5	5.0	6.0	7.0
2	α	3.99	3.95	3.91	3.85	3.73	3.63
3	Q	$5\cdot 10^{-6}$	$2.0\cdot 10^{-5}$	$2.45\cdot 10^{-5}$	$1.73\cdot 10^{-5}$	$4.6\cdot 10^{-6}$	$1.1\cdot 10^{-6}$
4	α	4.97	4.85	4.71	4.50	4.20	4.00
5	Q	$5.2\cdot 10^{-2}$	$4.3\cdot 10^{-2}$	$2.9\cdot 10^{-2}$	$1.2\cdot 10^{-2}$	$2.4\cdot 10^{-3}$	$3.1\cdot 10^{-4}$
6	σ	10	15	21	50	100	300
7	α	3.45	3.29	3.20	3.078	3.033	3.010
8	Q	$7.4\cdot 10^{-8}$	$6.2\cdot 10^{-9}$	$1.5\cdot 10^{-9}$	$1.9\cdot 10^{-10}$	$8.7\cdot 10^{-11}$	$5.9\cdot 10^{-11}$
9	α	3.67	3.45	3.33	3.16	3.11	3.07
10	Q	$3.7\cdot 10^{-6}$	$9.5\cdot 10^{-8}$	$1.3\cdot 10^{-8}$	$8.2\cdot 10^{-10}$	$3.2\cdot 10^{-10}$	$1.7\cdot 10^{-10}$

parameters k and Q in terms of it according to Eqs. (57) and (58), or the injection Q. In the latter case we must express the compression in terms of the injection. Furthermore, in both cases we must fix the external parameters of the problem: the velocity u_1 and density n_{g1} of the advancing plasma flux, as well as the injection momentum p_0 and limiting momentum p_m.

4. DISCUSSION OF RESULTS AND CONCLUSIONS

The results of numerical calculations are given in Table I. They are obtained under the assumptions $v_0 = u_1 = 10^{-2}$ s and $p_m/mc = 10^6$, which coincide in order of magnitude with an ''optimistic'' type of particle acceleration by a strong shock wave from the explosion of a supernova ($M \gg 1$). Lines 2, 3 and 7, 8 refer to a shock transition with a thermal jump, lines 4, 5 and 9, 10 to a degraded front. As $\sigma \to \infty$ the equations given above allow us to obtain $\alpha \to 3$ and $Q \to T_1/T_m \approx 5\cdot 10^{-11}$, where T is the kinetic energy. We now note some characteristic features of these results.

1. At global compressions $\sigma \geqslant 4$ there exist two branches of the solution, corresponding to a wave with a thermal jump and a completely degraded front. Both branches merge as $\sigma \to \infty$, where the thermal discontinuity disappears.

2. For a given compression of the medium, the regime with a thermal jump creates a harder spectrum of accelerated particles (smaller α) and requires lower injection power than the regime with a degraded front. This is explained by the fact that a flow profile with a large velocity gradient (thermal jump) accelerates particles more efficiently (Fig. 2).

3. All acceleration regimes shown in Table I require low relative injection power $Q \leqslant 5\cdot 10^{-2}$.

4. The branch with a thermal jump exists only over a bounded interval of injection power, $0 \leqslant Q \leqslant Q_{\max} \approx 2\cdot 10^{-5}$; it corresponds to a spectral index for accelerated particles in the range $4 \geqslant \alpha \geqslant 3$ (Fig. 3).

5. The branch with a degraded front exists for injection power $1 > Q \geqslant Q_{\min} = T_1/T_m \approx 5\cdot 10^{-11}$; in this case the spectral index varies from $\alpha \approx 5$ to $\alpha = 3$ (Fig. 3).

6. An increase in compression is accompanied by a decrease in spectral index and a decrease in injection (with the exception of the initial segment of the branch with the thermal jump). The decrease in injection is explained by the fact that as the index α decreases, the relative number of particles with maximum energy increases, and the prespecified injection is provided entirely by fewer and fewer ultrarelativistic particles. For the parameters chosen, the limit $\sigma \to \infty$ corresponds to vanishingly small injection $Q_{\min} \approx 5\cdot 10^{-11}$. Conversely, as injection increases, the relative number of relativistic particles in the spectrum decreases, since the original energy of the plasma flow is distributed over an increasing number of particles. A natural consequence of this is the increase in the spectral index and decrease in the compression.

7. The fraction of energy η transferred to the accelerated particles on the branch with the degraded front is very large and increases from 0.75 for $\sigma \to 4$ to 1 for $\sigma \to \infty$. On the branch with the thermal jump it varies for the same compressions from 0 to 1.

These results show (Fig. 2) that the solution to this nonlinear problem in the time-independent formulation has several branches. In particular, three values of compression of the medium are possible, as well as three values of the spectral index of the accelerated particles if the injection power lies in the range $Q_{\min} < Q < Q_{\max}$. Therefore, questions of stability of these states and their realizability must be addressed.

To study stability by traditional methods, it is necessary to go beyond the limits of the steady-state formulation of the problem, which leads to considerable difficulties. However, we can make arguments of a general character that favor the

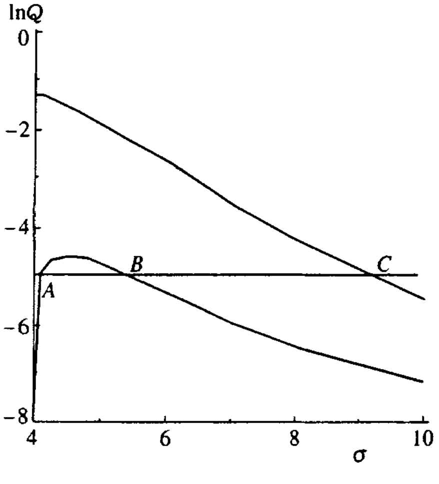

FIG. 2. Relation between the plasma compression σ and the rate Q of particle injection into the acceleration regime for $p_0/mc = 10^{-2}$ and $p_m/mc = 10^6$. The upper curve describes a shock wave with a degraded front, the lower curve a state with a thermal jump.

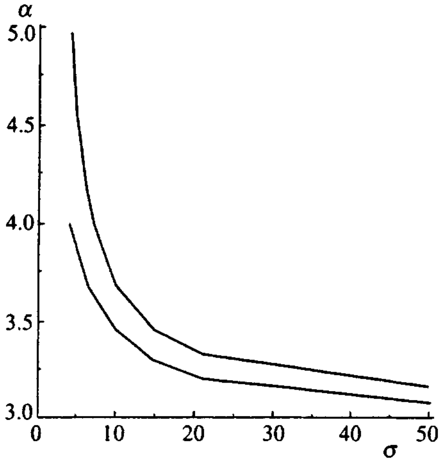

FIG. 3. Accelerated particle spectral index α as a function of global compression σ. The upper curve corresponds to the absence of a thermal jump, the lower curve to the presence of a thermal jump.

realization of the state with the smallest compression for a given rate of injection.

The shock transition can be regarded as a certain stage of approximation to the equilibrium state of a strongly nonequilibrium initial system (a flux of cold nonrelativistic plasma with a large excess of energy of directed motion). The relaxation of this system is accompanied by an increase in entropy. According the Boltzmann principle, the state that is most probable is the one with the highest entropy (i.e., which is realized by the largest number of microstates). Therefore, in nature we should expect those realizations of such a state (combined with the conservation laws and dynamic laws, i.e., the equations of motion) that correspond to the highest entropy per particle. Of the three states A, B, and C corresponding to the admissible solutions, only state A possesses these properties, because it corresponds to the highest average energy of the primary particle mass behind the shock transition. In state B the thermal jump is smaller than in state A, so that the heating of the primary plasma and its entropy turn out to be smaller; moreover, although the higher energy of a smaller faction of accelerated particles is accompanied by an increase in their entropy, this does not bring about a decrease in the entropy of the most numerous component. This tendency is manifested in state C, in which the entropy of the primary plasma remains constant, to an even stronger degree. It is not difficult to estimate this effect quantitatively: the entropy difference per particle for states A and C is given by

$$s_A - s_C = \ln(M^3/32) + \mathcal{O}(\sigma Q/4).$$

Starting with these considerations, we can propose the following sequence of plasma states at a shock transition with large Mach number for slow (quasistatic) growth of the level of injection. For $Q=0$ there are no accelerated particles, and we have a thermal jump with $\sigma_* = \sigma = 4$. As the injection increases from 0 to $Q_{\min} = T_1/T_m$ only one state can exist, with a thermal density jump close to 4. The appearance of relativistic particles increases the compression somewhat, while the spectral index is smaller than its original value $\alpha = 4$. For $Q > Q_{\min}$, three states are possible, but only the most stable one is realized—the one lying on the initial branch with the thermal jump.

As injection is further increased above $Q = Q_{\max}$, the only states that are compatible with the equations of motion and conservation laws are those with a degraded front; therefore, a jump should occur in the system to a different branch of the solution. This jump is accompanied by an increase in compression (by almost a factor of 2 for the parameters we have chosen) and according to what was said above, a decrease in entropy. However, there are no other states for levels of injection $Q > Q_{\max}$; therefore, realizations of the structure with a degraded front are inevitable under these conditions. The jump is also accompanied by a decrease in spectral index, and consequently an increase in the relative number of relativistic particles.

The behavior of the system in this range of injection power recalls that of a phase transition, accompanied by a change in some ‘‘order parameter’’—here the relative number of relativistic particles. Furthermore, in the neighborhood of $Q_{\max}$ there is also a region of fluctuations, in which small changes in injection lead to large changes in the state of the shock transition, which is analogous to the fluctuation region near the Curie point.

Further increases in injection lead to a decrease in compression and an increase in spectral index. When the injection increases to $Q \geqslant 3 \cdot 10^{-4}$, which corresponds to compression $\sigma \leqslant 7$, the spectral index increases to $\alpha > 4$, and monotonically increases after that as the rate of injection increases. Although in this case the fraction of energy transferred to the accelerated particles remains high, $\eta > 0.75$, since the number of accelerated particles increases their average energy decreases and the relative numbers of relativistic particles drops. The theory developed here is no longer valid at $\alpha \approx 5$, where this fraction becomes negligible.

As the rate of injection changes in the opposite direction, we might expect the reverse sequence of states. For injection $Q < Q_{\max}$, there will most likely be a jump in the system to the branch with a thermal jump. This does not exclude the possible appearance of a ‘‘superheated’’ state and hysteresis loops connected with possible stability within certain limits of the upper branch shown in Fig. 2 against small fluctuations, but ultimately this system will transition to the more stable state on the original branch of the lower curve.

Recall that the observed spectral index for galactic cosmic rays is $\alpha \approx 4.7$ in the energy range 10 GeV $\leqslant T \leqslant 10^6$ GeV. In a model where particles are accelerated by a single shock wave, this index can be generated in the linear regime by a shock wave of moderate strength ($\sigma \approx 2.76$, $M \approx 2.58$) and by a stong shock in the extreme nonlinear regime ($\sigma \approx 4.5$, $M \gg 1$). The main difference between these cases is the magnitude of the efficiency, i.e., the fraction of the energy transferred to accelerated particles: $\eta \ll 1$ in the linear regime and $\eta \approx 0.78$ in the nonlinear regime. It is likely that intermediate nonlinear regimes with $M > 2.58$ are possible as well; these are not considered in this paper.

We will also not discuss the rate of particle injection into the acceleration regime from the ambient medium in this paper. Several estimates of this quantity were given in Ref. 18 which indicate that under natural conditions any required injection can be realized within practically any regime. The consequences of the nonlinear effects discussed here for strong shock waves in astrophysical objects can be verified in principle by observing synchrotron radiation of the accelerated particles (the spectral index α) and thermal radiation due to the front, which strongly depends on the effective plasma temperature.

In conclusion, we present a brief summary of the overall properties of our model, which can be exhibited by other similar systems, for example shock waves with a spherical front.[8,19]

It has been shown that within a certain range of injection powers there exist certain states of the shock transition which correspond to the same injection, but which differ appreciably in their global compression, profile shape, and spectra of accelerated particles. The presence of several branches of the solution is a characteristic feature of many very different nonlinear systems.

There exist stable states of the shock transition from which the system is capable of executing transitions to other states that differ strongly from the original state. In this case a small change in injection power can lead to considerable changes in the observed parameters—global compression and accelerated particle spectrum.

In nonlinear regimes of particle acceleration, a decrease in injection leads to an increase in compression. High values of global relative compression at the shock transition (by factors of tens or hundreds) correspond to very low levels of injection. It is probable that such states (with relative compression >10) are unstable, and the possibility of their realization in nature is not clear.

[1] R. S. Sagdeev, in *Problems in Plasma Theory*, Vol. 4, [in Russian], Atomizdat, Moscow (1964).
[2] A. V. Gurevich and L. P. Pitaevskiĭ, Zh. Éksp. Teor. Fiz. **65**, 590 (1973) [Sov. Phys. JETP **38**, 291 (1973)]; Zh. Éksp. Teor. Fiz. **93**, 871 (1987) [Sov. Phys. JETP **66**, 490 (1987)].
[3] V. G. Eselevich, Space Sci. Rev. **32**, 56 (1982).
[4] W. I. Axford, E. Leer, and G. Scadron, in *Proc. 15th ICRC*, Plovdiv (1977), Vol. **11**, p. 132.
[5] G. F. Krymskiĭ, Dok. Akad. Nauk SSSR **234**, 1306 (1977) [Sov. Phys. Dokl. **22**, 327 (1977)].
[6] I. N. Toptygin, *Cosmic Rays in Interplanetary Magnetic Fields* [in Russian], Nauka, Moscow (1983).
[7] E. G. Berezhko and G. F. Krymskiĭ, Usp. Fiz. Nauk **154**, 49 (1988) [Sov. Phys. Usp. **31**, 27 (1988)].
[8] E. G. Berezhko, V. K. Eshlin, and L. T. Ksenofontov, Zh. Éksp. Teor. Fiz. **109**, 3 (1996) [JETP **82**, 1 (1996)].
[9] F. C. Jones and D. C. Ellison, Space Sci. Rev. **58**, 259 (1991).
[10] A. M. Bykov and I. N. Toptygin, Zh. Éksp. Teor. Fiz. **98**, 1255 (1990) [Sov. Phys. JETP **71**, 702 (1990)].
[11] J. F. McKenzie and H. J. Volk, Astron. Astrophys. **116**, 191 (1982).
[12] M. Scholer, in AIP Conf. Proc. 264, G. Zank and T. Gaisser (eds.) (1992), p. 125.
[13] K. B. Quest, in AIP Conf. Proc. 264, G. Zank and T. Gaisser (eds.) (1992), p. 348.
[14] A. M. Bykov and Yu. A. Uvarov, JETP Lett. **57**, 644 (1993).
[15] W. I. Axford, E. Leer, and J. F. McKenzie, Astron. Astrophys. **111**, 317 (1982).
[16] L. D. Landau and E. M. Lifshitz, *Fluid Mechanics*, Pergamon Press, Oxford (1987)
[17] M. Abramowitz and I. Stegun, *Handbook of Mathematical Functions*, Dover, New York (1965).
[18] I. N. Toptygin, in *Proc. 25th ICRC*, Durban (1997).
[19] L. O'C. Drury, H. J. Volk, and E. G. Berezhko, Astron. Astrophys. **299**, 222 (1995).

Translated by Frank J. Crowne

Equilibrium configuration of a nematic liquid crystal confined to a cylindrical cavity

S. V. Burylov*)

''Transmag'' Institute of Transport Systems and Technology, Ukrainian National Academy of Sciences, 320005 Dnepropetrovsk, Ukraine

(Submitted 28 April 1997)
Zh. Éksp. Teor. Fiz. **112**, 1603–1629 (November 1997)

A nematic liquid crystal confined to a cylindrical capillary with homeotropic anchoring to the sidewalls is considered. An analytic description of the planar polar director field configuration is proposed for arbitrary values of the system material parameters. Conditions for orientational transitions between planar radial, planar polar, and escaped radial structures are determined, with a discussion of similar considerations for planar-circular anchoring. *© 1997 American Institute of Physics.* [S1063-7761(97)00711-7]

1. INTRODUCTION

Equilibrium configurations of nematic liquid crystals (NLC) in a cylindrical cavity have been studied for approximately thirty years. Some dozens of papers have been written about this problem; therefore, the bibliographical citations listed below will naturally not encompass all of the available experimental and theoretical investigations. The reader can acquaint himself with additional information in, e.g., the review by Saupe[1] or the book by Kleman,[2] and for the results of more recent investigations the works of Allender and his coauthors.[3,4]

Here we will address some particular questions that in our view are of important practical interest. We note above all that the most convenient geometry in which to study nematic liquid crystals, after a geometry of plane-parallel cells, is the cylindrical geometry, both from a theoretical and an experimental point of view. In this case, essentially all experimentally observed[3–13] and theoretically possible[14,15] configurations of the director field **n** in a cylindrical cavity admit either a complete or approximate analytic description. This circumstance allows us to predict with some accuracy the transition points between configurations, starting with a specific set of material parameters of the system. On the other hand, values of the material parameters such as the NLC modulus of elasticity have been determined[3,4,11–13] by analyzing experimentally observed oriented structures.

The possible equilibrium configurations of a nematic in a cylindrical cavity depend primarily on how the director **n** is anchored to the lateral surface of the cylinder. The type of anchoring is specified by the unit vector $\mathbf{\Pi}$ for easy orientation of **n** at the walls of the liquid crystal sample. In essentially every experiment to date, the anchoring is of homeotropic type: the direction $\mathbf{\Pi}$ of easy orientation of the director is perpendicular to the lateral surface of the cylinder. The three theoretically possible configurations of an NLC corresponding to these boundary conditions are shown in Fig. 1. These structures are conventionally referred to in Refs. 3 and 4 as planar radial (PR), planar polar (PP), and escaped radial (ER). The first two configurations belong to the class of planar (two-dimensional) distortions of the director field, while the last belongs to the class of bulk (three-dimensional) deformations.

As shown in Refs. 3, 4, when the moduli of elasticity for transverse K_{11} and longitudinal K_{33} bending of the NLC are different, the minimum in the total free energy of this system in the class of two-dimensional distortions corresponds to the PP structure. However, this result cannot be extended to arbitrary values of K_{11} and K_{33}. This can be demonstrated for the example of liquid-crystal materials that exhibit not only the nematic but also the smectic A phase. In fact, near the point of transition to the smectic phase, where $K_{33} \gg K_{11}$, the molecules of the nematic tend to be located in ''smectic-like'' layers parallel to one another and of equal thickness. In this case, it is clear even on qualitative grounds that a PR structure (see Fig. 1a) with a line defect along the axis of the cylinder can allow a similar restructuring of the NLC, i.e., smectic-like layers forming concentric circles of equal thickness. At the same time, the internal restructuring of a nematic in the PP configuration (Fig. 1b) unavoidably leads to deformation of the layers along the thickness, which is extremely disadvantageous energetically. Consequently, there may be a certain relation between the elastic moduli K_{11} and K_{33} for which the minimum total free energy in the class of planar distortions turns out to correspond to the PR configuration. For a deeper analysis and quantitative estimates we require additional theoretical investigations.

The three-dimensional ER deformation (Fig. 1c) arises when a line defect in the planar radial configuration uniformly ''escapes'' in the third direction. Escape in the opposite energetically equivalent direction leads[3–13] to a more complicated three-dimensional structure with point defects (escaped radial with point defects, or ERPD). For infinitely long cylinders, which we discuss below, the ERPD configuration is metastable: point defects either attract and annihilate one another, or separate and disappear at infinity.[16] As a result, the ERPD structure is converted into a uniform ER configuration possessing lower energy in the class of three-dimensional distortions. We add that the ER configuration is also more energetically favorable than the ERPD structure for cylinders of finite length with absolutely degenerate end boundary conditions for the director **n**.

Optical[5–8,13] and nuclear magnetic resonance experiments[3,4,9–12] show that in cylinders with radii $R = 0.5-200\ \mu$m and homeotropic anchoring at the lateral surface, escape (ER or ERPD) structures are realized, while in cylinders with radii $R = 0.05-0.4\ \mu$m, depending on the

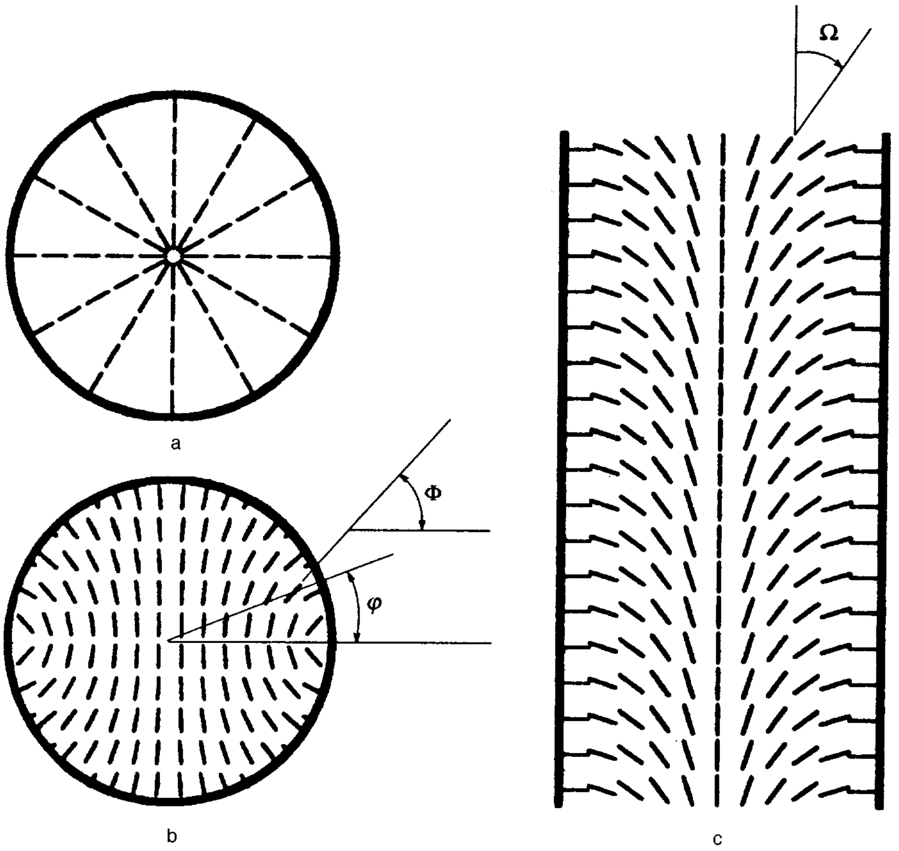

FIG. 1. Configurations of the director field **n** corresponding to homeotropic anchoring: a—planar radial (PR); b—planar polar (PP); c—escaped radial (ER).

relations between material parameters of the system, either ERPD or PP configurations can occur. The observed stable ERPD structures are associated with the presence of nondegenerate end boundary conditions (for example, of the same homeotropic nature). These boundary conditions are difficult to control and may differ from experiment to experiment. The existence of PR configurations in the cylindrical volume of an NLC has not been confirmed experimentally at this time; however, many authors (see, for example, Refs. 4, 5, 10, 15) assume that this structure can occur near the nematic–smectic A transition point in cylinders of radius $R \leqslant 0.1\ \mu\text{m}$. Note that such structures are seen fairly often in the pure smectic A-phase.[17,18]

Let us touch briefly on theoretical studies of the configurations shown in Fig. 1. The PR structure was completely described by Dzyaloshinskiĭ.[14] The analytic solution for the ER configuration for so-called rigid (see below) anchoring was obtained by Cladis and Kleman,[15] and in a more general form by Allender and his coauthors.[3,4] As for the PP structure, the exact solution obtained by the latter authors corresponds only to the two-constant approximation $K_{11} = K_{33}$. Numerical calculations for this structure when $K_{11} \neq K_{33}$ were recently carried out in Ref. 19.

In this paper we present an analytic description of the PP configuration for a system with arbitrary material parameters. The system always consists of a cylinder with infinite length; by analyzing exact solutions we find conditions for orientational transitions between PR, PP, and ER structures. For completeness of the theoretical investigation, along with homeotropic conditions we discuss in detail the cylindrical type of anchoring in which the direction $\mathbf{\Pi}$ of easy orientation of the director is perpendicular to the cylinder axis and tangent to its lateral surface. The circular type of anchoring has yet to be realized in practice. In order to do so it is necessary not only to fix the vector $\mathbf{\Pi}$ in the plane tangential to the lateral surface of the cylinder, as shown, e.g., in Ref. 20, but also to lift the degeneracy with respect to directions of $\mathbf{\Pi}$ in this plane; in other words, to orient the vector $\mathbf{\Pi}$ in the tangent plane that is perpendicular to the cylinder axis. For planar cells in an NLC, the problem of lifting the degeneracy in this way has been successfully solved experimentally;[21,22] therefore, we assume that in the future it will be solved for samples of cylindrical form as well. Three equilibrium structures analogous to those described above for the director field when the anchoring is of circular type are shown in Fig. 2. We refer to them in the following way: planar circular (PC), circularly planar polar (CPP), and escaped circular (EC). Of these three structures only the PC configuration admits even a semblance of a complete theoretical treatment;[14] the EC structure for rigid anchoring is treated in Ref. 15.

The sequence of exposition of the material in this paper is as follows. In Sec. 2 we present expressions for the total free energy functional of the NLC and describe the equilibrium equations for a cylindrical geometry. In Sec. 3 we formulate a general approach to describing plane oriented textures and briefly investigate the PR and PC configurations. The results of calculations for the polar PP and CPP structures are contained in Sec. 4. The escaped configurations are discussed in Sec. 5, in which we briefly describe the ER

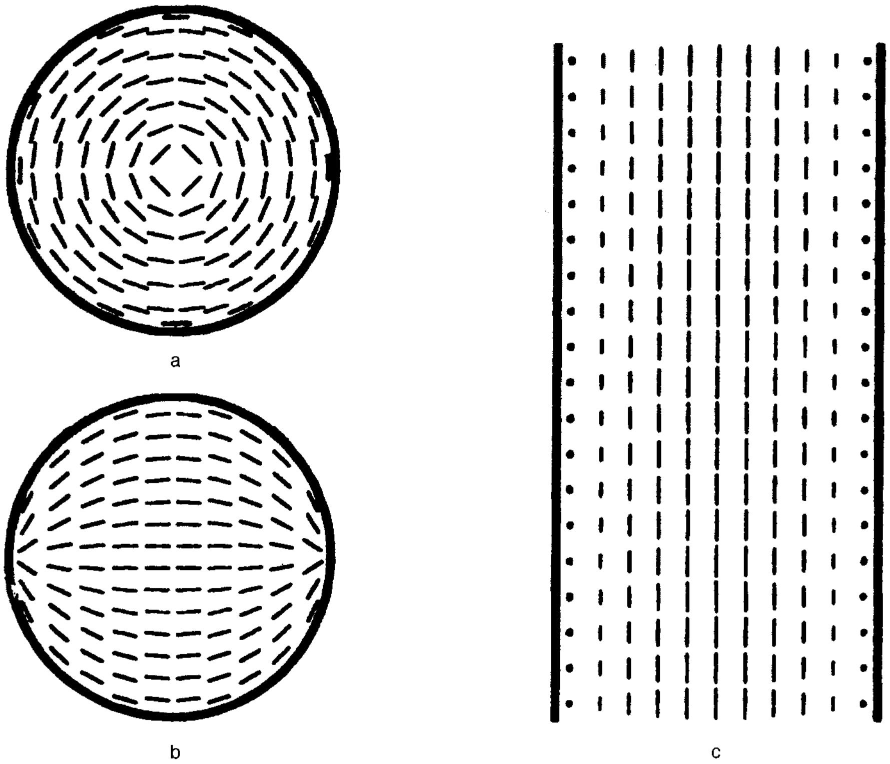

FIG. 2. Configurations of the director field **n** corresponding to circular anchoring: a—planar circular (PC); b—circular planar polar (CPP); c—escaped circular (EC). For the EC structure (c) the director on the cylinder axis lies in the plane of the figure, while near the walls of the capillary it is perpendicular to this plane.

structure, give a general calculation for the EC configuration, and discuss the ''total escape'' conditions that lead to a uniform axial structure with director **n** parallel to the cylinder axis. In Sec. 6 we analyze the conditions for orientational transitions among the possible configurations of the NLC for each of these types of anchoring. The conclusions are presented in Sec. 7.

2. CONTINUUM APPROACH TO THE DESCRIPTION OF NLC

2.1. Total free energy functional

In the static regime, and in the absence of external (magnetic or electric) fields, the total free energy F of a uniaxial NLC contains two contributions: the elastic free energy F_{EL} and the anchoring free energy F_A. Let us consider each of these contributions in detail.

According to Saupe,[23] the elastic free energy functional of the NLC, which is quadratic in the derivatives of the director, can be written in the following way:

$$F_{\mathrm{EL}}=\int_V dV\left\{f_V-\frac{1}{2}K_{24}\,\boldsymbol{\nabla}\cdot[\mathbf{n}\times(\boldsymbol{\nabla}\times\mathbf{n})+\mathbf{n}(\boldsymbol{\nabla}\cdot\mathbf{n})]\right\}. \tag{1}$$

Here dV is the volume element and f_V is the total free energy of Frank[24]:

$$f_V=\frac{1}{2}\{K_{11}(\boldsymbol{\nabla}\cdot\mathbf{n})^2+K_{22}[\mathbf{n}(\boldsymbol{\nabla}\cdot\mathbf{n})]^2+K_{33}[\mathbf{n}\times(\boldsymbol{\nabla}\times\mathbf{n})]^2\}. \tag{2}$$

The coefficient K_{22} is referred to as the torsion modulus, while the coefficients K_{11} and K_{33}, as mentioned above, are respectively the moduli of transverse and longitudinal bending. The divergence contribution of the coefficient K_{24} in the functional (1), by Gauss's theorem, can be written as a surface integral with energy density

$$f_{24}=-\frac{1}{2}K_{24}\mathbf{s}\cdot[\mathbf{n}\times(\boldsymbol{\nabla}\times\mathbf{n})+\mathbf{n}(\boldsymbol{\nabla}\cdot\mathbf{n})], \tag{3}$$

where **s** is the outward unit normal to the surface S of the sample. Since the coefficient K_{24} contributes only to the surface elastic energy of the NLC, it is referred to as the surface elastic modulus. Note that in the literature the constant K_{24} has been described in various ways; our choice of definition of this modulus follows from Eq. (1). We also note that, like the authors of Refs. 4, 9–13, 25, we neglect the influence of the other surface contribution $\int_V dVK_{13}\boldsymbol{\nabla}\cdot[\mathbf{n}(\boldsymbol{\nabla}\cdot\mathbf{n})]$, and assume that inclusion of this term in the functional (1) confers excessive accuracy. The results of individual experiments attest to this fact; see, for example, Ref. 26.

The functional (1) for the elastic free energy should have a minimum ($F_{\mathrm{EL}}=0$) for a uniform distribution of the director field. This condition imposes natural restrictions[27] on the elastic modulus of the NLC: the constants K_{11}, K_{22}, and K_{33} must be positive, and the constant K_{24} must lie in the interval $0\leqslant K_{24}\leqslant\min\{2K_{11},2K_{22}\}$.

Let us turn to the anchoring free energy functional; it can be written as a surface integral

$$F_A=\int_S dS\,f_A.$$

Here the anchoring energy density f_A is defined to be the anisotropic part of the surface tension at the walls (or boundaries) of the liquid crystal sample.[21,22] The walls, which are formed by mechanical means or with the help of surface-active materials, are found to act in an anisotropic orienting fashion on the NLC molecules, and thereby specify the type of anchoring, i.e., the direction $\mathbf{\Pi}$ of easy orientation of the director. In general, the unit vector $\mathbf{\Pi}$ at any point of the surface is described by two angles, α and β. The meridional angle α lies in the plane perpendicular to the surface, and is defined as the angle between $\mathbf{\Pi}$ and the normal $\mathbf{s}$. The azimuthal angle β lies in the tangent plane and is defined as the angle between the projection of $\mathbf{\Pi}$ on this plane and some direction of the polar axis. The actual direction of the director $\mathbf{n}$ at the surface of the liquid crystal sample is in turn given by two other angles, α' and β'. In the Rapini–Papoular[28] standard form, the anchoring free energy density, which depends on the mutual orientation of $\mathbf{n}$ and $\mathbf{\Pi}$, is given by

$$f_A=\frac{1}{2}\,(W_\theta \sin^2\,\varepsilon+W_\phi \sin^2\,\delta), \tag{4}$$

where $\varepsilon=\alpha-\alpha'$, $\delta=\beta-\beta'$; the positive constants W_θ and W_ϕ characterize the energies of the out-of-plane (meridional) and in-plane (azimuthal) perturbations of the director, respectively.

Thus, the total free energy of the system consisting of nematic plus bounding surface has the form

$$F=F_{\mathrm{EL}}+F_A=\int_V dV\, f_V+\int_S dS\,(f_{24}+f_A), \tag{5}$$

where the expressions for f_V, f_{24}, and f_A are given by Eqs. (2), (3), and (4), respectively.

2.2. Equilibrium equations for a cylindrical NLC sample

Consider an NLC located in an infinitely long cylindrical capillary of radius R with prespecified (homeotropic or circular) anchoring at the lateral surface S. We introduce a cylindrical coordinate system with a right-handed triad of unit vectors $\mathbf{e}_r$, $\mathbf{e}_\varphi$, $\mathbf{e}_z$, with the z axis directed along the cylinder axis. For homeotropic anchoring, the direction of easy orientation at the surface S is given by $\mathbf{\Pi}^{(H)}=\mathbf{e}_r$. In terms of the angles α and β entering into the anchoring energy density Eq. (4), we have $\alpha^{(H)}=0$, while the value of $\beta^{(H)}$ is degenerate. This implies that azimuthal surface perturbations do not occur for homeotropic anchoring, and f_A depends only on the term associated with W_θ. For anchoring of circular type $\mathbf{\Pi}^{(C)}=\mathbf{e}_\varphi$, i.e., $\alpha^{(C)}=\pi/2$ and $\beta^{(C)}=0$; here the angle β is reckoned from the direction of $\mathbf{e}_\varphi$. Since the angles $\alpha^{(C)}$ and $\beta^{(C)}$ are fixed in this case, both meridional and azimuthal perturbations can enter the problem through W_θ and W_ϕ respectively. A qualitative analysis of the structures shown in Fig. 2 leads us to conclude immediately that the PC configuration is unrelated to deviations of the director from the direction of $\mathbf{\Pi}^{(C)}$, i.e., $f_A=0$, while the CPP and EC structures correspond to the simplest type of surface perturbations: for the CPP structures f_A depends only on W_θ (meridional perturbations), while for the EC configuration f_A depends only on W_ϕ (azimuthal perturbations).

The equilibrium director field of the NLC can be determined by minimizing the functional (5) for the total free energy, following the usual variational procedures. The director field is parametrized by the two angles shown in Fig. 1: the slope $\Omega(\mathbf{r})$ and the torsion angle $\Phi(\mathbf{r})$. In our system of coordinates,

$$\mathbf{n}=\sin\,\Omega(\mathbf{r})\cos[\Phi(\mathbf{r})-\varphi]\mathbf{e}_r+\sin\,\Omega(\mathbf{r})\sin[\Phi(\mathbf{r})-\varphi]\mathbf{e}_\varphi+\cos\,\Omega(\mathbf{r})\mathbf{e}_z. \tag{6}$$

In the bulk of the NLC this minimization procedure yields the usual Euler equations:

$$\frac{\partial f_F}{\partial \chi}-\frac{1}{r}\,\partial_\nu r\,\frac{\partial f_F}{\partial \partial_\nu \chi}=0, \tag{7}$$

where $\chi=\Omega,\ \Phi$; $\partial_\nu=\partial/\partial\nu$; $\nu=r,\ \varphi$, and z.

The boundary conditions for Eqs. (7) require more information about the anchoring of NLC molecules to the bounding surface than simply its type. Two other anchoring subtypes are distinguished: ''hard'' and ''soft.'' For hard anchoring, the director at the surface S is strictly parallel to the direction of easy orientation, and in general the boundary condition for the angles Ω and Φ has the form

$$\mathbf{n}|_S=\pm\mathbf{\Pi}. \tag{8}$$

This is the situation when the specific energies W_ϕ and/or W_θ corresponding to homeotropic or circular anchoring from Eq. (4) are infinitely high. For soft anchoring, in which the corresponding specific energies are finite, the boundary conditions at the surface $r=R$ of the cylinder can be written in the form

$$\frac{\partial(f_A+f_{24})}{\partial\chi}+\frac{\partial f_F}{\partial\partial_r\chi}-\partial_\varphi\,\frac{\partial f_{24}}{\partial\partial_\varphi\chi}-\partial_z\,\frac{\partial f_{24}}{\partial\partial_z\chi}=0. \tag{9}$$

Note that although Eqs. (7) and the boundary condition (8) are general in form, and are valid for any geometry of the liquid crystal sample with a prespecified surface S, the boundary conditions (9) are here written in a simplified form that corresponds only to a cylindrical region.

3. REPRESENTATION OF A PLANAR DIRECTOR FIELD USING ANALYTIC FUNCTIONS

We consider a planar distortion of the director field

$$\mathbf{n}=\cos(\Phi-\varphi)\mathbf{e}_r+\sin(\Phi-\varphi)\mathbf{e}_\varphi,\quad \Phi=\Phi(r,\varphi). \tag{10}$$

This representation follows from Eq. (6) after making the substitution $\Phi(\mathbf{r})=\Phi(r,\varphi)$, and choosing the extremum $\Omega(\mathbf{r})=\pi/2$ of the corresponding Euler equation from the system (7). We note that in the planar case, the surface term associated with the constant K_{24} makes no contribution to the functional (1): $\nabla\cdot[\mathbf{n}\times(\nabla\times\mathbf{n})+\mathbf{n}(\nabla\cdot\mathbf{n})]=0$. Moreover, there is no torsion deformation $(\mathbf{n}\cdot(\nabla\times\mathbf{n})=0)$; therefore, the Frank free energy density (2), and consequently the Euler equation (7) for the angle Φ, include only terms associated with the elastic moduli K_{11} and K_{33}. We now analyze the general solution of the equilibrium Eqs. (7) for $\Phi(r,\varphi)$.

3.1. Two-constant approximation

At typical temperatures where the nematic phase exists, the elastic moduli K_{11} and K_{33} are comparable in magnitude[29]; therefore, in preliminary calculations the two-constant approximation is often used:

$$K_{11}=K_{33}=K. \tag{11}$$

In this case by K we mean the average value of the true elastic moduli K_{11} and K_{33}.

Substituting relations (10) and (11) into (7) yield the Laplace equation for the angle Φ:

$$\nabla^2\Phi=\frac{\partial^2\Phi}{\partial r^2}+\frac{1}{r}\,\frac{\partial\Phi}{\partial r}+\frac{1}{r^2}\,\frac{\partial^2\Phi}{\partial\varphi^2}=0. \tag{12}$$

From this equation it follows that there exists an irrotational and solenoidal field $\mathbf{E}$ such that $\mathbf{E}=-\nabla\Phi$; the minus sign is introduced by analogy with electrostatics.[30] Indeed, $\boldsymbol{\nabla}\times\mathbf{E}=-\boldsymbol{\nabla}\times\boldsymbol{\nabla}\Phi=0$ and $\boldsymbol{\nabla}\cdot\mathbf{E}=-\boldsymbol{\nabla}^2\Phi=0$. The first relation implies that the angle Φ plays the role of a scalar potential for the field $\mathbf{E}$. The second condition enables us to introduce a vector potential $\boldsymbol{\Psi}$ that satisfies $\mathbf{E}=\boldsymbol{\nabla}\times\boldsymbol{\Psi}$. Since the field $\mathbf{E}$ is planar, the vector $\boldsymbol{\Psi}$ can always be chosen to be parallel to the z axis, i.e., $\boldsymbol{\Psi}=\Psi\mathbf{e}_z$; here $\Psi=\Psi(r,\varphi)$. Then the components of the field $\mathbf{E}$ can be expressed in the form of derivatives of Φ or Ψ:

$$E_r=-\frac{\partial\Phi}{\partial r}=\frac{1}{r}\,\frac{\partial\Psi}{\partial\varphi},\quad E_\varphi=-\frac{1}{r}\,\frac{\partial\Phi}{\partial\varphi}=-\frac{\partial\Psi}{\partial r}. \tag{13}$$

The relations (13) are the Cauchy–Riemann conditions, which are well known in the theory of functions of a complex variable (see, e.g., Eq. (31)). These conditions imply that the expression

$$G=\Phi-i\Psi+A, \tag{14}$$

which is determined up to a certain complex constant $A=\Phi_0-i\Psi_0$, is an analytic function of the complex variable $\mathscr{Z}(r,\varphi)=r\ \exp(i\varphi)$. We refer to the function $G(\mathscr{Z})$ as the complex potential of the field $\mathbf{E}$, or simply the complex potential.

It is well known[31] that the real and imaginary parts of any analytic function are both solutions of the Laplace equation. Therefore, as a solution of the equilibrium Eqs. (12), we can take both the real and imaginary parts of the complex potential. In the latter case, we have in place of (14)

$$G=\Psi+i\Phi+iA.$$

For definiteness, in this paper we seek a complex potential in the form (14), and take the real part of $G(\mathscr{Z})$ for the angle Φ. It follows from (12) and (14) that the function $\Phi(r,\varphi)$ is determined up to a constant Φ_0, which can be found from some supplementary conditions, e.g., boundary conditions. Using the relations

$$\mathbf{e}_r=\cos\,\varphi+i\,\sin\,\varphi,\quad \mathbf{e}_\varphi=-\sin\,\varphi+i\,\cos\,\varphi$$

the director field Eq. (10) can be reconstructed using the known complex potential in the following way:

$$\mathbf{n}=\cos\,\Phi+i\,\sin\,\Phi=\exp\left[i\,\frac{G(\mathscr{Z})+G^*(\mathscr{Z})}{2}\right],$$

where $G^*(\mathscr{Z})$ is the complex conjugate function.

Since the function $\Phi(r,\varphi)$ is dimensionless, the argument $\mathscr{Z}$ must enter into the complex potential, G in the form $\mathscr{Z}/D$, where D is a characteristic dimension of the system. We must take for the characteristic dimension some general combination of material parameters having the dimensions of length. In an unbounded volume of NLC, where there are no dimensionless parameters, $\Phi(r,\varphi)$ can depend only on some angular variable φ'. In this case, the following function is an example of the complex potential:

$$G_m(\mathscr{Z},\mathscr{Z}_0)=-im\ \ln(\mathscr{Z}-\mathscr{Z}_0)+A, \tag{15}$$

whose real part

$$\Phi=\mathrm{Re}[G_m(\mathscr{Z},\mathscr{Z}_0)]=m\varphi'+\Phi_0 \tag{16}$$

specifies the director distribution around the disclination line[29,32] that passes through the point $\mathscr{Z}_0=\mathscr{Z}_0(r_0,\varphi_0)$. Here φ' is the polar angle in a coordinate system centered at the point $\mathscr{Z}_0$; m is the topological charge, and Φ_0 is the initial phase of the disclination. By virtue of the single-valuedness condition $\mathbf{n}(\varphi'+2\pi)=\pm\mathbf{n}(\varphi')$, the quantity m can take on only integer or half-integer values, i.e., $m=0,\pm1/2,\pm1,\ldots$. The existence of disclination lines at the point $\mathscr{Z}_0$ reflects the fact that this is a singular point, i.e., at that point the conditions of analyticity of the complex potential (15) are violated.

If the NLC is in a finite volume, boundary conditions like (8) or (9) are imposed on the real part of the complex potential $G(\mathscr{Z})$. Then for our specific sample geometry, the problem of determining the equilibrium planar field of the director reduces in the two-constant approximation to finding an analytic function $G(\mathscr{Z})$ whose real part satisfies the specified boundary conditions. In constructing the function $G(\mathscr{Z})$ we can use the well-developed method of conformal mapping.[31] This method is especially useful for hard anchoring in samples with complex geometry. In special cases it is possible to construct the function $G(\mathscr{Z})$ as a simple superposition of analytic functions. This procedure is correct because the resulting complex potential obtained will also be an analytic function. For example, we can use the required number of functions of the form Eq. (15). If as a result of constructing the function $G(\mathscr{Z})$ the specific point $\mathscr{Z}_0^{(j)}$ turns out to be within the NLC, it will correspond to a real line defect; if it is outside the NLC, it is a fictitious disclination line.

3.2. The general case $K_{11}\neq K_{33}$. PR and PC configurations

In the general case $K_{11}\neq K_{33}$, substituting the distribution (10) into the equilibrium Eq. (7) yields

$$\nabla^2\Phi+\kappa\Lambda(\Phi)=0. \tag{17}$$

Here

$$\kappa=\frac{K_{33}-K_{11}}{K_{11}+K_{33}},$$

$$\begin{aligned}\Lambda(\Phi)=&\left[\frac{1}{r^2}\left(\frac{\partial\Phi}{\partial\varphi}\right)^2-\left(\frac{\partial\Phi}{\partial r}\right)^2+\frac{2}{r}\,\frac{\partial^2\Phi}{\partial\varphi\partial r}\right.\\&\left.-\frac{2}{r^2}\left(\frac{\partial\Phi}{\partial\varphi}\right)\right]\sin(2\Phi-2\varphi)+\left[\frac{\partial^2\Phi}{\partial r^2}-\frac{1}{r}\,\frac{\partial\Phi}{\partial r}\right.\\&\left.+\frac{2}{r}\,\frac{\partial\Phi}{\partial r}\,\frac{\partial\Phi}{\partial\varphi}-\frac{1}{r^2}\,\frac{\partial^2\Phi}{\partial\varphi^2}\right]\cos(2\Phi-2\varphi).\end{aligned} \tag{18}$$

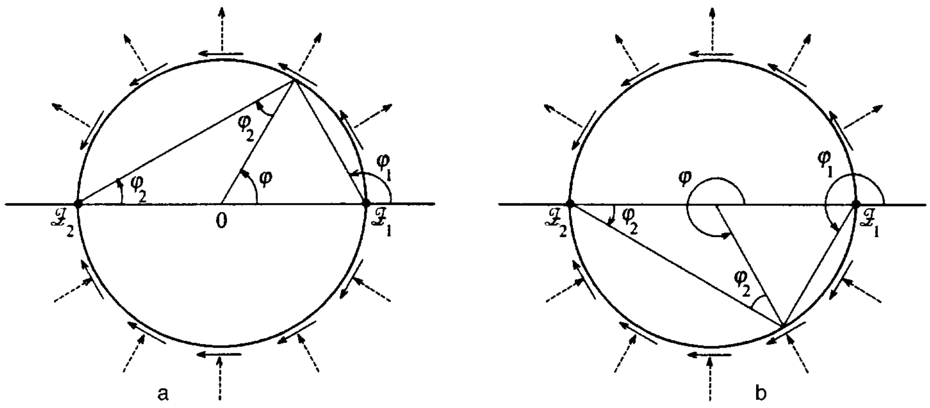

FIG. 3. Scheme for constructing a solution for polar structures with hard anchoring. In the upper half of the circle $\varphi_1=\varphi/2+\pi/2$, $\varphi_2=\varphi/2$(a); in the lower half of the circle $\varphi_1=\varphi/2+\pi/2$, $\varphi_2=\varphi/2-\pi$(b).

Equation (17) does not allow us to introduce a field **E** and complex potential G in a simple way, as we did above. Nevertheless, several special planar distortions of the director field can be described by the analytic function (14). Similar situations occur when the solutions of Eqs. (12) and (17) coincide with each other, i.e., when the operator function $\Lambda(\mathrm{Re}(G(\mathscr{Z})))$ from condition (18) is identically equal to zero. We note two cases that are of practical importance for this paper.

1. A distortion given by a single disclination line with topological charge $m=1$. According to Eq. (15), the complex potential of such a distortion is

$$G_1=-i\ \ln(\mathscr{Z}-\mathscr{Z}_0)+A.$$

Substituting this expression into Eq. (18) yields

$$\Lambda_1=\Lambda[\mathrm{Re}(G_1)]=-\frac{\sin(2\Phi_0)}{l^2}, \tag{19}$$

where $l=|\mathscr{Z}-\mathscr{Z}_0|$ is the distance from the current point $\mathscr{Z}$ to the disclination axis. Expression (19) shows that the equilibrium state ($\Lambda_1=0$) of a disclination line with topological charge $m=1$ corresponds to a phase Φ_0 that is a multiple of $\pi/2$. Distributions with phases $\Phi_0=\Phi_0+j\pi$, where $j=0, \pm1, \pm2, \dots$, give the same distribution of the director **n**. Therefore, only the two phases $\Phi_0=0$ and $\pi/2$ are independent. This result, which was first obtained in Ref. 14, is directly related to the PR and PC configurations of the NLC in a cylindrical volume (see Figs. 1a and 2a, respectively). If the disclination with $m=1$ is on the axis of the cylinder, then the director field Eq. (10) with the function $\Phi=\varphi+\Phi_0$ from Eq. (16) describes the PR structure for $\Phi_0=0$ and the PC structure for $\Phi_0=\pi/2$. The expressions obtained from relation (5) for the total free energy of these structures per unit length of cylinder have the form

$$F_{\mathrm{PR}}=\pi K_{11}\ \ln(R/\rho), \quad F_{\mathrm{PC}}=\pi K_{33}\ \ln(R/\rho), \tag{20}$$

where ρ is the radius of the disclination core.

2. Planar distortions given by two disclination lines with the same topological charge $m_1=m_2=1$. If the disclination lines pass through the points $\mathscr{Z}_1$ and $\mathscr{Z}_2$, then the complex potential (see Eq. (15)) is

$$G_{1+1}=-i\ \ln[(\mathscr{Z}-\mathscr{Z}_1)(\mathscr{Z}-\mathscr{Z}_2)]+A.$$

Measuring the total phase Φ_0 of the disclinations from the direction of the line joining the points $\mathscr{Z}_1$ and $\mathscr{Z}_2$, we obtain

$$\Lambda_{1+1}=\Lambda(\mathrm{Re}(G_{1+1}))=-\frac{d^2\ \sin(2\Phi_0)}{l_1^2 l_2^2}, \tag{21}$$

where $l_j=|\mathscr{Z}-\mathscr{Z}_j|$ is the distance from the current point $\mathscr{Z}$ to the axis of the jth disclination ($j=1,2$); and $d=|\mathscr{Z}_1-\mathscr{Z}_2|$ is the distance between the disclinations. From Eq. (21) it follows that for two separate ($d\neq0$) line defects the condition $\Lambda_{1+1}=0$ is realized if the total phase Φ_0 is a multiple of $\pi/2$; the values $\Phi_0=0$ and $\pi/2$ are independent. We use this result in the next section. (We add here that $\Lambda_{1+1}=0$ for $d=0$ as well, i.e., the case of an isolated disclination with charge $m=2$; see Ref. 14.)

4. PP AND CPP CONFIGURATIONS

4.1. Two-constant approximation

As noted above, the PP and CPP configurations (see Figs. 1b and 2b, respectively) belong to the class of planar distortions of the director field. The authors of Refs. 3 and 4 treated the PP structure in the two-constant approximation. Let us trace how this solution can be obtained using a representation involving the complex potential. We will also discuss the CPP configuration simultaneously with the PP structure.

The director field of the PP and CPP structures can be described by Eq. (10); the direction of easy orientation at the surface $r=R$ of the cylinder is determined by the function

$$\Phi_S(\varphi)=\begin{cases}\varphi+\dfrac{\pi}{4}(1-q), & 0<\varphi<\pi,\\[2ex] \varphi-\dfrac{\pi}{4}(3+q), & \pi<\varphi<2\pi.\end{cases} \tag{22}$$

Here $q=\pm1$: the value $q=1$ corresponds to homeotropic anchoring, while $q=-1$ corresponds to circular anchoring; the directions of the director given by the function (22) are shown in Fig. 3 (the solid arrows correspond to $q=-1$, the dashed to $q=1$). If the character of the anchoring is rigid, then the boundary condition (8) for the equilibrium Eq. (12) has the form

$$\Phi(R,\varphi)=\Phi_S(\varphi). \tag{23}$$

It is clear from Eq. (22) that at points $\mathscr{Z}_1=\mathscr{Z}(R,0)=R$ and $\mathscr{Z}_2=\mathscr{Z}(R,\pi)=-R$ on the surface of the cylinder the boundary function $\Phi_S(\varphi)$ undergoes a discontinuity. If the equilibrium Eq. (12) holds everywhere in the bulk of the NLC, then at these boundary points there must exist disclination lines with certain topological charges m_1 and m_2 respectively. Let us construct a trial complex potential as a sum of potentials (15) of the individual disclination lines:

$$G(\mathscr{Z})=-im_1\ \ln(\mathscr{Z}-R)-im_2\ \ln(\mathscr{Z}+R)+A. \tag{24}$$

The real part of this expression defines the trial function

$$\Phi=\mathrm{Re}[G(\mathscr{Z})]=m_1\varphi_1+m_2\varphi_2+\Phi_0;$$

the angles φ_1 and φ_2 are shown in Fig. 3. In order that the function $\Phi(r,\varphi)$ be single-valued in the region occupied by the NLC, we will make a cut in the $\mathscr{Z}$ plane along the rays $[-\infty,-R]$ and $[R,+\infty]$. Then the angles φ_1 and φ_2 can vary over the intervals $0\leqslant\varphi_1<2\pi$ and $-\pi\leqslant\varphi_2<\pi$.

We now find the phase Φ_0 and the topological charges m_1 and m_2 from the boundary conditions (23). Expressing the angles φ_1 and φ_2 from geometric considerations at the surface of the cylinder in terms of the angle φ (see Fig. 3) and using the function (22), we obtain a system of simple linear equations:

$$\frac{1}{2}\ \varphi(m_1+m_2)+\frac{1}{2}\ \pi m_1+\Phi_0=\varphi+\frac{1}{4}\ \pi(1-q),$$

$$\frac{1}{2}\ \varphi(m_1+m_2)-\pi\left(m_2-\frac{1}{2}\ m_1\right)+\Phi_0=\varphi-\frac{1}{4}\ \pi(3+q).$$

These equations can be satisfied for any value of φ; this is true if

$$m_1=m_2=1,\quad \Phi_0=-\frac{1}{4}\ \pi(1+q). \tag{25}$$

Thus, the equilibrium state of the NLC corresponds to a distortion which in the $\mathscr{Z}$ half-plane is given by two disclination lines with identical topological charges equal to unity. Homeotropic anchoring corresponds to a phase $\Phi_0(q=1)=-\pi/2$, and circular anchoring to $\Phi_0(q=-1)=0$. Substituting (25) into the function (24) and calculating its real part, we finally obtain an expression[1)] for the angle:

$$\Phi=\arctan\frac{r^2\ \sin 2\varphi}{r^2\ \cos 2\varphi-R^2}+\frac{\pi}{4}\ (3-q). \tag{26}$$

As follows from (25) and (26), the functions $\Phi(r,\varphi)$ for PP and CPP structures differ only by a phase $\pi/2$. In this case the overall pattern of the corresponding current lines comprises the orthogonal grid of a bipolar coordinate system, whose poles are located at the points $\mathscr{Z}_{1,2}=\pm R$.

In the two-constant approximation, the phase $\pi/2$ does not affect the total free energy Eq. (5); therefore, the total energies for the PP and CPP structures coincide with one another. They have the following form taken per unit length:

$$F_{\mathrm{PP}}=F_{\mathrm{CPP}}=\pi\ K\ \ln(R/2\rho). \tag{27}$$

Let us discuss the solution of the problem for soft $(0\leqslant W_\theta<\infty)$ anchoring. The equilibrium state of the NLC is described by the Laplace equation (12) with boundary condition (9), which in our case takes the form

$$\left[2KR\ \frac{\partial\Phi}{\partial r}+qW_\theta\ R\ \sin(2\Phi-2\varphi)\right]_{r=R}=0. \tag{28}$$

Rather than solve this problem, we note that the scale (conformal) transformation[31,33]

$$r'=cr,\quad \varphi'=\varphi, \tag{29}$$

where c is an expansion coefficient, transforms the Laplace equation (12) into a solution of the same equation. Consequently, a function of the form (compare with Eq. (26))

$$\Phi=\arctan\left[\frac{r^2\ \sin 2\varphi}{r^2\ \cos 2\varphi-(cR)^2}\right]+\frac{\pi}{4}\ (3-q) \tag{30}$$

is also a solution of the equilibrium equation (12). Indeed, the function (30) corresponds to two disclination lines located at $\mathscr{Z}_1=cR$ and $\mathscr{Z}_2=-cR$.

Substitution of the expression (30) into the boundary condition (28) enables us to determine the equilibrium value of c. This substitution leads to an equation that does not depend on the parameter q, i.e.,

$$\frac{\sin 2\varphi[W_\theta\ Rc^4-4Kc^2-W_\theta\ R]}{c^4-2c^2\ \cos 2\varphi+1}=0. \tag{31}$$

From this it follows that

$$c=\sqrt{\frac{1+\sqrt{1+w^2}}{w}},$$

where $w=W_\theta\ R/2K$. For any finite value of w, $c>1$. Consequently, the equilibrium field of the director within the cylindrical capillary corresponds to a distortion specified by two fictitious disclination lines. In other words, for soft anchoring, the effective radius of a particle increases by a factor of c (see the scale transformation (29)). When $w=0$ (the totally degenerate type of anchoring), the effective radius grows without bound, the fictitious disclination lines depart to infinity, and the field of the director becomes uniform within the capillary.

Substitution of the distribution (10) with the function (30) into Eq. (5) gives the total energy of the PP and CPP structures per length of cylinder:

$$F_{\mathrm{PP}}=F_{\mathrm{CPP}}=\pi K\left[-\ln\left(\frac{c^4-1}{c^4}\right)+w\left(\frac{c^2-1}{c^2}\right)\right]$$

$$=\pi K\left[-\ln(2\gamma\xi)+\frac{1-\gamma}{\xi}\right]. \tag{32}$$

The latter expression is written in the notation used in Refs. 3 and 4: here $\xi=1/w=2K/W_\theta\ R$, $\gamma=1/c^2=\sqrt{\xi^2+1}-\xi$. It follows from Eqs. (27) and (32) that in the two-constant approximation the PP and CPP structures are energetically completely equivalent.

4.2. The general case $K_{11}\neq K_{33}$

In Sec. 3.2 we showed that a distortion field specified by two disclination lines with topological charges $m_1=m_2=1$ and phase Φ_0 that is a multiple of $\pi/2$ satisfies the general equilibrium equation (17) for $K_{11}\neq K_{33}$. Therefore, for rigid anchoring, where the boundary conditions for the angle $\Phi(r,\varphi)$ have the form (23), the solution of the problem is determined by Eq. (26). Despite this coincidence, the PP and CPP structures are no longer energetically equivalent in general; the expressions obtained from Eq. (5) when $K_{11}\neq K_{33}$ for the total free energy per unit length of cylindrical capillary have the form

$$F_{\mathrm{PP}}=\pi K_{33}\ln(R/2\rho)-\pi(K_{33}-K_{11})(1-\ln 2),$$

$$F_{\mathrm{CPP}}=\pi K_{11}\ln(R/2\rho)+\pi(K_{33}-K_{11})(1-\ln 2). \tag{33}$$

It can be shown that these equations transform into Eq. (27) when $K_{11}=K_{33}$.

For soft anchoring, the boundary condition (9) for the equilibrium equation (17) can be written

$$\left\{2KR\frac{\partial\Phi}{\partial r}+qW_\theta R\sin(2\Phi-2\varphi)+2K\kappa\left[R\frac{\partial\Phi}{\partial r}\cos(2\Phi-2\varphi)+\frac{\partial\Phi}{\partial\varphi}\sin(2\Phi-2\varphi)\right]\right\}\Bigg|_{r=R}=0. \tag{34}$$

Recall that in the general case $K=(K_{11}+K_{33})/2$. By analogy with the solution of this problem in the two-constant approximation, we can use the scale transformation (29), and a trial function $\Phi(r,\varphi)$ can be found in the form (compare with Eqs. (26) and (30))

$$\Phi=\arctan\left[\frac{r^2\sin 2\varphi}{r^2\cos 2\varphi-(pR)^2}\right]+\frac{\pi}{4}(3-q), \tag{35}$$

where p is the expansion coefficient corresponding to the case $K_{11}\neq K_{33}$. The validity of this approach also follows from the fact that the general equilibrium equation (17), like the Laplace equation (12), is invariant under scale transformations (29).

Substitution of Eq. (35) into the boundary condition (34) yields an equation (compare with (31)) for the equilibrium value of p:

$$\frac{\sin 2\varphi[W_\theta Rp^4-4Kp^2-W_\theta R-4qK\kappa]}{p^4-2p^2\cos 2\varphi+1}=0.$$

From this equation we find

$$p=\sqrt{\frac{1+\sqrt{1+w^2+2q\kappa w}}{w}}. \tag{36}$$

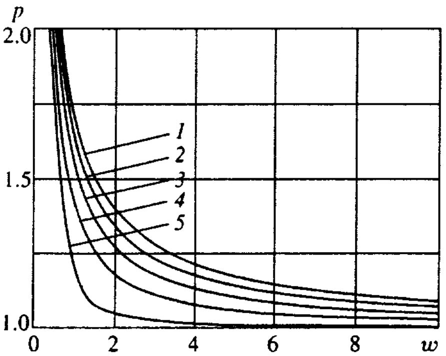

FIG. 4. Dependence of the expansion coefficient p on the dimensionless parameter w for $q\kappa=$ 0.9 (*1*), 0.45 (*2*), 0 (*3*), -0.45 (*4*), -0.9 (*5*).

Let us discuss Eq. (36) and consider the behavior of the disclination lines when $K_{11}\neq K_{33}$. The general behavior of the expansion coefficient p as a function of the dimensionless anchoring energy w for various values of $q\kappa$ is shown in Fig. 4; the asymptotic expansion of the function $p(w)$ is

$$p=\begin{cases}(4+q\kappa w^2)/\sqrt{8w}, & w\leqslant 1,\\ 1+(1+q\kappa)/2w, & w\geqslant 1.\end{cases} \tag{37}$$

From Fig. 4 and Eq. (37) it is clear that compared to the two-constant approximation $(p(w,\kappa=0)=c(w))$, the behavior of the disclination lines is qualitatively unchanged: for the rigid type of anchoring, where $w=\infty$, the lines are located at the lateral surface of the capillary $(p=1)$; for finite values of w they disappear from the surface and become purely fictitious $(1<p<\infty)$; as w tends to zero, the lines recede to infinity $(p\rightarrow\infty)$. The difference shows up in the actual value of the expansion coefficient p, which must depend on the sign and magnitude of the product $q\kappa$, i.e., on the type of anchoring of the director to the lateral surface of the capillary and on the ratio of elastic moduli K_{11} and K_{33}. For ordinary nematics $K_{33}>K_{11}$, i.e., $\kappa>0$. Therefore, other things being equal, we expect (see Fig. 4) that when the anchoring is homeotropic $(q\kappa>0)$, the expansion coefficient will be larger, i.e., the fictitious disclination lines will be farther from the capillary surface than in the case of circular $(q\kappa<0)$ boundary conditions. Note, in particular, that for a specified type of anchoring, the distortion of the director field, which in experiments is the ‘‘observed quantity,’’ depends only on the expansion coefficient p, and does not depend on the specific set of parameters $\{w,\kappa\}$ responsible for this value. In other words, any pair of parameters $\{w,\kappa\}$ corresponding to the same value of p (see, e.g., the lines of the horizontal grid in Fig. 4) yields a completely equivalent distribution of the director within the cylindrical capillary.

Substituting the director distribution (10) with the function $\Phi(r,\varphi)$ from Eq. (35) into Eq. (5) enables us to find the general expression for the energy per unit length of cylinder of the PP and CPP structures; this expression has the form

$$F_q=\pi K\left\{-\ln\left(\frac{p^4-1}{p^4}\right)-q\kappa\left[\ln\left(\frac{p^2-1}{p^2+1}\right)+\frac{2}{p^2}\right]+w\,\frac{p^2-1}{p^2}\right\}.$$

Here $F_{q=1}=F_{\mathrm{PP}}$, $F_{q=-1}=F_{\mathrm{CPP}}$, and the function $p=p(q,w,\kappa)$ is defined by Eq. (36). Asymptotic expansion of F_q for $w\ll 1$ yields

$$F_q \approx \pi K\left(w-\frac{w^2}{4}+\frac{q\kappa w^3}{12}\right)$$

$$=\frac{\pi W_\theta R}{2}\left[1-\frac{1}{4}\left(\frac{W_\theta R}{K_{11}+K_{33}}\right)+\frac{q}{12}\left(\frac{K_{33}-K_{11}}{K_{33}+K_{11}}\right)\left(\frac{W_\theta R}{K_{11}+k_{33}}\right)^2\right], \tag{38}$$

and for $w \gg 1$

$$F_q \approx \pi K\left\{(1+q\kappa)\ln\left(\frac{w}{1+q\kappa}\right)+(1-q\kappa)(1-\ln 2)+\frac{1}{2w}(1+4q\kappa+3q^2\kappa^2)\right\}$$

$$=\begin{cases}\pi K_{33}\ln\left(\dfrac{W_\theta R}{2K_{33}}\right)+\pi K_{11}(1-\ln 2) \\ \quad -\dfrac{\pi K_{33}(2K_{33}-K_{11})}{W_\theta R}, \quad q=1, \\ \pi K_{11}\ln\left(\dfrac{W_\theta R}{2K_{11}}\right)+\pi K_{33}(1-\ln 2) \\ \quad -\dfrac{\pi K_{11}(2K_{11}-K_{33})}{W_\theta R}, \quad q=-1.\end{cases} \tag{39}$$

From Eqs. (33) and (39) it follows that the transition from soft to hard anchoring takes place at values of the specific energy $W_\theta \sim 2K_{33}/e\rho$ and $W_\theta \sim 2K_{11}/e\rho$ for the PP and CPP structures, respectively. The various elastic moduli entering into these estimates correspond to the dominant distortions for each of the structures under discussion: for the PP structure the dominant deformation is longitudinal bending, which is associated with the constant K_{33}, while for the CPP configuration it is transverse bending associated with the constant K_{11}.

5. ''ESCAPED'' CONFIGURATIONS

5.1. The ER configuration and axial structure

For hard anchoring, the ER structure (Fig. 1c) was described in Ref. 15 (see also Ref. 34). The case of soft anchoring was considered in Refs. 3 and 4. Let us discuss the results obtained in Refs. 3 and 4 briefly.

The field of the director for the ER configuration is determined by the expression

$$\mathbf{n}=\sin\Omega(r)\mathbf{e}_r+\cos\Omega(r)\mathbf{e}_z, \tag{40}$$

which follows from Eq. (6) after the substitution $\Omega(\mathbf{r})=\Omega(r)$ and the choice of the extremum $\Phi(\mathbf{r})=\varphi$ of the corresponding Euler equation from system (7). The direction $\mathbf{\Pi}$ of easy orientation of the director at the cylinder surface corresponds to an angle $\Omega_S=\pi/2$. The distribution $\Omega(r)$, as usual, is found from the equilibrium equation (7) with the boundary condition (9) when $r=R$. Moreover, the absence of disclinations on the cylinder axis corresponds to an additional boundary condition at $r=0$:

$$\Omega(0)=0, \quad \lim_{r\to 0}|\partial\Omega(r)/\partial r|<\infty.$$

As shown in Refs. 3 and 4, the form of the function $\Omega(r)$ is governed by the dimensionless parameter

$$\sigma=\frac{W_\theta R}{K_{11}}+\frac{K_{24}}{K_{11}}-1,$$

which characterizes the surface interaction in the system. For $\sigma>1$, the equilibrium distribution $\Omega(r)$ is given by the implicit function

$$\frac{r}{R}=\sqrt{\frac{\sigma+1}{\sigma-1}\,\frac{\Delta-1}{\Delta+1}}\exp\left(\sqrt{\eta-1}\arctan\frac{\sqrt{\eta-1}(\Delta-\sigma)}{\Delta\sigma+\eta-1}\right). \tag{41}$$

Here $\Delta=\sqrt{1+\eta\tan^2\Omega(r)}$, $\eta=K_{33}/K_{11}$, $0\leqslant\Omega(r)\leqslant\pi/2$. Equation (41) is valid both for $\eta\geqslant 1$ and for $0<\eta<1$; in the latter case, we must use the following identity in the exponent:

$$\sqrt{\eta-1}\arctan[\sqrt{\eta-1}\mu(\eta,\ldots)] \equiv \sqrt{1-\eta}\operatorname{arctanh}[\sqrt{1-\eta}\mu(\eta,\ldots)], \tag{42}$$

where $\mu(\eta,...)$ is a function determined up to a sign for any value of $\eta>0$.

For $\sigma\leqslant 1$, the complicated function $\Omega(r)$ from Eq. (41) is replaced by a uniform distribution $\Omega(r)=\text{const}=0$ with director $\mathbf{n}$ parallel to the z axis. This latter structure is a qualitatively new (compared to the escaped radial) configuration of the director field; we refer to it as an axial structure (AX). In principle, the solution $\Omega(r)=0$ corresponding to the AX structure satisfies the equilibrium equation with given boundary conditions for any σ. However, for $\sigma>1$ this structure is energetically less favorable than the ER configuration, and can exist only in a metastable state.

Hence, in considering deformations of the form (40) it is advisable to consider two NLC configurations: the escaped radial, which corresponds to $\sigma>1$, and the axial, which is in fact realized for $\sigma\leqslant 1$. Using Eq. (41), we can show that as $\sigma\to +1$ the escaped ER configuration smoothly transforms (total escape) to the uniform axial structure. Expressions for the free energy per unit length of cylinder of the each of these structures have the form

$$F_{\mathrm{ER}}=\pi K_{11}\times\left\{2+\frac{\eta}{\sqrt{\eta-1}}\arctan\left[\frac{\sqrt{\eta-1}(\sigma-1)}{\sigma+\eta-1}\right]-\frac{K_{24}}{K_{11}}\right\}, \quad \sigma>1, \tag{43}$$

$$F_{\mathrm{AX}}=\pi R W_\theta, \quad \sigma\leqslant 1. \tag{44}$$

For $\eta<1$ we must use the identity (42) in relation (43).

5.2. The EC configuration and axial structure

An analytic description of the EC structure (Fig. 2c) for hard anchoring was given in Ref. 15. We now examine this configuration for the case of soft anchoring.

We seek a director field in the form

$$\mathbf{n}=\sin\Omega(r)\mathbf{e}_\varphi+\cos\Omega(r)\mathbf{e}_z. \tag{45}$$

This distribution follows from Eq. (6) if we make the substitution $\Omega(\mathbf{r})=\Omega(r)$ and use the extremum $\Phi(\mathbf{r})=\varphi+\pi/2$. The direction $\mathbf{\Pi}$ of easy orientation of the director at the surface of the cylinder is given by the angle $\Omega_S=\pi/2$. In the case of a distortion of the form Eq. (45), the surface anchoring energy density (4) contains only an azimuthal part (W_ϕ), while the Frank surface energy (2) depends only on the elastic moduli K_{22} and K_{33}, since the contribution associated with the constant K_{11} is identically zero ($\boldsymbol{\nabla}\cdot\mathbf{n}=0$). The equilibrium equation (7) and the boundary condition (9) take the form

$$r^2\,\frac{\partial^2\Omega(r)}{\partial r^2}+r\,\frac{\partial\Omega(r)}{\partial r}-\sin\,\Omega(r)\cos\,\Omega(r)[1+2(\tilde{\eta}-1)\sin^2\,\Omega(r)]=0, \tag{46}$$

$$R\left(\frac{\partial\Omega(r)}{\partial r}\right)_{r=R}-\tilde{\sigma}\,\sin\,\Omega(R)\cos\,\Omega(R)=0, \tag{47}$$

where $\tilde{\eta}=K_{33}/K_{22}$, $\tilde{\sigma}=(W_\phi\,R+K_{24}-K_{22})/K_{22}$.

From (46) and (47), it is clear that three solutions to the problem exist.

1. A solution $\Omega^{(1)}(r)=\Omega^{(1)}=\pi/2$ corresponding to the planar PC configuration.

2. A distribution $\Omega^{(2)}(r)=\Omega^{(2)}=0$ corresponding to the uniform AX structure.

3. A third solution $\Omega^{(3)}(r)$ corresponding to the nonuniform EC configuration. Let us obtain this configuration in explicit form; for the sake of brevity, the upper index that denotes the order number of the solution will be omitted.

The Euler equation (46) has a first integral

$$\left(r\,\frac{\partial\Omega(r)}{\partial r}\right)^2-\sin^2\,\Omega(r)[\cos^2\,\Omega(r)+\tilde{\eta}\,\sin^2\,\Omega(r)]=\text{const.} \tag{48}$$

It is obvious that total escape of the line defect of the PC structure in the third direction is realized when $\Omega(0)=0$ and $\lim_{r\to 0}|\partial\Omega(r)/\partial r|<\infty$; therefore, the constant is zero.

Substituting Eq. (48) into the boundary condition (47) yields an equation for the angle $\Omega(R)$:

$$\sin\,\Omega(R)\cos\,\Omega(R)\{\sqrt{1+\tilde{\eta}\,\tan^2\,\Omega(R)}-\tilde{\sigma}\}=0. \tag{49}$$

Note that $\tilde{\eta}>0$; therefore, the solution with $\Omega(R)\neq 0$ exists only for $\tilde{\sigma}>1$. In this case

$$\Omega(R)=\arctan\sqrt{\frac{\tilde{\sigma}^2-1}{\tilde{\eta}}}. \tag{50}$$

For $\tilde{\sigma}\leqslant 1$ the boundary angle $\Omega(R)=0$ (see Eq. (49)) and the general solution $\Omega(r)=\Omega^{(2)}=0$ corresponds to a uniform AX structure.

Integrating (48) while taking into account the boundary value (50) yields

$$\left(\frac{r}{R}\right)^2=\frac{\tilde{\sigma}+1}{\tilde{\sigma}-1}\,\frac{\sqrt{1+\tilde{\eta}\,\tan^2\,\Omega(r)}-1}{\sqrt{1+\tilde{\eta}\,\tan^2\,\Omega(r)}+1}.$$

Writing the function $\Omega(r)$ resulting from this in explicit form, we obtain the distribution

$$\Omega(r)=\arctan\left[\sqrt{\frac{\tilde{\sigma}^2-1}{\tilde{\eta}}}\,\frac{2r\;R}{R^2(\tilde{\sigma}+1)-r^2(\tilde{\sigma}-1)}\right], \tag{51}$$

corresponding to a value $\tilde{\sigma}>1$. From Eq. (51) it is clear that when $\tilde{\sigma}\to+1$ the escaped circular configuration transforms smoothly into the axial structure. Relations for the total free energy of the EC and AX structures coincide, upon making the replacements $K_{11}\to K_{22}$ and $W_\theta\to W_\phi$ (i.e., $\eta\to\tilde{\eta}$ and $\sigma\to\tilde{\sigma}$), with Eqs. (43) and (44) respectively. The EC configuration is energetically more favorable when $\tilde{\sigma}>1$.

6. ORIENTATIONAL TRANSITIONS BETWEEN CONFIGURATIONS

6.1. Homeotropic anchoring

Final expressions for the free energy corresponding to homeotropic anchoring for the structures discussed above are listed in Table I. Figure 5 shows the overall behavior of these energies as a function of the dimensionless parameter $w_\theta=W_\theta\,R/K_{11}$ for various relations between the elastic moduli K_{11}, K_{33}, and K_{24}. Note that the constant K_{22} makes no contribution to the energy of even one of the configurations discussed, while only the energy of the ER structure depends on the constant K_{24}. Let us discuss the values of the system material parameters for which a given configuration of the NLC is realized (i.e., which is energetically most favorable).

When the bulk elastic moduli K_{11} and K_{33} are equal, the relations listed in Table I for the energy coincide completely with analogous expressions obtained in Refs. 3 and 4. In this case the energy of the PP configuration is always lower than the energies of the PR and AX structures:

$$F_{\text{PP}}-F_{\text{PR}}<-\pi K\,\ln 2<0,\quad F_{\text{PP}}-F_{\text{AX}}<-\frac{W_\theta\,R}{2K}<0. \tag{52}$$

The latter estimate is obtained from Eq. (38), from which it follows that the initial slope of the function $F_{\text{PP}}(W_\theta)$ is half the slope of the linear function $F_{AL}(W_\theta)$; see Table I. From the behavior of curve *5* in Fig. 5, it is clear that as the specific energy W_θ (i.e., the dimensionless parameter w_θ) increases, the slope of the function $F_{\text{PP}}(W_\theta)$ decreases; therefore, the second condition in (52) is fulfilled for any value of W_θ. Thus, for $K_{11}=K_{33}$ the equilibrium configuration of the NLC is determined by the balance of the energies of the PP and ER structures (compare curve *5* with curves *1* and *2*, which were obtained for different values of the constant K_{24}).

In the general case $K_{11}\neq K_{33}$, the same considerations lead us to conclude that the AX structure will always have a higher energy than the PP configuration. Consequently, for homeotropic anchoring of a purely axial distribution, the director field should not be observed experimentally (except, of course, in the trivial case $W_\theta=0$ corresponding to completely degenerate anchoring).

At the same time, the PR configuration can occur when certain relationships hold among the system material param-

TABLE I. Total free energy per unit cylinder length of structures corresponding to homeotropic anchoring.

	Anchoring type	
Structure	Hard	Soft
PR	$\pi K_{11}\ \ln(R/\rho)$	$\pi K_{11}\ \ln(R/\rho)$
PP	$\pi K_{33}\ \ln(R/2\rho)-\pi(K_{33}-K_{11})(1-\ln 2)$	$\pi K\left\{-\ln\left(\frac{\zeta^2-1}{\zeta^2}\right)+w\,\frac{\zeta-1}{\zeta}-\kappa\left[\ln\left(\frac{\zeta-1}{\zeta+1}\right)+\frac{2}{\zeta}\right]\right\},$ $\zeta=\frac{1+\sqrt{1+w^2+2w\kappa}}{w},$ $K=\frac{K_{11}+K_{33}}{2},\quad \kappa=\frac{K_{33}-K_{11}}{K_{33}+K_{11}},$ $w=\frac{W_\theta\ R}{K_{11}+K_{33}}$
ER	$\pi K_{11}\left[2-\frac{K_{24}}{K_{11}}+\frac{\eta}{\sqrt{\eta-1}}\ \arctan\sqrt{\eta-1}\right],$ $\eta=K_{33}/K_{11},$ $\eta\geqslant 1^*$	$\pi K_{11}\left\{2-\frac{K_{24}}{K_{11}}+\frac{\eta}{\sqrt{\eta-1}}\ \arctan\frac{\sqrt{\eta-1}(\sigma-1)}{\sigma+\eta-1}\right\},$ $\sigma=W_\theta\ R/K_{11}+K_{24}/K_{11}-1,$ $\sigma>1,\quad \eta\geqslant 1^*$
AX	–	$\pi R W_\theta,$ $\sigma\leqslant 1$

Note. *For $\eta<1$ we must use an identity of the form Eq. (42).

eters. For example, when the anchoring is hard ($W_\theta=\infty$), the PR configuration becomes energetically more favorable than the PP structure if

$$\eta=\frac{K_{33}}{K_{11}}>1+\frac{\ln 2}{\ln(R/\rho)-1}, \tag{53}$$

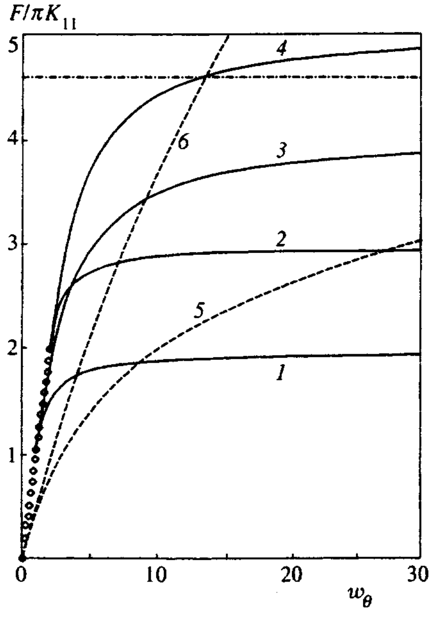

FIG. 5. Dependence of the total free energy on the dimensionless parameter w_θ for homeotropic anchoring. The energy of the ER structure is shown by the solid curves, the PP configuration by the dashed curves, the ER configuration by the dotted-dashed curves, and the AX structure by the dots. Curve *1* corresponds to $\eta=1$, $K_{24}=K_{11}$; for *2*, $\eta=1$, $K_{24}=0$; for *3*, $\eta=6$, $K_{24}=K_{11}$; for *4*, $\eta=6$, $K_{24}=0$; for *5*, $\eta=1$; for *6*, $\eta=6$ For the energy of the ER structure we have chosen a ratio $R/\rho=100$.

where we must set $R\gg\rho$ (or in any case $R>e\rho$) as in the expressions for F_{PP} and F_{ER} in Table I. Note that in the limit $R\rightarrow\infty$, (53) coincides with the results of Ref. 35: a line radial disclination with $m=1$ is stable against planar perturbations when $\eta>1$. As the radius R of the cylinder decreases, Eq. (53) shows that the energy of the PR structure in the class of planar distortions is minimized at larger values of η. It is natural that stability of the PR configuration also requires that $F_{\mathrm{PR}}<F_{\mathrm{ER}}$. The expression for the energy F_{ER} contains a complicated function of η, so this condition is unsuitable for a qualitative analysis. A more complete representation of the regions of existence of each of the three structures discussed here can be obtained from the diagram in Fig. 6, which shows the orientational states corresponding to $K_{24}=0$ and $K_{24}=1.5K_{11}$.

From Fig. 6 it is clear that for cylinders of large radius ($\ln(R/\rho)\geqslant 6$), the energy minimum corresponds to the ER structure over a wide range of values of η, a conclusion that is essentially independent of the value of K_{24}. This situation is relevant to the optical experiments described in Refs. 5–8, and 13, in which capillaries of radius $R=20-200\ \mu$m were used. In these experiments the ER (or ERPD) configurations were observed, and just this type of hard anchoring was realized. In fact, a comparison of the expressions for the ER structure energy corresponding to various anchoring types (see Table I) leads us to conclude that the transition from soft to hard anchoring takes place at $\sigma\gg\eta$. A cruder form of this estimate is $R\gg b_3$, where $b_3=K_{33}/W_\theta$ is the extrapolated de Gennes–Kleman length[2,29] corresponding to the elastic modulus K_{33}. Using the fact that for typical temperatures where the nematic phase exists $K_{33}\sim 10^{-6}$ dynes (see Ref. 29) and $W_\theta\sim 10^{-2}-10^{-1}$ erg/cm^2 (see Ref. 36), we obtain the estimate $b_3\sim 0.1-1\ \mu$m, i.e., the condition for hard anchoring is satisfied in the experiments of Refs. 5–8 and 13.

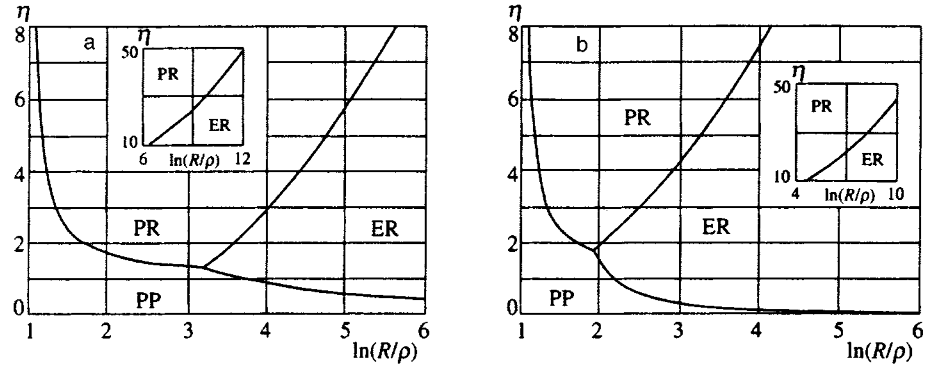

FIG. 6. Orientational states of an NLC, plotted in coordinates $\ln(R/\rho)$ and η for homeotropic boundary conditions and hard anchoring. The calculated values of the elastic modulus are $K_{24}=0$ (a) and $1.5K_{11}$ (b). The insets show the regions of large coordinate values.

Theoretically, orientational transitions to PR and PP configurations should occur in cylinders of small radius (see Fig. 6). However, in thin capillaries, the condition for hard anchoring $R \gg b_3$ ceases to hold; taking $\rho \sim 5 \cdot 10^{-7}$ (Refs. 9–12), we find that R is always smaller than or of the same order as b_3 for $\ln(R/\rho) \leqslant 3$. Thus, in order to assess the orientational stability of configurations in thin capillaries, it is necessary to use more general expressions for the energy corresponding to soft anchoring.

Diagrams for the orientational states of NLC for soft anchoring and values $K_{24}=0$ and $K_{24}=1.5K_{11}$ are shown in Fig. 7. On the whole, these diagrams show that the conditions for transitions between configurations depend strongly on the value of the surface elastic modulus K_{24}. Thus, the region of existence of the ER structure when $K_{24}=1.5K_{11}$ (Fig. 7b) is considerably broader than for the case $K_{24}=0$ (Fig. 7a). This is entirely natural, because as K_{24} increases, the energy of the ER configuration decreases (compare curves *2* and *4* with curves *1* and *3* in Fig. 5). The PP configuration essentially always occurs (even for $K_{24}=2K_{11}$) for small values of the dimensionless energy w_θ. For example, this configuration is observed in experiments[3,4] using cylinders with radii $R=0.3$ and $0.4\ \mu$m; theoretical analysis of the experimental data yields the estimates $w_\theta=1.8$ and 2.4 respectively.

The PR structure, on the other hand, can occur only at large values of η. Note that the region of existence of this configuration shown in Fig. 7 is somewhat provisional, and corresponds to a ratio $R/\rho=100$, i.e., to cylinders with radii $R \sim 0.5\ \mu$m. For $R/\rho > 100$ this region is shifted towards larger values of η, while for $R/\rho < 100$ it shifts to smaller values. Consequently, as the radius of the cylinder decreases, and near the nematic–smectic *A* transition where η is considerably larger than unity, the probability of experimentally observing the PR structure increases.

6.2. Circular anchoring

Let us briefly consider the conditions for transitions between configurations that correspond to circular anchoring. The final expressions for the free energies of these structures are listed in Table II. The set of material parameters that correspond to these configurations is broader than the corresponding set for homeotropic anchoring, and includes values of the torsion modulus K_{22} and specific anchoring energy W_ϕ. Increasing the number of material parameters complicates the qualitative analysis of the system as a whole. Despite this fact, we are at least able to find necessary existence conditions for individual structures such as the PC and AX configurations.

The PC configuration can occur only when it corresponds to an energy minimum in the class of planar distortions. For hard anchoring the requirement $F_{\mathrm{PC}} < F_{\mathrm{CPP}}$ leads to the condition

$$\eta = \frac{K_{33}}{K_{11}} < \frac{\ln(R/\rho)}{\ln(2R/e\rho)} \approx 1 + \frac{0.3}{\ln(R/\rho)}, \tag{54}$$

which in cylinders of large radius ($R \gg \rho$) coincides with the relation obtained in Ref. 35, $\eta < 1$. For soft anchoring, the energy of the CPP configuration is reduced; therefore, the

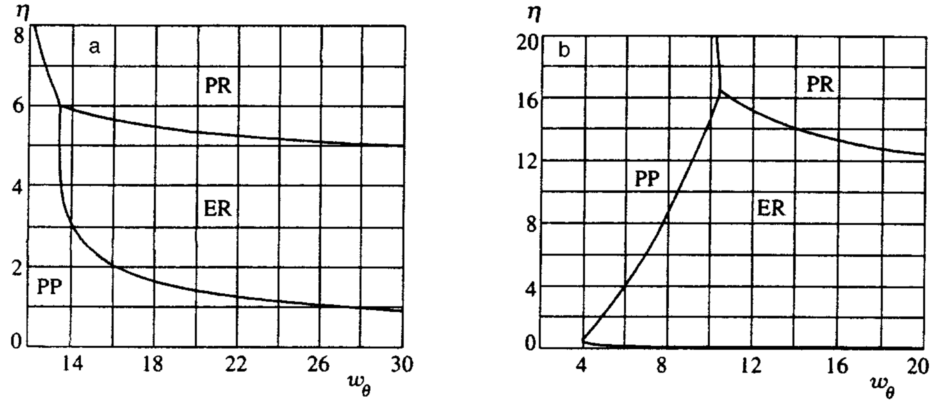

FIG. 7. Orientational states of NLC, plotted in the coordinates w_θ and η for homeotropic boundary conditions in the case of soft anchoring. The calculated values of the parameters are $R/\rho=100$, $K_{24}=0$ (a) and $K_{24}=1.5K_{11}$ (b).

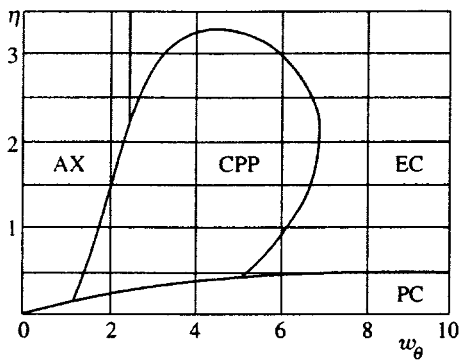

FIG. 8. Orientational states of the NLC, plotted in coordinates w_θ and η for circular boundary conditions in the case of soft anchoring. The computed values of the parameters are $\tilde{\eta}=1$, $K_{24}/K_{11}=1$, $W_\phi/W_\theta=0.4$, $R/\rho=20$.

region of existence of a PC structure with constant energy is shifted towards smaller values of η. Note that even in the case of hard anchoring the restriction (54) is a strong one, because in real NLC at typical temperatures where the nematic phase exists, the parameter η usually lies in the range $1\leqslant\eta\leqslant 2$.

The AX structure can only exist for $\tilde{\sigma}<1$, and only when the slope of the linear function $F_{\mathrm{AX}}(W_\phi)$ is less than the initial slope of the function $F_{\mathrm{CPP}}(W_\theta)$; see Eq. (38). This occurs when $W_\phi/W_\theta<1/2$.

As an example, Fig. 8 shows the orientational states of an NLC with soft anchoring and values $\tilde{\eta}=1$, $K_{24}/K_{11}=1$, $W_\phi/W_\theta=0.4$, $R/\rho=20$. Theoretically, in this case all four configurations of the NLC can occur. The region of existence of the PC structure, however, corresponds to values of η that are unrealistic in practical terms. Therefore, we assume that this configuration cannot be observed experimentally—if, of course, the circular anchoring is realized in practice. This conclusion is all the more obvious because as the radius of the cylinder increases, the region of existence of the PC structure narrows and corresponds to smaller values of η. It follows from Fig. 8 that in cylinders with large radius, the energy minimum corresponds to the EC structure, while in thin capillaries it corresponds to the AX or CPP configurations. Numerical calculations show that the region of existence of this CPP structure broadens as $\tilde{\eta}$ increases and K_{24} decreases.

7. CONCLUSION

Although our discussions have involved infinitely long cylinders, the results remain valid for capillaries whose length $L\gg R$ as well. In the latter case, the ratio of the energy associated with end effects to the overall free energy of the system is of order R/L. Therefore, deviations of the director near the ends of the cylinder can be neglected, and we can use the expressions from Tables I and II for the energy of the structures described above.

The situation changes considerably for the ERPD structure (and also for the theoretically possible EC structure with point defects). The ERPD configuration is stable in capillaries of finite length. As shown in Ref. 16, point defects attract one another and annihilate only for distances between them $h\leqslant 0.25R$. For distances $h>0.25R$, the defects repel one another. However, they cannot leave the liquid crystal sample, because near the ends of the cylinder point defects, like line disclinations,[29] repel each other and repel their mirror images. These repulsive forces cause real point defects to be located along the cylinder axis at the same distance from one

TABLE II. Total free energy per unit cylinder length of structures corresponding to circular anchoring.

	Anchoring type	
Structure	Hard	Soft
PC	$\pi K_{33}\ln(R/\rho)$	$\pi K_{33}\ln(R/\rho)$
CPP	$\pi K_{11}\ln(R/2\rho)+\pi(K_{33}-K_{11})(1-\ln 2)$	$\pi K\left\{-\ln\left(\frac{\tilde{\zeta}^2-1}{\tilde{\zeta}^2}\right)+w\frac{\tilde{\zeta}-1}{\tilde{\zeta}}+\kappa\left[\ln\left(\frac{\tilde{\zeta}-1}{\tilde{\zeta}+1}\right)+\frac{2}{\tilde{\zeta}}\right]\right\}$, $\tilde{\zeta}=\frac{1+\sqrt{1+w^2-2w\kappa}}{w}$, $K=\frac{K_{11}+K_{33}}{2}, \quad \kappa=\frac{K_{33}-K_{11}}{K_{33}+K_{11}}$ $w=\frac{W_\theta R}{K_{11}+K_{33}}$
EC	$\pi K_{22}\left[2-\frac{K_{24}}{K_{22}}+\frac{\tilde{\eta}}{\sqrt{\tilde{\eta}-1}}\arctan\sqrt{\tilde{\eta}-1}\right]$, $\tilde{\eta}=\frac{K_{33}}{K_{22}}$ $\tilde{\eta}\geqslant 1$*	$\pi K_{22}\left[2-\frac{K_{24}}{K_{22}}+\frac{\tilde{\eta}}{\sqrt{\tilde{\eta}-1}}\arctan\frac{\sqrt{\tilde{\eta}-1}(\tilde{\eta}-1)}{\tilde{\sigma}+\tilde{\eta}-1}\right]$, $\tilde{\sigma}=\frac{W_\phi R}{K_{22}}+\frac{K_{24}}{K_{22}}-1$, $\tilde{\sigma}>1 \quad \tilde{\eta}\geqslant 1$*
AX	–	$\pi R W_\phi$, $\tilde{\sigma}\leqslant 1$

Note. *For $\tilde{\eta}<1$ we must use the identity Eq. (42), replacing η with $\tilde{\eta}$.

another. Since all directions of escape are equally probable, in real situations the ERPD structure is observed more often than the uniform ER configuration. Moreover, the conditions described in Sec. 6 for transitions between planar and escape structures remain valid on the whole. For $L \gg R$ these conditions, which are in fact associated with instability of one of the planar structures, should depend weakly on which of the three-dimensional configurations (ER or ERPD) undergoes escape.

The authors of Refs. 3 and 4 observed a transition from the PP structure to the ERPD configuration, and used this fact to estimate the surface elastic modulus K_{24}. We note that for the constant K_{24} the amount of experimental data in the literature is extremely limited (see, e.g., Refs. 37 and 38). This is because the surface elastic modulus always enters into the defining relations in combination with at least one of the specific anchoring energies W_θ or W_ϕ. Separating these parameters in a single series of experiments is a complicated and not always soluble problem. In Refs. 3 and 4 this separation was made in a rather sketchy fashion. The object of investigation was the liquid crystal 5CB placed in cylindrical pores of length $L \approx 10\ \mu\text{m}$. The PP structure, as we have already mentioned above, was observed in pores of radii $R=0.3$ and $0.4\ \mu\text{m}$; the transition to the ERPD configuration occurred at $R=0.5\ \mu\text{m}$. The method of separating the contributions associated with W_θ and K_{24} was based on direct determination of the quantity W_θ by analyzing experimental data corresponding to the PP configuration. Recall that this structure does not depend on the elastic modulus K_{24}. In using the two-constant approximation $(\eta=1)$ an estimate $W_\theta/K \approx 6 \cdot 10^4\ \text{cm}^{-1}$ was obtained. From the condition $F_{\text{PP}} \approx F_{\text{ER}}$ at $R=0.5\ \mu\text{m}$ the value $K_{24} \approx 1.7\,K$ was found. Starting with the real value of the parameter $\eta=1.4$ (see Refs. 12 and 39), and based on the results of this paper, we can refine the values of W_θ and K_{24}. Using the average specific energies to estimate W_θ, which are found by equating the expansion coefficients $p(\eta=1.4)=p(\eta=1)$ at $R=0.3$ and $0.4\ \mu\text{m}$, and following the same method to determine K_{24}, we obtain $W_\theta/K_{11} \approx 7.7 \cdot 10^4\ \text{cm}^{-1}$ and $K_{24} \approx 1.61\,K_{11}$. The latter estimate, of course, is not definitive, because it does not follow from a direct comparison of theory with the experimental data: we have used the theoretical values $p(\eta=1)$ in place of ‘‘experimental’’ values. In this case the value $K_{24}=1.61\,K_{11}$ is closer to the value $K_{24}=1.1\,K$, which was obtained in the same papers by fitting the experimental data corresponding to the ERPD configuration. In the latter case, we used for the angle $\Omega(r,z)$ a trial function that qualitatively describes the real distribution of the director $\mathbf{n}(\mathbf{r})$ when $\eta=1$ (the two-constant approximation). For a more accurate estimate of the quantity K_{24} and verification of the results of this paper, further experiments would be very desirable.

The author is grateful to Yu. L Raĭkher for discussing these results and to K. M. Morozov for a number of useful comments.

The work was carried out with the partial financial support of NPK ‘‘ISTA.’’

[*] E-mail: burylov@tmg.dp.ua, burylov@transmag.vidrua.dp.ua

1) Naturally this result can be obtained by a number of other methods, for example, by substituting the boundary function (22) into the Poisson integral, as is usually done in problems of mathematical physics. In this procedure, however, when we directly compute the function (26), we would not be able to determine the exact charge of the disclination lines, i.e., we would lose the qualitative character of the field distribution of the director **n**.

---

[1] A. Saupe, Mol. Cryst. Liq. Cryst. **21**, 211 (1973).
[2] M. Kleman, *Points, Lines and Walls in Liquid Crystals, Magnetic Systems and Various Ordered Materials*, Wiley, New York (1983), p. 48.
[3] D. W. Allender, G. P. Crawford, and J. W. Doane, Phys. Rev. Lett. **67**, 1442 (1991).
[4] G. P. Crawford, D. W. Allender, and J. W. Doane, Phys. Rev. A **45**, 8693 (1992).
[5] R. B. Meyer, Phil. Mag. **27**, 405 (1973).
[6] C. Williams, P. Pieranski, and P. E. Cladis, Phys. Rev. Lett. **29**, 90 (1972).
[7] C. Williams, P. E. Cladis, and M. Kleman, Mol. Cryst. Liq. Cryst. **21**, 355 (1973).
[8] M. Kuzma and M. M. Labes, Mol. Cryst. Liq. Cryst. **100**, 103 (1983).
[9] G. P. Crawford, M. Vifan, J. W. Doane, and I. Vifan, Phys. Rev. A **43**, 835 (1991).
[10] R. J. Ondris-Crawford, G. P. Crawford, J. W. Doane *et al.*, Phys. Rev. E **48**, 1998 (1993).
[11] G. P. Crawford, D. W. Allender, and J. W. Doane, Phys. Rev. A **44**, 2570 (1991).
[12] A. Scharkowski, G. P. Crawford, S. Žumer, and J. W. Doane, J. Appl. Phys. **73**, 7280 (1993).
[13] R. D. Polak, G. P. Crawford, B. C. Kostival *et al.*, Phys. Rev. E **49**, R978 (1994).
[14] I. E. Dzyaloshinskiĭ, Zh. Éksp. Teor. Fiz. **58**, 1443 (1970) [Sov. Phys. JETP **31**, 773 (1970)].
[15] P. E. Cladis and M. Kleman, J. de Phys. **33**, 591 (1972).
[16] I. Vifan, M. Vifan, and S. Žumer, Phys. Rev. A **43**, 6875 (1991).
[17] P. E. Cladis, Philos. Mag. **29**, 641 (1974).
[18] F. Scudieri, Appl. Opt. **18**, 1455 (1979).
[19] S. Kralj and S. Žumer, Phys. Rev. E **51**, 366 (1995).
[20] R. J. Ondris-Crawford, M. Ambrožič, J. W. Doane, and S. Žumer, Phys. Rev. E **50**, 4773 (1994).
[21] L. M. Blinov, E. I. Kats, and A. A. Sonin, Usp. Fiz. Nauk **152**, 449 (1987) [Sov. Phys. Usp. **30**, 604 (1987)].
[22] Zh. Kon’yar, *Orientation of Liquid Crystals and their Mixtures* [in Russian], University Press, Minsk (1986).
[23] A. Saupe, J. Chem. Phys. **75**, 5118 (1981).
[24] F. C. Frank, Discuss. Faraday Soc. **25**, 19 (1958).
[25] E. I. Kats and V. V. Lebedev, *Dynamics of Liquid Crystals* [in Russian], Nauka, Moscow (1988), p. 18.
[26] S. Stallinga, J. A. M. M. van Haaren, and J. M. A. van den Eerenbeernd, Phys. Rev. E **53**, 1701 (1996).
[27] J. L. Eriksen, Phys. Fluids **9**, 1205 (1966).
[28] A. Rapini and M. Papoular, J. de Phys. **30**, C4-54 (1969).
[29] P. G. de Gennes, *The Physics of Liquid Crystals*, 2nd ed., Clarendon Press, Oxford (1993).
[30] L. D. Landau and E. M Lifshitz, *Electrodynamics of Continuous Media*, 2nd ed., Pergamon Press, New York (1984).
[31] M. A. Lavrent’ev and E. B. Shabat, *Methods in the Theory of Functions of a Complex Variable* [in Russian], Nauka, Moscow (1982).
[32] M. V. Kurik and O. D. Lavrentovich, Usp. Fiz. Nauk **154**, 381 (1988) [Sov. Phys. Usp. **31**, 196 (1988)].
[33] J. Ericsen, *Research on the Mechanics of Continuous Media* [Russian translation], Mir, Moscow (1977).
[34] L. D. Landau and E. M Lifshitz, *Theory of Elasticity*, 3rd Engl. ed., Pergamon Press, Oxford (1986).
[35] S. I. Anisimov and I. E. Dzyaloshinskiĭ, Zh. Éksp. Teor. Fiz. **63**, 1460 (1972) [Sov. Phys. JETP **36**, 774 (1972)].
[36] C. Rosenblatt, J. de Phys. **45**, 349 (1972).
[37] O. D. Lavrentovich, Phys. Scr. **39**, 349 (1991).
[38] A. Sparavigna, O. D. Lavrentovich, and A. Strigazzi, Phys. Rev. E **49**, 1344 (1994).
[39] P. P. Karat and N. V. Madhusudana, Mol. Cryst. Liq. Cryst. **36**, 51 (1976); Mol. Cryst. Liq. Cryst. **40**, 239 (1977).

Translated by Frank J. Crowne

Theory of parametric excitation of acoustic waves

A. R. Muratov

Institute for Oil and Gas Research, Russian Academy of Sciences, 117917, Moscow, Russia;
Department of Physics, Weizmann Institute of Science, 76100, Rehovol, Israel

(Submitted 26 May 1997)
Zh. Éksp. Teor. Fiz. **112**, 1630–1648 (November 1997)

A theory of parametric excitation of acoustic waves is constructed. It is shown that nonlinear attenuation is the main restriction mechanism for a parametrically generated sound wave. The intensity of generated waves is directly proportional to the difference ϵ between the value of pumping and bare attenuation. The calculated proportionality coefficient depends on the shape of the generated sound wave. Why an ordinary pattern does not form for acoustic waves is explained. The structure of the spectrum of excited waves was studied. It is shown that this structure has exponential asymptotic behavior at the frequency. The width of the intensity distribution depends on the shape of a wave. For different cases it behaves as ϵ^{α} with $\alpha=1$, 8/7, and 4/3. The results are compared with the experimental data of Ref. 5. © *1997 American Institute of Physics.* [S1063-7761(97)00811-1]

1. INTRODUCTION

Parametric excitation of waves is observed in a wide class of dynamical systems for waves with different dispersion relations.[1] These dispersion relations can be divided into two groups: nondecaying and decaying. As an example from the first group we have spin waves and from the second group waves on the free surface of a liquid. For spin waves conservation laws of frequency and wave vector, as a rule, do not permit three-wave interactions. The behavior of spin-wave systems in those cases is determined by four-wave interactions. The corresponding theory is well developed and is described elsewhere.[2,3] The main mechanism for saturation of the amplitude of generated wave in these systems is the so-called dephasing mechanism, i.e., renormalization of the pumping due to the interaction between secondary waves. Capillary waves on the free surface of a liquid have the dispersion relation $\omega \propto k^{3/2}$, where ω is the frequency and k is the wave vector of the wave. Three-wave interaction is allowed for this dispersion relation. The pattern selection and amplitude saturation for surface waves are determined by a nonlinear attenuation, as has been shown in Ref. 4.

The case of acoustic dispersion relation $\omega \propto k$ is the marginal case between these two possibilities. In this case the conservation laws allow three-wave interactions but only for the waves with collinear (parallel or antiparallel) wave vectors. This case, which we will consider in this paper, was not studied at all. We will show that nonlinear attenuation is the main mechanism for restriction of amplitude of a parametrically generated sound wave. The intensity of generated waves is directly proportional to the difference between the value of pumping and the bare attenuation. The proportionality coefficient depends on the shape of the excited sound wave.

Three-wave interaction of sound waves is allowed only if their wave vectors are almost collinear. This special interaction destroys the long-range order at an angle between the directions of propagation of waves; therefore, ordinary pattern formation does not occur in the case of acoustic waves. We will find the fine structure of the spectrum of generated waves. It turns out that it has exponential asymptotic behavior at the frequency which is known for the other nonlinear systems.[3] The behavior of the width of the spectrum for acoustic waves differs from the one known for spin waves. The width of the intensity distribution depends on the shape of the wave. For different cases it behaves as ϵ^{α} with $\alpha=1$, 8/7, and 4/3. The results of this paper were compared with many data obtained in experiments with parametric excitation of the second-sound waves in liquid helium by the first-sound wave.[5,6] We obtained good qualitative and quantitative agreement with the experimental results.

2. THE EFFECTIVE ACTION

It is suitable to use the Hamiltonian approach to describe nonlinear dynamics of waves. It is not a simple problem to find the corresponding canonical variables in general.[3,7] We will assume that this problem has already been solved. For the dynamics of liquid helium the canonical variables were found in Ref. 8. In canonical variables the Hamiltonian of a system can be written as

$$\begin{aligned} H=\int d^3r(&b^*(t,\mathbf{r})\omega(\nabla)b(t,\mathbf{r})\\ &+U[a^*(t,\mathbf{r})b(t,\mathbf{r})b(t,\mathbf{r})+\text{c.c.}]\\ &+V[b^*(t,\mathbf{r}))b(t,\mathbf{r})b(t,\mathbf{r})+\text{c.c.}]). \end{aligned} \tag{1}$$

Here $b(t,\mathbf{r})$ is the wave variable which describes the excited sound wave, $\omega=c\sqrt{-\nabla^2}$ is its dispersion relation, and c is the phase velocity of the sound wave. We will study parametric excitation of the sound wave $b(t,\mathbf{r})$ by the external wave field $a(t,\mathbf{r})$ (pumping wave). The parameter U in Eq. (1) is the vertex of the three-wave interaction of the pumping wave and the excited waves, and V is the vertex of the three-wave self-interaction.

Equation (1) is simply an expansion over the value of the excited wave; it can be used only if the amplitude of the excited wave is small, i.e., not far from the excitation threshold. In general, we can prolong expansion (1) and take into account four-wave interaction of the excited waves. It is necessary if the three-wave interaction is not allowed due to the conservation laws of frequency and wave vector. As will be shown below, for the sound waves we can consider only the three-wave interaction.

It is useful to make Fourier transform of the wave field:

$$b(t,\mathbf{r})=\int \frac{d^3k}{(2\pi)^3}\, b(t,\mathbf{k})e^{i\mathbf{kr}}. \tag{2}$$

We can then write the Hamiltonian as

$$\begin{aligned}H=\int \frac{d^3k}{(2\pi)^3}\bigg[&\omega(k)b(\mathbf{k})b^*(\mathbf{k})+\int \frac{d^3q}{(2\pi)^3}\,(U(\mathbf{k},\mathbf{q})\\ &\times[a^*(\mathbf{k})b(\mathbf{q})b(\mathbf{k}-\mathbf{q})+\text{c.c.}]+V(\mathbf{k},\mathbf{q})\\ &\times[b^*(\mathbf{k})b(\mathbf{q})b(\mathbf{k}-\mathbf{q})+\text{c.c.}])\bigg].\end{aligned} \tag{3}$$

Here ω and $\mathbf{k}$ are the frequency and the wave vector of the sound wave, and $\omega(k)$ is its dispersion relation. The expansion in (3) is an ordinary hydrodynamic expansion and its parameter is $\sqrt{\omega}b$. It means that the vertices U and V are proportional to

$$\sqrt{\omega(k_1)\omega(k_2)\omega(k_3)}. \tag{4}$$

We will use complex canonical variables, in which the dynamic equations have the form

$$i\partial_t b(\mathbf{k})=\frac{\delta H}{\delta b^*(\mathbf{k})},\quad -i\partial_t b^*(\mathbf{k})=\frac{\delta H}{\delta b(\mathbf{k})}. \tag{5}$$

In our case we have

$$\begin{aligned}i\partial_t b(\mathbf{k})=\omega(k)b(\mathbf{k})+\int \frac{d^3q}{(2\pi)^3}\,&(2Ua(\mathbf{k}+\mathbf{q})b^*(\mathbf{q})\\ &+V[2b(\mathbf{q})b^*(\mathbf{q}-\mathbf{k})+b(\mathbf{q})b(\mathbf{k}-\mathbf{q})]).\end{aligned} \tag{6}$$

The second equation is a complex conjugated equation (6).

Equation (6) is a conservative equation to which a dissipative term must be added. In general, this term is proportional to

$$\nabla^2\,\frac{\delta H}{\delta b^*(t,\mathbf{k})} \tag{7}$$

and small in the hydrodynamic parameter in comparison with the term ωb in Eq. (6). It means that we can ignore nonlinear terms in the dissipation part of the dynamic equation. Thus, to take into account the dissipation terms it is necessary to replace in Eq. (6) $\omega(k)\rightarrow\omega(k)-i\gamma_0(k)$, where $\gamma_0(k)=Dk^2$.

It is suitable to use for our problem the dynamic-diagram technique proposed by Wyld[9] and developed by the de Dominicis[10] and Jannsen.[11] Textbook description of this technique can be found in Ref. 12. The corresponding effective action can be written in the form

$$\begin{aligned}I=i\int \frac{dt\,d^3k}{(2\pi)^3}\bigg\{\bigg(&p^*(\mathbf{k})[\omega(k)-i\partial_t-i\gamma_0(k)]b(\mathbf{k})\\ &+\lambda\,\exp(-i2\omega_0 t)p^*(\mathbf{k})b^*(-\mathbf{k})\\ &+\int \frac{d^3q}{(2\pi)^3}\,Vp^*(\mathbf{k})b(\mathbf{q})[2b^*(\mathbf{q}-\mathbf{k})+b(\mathbf{k}-\mathbf{q})]\bigg)\\ &+\text{c.c.}+T\,\frac{\gamma_0(k)}{\omega(k)}\,p^*(\mathbf{k})p(\mathbf{k})\bigg\}.\end{aligned} \tag{8}$$

Here we have introduced an auxiliary field $p(t,\mathbf{r})$, which is conjugated to the wave field $b(t,\mathbf{r})$; $\lambda\equiv 2aU$ is the pumping field, and T is the temperature in units of energy. We assumed that the pumping wave is a monochromatic wave with a frequency $2\omega_0$. For simplicity, we will ignore below the nonzero value of the wave vector of the pumping wave. This can be done if the velocity of the pumping wave is significantly greater than the velocity of excited waves.

The equations of motion (6) with dissipation terms can be obtained as the extremum conditions for the effective action:

$$\frac{\delta I}{\delta p^*(t,\mathbf{k})}=0,\quad \frac{\delta I}{\delta p(t,\mathbf{k})}=0.$$

Various averages can be found as

$$\langle f(t,\mathbf{k})\rangle=\int \mathscr{D}p\mathscr{D}p^*\mathscr{D}b\mathscr{D}b^* f(t,\mathbf{k})e^{iI}. \tag{9}$$

3. THE CORRELATION FUNCTIONS

The quadratic part of the effective action (8) determines the bare correlation functions. There are three types of correlation functions in the Wyld diagram technique. The first $\langle pb\rangle$ is the Green's function, which is a response function on the external field. The second $\langle bb\rangle$ is the correlation function. The last average $\langle pp\rangle$ equals zero. In our system there are normal Green's and correlation functions, which are determined by the term with the coefficient $\omega-i\gamma_0$, and the abnormal functions, which are determined by the term with the pumping $\lambda=2aU$. Let us write the Fourier transform over time:

$$b(t,\mathbf{k})=\int \frac{d\omega}{2\pi}\, b(\omega,\mathbf{k})e^{-i\omega t}.$$

Further, for simplicity we introduce the notation

$$\kappa\equiv\{\omega,\mathbf{k}\},\quad \tilde{\varkappa}\equiv\{2\omega_0-\omega,-\mathbf{k}\},\quad \tilde{\omega}=\omega-\omega_0.$$

It is suitable to determine the Green's functions $\langle bp\rangle$ in the following way:

$$G(\kappa)=\begin{pmatrix}G_1(\kappa) & G_2(\kappa)\\ G_2^*(\tilde{\varkappa}) & G_1^*(\tilde{\varkappa})\end{pmatrix}, \tag{10}$$

where

$$\begin{aligned}&\langle b(\kappa)p^*(\kappa_1)\rangle=(2\pi)^4\delta(\omega-\omega_1)\,\delta(\mathbf{k}-\mathbf{k}_1)G_1(\omega,\mathbf{k}),\\ &\langle b(\kappa)p(\kappa_1)\rangle=(2\pi)^4\delta(\tilde{\omega}+\tilde{\omega}_1)\,\delta(\mathbf{k}+\mathbf{k}_1)G_2(\omega,\mathbf{k}).\end{aligned} \tag{11}$$

For the Green's functions $\langle pb\rangle$ we have

$$\tilde{G}(\kappa)=\begin{pmatrix}G_1^*(\kappa) & G_2(\tilde{\varkappa})\\ G_2^*(\kappa) & G_1(\tilde{\varkappa})\end{pmatrix}. \tag{12}$$

The bare Green's functions can be found as

$$G_0^{-1}(\kappa)=\begin{pmatrix} ck-\omega-i\gamma_0(k) & \lambda \\ \lambda^* & ck+\omega-2\omega_0+i\gamma_0(k)\end{pmatrix}, \tag{13}$$

where $\gamma_0(k)$ is the bare attenuation rate of the sound wave. It is easy to obtain the following expressions for the bare Green's functions from (13):

$$G_{10}(\kappa)=\Delta^{-1}(\kappa)[ck+\omega-2\omega_0+i\gamma_0(k)],$$
$$G_{20}(\kappa)=-\lambda\Delta^{-1}(\kappa). \tag{14}$$

Here

$$\Delta(\kappa)=(ck-\omega_0)^2-[\omega-\omega_0+i\gamma_0(k)]^2-|\lambda|^2,$$
$$\Delta(\widetilde{\varkappa})=\Delta^*(\kappa). \tag{15}$$

The off-diagonal components of the Green's function are essential only for $\omega\sim\omega_0$ and $k\sim k_0\equiv\omega_0/c$. Far from this region it is possible to use for the Green's function the expression

$$G_1(\kappa)=[ck-\omega-i\gamma_0(k)]^{-1}. \tag{16}$$

The full Green's function can be found as a solution of the Dyson equation in the form

$$G^{-1}(\kappa)=G_0^{-1}(\kappa)-\Sigma(\kappa), \tag{17}$$

where $\Sigma(\kappa)$ is a self-energy function. The self-energy matrix has the same properties as G; i.e., it can be written in the form

$$\Sigma(\kappa)=\begin{pmatrix}\Sigma_1(\kappa) & \Sigma_2(\kappa)\\ \Sigma_2^*(\widetilde{\varkappa}) & \Sigma_1^*(\widetilde{\varkappa})\end{pmatrix}. \tag{18}$$

The bare value of $\Sigma(\kappa)$ equals zero.

The correlation function F has a matrix structure also. It can be determined as

$$F(\kappa)=\begin{pmatrix}F_1(\kappa) & F_2(\kappa)\\ F_2(\widetilde{\kappa}) & F_1^*(\widetilde{\kappa})\end{pmatrix}, \tag{19}$$

where

$$\langle b(\kappa)b^*(\kappa_1)\rangle=(2\pi)^4\delta(\omega-\omega_1)\delta(\mathbf{k}-\mathbf{k}_1)F_1(\omega,\mathbf{k}),$$
$$\langle b(\kappa)b(\kappa_1)\rangle=(2\pi)^4\delta(\widetilde{\omega}+\widetilde{\omega}_1)\delta(\mathbf{k}+\mathbf{k}_1)F_2(\omega,\mathbf{k}).$$

It is easy to see that $F_1^*(\kappa)=F_1(\kappa)$ and $F_2(\overline{\varkappa})=F_2(\kappa)$. Therefore, we can write

$$F(\kappa)=\begin{pmatrix}F_1(\kappa) & F_2(\kappa)\\ F_2^*(\kappa) & F_1(\widetilde{\varkappa})\end{pmatrix}. \tag{20}$$

The Wyld correlation functions can be calculated as

$$F(\kappa)=G(\kappa)\Phi(\kappa)\widetilde{G}(\kappa), \tag{21}$$

where $\overline{G(\kappa)}$ is determined by (12), and $\Phi(\kappa)$ is a force function. Its bare value Φ_0 is determined by the casual force correlator, i.e.,

$$\Phi_0(\kappa)=\Gamma_0 E,\quad \Gamma_0=T\,\frac{\gamma_0(k)}{\omega(k)}, \tag{22}$$

where E is a unit 2×2 matrix. For the bare correlation functions we obtain

FIG. 1. Tree correction for the self-energy function.

$$F_{10}(\kappa)=\Gamma_0\,\frac{(ck+\omega-2\omega_0)^2+\gamma_0^2(k)+|\lambda|^2}{\Delta(\kappa)\Delta^*(\kappa)},$$
$$F_{20}(\kappa)=-\Gamma_0\,\frac{2\lambda[ck-\omega_0+i\gamma_0(k)]}{\Delta(\kappa)\Delta^*(\kappa)}. \tag{23}$$

The force function $\Phi(\kappa)$ can be written in the form

$$\Phi(\kappa)=\begin{pmatrix}\Phi_1(\kappa) & \Phi_2(\kappa)\\ \Phi_2^*(\kappa) & \Phi_1(\widetilde{\varkappa})\end{pmatrix}. \tag{24}$$

The force functions $\Phi(\kappa)$, by analogy with $F(\kappa)$, have the properties $\Phi_1(\kappa)=\Phi_1^*(\kappa)$ and $\Phi_2(\kappa)=\Phi_2(\overline{\varkappa})$.

4. SATURATION OF THE EXCITED WAVE

In this section we omit the term proportional to the temperature. In this case the fluctuations of the phase of the parametrically excited wave can be ignored and we can assume that there appears a nonzero value of average $\langle b\rangle$ if the pumping is over the threshold. The equations for this nonzero average coincide with (6). If we disregard the nonlinear terms on b, these equations will be linear equations with zero right-hand side:

$$G^{-1}\begin{pmatrix}b(\kappa)\\ b(\widetilde{\varkappa})\end{pmatrix}=0. \tag{25}$$

They can have a nonzero solution only if the main determinant of the system $\Delta(\kappa)$, which is determined by (15), equals zero:

$$\Delta(\kappa)=(ck-\omega_0)^2-[\omega-\omega_0+i\gamma_0(k)]^2-|\lambda|^2=0. \tag{26}$$

This equation can first be satisfied for waves with $\omega=\omega_0$ and $k=k_0=\omega_0/c$. The threshold value of pumping is $|\lambda|=\gamma_0(k_0)\equiv\gamma_0$; i.e.,

$$|a|=\gamma_0/2U. \tag{27}$$

If $|\lambda|>\gamma_0$, the nonzero value of average $\langle b\rangle$ appears. In order to determine its value, we must consider the nonlinear corrections. In a tree approximation it is necessary to take into account the corrections for the self-energy function, shown in Fig. 1. The solid lines in Fig. 1 correspond to the field b, the dashed lines correspond to the field p, and the points correspond to the vortices V. This diagram for $\mathbf{k}'\simeq\mathbf{k}$ gives the contribution to the diagonal part of the self-energy function and determines the nonlinear correction to the attenuation rate γ. The diagram in Fig. 1 for $\mathbf{k}'\simeq-\mathbf{k}$ corrects the off-diagonal terms of the self-energy function; it renormalizes the pumping λ.

The Green's function of the diagram in Fig. 1 has a frequency near $2\omega_0$ only if $\mathbf{k}'\simeq\mathbf{k}\simeq\mathbf{k}_1$ and has a frequency near zero for all other cases. Using Eq. (4), it is easy to see that in the first case the correction is greater than that in the second case by a factor of ω_0/γ_0. In particular, this means that for acoustic waves the nonlinear attenuation is significantly more important than renormalization of pumping. This result agrees with the corresponding conclusion for the surface waves, where the three-wave interactions are allowed.[4]

In general, the average of the wave field $b(t,\mathbf{r})$ has the form

$$\langle b(t,\mathbf{r})\rangle=\int d\Omega B(\theta,\varphi)\exp(-i\omega_0 t+ik_0\mathbf{er}),\tag{28}$$

where $\mathbf{e}\equiv\mathbf{e}(\theta,\varphi)$ is the unit vector in the direction which is determined by the angles θ, φ, and $d\Omega\equiv d\theta d\varphi\sin\theta$. We see that it is possible to disregard the renormalization of the pumping for the sound waves. We also see that there is no standard pattern formation for sound waves. This means that we can choose a real amplitude B and a real pumping λ. The correction for the self-energy function in Fig. 1 can be written as

$$\begin{aligned}\Sigma(\omega_0,\mathbf{k})&=4\int\frac{d\omega_1 d\mathbf{k}_1}{(2\pi)^4}V^2F_1(\kappa_1)G_1(\kappa+\kappa_1)\\&=4\int d\theta d\varphi\,\frac{V^2(\theta,\varphi)B^2(\theta,\varphi)\sin\theta}{\omega(\mathbf{k}+\mathbf{k}_1)-2\omega_0-i\gamma(\mathbf{k}+\mathbf{k}_1)}.\end{aligned}\tag{29}$$

In Eq. (29) θ is a polar angle between the wave vectors $\mathbf{k}$ and $\mathbf{k}_1$, and φ is the azimuthal angle. Since we use the tree approximation in this section, it is possible to replace

$$\langle b(\kappa)b^*(\kappa_1)\rangle=\langle b(\kappa)\rangle\langle b^*(\kappa_1)\rangle.$$

It is easy to see that the integral in (29) is determined by the small region at an angle θ, $\Delta\theta\simeq4\sqrt{\gamma_0/\omega_0}$. In this region it is possible to replace $V(\theta,\varphi)$ and $B(\theta,\varphi)$ by their values for $\theta=0$ and use instead of $\sin\theta$ the approximate expression $\sin\theta\simeq\theta$. As a result, we obtain $\omega(\mathbf{k}+\mathbf{k}_1)\simeq2\omega_0(1-\theta^2/8)$. The real part and the imaginary part of Σ are of the same order of magnitude. Since $\omega_0\gg\gamma_0$, it is possible to ignore the real part of Σ, which gives a small correction for the sound velocity. The imaginary part of Σ gives the correction for the attenuation rate γ:

$$\gamma=\gamma_0+\operatorname{Im}\Sigma.\tag{30}$$

For the imaginary part of Σ we have

$$\operatorname{Im}\Sigma(\omega_0,k_0\mathbf{e})\equiv\mu n(\mathbf{e}),\quad n(\mathbf{e})=B^2(\mathbf{e}),$$

$$\mu=4V^2\int d\theta d\varphi\,\frac{\gamma_0(2k_0)\sin\theta}{[\omega(\mathbf{k}+\mathbf{k}_1)-2\omega_0]^2+\gamma_0^2(2k_0)},\tag{31}$$

where $V\equiv V(\theta=0)$. The equilibrium value of the amplitude of the excited wave is defined as

$$\lambda\equiv\gamma_0(1+\epsilon)=\gamma_0+\mu n,\quad n=\gamma_0\epsilon/\mu.\tag{32}$$

Therefore, the equilibrium density n of the parametrically excited wave propagating in a given direction $\mathbf{e}$ is proportional to ϵ.

In further calculations it is necessary to make some assumptions about the shape of parametrically excited wave. If we ignore the nonzero value of the wave vector of the pumping wave and if the system is isotropic (in particular, if the vertex U of the interaction of the pumping wave with the excited waves depends only slightly on the angles), the excited wave will be a spherical wave (three-dimensional):

$$\langle b(t,\mathbf{r})\rangle_3=B\int d\Omega\,\exp(-i\omega_0 t+ik_0\mathbf{er}).\tag{33}$$

In this case the coefficient μ is

$$\mu_3=8\pi^2V^2\omega_0^{-1}.\tag{34}$$

The total density of the excited wave is

$$N_3=4\pi B^2=\frac{2}{\pi}\frac{\gamma_0\omega_0}{4V^2}\epsilon.\tag{35}$$

It is interesting to compare this result with the corresponding result for spin waves.[2] Saturation of the amplitude of the excited spin wave occurs due to the renormalization of pumping by the four-wave interaction (dephasing mechanism). The corresponding result for the density of the wave is $n\propto\sqrt{\epsilon}$. Estimate for the proportionality coefficient in this equation coincides with the estimate for the coefficient in (34), but it turns out that the coefficient for the four-wave interaction is larger numerically. Besides, near the threshold $\epsilon\ll\sqrt{\epsilon}$, so the nonlinear attenuation due to the three-wave interaction is more important than the renormalization of pumping by the four-wave interaction.

If the system has axial symmetry or if the pumping wave is a standing wave, as is the case in Ref. 5, it is possible that the excited wave will be a cylindrical wave:

$$\begin{aligned}\langle b(t,\mathbf{r})\rangle_2=B\int d\varphi\,\exp[&-i\omega_0 t+ik_0\\&\times(x\cos\varphi+y\sin\varphi)].\end{aligned}\tag{36}$$

In this case the coefficient μ and the total density of the wave are

$$\mu_2=2^{3/2}\frac{\pi V^2}{\sqrt{\omega_0\gamma_0}},\quad N_2=2\pi B^2=2^{3/2}\sqrt{\frac{\gamma_0}{\omega_0}}\frac{\gamma_0\omega_0}{4V^2}\epsilon.\tag{37}$$

A further decrease of the symmetry can render an excited wave flat. In this case the corresponding equations will be

$$\langle b(t,\mathbf{r})\rangle_1=2B\exp(-i\omega_0 t)\cos(k_0x),\quad \mu_1=4\frac{V^2}{\gamma_0},$$

$$N_1=B^2=\frac{\gamma_0}{\omega_0}\frac{\gamma_0\omega_0}{4V^2}\epsilon.\tag{38}$$

For the last two cases the restriction of the sound-wave amplitude by nonlinear attenuation is stronger than the corresponding saturation due to the dephasing mechanism by a factor of $\sqrt{\gamma_0/\omega_0}$ for a cylindrical wave and by a factor of γ_0/ω_0 for a flat wave.

The total intensity of parametrically excited sound wave is maximal for a spherical wave and minimal for a flat wave. This situation for sound waves is quite different from the situation for spin waves, where the integral intensity of parametrically excited wave depends only slightly on its shape. In general, it is natural to expect that a nonlinear system will try to have maximal full intensity and corresponding dissipa-

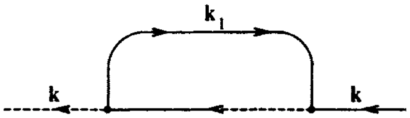

FIG. 2. One-loop correction for the normal self-energy function.

tion. This means that it is possible to expect transitions from a less symmetric shape to a more symmetric shape of the sound wave (for example, flat → cylindrical → spherical) as the intensity of the pumping wave increases. This means that it is necessary to expect the appearance of a sound wave with the maximum possible symmetry near the threshold.

Sound waves interact essentially only if the angle between their wave vectors is smaller than $\Delta\theta \simeq 4\sqrt{\gamma_0/\omega_0}$. This peculiar property of the interaction destroys the long-range order at an angle between the sound waves and leads to the absence of an ordinary pattern formation. Specific patterns which must appear over the threshold of excitation of sound waves have approximately equal intensities of the waves propagating in the range from $-\Delta\theta$ to $\Delta\theta$. In an anisotropic system the shape of parametrically excited wave is determined mainly by the shape of the pumping wave, by the properties of the interaction vertex between the pumping wave and the excited waves, and by the boundary conditions.

5. THERMAL BROADENING

Let us consider the influence of thermal fluctuations on the spectrum of a parametrically generated sound wave. It is necessary to take into account the diagram in Fig. 2, which contributes to the self-energy function $\Sigma_1(k)$. Analytical expression for this diagram is determined by (29), where now the function F_1 is irreducible. The matrix structure of the correlation functions is essential only for the frequencies near ω_0. For the diagram in Fig. 2 it is therefore necessary to take into account the nondiagonality of the function F_1 and use for it the expression (23). The Green's function G has the frequency $\omega \sim 2\omega_0$, so we can use for it the expression (16). Equation (29) now can be rewritten as

$$\Sigma_1(\omega,\mathbf{k}) = 4V^2 \int \frac{d\omega_1 d\mathbf{k}_1}{\Omega(2\pi)^4}\,\Gamma_0(k_1) \times \frac{(ck_1+\omega_1-2\omega_0)^2+\gamma^2+\lambda^2}{|(\omega_1-i\gamma)^2-(ck_1-\omega_0)^2+\lambda^2|^2} \int d\Omega G_1(\kappa). \tag{39}$$

The last integration in Eq. (39) must be made over all angles. For a flat wave it is absent, for a cylindrical wave it is an integral over an angle θ, and for a spherical wave it is an integral over $d\Omega = d\theta d\varphi \sin\theta$. In Eq.(39) the first integral is real and the imaginary part of the second integral is determined by (31). The integral from the correlation function F over $\mathbf{k}_1$ determines the spectral density of excited sound waves. This density can be determined from the equation

$$n = \int d\omega\ n(\omega) = \frac{1}{\Omega} \int \frac{d\omega d\mathbf{k}}{(2\pi)^4} F_1(\omega,\mathbf{k}). \tag{40}$$

Here n and $n(\omega)$ are the integral and spectral densities of the sound waves, which propagate in a given direction. The factor Ω in (39) and (40) depends on the shape of the wave. For a spherical wave $\Omega = 4\pi$, for a cylindrical wave $\Omega = 2\pi$, and for a flat wave $\Omega = 1$. The spectral density of a wave is introduced in such a way that the total density N of the sound wave is

$$N = \Omega n.$$

The first integral in Eq. (39) contains the function F, which is singular on ω_1, k_1, and the smooth function $\int d\Omega G$. It is possible to write instead of the second integral the expression (31) and consider it as a constant. Thus the renormalized attenuation rate of the sound wave is

$$\gamma = \gamma_0 + \mathrm{Im}\,\Sigma, \quad \mathrm{Im}\,\Sigma = \mu n. \tag{41}$$

Here n is the total spectral density of the excited sound waves, which propagate in a given direction, obtained with allowance for thermal broadening. Calculating the first integral in (39), we obtain the equation for the damping rate γ. We can consider this equation as self-consistent equation for γ, which means that we have summed the set of diagrams in Fig. 2:

$$\gamma = \gamma_0 + K\Gamma_0/\nu, \quad \nu \equiv \sqrt{\gamma^2-\lambda^2}. \tag{42}$$

For simplicity it is useful to choose real λ. The coefficient K is

$$K = \mu\,\frac{k_0^2(\gamma^2+\lambda^2)}{16\pi^2 c\gamma}. \tag{43}$$

Now the value of γ must be found from Eq. (42). We see that $\gamma > 0$ for all values of the pumping λ. The width of the distribution $n(\omega)$ is determined by the position of the singularity nearest to the real axis in the integral $\int d\omega_1 F_1$. For $\lambda > \gamma_0$ this width is of the order of ν. If $\lambda \gg \gamma_0$, the value of γ can be determined from the equation

$$\gamma \simeq \frac{K\Gamma_0}{\sqrt{\gamma^2-\lambda^2}}. \tag{44}$$

We see that thermal width of the spectrum leads to zero if $\lambda \to \infty$. It is easy to determine the spectral distribution $n(\omega)$. We have

$$n(\omega) = \Gamma_0\,\frac{k_0^2(\gamma^2+\lambda^2)}{(2\pi)^3 c}\,J,$$

$$J = \int \frac{dk}{|c^2k^2+(\gamma+i\omega)^2-\lambda^2|^2}. \tag{45}$$

The poles of the integrated function are $k = \pm i a_\pm$, where $a_\pm = \sqrt{(\gamma \pm i\omega)^2-\lambda^2}$. If $\omega < \nu^2/2\gamma$, then these poles lie near the real axis at a distance of the order of ν. If $\omega > \nu^2/2\gamma$, the corresponding distance is about $\gamma\omega/\sqrt{\gamma^2+\lambda^2}$. The main part of the integral is produced from the first region. Calculating this part, we obtain

$$J = \frac{\pi}{2\nu^3 f(\widetilde{\omega})}, \quad f(x) = \frac{r^2}{\sqrt{2}}\,\sqrt{r^2+1-x^2\nu^{-2}},$$

$$r^2 = \sqrt{(1-x^2\nu^{-2})^2+4\gamma^2x^2\nu^{-4}}. \tag{46}$$

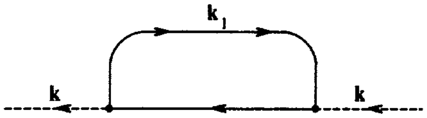

FIG. 3. One-loop correction for the normal force function.

For spectral distribution of the sound waves we have

$$n(\omega)=\frac{k_0^2}{(2\pi)^3c}\,\frac{\pi(\gamma^2+\lambda^2)}{2\nu^3}\,\frac{\Gamma_0}{f(\tilde{\omega})}. \tag{47}$$

Let us compare Eq. (41) and Eq. (32), which was obtained for the distribution of zero width. Let $(\Delta\omega)_T$ be the thermal width of the spectrum. For $\lambda-\gamma_0\gg(\Delta\omega)_T$ we have $\gamma-\lambda\ll\gamma_0$. Therefore, integrating the distribution $n(\omega)$ over ω, we obtain the integral intensity of excited sound waves, which coincides with the previous result (32) for the intensity.

In a one-loop approximation it is necessary to take into account the correction for the force function, which can be represented by the diagram in Fig. 3. The analytical expression for this correction is

$$(\Phi_1(\kappa))_1\sim\frac{V^2}{\Omega}\int\frac{d\omega_1 d\mathbf{k}_1}{(2\pi)^4}F_1(\kappa_1)F_1(\kappa+\kappa_1). \tag{48}$$

Here the first function F_1 has a frequency near ω_0 and the second function F_1 has a frequency near $2\omega_0$. We can calculate (48) as an analogous expression for Σ_1. For the second function F_1 we can use the expression

$$F_1(\kappa+\kappa_1)=\frac{2T\gamma_0}{\omega_0\{[\omega(|\mathbf{k}+\mathbf{k}_1|)-\omega-\omega_1]^2+\gamma_0^2(2k_0)\}}. \tag{49}$$

We can then write Eq. (48) in the form

$$(\Phi_1(\kappa))_1\sim\frac{V^2}{\Omega}\int\frac{d\omega_1 d\mathbf{k}_1}{(2\pi)^4}F_1(\kappa_1)\int d\Omega F(\kappa+\kappa_1). \tag{50}$$

The first integral was found in (39); for the second integral we have

$$\int d\Omega F(\kappa+\kappa_1)=\frac{T\mu}{\omega_0 V^2}. \tag{51}$$

Thus, for the force function we have

$$(\Phi_1)_1\sim V^2\frac{Tn}{\omega_0\sqrt{\omega_0\gamma_0}} \tag{52}$$

and

$$\frac{(\Phi_1)_1}{\Phi_{10}}\sim\frac{\mu nT}{\omega_0}\,\frac{\omega_0}{T\gamma_0}\propto\epsilon. \tag{53}$$

This correction is small near the excitation threshold. Therefore, in a one-loop approximation it is possible to consider only the broadening of parametrically excited waves due to the thermal fluctuations. Thermal width of the spectrum is very small, and its dependence on pumping does not agree with the experiment. This means that it is necessary to use a two-loop approximation in order to describe experimentally observed broadening of the spectrum.

6. TWO-LOOP CORRECTIONS

To study the broadening of excited sound waves due to their scattering we must take into account the two-loop corrections for the mass operators: the self-energy function Σ and the force function Φ. These corrections for Σ_1 and Σ_2 can be represented by the diagrams in Fig. 4.

Their analytical representation is

$$\begin{aligned}\Sigma_1(\kappa)=8V^4\int\frac{d^4k_1d^4\kappa_2}{(2\pi)^8}&[G_1^*(\kappa_1)F_1(\kappa_2)F_1\\&\times(\kappa_1+\kappa-\kappa_2)G(\kappa+\kappa_1)G^*(\kappa+\kappa_1)\\&+2G_1(\kappa_1)F_2(\kappa_2)F_2^*(\kappa_1+\kappa_2-\kappa)G\\&\times(\kappa_1+\kappa_2)G(\kappa-\kappa_2)],\\ \Sigma_2(\kappa)=8V^4\int\frac{d^4\kappa_1d^4\kappa_2}{(2\pi)^8}&[G_2^*(\kappa_1)F_2(\kappa_2)F_2\\&\times(\kappa_1+\kappa-\kappa_2)G(\kappa+\kappa_1)G(-\kappa-\kappa_1)\\&+2G_2(\kappa_1)F_1(\kappa_2)F_1(\kappa_1+\kappa_2-\kappa)G\\&\times(\kappa_1+\kappa_2)G^*(\kappa_2-\kappa)].\end{aligned} \tag{54}$$

The corresponding diagrams for Φ_1 and Φ_2 are presented in Figs. 5 and 6. Analytically, we have

$$\begin{aligned}\Phi_1(\kappa)=8V^4\int\frac{d^4\kappa_1d^4\kappa_2}{(2\pi)^8}&[F_1(\kappa_1)F_1(\kappa_2)F_1\\&\times(\kappa_1+\kappa-\kappa_2)G(\kappa+\kappa_1)G^*(\kappa+\kappa_1)\\&+2F_1(\kappa_1)F_2(\kappa_2)F_2^*(\kappa_1+\kappa_2-\kappa)G\\&\times(\kappa_1+\kappa_2)G^*(\kappa-\kappa_2)],\\ \Phi_2(\kappa)=8V^4\int\frac{d^4\kappa_1d^4\kappa_2}{(2\pi)^8}&[F_2^*(\kappa_1)F_2(\kappa_2)F_2\\&\times(\kappa_1+\kappa-\kappa_2)G(\kappa+\kappa_1)G(-\kappa-\kappa_1)\end{aligned}$$

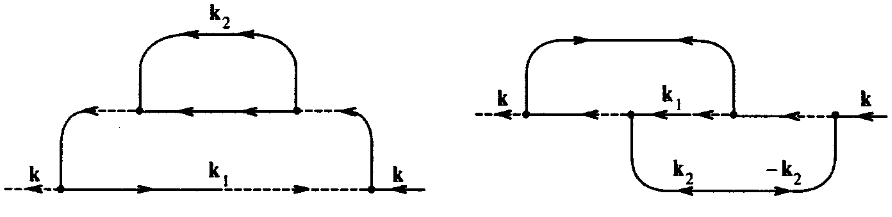

FIG. 4. Two-loop corrections for the normal self-energy function.

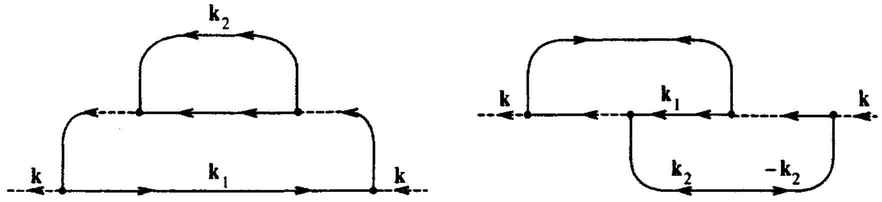

FIG. 5. Two-loop corrections for the normal force function.

$$+2F_2(\kappa_1)F_1(\kappa_2)F_1^*(\kappa_1+\kappa_2-\kappa)G \times(\kappa_1+\kappa_2)G(\kappa_2-\kappa)]. \tag{55}$$

It is easy to verify that the expressions for $\Phi_1(\kappa)$ and $\Phi_2(\kappa)$ satisfy the properties $\Phi_1(\kappa)=\Phi_1^*(\kappa)$ and $\Phi_2(\kappa)=\Phi_2\overline{(\varkappa)}$.

The corrections for the Green's functions and for the correlation functions, represented by the second terms in Eqs. (54) and (55), can be disregarded. In fact, it is necessary to take into account only the diagrams which contain the correlation functions $F(\omega)$ with $\omega\sim\omega_0$ and the Green's functions $G(\omega)$ with $\omega\sim\omega_0$ or $\omega\sim2\omega_0$. It is impossible to satisfy these conditions for the corrections mentioned above. The first correction term for $\Phi_2(\Sigma_2)$ will then be significantly smaller than the corresponding term for $\Phi_1(\Sigma_1)$, because the distance between the poles of the corresponding Green's functions is of the order of $2\omega_0$ in the first case and of the order of $8\gamma_0$ in the second case. This means that we can rewrite Eqs. (54) and (55) in the form

$$\Sigma_1(\kappa)=8V^4\int\frac{d^4\kappa_1d^4\kappa_2}{(2\pi)^8}G_1^*(\kappa_1)F_1(\kappa_2)F_1 \times(\kappa_1+\kappa-\kappa_2)G(\kappa+\kappa_1)G^*(\kappa+\kappa_1),$$

$$\Sigma_2(\kappa)\simeq0 \tag{56}$$

and

$$\Phi_1(\kappa)=8V^4\int\frac{d^4\kappa_1d^4\kappa_2}{(2\pi)^8}F_1(\kappa_1)F_1(\kappa_2)F_1 \times(\kappa_1+\kappa-\kappa_2)G(\kappa+\kappa_1)G^*(\kappa+\kappa_1),$$

$$\Phi_2(\kappa)\simeq0. \tag{57}$$

Here and below the functions $G(\kappa)$ have the frequencies $\omega\sim2\omega_0$; therefore, we can use for them the expression (16).

Equations (56) and (57) mean that in a two-loop approximation we have a situation similar to a one-loop approximation. It turns out that the corrections for the abnormal self-energy and for the abnormal force functions are significantly smaller than the corresponding corrections for the normal functions. The corrections for the self-energy functions can be used if we replace

$$\gamma_0(\kappa)\rightarrow\gamma(\kappa)=\gamma_0(\kappa)+\mu n+\mathrm{Im}\ \Sigma_1(\kappa))_2 \tag{58}$$

and if we use Eqs. (14) and (15). Here we took into account the tree correction for the self-energy function, shown in Fig. 1. Analogously, the corrections for the correlation functions can be taken into account if we replace

$$\Gamma_0(\kappa)\rightarrow\Gamma(\kappa)=\Gamma_0(\kappa)+\Phi_1(\kappa) \tag{59}$$

and if we use Eq. (23). In the last equation it is possible to ignore both the first term and the one-loop correction for the force function Φ_1, because they are very small.

Thus, we obtain the following equation for the two-loop correction for the self-energy functions:

$$(\Delta\gamma)_2=-8V^4\int\frac{d^4\kappa_1d^4\kappa_2}{(2\pi)^8}\frac{(ck_1+\omega_1-2\omega_0)^2+\gamma^2-\lambda^2}{\Delta(\kappa_1)\Delta^*(\kappa_1)} \times\gamma(k_1)F_1(\kappa_2)F_1(\kappa_1+\kappa-\kappa_2)G(\kappa+\kappa_1)G^* \times(\kappa+\kappa_1). \tag{60}$$

The corresponding equation for the force function has the form

$$\Gamma(\kappa)=8V^4\int\frac{d^4\kappa_1d^4\kappa_2}{(2\pi)^8}F_1(\kappa_1)F_1(\kappa_2) \times F_1(\kappa_1+\kappa-\kappa_2)G(\kappa+\kappa_1)G^*(\kappa+\kappa_1). \tag{61}$$

First, let us consider the case in which the excited sound wave is spherical. It is easy to integrate in (60) and (61) over the angles $\vartheta(\mathbf{k}_1,\mathbf{k})$ and $\varphi(\mathbf{k}_1,\mathbf{k})$. The only factor in these expressions, which depends on the angle ϑ, is $G\times(\kappa+\kappa_1)G^*(\kappa+\kappa_1)$. For the integral we have

$$\int\frac{d\vartheta(\mathbf{k}_1,\mathbf{k})d\varphi(\mathbf{k}_1,\mathbf{k})\sin\vartheta}{[\omega(\mathbf{k}+\mathbf{k}_1)-\omega-\omega_1]^2+16\gamma_0^2}=\frac{\pi^2}{2\omega_0\gamma_0}. \tag{62}$$

Note that it is proportional to γ_0^{-1} and therefore this expression is significantly greater than the analogous term for the direct fourth vertex. This statement is true irrespective of the shape of the excited sound wave. This means that broadening of the spectrum of parametrically excited acoustic wave is determined by the three-wave interaction.

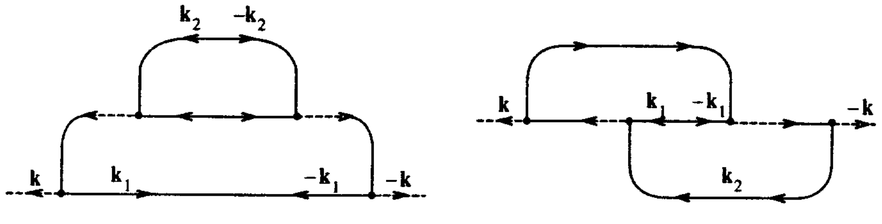

FIG. 6. Two-loop corrections for the abnormal force function.

Substituting expression (62) in (60) and (61), we obtain the system of equations

$$\gamma(\kappa)=\gamma_0+\mu n-C$$

$$\times\int \frac{d\omega_1 dk_1 d\omega_2 dk_2 d\theta \sin\,\theta}{(2\pi)^8}\,\gamma(k_1)$$

$$\times\frac{ck_1+\omega_1-2\omega_0)^2+\gamma^2-\lambda^2}{\Delta(\kappa_1)\Delta^*(\kappa_1)}\,F_1(\kappa_2)F_1$$

$$\times(\kappa_1+\kappa-\kappa_2),$$

$$\Gamma(\kappa)=C\int \frac{d\omega_1 dk_1 d\omega_2 dk_2 d\theta \sin\,\theta}{(2\pi)^8}$$

$$\times F_1(\kappa_1)F_1(\kappa_2)F_1(\kappa_1+\kappa-\kappa_2), \tag{63}$$

where $\theta\equiv\theta(\mathbf{k}_1+\mathbf{k},\mathbf{k}_2)$, and $C=\mu_3 V^2 k_0^4/2\gamma_0$.

As we will see below, the two-loop correction for the damping rate γ is not very important. Let us, therefore, first consider the correction for the force function. It is necessary to use the integrals over k_1, k_2, and θ. Experiment shows that broadening of parametrically excited waves is significantly smaller than $\gamma\sim\lambda$. Therefore, we can write

$$\gamma^2(k)-\lambda^2\equiv\nu^2,\quad \nu\ll\lambda,$$

$$\Delta(k)=(ck-\omega_0)^2-\tilde{\omega}^2+\nu^2-2i\gamma\tilde{\omega}. \tag{64}$$

The characteristic value of $ck-\omega_0$ is of the order of ν and the characteristic value of $\tilde{\omega}$ is of the order of $\nu^2/2\gamma\ll\nu$. It is easy to see that the dependence of $\Gamma(\omega,\mathbf{k})$ on the wave vector $\mathbf{k}$ is smooth, while its dependence on the frequency ω is singular. Therefore, integrating in (63) over k_1, k_2, and θ, we can assume Γ to be a constant, and the corresponding integrals are determined by the poles of $\Delta(k)\Delta^*(k)$. The integral over the angle $d\Omega=d\theta d\phi\sin\theta$ is

$$\int d\Omega\; F_1(\mathbf{k}_1+\mathbf{k}-\mathbf{k}_2)=\frac{\pi^2(\gamma^2+\lambda^2)}{2\omega_0\nu^3}\,\frac{\Gamma(\omega_1+\omega-\omega_2)}{f(\zeta)},$$

$$\zeta=\omega_1+\omega-\omega_2-\omega_0, \tag{65}$$

where $f(\zeta)$ and r are determined by (46). For $\zeta\sim\nu^2/2\gamma$ the function f can be written as

$$f(\zeta)=\frac{1}{\sqrt{2}}\,\sqrt{1+(2\gamma\zeta\nu^{-2})^2}\sqrt{\sqrt{1+(2\gamma\zeta\nu^{-2})^2}+1}. \tag{66}$$

It is easy to see that $f(\zeta)$ is an even function and that $f(0)=1$.

The integral over k_1 gives

$$\int dk_1 F_1(\mathbf{k})=\frac{\pi(\gamma^2+\lambda^2)}{2c\nu^3}\,\frac{\Gamma(\omega_1)}{f(\tilde{\omega}_1)}. \tag{67}$$

Thus we obtain the following equation for $n(\omega)$:

$$f(\tilde{\omega})n(\omega)=C_3\int d\omega_1 d\omega_2 n(\omega_1)n(\omega_2)n(\omega_1+\omega-\omega_2),$$

$$C_3=\frac{\mu_3^2(\gamma^2+\lambda^2)}{8\gamma_0\nu^3}, \tag{68}$$

where μ_3 is determined by (34).

Analogous equation was obtained for the distribution of parametrically excited spin waves.[3] It is easy to solve this equation for $f(x)=1+(x/\eta)^2$. In this case the solution is

$$n(\omega)=(\sqrt{2C_3}\,\eta\,\cosh(\pi\tilde{\omega}/2\eta))^{-1}.$$

General consideration shows that for our functions $f(x)$, which have no singularities in the immediate vicinity of the real axes, the solution of Eq. (68) has a symmetrical form with the center at $\tilde{\omega}=0$ and exponential frequency asymptotics. The characteristic width of the distribution can be estimated in the following way. Since $n=\int d\omega n(\omega)\simeq\sqrt{2/C_3}$, using the equation for equilibrium density of the sound wave (32), we obtain

$$\mu_3 n=\epsilon\gamma_0\simeq\sqrt{\frac{16\gamma_0\nu^3}{\gamma^2+\lambda^2}}. \tag{69}$$

Numerical coefficient in this equation cannot be found analytically; it is of the order of unity. Thus,

$$\nu\simeq\left(\frac{\gamma_0\epsilon^2}{8}\,\frac{\gamma^2+\lambda^2}{2}\right)^{1/3}. \tag{70}$$

We obtain

$$(\Delta\omega)_3\simeq\frac{1}{4\pi\gamma}\left(\gamma_0\epsilon^2\,\frac{\gamma^2+\lambda^2}{2}\right)^{2/3}. \tag{71}$$

Analogously, it is possible to obtain the corresponding equations for the excited cylindrical sound wave. The equation for n is

$$f(\tilde{\omega})n(\omega)=C_2\int d\omega_1 d\omega_2 n(\omega_1)n(\omega_2)n$$

$$\times(\omega_1+\omega-\omega_2)\tilde{f}(\zeta),$$

$$C_2=\frac{\mu_2^2(\gamma^2+\lambda^2)}{16\sqrt{\gamma_0\nu^7}},\quad \tilde{f}(\zeta)=\sqrt{\frac{1}{r}+\frac{\gamma|\zeta|}{\nu^2 f(\zeta)}}, \tag{72}$$

where μ_2 is determined by (37), and r is determined by (46). Equation (72) has the same asymptotic form as the corresponding Eq. (68) for a spherical wave. This means that the asymptotic properties of the solution of this equation are the same as for Eq. (68). By analogy with Eqs. (69)–(71), we can obtain for an excited cylindrical sound wave

$$\mu_2 n=\epsilon\gamma_0\simeq 4(\gamma_0\nu^7)^{1/4}\sqrt{\frac{2}{\gamma^2+\lambda^2}},$$

$$(\Delta\omega)_2\simeq\frac{\nu^2}{\pi\gamma}\simeq\frac{(\gamma_0^6\epsilon^8)^{1/7}}{4\pi\gamma}\left(\frac{\gamma^2+\lambda^2}{2}\right)^{4/7}. \tag{73}$$

Let us consider the one-dimensional case of a flat sound wave. In this case the dependence of Γ on k is not smooth. We can obtain the following equation for $n(\omega,k)$:

$$\tilde{f}(\omega,k)n(\omega,k)=C_1\int dk_1 d\omega_1 dk_2 d\omega_2 n(\omega_1,k_1)$$

$$\times n(\omega_2,k_2)n(\omega_1+\omega-\omega_2,k_1+k-k_2),$$

$$\tilde{f}(\omega,k)n(\omega,k)=\left[1+\left(\frac{ck-\omega_0}{\nu}\right)^2\right]^2+\left(\frac{2\gamma\tilde{\omega}}{\nu^2}\right)^2,$$

$$C_1=\frac{\mu_1^2}{32}\,\frac{\gamma^2+\lambda^2}{\nu^4}, \tag{74}$$

where μ_1 is determined by (36). Equation (74) means that

$$\mu_1 n=\epsilon\gamma_0\simeq 8\,\nu^2\sqrt{\frac{1}{\gamma^2+\lambda^2}}. \tag{75}$$

For the width of a sound spectrum we have

$$(\Delta\omega)_1\simeq\frac{\gamma_0\epsilon}{8\pi\gamma}\sqrt{\gamma^2+\lambda^2}. \tag{76}$$

Note that numerical coefficients in expressions (71), (73), and (76) are not correct; these equations are only estimates for the corresponding widths. It is necessary to solve the corresponding nonlinear equations numerically in order to determine accurate values of the coefficients.

Let us now estimate the two-loop correction for the self-energy function. It is easy to obtain from the first equation in (63):

$$\frac{(\Delta\gamma)_2}{(\Delta\gamma)_1}\sim\frac{1}{16}\,\epsilon^{1/7}. \tag{77}$$

We see that the two-loop correction is small numerically, and that it materially does not change the general picture. This result is logical, because the conservation laws allow us to obtain a not small one-loop correction for the self-energy function. It turns out that the corresponding two-loop correction is not essential. For the force function the one-loop correction is small. It is therefore necessary to take into account the two-loop corrections.

7. COMPARISON WITH THE EXPERIMENT

Let us compare the theory with the experiment.[5,6] Experimental studies[5,6] were performed for parametric generation of a second-sound wave by a first-sound wave in liquid helium near the superfluid transition temperature. The canonical variables for this system were found by Pokrovskii and Khalatnikov,[8] who calculated the triple vertex U of the first- and second-sound interaction (the correct vertex is greater than that found by Pokrovskii and Khalatnikov by a factor of 2, in agreement with the result of Lebedev[13]). The correct expression for this vertex is

$$U=\frac{1}{c_1}\sqrt{\frac{\omega_1^3}{32\rho}}\left[\frac{1}{\rho}\,\frac{P_{\sigma\sigma}}{T_\sigma}-\frac{\rho}{\rho_s}\left(\frac{\partial\rho_s}{\partial\rho}\right)_\sigma\right]. \tag{78}$$

Here ρ and ρ_s are the total and the superfluid density of liquid helium, P and T are the pressure and temperature, ω_1 is the frequency of the first sound, c_1 its velocity, $\sigma=S/\rho$; $T_\sigma=(\partial T/\partial\sigma)_\rho$, etc. For experimental conditions of Refs. 5 and 6, it is possible to ignore the weak dependence of this vertex on the angle between the wave vectors, which is small as ρ_s/ρ. Expression (78) can be rewritten in the variables P, and T in the following way:

$$U=\frac{1}{c_1}\sqrt{\frac{\omega_1^3}{32\rho}}\,(U_1+U_2), \tag{79}$$

where

$$U_1=-\frac{\rho}{J\phi}\left(\frac{C_P}{T}\,\frac{\partial\phi}{\partial P}+\frac{\beta_P}{\rho}\,\frac{\partial\phi}{\partial T}\right),$$

$$U_2=\rho^{-1}\left(\frac{\partial\psi}{\partial T}+\frac{\beta_P}{\kappa_T}\,\frac{\partial\psi}{\partial P}\right). \tag{80}$$

Here we introduce the notation

$$\phi=\frac{\rho_s}{\rho},\quad \psi=\frac{\rho\beta_P}{J},\quad J=\frac{\rho\kappa_T C_P}{T}-\beta_P^2,$$

$$\kappa_T=\frac{1}{\rho}\left(\frac{\partial\rho}{\partial p}\right)_T,\quad C_P=T\left(\frac{\partial\sigma}{\partial T}\right)_P,$$

$$\beta_P=-\rho\left(\frac{\partial\sigma}{\partial P}\right)_T=-\frac{1}{\rho}\left(\frac{\partial\rho}{\partial T}\right)_P. \tag{81}$$

Here ω_2 and c_2 are the frequency and the velocity of the second sound. These equations permit us to use the results of Ref. 14 to calculate this vertex.

Using the Pokrovskii–Khalatnikov equations for the canonical variables, we obtain the following expression for the triple vertex of the second-sound interaction:

$$V(\theta)=\sqrt{\frac{\omega_2}{16\rho T_\sigma}}\left\{\frac{T_{\sigma\sigma}}{T_\sigma}+\frac{1}{\rho_s}\left(\frac{\partial\rho_s}{\partial\sigma}\right)_\rho[\cos(2\theta)-2\cos\,\theta]\right\}, \tag{82}$$

where θ is the angle between the wave vectors of the second-sound waves. This vertex can be written in the variables P, and T as

$$V(\theta)=\sqrt{\frac{\omega_2^3}{16\rho}}\,X,$$

$$X=\sqrt{\chi}\left\{\frac{1}{\chi}\,\hat{D}(\chi)+\frac{1}{\phi}\,\hat{D}(\phi)[\cos(2\theta)-2\cos\,\theta]\right\}, \tag{83}$$

where

$$\chi=\frac{\rho\kappa_T}{J},\quad \hat{D}=\frac{\partial}{\partial T}+\frac{\beta_P}{\kappa_T}\,\frac{\partial}{\partial P}.$$

It is possible to compare the experimental results with theory for three parameters: the threshold of the second sound excitation, the equilibrium intensity of the second-sound over the threshold, and the form of the spectrum of the excited waves. The ratio of the velocities of the pumping first-sound wave and the excited second sound waves was about 10^{-2} in Ref. 5. The pumping wave was a standing wave. These results lead to a generation of cylindrical (or perhaps flat) but not spherical second-sound waves. It is possible to see that an accurate comparison of the data on the excitation threshold with Eqs. (27), (79), and (80) gives a good agreement, significantly better than that in Ref. 5. It is necessary to point out, however, that for the experiment[5] Eq. (27) must be modified. A special geometry of the experimental cell and pumping by a standing wave lead to the following modified equation for the excitation threshold:

$$|a|=\gamma_0/\sqrt{2}U.$$

A correlation of the second-sound waves for intermediate angles between the wave vectors was not observed experimentally. This result agrees with our assertion about the absence of long-range order at the angle for parametrically generated sound waves.

The thermal width near the threshold can be easily estimated for a given experiment.[5] In fact,

$$(\Delta\omega)_T = \frac{K\Gamma_0}{\sqrt{\gamma^2-\lambda^2}} \sim \mu \frac{\omega_0\gamma_0 T}{4\pi^2 c_2^3} \sim \gamma_0 \frac{\omega_0\gamma_0 T}{4\pi^2 c_2^3 n}. \tag{84}$$

The value of n can be found from the second-sound intensity $\tilde{I}$:

$$\tilde{I} = c_2\omega_2 n,$$

and we have

$$(\Delta\omega)_T = \gamma_0 \frac{\omega_0^2\gamma_0 T}{4\pi^2 c^2 \tilde{I}} \sim \gamma_0 \frac{\gamma_0 T}{\lambda_2^2 \tilde{I}}. \tag{85}$$

For the values

$$\gamma_0 \sim 25\ \mathrm{s}^{-1}, \quad \lambda_2 \sim 10^{-4}\ \mathrm{m}, \quad I \sim 10^{-5}\ \mathrm{W/m^2},$$
$$kT \sim 3\times 10^{-23}\ \mathrm{J}$$

we obtain

$$\frac{(\Delta\omega)_T}{\gamma_0} \sim 10^{-8},$$

which is negligible. In a real experiment there are always other sources of noise except temperature. Estimate (85) determines the condition under which it is necessary to take into account such noise source.

Experimental shape of the second-sound spectrum strongly fluctuates. For good experimental results it can be universally described as a symmetrical spectral line with exponential tails. The width of this spectral line is proportional to ϵ^α with $\alpha \sim 1-1.2$. This result agrees well with Eqs. (73)–(76).

The results for the intensity of the second-sound waves are not yet fully understood. Experimental values are significantly smaller than theoretical expressions (37) and (38). The reason for this discrepancy is not known. It was shown, in particular, that the intensity of the excited sound wave depends strongly on its shape. The excited second-sound wave in Ref. 5 is not spherical due to the pumping by a standing wave. Unfortunately, experimental information does not allow us to draw definite conclusion about the shape of a parametrically generated sound wave.

8. CONCLUSIONS

The theory of parametric excitation of sound waves considered by us differs significantly from the standard theory of spin waves.[3] The most important difference is that three-wave interaction is allowed for sound waves. This three-wave interaction produces nonlinear attenuation of the sound wave and determines the saturated value of the amplitude of an excited wave. The intensity of a parametrically excited sound wave is proportional to the difference between the value of pumping and bare attenuation rate of a sound wave, $\epsilon = \lambda/\gamma_0 - 1$.

Three-wave interaction between sound waves is essential only if the angle between their wave vectors is smaller than $4\sqrt{\gamma_0/\omega}$. This property destroys long-range order over the angle between waves and accounts for the absence of ordinary pattern formation. The total intensity of a parametrically excited sound wave crucially depends on the shape of the wave. It is maximal for a spherical wave and minimal for a flat wave. The shape of an excited wave is determined by the symmetry of the system (boundary conditions), by the shape of the pumping wave, and by the properties of the interaction vertex between the pumping wave and the sound waves. It is expected that the symmetry of an excited sound wave will be the same as the symmetry of a system due to the peculiar interaction between sound waves.

The spectrum of parametrically excited sound waves is similar to the spectrum of other waves. Thermal broadening of the spectrum is negligible for the experiment in Ref. 6. Significant broadening of the spectrum of excited waves takes place as a result of their scattering. The structure of a nonlinear integral equation, which determines the shape of the spectrum of sound waves, is similar to the structure of analogous equations for waves with other dispersion relations. This fact leads to universal shape of the spectrum with exponential asymptotic behavior over the frequency. The width of the spectrum essentially depends on the shape of the wave. Roughly, it is estimated as $\Delta\omega \sim \gamma_0\epsilon^\alpha/4\pi$. Here γ_0 is the bare damping rate of a sound wave, and the value of the parameter α depends on the shape of the wave. For a flat wave $\alpha = 1$, for a cylindrical wave $\alpha = 8/7$, and for a spherical wave $\alpha = 8/6$, whereas the corresponding index for spin waves is equal to 2/3.

I am deeply grateful to V. Lebedev for many useful discussions. I wish to thank D. Rinberg, V. Steinberg, and G. Falkovich for many discussions of the various aspects of the experimental studies[5,6] and for their hospitality. This work was supported, in part, by the Minerva Center for Nonlinear Physics, INTAS (grant No. 94-4078) and Russian Fund for Fundamental Research (Grant No. 96-02-18235).

[1] M. C. Cross and P. C. Hohenberg, Rev. Mod. Phys. **65**, 851 (1993).
[2] V. E. Zaharov, V. S. L'vov, and S. Starobinetz, Zh. Éksp. Teor. Fiz. **59**, 1200 (1970) [Sov. Phys. JETP **32**, 656 (1971)].
[3] V. S. L'vov, Wave Turbulence under Parametric Excitation, Springer-Verlag, Berlin (1994).
[4] W. Zhang and J. Vinals, submitted to J. Fluid. Mech.
[5] D. Rinberg, V. Cherepanov, and V. Steinberg, Phys. Rev. Lett. **76**, 2105 (1996).
[6] D. Rinberg, V. Cherepanov, and V. Steinberg, Phys. Rev. Lett. **78**, (1997).
[7] G. M. Zaslavskii and R. Z. Sagdeev, Introduction to Nonlinear Physics [in Russian], Nauka, Moscow (1988).
[8] V. L. Pokrovskii and I. M. Khalatnikov, Zh. Éksp. Teor. Fiz. **71**, 1974 (1976) [Sov. Phys. JETP **44**, 1036 (1976)].
[9] H. W. Wyld, Ann. Phys. **14**, 143 (1961).
[10] C. De Dominicis, J. de Phys. Colloque **37**, 247 (1976).

[11] H. K. Janssen, Z. Phys. B **23**, 377 (1976).
[12] E. I. Kats and V. V. Lebedev, Fluctuational Effects in the Dynamics of Liquid Crystals, Springer-Verlag, New York (1994).
[13] V. V. Lebedev, Zh. Éksp. Teor. Fiz, **72**, 2224 (1977) [Sov. Phys. JETP **45**, 1169 (1977)].
[14] G. Ahlers, in The Physics of Liquid and Solid Helium, ed. by K. H. Bennemann and J. B. Ketterson, John Wiley & Sons, New York (1976), p. 85.

Published in English in the original Russian journal. Reproduced here with stylistic changes by the Translation Editor.

The renormalization group in the problem of turbulent convection of a passive scalar impurity with nonlinear diffusion

N. V. Antonov*)

St. Petersburg State University, 199034 St. Petersburg, Russia

(Submitted 7 August 1996)
Zh. Éksp. Teor. Fiz. **112**, 1649–1663 (November 1997)

The problem of turbulent mixing of a passive scalar impurity is studied within the renormalization-group approach to the stochastic theory of developed turbulence for the case where the diffusion coefficient is an arbitrary function of the impurity concentration. Such a problem incorporates an infinite number of coupling constants (''charges''). A one-loop calculation shows that in the infinite-dimensional space of the charges there is a two-dimensional surface of fixed points of the renormalization-group equations. When the surface has an IR-stability region, the problem has scaling with universal critical dimensionalities, corresponding to the phenomenological laws of Kolmogorov and Richardson, but with nonuniversal (i.e., depending on the Prandtl number and the explicit form of the nonlinearity in the diffusion equation) scaling functions, amplitude factors in the power laws, and value of the ''effective Prandtl turbulence number.'' [S1063-7761(97)00911-6]

1. INTRODUCTION

The stochastic formulation of the theory of an isotropic developed turbulence in an incompressible viscous liquid uses the Navier-Stokes equation with an external random force (see the monographs of Monin and Yaglom[1] and McComb[2] and the review by Adzhemyan *et al.*[3]):

$$\mathscr{D}_t\varphi_i-\nu_0\partial^2\varphi_i+\partial_i p-f_i=0,\quad \mathscr{D}_t\equiv\partial_t+(\varphi\cdot\partial). \tag{1}$$

Here $\mathscr{D}_t$ is the Galilean-covariant derivative, φ is the transverse (in view of the incompressibility condition $\partial_i\varphi_i=0$) vector velocity field, p and f are the pressure and the transverse random force per unit mass (all these quantities depend on $x\equiv(t,\mathbf{x})$), ν_0 is the kinematic viscosity coefficient, and ∂^2 is the Laplacian. The force f_i is assumed to have a Gaussian distribution with a zero mean and a correlator

$$\langle f_i(x)f_j(x')\rangle=\frac{\delta(t-t')}{(2\pi)^d}\int d\mathbf{k}P_{ij}(\mathbf{k})d^{\varphi}(k)e^{i\mathbf{k}\cdot(\mathbf{x}-\mathbf{x}')}, \tag{2}$$

where $P_{ij}(\mathbf{k})=\delta_{ij}-k_ik_j/k^2$ is the transverse projector, $d>2$ is the arbitrary (for the sake of generality) dimensionality of the space $\mathbf{x}$, and $d^{\varphi}(k)$ is a function of $k\equiv|\mathbf{k}|$ and the model parameters. This function can be chosen in the form

$$d^{\varphi}(k)=D_0k^{4-d-2\epsilon}h\left(\frac{m}{k}\right),\quad h(0)=1,\quad D_0\equiv g_0\nu_0^3, \tag{3}$$

where $g_0>0$ is the bare coupling constant (''charge''), h is a fairly smooth but otherwise arbitrary function, $m\equiv1/L$ is the reciprocal external turbulence scale, $\epsilon\geqslant0$ is the renormalization-group expansion parameter, similar to $\epsilon=4-d$ in the theory of critical phenomena,[4] with a logarithmic value $\epsilon=0$. The random force models the interaction with large-scale ($k\sim m\equiv1/L$) movements, so that its physical range of values is $\epsilon\geqslant2$ (for more details see Refs. 3 and 5). For $\epsilon>2$ the problem arises of studying the dependence of the correlation functions on m, which proves to be quite nontrivial because of the presence in the theory of ''dangerous'' composite fields with negative critical dimensionalities.[5] Hence in what follows we limit our discussion to the region $0<\epsilon\leqslant2$, taking the limit $\epsilon=2$ of ''IR-pumping'' as the physical value of ϵ, as is done in the majority of papers on the renormalization-group theory of turbulence. Note that at $\epsilon=2$ the function (3) can be interpreted as a power model of the function $\delta(\mathbf{k})$.

De Dominicis and Martin[6] used the renormalization-group method to prove the existence in the problem (1)–(3) of IR scaling with exactly known critical dimensionalities

$$\Delta_{\varphi}=1-\frac{2\epsilon}{3},\quad \Delta_{\varphi'}=d-1+\frac{2\epsilon}{3},$$
$$\Delta_t=-\Delta_{\omega}=-2+\frac{2\epsilon}{3},\quad \Delta_m=1, \tag{4}$$

which at $\epsilon=2$ coincide with the well-known Kolmogorov values

$$\Delta_{\varphi}=-\tfrac{1}{3},\quad \Delta_{\varphi'}=d+\tfrac{1}{3},\quad \Delta_t=-\Delta_{\omega}=-\tfrac{2}{3},\quad \Delta_m=1 \tag{5}$$

(the auxiliary field φ' appears in the quantum-field formulation of the problem; see Sec. 2). The ''freezing'' of the dimensionalities[6] at their Kolmogorov values over the entire physical range $\epsilon\geqslant2$ and the fact that the correlation functions are independent of viscosity in the inertial interval (Kolmogorov's second hypothesis) were proved by Adzhemyan *et al.*[5]

Adzhemyan *et al.*[7] applied the renormalization-group technique to the problem of turbulent convection of a passive scalar impurity. In this case the problem (1)–(3) is supplemented by a diffusion equation (or by a heat equation in the heat transfer problem) of the form[1,2]

$$\mathscr{D}_t\theta=\partial_iJ_i+f^{\theta}, \tag{6}$$

where $\theta\equiv\theta(x)$ is the random component of the impurity concentration field (temperature). Adzhemyan *et al.*[7] considered a simplified version of the problem (6) without the random force f^θ, and the current J_i was chosen in the simplest form $J_i=u_0\nu_0\partial_i\theta$, where u_0 is the reciprocal Prandtl number. For such a problem Adzhemyan *et al.*[7] proved the existence of IR scaling, justified Richardson's phenomenological $\frac{4}{3}$-law,[1] and obtained the following expression for the effective reciprocal Prandtl number u_* in the IR asymptotic limit:

$$u_*=\frac{1}{2}\left(-1+\sqrt{1+\frac{8(d+2)}{d}}\right)+O(\epsilon).$$

In the papers[8–16] that followed, the results of Ref. 7 were reproduced and augmented, in particular, by calculations of the Batchelor constant in the passive impurity spectrum,[8–10] by studies of chemically decaying impurities,[13,14] and by allowing for anisotropy.[15,16]

In the present paper we will study the problem (6) in the presence of a random force and a current J_i of general form.

In view of the isotropy we have $\langle f_i f^\theta\rangle=0$ and the correlator

$$\langle f^\theta(x)f^\theta(x')\rangle=\frac{\delta(t-t')}{(2\pi)^d}\int d\mathbf{k}d^\theta(k)e^{i\mathbf{k}\cdot(\mathbf{x}-\mathbf{x}')} \tag{7}$$

can be written in the form (we will justify this later)

$$d^\theta(k)=D_0'k^2(k^2+m^2)^{-d/2-\alpha\epsilon}. \tag{8}$$

The exponent in (8) is selected in such a way that at $\epsilon=0$ both nonlinearities (''interactions'') in (6) are logarithmic (see Sec. 2), since otherwise one nonlinearity would be ''weaker'' (from the standpoint of the renormalization group) than the other and would provide only corrections to IR scaling, corrections which should be ignored in the leading term of the IR asymptotic limit (similar ideas were developed in Refs. 13 and 17). The most ''realistic'' value of an additional new parameter $\alpha>0$ should be considered equal to 1/2; then at $\epsilon=2$ we will have $d^\varphi,d^\theta\propto k^{-d}$ simultaneously for $k\gg m$. The parameter m guarantees IR regularization of perturbation diagrams.

Like the force f_i in Eq. (1), the random contribution f^θ to (6) models the interaction between the $k\gg m$ modes (for which the statistical model (1) and (6) is assumed meaningful) and the large-scale region $k\leqslant m$. In the case at hand the substance of the impurity ''disappears'' in the regions with $f^\theta<0$ and ''appears'' in the regions with $f^\theta>0$, passing in the process through the long-wave region with $k\leqslant m$. Here the conservation of the total amount of impurity (with allowance for the amount present in the long-wave region) is ensured by the condition $d^\theta(k)=0$ at $k=0$. The parameters D_0 and D_0' in the correlators (3) and (8) of the random forces can be expressed, via exact relationships, in terms of quantities that have direct physical meaning, namely, the average rates of energy and impurity-concentration dissipation (see Sec. 5). In analyzing the critical dimensionalities, we can eliminate the ''superfluous'' parameter D_0' in (8) by restretching the fields, so that below (with the exception of Sec. 5) we put $D_0'=1$.

Moreover, the choice of the correlators in the form $\langle f^\theta(t)f^\theta(t')\rangle\propto\delta(t-t')$ is typical of problems of Brownian movement and critical dynamics type (see, e.g., Ref. 4). Of course, the physics of developed turbulence is far from critical dynamics, but here too there are certain arguments in favor of such a choice: first, it corresponds to the maximum entropy principle (see Ref. 18), and second, because of strong IR singularities the two-time correlation function rapidly (superexponentially) increases with the increasing difference $t-t'$, the rate of decrease growing with the external turbulence scale L (see, e.g., Refs. 19 and 20), and if we are not interested in the dependence of these functions on L, we can replace them by the function $\delta(t-t')$.

In the expansion $J_i=\partial_i V_0(\theta)+O(\partial^2)$ of the current J_i in powers of the gradient ∂ we can immediately ignore the contributions containing more than one ∂, as being IR-weak. For the same reason we can ignore the lower bound θ on the value of the field, a bound that follows from the fact that the total impurity concentration is positive. However, we will see that in the expansion

$$V_0(\theta)=\sum_{n=1}^{\infty}\frac{\lambda_{n0}\theta^n}{n!} \tag{9}$$

we can ignore contributions of higher orders in θ in comparison to the first-order contribution $V_0\propto\theta$. Hence the corresponding quantum-field model is ''infinitely charged'' (here the parameters λ_{n0} reduced to dimensionless form act as coupling constants, or ''charges''). This essentially sets our problem apart from ordinary models of the theory of critical behavior of the φ^4 type,[4] where contributions with higher orders of derivatives and fields are found to be IR-unessential. Such an infinitely charged problem has recently been studied in Ref. 21 in the renormalization-group analysis of the stochastic model of a growing phase boundary, proposed in Ref. 22.

The main result achieved in this paper is the proof of multiplicative renormalizability of the quantum-field infinitely charged model corresponding to the problem (1)–(3) and (6)–(9), which makes it possible to apply the renormalization-group technique in the analysis of the IR behavior of the problem. The renormalization constants and the renormalization-group functions are found explicitly in the one-loop approximation by using the functional technique developed in Ref. 21. The corresponding β-functions in the infinite-dimensional space of charges have a two-dimensional surface of fixed points. When this surface has an IR-stability region, the problem has IR scaling with universal critical dimensionalities of fields and parameters, coinciding with those in Refs. 6 and 7 and corresponding to Kolmogorov scaling and the Richardson law at $\epsilon=2$, but with nonuniversal (i.e., depending on the choice of the fixed point or, in other words, on the value of the Prandtl number and the explicit form of the nonlinearity in the diffusion equation) scaling functions, amplitude factors in the power laws (such as the Batchelor constant in the passive impurity spectrum), and value of the ''effective Prandtl turbulence number'' u_*.

2. QUANTUM-FIELD STATEMENT OF THE PROBLEM: ANALYSIS OF ULTRAVIOLET DIVERGENCES

In accordance with a general theorem (see, e.g., Ref. 3), the stochastic problem (1)–(3) and (6)–(9) is the equivalent of the quantum theory of a double set of fields $\Phi\equiv\varphi,\varphi',\theta,\theta'$ with an action functional

TABLE I.

F	φ	φ'	θ	θ'	m,μ	ν,ν_0
d_F^k	-1	$d+1$	$1-\alpha\epsilon$	$d-1+\alpha\epsilon$	1	-2
d_F^ω	1	-1	$-1/2$	$1/2$	0	1
d_F	1	$d-1$	$-\alpha\epsilon$	$d+\alpha\epsilon$	1	0

F	λ_{n0}	λ_n	g_0	g_{n0}	g_n, g
d_F^k	$-(n+1)+(n-1)\alpha\epsilon$	$-(n+1)$	2ϵ	$(n-1)\alpha\epsilon$	0
d_F^ω	$(n+1)/2$	$(n+1)/2$	0	0	0
d_F	$(n-1)\alpha\epsilon$	0	2ϵ	$(n-1)\alpha\epsilon$	0

$$S(\Phi)=S_\varphi(\varphi,\varphi')+\frac{\theta' d^\theta \theta'}{2}+\theta'[-\mathscr{D}_t\theta+\partial^2 V_0(\theta)], \tag{10}$$

where $V_0(\theta)$ is specified in (9), and $S_\varphi(\varphi,\varphi')$ is the action functional[6] for a liquid without an impurity:

$$S_\varphi(\varphi,\varphi')=\frac{\varphi' d^\varphi \varphi'}{2}+\varphi'[-\mathscr{D}_t\varphi+\nu_0\partial^2\varphi]. \tag{11}$$

The nonlocal contribution of the random forces is written symbolically; in what follows the required summation over the field indices and integration over the arguments $x=(t,\mathbf{x})$ in (10), (11), and similar formulas are implied.

The action (10) is assumed to be unrenormalizable and its parameters to be bare; they are labeled by a zero, in contrast to their renormalizable counterparts (see below). The correlation functions (the Green's functions) $G_n=\langle\Phi(x_1)\ldots\Phi(x_n)\rangle$ of the model (10) are functional averages with a weight equal to $\exp S(\Phi)$. They have standard representations in the form of Feynman diagrams; the lines in the diagrams stand for the bare propagators $\langle\Phi\Phi\rangle_0$ determined by the free (quadratic in field) part of the action (10), while the leading (in Φ) terms in $S(\Phi)$ determine the vertices.

As is well known,[23] the analysis of UV divergences is related to the analysis of dimensionalities. In a dynamical model of the form (10), for each quantity F two independent canonical dimensionalities can be introduced, the momentum dimensionality d_F^k and the frequency dimensionality d_F^ω. Using these two dimensionalities, we can find the total dimensionality $d_F=d_F^k+2d_F^\omega$ (see Refs. 3 and 24). By definition, $d_\mathbf{x}^k=d_t^\omega=-1$ and $d_t^k=d_\mathbf{x}^\omega=0$, while the dimensionalities of the other quantities are found from the requirement that all terms in the action (10) be dimensionless (in momentum and frequency, separately). The data on dimensionalities are listed in Table I (it also lists the parameters of the renormalized theory, which we will need later).

We see that all the interactions in (10) and (11) become logarithmic simultaneously ($d_{g_0}=d_{\lambda_{n0}}=0$) at $\epsilon=0$, with the result that they must all be included in the analysis of the IR behavior of the model.

The UV divergences have the form of poles in ϵ in the Green's functions. The total canonical dimensionality of an arbitrary 1-irreducible diagram (the "formal divergence index") is

$$\delta=d+2-\sum_\Phi d_\Phi N_\Phi,$$

where the sum is over all types of field, and N_Φ is the number of the corresponding external legs in the diagram. The counterterms are generated by "surface-divergent" 1-irreducible diagrams; a diagram is surface-divergent if its real divergence index (see below) in the logarithmic theory (i.e., at $\epsilon=0$) is a nonnegative integer, with $\delta(\epsilon=0)$ determining the degree of homogeneity of a counterterm in momenta and frequencies. When analyzing the divergences in the model (10) and (11), the following additional considerations must be taken into account (cf. Refs. 6 and 24):

(1) In view of the passiveness of the impurity, the renormalization of the Green's functions in which only the fields φ and φ' participate is done in same way as for the model without an impurity. It is well known that the renormalization in this case amounts to introducing a counterterm of the form $\varphi'\partial^2\varphi$ or, what is the same thing, to introducing a single renormalization constant Z_ν into the corresponding term in the action (11).

(2) All the 1-irreducible Green's functions with $N_{\varphi'}=N_{\theta'}=0$ vanish.

(3) The operator ∂^2 at a vertex of (10) can be shifted to the field θ' via integration by parts. Hence in any 1-irreducible diagram, with each external leg θ' attached to such a vertex there is associated the square of the corresponding external momentum, and the "real divergence index" δ' (see Ref. 24) will be smaller than the formal divergence index δ by the appropriate number of units. Since the field φ is transverse, the derivative ∂ at the vertex $\theta'(\varphi\partial)\theta$ can be shifted to the field θ'. Hence each external leg θ or θ' attached to such a vertex is associated with a single momentum. Thus, in any 1-irreducible diagram, each external leg θ' is associated with at least a single momentum, and the index δ' obeys the conditions $\delta-2N_{\theta'}\leqslant\delta'\leqslant\delta-N_{\theta'}$.

(4) The Galilean invariance of the model (10) and (11) also implies that the necessary counterterms are invariants. In particular, the covariant derivative $\mathscr{D}_t$ must enter into the counterterms as single entity.

Taking these considerations into account, we can verify that in our model surface divergences in the Green's functions with impurity fields can appear only in the 1-irreducible diagrams $\theta'\theta\cdots\theta$ with any finite number of fields θ. For all these diagrams we have $\delta=2$ and $\delta'=0$, and the corresponding counterterms are sure to contain $\partial_i\theta'$ and thus can always be reduced to $\theta' \partial^2 \theta^n$ (other variants of the arrangement of gradients or the participation of $\mathscr{D}_t$ and m are forbidden). Hence renormalization of the model (10) and (11) generates counterterms only in the form of the structures already present in the action functional, which means that the theory under consideration is multiplicatively renormalizable.

3. RENORMALIZATION-GROUP EQUATIONS: CALCULATING THE RENORMALIZATION-GROUP FUNCTIONS IN THE ONE-LOOP APPROXIMATION

The results of Sec. 2 yield the following formula for the renormalized action of the model (10) and (11):

$$S_R(\Phi)=S_{\varphi R}(\varphi,\varphi')+\frac{\theta' d^\theta \theta'}{2}+\theta'[-\mathscr{D}_t\theta+\partial^2 V_R(\theta)], \tag{12}$$

where

$$V_R(\theta)=\sum_{n=1}^{\infty}\frac{Z_n\lambda_n\theta^n}{n!}, \tag{13}$$

and $S_{\varphi R}$ is the renormalized action of the problem without an impurity,

$$S_{\varphi R}(\varphi,\varphi')=\frac{\varphi' d^\varphi \varphi'}{2}+\varphi'[-\mathscr{D}_t\varphi+\nu Z_\nu \partial^2\varphi]. \tag{14}$$

All the functionals (12)–(14) depend on the variables $\{g,\nu,\lambda_n\}$, which are the renormalized analogs of the bare parameters $\{g_0,\nu_0,\lambda_{0n}\}$, and the renormalization mass μ, which is an additional arbitrary parameter in the renormalized theory. The correlator d^φ in (14) can be expressed in terms of g, ν, and μ through: $g_0\nu_0^3=g\nu^3\mu^{2\epsilon}$. The bare charges $\{g_{n0},\ n=1,2,3,\dots\}$ and their fully dimensionless renormalized counterparts $[g_n;\ n=1,2,3,\dots\}$ can be expressed in terms of the parameters λ_{n0} and λ_n in (9) and (13) by the following relationships:

$$\lambda_{n0}=g_{n0}\nu_0^{(n+1)/2},\quad \lambda_n=g_n\nu^{(n+1)/2}\mu^{(n-1)\alpha\epsilon}, \tag{15}$$

with $g_1\equiv u$ in the notation used in Ref. 7. The renormalization constants in the minimum subtraction (MS) scheme depend on the totally dimensionless charges $\{g,g_n\}$ (Z_ν depends only on g) and on the parameters ϵ, α, and d.

The action (12) can be obtained from (10) via the following renormalization of the parameters (it is unnecessary to renormalize the fields and the ''mass'' $m_0=m$):

$$\nu_0=\nu Z_\nu,\quad g_0=g\mu^{2\epsilon}Z_g,\quad g_{n0}=g_n\mu^{(n-1)\alpha\epsilon}Z_{g_n}. \tag{16}$$

The constants Z in (12) and (16) are linked by the following relationships:

$$Z_g=Z_\nu^{-3},\quad Z_{g_n}=Z_nZ_\nu^{-(n+1)/2}, \tag{17}$$

with the first equality being a consequence of the absence of renormalization in the contribution with d^φ in (12).

The relation $S(\Phi,e_0)=S_R(\Phi,e,\mu)$ (e_0 is the set of bare variables, and e is the set of renormalized variables) for the Green's functions $G_n=\langle\Phi\cdots\Phi\rangle$ of the model (10) yields the renormalization-group equation

$$\mathscr{D}_{RG}G_n=0,$$

$$\mathscr{D}_{RG}\equiv\mathscr{D}_\mu-\gamma_\nu\mathscr{D}_\nu+\beta_g\partial_g+\sum_{n=1}^{\infty}\beta_{g_n}\partial_{g_n}, \tag{18}$$

where we have used the notation $\mathscr{D}_x\equiv x\partial_x$ for any variable x. For any renormalization constant Z_i, the corresponding anomalous dimensionality γ_i is defined as $\gamma_i\equiv\widetilde{\mathscr{D}}_\mu \ln Z_i$, where $\widetilde{\mathscr{D}}_\mu$ is the operation $\mathscr{D}_\mu$ for fixed e_0, and the β-functions for all charges are defined by the expressions

$$\beta_g\equiv\widetilde{\mathscr{D}}_\mu g=g[-2\epsilon+3\gamma_\nu],$$

$$\beta_{g_n}\equiv\widetilde{\mathscr{D}}_\mu g_n=g_n[-(n-1)\alpha\epsilon-\gamma_{g_n}]=g_n[-(n-1)\alpha\epsilon$$

$$+(n+1)\gamma_\nu/2-\gamma_n]. \tag{19}$$

The last equality in (19) follows from the relationship between the renormalization constants in (17). Note that $\mathscr{D}_{RG}$ in (18) is the operation $\widetilde{\mathscr{D}}_\mu$ in the variables e and μ. We also note that because there is no field renormalization the initial Green's functions $G_n(e_0)$ and the renormalized Green's functions $G_{nR}(e,\mu)$ coincide (the difference lies in the choice of variables) and can equally be used to analyze the IR asymptotics.

The expressions for the constant Z_ν and the renormalization-group functions β_g and γ_ν for the problem without an impurity in the one-loop approximation can be found in Refs. 3 and 24:

$$Z_\nu=1-\frac{ag}{2\epsilon}+O(g^2),$$

$$\gamma_\nu(g)=ag+O(g^2),\quad a=\frac{d-1}{4(d+2)}\frac{S_d}{(2\pi)^d}, \tag{20}$$

where $S_d\equiv2\pi^{d/2}/\Gamma(d/2)$ is the surface area of a unit sphere in d-dimensional space. It is known[6,24] that the function β_g in (19) has an IR-stable fixed point $g_*=2\epsilon/3a+O(\epsilon^2)$ at which $\beta_g(g_*)\equiv0$ and $\beta_g'(g_*)>0$. The relation $\beta_g=g(-2\epsilon+3\gamma_\nu)$, which follows from (17), makes it possible to determine $\gamma_\nu^*\equiv\gamma_\nu(g_*)=2\epsilon/3$ exactly (with ϵ^2, ϵ^3, and higher-order corrections). The critical dimensionalities of simple fields and time can be expressed in terms of a single anomalous dimensionality γ_ν^* and can also be determined exactly (their explicit form is given in (4)).

Let us calculate the constants Z_n in (12) in the one-loop approximation by using the method developed earlier in Ref. 21. In the expansion of the generating functional $\Gamma_R(\Phi)$ of 1-irreducible functions of the model (12) in p (the number of loops),

$$\Gamma_R(\Phi)=\sum_{p=0}^{\infty}\Gamma^{(p)}(\Phi),\quad \Gamma^{(0)}(\Phi)=S_R(\Phi), \tag{21}$$

the loop-free (''tree'') contribution is the renormalized action (12), and the one-loop contribution is given by the expression (see, e.g., Ref. 25)

$$\Gamma^{(1)}(\Phi)=-\frac{1}{2}\,\mathrm{Tr}\ln\frac{W}{W_0}, \tag{22}$$

where W is a linear operator with a kernel

$$W(x,y)=-\frac{\delta^2 S_R(\Phi)}{\delta\Phi(x)\,\delta\Phi(y)}, \tag{23}$$

and W_0 is a similar expression for the free (quadratic in fields) part of the action (12). Both quantities, W and W_0, are 4-by-4 matrices in the fields $\Phi\equiv\varphi,\varphi',\theta,\theta'$, and the inverse of W_0 represents lines (propagators) in the diagrams of the model (12).

The constants Z_n can be found from the condition that UV divergences (poles in ϵ) in Eq. (21) must be cancelled; if the additional condition that Z equals unity plus only poles in ϵ (the MS scheme), the constants can be determined uniquely. To calculate the constants Z_n we need only the matrix (23) at $\varphi,\varphi'=0$ (see below); for single-loop calculations in (22) we must put $Z=1$, and in the loop-free contribution in (12) we must allow for terms of order g in the constants Z. Thus, for the nonzero elements of the matrix (23) we have (for the sake of brevity we drop indices on fields and derivatives)

$$\begin{gathered}
W^{(\theta\theta)}=-\partial^2\theta'\times V''(\theta),\quad W^{(\theta'\theta')}=-d^{\theta},\\
W^{(\theta\theta')}=L^T,\quad W^{(\theta'\theta)}=L,\quad W^{(\varphi\theta)}=\theta'\partial,\\
W^{(\theta\varphi)}=-\partial\theta',\quad W^{(\theta'\varphi)}=\partial\theta,\quad W^{(\varphi\theta')}=-\theta\partial,\\
W^{(\varphi\varphi')}=M^T,\quad W^{(\varphi'\varphi)}=M,\\
W^{(\varphi'\varphi')}=-d^{\varphi}.
\end{gathered} \tag{24}$$

Here d^{φ} and d^{θ} are the correlators (3) and (8), the function $V(\theta)$ can be obtained from $V_R(\theta)$ by replacing Z_n with unity (here and in what follows, V' and V'' stand for the derivatives of V with respect to the single variable $\theta(x)$), we have written $L=\partial_t-\partial^2 V'$ and $M=\partial_t-\nu\partial^2$, and $L^T=-\partial_t-V'\partial^2$ and $M^T=-\partial_t-\nu\partial^2$ are the transposed operations.

To find the Z_n we need not the entire exact expression (22) but only its divergent part (see Sec. 2)

$$\int dx\,\partial^2\theta'(x)R(\theta(x)),$$

with $R(\theta)$ similar to $V(\theta)$. This implies that it is sufficient to know the trace of the logarithm of the matrix (23) to first order in the matrix elements $(\theta\theta)$, $(\theta\varphi)$, and $(\varphi\theta)$ that are linear in θ' (see Eqs. (24)). Using the well-known formula $\delta(\mathrm{Tr}\ln K)=\mathrm{Tr}(K^{-1}\delta K)$, from (24) we find (with the necessary accuracy) that $\mathrm{Tr}\ln(W/W_0)\simeq -I_1+2I_2$, where

$$\begin{gathered}
I_1=\int dx\; D^{(\theta\theta)}(x,x)V''(\theta(x))\partial^2\theta'(x),\\
I_2=\int dx\int dy\;\partial_i\theta(x)D^{(\theta'\theta)}(x,y)D_{ij}^{(\varphi\varphi)}(x,y)\partial_j\theta(y),
\end{gathered} \tag{25}$$

and $D^{(\Phi\Phi)}$ are the corresponding elements of the matrix W^{-1} at $\varphi,\varphi',\theta=0$. By their very meaning, $D^{(\varphi\varphi)}$ is the ordinary bare propagator of the model (14) with $Z=1$, and $D^{(\theta\theta)}$ and $D^{(\theta'\theta)}$ are the propagator and the response function of the model (12) with $Z=1$ in the ''external field'' $\theta(x)$.

For the subsequent discussion it is important to note that after the derivatives ∂ have been shifted to the external factors $\theta(x)$ and $\theta'(x)$, the expressions that remain in $I_{1,2}$ diverge only logarithmically, and in calculating the divergent parts of the diagrams (25) all the external momenta can be set equal to zero (here IR regularization is ensured by the ''mass'' m). This means that in selecting the pole (in ϵ) part in (25) we can ignore the inhomogeneity of $\partial^2\theta'(x)$ and $\theta(x)$ in I_1 and of $\partial_i\theta(x)$, $\partial_i\theta'(x)$, and $\theta(x)$ in I_2, i.e., they can be considered constants. Then the necessary integrals can easily be calculated by passing to the momentum–frequency representation:

$$\begin{aligned}
D^{(\theta\theta)}(x,x)&=\int\!\!\int\frac{d\omega d\mathbf{k}}{(2\pi)^{d+1}}\,\frac{d^{\theta}(k)}{\omega^2+[k^2V'(\theta)]^2}\\
&=\frac{\mu^{-2\alpha\epsilon}}{2\alpha\epsilon}\,\frac{2a_1V''(\theta)}{V'(\theta)}+\cdots,
\end{aligned}$$

$$\begin{aligned}
&\int dy D^{(\theta'\theta)}(x,y)D_{ij}^{(\varphi\varphi)}(x,y)\\
&\quad=\int\!\!\int\frac{d\omega d\mathbf{k}}{(2\pi)^{d+1}}\,\frac{P_{ij}(\mathbf{k})d^{\varphi}(k)}{(\omega^2+\nu^2k^4)(i\omega+V'(\theta)k^2)}\\
&\quad=\delta_{ij}\frac{\mu^{-2\epsilon}}{2\epsilon}\,\frac{a_2g\nu^2}{2(\nu+V'(\theta))}+\cdots,
\end{aligned} \tag{26}$$

where we have introduced the quantities $a_1\equiv S_d/4(2\pi)^d$ and $a_2\equiv(d-1)S_d/2d(2\pi)^d$.

After the derivative in I_2 has been shifted to the field θ' via integration by parts and (25) and (26) have been substituted into (22), we arrive at the following expression for the divergent part $\Gamma^{(1)}(\Phi)$ with the necessary accuracy:

$$\begin{aligned}
\Gamma^{(1)}(\Phi)=\frac{a_1\mu^{-2\alpha\epsilon}}{2\alpha\epsilon}&\int dxF_1(\theta)\partial^2\theta'\\
&+\frac{a_2\mu^{-2\epsilon}}{2\epsilon}\int dxF_2(\theta)\partial^2\theta'.
\end{aligned} \tag{27}$$

The relationships

$$\begin{gathered}
F_1(\theta)=\frac{V''(\theta)}{V'(\theta)}=\sum_{n=0}^{\infty}\frac{\mu^{\alpha\epsilon(n+1)}\nu^{(n+1)/2}r_n\theta^n}{n!},\\
F_2(\theta)=\int_0^{\theta}d\vartheta\,\frac{g\nu^2}{\nu+V'(\vartheta)}=\sum_{n=0}^{\infty}\frac{\mu^{\alpha\epsilon(n+1)}\nu^{(n+1)/2}s_n\theta^n}{n!}
\end{gathered} \tag{28}$$

determine the functions $F_{1,2}$ in (27) and the totally dimensionless coefficients r_n and s_n (polynomials in the charges g and g_n). The value of the lower limit of integration in F_2 is indeed unimportant, since the coefficients r_0 and s_0 in (28) obviously contribute nothing to (27). From the above requirement of cancelling poles in ϵ and with allowance for (15) we obtain

$$Z_n=1-\frac{a_1r_n}{2\alpha\epsilon g_n}-\frac{a_2s_n}{2\epsilon g_n}+\cdots. \tag{29}$$

When doing calculations that involve the renormalization constants of renormalization-group functions, we must bear in mind that the operation $\widetilde{\mathscr{D}}_\mu$ on the functions of the form (29) which depend only on the charges g and g_n assumes the form

$$\widetilde{\mathscr{D}}_\mu=\beta_g\partial_g+\sum_{n=1}^{\infty}\beta_{g_n}\partial_{g_n}.$$

Here, to the adopted accuracy, it is sufficient to keep only the first terms in the β-functions (19), which yields

$$\widetilde{\mathscr{D}}_\mu=-2\epsilon\mathscr{D}_g-\alpha\epsilon\sum_{n=1}^{\infty}(n-1)\mathscr{D}_{g_n}. \tag{30}$$

Then we can use (29) to obtain an expression for the anomalous dimensionalities $\gamma_n\equiv\widetilde{\mathscr{D}}_\mu \ln Z_n$,

$$\gamma_n=\frac{a_1r_n+a_2s_n}{g_n},$$

which yields the following expression for the β-functions in (19):

$$\beta_{g_n}=g_n\left[-(n-1)\alpha\epsilon+\frac{(n+1)\gamma_\nu}{2}\right]-[a_1r_n+a_2s_n]. \tag{31}$$

From the definition (28) we can find the first coefficients r_n and s_n:

$$r_1=\frac{g_3}{u}-\left(\frac{g_2}{u}\right)^2,\quad r_2=\frac{g_4}{u}-\frac{3g_2g_3}{u^2}+\left(\frac{g_2}{u}\right)^3,$$

$$r_3=\frac{g_5}{u}-\frac{4g_2g_4}{u^2}-3\left(\frac{g_3}{u}\right)^2+\frac{12g_2^2g_3}{u^3}-6\left(\frac{g_2}{u}\right)^4,$$

$$s_1=\frac{g}{u+1},\quad s_2=-\frac{gg_2}{(u+1)^2},$$

$$s_3=-\frac{gg_3}{(u+1)^2}+\frac{2gg_2^2}{(u+1)^3}, \tag{32}$$

etc. (recall that $u\equiv g_1$).

4. FIXED POINTS; INFRARED SCALING

The renormalization-group fixed points $\{g_*,g_{n*}\}$ are determined by the conditions

$$\beta_g(g_*)=\beta_{g_n}(g_*,g_{n*})=0$$

for all $n=1,2,3,\dots$; here the known values $g_*,\gamma_\nu^*=2\epsilon/3$ for a liquid without an impurity must be used in Eq. (31) (see the text after (20)). The explicit form of the functions (31) and (32) implies that in defining g_{n*} the quantities $u\equiv g_{1*}$ and g_{2*} can be chosen arbitrarily, while the other g_{n*} for $n\geqslant3$ are then uniquely determined from the equations $\beta_{g_n}=0$ with $n\geqslant1$. This means that in the infinite-dimensional space of the charges g_n the renormalization-group equations (18) have a two-dimensional surface of fixed points g_{n*} parametrized by the values g_{1*} and g_{2*}.

A complete study of the stability of these points is a difficult task. According to the general rule (see, e.g., Ref. 4), a fixed point is IR-stable if the real parts of all the eigenvalues of the matrix $\omega\equiv\partial\beta/\partial g$ (for a complete set of charges and β-functions) for this point are positive. In view of the triangular block nature of the matrix ω for our model (the function β_g is independent of the charges g_n), one of the eigenvalues is known—it coincides with the diagonal element $\partial\beta_g/\partial g=2\epsilon+O(\epsilon^2)$ and is positive. The necessary condition for IR-stability is the positiveness of the other diagonal elements $\omega_{nn}\equiv\partial\beta_{g_n}/\partial g_n$, which from (28) can be found explicitly for all values of n,

$$\omega_{nn}=(1-n)\alpha\epsilon+\frac{(n+1)\epsilon}{3}+\frac{a_2g_*}{(u_*+1)^2}+\frac{a_1n(n+1)}{2u_*^2}\left(g_{3*}-\frac{2g_{2*}^2}{u_*}\right), \tag{33}$$

where g_{3*} must be expressed in terms of $u\equiv g_{1*}$ and g_{2*} via the condition $\beta_{g_1}=0$:

$$g_{3*}=\frac{2u_*^2\epsilon}{3a_1}-\frac{a_2g_*u_*}{a_1(u_*+1)}+\frac{g_{2*}^2}{u_*}.$$

An analysis of (33) shows that for $0<\alpha\leqslant1/3$ all the ω_{nn} are positive in the region $u\geqslant u_{1*}$ and for small values of g_{2*}^2/u_*^3, where

$$u_{1*}=\frac{1}{2}\left(-1+\sqrt{1+\frac{8(d+2)}{d}}\right)$$

is the positive root of the equation

$$u(u+1)=\frac{2(d+2)}{d},$$

which root coincides with the asymptotic value of the effective Prandtl number obtained in Ref. 7. This region also contains the point $u=u_{1*}$, $g_{n*}=0$, $n\geqslant2$, corresponding to the simplified model with $V(\theta)\propto\theta$ studied in Refs. 7–9. For $\alpha\geqslant1/3$ the point becomes IR-unstable, but in the region $1/3<\alpha\leqslant2/3$, which incorporates the "physical" value $\alpha=1/2$ (see Sec. 1), all the ω_{nn} are positive for $u\geqslant u_{2*}$ and small values of the ratio g_{2*}^2/u_*^3, where u_{2*} is the positive root of the equation

$$u(u+1)=\frac{2(d+2)}{d(2-3\alpha)}.$$

Although this is only a necessary condition, we can expect that at $\alpha=1/2$ the surface of the fixed points has a region of IR-stability. If this is the case, the model (10) has scaling with the same (as for a liquid without an impurity) dimensionalities (4) of the quantities φ, φ', ω, and m (this is a consequence of the passivity of the impurity); in the general case the dimensionality $\Delta[F]\equiv\Delta_F$ of a quantity F for a dynamical model of type (10) can be found from the following relationship:[3,24]

$$\Delta[F]\equiv\Delta_F=d_F^k+\Delta_\omega d_F^\omega+\gamma_F^*=d_F-\gamma_\nu^*d_F^\omega+\gamma_F^*, \tag{34}$$

where $\gamma_F^*=\gamma_F(g_*)=\widetilde{\mathscr{D}}_\mu \ln Z_F|_{g=g_*}$ is the anomalous dimensionality of the quantity if the quantity is renormalizable, $F=Z_FF_R$. In view of the absence of renormalization of the field θ and θ', we can write $\gamma_\theta=\gamma_{\theta'}=0$. This together with (34) and the data of Table I yields

$$\Delta[\theta]=\left(\frac{1}{3}-\alpha\right)\epsilon,\quad \Delta[\theta]+\Delta[\theta']=d. \tag{35}$$

As in (4), the result (35) is exact, i.e., contains no corrections of order ϵ^2, ϵ^3, etc.

5. SOLVING THE RENORMALIZATION-GROUP EQUATIONS FOR CORRELATORS: THE RICHARDSON AND KOLMOGOROV LAWS

The second equation in (35) corresponds to Richardson's empirical $\frac{4}{3}$-law for the rate of spread of a cloud of impurity particles in a turbulent atmosphere.[1] Indeed, if the field $\theta(\mathbf{x},t)$ is the concentration of impurity particles, the effective radius R at time $t>0$ of a cloud of such particles that at $t'=0$ started at the origin $\mathbf{x}'=0$ is given by the following expression:

$$R^2=\int d\mathbf{x}\,\mathbf{x}^2\langle\theta(\mathbf{x},t)\theta'(\mathbf{0},0)\rangle. \tag{36}$$

Combining (35) and (36) and allowing for the fact that $\Delta_R=-1$, we find that $\Delta[dR^2/dt]=-2-\Delta_t$, and from (4) at $\epsilon=2$ we have $\Delta_t=-2/3$, so that $dR^2/dt\propto R^{4/3}$, which is just what Richardson's law states.[1]

From the first equation in (35) with the real values $\epsilon=2$ and $\alpha=1/2$ we find that $\Delta_\theta=-1/3$, which corresponds to Kolmogorov's phenomenological $\frac{5}{3}$-law for the spectrum of a passive impurity.[1] To clarify this we note that the critical dimensionality of an arbitrary Green's function in the $(t,\mathbf{x})$-representation is simply the sum of the dimensionalities of the constituent fields, while in the momentum-frequency representation it can be obtained from Fourier-transformation formulas. In particular, for the correlators

$$D^\theta(\omega,k)=\langle\theta\theta\rangle(\omega,k),\quad D^\theta_{st}(k)=\frac{1}{2\pi}\int d\omega D^\theta(\omega,k) \tag{37}$$

we obtain

$$\Delta[D^\theta(\omega,k)]=2\Delta_\theta-d-\Delta_\omega,\quad \Delta[D^\theta_{st}(k)]=2\Delta_\theta-d. \tag{38}$$

Usually one studies not the static (single-time) correlator $D^\theta_{st}(k)$ but the one-dimensional spectrum of the passive impurity, $E^\theta(k)\propto k^{d-1}D^\theta_{st}(k)$ (see below). Here, from Eqs. (35) and (38) and the fact that $\Delta_\theta=-1/3$ we find that $\Delta[E^\theta]=d-1+\Delta[D^\theta_{st}]=-5/3$, i.e., $E^\theta(k)\propto k^{-5/3}$, as stated by the $\frac{5}{3}$-law.

The critical dimensionalities of the field, (4) and (35), and as result the exponents in the power laws of the Kolmogorov and Richardson type prove to be universal in the model (10), i.e., independent of the choice of a fixed point in the IR-stability region or, in other words, of the model parameters $\{g,g_i\}$. However, the scaling functions (and hence the amplitude factors in the power laws) are not universal, in contrast to the simplified model with $V_0\propto\theta$ in (10). Let us clarify this by using the example of the Batchelor constant in the spectrum of a passive impurity.

The one-dimensional spectra of the energy, $E^\varphi(k)$, and the passive impurity, $E^\theta(k)$, are related to the single-time pair correlators $D^\theta_{st}(k)$ of (37) and $\langle\varphi_i\varphi_j\rangle(k)=P_{ij}D^\varphi_{st}(k)$ as follows:

$$E^\theta(k)=\frac{S_d}{2(2\pi)^d}k^{d-1}D^\theta_{st}(k),$$
$$E^\varphi(k)=\frac{(d-1)S_d}{2(2\pi)^d}\,k^{d-1}D^\varphi_{st}(k) \tag{39}$$

(the additional factor $d-1$ in E^φ originates from the trace of the transverse projector, which is absent in D^θ_{st}). The phenomenological $\frac{5}{3}$-laws for the spectra (39) have the form[1]

$$E^\theta(k)=\mathrm{Ba}\,NW^{-1/3}k^{-5/3},\quad E^\varphi(k)=\mathrm{K}\,W^{2/3}k^{-5/3}, \tag{40}$$

where Ba and K are the Batchelor and Kolmogorov constants, W is the average energy-dissipation rate, and N is the average impurity-concentration rate. In the statistical model (1) and (6), the two rates are linked to the random-force correlators (3) and (8) via the exact relationships (see Refs. 2 and 3)

$$W=\frac{d-1}{2(2\pi)^d}\int d\mathbf{k}d^\varphi(k),\quad N=\frac{1}{2(2\pi)^d}\int d\mathbf{k}d^\theta(k) \tag{41}$$

(UV cutoff is implied at a value of k of the order of the reciprocal dissipation length $k_d\sim l_d^{-1}$). At the real values $\epsilon=2$ and $\alpha=1/2$ we have the following expressions for the correlators (3) and (8) with allowance for the fact that $k_d/m\gg1$:

$$W=D_0\frac{(d-1)S_d}{2(2\pi)^d}\ln\frac{k_d}{m},\quad N=D'_0\frac{S_d}{2(2\pi)^d}\ln\frac{k_d}{m} \tag{42}$$

(here we have reintroduced the factor D'_0 in the correlator (8) for proper normalization of the field θ).

From dimensionality considerations (see Table I), the correlators D_{st} can be expressed in terms of renormalized variables as

$$D^\theta_{st}(k)=D'_0\nu^{-1}k^{-d-2\alpha\epsilon}R^\theta(s,g,g_i,z),$$
$$D^\varphi_{st}(k)=\nu^2k^{2-d}R^\varphi(s,g,z), \tag{43}$$

with $s\equiv k/\mu$ and $z\equiv k/m$, where R^θ and R^φ are functions of totally dimensionless (with respect to momenta and frequencies) variables.

The correlators in (43) satisfy the renormalization-group equations (18), which lead to the following renormalization-group representation of the correlators:

$$D^\theta_{st}(k)=D'_0(\overline{\nu})^{-1}k^{-d-2\alpha\epsilon}R^\theta(1,\overline{g},\overline{g}_i,z),$$
$$D^\varphi_{st}(k)=(\overline{\nu})^2k^{2-d}R^\varphi(1,\overline{g},z), \tag{44}$$

where the "invariant variables" $\overline{g}=\overline{g}(s,g)$, $\overline{g}_i=\overline{g}_i(s,g,g_k)$, and $\overline{\nu}=\overline{\nu}(s,g,\nu)$ are the solutions of Eqs. (18) normalized at $s=1$ to g, g_i, and ν, respectively (see, e.g., Refs. 3 and 5). The identity $\overline{z}=z$ is a consequence of the absence of a contribution of $\mathscr{D}_m$ to the operator $\mathscr{D}_{RG}$ of Eq. (18). In the IR asymptotic limit $s\to0$, the invariant charges $\overline{g}$ and $\overline{g}_i$ tend to a fixed point of the renormalization group in the IR-stability region (see Sec. 4), $\overline{g}\to g_*$ and $\overline{g}_i\to g_{i*}$, while for the invariant viscosity we have

$$\overline{\nu}=\left(\frac{g_0\nu_0^3}{\overline{g}k^{2\epsilon}}\right)^{1/3}\to\frac{D_0}{g_*}k^{-2\epsilon/3}. \tag{45}$$

This yields the following expressions for the correlators (43):

$$D^{\theta}_{st}(k)=D_0'D_0^{-1/3}k^{-d-2\alpha\epsilon+2\epsilon/3}R^{\theta}(1,g_*,g_{i*},z)g_*^{1/3},$$

$$D^{\varphi}_{st}(k)=D_0^{2/3}k^{2-d-4\epsilon/3}R^{\varphi}(1,g_*,z)g_*^{-2/3}. \tag{46}$$

Combining (40), (42), and (43), we arrive at an expression for the ratio of the constants Ba and K:

$$\frac{\mathrm{Ba}}{\mathrm{K}}=\frac{g_*R^{\theta}(1,g_*,g_{i*},z)}{R^{\varphi}(1,g_*,z)}. \tag{47}$$

In the lowest order in the ϵ-expansion with $z\ll 1$ (the inertial interval) we have $R^{\varphi}=g_*/2$ and $R^{\theta}=1/2u_*$, so that (47) yields

$$\mathrm{Ba}/\mathrm{K}=u_*+O(\epsilon). \tag{48}$$

The value u_* for Ba/K at $d=3$ and $\epsilon=2$ was obtained earlier in another way for the model with $V_0\propto\theta$ by Yakhot and Orzsag,[10] who assumed it to be exact, although this is obviously not the case if we allow for (47).

Equation (47) implies, among other things, that the constant Ba, in contrast to the dimensionalities (4) and (35) and the constant K, is not universal, i.e., it depends on the fixed points $\{g_{n*}\}$ or, in other words, depends on the Prandtl number and the type of nonlinearity in the initial equation (6). Possibly, this explains the much larger (in comparison to K) spread of the experimental values of Ba (see, e.g., Ref. 26). Setting $\mathrm{K}=1.5$ (Ref. 26) and assuming that $u_*\geqslant u_{1*}=2.13$ at $\alpha=1/2$ and $d=3$ (see Sec. 4), we arrive at the estimate $\mathrm{Ba}\leqslant 0.704$, with the experimental values Ba lying in the 0.3–1.2 range ($\mathrm{Ba}=B_T^{(1)}$ in the notation used in Ref. 26). This is not bad, considering that (47) is only the first term in the ϵ-expansion for the realistic value $\epsilon=2$.

6. CONCLUSION

The general conclusion that can be drawn from this study is that the renormalization-group method for the problem of turbulent mixing of a passive scalar impurity with a diffusion coefficient that is an arbitrary function of the impurity concentration points to the presence of IR scaling with exactly known universal critical dimensionalities, corresponding to the phenomenological laws of Kolmogorov of Richardson, and nonuniversal (i.e., depending on the choice of the fixed point in the IR-stability region or, in other words, on the type of nonlinearity and the value of u_0 in the initial equation (6)) values of the effective charges g_{n*} (including the effective Prandtl number $u_*\equiv g_{1*}$), the amplitudes in the scaling laws (such as the Batchelor constant), and scaling functions. This sets the problem apart from the case of linear diffusion, where the scaling functions and the amplitudes are universal,[7] and from the problem of turbulent mixing of a chemically decaying impurity, where the theory predicts small deviations from Richardson's law.[14] Note, finally, that the current problem also differs from a similar infinite-charge problem, the model of a randomly growing phase boundary, which was proposed in Ref. 22. This model also has a two-dimensional surface of fixed points, but even the critical dimensionalities of the fields and parameters prove to be nonuniversal.[21] This means that infinite-charge problems exhibit different types of critical behavior uncharacteristic of ordinary models with a finite number of coupling constants, such as the standard φ^4-theory of critical behavior,[4] so that the renormalization-group technique can be effectively used to study such problems. In particular, we can expect that the functional technique developed in this paper for calculating counterterms and renormalization-group functions will be useful in studying such interesting infinite-charge problems as the complete U_N-symmetric 4-fermion model with the dimensionality $d=2+\epsilon$ (Ref. 27) and the problem of true random walks with self-avoidance.[28]

I am grateful to L. Ts. Adzhemyan, A. N. Vasil'ev, M. Gnatich, and D. Horvath for useful discussions. The work was supported financially by the Russian Fund for Fundamental Research (Grant No. 96-02-17-033) and the Grant Center of Natural Sciences of the State Committee of Institutions of Higher Learning (Grant No. 95-0-5.1-30).

[*)] E-mail: antonov@snoopy.phys.spbu.ru

---

[1] A. S. Monin and A. M. Yaglom, *Statistical Hydrodynamics*, Vol. 2, Nauka, Moscow (1967) [English transl.: MIT Press, Cambridge, Mass. (1975)]

[2] W. D. McComb, *The Physics of Fluid Turbulence*, Clarendon Press, Oxford (1990).

[3] L. Ts. Adzhemyan, N. V. Antonov, and A. N. Vasil'ev, Usp. Fiz. Nauk **166**, 1257 (1996) [Phys. Usp. **39**, 1193 (1996)].

[4] J. Zinn-Justin, *Quantum Field Theory and Critical Phenomena*, Clarendon Press, Oxford (1989).

[5] L. Ts. Adzhemyan, N. V. Antonov, and A. N. Vasil'ev, Zh. Éksp. Teor. Fiz. **95**, 1272 (1989) [Sov. Phys. JETP **68**, 733 (1989)].

[6] C. De Dominicis and P. C. Martin, Phys. Rev. A **19**, 419 (1979).

[7] L. Ts. Adzhemyan, A. N. Vasil'ev, and M. Gnatich, Teoret. Mat. Fiz. **58**, 72 (1984) [Theor. Math. Phys. **58**, 47 (1984)].

[8] V. Yakhot and S. A. Orszag, Phys. Rev. Lett. **57**, 1722 (1986); J. Sc. Comp. **1**, 3 (1986).

[9] W. P. Dannevik, V. Yakhot, and S. A. Orzsag, Phys. Fluids **30**, 2021 (1987).

[10] V. Yakhot and S. A. Orzsag, Phys. Fluids **30**, 3 (1987).

[11] V. Yakhot, Phys. Fluids A **1**, 175 (1989).

[12] É. V. Teodorovich, Prikl. Mat. Mekh. **52**, 218 (1988) [Appl. Math. Mech. **52**, 170 (1988)].

[13] M. Gnatich, Teor. Mat. Fiz. **83**, 374 (1990).

[14] M. Hnatich, *Talk at the Int. Conf. ''Renormalization Group 96''*, JINR, Dubna, August 1996.

[15] D. Carati and Brenig, Phys. Rev. A **40**, 5193 (1989).

[16] T. L. Kim and A. V. Serdyukov, Teor. Mat. Fiz. **105**, 412 (1995).

[17] L. Ts. Adzhemyan, A. N. Vasil'ev, and M. Gnatich, Teoret. Mat. Fiz. **64**, 196 (1985) [Theor. Math. Phys. **64**, 777 (1985)].

[18] R. H. Kraichnan, J. Fluid Mech. **5**, 407 (1959).

[19] R. H. Kraichnan, Phys. Fluids **7**, 1723 (1964); S. Chen and R. H. Kraichnan, Phys. Fluids A **1**, 2109 (1989).

[20] N. V. Antonov, Zh. Éksp. Teor. Fiz. **105**, 614 (1994) [JETP **78**, 327 (1994)].

[21] N. V. Antonov and A. N. Vasil'ev, Zh. Éksp. Teor. Fiz. **108**, 885 (1995) [JETP **81**, 485 (1995)].

[22] S. I. Pavlik, Zh. Éksp. Teor. Fiz. **106**, 553 (1994) [JETP **79**, 303 (1994)].

[23] J. Collins, *Renormalization*, Cambridge Univ. Press, London (1984).

[24] L. Ts. Adzhemyan, A. N. Vasil'ev, and Yu. M. Pis'mak, Teoret. Mat. Fiz. **57**, 286 (1983) [Theor. Math. Phys. **57**, 1131 (1983)].

[25] A. N. Vasil'ev, *Functional Methods in Quantum Field Theory and Statistics* [in Russian], Leningrad Univ. Press, Leningrad (1976).

[26] A. M. Yaglom, Izv. Akad. Nauk SSSR, Fiz. Atmos. Okeana **17**, 1235 (1981).

[27] A. Bondi, G. Curci, G. Paffuti, and R. Rossi, Ann. Phys. (N.Y.) **199**, 268 (1990); A. N. Vasil'ev, M. I. Vyazovskiĭ, S. É. Derkachyov, and K. A. Kivel', Teor. Mat. Fiz. **107**, 27 (1996).

[28] S. É. Derkachov, J. Honkonen, and A. N. Vasil'ev, J. Phys. A **23**, 2479 (1990).

Translated by Eugene Yankovsky

Fluctuation background due to incompressible disturbances in laminar shear flows

G. D. Chagelishvili*) and G. R. Khudzhadze

Abastumani Astrophysical Observatory, Georgian Academy of Sciences, 380060 Tbilisi, Georgia;
Space Research Institute, Russian Academy of Sciences, 117810 Moscow, Russia

(Submitted 4 October 1996)
Zh. Éksp. Teor. Fiz. **112**, 1664–1674 (November 1997)

The incompressible fluctuation background in laminar shear flows with a smooth velocity profile is investigated. Concrete calculations are performed for parallel Couette flow using nonmodal analysis of the linear dynamics of the disturbances. Nonmodal analysis makes it possible to grasp phenomena that could not be grasped in the early investigations, and thereby makes it possible to represent the fluctuation background in a completely new light: In incompressible shear flows the spatial spectral energy density of the fluctuation background is anisotropic, and furthermore in certain regions of wave-number space it is higher than that of the thermal noise. It is also shown that in the stationary state of the nonequilibrium system studied there exists a new, indirect channel for thermalization of the energy of the mean flow—energy is constantly transferred from the mean flow into the spatial Fourier harmonics of vortex pertubations and ultimately into heat. Possible manifestations of the fluctuation background described in this paper are listed.
[S1063-7761(97)01011-1]

1. INTRODUCTION

The standard method of investigating linear processes—spectral expansion in time of disturbances followed by eigenvalue analysis—in shear flows cannot make sense of the energy-intensive processes occurring in such flows.[1–4] Moreover, some phenomena of paramount importance (which will be listed below) remain hidden from view. The reasons for these difficulties were rigorously described mathematically in the 1990s.[1] The essence of the difficulties is as follows: in the standard (modal) analysis of linear processes in shear flows, the operators appearing in the equations are not self-adjoint, and in consequence the eigenfunctions of the problem are not orthogonal to one another—they strongly interfere with one another. As a result, the information obtained from an analysis of individual modes (eigenfunctions and eigenvalues) is far from complete. These circumstances make it necessary to calculate accurately the results of the interference of the eigenfunctions in order to describe the phenomena correctly, which at present is a problem of insurmountable difficulty.

There exists another method, the so-called nonmodal method,[2] dating back to Kelvin[5] and Orr,[6] for analyzing linear processes in shear flows. In this approach the original problem is solved by following the temporal evolution of the spatial Fourier harmonics of the disturbances.[7–23] The effectiveness of the second approach is confirmed by the progress made in the last few years with its help in understanding the diversity of processes occurring in shear flows: many new and unexpected results concerning the evolution of both vortex[7–13] and acoustic[14] disturbances have been obtained. This method is also used successfully to study MHD waves[15–18]; a new concept of the transition to turbulence in shear flows has been formulated[13,19–22]; and, a new mechanism of the linear transformation of waves in shear flows has been discovered.[18,23,24] In short, the nonmodal approach, revealing new features in different aspects of the linear dynamics of shear flows, has led to a new understanding of these aspects. This experience suggests that nonmodal analysis might be useful in studying hydrodynamic fluctuations in shear flows. Indeed, the first steps taken in this direction in the present paper have cast the incompressible (vortex) fluctuation background disturbances in laminar Couette flow in a completely new light:

1) The spatial spectral energy density of incompressible fluctuations in laminar Couette flow (SEDCF) is strongly anisotropic and in certain regions of **k** space it is much higher than that of the thermal noise.

2) In a stationary state of the nonequilibrium system which we investigated there exists a new, indirect channel for thermalization of the energy of the mean flow—under constant fluctuation background conditions energy is constantly transferred from the mean flow into the spatial Fourier harmonics and ultimately into heat.

These features of the fluctuation background are explained by the fact that besides random (Langevin) and dissipative forces two other physical phenomena, which modal analysis describes inadequately or not at all, play a decisive role in its formation: a) linear drift of the spatial Fourier harmonics in **k** space and b) energy transfer between the mean flow and the spatial Fourier harmonics.

This paper is organized as follows. In Sec. 2 the phenomena a and b are described phenomenologically on the basis of Refs. 7–9 and 13. In Sec. 3, the dynamical equation for the SEDCF is obtained, allowing for Langevin and dissipative forces in the equations of incompressible hydrodynamics, by nonmodal analysis. The calculations are performed for two-dimensional disturbances in the linear approximation. The simplicity and clarity of the equation obtained make possible a detailed interpretation of the process leading to the formation of the fluctuation background. This is done in Sec. 4. In addition, computational results for the SEDCF in the three-dimensional case are presented in

1063-7761/97/110907-07$10.00

Sec. 4. In the concluding Sec. 5, a new, indirect channel of thermalization of the energy of the mean flow is discussed and possible manifestations of the fluctuation background that is described in the paper are indicated.

2. LINEAR DYNAMICS OF SPATIAL FOURIER HARMONICS

The processes a and b are described well in works that cultivate nonmodal analysis. Their essence consists of the following.

a) In Couette flow, the wave number of the spatial Fourier harmonic along an axis orthogonal to the flow (i.e., along the velocity shear) changes in time. In the linear approximation the spatial Fourier harmonics undergo ''drift'' in **k** space.

Indeed (see Refs. 5–24), in parallel flows with a linear velocity shear (Couette flow)

$$\mathbf{U}_0=\mathbf{U}_0(Ay,0,0) \tag{1}$$

(A is the shear parameter, assumed to be positive) disturbances do not have the form of a simple wave because the wave crest curves as a result of the nonuniform character of the flow. In such a case the wave number of the spatial Fourier harmonic depends on the time:[7–24] If the spatial Fourier harmonic with wave numbers k_x, $k_y(0)$, and k_z is disturbed initially, i.e.

$$v_x(0)=\tilde{v}_x(k_x,k_y(0),k_z,0)\exp[ik_xx+ik_y(0)y+ik_zz], \tag{2}$$

then the evolution of its phase at times $t>0$ is determined by the equations

$$v_x(t)\propto\exp[ik_xx+ik_y(t)y+ik_zz],$$

$$k_y(t)=k_y(0)-k_xAt, \tag{3}$$

which describe linear drift of the Fourier harmonic in wavenumber space. The values of the spatial characteristics $(k_x,k_y(t),k_z)$ largely determine the intensity of energy transfer between the spatial Fourier harmonics and the shear flow. Therefore linear drift changes the intensity of this transfer.

b) Not all spatial Fourier harmonics can draw energy from the shear and be amplified. Only harmonics from a definite region in **k** space (called in what follows the region of amplification) are amplified. Each harmonic is amplified for a finite time until it leaves the region of amplification as a result of linear drift. Furthermore, the fact that spatial Fourier harmonics are located in this region imposes mainly a condition on the direction of their wave vector. Therefore, energy transfer between vortex disturbances and the shear flow is strongly anisotropic in **k** space.

Thus, at the linear stage of evolution incompressible vortex spatial Fourier harmonics can draw energy from the shear and be amplified for only a finite time, undergoing temporary growth. The dynamics of two-dimensional Fourier harmonics ($k_z=0$) is substantially different from that of three-dimensional Fourier harmonics ($k_z\neq 0$). This difference can be easily traced by comparing the evolution of their energy (see Fig. 1). Spatial Fourier harmonics initially satisfying the inequality $k_y(0)/k_x=30\gg 1$ were studied. With time, $k_y(t)$ starts to decrease as a result of linear drift, but as long as $k_y(t)\gg k_x$ little energy is transferred between the flow and spatial Fourier harmonics. At times when $k_y(t)\approx k_x$ both two- and three-dimensional Fourier harmonics start to draw energy from the shear intensively and grow. The amplification of two-dimensional harmonics stops when $k_y(t)=0$ (in Fig. 1, when $At=30$) and when $k_y(t)/k_x<0$ they return energy back into the medium (lower curve in Fig. 1). The three-dimensional Fourier harmonics continue to grow even when $k_y(t)/k_x<0$. In reality, this growth continues until $k_y(t)\approx -k_x$ (the dashed curve in Fig. 1), i.e., the region of amplification in **k** space is wider for three- than for two-dimensional Fourier harmonics. Moreover, the energy of the three-dimensional harmonics, in contrast to that of two-dimensional harmonics, does not decrease after the harmonics pass through the region of amplification (the three-dimensional Fourier harmonics do not return energy back into the flow), but rather it saturates and approaches a value much greater than the initial value. These arguments are valid when viscous and random forces are neglected. It is easy to understand that in reality, as $|k_y(t)|$ increases ($|k_y(t)|\rightarrow\infty$), viscous dissipation becomes important and converts the energy of the three-dimensional Fourier harmonics into heat.

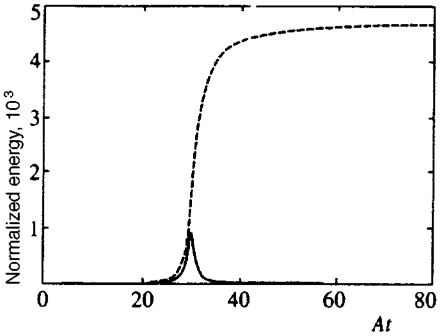

FIG. 1. Evolution of the energy, normalized to the initial value, of two- and three-dimensional Fourier harmonics. The solid curve is for a two-dimensional Fourier harmonic (with $k_y(0)/k_x=30$ and $k_z=0$). The dashed curve is for a three-dimensional Fourier harmonic (with $k_y(0)/k_x=30$, $k_x/k_z=1$, and $\bar{v}_x(0)/\bar{v}_y(0)=-20$).

3. DERIVATION OF THE DYNAMICAL EQUATION FOR THE SEDCF

Looking ahead somewhat, the dynamical equation obtained for the SEDCF in this section clearly describes the basic processes (random and dissipative) of the Landau–Lifshitz theory as well as the processes a and b. This is why this equation makes it possible to understand quite deeply the physics of the formation of the fluctuation background in shear flows. Specifically, it makes it possible to delimit the regions in **k** space where each process dominates; it makes it possible to show that the processes a and b do more than play a significant role in the formation of the fluctuation background—they determine its peculiar character.

In nonequilibrium systems (which nonuniform flows are), hydrodynamic fluctuations are best calculated on the basis of the Landau–Lifshitz theory[25]—the fluctuation–dissipation theorem. A discussion of this is given in Ref. 26.

For simplicity, we study a parallel incompressible Couette flow (see Eq. (1)). We confine ourselves to subcritical values of the Reynolds number, for which the flow is still laminar. In this case the fluctuations are considered to be so weak that the linear dynamical equations are sufficient.[26] The nonlinear terms become important only when the medium is in a state close to a critical point, after which the flow becomes turbulent (a detailed discussion is given in Ref. 27). To achieve the objective of the present section (derivation of the dynamical equation for the SEDCF), we impose one more constraint—we study two-dimensional disturbances. We discuss the fluctuation background of three-dimensional disturbances in the next section.

Thus, we base our investigation on the fluctuation–dissipation theory, we study incompressible disturbances, and we limit ourselves to an approximation that is linear in the these disturbances. Then, in the two-dimensional case we can start with the following equations:[25,28,29]

$$\frac{\partial v_x}{\partial x}+\frac{\partial v_y}{\partial y}=0, \tag{4}$$

$$\left(\frac{\partial}{\partial t}+Ay\,\frac{\partial}{\partial x}\right)v_x+Av_y =-\frac{1}{\rho_0}\,\frac{\partial p}{\partial x}+\nu\left(\frac{\partial^2}{\partial x^2}+\frac{\partial^2}{\partial y^2}\right)v_x+\frac{1}{\rho_0}\,f_x, \tag{5}$$

$$\left(\frac{\partial}{\partial t}+Ay\,\frac{\partial}{\partial x}\right)v_y=-\frac{1}{\rho_0}\,\frac{\partial p}{\partial y}+\nu\left(\frac{\partial^2}{\partial x^2}+\frac{\partial^2}{\partial y^2}\right)v_y+\frac{1}{\rho_0}\,f_y, \tag{6}$$

where ρ_0 is the undisturbed density; p, v_x, and v_y are, respectively, the disturbances of the pressure and velocity components; and, ν is the kinematic velocity of the medium. The components f_x and f_y of the random force are given by the spontaneous stress tensor $S_{ij}(\mathbf{r},t)$:

$$f_i=\frac{\partial S_{ij}}{\partial x_j},\quad i,j=x,y. \tag{7}$$

Since we are concerned with two-dimensional disturbances, we assume that they do not depend on the coordinate z. In accordance with the fluctuation–dissipation theory, the statistical properties of the spontaneous stress tensor are described by the following correlation function:[25,28,29]

$$\langle S_{ij}(t,\mathbf{r})S_{kl}(t',\mathbf{r}')\rangle =2T\rho_0\nu\left(\delta_{ik}\delta_{jl}+\delta_{il}\delta_{kj}-\frac{2}{3}\,\delta_{ij}\delta_{kl}\right)\delta(\mathbf{r}-\mathbf{r}')\,\delta(t-t'). \tag{8}$$

For simplicity, we consider liquids whose second viscosity coefficient ξ equals zero. In Eq. (8) and below, angular brackets denote averaging over an ensemble. Proceeding in the spirit of the nonmodal approach, we expand the disturbances in a Fourier integral with respect to the spatial coordinates only:

$$\left\{\begin{matrix} v_x\\ v_y\\ p\\ S_{ij}\end{matrix}\right\}=\int_{-\infty}^{\infty}dk_xdk_y \times\left\{\begin{matrix}\tilde{v}_x(k_x,k_y,t\\ \tilde{v}_y(k_x,k_y,t)\\ \tilde{p}(k_x,k_y,t)\\ \tilde{S}_{ij}(k_x,k_y,t)\end{matrix}\right\}\exp(ik_xx+ik_yy), \tag{9}$$

and then follow the temporal evolution of the SEDCF $(e_{\mathbf{k}}(t))$. A relation between the SEDCF and the average energy $\langle e\rangle$ of a disturbance is obtained using the following chain of equations:

$$\langle e\rangle=\left\langle\rho_0\,\frac{v_x^2+v_y^2}{2}\right\rangle=\frac{1}{2}\int dk_xdk_y[\rho_0(|\tilde{v}_x|^2+|\tilde{v}_y|^2)] =\frac{1}{2}\int dk_xdk_y\left(\rho_0\,\frac{k_x^2+k_y^2}{k_y^2}\,|\tilde{v}_x|^2\right)\equiv\int dk_xdk_ye_{\mathbf{k}}(t). \tag{10}$$

Substituting the expression (9) into Eqs. (4)–(8), we obtain, after tedious but simple manipulations, the following dynamical equation for $e_{\mathbf{k}}(t)$:

$$\frac{\partial e_{\mathbf{k}}}{\partial t}=Ak_x\,\frac{\partial e_{\mathbf{k}}}{\partial k_y}+\frac{2Ak_xk_y}{k_x^2+k_y^2}\,e_{\mathbf{k}} -2\nu(k_x^2+k_y^2)e_{\mathbf{k}}+2\nu(k_x^2+k_y^2)T. \tag{11}$$

The four terms on the right-hand side of Eq. (11) correspond to the four processes that participate in the formation of the SEDCF. The first term describes ''linear drift'' of the spatial Fourier harmonics in **k** space, i.e., the process a, described by Eq. (3). The second term describes energy transfer between the mean flow and the spatial Fourier harmonics (process b). The third and fourth terms describe the effect of dissipative and random forces, respectively.

4. PHYSICS OF THE FORMATION OF THE FLUCTUATION BACKGROUND

In the absence of shear $(A=0)$, the first two terms in Eq. (11) identically equal zero, and therefore the last two terms are the only ones that form the fluctuation background. In this (equilibrium) case, as expected (see, for example, Refs. 25, 28 and 29), dissipative and random forces lead in the stationary limit $(\partial e_{\mathbf{k}}/\partial t=0)$ to white noise

$$e_{\mathbf{k}}=T. \tag{12}$$

To describe the SEDCF with $A\neq 0$, it is convenient to transform to dimensionless variables:

$$\frac{e_{\mathbf{k}}}{T}\equiv E_{\mathbf{K}},\quad At\equiv\tau,\quad k_\nu\equiv\sqrt{\frac{V_0}{L_0\nu}}\equiv\sqrt{\frac{4}{\nu}}, \quad \frac{k_x}{k_\nu}\equiv K_x,\quad \frac{k_y}{k_\nu}\equiv K_y,\quad K_x^2+K_y^2\equiv K^2, \tag{13}$$

where the relation between the shear parameter A and the width L_0 of the Couette flow channel and the flow velocity

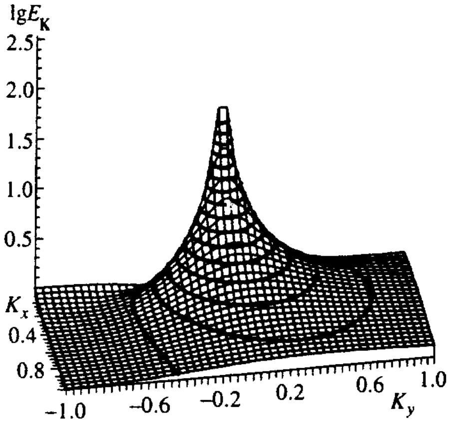

FIG. 2. Curves of constant log $E_{\mathbf{k}}$ (for the two-dimensional fluctuation background $K_z=0$) in the (K_x, K_y) plane for $K_x>0$. The maximum (peak) value log $E_{\mathbf{K}}=1.8$ is reached near $K_y=0$.

differential V_0 $(A \equiv V_0/L_0)$ is taken into account in the expression for k_ν. In the notation (13), Eq. (11) assumes the form

$$\frac{\partial E_{\mathbf{K}}}{\partial \tau}=K_x\frac{\partial E_{\mathbf{K}}}{\partial K_y}+2\frac{K_xK_y}{K^2}E_{\mathbf{K}}-2K^2E_{\mathbf{K}}+2K^2. \tag{14}$$

It is easy to see from the last equation that these four processes, leading to the formation of $E_{\mathbf{K}}$, operate with different efficiencies in different regions of **K** space. The last two terms dominate for spatial Fourier hamonics with large wave numbers $(K \geqslant 1)$, and the first two terms dominate for $K<1$. The process b is more efficient at moderate values of the ratio K_y/K_x. This last circumstance determines the peculiar character of the fluctuation background that we are studying—its anisotropy in **K** space and the strong deviation of $E_{\mathbf{K}}$ from white noise.

The solution of Eq. (13) in the stationary limit $(\partial E_{\mathbf{K}}/\partial \tau=0)$ is shown in Figs. 2 and 3 (for clarity, plots of the function log $E_{\mathbf{K}}$ are presented). The plots in these and all subsequent figures are constructed for positive K_x. For negative K_x the plots can be constructed using the identity $E_{-\mathbf{K}} \equiv E^*_{\mathbf{K}}$, which follows from the condition that the disturbances are real $(\mathbf{v}^*=\mathbf{v})$. Figure 2 displays curves of constant log $E_{\mathbf{K}}$ in the (K_x, K_y) half-plane with $K_z=0$. As one can see from this figure, for small K_x and K_y the contour lines are symmetric. The maximum (peak) value log $E_{\mathbf{K}}=1.8$ is reached near $K_y=0$. Figure 3 also shows a plot of log $E_{\mathbf{k}}$ versus K_x and K_y for $K_z=0$.

It would seem that the channel width determines the minimum value of the wave number of the fluctuation background $(k_{\min} \sim 1/L_0)$. In addition, this minimum value refers only to the wave number along the x axis, since k_y also easily ''passes'' through zero on account of linear drift (see Eq. (3)). Therefore we can write in dimensionless units (Eqs. (13))

$$|K_x|>K_{x,\min}\sim\sqrt{\frac{\nu}{V_0L_0}}\equiv\frac{1}{\sqrt{\mathscr{R}}}, \tag{15}$$

where $\mathscr{R}$ is the Reynolds number.

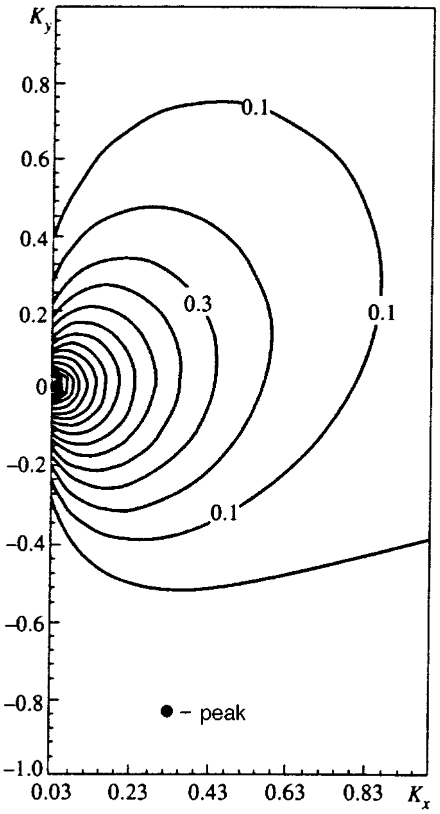

FIG. 3. Log $E_{\mathbf{K}}$ versus K_x and K_y for a two-dimensional fluctuation background $(K_z=0)$ in the (K_x, K_y) plane for $K_x>0$.

We describe the physics of the formation of the fluctuation background for the example of the two-dimensional Fourier harmonics. For clarity, we present a qualitative picture in Fig. 4. In this figure, in the horizontally hatched region, where $K \geqslant 1$, the random and dissipative forces produce a spectrum of spatial Fourier harmonics that is close to white noise $(E_{\mathbf{K}} \approx 1)$ over quite a short time interval $(\tau' \approx 1/K^2 \approx 1)$. These harmonics serve as the initial ''data'' for the formation of the spectrum in the region $K<1$. Indeed, on account of ''linear drift'' (process a), the spatial Fourier harmonics drift in **K** space in the direction of small K_y (K_x does not change during drift). The direction of drift in Fig. 4 is shown by the vertical arrows pointing downward. Energy transfer between the flow and the spatial Fourier harmonics comes into play as K_y decreases, and the ratio K_y/K_x becomes of the order of 1 (the region with the inclined hatching in Fig. 4). This transfer process is weak for harmonics with K_x of the order 1 (since viscous dissipation dominates for $K \approx 1$) and dominates for harmonics with small K_x. As K_y decreases, the latter spatial Fourier harmonics draw more and more energy from the shear (see paragraph b above). This outflow of energy causes $E_{\mathbf{K}}$ to deviate strongly from white noise and leads to formation of a peak for small K_x and K_y (see Fig. 3). The peak value is the greater, the smaller the value of $K_{x,\min}$, i.e., the larger the Reynolds number.

It is clear from paragraph b above that the maximum of log $E_{\mathbf{K}}$ should be larger for the three- than the two-dimensional Fourier harmonics, and it should be reached in

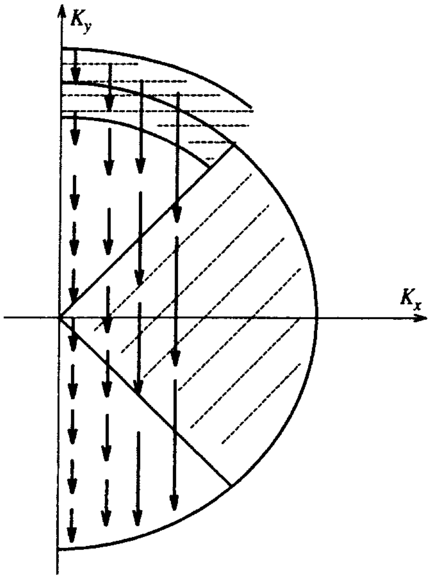

FIG. 4. Qualitative diagram describing the dynamics of the spatial Fourier harmonics in **K** space. The horizontal and inclined hatching distinguish regions where the individual basic processes dominate. Random and dissipative forces dominate in the horizontally hatched region. Energy transfer between the flow and the spatial Fourier harmonics comes into play in the region with inclined hatching. The arrows indicate the direction of drift of the Fourier harmonics in **K** space.

the region $K_y/K_x<0$. Calculations of the three-dimensional problem confirm these facts quantitatively. The three-dimensional calculations are not complicated, but they are very tedious. For this reason we shall not present them here. The results of the three-dimensional calculations are presented in Figs. 5, 6, and 7. For comparison, the results of two- and three-dimensional calculations are presented together in Fig. 5. The solid curve refers to the two-dimensional Fourier harmonic $K_x=0.03$, $K_y=0$—this is the section of the surface presented in Fig. 2 (but not for the logarithm). The dashed curve describes the three-dimensional fluctuation background $E_{\mathbf{K}}$ as a function of K_y for $K_x=K_z=0.03$. The drop in the three-dimensional fluctuation background to $E_{\mathbf{K}}\approx 1$ as $K_y\rightarrow -1$ is due to viscosity.

The three-dimensional fluctuation background is more clearly shown in Figs. 6 and 7. Figure 6 displays curves of constant $\log E_{\mathbf{K}}$ in the (K_x, K_y) plane for $K_z=0.03$. One can see from this figure that in the three-dimensional case, the peak value of $\log E_{\mathbf{K}}$ is strongly shifted, compared with the two-dimensional case, into the region $K_y/K_x<0$, i.e., the real, three-dimensional fluctuation background in shear flows is strongly anisotropic in **K** space. As one can see from Fig.

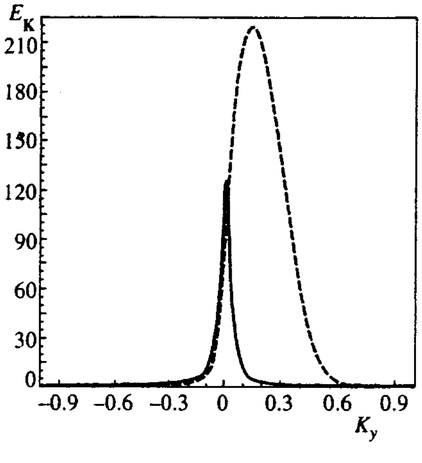

FIG. 5. The function $E_{\mathbf{K}}(K_y)$. The solid curve represents a section of the surface presented in Fig. 2 for $K_x=0.03$ (but not for the logarithmic function). The dashed curve describes the three-dimensional fluctuation background $E_{\mathbf{K}}$ as a function of K_y for $K_x=K_z=0.03$.

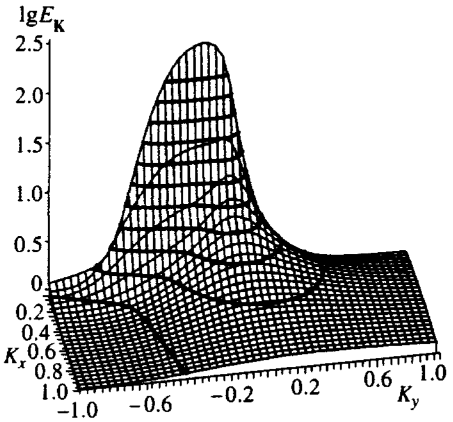

FIG. 6. Curves of constant $\log E_{\mathbf{K}}$ (for the three-dimensional fluctuation background) in the (K_x, K_y) plane for $K_x>0$ and $K_z=0.03$. The maximum peak value $\log E_{\mathbf{K}}=2.37$ is reached near $K_y=-0.14$, i.e., it is substantially shifted into the region $K_y<0$.

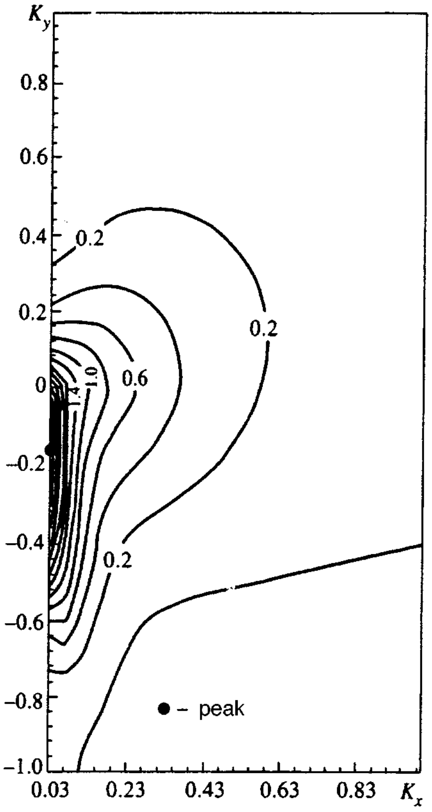

FIG. 7. Log $E_{\mathbf{K}}$ versus K_x and K_y for a three-dimensional fluctuation background in the (K_x, K_y) plane for $K_x>0$ and $K_z=0.03$.

7, the maximum value of $\log E_{\mathbf{K}}$ is greater for three-dimensional than for two-dimensional Fourier harmonics, and the plot itself is more spread out along the K_y axis.

Note that the form of the fluctuation background shown in Figs. 2–3 and 5–7 remains outside the purview of Ref. 30. Even though a rather general problem is investigated there (using, just as we do, the Navier–Stokes–Langevin equations in the linear approximation), Fourier analysis of the disturbances in time is ultimately performed to obtain concrete results, and as noted in the introduction, this is a suboptimal procedure which describes the processes a and b inadequately.

5. CONCLUSIONS

The most important results obtained in this paper are that the spatial spectral energy density of incompressible fluctuations in laminar Couette flow is anisotropic and differs strongly from white noise. Specifically, in certain regions of $\mathbf{k}$ space it is much higher than that of the thermal noise. Moreover, it follows directly from the dynamics of the spatial Fourier harmonics (see Fig. 4) that in a real three-dimensional case, energy is constantly transferred from the mean flow to the background (incompressible, vortex) disturbances and ultimately into heat.

It is easy to see that this new, indirect, channel of thermalization of the flow energy depends on the rate at which energy is drawn from the mean flow by background disturbances. This intensity of this channel increases with Reynolds number.[2,7,8] Therefore the efficiency of this channel should increase (!), and not decrease, with increasing Reynolds number. Concrete quantitative estimates that would make it possible to judge the system parameters for which this process can become effective (comparable to other processes that lead to the production of the mean entropy) fall outside the scope of the present work—such estimates require detailed numerical calculations of the three-dimensional problem.

Note that the characteristics of the fluctuation background described in the present paper are also typical of other shear flows. They should be manifested when hydrodynamic processes are important, for example, in the Brownian motion of small macroscopic particles. The significance of macroscopic (hydrodynamic) processes for the Brownian motion of small macroscopic particles is discussed in detail by Klimontovich.[28,29] The anisotropy of the Brownian motion of macroparticles in shear flows at high Reynolds numbers is most likely due to the anisotropy that we have found, and the high level of the fluctuation background (as compared with the thermal noise).

In conclusion, we briefly discuss the possible significance of the fluctuation background, described in this paper, for the transition to turbulence in some shear flows. It is known, for example, that in Couette flow the transition to turbulence occurs only as a result of finite disturbances. In accordance with a concept developed in the last few years (see Refs. 13 and 19–22), Couette flows become turbulent as a result of ''positive feedback'' (the crux of which is regeneration of spatial Fourier harmonics drawing energy from the mean flow) due to nonlinear phenomena. Therefore the transition to turbulence requires the presence of finite disturbances in the flow. It is obvious that such disturbances can be produced externally. But, according to the results of our investigations, finite disturbances can also originate in fluctuations. Indeed, at high Reynolds numbers fluctuations with small wave numbers can be strong, far exceeding the thermal noise level (see the discussion and figures in the preceding section). This in turn results in the ''turning on'' of nonlinear phenomena at certain Reynolds numbers, and leads to turbulence in the presence of ''positive feedback.''[13,19–22]

We thank S. S. Moiseev, V. G. Morozov, and O. G. Chkhetiani for helpful discussions and valuable suggestions.

This work was supported by the Ministry of Science of the Russian Federation and the International Science Foundation (Grant RVO 200).

*)e-mail: georgech@mx.iki.rssi.ru

---

[1] S. C. Reddy, P. J. Schmid, and D. S. Henningson, SIAM (Soc. Ind. Appl. Math.) J. Appl. Math. **53**, 15 (1993).

[2] L. N. Trefethen, A. E. Trefethen, S. C. Reddy, and T. A. Driscoll, Science **261**, 578 (1993).

[3] L. H. Gustavsson, J. Fluid Mech. **224**, 241 (1991).

[4] S. C. Reddy and D. S. Henningson, J. Fluid Mech. **252**, 209 (1993).

[5] Lord Kelvin (W. Thomson), Philos. Mag. **24(5)**, 188 (1887).

[6] W. M. F. Orr, Proc. Roy. Irish Acad. A **27**, 9 (1907).

[7] A. D. D. Craik and W. O. Criminale, Proc. R. Soc. London, Ser. A **406**, 13 (1986).

[8] K. Moffatt, in *Atmospheric Turbulence and Radio Wave Propagation*, A. M. Yaglom and V. I. Tatarskii (eds.), Nauka Press, Moscow (1967), p. 139.

[9] S. Marcus and W. H. Press, J. Fluid Mech. **79**, 525 (1977).

[10] W. O. Criminale and P. G. Drazin, Stud. Appl. Math. **83**, 123 (1990).

[11] Dzh. G. Lominadze, G. D. Chagelishvili, and R. G. Chanishvili, Pis'ma Astron. Zh. **1**, 856 (1988) [Sov. Astron. Lett. **14**, 364 (1988)].

[12] B. F. Farrell and P. J. Ioannou, Phys. Fluids A **5**, 1390 (1993).

[13] G. D. Chagelishvili, R. G. Chanishvili, J. G. Lominadze, and I. N. Segal in *Proc. of the 4th Inter. Conf. on Plasma Physics and Controlled Nuclear Fusion*, Japan, November 17–20, 1992, ESA SP-351 (1993), p. 23.

[14] G. D. Chagelishvili, A. D. Rogova, and I. N. Segal, Phys. Rev. E **50**, R4283 (1994).

[15] G. D. Chagelishvili, T. S. Christov, R. G. Chanishvili, and J. G. Lominadze, Phys. Rev. E **47**, 366 (1993).

[16] S. A. Balbus and J. H. Hawley, Astrophys. J. **400**, 610 (1992).

[17] S. H. Lubow and H. C. Spruit, Astrophys. J. **445**, 337 (1995).

[18] G. D. Chagelishvili, R. G. Chanishvili, J. G. Lominadze, and A. G. Tevzadze, Phys. Plasmas **4**, 259 (1997).

[19] G. D. Chagelishvili, R. G. Chanishvili, and J. G. Lominadze in *High Energy Astrophysics: American and Soviet Perspectives*, National Academy Press, Washington (1991).

[20] T. Gebhardt and S. Grossmann, Phys. Rev. E **50**, 3705 (1994).

[21] J. S. Baggett, T. A. Driscoll, and L. N. Trefethen, Phys. Fluids **7**, 833 (1995).

[22] G. D. Chagelishvili, R. G. Chanishvili, T. S. Christov, J. G. Lominadze, and I. N. Segal, Preprint No. 126, Space Research Institute, Russian Academy of Sciences, Moscow (1995).

[23] G. D. Chagelishvili, A. D. Rogova, and D. G. Tsiklauri, Phys. Rev. E **53**, 6028 (1996).

[24] G. D. Chagelishvili and O. G. Chkhetiani, JETP Lett. **62**, 314 (1995).

[25] L. D. Landau and E. M. Lifshitz, *Statistical Physics*, Pergamon Press, New York (1980).

[26] R. Schmitz, Phys. Rep. **171(1)**, 1 (1988).

[27] R. Graham in *Fluctuations, Instabilities, and Phase Transitions*, T. Riste (ed.), Plenum Press, New York (1975), p. 215; R. Graham and H. Pleiner, Phys. Fluids **18**, 130 (1975).
[28] Yu. L. Klimontovich, *Statistical Physics*, Harwood, Chur (1986).
[29] Yu. L. Klimontovich, *Turbulent Motion and the Structure of Chaos: A New Approach to the Statistical Theory of Open Systems* [in Russian], Nauka, Moscow (1990).
[30] J. Lutsko and J. W. Dufty, Phys. Rev. A **32**, 3040 (1985).

Translated by M. E. Alferieff

Fluctuations in liquid crystals in the presence of a flexoelectric effect

V. P. Romanov and G. K. Sklyarenko

St. Petersburg State University, 198904 St. Petersburg, Russia

(Submitted 4 March 1997)
Zh. Éksp. Teor. Fiz. **112**, 1675–1693 (November 1997)

We examine director fluctuations in nematic liquid crystals in an electric field in the presence of a flexoelectric effect. For the planar and homeotropic orientations we calculate the correlation functions and analyze these functions near the Freedericksz transition and the flexoelectric instability threshold. For both geometries we calculate the angular dependence of the intensity of light scattered by director fluctuations and examine its behavior at electric field strengths close to critical. © *1997 American Institute of Physics.* [S1063-7761(97)01111-6]

1. INTRODUCTION

Thanks to the anisotropy of the dielectric constant and the magnetic susceptibility, liquid crystals (LCs) undergo various structural transformations when placed in external electric and magnetic fields.[1–3] Here, as a rule, one deals with the instability of a homogeneously oriented state of an LC at field strengths above the threshold value. Physically such a change in the macroscopic orientation of a structure is equivalent to a second-order phase transition.[1,4] The threshold nature of these phenomena is due to the finite size of the liquid crystal layer and to a certain rigidity in the boundary conditions, which causes finite-gradient orientational perturbations to emerge, perturbations that are admissible only when the values of the external field strength are finite.

The best-known and most thoroughly studied effect of an orientational phase transition in a nematic liquid crystal (NLC) is the Freedericksz effect.[1–3] This transition, which occurs both in static fields and in light,[5–9] have been studied for different boundary conditions and orientations of the NLC.[10–14] Different types of distortions, periodic and aperiodic, that occur at field strengths higher than the threshold value have been investigated.[14–16]

Several groups of researchers (see Refs. 10–12, and 14) studied the various dynamical aspects of the effect of external fields on NLC behavior. Here the pre-transition processes were studied by analyzing the most unstable mode, whose amplitude increases substantially when the strength of the external field approaches the threshold value.

In 1969, Meyer[17] found that NLCs with a center of symmetry can exhibit a special piezoelectric effect, which became known as the flexoelectric effect. This linear effect of formation of a modulated structure induced by a uniform electric field is related to the highly anisotropic shape of molecules with constant dipole moments.[1–3]

In the present paper we study the thermal fluctuations in a limited NLC in the presence of the flexoelectric effect. The standard approach to studying fluctuations in nematic liquid crystals is to expand the fluctuations in natural modes.[10–16,18–20] The solution is given in the form of an infinite series, and finding each terms in the series involves solving a complicated transcendental equation. A method that makes it possible to derive closed expressions for the correlation functions of the director fluctuations in the cases of weak and strong adhesion to the substrate was proposed in Refs. 21 and 22. Here we use this approach to calculate thermal fluctuations in NLCs with solid-wall boundary conditions in an external electric field in the presence of the flexoelectric effect and the dielectric-constant anisotropy effect. As a result we arrive at expressions for the correlation functions of director fluctuations and the scattered-light intensity for homeotropic and planar orientations of the nematic. We find that the angular distribution of the scattered light intensity depends on the strength of the applied field. Finally, we analyze the results near the Freedericksz transition and near the flexoelectric instability threshold.

2. THE CORRELATION MATRIX IN THE PRESENCE OF AN ELECTRIC FIELD

Suppose that a nematic liquid crystal where the flexoelectric effect can occur is contained in a cell of thickness L placed between two plane-parallel plates with rigid boundary conditions in an external electric field. We introduce a Cartesian system of coordinates with its origin at the cell center and the z axis directed at right angles to the plates (Fig. 1).

The variation of the free energy, ΔF, consists of the elastic contribution, ΔF_{el}, the contribution ΔF_E related to the director orientation in the external field, and the contribution ΔF_{flex} due to flexoelectric polarization:[1–3,14]

$$\Delta F=\Delta F_{\mathrm{el}}+\Delta F_E+\Delta F_{\mathrm{flex}}=\frac{1}{2}\int d^3r\Big\{K_1(\mathbf{n}\ \mathrm{div}\ \mathbf{n})^2+K_2(\mathbf{n}\cdot\mathrm{curl}\ \mathbf{n})^2+K_3(\mathbf{n}\times\mathrm{curl}\ \mathbf{n})^2-\frac{\varepsilon_a}{4\pi}(\mathbf{n}\cdot\mathbf{E})^2-2\mathbf{E}\cdot(e_1\ \mathbf{n}\ \mathrm{div}\ \mathbf{n}+e_3(\mathrm{curl}\ \mathbf{n}\times\mathbf{n}))\Big\}, \tag{2.1}$$

where K_1, K_2, and K_3 are the Franck moduli, $\mathbf{n}$ is the director vector, $\mathbf{E}$ is the electric field strength, $\varepsilon_a=\varepsilon_\parallel-\varepsilon_\perp$ is the anisotropy of the dielectric constant (for the sake of definiteness we assume that ε_a is positive), with $\varepsilon_\parallel$ and $\varepsilon_\perp$ the dielectric constants parallel to the nematic axis and perpendicular to it, respectively, and e_1 and e_3 are the flexoelectric coefficients.

1063-7761/97/110914-11$10.00

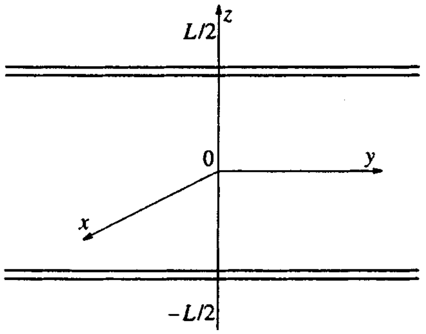

FIG. 1. The geometry of a cell with a liquid crystal.

Let us examine the contribution to the free energy related to director fluctuations. We write the vector $\mathbf{n}$ as $\mathbf{n}=\mathbf{n}_0+\delta\mathbf{n}$, where $\mathbf{n}_0$ is the equilibrium director orientation, and $\delta\mathbf{n}$ is the director fluctuation. Because of the solid-wall boundary conditions at the boundary of the region,

$$\delta\mathbf{n}(x,y,z=\pm L/2)=0. \tag{2.2}$$

Assuming that the director deviation $\delta\mathbf{n}=\mathbf{n}-\mathbf{n}_0$ is small, in the $\delta\mathbf{n}$-linear approximation we can write $\mathbf{n}^2=\mathbf{n}_0^2+2\mathbf{n}_0\cdot\delta\mathbf{n}$, i.e., $\mathbf{n}_0\cdot\delta\mathbf{n}=0$. This means that the vectors $\mathbf{n}_0$ and $\delta\mathbf{n}$ are orthogonal. Integration (2.1) by parts with allowance for the boundary conditions (2.2), we can Eq. (2.1) to within second-order terms in $\delta\mathbf{n}$ as follows:

$$\Delta F=\frac{1}{2}\int d^3r\,\delta\mathbf{n}(\mathbf{r})\hat{A}\,\delta\mathbf{n}^T(\mathbf{n}), \tag{2.3}$$

where $\hat{A}$ is a differential operator, and the superscript T stands for ''transposed.''

It is known that the director-fluctuation correlation matrix $\hat{G}(\mathbf{r},\mathbf{r}')=\langle\delta\mathbf{n}(\mathbf{r})\delta\mathbf{n}^T(\mathbf{r})\rangle$ must satisfy the following relationship:[4]

$$\hat{A}\hat{G}(\mathbf{r},\mathbf{r}')=k_BT\hat{I}\delta(\mathbf{r}-\mathbf{r}'), \tag{2.4}$$

where $\hat{I}$ is the identity matrix, T stands for temperature, and k_B is Boltzmann's constant. It is convenient to write the fluctuation $\delta\mathbf{n}(\mathbf{r})$ in the form of a two-dimensional Fourier integral:

$$\delta\mathbf{n}(\mathbf{r})=\frac{1}{(2\pi)^2}\int d^2q\,\exp[-i(\mathbf{q}\cdot\mathbf{r}_\perp)]\,\delta\mathbf{n}(\mathbf{q},z), \tag{2.5}$$

where $\mathbf{r}=(\mathbf{r}_\perp,z)$, and $\mathbf{q}$ is the wave vector in the xy plane, $\mathbf{q}=(q\cos\varphi,\ q\sin\varphi)$, with φ the angle between $\mathbf{q}$ and the x axis. Then the variation (2.3) of the free energy can be written as

$$\Delta F=\frac{1}{(2\pi)^2}\int d^2q\,\Delta F_{\mathbf{q}}, \tag{2.6}$$

where

$$\Delta F_{\mathbf{q}}=\frac{1}{2}\int_{-L/2}^{L/2}dz\ \delta\mathbf{n}^*(\mathbf{q},z)\hat{A}_{\mathbf{q}}\delta\mathbf{n}^T(\mathbf{q},z), \tag{2.7}$$

with the asterisk denoting complex conjugation, and $\hat{A}_{\mathbf{q}}$ the operator $\hat{A}$ in the $(\mathbf{q},z)$-representation. After we pass to the Fourier representation, Eq. (2.4) becomes

$$\hat{A}_{\mathbf{q}}\hat{G}(\mathbf{q},z,z')=k_BT\hat{I}\delta(z-z'). \tag{2.8}$$

Hence to find the correlation matrix, we must find the inverse of the operator $\hat{A}_{\mathbf{q}}$ with allowance for the boundary conditions

$$\hat{G}(\mathbf{q},z=\pm L/2,\ z')=0. \tag{2.9}$$

Let us examine the solution of this problem for two orientations of the NLC; homeotropic and planar.

3. DIRECTOR FLUCTUATIONS IN A HOMEOTROPICALLY ORIENTED CELL

When the cell is oriented homeotropically, the equilibrium direction of the director has the form $\mathbf{n}_0=(0,0,1)$ and the director fluctuation has the form $\delta\mathbf{n}(\mathbf{r})=(n_x,n_y,0)$, with

$$n_x(x,y,z=\pm L/2)=n_y(x,y,z=\pm L/2)=0$$

at the boundaries.

Suppose that the cell is placed in a uniform electric field directed along the x axis, $\mathbf{E}=(E,0,0)$. Then, to within second-order terms in $\delta\mathbf{n}$, the free-energy variation (2.1) assumes the form

$$\begin{aligned}\Delta F^{(h)}=\frac{1}{2}\int d^3r\Big\{&K_1(\partial_xn_x+\partial_yn_y)^2+K_2(\partial_xn_y-\partial_yn_x)^2\\&+K_3[(\partial_zn_x)^2+(\partial_zn_y)^2]-\frac{\varepsilon_a}{4\pi}E^2n_x^2-2E\\&\times[e_1n_x(\partial_xn_x+\partial_yn_y)+e_3(\partial_zn_x-n_y\partial_xn_y\\&+n_y\partial_yn_x)]\Big\},\end{aligned} \tag{3.1}$$

where ∂_j $(j=x,y,z)$ stands for the partial derivative with respect to the corresponding coordinate.

After integrating by parts and passing to the two-dimensional Fourier spectrum, we can write (3.1) in the form (2.7):

$$\Delta F_{\mathbf{q}}^{(h)}=\frac{1}{2}\int_{-L/2}^{L/2}dz(n_x^*,n_y^*)\hat{A}_{\mathbf{q}}^h\begin{pmatrix}n_x\\n_y\end{pmatrix}, \tag{3.2}$$

where $n_i\equiv n_i(\mathbf{q},z)$, $i=x,y$, and

$$\hat{A}_{\mathbf{q}}^h=\begin{pmatrix}K_1q_x^2+K_2q_y^2-K_3\partial_z^2-\dfrac{\varepsilon_a}{4\pi}E^2\\(K_1-K_2)q_xq_y+i(e_1-e_3)Eq_y\\(K_1-K_2)q_xq_y-i(e_1-e_3)Eq_y\\K_1q_y^2+K_2q_x^2-K_3\partial_z^2\end{pmatrix}.$$

The matrix $\hat{A}_{\mathbf{q}}^h$ is diagonalized by a transformation of the form $\hat{U}^{-1}\hat{A}_{\mathbf{q}}^h\hat{U}$, where $\hat{U}$ is a matrix consisting of the eigenvectors of $\hat{A}_{\mathbf{q}}^h$:

$$\hat{U}=\begin{pmatrix} (K_1-K_2)q_xq_y+i(e_1-e_3)Eq_y \\ (K_1-K_2)q_xq_y+i(e_1-e_3)Eq_y \\ \frac{1}{2}\left[\frac{\varepsilon_a}{4\pi}E^2+(K_1-K_2)(q_y^2-q_x^2)+g\right] \\ \frac{1}{2}\left[\frac{\varepsilon_a}{4\pi}E^2+(K_1-K_2)(q_y^2-q_x^2)-g\right] \end{pmatrix},$$

with

$$g=\left[(K_1-K_2)^2q^4+\left(\frac{\varepsilon_a}{4\pi}E^2\right)^2+4(e_1-e_3)^2E^2q_y^2 + \frac{\varepsilon_a}{2\pi}E^2(q_y^2-q_x^2)(K_1-K_2)\right]^{1/2}.$$

Equation (2.8) can be written in the equivalent form

$$\hat{U}^{-1}\hat{A}_{\mathbf{q}}^h\hat{U}\hat{U}^{-1}\hat{G}^h\hat{U}=k_BT\hat{I}\delta(z-z'). \tag{3.3}$$

Using the explicit expression for the matrices $\hat{A}_{\mathbf{q}}^h$, $\hat{U}$, and $\hat{U}^{-1}$, we get

$$\begin{pmatrix} \partial_z^2-P_{(h)}^2 & 0 \\ 0 & \partial_z^2-Q_{(h)}^2 \end{pmatrix}\hat{X}=-\frac{k_BT}{K_3}\hat{I}\delta(z-z'), \tag{3.4}$$

where

$$\hat{X}=\hat{U}^{-1}\hat{G}^h\hat{U}, \tag{3.5}$$

$$P_{(h)}^2=\frac{1}{2K_3}\left[(K_1+K_2)q^2-\frac{\varepsilon_a}{4\pi}E^2+g\right], \tag{3.6}$$

$$Q_{(h)}^2=\frac{1}{2K_3}\left[(K_1+K_2)q^2-\frac{\varepsilon_a}{4\pi}E^2-g\right]. \tag{3.7}$$

The boundary conditions (2.9) imply

$$\hat{X}(z=\pm L/2,\, z')=0. \tag{3.8}$$

Thus, Eqs. (3.4) and (3.8) constitute a system of closed differential equations with boundary conditions for the four elements of the matrix $\hat{X}$. Obviously,

$$X_{12}(z,z')=X_{21}(z,z')=0. \tag{3.9}$$

Finding the diagonal elements of $\hat{X}$ amounts to solving a boundary-value problem of the form

$$\begin{aligned} &\partial_z^2X_{ii}(z,z')-a_{ii}^2X_{ii}(z,z')=b_{ii}\delta(z-z'), \\ &X_{ii}(z=\pm L/2,\, z')=0, \quad i=1,2. \end{aligned} \tag{3.10}$$

Its solution is

$$X_{ii}(z,z')=\begin{cases} X_{ii}^{(+)}=C^{(+)}\sinh[a_{ii}(z-L/2)], & z>z', \\ X_{ii}^{(-)}=C^{(-)}\sinh[a_{ii}(z+L/2)], & z<z', \end{cases} \tag{3.11}$$

where $C^{(+)}$ and $C^{(-)}$ are constants. They can be determined from the conditions imposed on the solutions $X_{ii}^{(+)}$ and $X_{ii}^{(-)}$ at the point $z=z'$

$$\begin{aligned} &X_{ii}^{(+)}(z=z')=X_{ii}^{(-)}(z=z'), \\ &\partial_zX_{ii}^{(+)}(z=z')-\partial_zX_{ii}^{(-)}(z=z')=b_{ii}. \end{aligned} \tag{3.12}$$

Solving the system (3.12) and inserting the values of $C^{(+)}$ and $C^{(-)}$ into (3.11), we get

$$X_{ii}(z,z')=\frac{b_{ii}}{a_{ii}\sinh(a_{ii}L)} \times\begin{cases} \sinh[a_{ii}(z-L/2)]\sinh[a_{ii}(z'+L/2)], & z>z', \\ \sinh[a_{ii}(z+L/2)]\sinh[a_{ii}(z'-L/2)], & z<z'. \end{cases} \tag{3.13}$$

This formula can be written in the compact form

$$\begin{aligned} X_{ii}(z,z')=\frac{b_{ii}}{2a_{ii}\sinh(a_{ii}L)}\{&\cosh[a_{ii}(z+z')] \\ &-\cosh(a_{ii}L)\cosh[a_{ii}(z-z')] \\ &+\sinh(a_{ii}L)\sinh(a_{ii}|z-z'|)\}. \end{aligned} \tag{3.14}$$

Now if we substitute the corresponding expressions for the coefficients a_{ii} and b_{ii} taken from (3.4) in (3.14), we get

$$\begin{aligned} X_{11}(z,z')=\frac{k_BT}{2K_3P_{(h)}\sinh(P_{(h)}L)}\{&-\cosh[P_{(h)}(z+z')] \\ &+\cosh(P_{(h)}L)\cosh[P_{(h)}(z-z')] \\ &-\sinh(P_{(h)}L)\sinh(P_{(h)}|z-z'|)\} \\ \equiv-\frac{1}{K_3}J(P_{(h)}),& \end{aligned} \tag{3.15}$$

$$\begin{aligned} X_{22}(z,z')=\frac{k_BT}{2K_3Q_{(h)}\sinh(Q_{(h)}L)}\{&-\cosh[Q_{(h)}(z+z')] \\ &+\cosh(Q_{(h)}L)\cosh[Q_{(h)}(z-z')] \\ &-\sinh(Q_{(h)}L)\sinh(Q_{(h)}|z \\ &-z'|)\}\equiv-\frac{1}{K_3}J(Q_{(h)}). \end{aligned} \tag{3.16}$$

Equation (3.5) implies that the correlation matrix satisfies $\hat{G}^h=\hat{U}\hat{X}\hat{U}^{-1}$. If in this expression we insert (3.9), (3.15), and (3.16), we arrive at the following formulas for the matrix elements of $\hat{G}^h$:

$$\begin{aligned} G_{11}^h&=\langle n_x(\mathbf{q},z)n_x^*(\mathbf{q},z')\rangle \\ &=\frac{1}{2K_3}\left\{\frac{1}{g}\left[\frac{\varepsilon_a}{4\pi}E^2+(K_1-K_2)(q_y^2-q_x^2)\right]\right. \\ &\quad\left.\times[J(P_{(h)})-J(Q_{(h)})]-[J(P_{(h)})+J(Q_{(h)})]\right\}, \\ G_{22}^h&=\langle n_y(\mathbf{q},z)n_y^*(\mathbf{q},z')\rangle \\ &=-\frac{1}{2K_3}\left\{\frac{1}{g}\left[\frac{\varepsilon_a}{4\pi}E^2+(K_1-K_2)(q_y^2-q_x^2)\right]\right. \\ &\quad\left.\times[J(P_{(h)})-J(Q_{(h)})]+[J(P_{(h)})+J(Q_{(h)})]\right\}, \end{aligned} \tag{3.17}$$

$$G_{12}^h=\langle n_x(\mathbf{q},z)n_y^*(\mathbf{q},z')\rangle$$

$$= -\frac{1}{gK_3}[(K_1-K_2)q_xq_y$$
$$+i(e_1-e_3)Eq_y][J(P_{(h)})-J(Q_{(h)})],$$

$$G^h_{21} = \langle n_y(\mathbf{q},z)n_x^*(\mathbf{q},z')\rangle$$
$$= -\frac{1}{gK_3}[(K_1-K_2)q_xq_y - i(e_1-e_3)Eq_y]$$
$$\times[J(P_{(h)})-J(Q_{(h)})].$$

Note that at $E=0$ these correlation functions coincide with those obtained in Refs. 18, 19, and 21 in the limit of strong adhesion to the substrate ($W\to\infty$).

4. DIRECTOR FLUCTUATIONS IN A PLANAR-ORIENTED CELL

When the cell orientation is planar, the equilibrium direction of the director and the director fluctuation have the form $\mathbf{n}_0=(1,0,0)$ and $\delta\mathbf{n}(\mathbf{r})=(0,n_y,n_z)$, with

$$n_y(x,y,z=\pm L/2)=n_z(x,y,z=\pm L/2)=0. \qquad (4.1)$$

Suppose that a uniform electric field is directed along the z axis, $\mathbf{E}=(0,0,E)$. In this geometry the free-energy variation (2.1) can be expressed, to within second-order terms in $\delta\mathbf{n}$, as

$$\Delta F^{(p)} = \frac{1}{2}\int d^3r\left\{K_1(\partial_y n_y+\partial_z n_z)^2 + K_2(\partial_y n_z-\partial_z n_y)^2 + K_3[(\partial_x n_y)^2 + (\partial_x n_z)^2] - \frac{\varepsilon_a}{4\pi}E^2 n_z^2 - 2E[e_1 n_z(\partial_z n_z+\partial_y n_y) + e_3(\partial_x n_z + n_y\partial_y n_z + n_z\partial_z n_z)]\right\}. \qquad (4.2)$$

Integrating by parts and passing to the two-dimensional Fourier spectrum, we obtain

$$\Delta F^{(p)}_{\mathbf{q}} = \frac{1}{2}\int_{-L/2}^{L/2} dz(n_y^*,n_z^*)\hat{A}^p_{\mathbf{q}}\begin{pmatrix} n_y \\ n_z\end{pmatrix},$$

where $n_j\equiv n_j(\mathbf{q},z)$, $j=y,z$, and

$$\hat{A}^p_{\mathbf{q}} = \begin{pmatrix} K_3q_x^2+K_1q_y^2-K_2\partial_z^2 \\ -i(K_1-K_2)q_y\partial_z + i(e_1-e_3)Eq_y \\ -i(K_1-K_2)q_y\partial_z - i(e_1-e_3)Eq_y \\ K_3q_x^2+K_2q_y^2-K_1\partial_z^2-\dfrac{\varepsilon_a}{4\pi}E^2\end{pmatrix}.$$

In contrast to $\hat{A}^h_{\mathbf{q}}$, the matrix $\hat{A}^p_{\mathbf{q}}$ cannot be diagonalized by an appropriate similarity transformation, since it is not self-adjoint. Hence Eq. (2.8) must be transformed in such a way so that its left-hand side contains an operator $\hat{B}^p_{\mathbf{q}}$ that allows for diagonalization. To this end we write (2.8) in the form

$$(\hat{A}_0 + i\hat{C}\partial_z + \hat{D}\partial_z^2)\hat{G}^p = k_BT\hat{I}\delta(z-z'), \qquad (4.3)$$

where

$$\hat{A}_0 = \begin{pmatrix} K_3q_x^2+K_1q_y^2 & i(e_1-e_3)Eq_y \\ -i(e_1-e_3)Eq_y & K_3q_x^2+K_2q_y^2-\dfrac{\varepsilon_a}{4\pi}E^2\end{pmatrix},$$

$$\hat{C} = \begin{pmatrix} 0 & -(K_1-K_2)q_y \\ -(K_1-K_2)q_y & 0\end{pmatrix},$$

$$\hat{D} = \begin{pmatrix} -K_2 & 0 \\ 0 & -K_1\end{pmatrix}.$$

Multiplying both sides of (4.3) by $\hat{D}^{-1}$ and separating out a perfect square, we obtain

$$\left[\left(\hat{I}\partial_z + \frac{i}{2}\hat{D}^{-1}\hat{C}\right)^2 + \hat{H}\right]\hat{G}^p = k_BT\hat{D}^{-1}\delta(z-z'), \qquad (4.4)$$

where

$$\hat{H} = \frac{(\hat{D}^{-1}\hat{C})^2}{4} + \hat{D}^{-1}\hat{A}_0. \qquad (4.5)$$

Passing to the new variable

$$\hat{G}^p_0 = \exp\left(\frac{i}{2}\hat{D}^{-1}\hat{C}z\right)\hat{G}^p \qquad (4.6)$$

and allowing for the boundary conditions (2.9), we get

$$(\hat{H}'+\hat{I}\partial_z^2)\hat{G}^p_0(\mathbf{q},z,z') = k_BT\exp\left(\frac{i}{2}\hat{D}^{-1}\hat{C}z\right)\hat{D}^{-1}\delta(z-z'), \qquad (4.7)$$

$$\hat{G}^p_0(\mathbf{q},z=\pm L/2,\ z')=0, \qquad (4.8)$$

where

$$\hat{H}' = \exp\left(\frac{i}{2}\hat{D}^{-1}\hat{C}z\right)\hat{H}\exp\left(-\frac{i}{2}\hat{D}^{-1}\hat{C}z\right). \qquad (4.9)$$

The operator $\hat{B}^p_{\mathbf{q}}\equiv\hat{H}'+\hat{I}\partial_z^2$ has the following form (see the Appendix):

$$\hat{B}^p_{\mathbf{q}} = \begin{pmatrix} -a\sin^2\alpha - b\cos^2\alpha + f\sin 2\alpha + \partial_z^2 \\ i\sqrt{\dfrac{K_1}{K_2}}\left(\dfrac{a-b}{2}\sin 2\alpha - f\cos 2\alpha\right) \\ -i\sqrt{\dfrac{K_2}{K_1}}\left(\dfrac{a-b}{2}\sin 2\alpha - f\cos 2\alpha\right) \\ -a\cos^2\alpha - b\sin^2\alpha - f\sin 2\alpha + \partial_z^2\end{pmatrix}, \qquad (4.10)$$

where

$$a = \frac{K_3}{K_1}q_x^2 + \left(\frac{1}{2}+\frac{3}{4}\frac{K_2}{K_1}-\frac{1}{4}\frac{K_1}{K_2}\right)q_y^2 - \frac{\varepsilon_a}{4\pi K_1}E^2,$$

$$b = \frac{K_3}{K_2}q_x^2 + \left(\frac{1}{2}+\frac{3}{4}\frac{K_1}{K_2}-\frac{1}{4}\frac{K_2}{K_1}\right)q_y^2, \qquad (4.11)$$

$$f = \frac{e_1-e_3}{\sqrt{K_1K_2}}Eq_y, \quad \alpha = -\frac{1}{2}\frac{K_1-K_2}{\sqrt{K_1K_2}}q_yz.$$

This operator is diagonalized by the transformation $\hat{V}^{-1}\hat{B}^p_{\mathbf{q}}\hat{V}$, where the matrix $\hat{V}$ composed of the eigenvectors of the operator $\hat{B}^p_{\mathbf{q}}$ is given by the following expression:

$$\hat{V}=\begin{pmatrix} u & u \\ \sqrt{\dfrac{K_2}{K_1}}\,(w-p) & \sqrt{\dfrac{K_2}{K_1}}\,(w+p) \end{pmatrix},$$

with

$$\begin{gathered} u=i\left(\frac{b-a}{2}\sin 2\alpha+f\cos 2\alpha\right), \\ w=f\sin 2\alpha+\frac{a+b}{2}-a\sin^2\alpha-b\cos^2\alpha, \\ p=\sqrt{\left(\frac{a-b}{2}\right)^2+f^2}. \end{gathered} \tag{4.12}$$

We can write Eq. (4.7) in an equivalent form:

$$\hat{V}^{-1}\hat{B}^p_{\mathbf{q}}\hat{V}\hat{V}^{-1}\hat{G}^p_0\hat{V}=k_BT\left[\hat{V}^{-1}\exp\left(\frac{i}{2}\hat{D}^{-1}\hat{C}z\right)\hat{D}^{-1}\hat{V}\right]\times\delta(z-z'). \tag{4.13}$$

If we introduce the notation

$$\begin{gathered} \hat{W}=\hat{V}^{-1}\hat{G}^p_0\hat{V},\quad \hat{S}=\hat{V}^{-1}\exp\left(\frac{i}{2}\hat{D}^{-1}\hat{C}z\right)\hat{D}^{-1}\hat{V}, \\ P_{(p)}=\sqrt{\frac{a+b}{2}+p},\quad Q_{(p)}=\sqrt{\frac{a+b}{2}-p}, \end{gathered} \tag{4.14}$$

then, combining (4.8) and (4.13), we arrive at an equation for $\hat{W}$,

$$\begin{pmatrix} \partial_z^2-Q_{(p)} & 0 \\ 0 & \partial_z^2-P_{(p)} \end{pmatrix}\hat{W}=k_BT\hat{S}\,\delta(z-z'), \tag{4.15}$$

with

$$\hat{W}(z=\pm L/2,\ z')=0. \tag{4.16}$$

The matrix $\hat{S}$ can be obtained through multiplication of four matrices, with the expression for $\exp[(i/2)\hat{D}^{-1}\hat{C}z]$ taken from the Appendix. The result is

$$\begin{aligned} S_{11}&=\frac{1}{2pu}\left[\left(\frac{w-p}{K_1}-\frac{w+p}{K_2}\right)u\cos\alpha+i\left(\frac{1}{K_1}-\frac{1}{K_2}\right)u^2\sin\alpha\right], \\ S_{22}&=\frac{1}{2pu}\left[\left(\frac{w-p}{K_2}-\frac{w+p}{K_1}\right)u\cos\alpha+i\left(\frac{1}{K_2}-\frac{1}{K_1}\right)u^2\sin\alpha\right], \\ S_{12}&=\frac{1}{2pu}\left[\left(\frac{1}{K_1}-\frac{1}{K_2}\right)(w+p)u\cos\alpha+i\left(\frac{(w+p)^2}{K_1}-\frac{u^2}{K_2}\right)\sin\alpha\right], \\ S_{21}&=\frac{1}{2pu}\left[\left(\frac{1}{K_2}-\frac{1}{K_1}\right)(w-p)u\cos\alpha+i\left(\frac{u^2}{K_2}-\frac{(w-p)^2}{K_1}\right)\sin\alpha\right]. \end{aligned} \tag{4.17}$$

Equations (4.15) and (4.16) constitute a system of four differential equations with boundary conditions for the matrix elements of $\hat{W}$. They are similar to Eqs. (3.10) and have the following solutions:

$$W_{ij}(z,z')=S_{ij}Y_{ii},\quad i,j=1,2, \tag{4.18}$$

where

$$\begin{aligned} Y_{11}=\frac{k_BT}{2P_{(p)}\sinh(P_{(p)}L)}&\times\{\cosh[P_{(p)}(z+z')]-\cosh(P_{(p)}L) \\ &\times\cosh[P_{(p)}(z-z')]+\sinh(P_{(p)}L) \\ &\times\sinh(P_{(p)}|z-z'|)\}=J(P_{(p)}), \end{aligned} \tag{4.19}$$

$$\begin{aligned} Y_{22}=\frac{k_BT}{2Q_{(p)}\sinh(Q_{(p)}L)}&\times\{\cosh[Q_{(p)}(z+z')]-\cosh(Q_{(p)}L) \\ &\times\cosh[Q_{(p)}(z-z')]+\sinh(Q_{(p)}L) \\ &\times\sinh(Q_{(p)}|z-z'|)\}=J(Q_{(p)}), \end{aligned} \tag{4.20}$$

with the function J defined in (3.15).

Combining (4.6) and (4.14), we can write the correlation matrix in the following form:

$$\hat{G}^p=\exp\left(-\frac{i}{2}\hat{D}^{-1}\hat{C}z\right)\hat{V}\hat{W}\hat{V}^{-1}.$$

If we use Eqs. (A5), (4.17), and (4.18), we can write the following expression for the matrix elements of $\hat{G}^p$:

$$\begin{aligned} G^p_{11}&=\langle n_y(\mathbf{q},z)n_y^*(\mathbf{q},z')\rangle \\ &=-\frac{1}{2K_2}\left\{\frac{1}{p}[w\cos 2\alpha+iu\sin 2\alpha]\times[J(P_{(p)})-J(Q_{(p)})]+[J(P_{(p)})+J(Q_{(p)})]\right\}, \\ G^p_{22}&=\langle n_z(\mathbf{q},z)n_z^*(\mathbf{q},z')\rangle \\ &=\frac{1}{2K_1}\left\{\frac{1}{p}[w\cos 2\alpha+iu\sin 2\alpha]\times[J(P_{(p)})-J(Q_{(p)})]-[J(P_{(p)})+J(Q_{(p)})]\right\}, \\ G^p_{12}&=\langle n_y(\mathbf{q},z)n_z^*(\mathbf{q},z')\rangle \\ &=\frac{1}{2\sqrt{K_1K_2}}\left\{\frac{1}{p}[w\cos 2\alpha+iu\sin 2\alpha]\times[J(P_{(p)})-J(Q_{(p)})]\right\}, \end{aligned} \tag{4.21}$$

$$G^p_{21}=\langle n_z(\mathbf{q},z)n^*_y(\mathbf{q},z')\rangle=-G^p_{12}.$$

As in the case of homeotropic orientation, at $E=0$ the results coincide with those of Refs. 18, 19, and 21 for solid-wall boundary conditions.

5. CORRELATION FUNCTIONS NEAR THE INSTABILITY THRESHOLD

We see that for both orientations the correlation functions of the director fluctuations in an external electric field, Eqs. (3.17) and (4.21), have simple poles (if we adopt the notation (3.15), (3.16), (4.19), and (4.20)). In the single-constant approximation, $K_i=K$, $i=1,2,3$, the poles are at

$$Q_{(h)}=Q_{(p)}=\pm i\frac{\pi}{L}m, \quad m=1,2,\ldots .$$

Note that at $Q_{(h)}=Q_{(p)}=0$ the expressions for the correlation functions are finite since

$$\begin{aligned}\lim_{Q\to 0}\Big\{&\frac{1}{Q\,\sinh(QL)}(\cosh[Q(z+z')]\\ &-\cosh(QL)\cosh[Q(z-z')]\\ &+\sinh(QL)\sinh(Q|z-z'|))\Big\}\\ &=-\frac{L}{2}+\frac{2zz'}{L}+|z-z'|.\end{aligned} \tag{5.1}$$

If we consider $Q_{(h)}$ and $Q_{(p)}$ as functions of the field, i.e., assume $\mathbf{q}$ fixed, we see that the number of poles increases with E. Let us find the values $E^{(h)}_0$ and $E^{(p)}_0$ corresponding to the first pole. For the case of homeotropic orientation, $E^{(h)}_0$ can be found from the relationship

$$Q_{(h)}=\sqrt{q^2-\frac{\varepsilon_a}{8\pi K}(E^{(h)}_0)^2-\frac{1}{2K}\sqrt{\left[\frac{\varepsilon_a}{4\pi}(E^{(h)}_0)^2\right]^2+4(e_1-e_3)^2(E^{(h)}_0)^2q^2_y}}=\pm i\frac{\pi}{L}. \tag{5.2}$$

Solving (5.2) for $E^{(h)}_0$ yields

$$E^{(h)}_0=\frac{K(q^2+\pi^2/L^2)}{\sqrt{(e_1-e_3)^2q^2_y+(\varepsilon_a/4\pi)K(q^2+\pi^2/L^2)}}. \tag{5.3}$$

Similarly, if we use (4.11), (4.12), and (4.14), for the case of planar orientation we arrive at an equation that coincides with (5.2). Hence the first pole in the correlation functions for both orientations appears at

$$E=E^{(h)}_0=E^{(p)}_0\equiv E_0(q_x,q_y).$$

Equation (5.3) implies that $E_0(q_x,q_y)$ monotonically increases with q_x. Hence $q_x=0$ corresponds to the lowest value of the field at which the correlation functions have a pole. There are two reasons for such a pole: the Freedericksz transition and the flexoelectric instability threshold in cells of finite thickness.[3,14] This instability manifests itself in the emergence of a specific domain structure at field strengths above the critical value E_c. This type of transition depends on the parameters of the nematic liquid crystal and the system geometry.

A detailed discussion of the flexoelectric effects in a planar-oriented cell can be found in Ref. 3. Using the same method, we can easily calculate the critical value of the field strength for a homeotropically oriented cell. In the single-constant approximation, the value coincides with that obtained in Ref. 3 for a planar-oriented cell:

$$\begin{aligned}E(q_y)&=\frac{K[q^2_y+(\pi/L)^2]}{\sqrt{(e_1-e_3)^2q^2_y+(\varepsilon_a/4\pi)K[q^2_y+(\pi/L)^2]}}\\ &=E_0(q_x=0,\ q_y).\end{aligned} \tag{5.4}$$

The minimum in $E(q_y)$ determines the threshold values E_c and q_c:

$$\begin{aligned}q_c&=\frac{\pi}{L}\sqrt{\frac{(e_1-e_3)^2-(\varepsilon_a/4\pi)K}{(e_1-e_3)^2+(\varepsilon_a/4\pi)K}},\\ E_c&=\frac{\pi}{L}\,\frac{2K(e_1-e_3)}{(e_1-e_3)^2+(\varepsilon_a/4\pi)K}.\end{aligned} \tag{5.5}$$

We see that flexoelectric instability occurs only if

$$\varepsilon_a<\frac{4\pi(e_1-e_3)^2}{K}. \tag{5.6}$$

The other minimum in $E(q_y)$ is at $q_y=0$,

$$E_c=\frac{\pi}{L}\sqrt{\frac{4\pi K}{\varepsilon_a}},$$

which corresponds to the Freedericksz transition.

Thus, our formulas describe the correlation functions of director fluctuations at field strengths below the critical. If $E\geqslant E_c$ holds, the analysis becomes invalid, since the initial orientation cannot be considered homogeneous. In the limit $E\to E_c$, the correlation functions of modes whose wave vectors are close to $\mathbf{q}=(0,q_c)$ substantially increase. A detailed analysis of critical-mode behavior was done by Galatola *et al.*[14]

6. LIGHT SCATTERING BY DIRECTOR FLUCTUATIONS IN THE PRESENCE OF AN ELECTRIC FIELD

A nematic liquid crystal is an optically anisotropic medium, with the dielectric constant tensor $\varepsilon_{\alpha\beta}$ linked to the director field through the following relationship:

$$\varepsilon_{\alpha\beta}(\mathbf{r})=\varepsilon_\perp\delta_{\alpha\beta}+\varepsilon_a n_\alpha(\mathbf{r})n_\beta(\mathbf{r}).$$

The director fluctuations $\delta\mathbf{n}(\mathbf{r})$ change the tensor $\varepsilon_{\alpha\beta}(\mathbf{r})$:

$$\delta\varepsilon_{\alpha\beta}(\mathbf{r})=\varepsilon_a[n_\alpha\delta n_\beta(\mathbf{r})+n_\beta\delta n_\alpha(\mathbf{r})]. \tag{6.1}$$

This in turn causes the light propagating through the medium to scatter.

The intensity I of the scattered light is proportional to $\langle E'_\alpha(\mathbf{r})E'^*_\beta(\mathbf{r})\rangle$, where $\mathbf{E}'$ is the field of the scattered wave.[23] If a plane wave with an amplitude $\mathbf{E}^0$ and a wave vector $\mathbf{k}_i$ is propagating in the medium, the value of $\langle E'_\alpha(\mathbf{r})E'^*_\beta(\mathbf{r})\rangle$ for singly scattered waves $\mathbf{E}'$ is determined by an integral over the scattering volume:[23,24]

$$\begin{aligned}\langle E'_\alpha(\mathbf{r})E'^*_\beta(\mathbf{r})\rangle=\frac{\omega^4}{c^4}\int d^3r'\,d^3r''\,T_{\alpha\gamma}(\mathbf{r},\mathbf{r}')T^*_{\beta\lambda}(\mathbf{r},\mathbf{r}'')\\ \times\langle\delta\varepsilon_{\gamma\mu}(\mathbf{r}')\,\delta\varepsilon_{\lambda\nu}(\mathbf{r}'')\rangle E^0_\mu E^0_\nu\\ \times\exp\{i\mathbf{k}_i\cdot(\mathbf{r}'-\mathbf{r}'')\},\end{aligned} \tag{6.2}$$

where ω is the circular frequency, c is the speed of light, and $T_{\alpha\beta}(\mathbf{r}',\mathbf{r}'')$ is the Green's function of the Maxwell equations.

To simplify the description of light scattering we limit ourselves to the approximation of an isotropic medium, i.e., we assume that at large distances

$$T_{\alpha\beta}(\mathbf{r})=\frac{1}{4\pi r}e^{i\mathbf{k}\cdot\mathbf{r}}(\delta_{\alpha\beta}-s_\alpha s_\beta), \tag{6.3}$$

where $k=(\omega/c)\sqrt{\varepsilon}$, with ε the average dielectric constant, and $\mathbf{s}=\mathbf{r}/r$ is the unit vector pointing in the direction of the observer.

Substituting (6.3) in (6.2), we obtain

$$\begin{aligned}\langle E'_\alpha(\mathbf{r})E'^*_\beta(\mathbf{r})\rangle=\frac{\omega^4 V}{c^4(4\pi)^2r^2}(\delta_{\alpha\gamma}-s_\alpha s_\gamma)(\delta_{\beta\lambda}-s_\beta s_\lambda)\,\frac{1}{L}\\ \times\int_{-L/2}^{L/2}dz'\int_{-L/2}^{L/2}dz''\,\exp[-iq_{sc,z}(z\\ -z')]\langle\delta\varepsilon_{\gamma\mu}(\mathbf{q}^\perp_{sc},z')\,\delta\varepsilon^*_{\lambda\nu}(\mathbf{q}^\perp_{sc},z'')\rangle E^0_\mu E^0_\nu,\end{aligned} \tag{6.4}$$

where V is the scattering volume, $\mathbf{q}_{sc}=\mathbf{s}k-\mathbf{k}_i$ is the scattering vector, and $\mathbf{q}^\perp_{sc}=(q_{sc,x},q_{sc,y},0)$ is the transverse component of $\mathbf{q}_{sc}$.

According to (6.1), the correlation functions of the fluctuations of the dielectric−constant tensor are linked to the director fluctuations by the following relationship:

$$\begin{aligned}&\langle\delta\varepsilon_{\gamma\mu}(\mathbf{q}^\perp_{sc},z')\,\delta\varepsilon^*_{\lambda\nu}(\mathbf{q}^\perp_{sc},z'')\rangle\\ &\quad=\varepsilon_a[n^0_\gamma n^0_\lambda\langle\delta n_\mu(\mathbf{q}^\perp_{sc},z')\,\delta n_\lambda(\mathbf{q}^\perp_{sc},z'')\rangle\\ &\qquad+n^0_\mu n^0_\nu\langle\delta n_\gamma(\mathbf{q}^\perp_{sc},z')\,\delta n_\lambda(\mathbf{q}^\perp_{sc},z'')\rangle\\ &\qquad+n^0_\gamma n^0_\nu\langle\delta n_\mu(\mathbf{q}^\perp_{sc},z')\,\delta n_\lambda(\mathbf{q}^\perp_{sc},z'')\rangle\\ &\qquad+n^0_\mu n^0_\lambda\langle\delta n_\gamma(\mathbf{q}^\perp_{sc},z')\,\delta n_\nu(\mathbf{q}^\perp_{sc},z'')\rangle].\end{aligned} \tag{6.5}$$

Let us take the case of normal incidence, i.e., $\mathbf{k}_i=(0,0,k)$. If the scattering is in the direction $\mathbf{s}=(\sin\theta\cos\varphi,\sin\theta\sin\varphi,\cos\theta)$, the scattering vector has the form

$$\mathbf{q}_{sc}=k(\sin\theta\cos\varphi,\sin\theta\sin\varphi,\cos\theta-1),$$

$$q_{sc}=2k\sin\frac{\theta}{2}. \tag{6.6}$$

By combining (6.4), (6.5), (3.17), and (4.21) we can find the scattered light intensity for both director orientations.

Suppose that the light propagating in the medium is linearly polarized along the y axis, i.e., in (6.4) and (6.5) we must put $\mu=\nu=y$. Then in the single-constant approximation $K_i=K$, $i=1,2,3$, we have the following expressions for the scattered light intensity for the cases of homeotropic and planar orientations, respectively:

$$\begin{aligned}I^{(h)}(\theta,E)=I_0\frac{\omega^4}{c^4}\frac{V\varepsilon_a^2}{(4\pi)^2r^2}\frac{1}{L}\sin^2\theta\int_{-L/2}^{L/2}\int_{-L/2}^{L/2}dz'\,dz''\\ \times\exp[-iq_{sc,z}(z'-z'')]G^h_{22}(\mathbf{q}^\perp_{sc},z',z''),\end{aligned} \tag{6.7}$$

$$\begin{aligned}I^{(p)}(\theta,E)=I_0\frac{\omega^4}{c^4}\frac{V\varepsilon_a^2}{(4\pi)^2r^2}\frac{1}{L}(1-\sin^2\theta\cos^2\varphi)\\ \times\int_{-L/2}^{L/2}\int_{-L/2}^{L/2}dz'\,dz''\,\exp[-iq_{sc,z}(z'-z'')]\\ \times G^p_{11}(\mathbf{q}^\perp_{sc},z',z'').\end{aligned} \tag{6.8}$$

Here

$$\begin{aligned}G^h_{22}(\mathbf{q}^\perp_{sc},z',z'')=G^p_{11}(\mathbf{q}^\perp_{sc},z',z'')=\frac{1}{4K}\left\{-\frac{\varepsilon_aE^2}{4\pi g}[J(P)\right.\\ \left.-J(Q)]+[J(P)+J(Q)]\right\},\end{aligned}$$

$$g=E\sqrt{\left(\frac{\varepsilon_aE}{4\pi}\right)^2+4(e_1-e_3)^2q^2_{sc,y}}, \tag{6.9}$$

$$P=\sqrt{q^{\perp2}_{sc}+\frac{g}{2K}-\frac{\varepsilon_aE^2}{8\pi K}},\quad Q=\sqrt{q^{\perp2}_{sc}-\frac{g}{2K}-\frac{\varepsilon_aE^2}{8\pi K}}.$$

Here we are interested in the fluctuation modes with $q_x=0$ ($\varphi=\pi/2$), since in our geometry they are the modes that increase most rapidly near the instability threshold. To obtain the expressions for the scattered light intensity we must evaluate the integrals in (6.7) and (6.8). The integrals are

$$\begin{aligned}&\int_{-L/2}^{L/2}\int_{-L/2}^{L/2}dz'\,dz''\,\exp[-iq_{sc,z}(z'-z'')]\\ &\quad\times\cosh[\gamma(z'+z'')]=\frac{2}{\gamma^2+q^2_{sc,z}}\\ &\quad\times[\cosh(\gamma L)-\cos(q_{sc,z}L)],\\ &\int_{-L/2}^{L/2}\int_{-L/2}^{L/2}dz'\,dz''\,\exp[-iq_{sc,z}(z'-z'')]\\ &\quad\times\cosh[\gamma(z'-z'')]=\frac{2}{(\gamma^2+q^2_{sc,z})^2}\{(\gamma^2-q^2_{sc,z})\\ &\quad\times[\cosh(\gamma L)\cos(q_{sc,z}L)-1]\\ &\quad+2\gamma q_{sc,z}\sinh(\gamma L)\sin(q_{sc,z}L)\},\end{aligned} \tag{6.10}$$

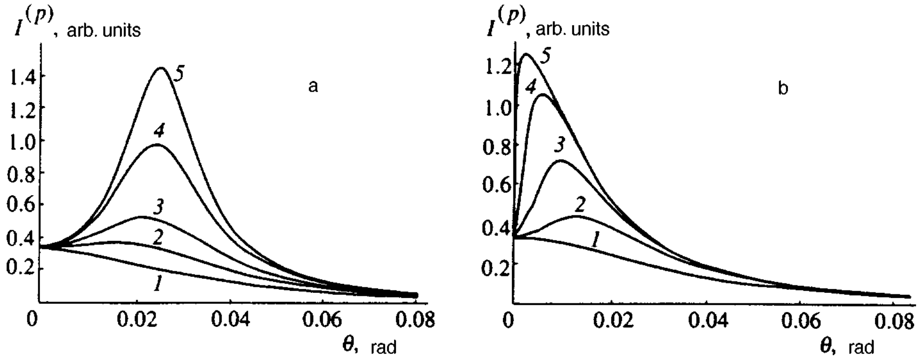

FIG. 2. Angular dependence of the scattered light intensity in a planar-oriented NLC cell for different values of the dielectric-constant anisotropy and different electric field strengths: (a) $\varepsilon_a = 0.1$ (curve *1* corresponds to $U=0$, curve *2* to $U=4.5$ V, curve *3* to $U=5.4$ V, curve *4* to $U=6.03$ V, and curve *5* to $U=6.12$ V); (b) $\varepsilon_a=0.7$ (curve *1* corresponds to $U=0$, curve *2* to $U=3.15$ V, curve *3* to $U=3.312$ V, curve *4* to $U=3.339$ V, and curve *5* to $U=3.3408$ V).

$$\int_{-L/2}^{L/2}\int_{-L/2}^{L/2} dz'dz'' \exp[-iq_{sc,z}(z'-z'')]$$

$$\times \sinh(\gamma|z'-z''|) = \frac{2}{\gamma^2+q_{sc,z}^2}$$

$$\times \left\{ -\gamma L + \frac{1}{\gamma^2+q_{sc,z}^2}[(\gamma^2-q_{sc,z}^2)\right.$$

$$\times \sinh(\gamma L)\cos(q_{sc,z}L)$$

$$\left. + 2\gamma q_{sc,z}\cosh(\gamma L)\sin(q_{sc,z}L)]\right\},$$

where γ is a constant. Combining Eqs. (3.6), (3.7), (3.15), (3.16), and (6.7)–(6.10), we obtain

$$I^{(h)} = \frac{1}{2} I_0 C \frac{\sin^2\theta}{L} F(P,Q), \quad I^{(p)} = \frac{1}{4} I_0 C \frac{1}{L} F(P,Q), \tag{6.11}$$

where

$$F(P,Q) = -\left(1+\frac{\varepsilon_a E^2}{4\pi g}\right)$$

$$\times \left\{ \frac{2P[\cosh(PL)-\cos(q_{sc,z}L)]}{(P^2+q_{sc,z}^2)^2\sinh(PL)} - \frac{L}{P^2+q_{sc,z}^2}\right\}$$

$$+\left(\frac{\varepsilon_a E^2}{4\pi g}-1\right)\left\{\frac{2Q[\cosh(QL)-\cos(q_{sc,z}L)]}{(Q^2+q_{sc,z}^2)^2\sinh(QL)}\right.$$

$$\left. - \frac{L}{Q^2+q_{sc,z}^2}\right\}, \tag{6.12}$$

$$C = \frac{\omega^4}{c^4}\frac{V\varepsilon_a^2 k_B T}{(4\pi)^2 r^2 K}, \quad q_{sc,z} = k(\cos\theta - 1),$$

$$q_{sc}^{\perp} = q_{sc,y} = k\sin\theta.$$

Since the expressions for $I^{(h)}$ and $I^{(p)}$ differ in the angular factors, we examine the angular dependence of the scattered light intensity in the planar orientation. Figure 2 depicts this dependence for different strengths of the external electric field and for typical values of NLC parameters:[1–3] $e_1-e_3 = 0.57\times10^{-11}$ C m^{-1} and $K=0.7\times10^{-6}$ dyn. The type of transition depends on the anisotropy of the dielectric constant. The limiting value of the anisotropy can be found from (5.6): $\varepsilon_a = 4\pi(e_1-e_3)^2/K = 0.52$. The specimen thickness is set equal to $L=10^{-3}$ cm and the length of the wave vector, to $k=10^5$ cm^{-1}.

Figure 2a corresponds to $\varepsilon_a=0.1$ (flexoelectric instability). In this case the critical values of the parameters are $U_c = E_c L = 6.5$ V and $q_{sc}^{\perp} = q_c = 2.6\times10^3$ cm^{-1}.

Figure 2b depicts the $I^{(p)}$ vs. θ dependence at $\varepsilon_a = 0.7$. In this case we have $q_c=0$, and at $U_c = 3.341$ V we have the Freedericksz transition.

Figures 2a and b show that the scattered light intensity has a peak near $q_{sc}^{\perp}=q_c$, with its height increasing as $E\to E_c$. The existence of such a sharp peak in the intensity of the scattered light provides a good possibility for experimental verification of the results and for measuring the difference of the flexoelectric coefficients, e_1-e_3.

Note that near the transition point Eqs. (6.9), (6.11), and (6.12) can be made much simpler if we restrict ourselves to an approximation that is linear in $E-E_c$. Then at $q_{sc}^{\perp}=q_c$ we have

$$g_c \approx \left\{\frac{2\pi(e_1-e_3)^3}{[(e_1-e_3)^2+\varepsilon_a K/4\pi]L} + \frac{(\varepsilon_a/4\pi)^2 K}{(e_1-e_3)^2}(E-E_c)\right\}E, \tag{6.13}$$

$$Q_c \approx i\left[\frac{\pi}{L} + \frac{\varepsilon_a K/4\pi + (e_1-e_3)^2}{2K(e_1-e_3)}(E-E_c)\right], \tag{6.14}$$

$$F_c(P,Q) \approx \left[\frac{\varepsilon_a K}{4\pi(e_1-e_3)^2} - 1\right]$$

$$\times\left\{\frac{2Q_c[\cosh(Q_cL)-\cos(q_{sc,z}L)]}{(Q_c^2+q_{sc,z}^2)^2\sinh(Q_cL)}\right.$$

$$\left. - \frac{L}{Q_c^2+q_{sc,z}^2}\right\}. \tag{6.15}$$

Plugging (6.14) into (6.15) yields

$$F_c(P,Q) \approx \frac{4\pi K[1+\cos(q_{sc,z}L)]}{(q_{sc,z}^2-\pi^2/L^2)^2 L^2 (e_1-e_3)}$$

$$\times\left[\frac{\varepsilon_a K - 4\pi(e_1-e_3)^2}{\varepsilon_a K + 4\pi(e_1-e_3)^2}\right](E-E_c)^{-1}. \tag{6.16}$$

Note that at $q_{sc,z}=\pi/L$ the expression for $F_c(P,Q)$ remains finite. In this case we cannot ignore the term $L/(Q_c^2+q_{sc,z}^2)$ in (6.15), and in view of the fact that

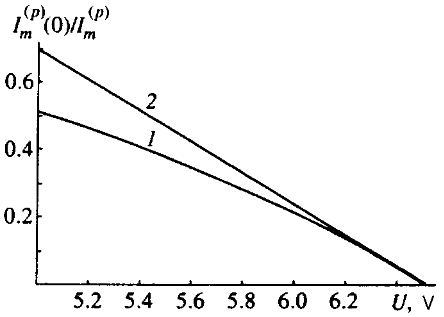

FIG. 3. The normalized reciprocal scattered light intensity at the maximum point $q_{sc}^{\perp}=q_c=2.6\times10^3\ \mathrm{cm}^{-1}$ as a function of the applied electric field for the case of planar orientation of the director, where $I^{(p)}(0)$ is the scattered light intensity at $q_{sc}^{\perp}=q_c$ and $E=0$. Curve *1* represents the results of calculations via (6.12) and (6.18) and curve *2* the results of calculations via the linear-approximation formula (6.16). Here we used the same parameter values as in Fig. 2a, which correspond to $\beta=553.7\ \mathrm{cm\,dyn}^{-1}$ and $F_c(0)=10^{-10}\ \mathrm{cm}^3$.

$$\lim_{q_{sc,z}\to -iQ_c}\left\{\frac{2Q_c[\cosh(Q_cL)-\cos(q_{sc,z}L)]}{(Q_c^2+q_{sc,z}^2)^2\sinh(Q_cL)} - \frac{L}{Q_c^2+q_{sc,z}^2}\right\} = \frac{L[QL\cosh(QL)+\sin(QL)]}{4Q^2\sinh(QL)},$$

we have

$$F_c(P,Q)\approx -\frac{KL^2}{2\pi(e_1-e_3)}\left[\frac{\varepsilon_aK-4\pi(e_1-e_3)^2}{\varepsilon_aK+4\pi(e_1-e_3)^2}\right]\times(E-E_c)^{-1}. \qquad (6.17)$$

Figure 3 depicts the field dependence of the normalized reciprocal scattered light intensity, $I_m^{(p)}(0)/I_m^{(p)}(E)$, at the maximum point $q_{sc,z}=q_c$:

$$\frac{I^{(p)}(0)}{I_m^{(p)}(E)}=\frac{F_c(0)}{F_c(P,Q)}, \qquad (6.18)$$

where $I_m^{(p)}(0)$ is the scattered light intensity in the absence of a field, and

$$F_c(0)\equiv F(P,Q)|_{q_{sc,z}=q_c,E=0} = \frac{2}{q_{sc}^2}\left\{L-\frac{2q_{sc}^{\perp}[\cosh(q_{sc}^{\perp}L)-\cos(q_{sc,z}L)]}{q_{sc}^2\sinh(q_{sc}^{\perp}L)}\right\}.$$

We see that within a fairly broad neighborhood of E_c the reciprocal intensities calculated via the exact formula (6.12) and in the linear approximation (6.16) coincide. At $E\approx E_c$ the slope ξ of the curve representing the field dependence of $I_m^{(p)}(0)/I_m^{(p)}(E)$ is

$$\xi|_{E=E_c}=\beta(e_1-e_3)\left[\frac{\varepsilon_aK-4\pi(e_1-e_3)^2}{\varepsilon_aK+4\pi(e_1-e_3)^2}\right],$$

where

$$\beta=\frac{(q_{sc,z}^2-\pi^2/L^2)^2L^2F_c(0)}{4\pi K[1+\cos(q_{sc,z}L)]}.$$

By measuring ξ we can calculate the difference of the flexoelectric coefficients, e_1-e_3.

7. DISCUSSION

We have examined the correlation functions of the director fluctuations in a nematic liquid crystal placed an external electric field with allowance for the flexoelectric effect with rigid boundary conditions, i.e., with a fixed director orientation at the surface. In this case the formation of spatially periodic flexoelectric structures is of a threshold nature, with the fluctuation mode corresponding to the period of the structure increasing without limit as the external field strength approaches the critical value. In an optical experiment such a pattern corresponds to the emergence of a peak in the angular dependence of the scattered light intensity.

In real liquid crystals the energy of adhesion to the substrate, W, is finite. A consistent analysis of the correlation functions in this case requires a separate investigation. However, some qualitative conclusions concerning the behavior of the director fluctuations can be drawn if we compare the results of two limiting cases: a fixed orientation at the surface, which is considered in this paper, and an infinitely large specimen, when the surface effects play no role. The correlation matrix of the director fluctuations in an external electric field for an infinite medium can easily be calculated via the method used in Secs. 3 and 4. If for the sake of definiteness we assume that the nematic is oriented along the x axis, $\mathbf{n}_0=(1,0,0)$, and that the external field is directed along the z axis, $\mathbf{E}=(0,0,E)$, the Fourier transform of the correlation matrix $\hat{G}^{\infty}$ of the fluctuations $\delta\mathbf{n}=(0,n_y,n_z)$ can be written as

$$\hat{G}_{\mathbf{q}}^{\infty}=\frac{k_BT}{K^2q^4-[(\varepsilon_a/4\pi)Kq^2+(e_1-e_3)^2q_y^2]E^2}\times\begin{pmatrix} Kq^2-\dfrac{\varepsilon_a}{4\pi}E^2 & -i(e_1-e_3)Eq_y \\ i(e_1-e_3)Eq_y & Kq^2\end{pmatrix}, \qquad (7.1)$$

where $\mathbf{q}=q(\sin\theta\cos\varphi,\sin\theta\sin\varphi,\cos\theta)$.

We see that in this case for any value of the electric field strength there are wave vectors

$$q=E\left\{\frac{\varepsilon_a}{4\pi K}+\left[\frac{(e_1-e_3)\sin\varphi\sin\theta}{K}\right]^2\right\}^{1/2},$$

for which the correlation functions have a pole. This corresponds to Meyer's well-known result,[3,10] which states that there is a periodic director distribution with a wave number

$$q\sim\frac{e_1-e_3}{K}E.$$

The formation of a spatial structure becomes a threshold effect when the surface contribution to the free energy begins to exceed the bulk contribution: $W>K/L$ (see Refs. 25 and 26). For $W\ll K/L$, as in an infinite medium, the effect has no threshold, which corresponds to the limit in which $E_c\to 0$ and $q_c\to 0$. This suggests that as the adhesion energy increases, both q_c and E_c increase, tending to the limit values (5.5) as $W\to\infty$.

In an optical experiment, the transition from $W=\infty$ to a finite value of the adhesion energy shifts the peak in the scattered light intensity toward smaller angles and decreases the value of the critical field.

APPENDIX

Let us derive Eq. (4.10) for the matrix

$$\hat{B}^p_{\mathbf{q}}=\hat{H}'+\hat{I}\partial_z^2 . \tag{A1}$$

Substituting (4.5) in (4.9), we get

$$\hat{H}'=\exp\left(\frac{i}{2}\,\hat{D}^{-1}\hat{C}z\right)\left[\frac{1}{4}(\hat{D}^{-1}\hat{C})^2+\hat{D}^{-1}\hat{A}_0\right]\times\exp\left(-\frac{i}{2}\,\hat{D}^{-1}\hat{C}z\right). \tag{A2}$$

If we now insert the explicit expressions for the matrices $\hat{A}_0$, $\hat{D}$, and $\hat{C}$ that enter into (A2), we get the following formulas for the combinations of matrices in (A2):

$$\hat{D}^{-1}\hat{C}=\begin{pmatrix} 0 & \dfrac{K_1-K_2}{K_2}q_y \\ \dfrac{K_1-K_2}{K_1}q_y & 0 \end{pmatrix},$$

$$\hat{D}^{-1}\hat{A}_0 =\begin{pmatrix} -\dfrac{K_3}{K_2}q_x^2-\dfrac{K_1}{K_2}q_y^2 & -i\dfrac{e_1-e_3}{K_2}Eq_y \\ i\dfrac{e_1-e_3}{K_1}Eq_y & -\dfrac{K_3}{K_1}q_x^2-\dfrac{K_2}{K_1}q_y^2+\dfrac{\varepsilon_a}{4\pi K_1}E^2 \end{pmatrix}, \tag{A3}$$

$$\frac{1}{4}(\hat{D}^{-1}\hat{C})^2+\hat{D}^{-1}\hat{A}_0 =\begin{pmatrix} -\dfrac{K_3}{K_2}q_x^2-\left(\dfrac{1}{2}+\dfrac{3}{4}\dfrac{K_1}{K_2}-\dfrac{1}{4}\dfrac{K_2}{K_1}\right)q_y^2 \\ -i\dfrac{e_1-e_3}{K_2}Eq_y \\ i\dfrac{e_1-e_3}{K_1}Eq_y \\ -\dfrac{K_3}{K_1}q_x^2-\left(\dfrac{1}{2}+\dfrac{3}{4}\dfrac{K_2}{K_1}-\dfrac{1}{4}\dfrac{K_1}{K_2}\right)q_y^2+\dfrac{\varepsilon_a}{4\pi K_1}E^2 \end{pmatrix}.$$

The rotation matrix $\exp(\pm(i/2)\hat{D}^{-1}\hat{C}z)$ has the following form

$$\exp\left(\pm\frac{i}{2}\,\hat{D}^{-1}\hat{C}z\right)=\exp[\hat{M}\times(\pm z)] =\hat{T}\begin{pmatrix}\exp(\pm\lambda_1 z) & 0 \\ 0 & \exp(\pm\lambda_2 z)\end{pmatrix}\hat{T}^{-1}, \tag{A4}$$

where

$$\hat{M}=\begin{pmatrix} 0 & -\tau\sqrt{\dfrac{K_1}{K_2}} \\ -\tau\sqrt{\dfrac{K_2}{K_1}} & 0 \end{pmatrix},$$

$$\tau=\frac{1}{2i}\,\frac{K_1-K_2}{\sqrt{K_1K_2}}q_y ,$$

$$\hat{T}=\begin{pmatrix} 1 & 1 \\ -\sqrt{\dfrac{K_2}{K_1}} & \sqrt{\dfrac{K_2}{K_1}} \end{pmatrix},$$

$\hat{T}$ a matrix composed of eigenvectors, and $\lambda_{1,2}=\pm\tau$ are the eigenvalues of $\hat{M}$.

Plugging these expressions into (A4), we obtain

$$\exp\left(\frac{i}{2}\,\hat{D}^{-1}\hat{C}z\right)=\hat{T}\begin{pmatrix} e^{\tau z} & 0 \\ 0 & e^{-\tau z}\end{pmatrix}\hat{T}^{-1} =\begin{pmatrix} \cos\alpha & -i\sqrt{\dfrac{K_1}{K_2}}\sin\alpha \\ -i\sqrt{\dfrac{K_2}{K_1}}\sin\alpha & \cos\alpha \end{pmatrix},$$

$$\exp\left(-\frac{i}{2}\,\hat{D}^{-1}\hat{C}z\right) =\begin{pmatrix} \cos\alpha & i\sqrt{\dfrac{K_1}{K_2}}\sin\alpha \\ i\sqrt{\dfrac{K_2}{K_1}}\sin\alpha & \cos\alpha \end{pmatrix}, \tag{A5}$$

where

$$\alpha=-i\tau z=-\frac{1}{2i}\,\frac{K_1-K_2}{\sqrt{K_1K_2}}q_y z.$$

Inserting (A3) and (A5) into (A2) and multiplying the matrices, we arrive at the expression (4.10) for $\hat{B}^p_{\mathbf{q}}$.

[1] P. G. de Gennes, *The Physics of Liquid Crystals*, Oxford Univ. Press, London (1974).

[2] S. Chandrasekhar, *Liquid Crystals*, Cambridge Univ. Press, London (1977).

[3] S. A. Pikin, *Structural Transformations in Liquid Crystals* [in Russian], Nauka, Moscow (1981).

[4] L. D. Landau and E. M. Lifshitz, *Statistical Physics*, Part 1, 3 rd ed., Pergamon Press, Oxford (1980).

[5] B. Ya. Zel'dovich, N. F. Pilipetskiĭ, A. V. Sukhov, and N. V. Tabiryan, JETP Lett. **31**, 263 (1980).

[6] A. S. Zolot'ko, V. F. Kitaeva, N. Kroo, N. N. Sobolev, and L. Chillag, JETP Lett. **32**, 158 (1980).

[7] I. C. Khoo, Phys. Rev. A **25**, 1040 (1982).

[8] S. J. Elson, I. Solymar, and D. J. Webb, Phys. Rev. E **48**, 1172 (1993).

[9] V. P. Romanov and D. O. Fedorov, Opt. Spektrosk. **79**, 313 (1995) [Opt. Spectrosc. **79**, 288 (1995)].

[10] P. Galatola and M. Rajteri, Phys. Rev. E **49**, 623 (1994).

[11] K. Eidner, M. Lewis, H. K. M. Vithana, and D. L. Johnson, Phys. Rev. A **40**, 6388 (1989).

[12] M. San Miguel and F. Sagues, Phys. Rev. A **36**, 1883 (1987).
[13] F. Sagues and M. San Miguel, Phys. Rev. A **39**, 6567 (1989).
[14] P. Galatola, C. Oldano, and M. Rajteri, Phys. Rev. E **49**, 1458 (1994).
[15] C. Oldano, Phys. Rev. Lett. **56**, 1098 (1986).
[16] E. Miraldi, C. Oldano, and A. Strigazzi, Phys. Rev. A **34**, 4348 (1986).
[17] R. B. Meyer, Phys. Rev. Lett. **22**, 918 (1969).
[18] B. Ya. Zel'dovich and N. V. Tabiryan, Zh. Éksp. Teor. Fiz. **81**, 1738 (1981) [Sov. Phys. JETP **54**, 922 (1981)].
[19] T. Ya. Marusiĭ, Yu. A. Reznikov, V. Yu. Reshetnyak, M. S. Siskin, and A. I. Khizhnyak, Zh. Éksp. Teor. Fiz. **91**, 851 (1986) [Sov. Phys. JETP **64**, 502 (1986)].
[20] F. Lonberg and R. B. Meyer, Phys. Rev. Lett. **55**, 718 (1985).
[21] V. P. Romanov and A. N. Shalaginov, Zh. Éksp. Teor. Fiz. **102**, 884 (1992) [Sov. Phys. JETP **75**, 483 (1992)].
[22] A. Yu. Val'kov, V. P. Romanov, and A. N. Shalaginov, Usp. Fiz. Nauk **164**, 149 (1994) [Phys. Usp. **36**, 139 (1994)].
[23] L. D. Landau and E. M. Lifshitz, *Electrodynamics of Continuous Media*, Pergamon Press, Oxford (1984).
[24] V. L. Kuz'min, V. P. Romanov, and L. A. Zubkov, Phys. Rep. **248**, 71 (1994).
[25] S. A. Pikin, V. G. Chigrinov, and V. L. Indenbom, Mol. Cryst. Liq. Cryst. **37**, 313 (1976).
[26] Y. P. Bobylev, V. G. Chigrinov, and S. A. Pikin, J. de Phys. Coll. **40**, C3–331 (1979).

Translated by Eugene Yankovsky

Optical and magneto-optical properties of Fe/Cu multilayered films: influence of the modulation period and the bcc-fcc phase transition in iron

M. M. Kirillova, I. D. Lobov, V. M. Maevskiĭ, L. V. Nomerovannaya, A. A. Makhnev,
G. A. Bolotin, and F. A. Pudonin

Institute of the Physics of Metals, Russian Academy of Sciences, Ural Branch, 620219 Ekaterinburg, Russia

(Submitted 11 June 1996)
Zh. Éksp. Teor. Fiz. **112**, 1694–1709 (November 1997)

The optical and magneto-optical properties of multilayered film samples of the Fe/Cu system prepared by high-frequency sputtering on an Si(100) substrate are studied by ellipsometry and by measuring the equatorial Kerr effect (the δ_p effect) in the spectral range 0.25–7 μm. The optical characteristics, the plasma frequency ω_p and the relaxation frequency γ_0 of the conduction electrons, and the δ_p effect are found as functions of the modulation period $D = 12.5 - 100$ Å. Anomalous behavior of the optical and magneto-optical characteristics is discovered in short-period Fe/Cu structures. The results are discussed within a phenomenological theory of optical and magneto-optical properties for layered structures. Several factors, such as the indirect exchange interaction between the iron layers, the presence of a transition layer on the internal boundaries, the possible ''magnetizing'' of copper, and the formation of an fcc iron phase in the thin layers, are taken into account in the analysis of the experimental data. © *1997 American Institute of Physics.* [S1063-7761(97)01211-0]

1. INTRODUCTION

The interest in investigating metallic superlattices with alternating ultrathin magnetic and nonmagnetic layers has been stimulated by the search for new electronic phenomena associated with lowering of the dimensionality of the layers (the 3D→2D transition) and the need to deepen our understanding of their magnetic state. Giant magnetoresistance due to the antiferromagnetic type of indirect exchange interaction between magnetic layers has been discovered in these superlattices (see Refs. 1–3 for Fe/Cr and Co/Cu). The character of the interlayer exchange interaction also has a decisive influence on the magneto-optical properties of layered systems.[4] The most important feature of structures of this class is the enhancement of the magneto-optical activity in the ultraviolet region of the spectrum [for example, in Pt/Co (Ref. 5)]. A resonant increase in the Kerr effect in the visible region has been observed in Fe/Ag/Fe and Fe/Au/Fe sandwiches.[6,7] The nature of these phenomena has not been conclusively ascertained and is being actively discussed.

In recent years a great deal of attention has been focused on the study of Fe/Cu thin-film systems, particularly their magnetic characteristics. It has been established by structural investigations that as the thickness d_{Fe} of the layer adjacent to copper decreases, the iron crystal lattice changes from the bcc (α) to the fcc (γ) phase, and the critical thickness for the $\alpha \rightarrow \gamma$ transformation is estimated as $d_{\mathrm{Fe}} \leqslant 1.5$ nm.[8,9] The experimental information on the magnetic state of γ-Fe obtained by different methods, including neutron diffraction analysis and Mössbauer spectroscopy, are extremely contradictory (see Refs. 10 and 11, as well as the review in Ref. 12). It is already clear that there is a difference between the magnetic states of γ-Fe obtained in the form of particles in a copper matrix and in the form of thin films in a layered system with copper. In the former case an antiferromagnetic state with a Néel temperature $T_N = 69$ K forms.[13] In the latter case either an antiferromagnetic or a ferromagnetic state can form, and, according to Ref. 14, the Curie temperature can reach values of 400–578 K. Bennett *et al.*[15] observed a polar Kerr effect on an epitaxially grown γ-Fe/Cu/γ-Fe sandwich at $\lambda = 0.63$ μm and room temperature. Along with enhancement of the effect, they also noticed its oscillatory dependence on d_{Cu}. Enhancement of the Kerr effect in an α-Fe/Cu multilayered film at $\lambda = 0.56$ μm (the ''plasma'' absorption edge in copper) was also noted in Ref. 16. There is a school of thought which holds that the increase in magneto-optical activity is attributable to induction of a magnetic moment in the *d* and *p* subshells of the copper atoms adjacent to the ferromagnetic iron, i.e., to the ''magnetizing'' of copper under the influence of the Fe–Fe exchange interaction. A great deal of attention has been focused on the search for evidence in support of the spin polarization of copper in Fe/Cu and Co/Cu systems.[17–19] On the other hand, an active theoretical search is being conducted for the changes in the electronic structure of thin layers that are associated with the lowering of their dimensionality. The available experimental data on this subject are very limited.

In the present work the optical and magneto-optical properties of an Fe/Cu periodic multilayered structure were studied by several methods on a single system of samples. The main purpose of the work was to study the evolution of the electronic characteristics and magnetic state in response to variation of the modulation period of the layered structure and to the $\alpha - \gamma$ phase transition in the iron layers. Another objective was to theoretically analyze the optical and magneto-optical spectra of Fe/Cu within a phenomenological theory that takes into account multiple reflections from the interface.

2. EXPERIMENT

We investigated a system of Fe/Cu multilayered films with a fixed ratio $d_{\mathrm{Fe}}/d_{\mathrm{Cu}} = 2/3$ between the layer thicknesses: (Fe 40 Å/Cu 60 Å)$_{10}$, (Fe 30 Å/Cu 45 Å)$_{14}$, (Fe 20 Å/Cu 30 Å)$_{20}$, (Fe 15 Å/Cu 22.5 Å)$_{27}$, (Fe 10 Å/Cu 15 Å)$_{40}$, (Fe 8 Å/Cu 12 Å)$_{50}$, and (Fe 5 Å/Cu 7.5 Å)$_{80}$. The modulation period $D = d_{\mathrm{Cu}} + d_{\mathrm{Fe}}$ in these structures varied in the range 12.5–100 Å. The samples were prepared at room temperature by high-frequency sputtering in an argon atmosphere with a pressure equal to 1.1×10^{-3} Torr in the apparatus described in Ref. 20. The deposition rate for iron was 54.7 Å/min, and the rate for copper was 36.4 Å/min. Silicon(100) wafers served as substrates. In all cases the uppermost layer was an iron film. Pure Fe and Cu films with $d = 1000$ Å were also deposited in the same chamber. The thicknesses of the layers were determined from the deposition rate and time. An investigation of transverse sections of several samples by transmission electron microscopy confirmed the periodicity of the multilayered films across their thickness.

The crystal structure of the samples was studied by x-ray diffraction analysis on a DRON-3M diffractometer in Cu K_α radiation. The investigations showed that the crystalline state of Fe and Cu is manifested fairly clearly in all the samples. In ultrathin layers ($d \leqslant 10$ Å) the grain size is strongly reduced, and partial destruction of the long-range order takes place. However, a halo, which would attest to the presence of an amorphous phase, was not discovered on the x-ray diffraction patterns. The form of the diffraction reflections indicates the presence of stresses in the iron crystal lattice, which grow as the thickness of the layers decreases. The data that we obtained confirmed the results of the earlier x-ray diffraction studies, which revealed that the copper layers have a well defined fcc lattice with a very small distortion that does not depend on the thickness of the layers or the ratio $d_{\mathrm{Fe}}/d_{\mathrm{Cu}}$ and that the iron crystal lattice undergoes a bcc-fcc phase transition as the layer thickness decreases. It has been reported[11] that stabilization of the γ phase of Fe in the Fe/Cu system is largely determined by the deposition conditions, including the substrate temperature. Our analysis showed that there are only ‘‘traces’’ of γ-Fe in (Fe 15 Å/Cu 22.5 Å)$_{27}$. The fractions of the α and γ phases in the (Fe 10 Å/Cu 15 Å)$_{40}$ and (Fe 8 Å/Cu 12 Å)$_{50}$ phases are almost equivalent, and in (Fe 5 Å/Cu 7.5 Å)$_{80}$ the contribution of γ-Fe becomes dominant ($\sim$80%).

The effective refractive index (n_{eff}) and absorption coefficient (k_{eff}) were measured on an automatic ellipsometer with one ($\lambda = 0.25 - 2.5$ μm) and two ($\lambda = 2.5 - 7$ μm) reflections from the sample. The angle of incidence of light onto the sample was $\varphi_1 = 76°$ at wavelengths $\lambda < 1.5$ μm and $\varphi_2 = 81°$ for $\lambda > 1.5$ μm. The optical properties of iron and copper were measured on the same instrument. The error in the measurements of n_{eff} and k_{eff} was 2–5%. The values of n_{eff} and k_{eff} were used to calculate the effective values of the real ($\varepsilon'_{\mathrm{eff}}$) and imaginary ($\varepsilon''_{\mathrm{eff}}$) parts of the dielectric constant, as well as the optical conductivity σ_{eff}.

Measurements of the equatorial Kerr effect (an effect which is odd with respect to the magnetization and associated with the relative variation of the intensity of the reflected light $\Delta I/I$ upon equatorial magnetization of the sample and p polarization of the incident wave) were performed on the system described in Ref. 21 in the spectral range 0.3–2.4 μm when light was incident on the sample at an angle $\varphi = 70°$. The field dependence of the equatorial Kerr effect was studied at $\lambda = 0.6$ μm and fields $H \leqslant 9$ kOe.

3. DISCUSSION

3.1. Optical properties

As we know, the ellipsometric determination of the optical constants and the dielectric constant of a metal is based on the difference between the reflection coefficients for light polarized in the plane of incidence (p polarization) and perpendicularly to it (s polarization). When light is reflected from a metal boundary at an angle φ, the amplitude reflection coefficients r_p and r_s are given by the Fresnel formulas, and the complex refractive index N is expressed in terms of the ratio r_p/r_s:

$$N = \sin\varphi\left[1 + \tan^2\varphi\left(\frac{1 - r_p/r_s}{1 + r_p/r_s}\right)^2\right]^{1/2}. \tag{1}$$

If the medium is continuous, Eq. (1) defines the effective complex refractive index N_{eff} in terms of the measurable quantity r_p/r_s.[22]

The experimental data on the frequency dependence of the effective dielectric constant $\varepsilon_{\mathrm{eff}} = N^2_{\mathrm{eff}}(\omega)$ will be discussed within a theory derived from a simple model of a superlattice consisting of alternating layers of two metals with the possible inclusion of a transition layer on the boundary between them. Regardless of the value of the modulation period, the optical properties of a periodic multilayer can be described with consideration of the macroscopic dimensions of the samples across their thickness by introducing a macroscopic characteristic, viz., the dielectric constant $\varepsilon(z)$, where z is the coordinate transverse to the plane of the layers. In solving the reflection problem, it is permissible to go over to the simulation of an inhomogeneous medium with a periodic dependence of the dielectric constant on z and to treat the repeating fragment of the periodic multilayer as a set of layers with individual dielectric constants ε_j. The thicknesses d_j of the layers so distinguished should correspond to regions of relatively uniform $\varepsilon_j(z)$. If we start out from the simplest case of a periodic bilayer structure, a calculation of the reflection coefficients r_p and r_s with consideration of multiple reflections on the interfaces and the phase shifts across the thickness of the layers[22] using Eq. (1) under the condition that the dielectric constants are large and the thicknesses of the layers are small compared with the skin depth in the material under consideration, i.e.,

$$|\varepsilon_j| \gg 1, \quad \frac{\omega}{c}|\sqrt{\varepsilon_j}|d_j \ll 1 \tag{2}$$

(ω is the frequency and c is the velocity of light in vacuum), leads to the following expression for the effective refractive index:

$$N_{\mathrm{eff}} = \left[\frac{1}{D}(\varepsilon_1 d_1 + \varepsilon_2 d_2)\right]^{1/2} + \frac{i\omega}{2c}(\varepsilon_1 - \varepsilon_2)\,\frac{d_1 d_2}{D}, \tag{3}$$

where $D = d_1 + d_2$ is the period of the bilayer superlattice and i is the unit imaginary number. The second term in (3), which is determined by the difference between the dielectric constants of the layers, is a small correction because of the inequalities (2), and in the approximations indicated (layer thickness small in comparison to the skin depth) a metallic superlattice is an effective optical medium with a thickness-weighted dielectric constant

$$\varepsilon_{\text{eff}}(\omega) = \frac{1}{D} \sum_j \varepsilon_j d_j \tag{4}$$

regardless of the number of layers in the repeating fragment. Therefore, the real ($\varepsilon'_{\text{eff}}$) and imaginary ($\varepsilon''_{\text{eff}}$) parts of the dielectric constant, as well as the optical conductivity

$$\sigma_{\text{eff}}(\omega) = \frac{\omega}{4\pi} \operatorname{Im} \varepsilon_{\text{eff}}, \tag{5}$$

are weighted means.

We now proceed to a discussion of the experimental data. Let us consider the optical response of the Fe/Cu system in the infrared region $\lambda = 3 - 7\ \mu$m, where monotonic increases in $\varepsilon'_{\text{eff}}$ and $\varepsilon''_{\text{eff}}$ with increasing λ are observed. Under conditions such that the electron mean free path in the field of a light wave is comparable to or greater than the thickness of the layers ($l \geqslant d_j$), size effects have an influence on ε_j. Therefore, the use of the bulk values of the dielectric constants of Fe and Cu in Eq. (4) is now incorrect. For this reason, we did not simulate ε_{eff} in the infrared region. However, the Drude character of the spectral dependence of $\varepsilon'_{\text{eff}}$ and $\varepsilon''_{\text{eff}}$ makes it possible to estimate the parameters of the conduction electrons, viz., the plasma frequency ω_p and the relaxation frequency γ_0, and to trace their evolution as the modulation period D varies. We obtained the values of ω_p from the linear segment of a plot of

$$1/(1 - \varepsilon'_{\text{eff}}) = \omega^2/\omega_p^2 + \gamma_0^2/\omega_p^2$$

(the contribution from the virtual electronic transition was neglected here). As expected, the variation of ω_p with decreasing D is insignificant. For thick-layered bcc-Fe/Cu samples ($D = 50 - 100$ Å) the average value of $\hbar\omega_p$ is 4.4 eV. In structures with ultrathin layers ($D \leqslant 37.5$ Å), in which the fraction of fcc Fe amounts to 50–80%, $\hbar\omega_p$ decreases to 3.8 eV. The dependence of the relaxation frequency $\gamma_0(D)$ has a significantly different character (Fig. 1). The observed sharp increase in γ_0 is an indication of additional scattering of electrons from the internal interlayer boundaries, whose number within the skin depth increases as the period of the multilayered structure decreases. An increase in γ_0 also promotes additional scattering of electrons from the grain boundaries because of the sharp drop in their grain size, especially in the samples with $D \leqslant 20$ Å. Figure 1 also presents data on the optical resistivity $\rho_{\text{opt}} = 4\pi\gamma_0/\omega_p^2$, which is calculated in the low-frequency limit $\omega \to 0$ from the values of ω_p and γ_0. It can be concluded that the characteristic dependence of ρ_{opt} on D in thin-layer periodic multilayers is determined mainly by processes involving the scattering of conduction electrons.

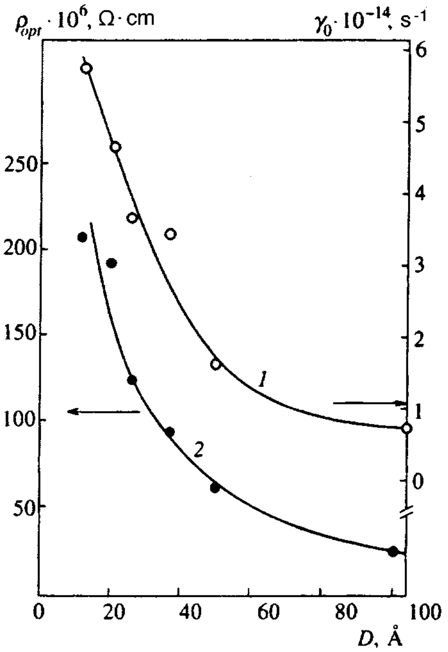

FIG. 1. Dependence of the relaxation frequency of the conduction electrons (*1*) and the optical resistivity (*2*) on the modulation period in an Fe/Cu system with $d_{\text{Fe}}/d_{\text{Cu}} = 2/3$.

Let us now turn to a discussion of the optical response of the Fe/Cu system in the spectral range 0.5–5 eV. The dispersion curves of σ_{eff} for Fe/Cu samples and the optical conductivities of pure iron and copper are presented in Figs. 2a and 2b. In the spectral region considered the optical properties of iron are determined by the interband mechanism of optical absorption. The optical spectrum of bcc Fe contains an intense absorption band with a maximum at 2.2 eV. Numerical calculations of the optical properties of ferromagnetic α-Fe performed in the one-electron approximation (see, for example, Refs. 23 and 24) established that this band is formed by the superposition of several partial contributions from interband transitions within the $3d$ subband with orientation of the spin opposite to the magnetization (↓) ($d-d$, p transitions). The contribution of interband transitions in the system of bands with spins oriented with the magnetization (↑) to σ_{Fe} is insignificant because of the almost completely filled state of the $3d_{\uparrow}$ band and the sharp contraction of the phase volume for electron excitation. In copper the optical properties are determined by an intraband mechanism of optical absorption at photon energies $E < 2$ eV. The interband absorption edge at $E \approx 2.1$ eV is caused by the excitation of electrons from the top of the $3d$ band into the conduction band [the $L_3 \to L'_2(E_F)$ transition]. Within the effective-medium model considered above [expression (4)], the high optical conductivity of α-Fe will be ''diluted'' by contributions to $\sigma_{\text{Cu}}(\omega)$ of small magnitude as the thickness of the copper layer increases. Because of the strong contrast between the optical properties of these metals, the resultant spectra of σ_{eff} acquire new dispersion features. In particular, as has already been noted in Ref. 25, the absorption peak at 2.4–2.6 eV, which is formed by the superposition of contributions from interband transitions of electrons in both the

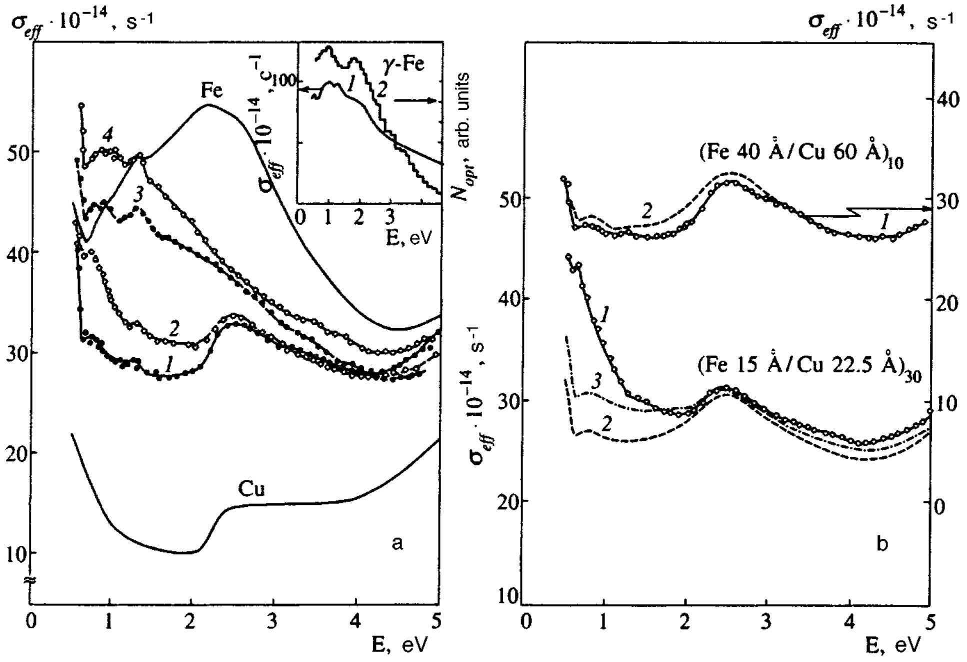

FIG. 2. Dispersion of the optical conductivity $\sigma_{\rm eff}$: a) *1*—(Fe 30 Å/Cu 45 Å)$_{14}$, *2*—(Fe 20 Å/ Cu 30 Å)$_{20}$, *3*—(Fe 8 Å/Cu 12 Å)$_{50}$, *4*—(Fe 5 Å/Cu7.5 Å)$_{80}$. Inset: *1*—optical conductivity of γ-Fe, *2*—histogram of the density of optical interband transitions in γ-Fe. b) *1*—Experimental data for $\sigma_{\rm eff}$, *2*—calculation in the sharp-boundary model, *3*—calculation based on a model with a transition layer of thickness $d_0 = 4$ Å.

iron and copper layers, becomes the dominant feature on the $\sigma_{\rm eff}$ curve.

The results of the simulation of the optical spectra of periodic multilayers using Eq. (4) and the values of the optical constants that we obtained in thick-film samples of iron and copper are presented in Fig. 2b. It can be seen that the theory which takes into account the multiple reflections of a light wave from a sharp boundary between media provides a fully satisfactory description of the dispersion of $\sigma_{\rm eff}$ by a layered system with ''thick'' metallic layers. The (Fe 40 Å/Cu 60 Å)$_{10}$ sample is an example. However, for the samples with thinner layers of bcc iron and copper the fit between the experimental and simulated $\sigma_{\rm eff}$ curves is maintained only at photon energies $E \geqslant 2$ eV. As an example we present the simulated optical conductivity curves for the (Fe 15 Å/Cu 22.5 Å)$_{27}$ sample. Figure 2b shows that for $E \leqslant 1.5$ eV the calculated curves predict optical absorption lower than the experimentally observed value. It is perfectly reasonable to attribute this disparity to the presence in real systems of a transition layer between iron and copper, which can be a mixture of the bcc and fcc iron fractions and copper. It was found that consideration of a transition layer of thickness $d_0 = 4$ Å having optical constants that correspond to the data for the (Fe 5 Å/Cu 7.5 Å)$_{80}$ sample improves the agreement between the experimental and simulated $\sigma_{\rm eff}$ curves in the spectral region indicated, although the disparity between the absorption amplitudes persists. As D decreases the differences in the dispersion of the experimental and simulated $\sigma_{\rm eff}$ curves increases significantly.

It might be expected that the enhancement of the low-energy absorption in short-period Fe/Cu structures is caused by the influence of the intraband absorption mechanism. However, estimates of the contributions $\sigma_{\rm intra}$ obtained using the values of ω_p and γ_0 presented above showed that this influence is insignificant in the spectral region $E = 0.5 - 2$ eV of interest to us. For example, at a photon energy $E = 1$ eV, the value of $\sigma_{\rm intra}$ in the samples with a modulation period $100 \leqslant D \leqslant 12.5$ Å varies from 17×10^{14} to 6×10^{14} s^{-1}, while the experimentally observed increase in the optical conductivity is $\Delta\sigma_{\rm eff} = 26 \times 10^{14}$ s^{-1}.

In our opinion, one of the causes of the appearance of additional low-energy absorption is the modification of the electronic structure in thin layers of iron and copper, particularly the formation of surface electronic states near the Fermi level E_F. This question was thoroughly investigated for Fe/Cu bilayers and Cu/Fe/Cu sandwiches in Ref. 12 via self-consistent calculations of the energy bands of iron by the linear APW method. In thick films the role of the surface states in shaping the optical spectra is small; however, as the layers thin, the contribution of the electronic surface states to the low-energy interband excitation processes increases considerably. Just such a tendency can be traced in the behavior of the optical spectra of Fe/Cu (Fig. 2a).

We noticed an even more significant transformation of the optical conductivity curve associated with the $\alpha - \gamma$ phase transition in iron layers. For example, the (Fe 8 Å/Cu 12 Å)$_{50}$ sample with almost equivalent fractions of α and γ-iron exhibits enhancement of the interband absorption in the near-infrared region of the spectrum (Fig. 2a, curve *3*), as a result of which the fundamental absorption peak is centered at $E = 0.7 - 1.4$ eV. The further increase in the γ-Fe fraction in (Fe 5 Å/Cu 7.5 Å)$_{50}$ leads to an increase in the intensity of that peak (Fig. 2a, curve *4*). We applied Eq. (4) to two thin-film samples with $D = 12$ and 20 Å to determine the spectral dependence of the optical conductivity of γ-Fe. Although the procedure for subtracting the contributions of $\sigma_{\rm Cu}$ and $\sigma_{\alpha-{\rm Fe}}$ from the resultant $\sigma_{\rm eff}$ curve is approximate, the spectral profile of $\sigma_{\gamma-{\rm Fe}}$ is practically identical in both cases. Thus, in the $\alpha - \gamma$ phase transition, which is accompanied by an approximately 26% increase in

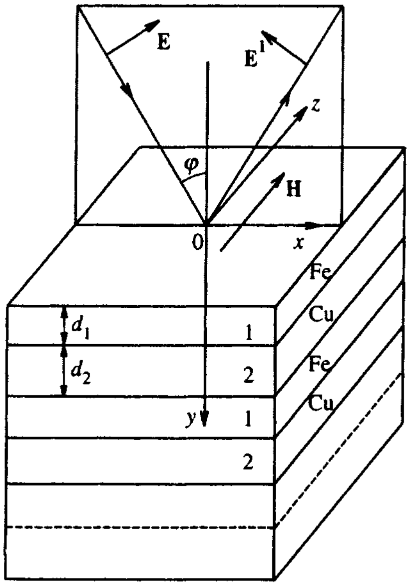

FIG. 3. Diagram illustrating the measurement of the equatorial Kerr effect in a periodic multilayer. The electric intensity vector **E** of the incident beam lies in the xy plane (p polarization). The magnetizing field **H** is parallel to the z axis, and φ is the angle of incidence of the light.

the crystal lattice parameter of iron, the maximum of the fundamental interband absorption band shifts from 2.2 eV to 1.1 eV. The shape of the $\sigma_{\gamma-\mathrm{Fe}}$ curve correlates with the energy dependence of the density of optical transitions N_{opt} obtained using Spicer's formula.[26] To calculate N_{opt} we used the data on the electronic density of states $N(E)$ in thin ferromagnetic fcc Fe layers having two-dimensional translational symmetry.[27] We shall address the question of the character of the magnetic ordering of the γ phase in our samples when we discuss the magneto-optical data in the next section.

3.2. Magneto-optical properties

a) Theory of the equatorial Kerr effect for a periodic multilayer. A diagram of the observation of the equatorial Kerr effect is shown in Fig. 3. We assume that all the media in the periodic multilayer have symmetry no lower than cubic and are uniformly magnetized. For an assigned thickness d_j in the approximation that is linear with respect to the magnetization each layer is described by a dielectric tensor

$$\hat{\varepsilon}=\varepsilon_j\begin{pmatrix} 1 & -iQ_j & 0 \\ iQ_j & 1 & 0 \\ 0 & 0 & 1 \end{pmatrix}, \quad j=1,2, \tag{6}$$

where ε_j is the diagonal dielectric constant and Q_j is the magneto-optical parameter of the medium, which is proportional to its saturation magnetization ($|Q_j|\ll 1$). In the sharp-boundary model the magnitude of the equatorial Kerr effect for the reflection of p-polarized light from an infinite periodic multilayered structure (with a number of periods $N\rightarrow\infty$) is found, according to Ref. 22, from the expression

$$\delta_p=\frac{\Delta I}{I}=2\,\mathrm{Im}\,\frac{[(G^2-G_1^2)a_2+(G_2^2-G^2)a_1]\sin 2\varphi}{(\cos^2\varphi-G^2)(G_1^2-G_2^2)}, \tag{7}$$

where φ is the angle of incidence of the light,

$$G_j=\frac{g_j}{\varepsilon_j}, \quad a_j=\frac{Q_j\cos\beta_j}{\varepsilon_j}, \quad g_j=\sqrt{\varepsilon_j-\sin^2\varphi}, \tag{8}$$

and β_j is the angle between the magnetization vector of the jth layer and the z axis (the equatorial angle). The parameter G in (7) is defined by the expression

$$G=\frac{(1-r_p)\cos\varphi}{1+r_p}, \tag{9}$$

where r_p is the reflection coefficient from a periodic multilayer in the absence of magnetization, which can be calculated using the formulas presented in Refs. 22 and 28. We note that the infinite character of the periodic multilayer actually means that its total thickness exceeds the thickness of the effective skin layer.

Let us consider periodic multilayers (Fig. 3) in which the ratio d_2/d_1 between the thicknesses of the layers is constant. The conditions $d_j/\lambda\ll 1$, where λ is the wavelength of the optical wave in a vacuum, usually hold in periodic multilayers. If we confine ourselves in expansions of differences of the form $1-\exp(-i4\pi g_j d_j/\lambda)$ in powers of d_j/λ to the linear and quadratic terms, Eq. (7) can be represented in the form

$$\delta_p=\mathrm{Im}\left(\sum_{j=1}^{2}\frac{d_j}{D}A_jQ_j\cos\beta_j+\frac{D}{\lambda}\sum_{j=1}^{2}B_jQ_j\cos\beta_j\right), \tag{10}$$

where D is the period of the structure, and the coefficients A_j and B_j are functions of the dielectric constants ε_1 and ε_2, the angle of incidence φ of the light, and the ratio d_1/d_2. Explicit expressions for A_j and B_j were presented in Ref. 22. Thus, in the linear approximation with respect to d_j/λ (the Drude approximation) the expression for the equatorial Kerr effect contains a term that does not depend on D and a correction that is linear with respect to D/λ (or d_j/λ).

However, it can be expected that a more complicated dependence of the equatorial Kerr effect on D can appear in real objects because of the variation of the electronic structure and the magnetic characteristics in thin-layer periodic structures.

b) Field and spectral dependence of the δ_p effect. Figures 4 and 5 present the field dependence of the equatorial Kerr effect, which characterizes the magnetizing process of an Fe/Cu structure in a magnetic field **H** parallel to the plane of the film. Note that the samples with $d_{\mathrm{Fe}}>10$ Å containing iron in the bcc phase are magnetized to saturation in weak fields of ~50 Oe, in analogy to a thick ($d\approx 1000$ Å) layer of bcc Fe. At the same time, in the sample with $d_{\mathrm{Fe}}=8$ Å, in which iron is present in a mixture of α and γ phases, the saturation field increases to 300 Oe. The field dependence for the (Fe 5 Å/Cu 7.5 Å)$_{80}$ sample, which contains iron predominantly in the γ phase, has a unique form (Fig. 5a). The magnetization curve has three clearly distinguishable regions: an initial segment at 0–30 Oe, where the δ_p effect is

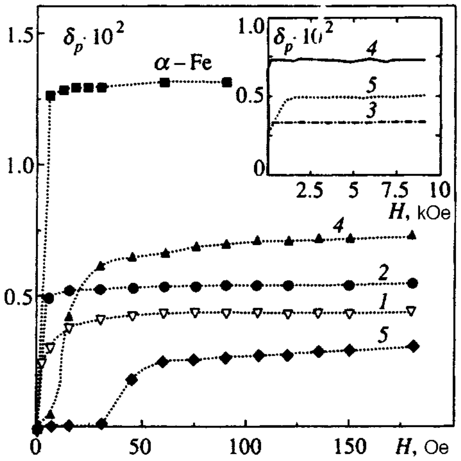

FIG. 4. Dependence of the equatorial Kerr effect for Fe/Cu samples (curves *1–5*) and for a thick film of bcc iron on the magnetizing field H: *1*—(Fe 30 Å/Cu 45 Å)$_{14}$, *2*—(Fe 20 Å/Cu 30 Å)$_{20}$, *3*—(Fe 10 Å/Cu 15 Å)$_{40}$, *4*—(Fe 8 Å/Cu 12 Å)$_{50}$, *5*—(Fe 5 Å/Cu 7.5 Å)$_{80}$.

slightly nonzero, the range from 30 to 60 Oe, where the effect increases sharply, and, finally, a segment with a gently sloping increase in $\delta_p(H)$ up to complete saturation at $H=1600$ Oe.

Let us discuss the results obtained on the basis of the hypothesis that the indirect exchange interaction between the ferromagnetically ordered iron layers influences the magnetic structure of a particular sample. The existence of such an interaction in Fe/Cu periodic multilayered systems is confirmed by the results of magnetoresistance measurements.[29] In addition, it was shown in Ref. 4 within a biquadratic exchange model that in magnetic superlattices (of the Fe/Cr type) the indirect exchange interaction (which depends on the thickness of the intervening nonmagnetic layer) leads to noncollinear ordering of the magnetic moments in neighboring ferromagnetic layers, i.e, to their misalignment by an angle θ_0 differing from 0° and 180°, in a certain range of values of the exchange coupling constants. Ustinov *et al.*[4] also proposed a method, which was used to determine values of θ_0 lying in the range $80°-144°$ from measurements of the equatorial Kerr effect in Fe/Cr superlattices with easy-plane magnetization. We shall use a similar approach to account for the shape of the magnetization curve of the (Fe 5 Å/Cu 7.5 Å)$_{80}$ sample. Figure 5b is a schematic representation of a model of the magnetic structure of the sample in the ground state ($H=0$) and its variation during the magnetizing process in a field **H** applied along the z axis (Fig. 3). When $H=0$ holds, the magnetic moments $\mathbf{M}_1$ and $\mathbf{M}_2$ of neighboring layers of fcc iron are at an angle θ_0, which depends on the exchange coupling energy. It can be assumed that the difference between the vectors $\mathbf{M}_1$ and $\mathbf{M}_2$ lies in a plane parallel to the y axis. The cones drawn in the figure illustrate the fact that the mean magnetization vector $\mathbf{M}=(1/2)(\mathbf{M}_1+\mathbf{M}_2)$ for different domains has directional isotropy at $H=0$, so that the projection of the resultant magnetization $\mathbf{M}_R$ onto the z axis equals zero. This model is based on the data obtained for periodic multilayered structures and γ-Fe/Cu/γ-Fe three-layer structures in Refs. 6, 14, and 30. It was shown in those studies that thin layers of γ-Fe ($d_{\mathrm{Fe}} \leqslant 5.5$ Å) are ferromagnetic for $T \leqslant 400$ K and have perpendicular anisotropy. In addition, the plots of the polar Kerr effect and the saturation field (H_s) versus the thickness of the intervening copper layer in the three-layer structures exhibited maxima, which were interpreted as a manifestation of an indirect exchange interaction of the antiferromagnetic type between the magnetic moments of neighboring iron layers. In weak fields between 0 and 30 Oe, which are lower than the magnetic anisotropy field H_A, this structure is basically preserved (only a small component M_{Rz} appears), and the values of the equatorial Kerr effect in this region are close to zero. In the range of fields 30–60 Oe ($H>H_A$) the vectors **M** of all the domains turn rapidly about the y axis, so that at $H=60$ Oe they are all directed along the field **H**. If the exchange coupling energy significantly exceeds the magnetic anisotropy energy, it can be assumed in a first approximation that this turning takes place without variation of the angle θ_0. In the last range from 60 to 1600 Oe an increase in the field results only in a decrease in the misalignment angle θ of $\mathbf{M}_1$ and $\mathbf{M}_2$ from the value of θ_0 at 60 Oe to 0° at the saturation field of 1600 Oe. According to Ref. 4, the magnitude of the equatorial Kerr effect on this portion of the magnetization curve is specified by the expression

$$\delta_p(H)=A\cos\frac{\theta(H)}{2}, \tag{11}$$

where the coefficient A does not depend on H. Formula (11) was used to find the value of θ_0 for the

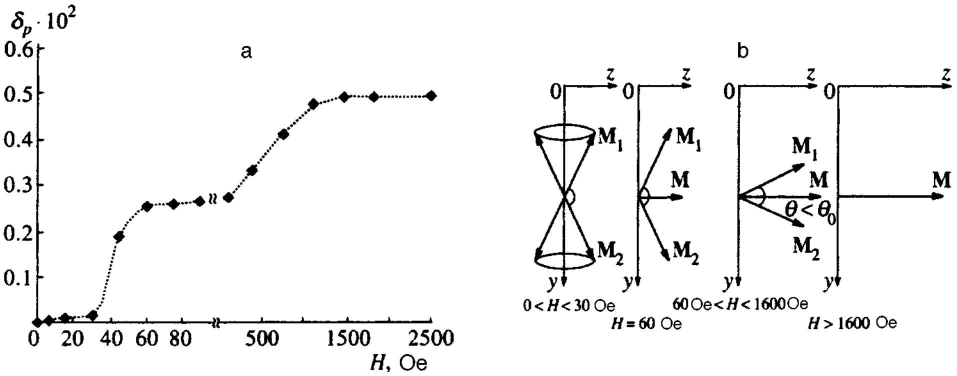

FIG. 5. Dependence of the equatorial Kerr effect for the (Fe 5 Å/Cu 7.5 Å)$_{80}$ sample on the magnetizing field H (a) and model of the magnetic structure of the sample during the magnetizing process (b).

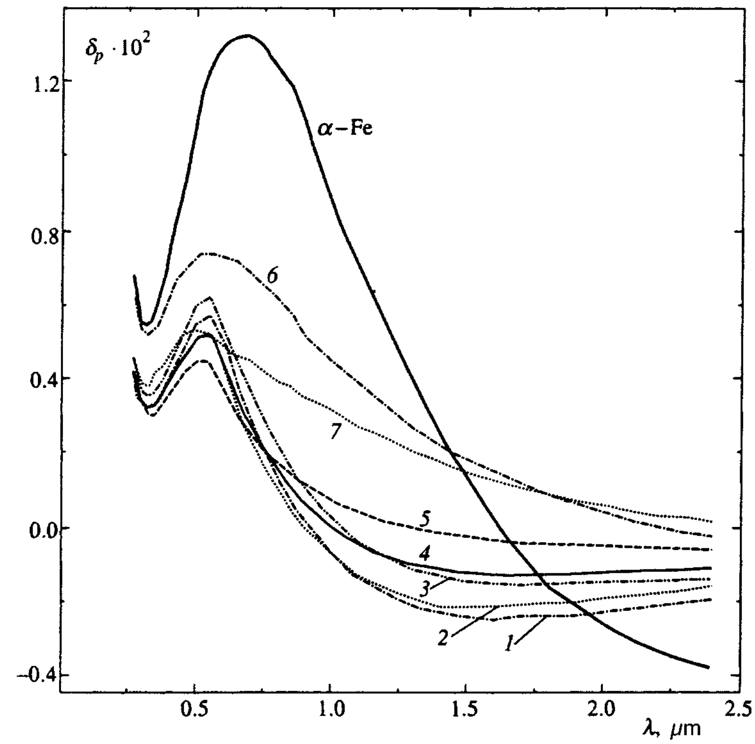

FIG. 6. Spectral dependence of the equatorial Kerr effect for Fe/Cu structures (curves *1–7*) and for a thick film of bcc iron: *1*—$(\mathrm{Fe}\ 40\,\text{Å}/\mathrm{Cu}\ 60\,\text{Å})_{10}$, *2*—$(\mathrm{Fe}\ 30\,\text{Å}/\mathrm{Cu}\ 45\,\text{Å})_{14}$, *3*—$(\mathrm{Fe}\ 20\,\text{Å}/\mathrm{Cu}\ 30\,\text{Å})_{20}$, *4*—$(\mathrm{Fe}\ 15\,\text{Å}/\mathrm{Cu}\ 22.5\,\text{Å})_{27}$, *5*—$(\mathrm{Fe}\ 10\,\text{Å}/\mathrm{Cu}\ 15\,\text{Å})_{40}$, *6*—$(\mathrm{Fe}\ 8\,\text{Å}/\mathrm{Cu}\ 12\,\text{Å})_{50}$, *7*—$(\mathrm{Fe}\ 5\,\text{Å}/\mathrm{Cu}\ 7.5\,\text{Å})_{80}$.

$(\mathrm{Fe}\ 5\,\text{Å}/\mathrm{Cu}\ 7.5\,\text{Å})_{80}$ structure from the values of $\delta_p(60\,\mathrm{Oe})$ and $\delta_p(1600\,\mathrm{Oe})$. It was found to be equal to 120°.

The results of spectral measurements of the equatorial Kerr effect in Fe/Cu structures in saturation fields at $\varphi = 70°$ are presented in Fig. 6, in which a plot of $\delta_p(\lambda)$ for a thick ($d \approx 1000$ Å) film of bcc iron is also presented. It can be seen that the spectral curves for the four long-period periodic multilayered structures with $d_{\mathrm{Fe}} > 10$ Å, which contain iron only (or mainly) in the α phase ($D = 37.5 - 100$ Å), form a separate group. These curves are similar to one another, and their characteristic features (a minimum at $\lambda = 0.3\ \mu$m, a maximum in the region 0.55–0.60 μm, passage through zero, and a second weakly expressed maximum at 1.5 μm) mimic the spectral behavior of the equatorial Kerr effect for pure bcc iron. This means that the form of the $\delta_p(\lambda)$ curves for Fe/Cu structures is determined mainly by the dispersion of the off-diagonal dielectric constant $\varepsilon_{xy}(\lambda)$ of iron. The spectral plots of the equatorial Kerr effect for the short-period samples with $d_{\mathrm{Fe}} \leqslant 10$ Å ($D = 12 - 25$ Å), in which the γ phase of iron is present in considerable amounts, differ significantly from the group just described.

This difference is especially noticeable when the experimental curves are compared with the results of a theoretical calculation of the equatorial Kerr effect. Figure 7 compares the experimental curves with theoretical curves calculated from Eq. (7) using the bulk values of $\varepsilon_{\mathrm{Cu}}(\lambda)$, $\varepsilon_{\mathrm{Fe}}(\lambda)$, and $Q_{\mathrm{Fe}}(\lambda)$ found from measurements performed on thick ($d \sim 1000$ Å) films of the metals for two structures, which represent the long-period and short-period samples. The

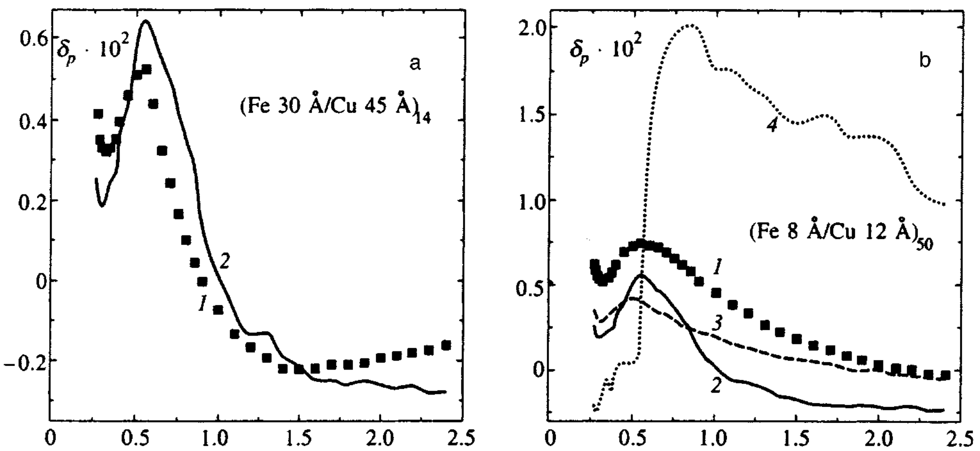

FIG. 7. Comparison of the measured spectral dependences of the equatorial Kerr effect for $(\mathrm{Fe}\ 30\,\text{Å}/\mathrm{Cu}\ 45\,\text{Å})_{14}$ (a) and $(\mathrm{Fe}\ 8\,\text{Å}/\mathrm{Cu}\ 12\,\text{Å})_{50}$ (b) with theory: *1*—experiment, *2*—calculation based on Eq. (7), *3*—calculation with consideration of a transition layer, *4*—calculation under the assumption that copper is magnetized in the free-electron model.

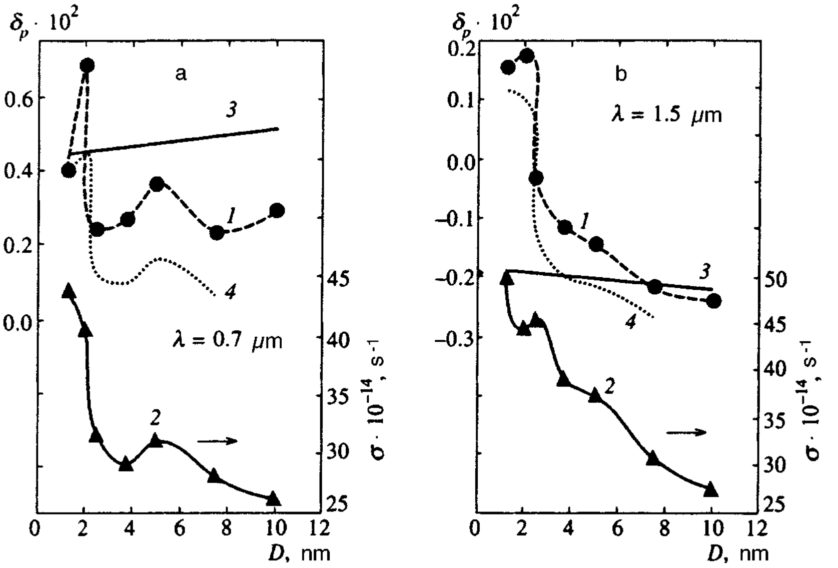

FIG. 8. Dependence of the δ_p effect and σ_{eff} of Fe/Cu structures on the modulation period D for $\lambda = 0.7\ \mu$m (a) and $\lambda = 1.5\ \mu$m (b): *1*—δ_p effect (experiment), *2*—σ_{eff} (experiment), *3*—calculation of the δ_p effect using Eq. (7), *4*—calculation of the δ_p effect using Eq. (12) with consideration of the values of σ_{eff}.

comparison shows that while the first group exhibits fairly good agreement between the calculation and experiment, the experimental data for the short-period samples significantly exceed the calculated values of δ_p.

There are several possible reasons for this disparity. Among them we mention the following: reorganization of the electronic structure of the metals when we go over to ultrathin layers, the formation of an fcc phase of iron, the ''magnetizing'' of copper, and the formation of a transition layer on the iron-copper boundaries. We attempted to evaluate the influence of the last two factors. To this end we calculated the equatorial Kerr effect for the $(\text{Fe}\ 8\ \text{Å}/\text{Cu}\ 12\ \text{Å})_{50}$ sample with consideration of the possible magnetizing of copper, for which we introduced the magneto-optical parameter of copper $Q_{\text{Cu}} = i\varepsilon_{xy}/\varepsilon_{xx}$ into Eq. (7). Here the off-diagonal dielectric constant ε_{xy} of copper was calculated on the basis of the free-electron model, as was done, for example, in Ref. 31 in an analysis of the magneto-optical spectra of Fe/Ag films. The calculation results presented in Fig. 7b show that the hypothesis that the copper layer is magnetized (in the free-electron model) leads to sharp disparity with the experimental data. The introduction of a transition layer likewise does not provide for complete agreement with experiment, especially in the visible portion of the spectrum.

In conclusion, let us examine the thickness dependence of the optical and magneto-optical properties of the Fe/Cu system in the spectral range that we investigated. Figure 8 presents the values of the equatorial Kerr effect and the effective optical conductivity σ_{eff} as a function of the modulation period D for two wavelengths. The figure also presents $\delta_p(D)$ curves calculated from Eq. (7) using the bulk values of ε_{Cu}, ε_{Fe}, and Q_{Fe}. An analysis of the results obtained reveals that the experimental $\delta_p(D)$ curves differ significantly from the theoretical curves and have a sharply nonmonotonic (oscillating) form in the wavelength range 0.3–1 μm (Fig. 8a). At $\lambda > 1\ \mu$m the oscillations are smoothed, and the dependence of the equatorial Kerr effect on D takes on a monotonically decreasing character (Fig. 8b). We have already noted above that an investigation of Fe 6 Å/X/Fe 6 Å sandwiches (X=Au, Ag) revealed oscillations of the polar Kerr effect with variation of the thickness of the X layer in the spectral ranges $E = 2.5-3.8$ eV and $E = 2.8-4.5$ eV, respectively.[7] A similar thickness dependence of the polar Kerr effect was observed by Bennett *et al.*[15] in a γ-Fe/Cu/γ-Fe sandwich at $\lambda = 0.628\ \mu$m. The anomalous behavior of the magneto-optical effect in iron sandwiches with noble metals has recently been attributed to the formation of quantum-well states in the band spectrum of ultrathin films.[7,32] The influence of the latter on the total density of states and the oscillating dependence of the magnetic moment in the paramagnetic space of copper in the Fe/Cu/Fe system was considered in Ref. 32 on the basis of first-principles calculations. This approach to the interpretation of magneto-optical data is probably the most preferable. The results of the present work show that in the Fe/Cu system the oscillatory thickness dependence is also characteristic of the optical parameters (Fig. 8, curve *2*). Since the values of the equatorial Kerr effect were measured at magnetic saturation, it can be theorized that the thickness dependence of the δ_p effect reflects (at least partially) the nonmonotonic dependence of the optical properties of the Fe/Cu structure on the modulation period. To test this hypothesis, we calculated the equatorial Kerr effect of Fe/Cu using the formula for a monolithic sample,

$$\delta_p = -4\,\text{Im}\,\frac{\varepsilon_{\text{eff}}\,Q_{\text{Fe}}\tan\varphi}{(\varepsilon_{\text{eff}}-1)(\varepsilon_{\text{eff}}-\tan^2\varphi)}\,\frac{d_{\text{Fe}}}{D}, \tag{12}$$

where Q_{Fe} is the bulk magneto-optical parameter of α-iron. The results of the calculation (Fig. 8, curve *4*) confirm the validity of the hypothesis. A more general conclusion is that the nonmonotonic character of the thickness dependence of magneto-optical effects is clearly related to the variation of the entire dielectric tensor of the layered system.

4. CONCLUSIONS

A combined analysis of the experimental $\sigma_{\mathrm{eff}}(D,\lambda)$ and $\delta_p(D,\lambda)$ curves for Fe/Cu samples and a comparison with the results of calculations within a phenomenological theory for metallic superlattices imply that the entire dielectric tensor (the diagonal component ε_{xx} and the off-diagonal component ε_{xy}) of a layered system varies as the modulation period decreases. This variation is associated both with the presence of fractions of iron in the fcc phase in samples with $D<25$ Å and with a general reorganization of the electronic structure of the metallic layers as a consequence of the lowering of their dimensionality and the influence of quantum size effects.

Let us enumerate the main results of this work.

1. No decrease in the magnitude of the equatorial Kerr effect in short-period Fe/Cu structures has been noted in connection with the bcc-fcc phase transition in iron layers, which implies that the fcc-Fe fraction obtained has ferromagnetic ordering.

2. The plasma frequency ω_p of the conduction electrons depends weakly on the modulation period and the structural state of iron. In short-period multilayered structures ($D<37.5$ Å) there is an increase in the relaxation frequency γ_0, which indicates enhancement of the scattering of the conduction electrons on the interlayer and intergrain boundaries.

3. Nonmonotonic (oscillating) dependences of both the magneto-optical (the δ_p effect) and optical (σ_{eff}) properties of Fe/Cu on the period D have been discovered for the first time in the broad spectral range $\lambda=0.3-1.5\ \mu$m. The analysis of the magneto-optical data that we performed in the free-electron model did not support the conception of uniform ''magnetizing'' of the copper layers in these objects. The nature of the enhancement of the magneto-optical activity in Fe/Cu with ultrathin layers and the oscillating $\sigma_{\mathrm{eff}}(D)$ and $\delta_p(D)$ curves requires further investigation.

4. We have interpreted the special form of the field dependence of the equatorial Kerr effect for the (Fe 5 Å/Cu 7.5 Å)$_{80}$ sample as a manifestation of an indirect exchange interaction, which leads to noncollinear ordering of the magnetic moments $\mathbf{M}_1$ and $\mathbf{M}_2$ in neighboring iron layers. The initial misalignment angle of these magnetic moments $\theta_0=120°$ has been determined on the basis of the proposed model of the magnetic structure of the sample.

We thank V. A. Sazonova for performing the x-ray structural analysis of the samples.

This work was performed with financial support from the Russian Fund for Fundamental Research (Project No. 96-02-16370).

[1] S. S. Parkin, N. More, and K. P. Roche, Phys. Rev. Lett. **64**, 2304 (1990).
[2] E. E. Fullerton, M. J. Conover, J. E. Mattson, C. H. Sowers, and S. D. Bader, J. Appl. Phys. **75**, 6461 (1994).
[3] D. H. Mosca, F. Petroff, A. Fert, P. A. Schroeder, W. P. Pratt Jr., and R. Loloel, J. Magn. Magn. Mater. **94**, L1-L2 (1991).
[4] V. V. Ustinov, M. M. Kirillova, I. D. Lobov, V. M. Maevskiĭ, A. A. Makhnev, V. I. Minin, L. N. Romashev, A. R. Del', A. V. Semerikov, and F. I. Shreder, Zh. Éksp. Teor. Fiz. **109**, 477 (1996) [JETP **82**, 253 (1996)].
[5] D. Weller, W. Reim, and K. Sporl, J. Magn. Magn. Mater. **93**, 183 (1991).
[6] A. Fuss, S. Demokritov, P. Grünberg, and W. Zinn, J. Magn. Magn. Mater. **103**, L221 (1992).
[7] T. Katayama, Y. Suzuki, M. Hayashi, and A. Thiaville, J. Magn. Magn. Mater. **126**, 527 (1993).
[8] N. Tanaka, O. Kayayama, and T. Kizuka, J. Magn. Magn. Mater. **126**, 55 (1993).
[9] K. B. Hathaway, S. F. Cheng, and A. N. Mansour, J. Magn. Magn. Mater. **126**, 79 (1993).
[10] F. Badia, G. Fratucello, B. Mastinez, D. Fioran, A. Labarta, and J. Tejada, J. Magn. Magn. Mater. **93**, 425 (1991).
[11] S. F. Cheng, A. N. Mansour, J. P. Teter, K. B. Hathaway, and L. T. Kabacoff, Phys. Rev. B **47**, 205 (1993).
[12] C. L. Fu and A. J. Freeman, Phys. Rev. B **35**, 925 (1987).
[13] Y. Tsunoda, S. Imada, and N. Kunitomi, J. Phys. F: Met. Phys. **18**, 1421 (1988).
[14] M. Doyama, M. Matsui, H. Matsuoka, S. Mitani, and K. Doi, J. Magn. Magn. Mater. **93**, 374 (1991).
[15] W. R. Bennett, W. Schwarzacher, W. F. Egelhoff Jr., Phys. Rev. Lett. **65**, 3169 (1990).
[16] T. Katayama, H. Awano, and Y. Nishihara, J. Phys. Soc. Jpn. **55**, 2539 (1986).
[17] S. Pizzini, A. Fontaine, C. Giorgetti, E. Dastyge, J. F. Bobo, M. Piecuch, and F. Baudelet, Phys. Rev. Lett. **74**, 1470 (1995).
[18] Y. B. Xu, M. Lu, Q. Y. Jin, C. Hu, Y. Z. Miao, Y. Zhai, Q. S. Bie, H. R. Zhai, G. L. Dunifer, R. Naik, and M. Ahmad, J. Appl. Phys. **75**, 6190 (1994).
[19] M. G. Samant, J. Stöhr, S. S. Parkin, G. A. Held, B. D. Hermsmeier, F. Herman, M. Van Schilfgaarde, L.-C. Duda, D. C. Mancini, N. Wassdane, and R. Nakajima, Phys. Rev. Lett. **72**, 1112 (1994).
[20] A. F. Plognikov, F. A. Pudonin, V. B. Stonchanskiĭ, JETP Lett. **46**, 560 (1987).
[21] I. D. Lobov, A. V. Druzhinin, S. L. Beremsenko, A. A. Makhnev, Document deposited in the All-Union Institute of Scientific and Technical Information of the Academy of Sciences of the USSR (VINITI), Novosibirsk, No. 2324 (1988).
[22] G. A. Bologin and V. M. Maevskiĭ, Fiz. Met. Metalloved. **79**, 8 (1995).
[23] D. G. Laurent, J. Callaway, and C. S. Wang, Phys. Rev. B **20**, 1134 (1979).
[24] Yu. A. Uspenskiĭ and S. V. Khalilov, Zh. Éksp. Teor. Fiz. **95**, 1022 (1989) [Sov. Phys. JETP **68**, 588 (1989)].
[25] Yu. V. Kudryavtsev, O. Yu. Bzhestovskiĭ, and L. Smardz, Fiz. Met. Metalloved. **76(1)**, 65 (1993).
[26] C. N. Berglund and W. E. Spicer, Phys. Rev. **136**, A1044 (1964).
[27] D. Guenzberger and D. E. Ellis, Phys. Rev. B **52**, 13 390 (1995).
[28] A. V. Rzhanov, K. K. Svitashev, A. S. Mardezhov, and V. A. Shvets, Dokl. Akad. Nauk SSSR **298**, 862 (1988) [Sov. Phys. Dokl. **33**, 146 (1988)].
[29] M. Doi, T. Kanbe, and M. Matsui, J. Magn. Magn. Mater. **126**, 443 (1993).
[30] J. F. Cochran, J. M. Rudd, M. Form, B. Heinrich, W. Bennett, W. Schwarzacher, and M. F. Egelhoff Jr., Phys. Rev. B **45**, 4676 (1992).
[31] Y. B. Xu, H. R. Zhai, M. Lu, Q. Y. Jin, and Y. Z. Miao, Phys. Lett. A **168**, 213 (1992).
[32] W. Geerts, Y. Suzuki, T. Katayama, K. Tanaka, K. Ando, and S. Yoshida, Phys. Rev. B **50**, 12 581 (1994).
[33] A. M. N. Niklasson, S. Mirbt, H. L. Skriver, and B. Johansson, Phys. Rev. B **53**, 8509 (1996).

Translated by P. Shelnitz

Anomalous behavior of the electrical conductivity tensor in strong magnetic fields

A. Ya. Mal'tsev*)

L. D. Landau Institute of Theoretical Physics, Russian Academy of Sciences, 142432 Moscow, Russia

(Submitted 27 March 1997)
Zh. Éksp. Teor. Fiz. **112**, 1710–1726 (November 1997)

The behavior of the electrical conductivity tensor in strong magnetic fields in the presence of unclosed quasiclassical electron trajectories of complex form near the Fermi surface is considered. It is shown that the asymptotic behavior of the conductivity tensor in the limit $B \to \infty$ differs in this case from the picture previously described for trajectories of simpler form. The possibility of blocking the longitudinal conductivity in strong magnetic fields at low temperatures in the case of a Fermi surface of special form is also treated theoretically.
[S1063-7761(97)01311-5]

1. INTRODUCTION

This paper is a continuation of Refs. 1 and 2 and is devoted to the galvanomagnetic phenomena in metals with complicated Fermi surfaces. The study of the galvanomagnetic phenomena in metals with a complex Fermi surface was begun in Refs. 3–5, in which the influence of unclosed quasiclassical electron trajectories lying at the Fermi surface on the electrical conductivity tensor in strong magnetic fields was studied. In particular, Refs. 4 and 5 presented calculations of the contribution to the conductivity tensor that does not vanish in the limit $B \to \infty$ from an unclosed electron trajectory which lies in a band of finite width in a plane $\Pi(\mathbf{B})$ perpendicular to the magnetic field and passes completely through it. It was shown that the contribution of such trajectories to $\sigma_{\alpha\beta}$ in the limit $\beta \to \infty$ is a degenerate tensor with a kernel coinciding with the mean direction of the trajectory. This situation was subsequently utilized to experimentally investigate complicated Fermi surfaces of metals.[6–9] A detailed presentation of the theoretical and experimental results previously obtained in this area can be found in Refs. 10–13. The topological problem of classifying unclosed electron trajectories in a strong uniform magnetic field for an arbitrary Fermi surface was then posed in Refs. 14–17 and investigated in Refs. 18–24. The topological theorems obtained in those papers provide a complete picture of the various situations that arise for an arbitrary direction of **B** on an arbitrary level surface $\epsilon(\mathbf{p}) = \text{const}$, where $\epsilon(\mathbf{p})$ is the dispersion law. We shall describe this picture here.

2. FORMULATION OF TOPOLOGICAL THEOREMS

The presence of a periodic potential causes the state of an electron in a single crystal to be characterized by the number s of the allowed energy band and the value of the quasimomentum $\mathbf{p}$ determined to within the reciprocal lattice vectors. The value of the electron energy $\epsilon_s(\mathbf{p})$ is then a periodic function in quasimomentum space with periods equal to the reciprocal lattice vectors. Thus, from the topological standpoint, $\epsilon_s(\mathbf{p})$ is a function on a three-torus $\mathcal{T}^3$ (which we shall identify with the first Brillouin zone) obtained from the Euclidean space $\mathcal{R}^3$ by factorization with respect to the reciprocal lattice vectors.

In the presence of a strong uniform magnetic field **B**, quasiclassical electron trajectories are described as a function of time by the solutions of the system of equations

$$\frac{dx^i}{dt} = \partial_i \epsilon_s(\mathbf{p}), \tag{1}$$

$$\frac{dp_i}{dt} = \frac{e}{c}[\nabla \epsilon_s(\mathbf{p})\mathbf{B}]^i. \tag{2}$$

The system of equations (1) and (2) is a Hamiltonian system relative to the Poisson brackets $\{x^i, x^j\} = 0$, $\{x^i, p_j\} = \delta^i_j$, and $\{p_i, p_j\} = eB_{ij}/c$, where $B_{23} = B^1$, $B_{31} = B^2$, etc., with the Hamiltonian $H = \epsilon_s(\mathbf{p})$.

The electron trajectories in quasimomentum space that are specified by the solutions of system (2) are given by the intersections of the 3-period level surfaces $\epsilon_s = \text{const}$ with planes that are orthogonal to the magnetic field **B**. In the three-torus $\mathcal{T}^3$ obtained from the Euclidean space $\mathcal{R}^3$ by factorization with respect to the reciprocal lattice vectors, the electron trajectories on the level surface $\epsilon_s(\mathbf{p}) = \text{const}$ are given by the level lines of the 1-form $\omega = B^1 dp_1 + B^2 dp_2 + B^3 dp_3$ confined to that surface. Below, following Ref. 21, for the set of points A in $\mathcal{T}^3$ [for example, trajectories or parts of the level surface $\epsilon(\mathbf{p}) = \text{const}$] we shall use $\hat{A}$ to denote its complete progenitor in $\mathcal{R}^3$ under the mapping $\mathcal{R}^3 \to \mathcal{T}^3$ and thus establish the correspondence between these objects.

Here we shall presume that the magnetic field **B** has a direction of irrationality 3, i.e., $\Pi(\mathbf{B})$ does not contain reciprocal lattice vectors. In this case for closed and open trajectories in the three-torus $\mathcal{T}^3$ there will be corresponding periodic sets of closed and open trajectories, respectively, in $\mathcal{R}^3$. It is easy to see that any closed trajectory in $\mathcal{T}^3$ can be pasted over by a disk perpendicular to the magnetic field in this case, i.e., it is homologous to zero in $\mathcal{T}^3$. In the general case we shall assume that the restriction of the form ω to the energy levels $\epsilon_s(\mathbf{p}) = \text{const}$ has a Morse character, i.e., we shall assume that after restriction, all of its critical points [the points at which the tangent plane to the surface coincides with $\Pi(\mathbf{B})$] are nondegenerate. The critical points of ω are then trajectories of system (2). We shall call these trajectories, as well as the trajectories directly adjacent to them in the case of the saddle points (see Fig. 1), singular trajecto-

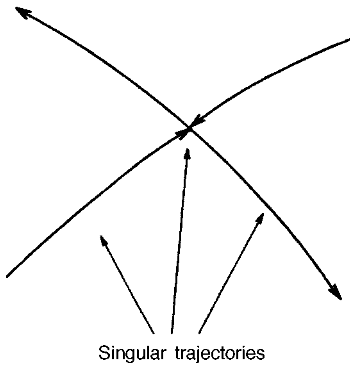

FIG. 1. Singular trajectories.

ries. The remaining trajectories, which do not pass through singular points of ω, will be called nonsingular or regular trajectories.

Each constant-energy surface $\epsilon_s(\mathbf{p}) = \text{const}$ can now be divided into connected components, each of which consists entirely of closed or open trajectories. The components bound one another along singular cycles (see Ref. 21). The images of these components will consist entirely of closed or open trajectories, respectively, and will bound one another along closed singular trajectories (see Fig. 2).

Next, together with the energy surfaces $\mathcal{F}_\epsilon : \epsilon(\mathbf{p}) = \text{const}$, for the fields $\mathbf{B}$ having a direction of irrationality 3 we shall also consider the reduced surfaces $\mathcal{F}_\epsilon^\dagger$ in the torus $\mathcal{T}^3$, which are obtained from $\mathcal{F}_\epsilon$ by removing components consisting of closed trajectories and pasting by disks that are perpendicular to the magnetic field $\mathbf{B}$ over the resulting openings. Thus, an arbitrary $\mathcal{F}_\epsilon^\dagger$ is a piecewise smooth, generally unconnected, non-self-intersecting [see Ref. 21) surface, which depends on the direction of the magnetic field $\mathbf{B}$.

The open trajectories in $\mathcal{R}^3$ will now be prescribed by the intersection of the image $\mathcal{F}_\epsilon^\dagger$, $\hat{\mathcal{F}}_\epsilon^\dagger$ with planes that are orthogonal to $\mathbf{B}$ (the disks pasted on lie in such planes). Each of the connected components of $\mathcal{F}_\epsilon^\dagger$ in the torus $\mathcal{T}^3$ is a compact two-dimensional oriented surface and thus has the form of a sphere with g arms pasted on it (g is the kind of the surface) enclosed (see Ref. 21) in $\mathcal{T}^3$. We note that g cannot be equal to zero (the case corresponding to a sphere), since in that case the corresponding image surface would consist of compact components and would therefore be able to contain only closed trajectories.

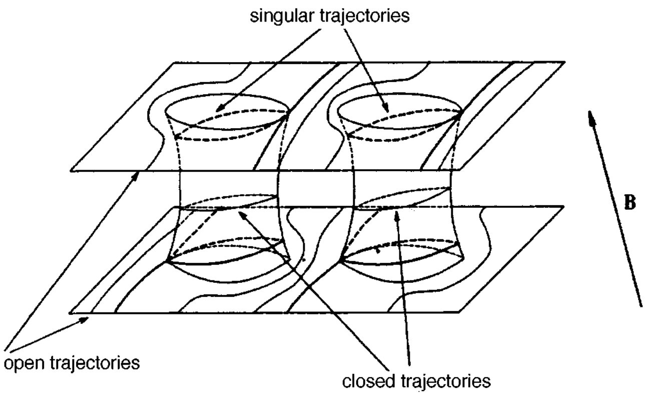

FIG. 2. Portion of a Fermi surface containing closed and open trajectories separated by singular cycles.

Let us now formulate the topological theorems (see Refs. 18–24) which describe families of the surfaces $\mathcal{F}_\epsilon^\dagger$ for different directions of the magnetic field.

Let there be an arbitrary 3-period function $\epsilon_s(\mathbf{p})$ with periods equal to reciprocal lattice vectors, which takes values in the range $\epsilon_{\min} \leqslant \epsilon(\mathbf{p}) \leqslant \epsilon_{\max}$. Then

1) For any direction of the magnetic field unclosed trajectories exist either at all the energy levels belonging to a certain connected interval $\epsilon_1(\mathbf{B}) \leqslant \epsilon(\mathbf{p}) \leqslant \epsilon_2(\mathbf{B})$, where $\epsilon_1(\mathbf{B}) > \epsilon_{\min}$ and $\epsilon_2(\mathbf{B}) < \epsilon_{\max}$, or at a single energy level corresponding to a certain value $\epsilon_0(\mathbf{B})$. (In particular, it cannot happen that there are no unclosed trajectories at any of the levels.)

2) In the former case the set $\mathcal{F}_\epsilon^\dagger$ for any value of ϵ, $\epsilon_1(\mathbf{B}) \leqslant \epsilon \leqslant \epsilon_2(\mathbf{B})$, is an unconnected union of nonintersecting two-tori $\mathcal{T}^2$, which are nonhomologous to zero in $\mathcal{T}^3$ [for fields $\mathbf{B}$ having a direction of irrationality 3, so that $\Pi(\mathbf{B})$ does not contain reciprocal lattice vectors], i.e., $g = 1$ for any connected component of $\mathcal{F}_\epsilon^\dagger$. Two-tori lying at different energy levels likewise do not intersect one another. In $\mathcal{R}^3$ the map of such components is a family of parallel, periodically deformed integer (i.e., generated by two reciprocal lattice vectors) surfaces. All the open trajectories lie in bands of finite width, whose direction is assigned by the intersection of $\Pi(\mathbf{B})$ with the planes described above, and pass completely through them (see Ref. 21). In addition, there is a stability zone near the direction of $\mathbf{B}$ in the form of a region of finite size with a piecewise smooth boundary on the unit sphere $\mathcal{S}^2$, which is such that the same situation is observed from this zone for a direction of $\mathbf{B}$ of irrationality 3. The homology class of each of the two-tori remains unchanged, although the values of $\epsilon_1(\mathbf{B})$ and $\epsilon_2(\mathbf{B})$, as well as the measure of the open trajectories at each energy level generally vary. On the boundaries of the stability zone the values of $\epsilon_1(\mathbf{B})$ and $\epsilon_2(\mathbf{B})$ coincide; however, $\mathcal{F}_{\epsilon_1}^\dagger$ ($\epsilon_1 = \epsilon_2$) consists, as previously, of two-tori with the same homology class. The physical effects associated with the situation considered above were described in Refs. 1 and 2.

However, generally speaking, in the other case, i.e., when open trajectories exist at a single energy level, they may also not lie in a band of finite width[22–25] (then the direction of the magnetic field does not lie on the boundary of any of the stability zones), and, in addition, for directions of $\mathbf{B}$ of irrationality 3 (see Refs. 22–24) they will then not have an asymptotic direction. This situation corresponds to the case where all the connected components of $\mathcal{F}_{\epsilon_0}^\dagger$ are of a kind greater than or equal to 3 (see Refs. 21 and 24). Here we are interested in physical effects associated specifically with such a situation.

We note here that the unit sphere $\mathcal{S}^2$ (see Ref. 22), which parametrizes the directions of the magnetic field $\mathbf{B}$, can either consist entirely of one stability zone or contain an infinite number of such zones and that in the latter case any two stability zones can have no more than one common boundary point. The picture then appearing is quite non-

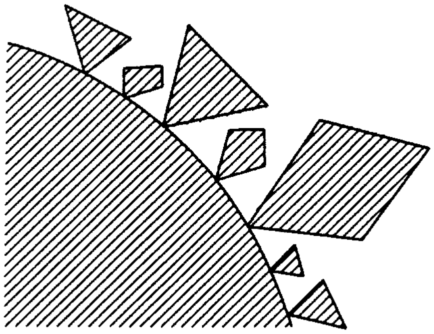

FIG. 3. Arrangement of the stability zones corresponding to the case of trajectories which lie in straight bands of finite width and pass completely through them on a two-sphere.

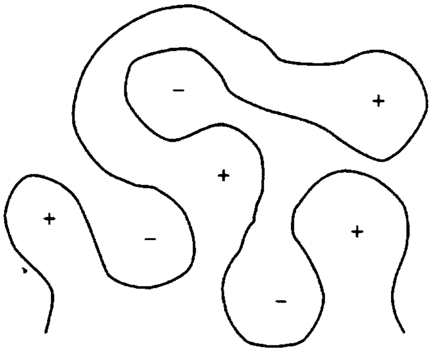

FIG. 4. Trajectory of the "diffusion" type that we considered. The plus and minus signs denote regions of relatively large and small energy values.

trivial. More specifically, on the unit sphere $\mathcal{S}^2$ there is an infinite number of stability zones with piecewise smooth boundaries, which tightly fill $\mathcal{S}^2$ everywhere, and an infinite number of smaller zones adjoin the boundary of each zone at an infinite number of points (Ref. 22, see Fig. 3). The union of all the zones densely fills $\mathcal{S}^2$, but it is still not known whether their total measure is equal to the measure of $\mathcal{S}^2$. The addition to the union of zones on the sphere has the form of an everywhere dense set of continual capacity, whose measure has not yet been established. In addition, there is a theorem (see Refs. 22–24), which states that each of the directions of **B** on the unit sphere at which the situation of interest to us is observed (open trajectories existing at a single energy level and not lying in bands of finite width) is a point for the accumulation of directions having this same property. In addition, all such directions near the original direction under consideration have the property that open trajectories exist at the same energy level ϵ_0 as for the original direction and lie on a certain smooth curve on $\mathcal{S}^2$, which passes through the original direction $\mathbf{B}_0$. [This is due to the need for the special topological characteristic to vanish when the situation of interest to us is observed (see Refs. 22–24) and thus locally specifies a one-submanifold at a fixed energy level (near the Fermi level in the present case). We note that this condition is not sufficient and directions of interest to us do not lie at all points on the curve described].

The situation described thus allows us to state that in the case of fairly complicated Fermi surfaces it is possible, in principle, to observe the second of these situations, which corresponds to high genera for the associated components of $\mathcal{F}^{\dagger}_{\epsilon_F}$ and will also be of interest to us, by specially selecting the magnetic field **B**.

As we have already noted above, in the case just indicated there are unclosed trajectories at only one energy level (we shall assume that the direction of **B** has been selected such that this level would coincide with the Fermi level ϵ_F or lie very close to it). Each of these open trajectories lacks an asymptotic direction and fills the entire plane corresponding to it, which is orthogonal to the magnetic field, so that the motion of an electron in that plane is reminiscent of ordinary diffusion (see Fig. 4). The existing analytical examples of such trajectories (see Ref. 22), however, allow us to state that in the general case the laws of ordinary diffusion are replaced by more general behavior, i.e., there are two directions (they can be considered orthogonal) in $\Pi(\mathbf{P})$ such that the mean (in absolute value) deviations from the initial position over the course of time along each of these directions are proportional to $p_F(l/p_F)^{\alpha}$ and $p_F(l/p_F)^{\beta}$, respectively (in all planes perpendicular to **B**), where l is the length of the portion of the trajectory traversed, p_F is the Fermi momentum, and $0\leqslant\alpha,\ \beta\leqslant 1$. From the condition that the area covered by the trajectory increases linearly with time, it can then be concluded that

$$\alpha+\beta=1. \qquad (3)$$

In the subsequent treatment we shall start out from this general assumption and retain the term diffusion for the trajectories just described. The value $\alpha=\beta=1/2$ corresponds to the case of ordinary diffusion, while in the general case the region in $\Pi(\mathbf{B})$ covered by a diffusion trajectory becomes increasingly more extended in one direction with the passage of time.

At energy levels not coinciding with the Fermi level there are only closed trajectories. The mean length of the trajectories that lie near the Fermi level and are obtained from open trajectories on the Fermi surface as a result of the rearrangements of the latter shown in Fig. 5 (see Ref. 21) in planes perpendicular to **B** upon departure from the Fermi surface can be estimated as

$$L_{\epsilon}\sim p_F\frac{\epsilon_F}{|\epsilon-\epsilon_F|}, \qquad (4)$$

where ϵ is the energy of the level. The mean length of such trajectories corresponding to the temperature spreading T can accordingly be estimated as $p_F(\epsilon_F/T)$, where $\epsilon_F/T\sim 10^4$ for ordinary metals. Thus, for magnetic fields B that are considered strong in the theory of galvanomagnetic phenomena (the condition for this is $\omega_B\tau\gg 1$, where τ is the electron

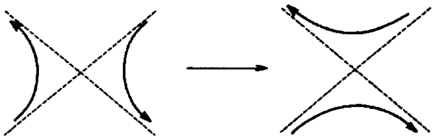

FIG. 5. Rearrangement of trajectories near saddle points when the energy level or the direction of the magnetic field is varied.

mean free transit time), which, however, satisfy the condition $\omega_B\tau\ll\epsilon_F/T$, trajectories of the type just described behave as open trajectories, since the transit time along such a trajectory significantly exceeds the electron mean free transit time. The contribution of such trajectories to the conductivity tensor differs significantly from the contribution of the previously known trajectories which lie in bands of finite width and pass completely through them (Refs. 4 and 5; see also Ref. 1). We shall now proceed to an investigation of this contribution.

3. PROPERTIES OF A SINGLE-PARTICLE DISTRIBUTION FUNCTION AS A FUNCTION OF THE TOPOLOGY OF THE OPEN TRAJECTORIES

Let us briefly describe the physical assumptions which we shall use below. We shall assume that the state of electrons is described well within the quasiclassical approximation by a single-particle distribution function $f(\mathbf{x},\mathbf{p},t)$, which satisfies the Boltzmann equation[1]

$$f_t+v^i_{\mathrm{gr}}(\mathbf{p})\frac{\partial f}{\partial x^i}+F^i_{\mathrm{ext}}\frac{\partial f}{\partial p_i}=I[f](\mathbf{x},\mathbf{p},t), \tag{5}$$

where $\mathbf{v}_{\mathrm{gr}}(\mathbf{p})=\nabla\epsilon_s(\mathbf{p})$ is the value of the electron group velocity, $\mathbf{F}_{\mathrm{ext}}$ is the external force, and $I[f]$ is the collision integral. In a state of thermodynamic equilibrium the electron distribution function is given by the expression

$$f_0(\mathbf{p})=\frac{1}{\exp[(\epsilon_s(\mathbf{p})-\epsilon_F)/T]+1}. \tag{6}$$

As can easily be seen, the application of a uniform magnetic field $\mathbf{B}$ does not alter the distribution function (6), since it generates a flux in quasimomentum space which maintains a volume element d^3p and does not alter the electron energies.

We are interested in the properties of the stationary, spatially homogeneous distributions that appear in such a situation when a weak electric field is applied, i.e., we are interested here in the conductivity tensor in strong magnetic fields. We assume, as is usually done in such cases, that to first order in E

$$f(\mathbf{p},\mathbf{E})=f_0(\epsilon)-\frac{\partial f_0}{\partial\epsilon}F^i\psi^i(\mathbf{p}), \tag{7}$$

and take the collision integral $I[f](\mathbf{p})$ (in the case of elastic scattering on impurities) in the form

$$\begin{aligned}I[f](\mathbf{p})&=\frac{2\pi n_{\mathrm{imp}}}{\hbar}\int|w_{\mathbf{pp}'}|^2[f(\mathbf{p}')(1-f(\mathbf{p}))-f(\mathbf{p})\\&\quad\times(1-f(\mathbf{p}'))]\delta(\epsilon_s(\mathbf{p})-\epsilon_s(\mathbf{p}'))\frac{d^3p'}{(2\pi\hbar)^3}V\\&=\frac{2\pi n_{\mathrm{imp}}}{\hbar}\int|w_{\mathbf{pp}'}|^2[f(\mathbf{p}')-f(\mathbf{p})]\delta(\epsilon_s(\mathbf{p})\\&\quad-\epsilon_s(\mathbf{p}'))\frac{d^3p'}{(2\pi\hbar)^3}V,\end{aligned} \tag{8}$$

where n_{imp} is the concentration of impurities and $w_{\mathbf{pp}'}$ is the scattering amplitude on an isolated impurity center. It is not difficult to obtain the following relation for $\psi(\mathbf{p})$:

$$\begin{aligned}&-\frac{e}{c}[\mathbf{v}_{\mathrm{gr}}(\mathbf{p})\mathbf{B}]^k\frac{\partial\psi^i}{\partial p^k}+ev^i_{\mathrm{gr}}(\mathbf{p})\\&\quad=\frac{2\pi n_{\mathrm{imp}}}{\hbar}\int|w_{\mathbf{pp}'}|^2[\psi^i(\mathbf{p})-\psi^i(\mathbf{p}')]\delta(\epsilon_s(\mathbf{p})\\&\quad-\epsilon_s(\mathbf{p}'))\frac{d^3p'}{(2\pi\hbar)^3}V,\end{aligned} \tag{9}$$

In the case of strong magnetic fields (see Refs. 4 and 5) it is usually assumed (we shall now consider the case of closed trajectories only) that

$$\psi^i(\mathbf{p},\mathbf{B})=\sum_{k=0}^{\infty}\psi^i_{(k)}(\mathbf{p})B^{-k}. \tag{10}$$

Assuming that the collision integral does not depend on the magnetic field in the quasiclassical approximation, for the functions $\psi^i_{(0)}(\mathbf{p})$ we obtain

$$[\mathbf{v}_{\mathrm{gr}}(\mathbf{p})\mathbf{B}]^k\frac{\partial\psi^i_{(0)}(\mathbf{p})}{\partial p^k}=0, \tag{11}$$

i.e., the $\psi^i(\mathbf{p})$ are constant on the trajectories of the system (2). For the next terms in the series (10) we obtain (see Refs. 4 and 5) the relations

$$\begin{aligned}&-\frac{e}{Bc}[\mathbf{v}_{\mathrm{gr}}(\mathbf{p})\mathbf{B}]^k\frac{\partial\psi^i_{(1)}(\mathbf{p})}{\partial p^k}+ev^i_{\mathrm{gr}}(\mathbf{p})\\&\quad=\frac{2\pi n_{\mathrm{imp}}}{\hbar}\int|w_{\mathbf{pp}'}|^2[\psi^i_{(0)}(\mathbf{p}')-\psi^i_{(0)}(\mathbf{p})]\delta(\epsilon_s(\mathbf{p})\\&\quad-\epsilon_s(\mathbf{p}'))\frac{d^3p'}{(2\pi\hbar)^3}V,\end{aligned} \tag{12}$$

$$\begin{aligned}&-\frac{e}{Bc}[\mathbf{v}_{\mathrm{gr}}(\mathbf{p})\mathbf{B}]^k\frac{\partial\psi^i_{(m)}(\mathbf{p})}{\partial p^k}\\&\quad=\frac{2\pi n_{\mathrm{imp}}}{\hbar}\int|w_{\mathbf{pp}'}|^2[\psi^i_{(m-1)}(\mathbf{p}')\\&\quad-\psi^i_{(m-1)}(\mathbf{p})]\delta(\epsilon_s(\mathbf{p})-\epsilon_s(\mathbf{p}'))\frac{d^3p'}{(2\pi\hbar)^3}V,\quad m>1.\end{aligned} \tag{13}$$

Averaging Eqs. (12) and (13) over the action of the one-parameter group generated by system (2), we obtain

$$\begin{aligned}e\langle v^i_{\mathrm{gr}}(\mathbf{p})\rangle&=\frac{2\pi n_{\mathrm{imp}}}{\hbar}\Big\langle\int|w_{\mathbf{pp}'}|^2[\psi^i_{(0)}(\mathbf{p}')\\&\quad-\psi^i_{(0)}(\mathbf{p})]\delta(\epsilon_s(\mathbf{p})-\epsilon_s(\mathbf{p}'))\frac{d^3p'}{(2\pi\hbar)^3}V\Big\rangle,\end{aligned} \tag{14}$$

$$\begin{aligned}&\Big\langle\int|w_{\mathbf{pp}'}|^2[\psi^i_{(m)}(\mathbf{p}')-\psi^i_{(m)}(\mathbf{p})]\delta(\epsilon_s(\mathbf{p})\\&\quad-\epsilon_s(\mathbf{p}'))\frac{d^3p'}{(2\pi\hbar)^3}V\Big\rangle=0,\quad m>0.\end{aligned} \tag{15}$$

where $\langle ... \rangle$ denotes an averaged quantity, which is constant on the trajectories of system (2).

Equation (14) permits the determination of $\psi^{i}_{(0)}(\mathbf{p})$ [which is constant on the trajectories of system (2)] as the solution of a linear inhomogeneous integral equation (see Refs. 4 and 5), and afterwards the functions $\psi^{i}_{(m)}(\mathbf{p})$, $m \geqslant 1$, can be found [with consideration of (14) and (15)] from the differential equations (12) and (13) to within functions that are constant on the trajectories of system (2) and can be found from Eq. (15) (we recall that we are considering the case of closed trajectories). Thus, Eqs. (12)–(15) enable us to find the functions $\psi^{i}(\mathbf{p},\mathbf{B})$ defined by the series (10).

As is easily seen, the functions $\psi^{i}_{(m)}(\mathbf{p})$ are determined from (12)–(15) to within functions which depend only on the energy. This is a property of the model of elastic scattering on impurity centers we have adopted and is, generally speaking, not observed for collision integrals of a more general form. Since such additions do not influence the value of the electric current $\mathbf{j}$, here we shall construe $\psi^{i}_{(m)}(\mathbf{p})$ as the difference between the function and its mean value at the respective energy level. As is easily seen, this does not alter the system of equations (12)–(15) except for imposing a normalization condition on $\psi^{i}_{(m)}(\mathbf{p})$. Henceforth we shall not use a specific form of the collision integral and shall estimate only its order of magnitude.

On the basis of Eqs. (13), the ratio of the $(m+1)$th term of the series (10) to the mth term can be estimated as

$$\frac{1}{B}\,\frac{\psi_{(m+1)}}{\psi_{(m)}} \sim \frac{L}{(e/c)v_F B\tau}, \tag{16}$$

where L is the length of the closed trajectories in quasimomentum space, and τ is the previously introduced electron mean free transit time. Setting $L \sim p_F$ for ''short'' closed trajectories (i.e., which have dimensions of the order of the dimensions of the first Brillouin zone), we obtain

$$\frac{\psi_{(m+1)}}{B\psi_{(m)}} \sim (\omega_B\tau)^{-1}, \tag{17}$$

and, thus, $(\omega_B\tau)^{-1}$ plays the role of a small expansion parameter. The asymptotic behavior of the conductivity tensor in the limit $B\rightarrow\infty$ can now be written (see Refs. 4 and 5) as

$$\sigma^{ik} \sim \begin{pmatrix} (\omega_B\tau)^{-2} & (\omega_B\tau)^{-1} & (\omega_B\tau)^{-1} \\ (\omega_B\tau)^{-1} & (\omega_B\tau)^{-2} & (\omega_B\tau)^{-1} \\ (\omega_B\tau)^{-1} & (\omega_B\tau)^{-1} & 1 \end{pmatrix}, \tag{18}$$

and, accordingly, the resistivity tensor is

$$\rho_{ik} \sim \begin{pmatrix} 1 & \omega_B\tau & 1 \\ \omega_B\tau & 1 & 1 \\ 1 & 1 & 1 \end{pmatrix} \tag{19}$$

(see also Ref. 13).

In the case of open trajectories which lie in bands with a width of order p_F and pass completely through them (see Refs. 4 and 5), the same treatment2) gives

$$\sigma^{ik} \sim \begin{pmatrix} (\omega_B\tau)^{-2} & (\omega_B\tau)^{-1} & (\omega_B\tau)^{-1} \\ (\omega_B\tau)^{-1} & 1 & 1 \\ (\omega_B\tau)^{-1} & 1 & 1 \end{pmatrix}, \tag{20}$$

$$\rho_{ik} \sim \begin{pmatrix} (\omega_B\tau)^{2} & \omega_B\tau & \omega_B\tau \\ \omega_B\tau & 1 & 1 \\ \omega_B\tau & 1 & 1 \end{pmatrix}. \tag{21}$$

As can be seen from (19) and (21), the resistivity in a plane perpendicular to $\mathbf{B}$ reaches saturation in the limit $\omega_B\tau \gg 1$ and $B\rightarrow\infty$, if there are only closed short trajectories, and it obeys the law $\rho \sim B^2 \cos^2\varphi$, where φ is the angle between the direction of the current and the x axis, in the presence of open trajectories lying in narrow (of width $\sim p_F$) bands parallel to p_x.

In our case, however, as we have already indicated, $L \sim p_F\epsilon_F/|\epsilon_F-\epsilon|$, and the estimate (17) is thus inapplicable. Setting $|\epsilon_F-\epsilon| \sim T$, from (16) we obtain

$$\psi_{(m+1)}/B\psi_{(m)} \sim (\epsilon_F/T)(\omega_B\tau)^{-1},$$

and, thus, the range of magnetic fields satisfying the condition

$$\tau^{-1} \ll \omega_B \ll \frac{\epsilon_F}{T}\tau^{-1}, \tag{22}$$

requires a separate treatment in our case. For example, from (14) we obtain

$$\psi^{x}_{(0)}(\mathbf{p}) = \psi^{y}_{(0)}(\mathbf{p}) \equiv 0,$$

after which, taking into account Eq. (2), from (12) we can easily find that

$$\begin{aligned} \max|\psi^{x}_{(1)}(\mathbf{p})-\psi^{x}_{(1)}(\mathbf{p}')| &= c\,\max|p_y-p'_y| \sim c p_F(L/p_F)^{\beta} \\ &\sim c p_F(\epsilon_F/T)^{\beta}, \end{aligned}$$

$$\begin{aligned} \max|\psi^{y}_{(1)}(\mathbf{p})-\psi^{y}_{(1)}(\mathbf{p}')| &= c\,\max|p_x-p'_x| \\ &\sim c p_F(\epsilon_F/T)^{\alpha}. \end{aligned}$$

We shall henceforth use the so-called mean free path concept (see Refs. 12 and 13). More specifically, neglecting the dependence of the mean free path on the quasimomentum, we assume that the fraction of electrons which undergo their first scattering act after the beginning of observation in the time interval $(t,\ t+dt)$ equals

$$\nu = \frac{1}{\tau}e^{-t/\tau}. \tag{23}$$

We use $\mathbf{v}(t,\mathbf{p})$ to denote the value of the group velocity at the point obtained from $\mathbf{p}$ by shifting system (2) by the time $(-t)$ along the trajectory, and we introduce the quantity

$$\mathbf{S}(t,\mathbf{p}) = \int_0^t \mathbf{v}(t',\mathbf{p})\,dt', \tag{24}$$

which is equal to the integral of $\mathbf{v}(t,\mathbf{p})$ over the corresponding portion of the trajectory ending at the point $\mathbf{p}$. The quantity

$$W(t,\mathbf{p}) = e\mathbf{E}\mathbf{S}(t,\mathbf{p}) \tag{25}$$

will then characterize the energy (to first order in $\mathbf{E}$) gained by an electron as it moves during the time t along the portion of the trajectory ending at the point $\mathbf{p}$. Now, assuming that the election moves along a trajectory of system (2) between two scattering acts, acquiring or losing energy in the electric field and thereby escaping to higher or lower energy levels, while electrons from more filled lower levels or less filled higher levels arrive in its place, and that scattering subsequently occurs in some other element of quasimomentum space, we can write a correction to the distribution function that is linear in $\mathbf{E}$ in the form

$$f_1(\mathbf{p}) = -\frac{\partial f_0(\epsilon)}{\partial \epsilon}\,\frac{1}{\tau}\int_0^\infty e^{-t/\tau}W(t,\mathbf{p})\,dt, \tag{26}$$

and, accordingly, the value of the current density $\mathbf{j}$ equals

$$\begin{aligned}\mathbf{j} &= -e^2\int \mathbf{v}_{\mathrm{gr}}(\mathbf{p})\,\frac{\partial f_0(\epsilon)}{\partial \epsilon}\\ &\quad\times\left[\frac{1}{\tau}\int_0^\infty e^{-t/\tau}\int_0^t \mathbf{E}\mathbf{v}(t',\mathbf{p})\,dt'\,dt\right]\frac{d^3p}{(2\pi\hbar)^3}\\ &= -e^2\int \mathbf{v}_{\mathrm{gr}}(\mathbf{p})\frac{\partial f_0(\epsilon)}{\partial \epsilon}\\ &\quad\times\int_0^\infty e^{-t'/\tau}(\mathbf{E}\mathbf{v}(t',\mathbf{p}))\,dt'\,\frac{d^3p}{(2\pi\hbar)^3}.\end{aligned} \tag{27}$$

With no loss of generality, we shall next assume that the z axis coincides with the direction of the magnetic field $\mathbf{B}$. In this case, following Refs. 4 and 5, it will be convenient for us to introduce new coordinates at each of the energy levels near the Fermi level. More specifically, since there are only closed trajectories at each of the levels with $\epsilon \neq \epsilon_F$, singular closed trajectories cut each of the levels into cylinders of height h_i, which consist of nonsingular closed trajectories (here we consider only essentially different cylinders, which are not obtained from one another by displacement by a reciprocal lattice vector). The bases of some of the cylinders can then be constricted into a point (see Fig. 6).

We take the values of p_z and $s = teB/c$, where t is the transit time along the trajectory of system (2), as the coordinates in each such cylinder. The sum of the heights of the cylinders consisting of trajectories obtained by rearranging open trajectories lying on the Fermi surface (apart from them, in the general case there are also ‘‘short’’ trajectories, which were previously excluded from the treatment) then tends to zero as $\epsilon \to \epsilon_F$ and can be estimated in order of magnitude as

$$H = {\sum}'\, h_i \sim p_F\frac{|\epsilon_F - \epsilon|}{\epsilon_F},$$

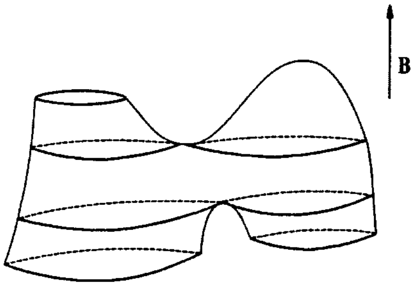

FIG. 6. Portion of a Fermi surface separated by singular cycles into cylinders of closed trajectories.

while the mean length along s of such trajectories is of order

$$\frac{p_F}{v_F}\,\frac{|\epsilon_F - \epsilon|}{\epsilon_F} \sim m^*\frac{|\epsilon_F - \epsilon|}{\epsilon_F},$$

where m^* is the electron effective mass. Taking into account the fact that the Jacobian for passing from the coordinates (p_x, p_y, p_z) to (ϵ, p_z, s) equals unity (see Refs. 4 and 5), the contribution of such trajectories to the conductivity tensor can be written, using (27), in the form

$$\begin{aligned}\sigma^{ik} &= -e^2\left(\frac{c}{eB}\right)\int{}'\ \frac{\partial f_0(\epsilon)}{\partial \epsilon}\left[\int_0^\infty v^i_{\mathrm{gr}}(\epsilon, p_z, s)\right.\\ &\quad\left.\times\exp\left(-\frac{cs'}{eB\tau}\right)v^k_{\mathrm{gr}}(\epsilon, p_z, s - s')\,ds'\right]\frac{d\epsilon\,dp_z\,ds}{(2\pi\hbar)^3},\end{aligned} \tag{28}$$

where the prime on the integral sign means that for each energy value the integration is performed along the cylinders described above of long trajectories obtained from open trajectories lying on the Fermi surface. We note that after the replacement of $\mathbf{B}$ by $-\mathbf{B}$, which entails the replacement $s \to -s$, it is not difficult to obtain the relation $\sigma^{ik}(\mathbf{B}) = \sigma^{ki}(-\mathbf{B})$ in accordance with the Onsager principle from Eq. (28).

Expanding the functions $\mathbf{v}_{\mathrm{gr}}(\epsilon, p_z, s)$, which are periodic in s, into a Fourier series

$$\mathbf{v}_{\mathrm{gr}}(\epsilon, p_z, s) = \sum_{n=-\infty}^{\infty}\mathbf{v}_{\mathrm{gr}}(\epsilon, p_z, n)\exp\left(i\frac{2\pi n}{S_0}s\right), \tag{29}$$

where $S_0 = S_0(\epsilon, p_z)$ is the length (along s) of the respective closed trajectory, we can rewrite Eq. (28) in the form

$$\begin{aligned}\sigma^{ik} &= -e^2\left(\frac{c}{eB}\right)\int{}'\ \frac{\partial f_0(\epsilon)}{\partial \epsilon}\\ &\quad\times\left[\sum_{n=-\infty}^{\infty}\frac{v^i_{\mathrm{gr}}(\epsilon, p_z, n)v^k_{\mathrm{gr}}(\epsilon, p_z, -n)}{c/eB\tau + i2\pi n/S_0}\right]\frac{d\epsilon\,dp_z}{(2\pi h)^3},\end{aligned} \tag{30}$$

where the components $\mathbf{v}_{\rm gr}(\epsilon,p_z,n)$ are of the same order of magnitude up to $n_0\sim S_0/m^*$ (note that s has the dimensions of mass and that m^* corresponds to the size of the Brillouin zone), after which they begin to decrease. From (22) we now have $S_0/m^*\gg cS_0/eB\tau\gg 1$.

To evaluate the integrals (28), we replace the quantity

$$\int_0^{\infty} e^{-cs'/eB\tau} v_{\rm gr}^k(\epsilon,p_z,s-s')ds'$$

by

$$\int_0^{eB\tau/c} v_{\rm gr}^k(\epsilon,p_z,s-s')ds', \tag{31}$$

and we replace $v_{\rm gr}^i(\epsilon,p_z,s)$ by the quantity averaged over the interval $eB\tau/c$ [in order to discard the higher harmonics that are orthogonal to (31)]:

$$v_{\rm gr}^i(\epsilon,p_z,s)\rightarrow \frac{c}{eB\tau}\int_0^{eB\tau/c} v_{\rm gr}^i(\epsilon,p_z,s-s')ds'. \tag{32}$$

We now note that for $i,k=1,2$ the quantities (31) and (32) can be expressed by virtue of (2) in terms of the differences between p_x and p_y at the ends of a trajectory segment of length $eB\tau/c$, which, in turn, can (when the p_x and p_y axes are appropriately selected) be estimated in order of magnitude according to the foregoing as $p_F(eB\tau/m^*c)^{\alpha}$ and $p_F(eB\tau/m^*c)^{\beta}$. For the corresponding components σ^{ik} we thus have the estimates

$$\sigma^{xx}\sim e^2\left(\frac{c}{eB}\right)^2\frac{1}{\tau}p_F^2(\omega_B\tau)^{2\beta}\frac{p_Fm^*}{(2\pi\hbar)^3}\frac{\epsilon_F}{|\epsilon_F-\epsilon|}\frac{|\epsilon_F-\epsilon|}{\epsilon_F}$$

$$\sim\frac{ne^2\tau}{m^*}\frac{1}{(\omega_B\tau)^{2-2\beta}}, \tag{33}$$

where $n\sim p_F^3/(2\pi\hbar)^3$ is the electron density. Similarly,

$$\sigma^{yy}\sim\frac{ne^2\tau}{m^*}\frac{1}{(\omega_B\tau)^{2-2\alpha}}, \tag{34}$$

$$\sigma^{xy}\sim\sigma^{yx}\sim\frac{ne^2\tau}{m^*}\frac{1}{(\omega_B\tau)^{2-\alpha-\beta}}=\frac{ne^2\tau}{m^*}\frac{1}{(\omega_B\tau)} \tag{35}$$

(so that $\alpha+\beta=1$).

Let us now consider the values for $v_{\rm gr}^z$ corresponding to (31) and (32). We assume that the set $F_{\epsilon_F}^{\dagger}$ described above consists in our case of one connected component (otherwise, the Fermi surface must be of genus no less than 6). In this case the part of $F_{\epsilon_F}^{\dagger}$ covered by open trajectories is a connected surface that is invariant to the replacement $p\rightarrow -p$, and, thus, the mean value of $v_{\rm gr}^z(\mathbf{p})$ on any open nonsingular trajectory on the Fermi surface is equal to zero. As we move away from the Fermi surface, however, the mean value of $v_{\rm gr}^z$ on the closed trajectories obtained from open trajectories, unlike $v_{\rm gr}^x$ and $v_{\rm gr}^y$, is, generally speaking, not equal to zero and can be estimated in order of magnitude as $v_F|\epsilon_F-\epsilon|/\epsilon_F$. For the quantity $v_{\rm gr}^z(\epsilon,p_z,s)-\langle v_{\rm gr}^z\rangle(\epsilon,p_z)$ on each of the trajectories it is then natural to use relations that are analogous to the corresponding $v_{\rm gr}^x$ and $v_{\rm gr}^y$ and to write within an order of magnitude

$$\int_0^{eB\tau/c}(v_{\rm gr}^z(\epsilon,p_z,s)-\langle v_{\rm gr}^z\rangle(\epsilon,p_z))ds'\sim v_F\left(\frac{eB\tau}{m^*c}\right)^{\gamma}, \tag{36}$$

where $0<\gamma<1$.

After the assumptions made, the remaining components of the conductivity tensor can be estimated from Eq. (28) as

$$\sigma^{zz}\sim e^2\left(\frac{c}{eB}\right)\int{}'\,\frac{1}{4T\cosh^2(\epsilon-\epsilon_F)/2T}$$

$$\times\frac{eB\tau}{c}v_F^2\frac{(\epsilon-\epsilon_F)^2}{\epsilon_F^2}\frac{d\epsilon dp_z ds}{(2\pi\hbar)^3}$$

$$+e^2\left(\frac{c}{eB}\right)\frac{1}{\tau}\int{}'\,\frac{\partial f_0(\epsilon)}{\partial\epsilon}p_F^2$$

$$\times\left(\frac{eB\tau}{m^*c}\right)^{2\gamma}\frac{d\epsilon dp_z ds}{(2\pi\hbar)^3}$$

$$\sim e^2\tau\frac{T^2}{\epsilon_F^2}v_F^2\frac{p_Fm^*}{(2\pi\hbar)^3}$$

$$+e^2\left(\frac{c}{eB}\right)^2\frac{1}{\tau}p_F^2(\omega_B\tau)^{2\gamma}\frac{p_Fm^*}{(2\pi\hbar)^3}$$

$$\sim\frac{ne^2\tau}{m^*}\frac{T^2}{\epsilon_F^2}+\frac{ne^2\tau}{m^*}\frac{1}{(\omega_B\tau)^{2-2\gamma}}; \tag{37}$$

[Formula (37), like (33)–(35), can be regarded only as an estimate, in which we have distinguished the two principal terms, one of which corresponds to nonzero values of $v_{\rm gr}^z$ near the Fermi surface and decreases with decreasing T, while the other corresponds to diffusive motion and decreases with increasing B]:

$$\sigma^{xz}\sim\sigma^{zx}\sim\frac{ne^2\tau}{m^*}\frac{1}{(\omega_B\tau)^{2-\beta-\gamma}}; \tag{38}$$

$$\sigma^{yz}\sim\sigma^{zy}\sim\frac{ne^2\tau}{m^*}\frac{1}{(\omega_B\tau)^{2-\alpha-\gamma}}. \tag{39}$$

Equations (33)–(35) and (37)–(39) thus describe the contribution to the conductivity tensor of the long trajectories that we considered. Comparing it to the contribution (18) of ordinary trajectories, we readily see that because of the slower decay of σ^{xx} and σ^{yy}, as well as, possibly (although not necessarily), σ^{xz}, σ^{zx}, σ^{yz}, and σ^{zy}, with increasing B in the range (22) considered here in comparison to the usual case, the case considered here can be distinguished experimentally from other cases. For the resistivity tensor $\rho_{\alpha\beta}$, $\alpha,\beta=1,2$, in a plane perpendicular to $\mathbf{B}$ we can easily obtain (when there is also a contribution from short trajectories, so that $\sigma^{zz}\neq 0$ holds for $B\rightarrow\infty$ and $T\rightarrow 0$) the estimate

$$\rho_{\alpha\beta}\sim\begin{pmatrix}(\omega_B\tau)^{2\alpha} & \omega_B\tau\\ \omega_B\tau & (\omega_B\tau)^{2\beta}\end{pmatrix} \tag{40}$$

in the range (22), and, thus, the resistivity in a plane orthogonal to the magnetic field increases in the principal term proportionally to $\rho\sim B^n\cos^2\varphi$, $1<n<2$ (here $n=2\max\{\alpha,\beta\}$, and φ is the angle between the direction of the current and the direction of maximum resistivity).

We now note that formulas (33)–(35) and (37)–(39), which follow from the general formula (28) after the assumptions which we made, can also be used in the range (22) and in the previously described cases[4,5] of short (with length $\sim p_F$) closed trajectories and open trajectories which lie in bands of finite width (also of order p_F) in $\Pi(\mathbf{B})$ and pass completely through them. In the former case, as is easily seen, we must set $\alpha=\beta=0$ and $\gamma=1$ (the integrals of v_{gr}^x and v_{gr}^y are constrained during motion along a trajectory, while the integral of v_{gr}^z increases linearly with the distance traversed), and in the latter case we must set $\beta=0$ and $\alpha=\gamma=1$ (assuming that motion in quasimomentum space occurs along the p_x axis). As for the case where the lengths L of the closed trajectories or the minimum width a of the band containing the open trajectories satisfy the condition

$$p_F<L,\quad a<p_F(\epsilon_F/T), \tag{41}$$

the motion of an electron along trajectories in quasimomentum space in the range of magnetic fields (22) can be regarded in such a situation as diffusive motion only for $1\ll\omega_B\tau\ll L/p_F$, while the expansion (10) can be used for $\omega_B\tau\gg L/p_F$. Thus, a more general dependence of σ^{ik} on B will be observed in the range (22), so that the $Bd(\ln\sigma^{ik})/dB$ [which play the role of the exponents in formulas (33)–(35), and (37)–(39)] will vary smoothly from the values corresponding to the case of electron diffusion in p-space to the case in which Eq. (18) or (20) holds. Formulas (33)–(35) and (37)–(39) can be considered valid in this more general case, if we assume that α, β, and γ are already arbitrary [not related by Eq. (3)] functions of B that vary slowly in range (22). This argument is important, since the treatments presented above, unlike the previously mentioned general cases (see Refs. 1 and 2), which correspond to stability zones of directions of $\mathbf{B}$, correspond to the situation observed when the direction of the magnetic field is fixed. In this case the maximum angle of deviation allowing the trajectories described above to be rearranged so that the mean length of the trajectory segment in which rearrangements do not occur (see Fig. 5) is equal to L can be estimated as $\sim(p_F/L)^{1+\max\{\alpha,\beta\}}$ and is thus very small under the condition that the regime described is maintained with the same α, β, and γ in the range (22) [this requires fulfillment of the condition $L\sim p_F(\epsilon_F/T)$]. Let us now consider the situation corresponding to the physical case in which because of the nonuniformity of $\mathbf{B}$ the measured value of the conductivity tensor σ^{ik} (or ρ_{ik}, depending on the conditions of the experiment) is averaged over a certain neighborhood O_δ near the direction of the field under consideration $\mathbf{B}_0$, the dimensions of O_δ exceeding the value indicated above for the angle of deviation. As was noted above, the addition to the set of directions of $\mathbf{B}$ in which the situation that we described is observed (not necessarily at the Fermi level) is the union of the stability zones in which open trajectories exist in an energy interval $[\epsilon_1,\epsilon_2]$ of nonzero length and lie in bands of finite width in planes perpendicular to the magnetic field $\mathbf{B}$, passing completely through them. The union of stability zones densely fills the unit sphere $\mathscr{S}^2$ everywhere, and, thus, the neighborhood O_δ will be tightly filled by such zones everywhere. The dimensions of the zones converging toward $\mathbf{B}_0$ tend to zero, and the values of the limits of the energy ranges corresponding to them ϵ_1 and ϵ_2 converge toward the value of ϵ_0, at which there are open trajectories for the direction of $\mathbf{B}_0$. The width a of the bands in which open trajectories lie tends to infinity. The situation that we described will be observed for directions of $\mathbf{B}$ from O_δ that do not lie in any of the stability zones, the energy values at which there are open trajectories also tending to ϵ_0 as $\mathbf{B}\rightarrow\mathbf{B}_0$ (we note that we assume that the direction of $\mathbf{B}_0$ was selected such that $\epsilon_0-\epsilon_F<T$). Thus, if $\mathbf{B}$ belongs to O_δ, the trajectories lying near the Fermi surface can be either closed or open. In addition, if the maximum angle of deviation from $\mathbf{B}_0$ (because of nonuniformity of the field, crystal defects, etc.) is equal to $\delta\theta$, the lengths of the segments of the original trajectories in which intersections did not occur are

$$L\sim p_F/(\delta\theta)^{1/(1+\max\{\alpha,\beta\})}.$$

The value of L thus determined is a lower estimate either for the lengths of the closed trajectories obtained or for the widths of the bands of open trajectories and, on the basis of reasonable experimental estimates for $\delta\theta$, satisfy (41). On the basis of the foregoing it can thus be expected that, if the magnetic field in a metal with a complicated Fermi surface is specially selected (so that the diffusive motion of electrons takes place on the Fermi surface in p-space in the magnetic field), the behavior of σ^{ik} described by (33)–(35) and (37)–(39) can be observed with *a priori* unknown values of α, β, and γ [which, generally speaking, are not related by (3) due to averaging over O_δ, if $\delta\theta$ is not so small that the regime observed for $\mathbf{B}=\mathbf{B}_0$ is maintained]. The behavior of the resistivity in a plane perpendicular to the magnetic field is then described by Eq. (40).

Here we note that a description of such behavior was given in a report of experimental work,[9] in which the dependence of the resistivity ρ in a plane perpendicular to a magnetic field $\mathbf{B}$ on its direction was investigated in a gold single crystal. More specifically, the measurements revealed pronounced anisotropy (as a function of the direction of $\mathbf{B}$) of the resistivity, and maximum points were discovered, at which the resistivity increases with B according to the law $\rho\sim B^n$, where n varies from 1 to 1.8. In addition, it can be seen from an angular diagram that groups of such maxima lie on one-dimensional curves on the unit sphere $\mathscr{S}^2$ in accordance with our previous statements (see Sec. 2), allowing us to state that the situation which we described is probably observed on the Fermi surface in a gold single crystal for these directions of the magnetic field.

As we have already mentioned, mathematical theorems allow us to state that the situation described can be observed for a fairly extensive list of metals with complicated Fermi surfaces when the direction of $\mathbf{B}$ is specially selected.

We now note that, according to Eqs. (33)–(35) and (37)–(39), the contribution of the diffusion trajectories described here to the longitudinal conductivity σ^{zz} (in the case of a Fermi surface of a low genus, so that $\mathscr{F}^{\dagger}_{\epsilon_F}$ consists of one connected component in our situation) vanishes when $T\rightarrow 0$ and $B\rightarrow\infty$. Moreover, if the Fermi surface is of genus 3 and has a negative (more precisely, nonpositive) Gaussian curvature at all of its points, there cannot be any closed trajectories on it in our situation. In fact, in this case there cannot be any closed trajectories demarcating a two-dimensional disk $\mathscr{D}^2$ on the Fermi surface, since there must be a singularity of the pole type within such a disk in this case, in contradiction to the nonpositive Gaussian curvature of the surface. As for closed trajectories of any other type, as is easily seen, after they are removed and the openings formed are pasted over by disks perpendicular to the magnetic field, the Fermi surface breaks up into components of a lower genus, and the previously described surface $\mathscr{F}^{\dagger}_{\epsilon}$ will thus not contain components of genus 3, in contradiction to our original assumptions regarding the situation. In this case Eqs. (33)–(35) and (37)–(39) will describe the complete conductivity tensor, and when $T\rightarrow 0$ and $B\rightarrow\infty$, the conductivity tensor (including σ^{zz}) becomes equal to zero, i.e., the substance will behave as an insulator in the limit $T\rightarrow 0$ in strong magnetic fields for special directions of **B**. It should, however, be noted that the condition described for a Fermi surface (which must be unique) is quite strong, so that the known metals with complicated Fermi surfaces (for example, Au), which are such that there is a possibility of observing the contribution of (33)–(35) and (37)–(39) described in them for special directions of the magnetic field, will not satisfy it, and contribution (18) will always be present in them in addition to (33)–(35) and (37)–(39). It is possible, however, to observe a sharp decrease in σ^{zz} for special directions of the magnetic field in metals with complicated Fermi surfaces, if the area covered by closed trajectories (of length $\sim p_F$) on the Fermi surface is small compared with the total area of the Fermi surface.

In conclusion, we thank S. P. Novikov and L. A. Fal'kovskiĭ for formulating the problem, and I. A. Dynnikov and the participants in the Theoretical Seminar of the L. D. Landau Institute of Theoretical Physics of the Russian Academy of Sciences for some fruitful discussions.

This work was performed with financial support from KFA Forschungzentrum Jülich GmbH and the Russian Fund for Fundamental Research (Project 96-01-01623).

---

*)e-mail: maltsev@itp.ac.ru

1)We shall carry out the treatment for a model of noninteracting electrons with a prescribed dispersion law. As can be shown (see Ref. 13), consideration of the Fermi-liquid effects, i.e., the dependence of the form of the dispersion law on the electron distribution, does not influence the result when the conductivity tensor is calculated.

2)The validity the of expansion (10) in the range (22) can be proved separately in this case, and we shall not dwell on it here.

[1] S. P. Novikov and A. Ya. Mal'tsev, JETP Lett. **63**, 855 (1996).

[2] I. A. Dynnikov and A. Ya. Mal'tsev, Zh. Éksp. Teor. Fiz. **112**, 371 (1997) [JETP **85**, 205 (1997)].

[3] I. M. Lifshits, M. Ya. Azbel', and M. I. Kaganov, Zh. Éksp. Teor. Fiz. **31**, 63 (1956) [Sov. Phys. JETP **4**, 41 (1957)].

[4] I. M. Lifshits and V. G. Peschanskiĭ, Zh. Éksp. Teor. Fiz. **35**, 1251 (1958) [Sov. Phys. JETP **8**, 875 (1959)].

[5] I. M. Lifshits and V. G. Peschanskiĭ, Zh. Éksp. Teor. Fiz. **38**, 188 (1960) [Sov. Phys. JETP **11**, 137 (1960)].

[6] N. E. Alekseevskiĭ and Yu. P. Gaĭdukov, Zh. Éksp. Teor. Fiz. **35**, 554 (1958) [Sov. Phys. JETP **8**, 383 (1959)].

[7] N. E. Alekseevskiĭ and Yu. P. Gaĭdukov, Zh. Éksp. Teor. Fiz. **36**, 447 (1959) [Sov. Phys. JETP **9**, 311 (1959)].

[8] N. E. Alekseevskiĭ and Yu. P. Gaĭdukov, Zh. Éksp. Teor. Fiz. **37**, 672 (1959) [Sov. Phys. JETP **10**, 481 (1960)].

[9] Yu. P. Gaĭdukov, Zh. Éksp. Teor. Fiz. **37**, 1281 (1959) [Sov. Phys. JETP **10**, 913 (1960)].

[10] I. M. Lifshits and M. I. Kaganov, Usp. Fiz. Nauk **69**, 419 (1959) [Sov. Phys. Usp. **2**, 831 (1960)].

[11] I. M. Lifshits and M. I. Kaganov, Usp. Fiz. Nauk **78**, 411 (1962) [Sov. Phys. Usp. **5**, 411 (1962)].

[12] I. M. Lifshits, M. Ya. Azbel', and M. I. Kaganov, *Electron Theory of Metals*, Consultants Bureau, New York (1973).

[13] A. A. Abrikosov, *Fundamentals of the Theory of Metals*, Elsevier, New York (1988).

[14] S. P. Novikov, Usp. Mat. Nauk **37**, 3 (1982).

[15] S. P. Novikov, Tr. Mat. Inst. im. V. A. Steklova, Akad. Nauk SSSR **166**, 201 (1984).

[16] S. P. Novikov, in *Proceedings of the Conference on Topological Methods in Mathematics*, dedicated to the 60th birthday of J. Milnor, June 15–22, 1991, State University of New York, Stony Brook (1993).

[17] S. P. Novikov, in *Proceedings of the Conference of Geometry, December 15–26*, 1993, Tel Aviv University (1995).

[18] A. V. Zorich, Usp. Mat. Nauk **39**, 235 (1984).

[19] I. A. Dynnikov, Usp. Mat. Nauk **47**, 161 (1992).

[20] I. A. Dynnikov, Usp. Mat. Nauk **48**, 179 (1993).

[21] I. A. Dynnikov, Mat. Zametki **53**, 57 (1993).

[22] I. A. Dynnikov, submitted to Adv. Sov. Math. (1997).

[23] I. A. Dynnikov, in *Surfaces in 3-Torus Geometry of Plane Sections, Proceedings of ECM2*, BuDA (1996).

[24] I. A. Dynnikov, Dissertation for the degree of Candidate of Physical and Mathematical Sciences, M. B. Lomonosov Moscow State University, Moscow (1996).

[25] S. P. Tsarev, Private communication (1992–1993).

Translated by P. Shelnitz

ESR millimeter-band spectroscopy of magnetic ordering in the low-dimensional magnet $CuGeO_3$

S. V. Demishev, A. V. Semeno, N. E. Sluchanko, and N. A. Samarin

Institute of General Physics, Russian Academy of Sciences, 117942, Moscow, Russia

A. N. Vasil'ev and L. I. Leonyuk

M. V. Lomonosov Moscow State University, 119899 Moscow, Russia

(Submitted 3 April 1997)
Zh. Éksp. Teor. Fiz. **112**, 1727–1738 (November 1997)

Resonant absorption of microwaves in $CuGeO_3$ single crystals in a frequency band of 40 to 120 GHz, in magnetic field $B \leqslant 15$ T, at temperatures ranging between 0.5 and 300 K, and in the configuration $\mathbf{B} \parallel \mathbf{a}$ has been investigated. Several absorption lines (S_0, S_a, and S_b) whose parameters strongly depend on temperature have been detected close to ESR. The temperature dependence of the total absorption in the main line S_0 with the Landé g-factor $g_0 = 2.154$ at temperatures above the spin-Peierls transition temperature is in good agreement with Bonner and Fisher's theoretical prediction for a one-dimensional Heisenberg spin chain. In addition to the main resonance, a resonance of smaller amplitude, S_a, with the g-factor $g_a = 2.72$ has been detected at temperatures ranging down to a characteristic temperature $T \simeq 1$ K, below which the amplitude of this feature drops to zero. A radical restructuring of the magnetoabsorption spectrum occurs at the temperature of the spin–Peierls transition $T_{SP} \approx 14$ K. At $T < 12$ K new features emerge in the spectrum, namely, a broad absorption line overlapping with the narrow lines S_0 and S_a, and a line S_b with $g_b = 1.83$, which is not detected at temperatures above T_{SP}. An analysis of amplitudes and total absorption of ESR lines as functions of temperature has shown that the temperature range below 1 K is anomalous, which may be caused by an additional ordering in the $CuGeO_3$ magnetic subsystem at low temperatures. © *1997 American Institute of Physics.* [S1063-7761(97)01411-X]

1. INTRODUCTION

Since the pioneering research by Hase *et al.*,[1] the low-dimensional magnet $CuGeO_3$ has attracted considerable attention from investigators as a sample of nonorganic material with a spin–Peierls instability. The common viewpoint is that Cu^{2+} ions ($S = 1/2$) arranged along the **c** axis form antiferromagnetic Heisenberg chains, which are known to be unstable against dimerization.[1] At temperatures below the spin–Peierls transition, T_{SP}, the spectrum of magnetic excitations of a one-dimensional Heisenberg chain is significantly changed, namely, the singlet ground state is separated from the excited triplet state by an energy gap.[2] As a result, one should expect an abrupt drop in the magnetic susceptibility in the temperature range below the spin-Peierls transition.

An abrupt drop in the magnetic susceptibility of $CuGeO_3$ (by almost an order of magnitude) was detected for $T < T_{SP} \approx 14$ K, and X-ray diffraction measurements produced evidence in favor of dimerization.[3] Neutron diffraction measurements demonstrated, however, that the nature of the magnetic interactions in $CuGeO_3$ is more complicated.[4,5] First, in addition to the antiferromagnetic exchange along the chains characterized by an exchange integral $J_c = 61.5$ K, there is a fairly strong antiferromagnetic coupling between chains in the **bc** plane with $J_b = 6.8$ K.[5] Second, the anisotropic antiferromagnetic interaction in the **bc** plane occurs alongside an antiferromagnetic interaction between planes along the **a**-axis with an exchange integral $J_a = 0.7$ K.[5]

Since the $CuGeO_3$ magnetic susceptibility is relatively low,[1] the ESR technique is the most efficient tool in studies of magnetic ordering. In the general case, formation of a collective spin mode or antiferromagnetic order, when individual spins are frozen, should lead to a decrease in the ESR signal, which is due to uncoupled spins. Several publications[6–11] were dedicated to ESR studies of $CuGeO_3$. It has been established that the ESR line amplitude drops with the temperature above T_{SP} in qualitative agreement with the behavior of the magnetic susceptibility. On the other hand, it is noteworthy that the susceptibility and ESR amplitude cannot be described using the theoretical formulas for a Heisenberg chain (see, for example, Ref. 1). Below the spin–Peierls transition, the ESR line amplitude drops rapidly with decreasing temperature in the range between $T_{SP} \approx 14$ K and $T \approx 6$ K.[6–11]

The published data on the ESR line width for $T < T_{SP}$ are very controversial. Some authors have observed a tendency toward linewidth saturation as the temperature decreased,[6,8,9] whereas others[10] detected a nonmonotonic dependence with a maximum about 6 K in the case when the magnetic field was aligned with the **c**-axis ($\mathbf{B} \parallel \mathbf{c}$). Note that, even in the case of the $\mathbf{B} \parallel \mathbf{c}$ configuration, which has been studied more thoroughly, the fine structure of the ESR absorption in the range $T < T_{SP}$ has not been interpreted. Honda *et al.*[10] detected narrow lines of small amplitude which were resolved in spectra at temperatures $T < 6$ K and arranged symmetrically about the main resonance, whose amplitude was more

1063-7761/97/110943-06$10.00

than ten times the amplitude of the weaker lines. Smirnov *et al.*,[11] on the contrary, for $T<T_{\rm SP}$ recorded a wide absorption line overlapping with up to four spectral components, and two lines of comparable amplitudes were located about the main resonance. Neither group of researchers[10,11] measured in detail the parameters of the spectral components, except the main resonance corresponding to $g\approx 2$.

The substantial ESR signal for $T<T_{\rm SP}$ indicates that the spin–Peierls phase cannot include 100% of the spins, which is, naturally, ascribed to defects in the $\rm CuGeO_3$ crystalline structure and/or internal disruptions of the magnetic order of the spin–Peierls state. The subsystem of uncoupled spins, which are not included in the collective mode, can also be ordered; in particular, experimental data of Ref. 11 provide evidence in favor of antiferromagnetic order coexisting with the spin–Peierls dimerization at low temperatures. Thus, the magnetic order in real $\rm CuGeO_3$ crystals is fairly complicated, and new effects can be expected in the temperature range below 1 K, where the temperature is comparable to the third exchange integral. This temperature range, however, has been little investigated.

The aim of the present work derives directly from the above discussion of available experimental results. Significant changes in ESR parameters at temperatures above the spin–Peierls transition and tentative changes in the ESR absorption spectrum below the transition require a detailed quantitative analysis of ESR line shapes as functions of temperature. It is obvious that the most interesting temperature range is below 1 K, in which new effects of magnetic ordering could be expected.

Note that most of the earlier measurements were performed at frequencies $\nu<35$ GHz,[6,10] i.e., in the conventional ESR band, or at frequencies ranging between 90 and 1600 GHz.[7–9] But the magnetic ordering can be destroyed at frequencies $\nu>200-300$ GHz, because the resonant magnetic field is too high.[7–9] The importance of experiments in the intermediate band was demonstrated in a recent publication[11] reporting on an anomalous low-temperature behavior of ESR absorption at frequencies $\nu=22-75$ GHz and $\mathbf{B}\|\mathbf{c}$. Note that this is the configuration that has been studied most comprehensively, unlike, for example, the case of $\mathbf{B}\|\mathbf{a}$. For this reason, we have undertaken an experimental study of resonant microwave absorption near the ESR line in $\rm CuGeO_3$ single crystals at temperatures $T=0.5-300$ K, in a frequency band of 40 to 120 GHz, and in the $\mathbf{B}\|\mathbf{a}$ configuration.

2. EXPERIMENTAL TECHNIQUES

$\rm CuGeO_3$ single crystals were synthesized at M. V. Lomonosov Moscow State University. Their quality was checked using X-ray diffraction, and the absence of technological impurities in the prepared crystals was checked by chemical analysis. A detailed description of the sample synthesis technique is given elsewhere.[12]

Microwave absorption in a magnetic field of up to 15 T in the frequency band of 40 to 120 GHz was measured using two techniques. The first was direct measurement of absorption in the magnetic field. Millimeter waves were generated by a set of sources built around backward-wave oscillators (BWO) and conducted via a waveguide into the cryostat with a superconducting magnet generating a field of up to 7 T. A single crystal with typical dimensions of $3\times 3\times 0.1$ mm was set on a copper diaphragm, whose temperature could be varied between 1.8 and 4.2 K with a stability within 0.05 K. The microwave radiation transmitted through the sample was detected by a carbon bolometer. This facility was used in detailed measurements of resonant features of spectra at different frequencies at temperatures below the spin-Peierls transition. A detailed description of this facility can be found in an earlier publication.[13]

A second facility was employed in studies of the ESR spectrum as a function of temperature. A sample was placed in a tunable cavity with $Q=8\cdot 10^3$, and the signal transmitted through the cavity was recorded as a function of magnetic field. A special device allowed us to shift the cavity bottom inside the bore of the superconducting solenoid generating a field of up to 15 T and thus roughly tune the resonant frequency between 50 and 75 GHz. Fine tuning to the resonance was performed by varying the microwave frequency. The loaded cavity transmission was measured by a millimeter-wave vector network analyzer (MNVA) manufactured by ABmm (France) and using solid-state generators and detectors.[14] Measurements in the 1.5–300-K temperature range were performed in a cryostat with a continuous flow of a cooling agent, and for $T<1.5$ K in a ^{3}He cryostat.

At temperatures below the spin–Peierls transition, namely in the range of 1.8 K to 4.2 K, the two experimental facilities recorded similar spectra of resonant absorption in a magnetic field. In magnetic fields of up to 15 T, only features near the ESR with $g\approx 2$ were detected in all samples, and no additional resonances whatever were recorded. The resonant frequencies of all detected features in absorption spectra were linear in the magnetic field within the experimental error.

Since defects in $\rm CuGeO_3$ crystals could affect shapes of ESR spectra, we checked spectra of the samples cleaved from different parts of the ingot. Samples cleaved from the central part, in which minimal impurity contents were detected by chemical analysis, produced a single main ESR line alongside weaker spectral components both above and below the spin-Peierls transition temperature, and the spectrum shapes were reproducible from sample to sample. The spectra of the samples from the ends of the bar, where the impurity content was higher, contained a doublet in the region of the main resonance and satellites of smaller amplitudes. As an additional check of the sample quality, we recorded ESR spectra of samples fabricated at Université de Paris Sud by G. Dhalenne and A. Revcolevschi. They were identical to spectra of single crystals cleaved from the central section of the bar. In this paper we specifically discuss measurements of samples of the highest quality.

3. EXPERIMENTAL RESULTS

3.1. Resonant magnetoabsorption of $\rm CuGeO_3$

Typical normalized transmission spectra $Tr(B)$ at $\nu=66.3$ GHz are given in Fig. 1. They are normalized so that $Tr(B)=1$ holds far from resonances.

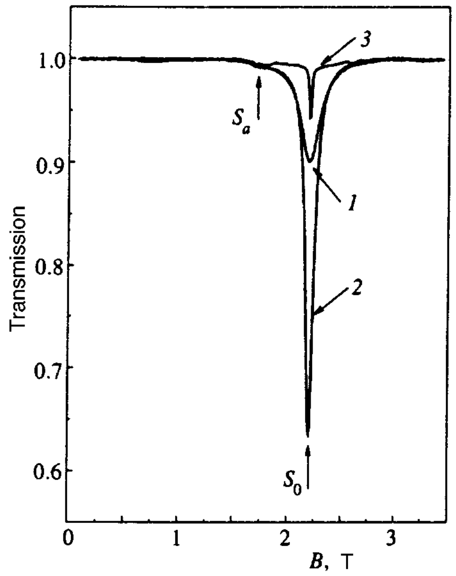

FIG. 1. Normalized transmission spectra around ESR in $CuGeO_3$ at $\nu = 66.3$ GHz and various temperatures: (*1*) $T = 256$ K; (*2*) $T = 78$ K; (*3*) $T = 4.2$ K.

At temperatures above that of the spin–Peierls transition, the ESR spectrum consists of two components, namely, the main line S_0 with a Lorentzian shape and the weaker line S_a. The amplitude and width of the S_0 line strongly depend on temperature. As the temperature is lowered to the transition temperature, its amplitude increases, while its width drops (Fig. 1, curves *1* and *2*). In this temperature range the parameters of the S_a line are almost constant with temperature.

For $T < T_{SP} \approx 14$ K the S_0 line amplitude drops abruptly (Fig. 1, curve *3*), and the shape of the magnetoabsorption spectrum near the ESR changes radically. In contrast to the range $T > T_{SP}$, the lines S_0 and S_a at temperatures $T < 12$ K are superposed on a new broad absorption line (see also Fig. 2, where details of the transmission spectrum are plotted on an enhanced scale). Moreover, the spectrum contains a new narrow line (Fig. 2). The broad line was first reported in Ref. 11 for the configuration $\mathbf{B} \| \mathbf{c}$, but our absorption spectra, unlike those in Ref. 11, do not have an asymmetric pattern of narrow ESR lines. With the exception of the broad line, the recorded spectra (Figs. 1 and 2) are similar to those in Ref. 10 for the configuration $\mathbf{B} \| \mathbf{c}$, where two weaker lines were also detected around the central absorption peak. It is remarkable that in the low-temperature range the main S_0 absorption line is accompanied by two weak satellites α and β, which are clearly seen for $T < 1.5$ K (Fig. 2).

All the components detected at temperatures both above and below the spin–Peierls transition, namely S_0, S_a, and S_b, and the broad line, depend sensitively on temperature. A detailed description of this dependence will be given in the following sections.

3.2. Positions and amplitudes of resonances

Positions of different resonances expressed in terms of g-factors are plotted in Fig. 3. One sees that the g-factors of S_0, S_a, and S_b lines are constant with temperature. The main resonance corresponds to $g_0 = 2.154 \pm 0.002$, in agreement with the published data for the configuration $\mathbf{B} \| \mathbf{a}$.[6] The g-factors of the S_a and S_b lines reported for the first time in this paper are $g_a = 2.72 \pm 0.01$ and $g_b = 1.83 \pm 0.01$ (Fig. 3).

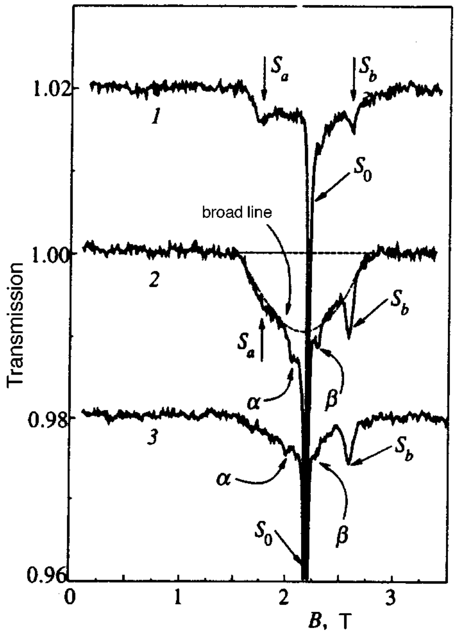

FIG. 2. Fine structure of $CuGeO_3$ transmission spectra around ESR at $\nu = 66.3$ GHz and below the spin–Peierls transition: (*1*) $T = 12$ K; (*2*) $T = 1.35$ K; (*3*) $T = 0.53$.

The standard procedure of ESR spectrum analysis includes calculation of the total absorption, which is proportional to the susceptibility of the free spins:[15]

$$I(T) = \int_0^{\infty} [1 - Tr(B)] dB \propto \chi_0(T). \tag{1}$$

In the case of $CuGeO_3$, $I(T)$ can be calculated for S_0 and the broad line, whereas the uncertainty in this integral for the weak S_a and S_b lines is too large. Therefore, let us first

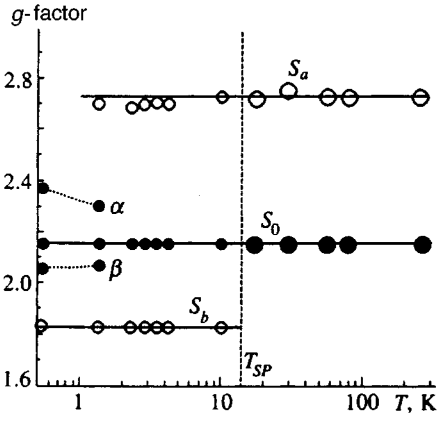

FIG. 3. g-factors of $CuGeO_3$ resonances versus temperature. The notations for the resonances in Figs. 1–5 are identical. The vertical dashed line in Figs. 3–5 shows the temperature of the spin–Peierls transition.

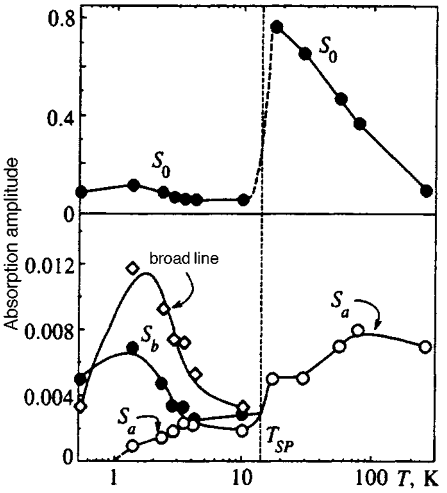

FIG. 4. Amplitudes of $CuGeO_3$ absorption lines as functions of temperature.

consider the amplitudes of the absorption maxima versus temperature, which can be measured for all components of the ESR spectra.

Unlike the resonance positions, their amplitudes strongly depend on temperature (Fig. 4). The amplitude of the S_0 line monotonically increases as the temperature drops, then drops abruptly by a factor of about 13 around $T_{SP} \approx 14$ K (a detailed description of this region will be given in the next section, in which we will discuss the total absorption as a function of temperature).

In the temperature range below the spin–Peierls transition, the S_0 line amplitude increases by a factor of about two as the temperature drops from 4.2 to 1.3 K, and then at $T \approx 0.5$ K it decreases by about 30% with respect to the local maximum (Fig. 4). A similar nonmonotonic behavior is displayed by the S_b line and the broad line, whose amplitudes have maxima around 1.3 K (Fig. 4).

It is remarkable that the relative change in the amplitude due to the temperature drop to $T \approx 0.5$ K is larger for the broad line than for the S_0 line and S_b line. Figures 2 and 4 clearly demonstrate that the broad line amplitude decreases substantially (by a factor of almost three) as the temperature drops from 1.3 to 0.5 K.

The S_a line amplitude has a different temperature dependence (Fig. 4). This parameter gradually decreases in the range $T < 100$ K, and near T_{SP} it is about 2.5 times smaller (recall that the S_0 line amplitude varies in this range by more than an order of magnitude). In the temperature range down to 1 K the S_a line amplitude decreases further, and at lower temperatures this feature is not detected in the magnetoabsorption spectra (see also Fig. 2).

3.3. Total absorption and line widths

The total absorption $I(T)$ was calculated by numerically integrating the transmission curves (Figs. 1 and 2). One can see in Fig. 2 that the broad line and S_0 line can be resolved below the spin–Peierls transition temperature, so for $T < T_{SP}$

$$I(T) = I_0(T) + I_1(T), \qquad (2)$$

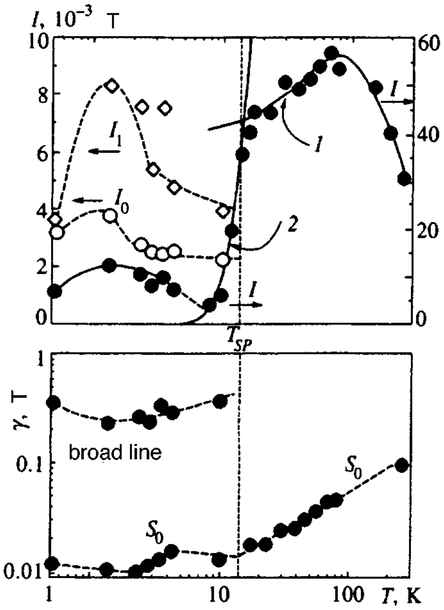

FIG. 5. Integral absorption I and line widths γ for features of ESR absorption spectra of $CuGeO_3$ versus temperature. Solid lines *1* and *2* for $I(T)$ show calculations by different models: (*1*) Bonner–Fisher model; (*2*) Bulaevskii model. The rest of the lines are plotted in accordance with experimental data.

where $I_0(T)$ and $I_1(T)$ are the total absorptions in the main S_0 line and broad line, respectively. The processing of these lines is illustrated by the middle graph in Fig. 2, where the dashed line shows the suggested contour of the broad line.

Calculations of the total absorption are plotted in Fig. 5. For $T > T_{SP}$ the experimental curves of $I(T) = a\chi_0(T)$ should, obviously, be compared with the magnetic susceptibility of a one-dimensional Heisenberg spin chain calculated by Bonner and Fisher.[16] The feature of the Bonner–Fisher model is that the exchange integral along the chain and the g-factor unambiguously determine both the temperature scale and amplitude of the effect, i.e., the model is free from adjustable parameters. In our calculations, we have used $J_c = 61.5$ K[5] and the g-factor of the main resonance (Fig. 3).

Theoretical calculations using this model are shown in Fig. 5 (curve *1*). It is clear that for $T > T_{SP}$ measurement data for $I(T)$ are approximated by the theoretical curve to within $\simeq 5\%$ for an ideal one-dimensional spin chain. The model adequately describes the drop in the total absorption by about 25% at $T = T_{SP}$ as compared to its peak value corresponding to $T \simeq 80$ K. Note that measurements of $I(T)$ by Ohta *et al.*,[8] who also studied the configuration $\mathbf{B} \| \mathbf{a}$, had an uncertainty of 30–40% for $T > T_{SP}$, and the uncertainty of measurements in the configuration $\mathbf{B} \| \mathbf{c}$ in Ref. 10 was about 20%, i.e., the accuracy of those measurements[8,10] was insufficient for checking theoretical predictions. To the best of our knowledge, the data in Fig. 5 illustrate the first-ever successful application of the Bonner–Fisher model to properties of $CuGeO_3$, since all previously reported measurements of magnetic susceptibility differed considerably from theoretical calculations[1,17] in both the effect amplitude and shape of the $\chi(T)$ curve. Possible reasons for such discrepancies will be discussed in the next section.

Bonner and Fisher did not take into account the spin–Peierls instability in their calculations. In accordance with Refs. 6 and 10, the total absorption versus temperature below T_{SP} is well described by the Bulaevskii formula[18]

$$I(T)\propto\frac{1}{T}e^{-m/T}, \tag{3}$$

where $m=46$ K [calculations made with Eq. (3) are shown by curve *2* in Fig. 5].

The total absorption $I(T)$ has a minimum at $T\sim4$ K. A further decrease in the temperature leads to an increase in $I(T)$, and the curves of $I_0(T)$ and $I_1(T)$ are similar (Fig. 5). Such behavior should be expected if most spins in chains are assumed to be dimerized, and the remaining uncoupled spins due to defects in the crystal lattice or irregularities in the spin-Peierls phase, which are not included in one-dimensional ordered structures, have a magnetic susceptibility described by the Curie law. A similar behavior of $I(T)$ for $\mathbf{B}\|\mathbf{c}$ was qualitatively described earlier,[11] but without distinguishing contributions from the broad and narrow features of the ESR spectrum. Measurements by Honda *et al.*[10] for the same configuration produced a different result: in the range $T<6$ K the susceptibility $\chi(T)$ increased with decreasing temperature, while the total absorption was constant.

Below $T=1$ K the total absorption drops (Fig. 5) largely due to a large drop in the contribution from the broad line, $I_1(T)$, and $I_0(T)$ changes similarly, although the amplitude of its change is considerably smaller.

Given the measured values of the total absorption and amplitudes, we can calculate line widths. Assuming that all lines have Lorentzian shapes, we can derive the Lorentzian width γ in units of magnetic field from the formula

$$\gamma=\frac{I(T)}{\pi A(T)}, \tag{4}$$

where $A(T)=1-\min\{Tr(B,T)\}$ is the amplitude of an absorption line with total intensity $I(T)$. This approximation is perfectly suitable for the S_0 line, whereas it yields a reasonable estimate for the broad line.

Calculated line widths are plotted in Fig. 5. Note that the gradual decrease in γ for the main line S_0 is in agreement with previously reported results.[6,8,9] The width of the broad line as a function of temperature is nonmonotonic, and a broad minimum can be seen on $\gamma(T)$ curve around $T\simeq1$ K.

3.4. Low-temperature anomaly in CuGeO$_3$

Experimental data described in the previous sections indicate a low-temperature anomaly in CuGeO$_3$. As can be seen in Figs. 1–5, the amplitude and total absorption of both the broad line and S_0 line drop considerably below 1 K. Moreover, the S_a line amplitude vanishes in this temperature range.

These qualitative and quantitative changes in ESR absorption spectra allow us to suggest that additional magnetic ordering occurs in CuGeO$_3$ at temperatures $T<1$ K, since in this case the susceptibility of uncoupled spins should decrease. Note also that these changes in the ESR spectrum occur in the region where the temperature is comparable to the third exchange integral, $T\sim J_a\approx0.7$ K,[5] so changes in the magnetic subsystem of spins not included in the spin–Peierls phase can be expected, namely, these spins can be ordered at lower temperatures or ''frozen'' by forming a spin–glass phase.

A comprehensive study and interpretation of the possible low-temperature anomaly in CuGeO$_3$ is beyond the scope of this publication. Here we only make several remarks. First, in our opinion, the formation of the broad line below the spin–Peierls transition should be taken into account. One can see in Figs. 4 and 5 that this feature is most susceptible to changes in temperature around $T\simeq1$ K. Usually broadening of an absorption line can be attributed to disorder, in this specific case, in the spin subsystem, so, the drop in the amplitude of this feature (Figs. 4 and 5) can be interpreted as additional ordering of spins in CuGeO$_3$ at $T\simeq1$ K.

Second, in addition to the possible order–disorder transition, the condition $T\sim J_a$ may be important. Since the exchange interaction along the **a**-axis is ferromagnetic, and a purely ferromagnetic interaction cannot decrease the susceptibility, it is likely that an additional interaction should lead to some change in the magnetic ordering, while the antiferromagnetic spin alignment should largely persist. As a result of the change in the magnetic structure, a fraction of spins, for example, can be redistributed between the spin–Peierls phase and the phase of free spins, and the number of the latter can decrease.

Third, we can see that measured total ESR absorption and static magnetic susceptibility in CuGeO$_3$ diverge. It seems likely that only free spins contribute to ESR, $I\sim\chi_0$, whereas the magnetic susceptibility measured by a magnetometer also includes a contribution χ_c of the collective mode, so that $\chi(T)=\chi_0(T)+\chi_c(T)$. As a result, on one hand the ESR technique can be more susceptible to changes in the magnetic ordering of a sample (especially in the subsystem of free spins), and on the other hand, ESR measurements are difficult to check independently. For this reason, more experiments on the magnetic susceptibility and ESR spectra are required for elucidating the nature of the suspected magnetic anomaly in CuGeO$_3$ indicated by our measurements, and this will be the subject of our future research.

4. CONCLUSIONS

The main results of our research in resonant microwave absorption around ESR in CuGeO$_3$ single crystals in the configuration $\mathbf{B}\|\mathbf{a}$ can be summarized as follows.

(1) The temperature dependence of the total absorption in the main resonance with $g_0=2.154$ in the temperature range above the spin–Peierls transition is in a good agreement with Bonner and Fisher's calculations for a one-dimensional Heisenberg chain.

(2) In addition to the main resonance, a new line of a smaller amplitude and with $g_a=2.72$ has been detected throughout the temperature range above the point $T\simeq1$ K, below which its amplitude is zero.

(3) When the temperature drops below that of the spin–Peierls transition, $T_{\mathrm{SP}}\approx14$ K, the shape of the magnetoabsorption spectrum in a magnetic field changes radically. A

new broad feature emerges in the magnetoabsorption spectrum with narrow lines superposed on it, including a new line with $g_b = 1.83$ not observed above T_{SP}.

(4) The quantitative analysis of ESR spectrum parameters indicates that the region below 1 K is anomalous, which may be caused by additional magnetic ordering in the magnetic subsystems of $\mathrm{CuGeO_3}$.

The character of the ESR spectrum restructuring due to the transition through T_{SP} for the $\mathbf{B}\parallel\mathbf{a}$ configuration is different from those described in Refs. 10 and 11 for $\mathbf{B}\parallel\mathbf{c}$, and our picture is intermediate between those reported in these two publications. As in Ref. 11, we have observed a broad feature in the ESR absorption spectrum, but the pattern of narrow resonances is closer to that in Ref. 10. The causes of such discrepancies remain unclear, although differences in the defect structures of samples investigated by different groups should be taken into account.

It also seems interesting to clarify the nature of the weak S_a line detected at temperatures both above and below the spin–Peierls transition. Our data do not allow us to ascribe this line to a chemical impurity, because it is highly unlikely that an impurity contributing to the ESR spectrum in a temperature range of 1 to 300 K could lose its ESR activity for $T < 1$ K. Given the strong temperature dependence of this line and the section with the abrupt change in its amplitude near T_{SP}, the S_a line can be tentatively attributed to intrinsic structural irregularities in the copper chains. An additional ordering in the subsystem of free spins for $T < 1$ K can ''heal'' defects of the spin–Peierls phase and thus suppress the corresponding feature in ESR spectra (Fig. 4). Unfortunately, the problem of defects in $\mathrm{CuGeO_3}$ is far from its ultimate solution at present as regards both technology and structural research, on one hand, and models of electronic structure, on the other. The results of our research indicate that defects of different nature determine the complicated structure and fine features of low-temperature ESR absorption, so studies of structural irregularities in undoped $\mathrm{CuGeO_3}$ single crystals assume primary importance.

We acknowledge the help of A. Ardavan and J. Singleton in some experiments. This work was a part of a joint project supported by the Royal Society (Great Britain), and projects INTAS 93-2400 and INTAS 94-1788. Some stages of this research were supported by the *Physics of Microwaves* and *Fundamental Spectroscopy* program sponsored by the Ministry of Science and Technology of Russia, and by the Russian Fund for Fundamental Research (Grant 96-02-1974a).

[1] M. Hase, I. Terasaki, and K. Uchinokura, Phys. Rev. Lett. **70**, 3651 (1993).
[2] I. S. Jacobs, J. W. Bray, H. R. Hart, L. V. Interrante, J. S. Kasper, G. D. Watkins, D. E. Prober, and J. C. Bonner, Phys. Rev. B **14**, 3036 (1976).
[3] M. D. Lumsden, B. D. Gaulin, H. Dabkowska, and M. L. Plumer, Phys. Rev. Lett. **76**, 4919 (1996).
[4] M. Nishi, O. Fujita, and J. Akimitsu, Phys. Rev. B **50**, 6508 (1994).
[5] L. P. Regnault, M. Ain, B. Hennion, G. Dhalenne, and A. Revcolevschi, Phys. Rev. B **53**, 5579 (1996).
[6] S. Oseroff, S.-W. Cheong, A. Fondado, B. Aktas, and Z. Fisk, J. Appl. Phys. **75**, 6819 (1994).
[7] T. M. Brill, J. P. Boucher, J. Voiron, G. Dhalenne, A. Revcolevschi, and J. P. Renard, Phys. Rev. Lett. **73**, 1545 (1994).
[8] H. Ohta, S. Imagawa, H. Ushiroyama, M. Motokawa, O. Fujita, and J. Akimitsu, J. Phys. Soc. Jpn. **63**, 2870 (1994).
[9] H. Ohta, Y. Yamamoto, S. Imagawa, T. Nanba, K. Watanabe, M. Arai, M. Motokawa, O. Fujita, and J. Akimitsu, Int. J. Infrared Millim. Waves **16**, 501 (1995).
[10] M. Honda, T. Shibata, K. Kindo, S. Sugai, T. Takeuchi, and H. Hori, J. Phys. Soc. Jpn. **65**, 691 (1996).
[11] A. I. Smirnov, V. N. Glushkov, A. N. Vasil'ev, D. I. Leonyuk, S. Coad, D. MacPaul, G. Dhalennl, and A. Revcolevschi, JETP Lett. **64**, 305 (1996).
[12] L. I. Leonyuk, G. Babonas, A. Resa, in *Proceedings of the 20-th Workshop on Compound Semiconductor Devices and Integrated Circuits*, Vilnius (1996), p. 41.
[13] S. V. Demishev, A. V. Semeno, N. E. Sluchanko, N. A. Samarin, I. B. Voskoboinikov, V. V. Glushkov, J. Singleton, S. J. Blundell, S. O. Hill, W. Hayes, M. V. Kartsovnik, A. E. Kovalev, M. Kurmoo, P. Day, and N. D. Kushch, Phys. Rev. B **53**, 12794 (1996).
[14] S. Hill, Ph.D. Thesis, Oxford University (1994).
[15] S. A. Al'tshuler and B. M. Kozyrev, *Electron Paramagnetic Resonance*, Fizmatgiz, Moscow (1961).
[16] J. C. Bonner and M. E. Fisher, Phys. Rev. **135**, A640 (1964).
[17] H. Hori, M. Furusawa, T. Takeuchi, S. Sugai, K. Kindo, and A. Yamagishi, J. Phys. Soc. Jpn. **63**, 18 (1994).
[18] L. N. Bulaevskiĭ, Fiz. Tverd. Tela **11**, 921 (1969) [*sic*].

Translation provided by the Russian Editorial office.

Chain ordering in molecular dynamics and kinetics

A. É. Filippov

Donetsk Physicotechnical Institute, Ukrainian National Academy of Sciences, 340114 Donetsk, Ukraine

(Submitted 23 January 1997)
Zh. Éksp. Teor. Fiz. **112**, 1739–1755 (November 1997)

The molecular dynamics method is used to study ordering processes in a two-component two-dimensional Coulomb gas consisting of equal numbers of positively and negatively charged particles, a gas that models the behavior of a system of interacting vortices. It is found that as the system temperature decreases, starting from the well-known Kosterlitz–Thouless transition point the system exhibits additional vortex-chain ordering. This process is found to stimulate the production of vortex chains, which can be observed in real superfluids, magnetic materials, and superconducting systems. The results are compared with those obtained by modeling the kinetics in similar systems via the time-dependent continuum Heisenberg–Landau model. © *1997 American Institute of Physics.* [S1063-7761(97)01511-4]

1. INTRODUCTION

In recent decades the dynamics of the ordering of spatially inhomogeneous structures and phase separation have attracted the attention of researchers. During this time the development of computational techniques refined the approximations needed to solve the problem. As a rule, such approximations of the problem amounted to transforming it into one that originated in the multiparticle dynamical problem of the motion of an ensemble of interacting subsystems, i.e., a continuum description on the base of collective fields (densities). The current level of computational techniques makes possible direct numerical modeling of fairly complicated systems with long-range interaction. On the one hand, this method makes it possible to verify the result of continuum theories, and on the other, to detect the structural features of the system that are sure to be lost in the approximation process.

Many publications (see, e.g., Refs. 1–12) give examples of both directions of research. For instance, computer simulation of phase separation and spinodal decay in simple and binary liquids[1–3] is to great extent aimed at reproducing the results of the analytical theory,[4] while the tangled dipole chains obtained by numerical methods[5–7] are extremely difficult objects for detection via analytical methods. By varying the dynamical scenarios it is possible to predict not only the structures proper but also ways of attaining them through experiments. Here the model incorporates fairly realistic potentials, as is the case, say, with modeling the crystallization of molecular liquids.[8,9]

In turn, the nontrivial results of modeling by the molecular dynamics method stimulates the search for similar structures by using methods based on the analysis of continuum fields and through experiments. For instance, proof of formation of orientation-ordered structures in liquids obtained by the molecular dynamics method for a system of dipoles with a hard spherical core[5,6] facilitated studies of long-range order in dipole liquids based on the idea of the density functional.[10] The numerical experiments in the quasicrystallization of vortices in two-dimensional turbulence[10,11] have been followed by experiments in observing the relaxation of the chaotic motion of magnetized electrons, which reproduce an almost ideal two-dimensional liquid, to a vortex crystal.[12]

2. DIPOLE AND VORTEX CHAINS

In this paper we give some results of modeling the dynamics of a two-dimensional electron gas as applied to the description of a system of vortices. Starting with the well-known papers of Berezinskiĭ[13] and Kosterlitz and Thouless,[14,15] the model of a two-dimensional Coulomb gas has been widely used to describe the thermodynamics of various systems (see Ref. 16). Under certain assumptions, the description of superfluids, the melting of crystals, and the two-dimensional $x-y$ model for spin lattices can be reduced to this model. This has made it possible to define the idea of topological order for two-dimensional systems, for which in accordance with the Mermin–Wagner–Hohenberg theorem[17,18] an ordered state in the ordinary sense of the word is impossible. A phase transition in such systems was compared to a dissociation of vortex pairs in which the average vortex–antivortex distance in an emerging fluctuation pair of excitations grows without limit. Bearing in mind the spatial dependence of the interaction between vortices, we use the model Hamiltonian

$$\mathbf{H}=\sum_{i\neq j} U(\mathbf{r}_{ij})S_iS_j\,,$$

where S_i are Coulomb charges and the potential $U(\mathbf{r}_{ij})$ is defined as

$$U(\mathbf{r}_{ij})=\int d\mathbf{r}'d\mathbf{r}''f(|\mathbf{r}'-\mathbf{r}''|)V(|\mathbf{r}'-\mathbf{r}''|)f(|\mathbf{r}''|),$$

with $f(|\mathbf{r}-\mathbf{r}'|)$ the normalized density of the spatial distribution of charge, and has the following limits:

$$U(\mathbf{r})\simeq\ln\frac{\lambda}{\zeta}\quad\text{for}\ \ r\ll\zeta\ll\lambda,$$

$$U(\mathbf{r})\simeq-\ln\frac{r}{\lambda}\quad\text{for}\ \ \zeta\ll r\ll\lambda,$$

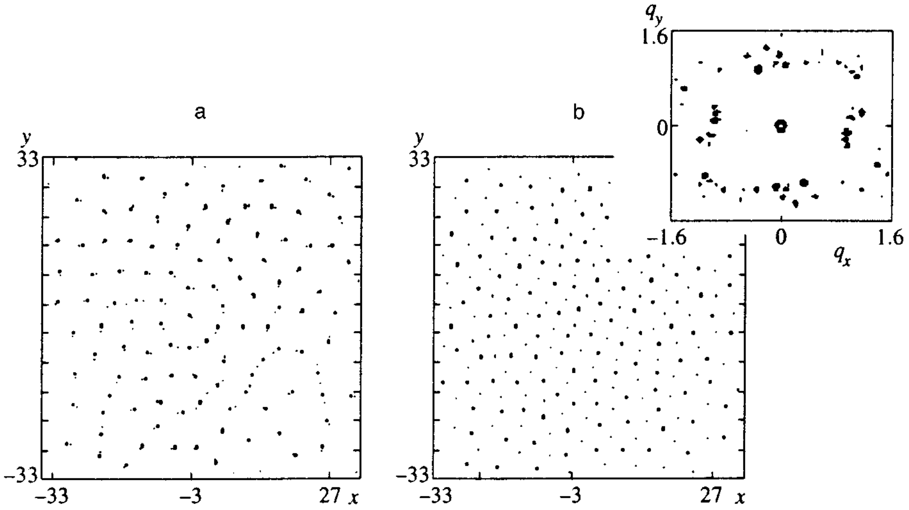

FIG. 1. Fragments of two characteristic structures (containing $N=10^3$ particles each) that occur for $T \ll T_{KT}$ and have a chaotic initial distribution of vortices: (a) chains consisting of vortex pairs ($r_0 \ll a$), and (b) a quasicrystalline vortex structure ($r_0 \simeq a$). Particles belonging to different species (vortices and antivortices) are depicted by dots of different sizes. The inset shows the distribution of the maxima of the Fourier transform of the correlation function.

$$U(\mathbf{r}) \sim r^{-1/2} \exp\left(-\frac{r}{\lambda}\right) \quad \text{for } \lambda \ll r,$$

which ensures the proper UV and IR cutoff.[16] A similar cutoff procedure can be used in numerical experiments.

The corresponding dynamical equation for such systems can be derived from the description of the motion of a superfluid (superconducting) liquid.[19,20] In the lowest kinetic approximation (in particular, in the approximation that ignores the electrostatic contribution to energy), vortices are inertialess.[16] In this approximation the vortex motion is determined by the condition that the total force acting on a vortex (and consisting of $-\partial U(\mathbf{r}_{ij})/\partial \mathbf{r}_i$, noise, and relaxation) vanishes, so that the equation of motion has the Langevin form[16]

$$\frac{d\mathbf{r}_i}{dt} = -\gamma \frac{\partial U(\mathbf{r}_{ij})}{\partial \mathbf{r}_i} + \xi(\mathbf{r}_i,t) \tag{1}$$

with delta-correlated noise ξ

$$\langle \xi(\mathbf{r},t) \rangle = 0,$$
$$\langle \xi(\mathbf{r},t)\xi(\mathbf{r}',t) \rangle = 2D\,\delta(\mathbf{r}-\mathbf{r}')\,\delta(t-t'). \tag{2}$$

In the general case the equation also contains $d^2\mathbf{r}_i/dt^2$:

$$\frac{d^2\mathbf{r}_i}{dt^2} = -\gamma \frac{d\mathbf{r}_i}{dt} - \frac{\partial U(\mathbf{r}_{ij})}{\partial \mathbf{r}_i} + \xi(\mathbf{r}_i,t). \tag{3}$$

In this form the model can be applied to a much broader class of objects. For instance, we can expect that by combining into pairs the charged particles form a dipole molecular liquid with properties similar to those discussed in Refs. 5–7 and yet retain all degrees of freedom (rotational, vibrational, ability to dissociate and recombine, etc.) inherent in real molecules. The last feature opens broader possibilities than does the traditional modeling of long-range orientational order in dipole systems that is based on a combination of Lennard–Jones potentials,[5–7,21]

$$\mathbf{w}_{LJ}(r) = 4\varepsilon\left[\left(\frac{\sigma}{r}\right)^{12} - \left(\frac{\sigma}{r}\right)^{6}\right], \tag{4}$$

which is used to simulate spherical particles (molecules carrying a dipole), and the dipole potential

$$\mathbf{w}_{\rm dip}(r) = -\frac{3(\mu_2\mathbf{r})\cdot(\mu_1\mathbf{r})}{r^5} + \frac{\mu_2\mu_1}{r^3}, \tag{5}$$

where μ is the dipole moment.

Moreover, the equations in which the elementary interactions have the simplest structure can be solved much faster, so that all process can be observed on a display in ‘‘real time’’ for fairly large data arrays (about 10^3 particles moving in three or two dimensions).

In modeling dipole moments, the repulsive core at small distances must be modeled by an appropriate short-range correction to the potential, $\Delta U(\mathbf{r}_{ij})$. However, at room temperature ($D \neq 0$), because of the Coulomb contribution to the energy,

$$\Delta U(\mathbf{r}_{ij}) \sim 1/r_{ij}^2, \tag{6}$$

which sets the average scale of the energy minimum at $r_0 \sim D$, this effect appears even in a purely Coulomb problem with the an initial potential $U(\mathbf{r}) \simeq -\ln(r/\lambda)$. For the given number density of particles (vortices) $\rho \sim 1/a^2$, the r_0-to-a ratio determines the type of the emerging structure.

Direct experiments make it possible to verify that when the noise is intense (i.e., exceeds the temperature $T \sim D = T_{KT} \approx \min[U(\mathbf{r}_{ij}) + \Delta U(\mathbf{r}_{ij})]$), all vortices move independently; they form stable pairs only when the temperature is below T_{KT}, so that the model reproduces in a stable manner the well-known topological transition. Below we discuss only the new results related to the formation of fine structure in the system when the molecular dynamics method is employed, results absent from an approximate theory.

Figure 1 depicts fragments of two characteristic structures (containing $N=10^3$ particles each) that occur for $T \ll T_{KT}$ and have a chaotic initial distribution of vortices for, respectively, $r_0 \ll a$ and $r_0 \simeq a$. The directly observable chains consisting of vortex pairs can be described by the parameter

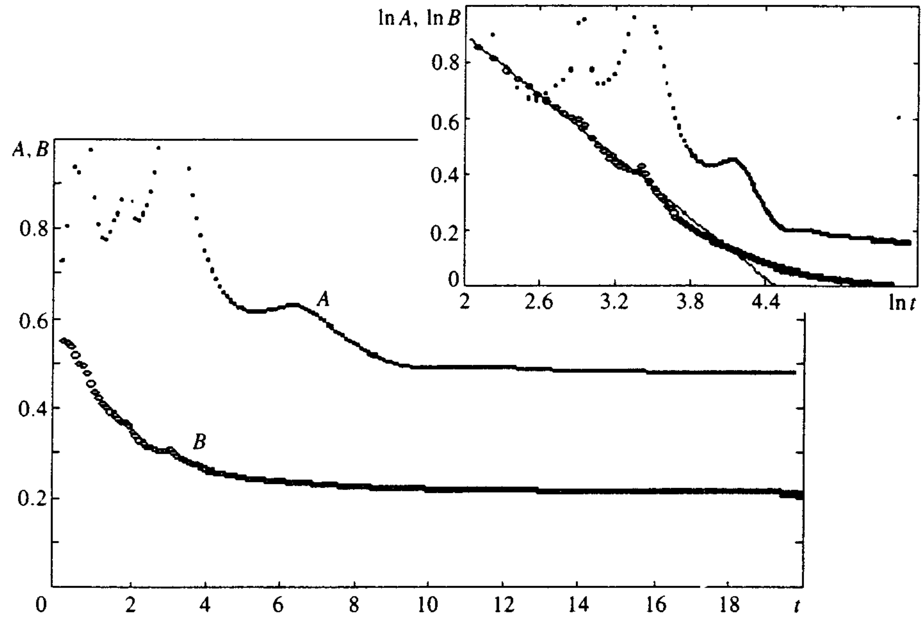

FIG. 2. The temporal evolution of the parameters $A=\{\Sigma_j[1/|\mathbf{r}_{jj'}|]+\Sigma_i\ [1/|\mathbf{r}_{ii'}|]\}/2-\Sigma_{ij}[1/|\mathbf{r}_{ij}|]$ and $B=\Sigma_k[1/|\mathbf{r}_{kk'}|]$. The inset depicts the same curves plotted on the log–log scale.

$$A=\frac{1}{2}\left\{\sum_j\left[\frac{1}{|\mathbf{r}_{jj'}|}\right]+\sum_i\left[\frac{1}{|\mathbf{r}_{ii'}|}\right]\right\}-\sum_{ij}\left[\frac{1}{|\mathbf{r}_{ij}|}\right], \tag{7}$$

which characterizes the difference in the average distances within the vortex subsystem ($\mathbf{r}_{ii'}\in\mathbf{R}^{(+)}$) and the antivortex subsystem ($\mathbf{r}_{jj'}\in\mathbf{R}^{(-)}$) and between the two subsystems ($\mathbf{r}_{ij}=\mathbf{r}_i-\mathbf{r}_j$) on the small scale.

The curve representing the parameter A in Fig. 2 shows that A rapidly increases in the early stages of the evolution of the system (randomly distributed at time $t=0$), when pairing leads to rapid screening of the Coulomb interaction. Later the system is slowly attracted to the attractor, at which the correlation of the pairs in the chains increases and the chains combine. The structures related to this transformation lead to temporary bursts in the value of A, which are especially evident in systems with a relatively small number of particles (to make the pattern more dramatic, the curves in Fig. 2 correspond to the case $N=10^2$). Here the parameter characterizing the distance between vortices of the two signs,

$$B=\sum_k\left[\frac{1}{|\mathbf{r}_{kk'}|}\right], \tag{8}$$

where $\mathbf{r}_{kk'}\in\mathbf{R}^{(+)}\oplus\mathbf{R}^{(-)}$, changes more smoothly and tends to the equilibrium value according to the power law $|B-B_0|\propto t^{1/3}$ (see the inset in Fig. 2, where the same curves are plotted on the log–log scale).

At $r_0\simeq a$ the system forms a vortex (quasi)crystal (see the second structure in Fig. 1), whose periodic structure is reflected in the maxima of the Fourier transform of the correlation function,

$$G(\mathbf{q})=\int d\mathbf{r}\,d\mathbf{r}'\exp(i\mathbf{r}\cdot\mathbf{q})\langle\rho(\mathbf{r})\rho(\mathbf{r}+\mathbf{r}')\rangle, \tag{9}$$

for finite wave vectors, $\mathbf{q}_j\neq 0$. These nontrivial maxima are clearly seen in Fig. 3 both in the total function $G(\mathbf{q})$, calculated by summing the discrete density over both subsystems,

$$\rho(\mathbf{r})=\rho_1(\mathbf{r})+\rho_2(\mathbf{r})=\sum_k\ \delta(\mathbf{r}-\mathbf{r}_k),\quad \mathbf{r}_k\in\mathbf{R}^{(+)}\oplus\mathbf{R}^{(-)}, \tag{10}$$

and in the partial form factors

$$S_{1,2}(\mathbf{q})=\int d\mathbf{r}\,d\mathbf{r}'\exp(i\mathbf{r}\cdot\mathbf{q})[\langle\rho_{1,2}(\mathbf{r})\rho_{1,2}(\mathbf{r}+\mathbf{r}')\rangle -|\langle\rho_{1,2}(\mathbf{r})\rangle|^2], \tag{11}$$

calculated for each subsystem separately. By way of an example, Fig. 3 depicts the section of one of the form factors, $S_1(\mathbf{q})$, along the direction $q_y=0$ normalized to the same value as $G(\mathbf{q})$, so it is convenient to compare the two.

Visually, the distribution of vortices in the xy plane resembles a sixth-order lattice, but the typical distribution of the maxima of $G(\mathbf{q})$ in the q_xq_y plane depicted in the inset to Fig. 1 has a symmetry that is closer to rhombic. Periodicity occurs only on the average. The distribution of the maxima of the functions $G(\mathbf{q})$ and $S_{1,2}(\mathbf{q})$ resembles a fractal, so that the periods are pronounced only for averaged values of $G(\mathbf{q})$ and $S_{1,2}(\mathbf{q})$ (the heavy curves in Fig. 3).

The structure that develops in time usually consists of several rhombuses rotated relative to one another. Visually one can detect sixth-, fifth-, and fourth-order local axes in such a structure, which makes the structure look more like a two-dimensional quasicrystal[22–24] than like a ''slightly melted'' crystal. This can be confirmed if we construct the distribution function in angle for pairs of vectors that connect each site of the structure with its two nearest neighbors. The distribution has pronounced maxima at certain values of the angles (instead of a single smooth maximum at $\pi/6$).

In free space, a finite number of particles (vortices) of the same sign, being stabilized by the total field of the particles of the opposite sign, form a spot consisting of fragments of a rhombic lattice and the chains correlated with the fragments. The pattern that develops in time is close to the

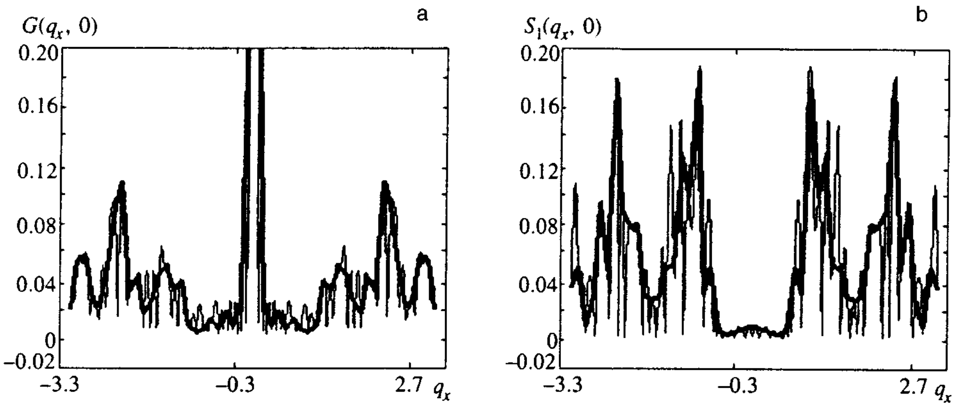

FIG. 3. (a) The Fourier transforms (light curves) of (a) the total correlation function, $G(\mathbf{q})=\int d\mathbf{r}\,d\mathbf{r}'\exp[i(\mathbf{r}\cdot\mathbf{q})]\times\langle\rho(\mathbf{r})\rho(\mathbf{r}+\mathbf{r}')\rangle\neq 0$, calculated by summing the discrete density over the two subsystems, $\rho(\mathbf{r})=\rho_1(\mathbf{r})+\rho_2(\mathbf{r})=\Sigma_k\delta(\mathbf{r}-\mathbf{r}_k)$, and (b) the partial form factor, $S_1(\mathbf{q})=\int d\mathbf{r}\,d\mathbf{r}'\exp[i(\mathbf{r}\cdot\mathbf{q})]\times[\langle\rho_1(\mathbf{r})\rho_1(\mathbf{r}+\mathbf{r}')\rangle-|\langle\rho_1(\mathbf{r})\rangle|^2]$, calculated for one subsystem (the first). The heavy curves depict the same quantities averaged over ten neighboring wave vectors.

recently discovered ordered structure that emerges in the positive column of a glow discharge in Ne (see Ref. 25). Here the Coulomb quasicrystal was formed by spherical glass particles under conditions close to those of the described numerical experiments. To model the process the experiment can be simplified somewhat by replacing the collective field of one subsystem with an external potential.

By itself, the appearance of vortex chains in an ordered state constitutes nothing new. For instance, vortex chains have been studied by Grishin *et al.*,[26] who investigated the magnetic structure of vortices in superconductors with single-axis anisotropy. They described the phenomenon of magnetic field inversion, related to the fact that in certain directions inside the anisotropic crystal the magnetic field is directed opposite to the total magnetic flux of the vortices. Because of this the vortices attract each other and form chains oriented along the crystal symmetry axis. This phenomenon became especially important when highly anisotropic high-T_c superconductors were discovered[27,28] and chains were actually observed.

Note that the multicomponent nature of the order parameter in the new superconductors, systems with heavy fermions, and other superfluid systems can in itself be the reason for the emergence of vortex chains.[29–32] In this case low-dimensional regions (channels) with a reduced total magnitude are formed in the order parameter. Singular vortices (containing a puncture of the modulus of the order parameter to zero) is attracted to these regions and become ordered vortex chains inside the regions. Lately it has been established that this phenomenon occurs in superfluid systems[29–31] and in superconducting systems.[32]

The molecular dynamics method has certain limitations that may become important when it is used to describe real systems. The phenomena detected within this approach can be related, in principle, to such features of the method as the fixing of the number of vortices or the specific type of interaction. At present there is no way in which these difficulties can be resolved. Yet we can try to obtain similar effects within other approaches and interpret them as indirect verification of the results of molecular dynamics.

Ordinarily (and this is also true of Refs. 29–32), the evolution of structures formed by interacting vortices is studied within the framework of the kinetic theory based on the time-dependent Ginzburg–Landau model (TDGLM).[33] In its gauge-invariant form this model is based on the analysis of a system of several interacting, fluctuating fields (the components φ_j of the order parameter and the vector potential $\mathbf{A}$), with noise and relaxation taken into account.[34–37] The gradient expansion within this approach reduces the problem to a system of local equations, which can be written in terms of the real-valued components of the complex-valued order parameter $\Psi=[\varphi_1, i\varphi_2]$ as follows:

$$\begin{aligned}\frac{1}{\gamma_1}\frac{\partial\varphi_1}{\partial t}&=\Delta\varphi_1+g(2\mathbf{A}\cdot\nabla\varphi_2+\varphi_2\nabla\mathbf{A})-\varphi_1[(\tau+g^2A^2)\\&\quad+\beta(\varphi_1^2+\varphi_2^2)]+\xi_1(\mathbf{r},t),\\ \frac{1}{\gamma_2}\frac{\partial\varphi_2}{\partial t}&=\Delta\varphi_2-g(2\mathbf{A}\cdot\nabla\varphi_1+\varphi_1\nabla\mathbf{A})-\varphi_2[(\tau+g^2A^2)\\&\quad+\beta(\varphi_1^2+\varphi_2^2)]+\xi_2(\mathbf{r},t),\\ \frac{1}{\gamma_3}\frac{\partial\mathbf{A}}{\partial t}&=\theta[\Delta\mathbf{A}-\mathbf{A}\nabla\mathbf{A}]-g(\varphi_1\nabla\varphi_2-\varphi_2\nabla\varphi_1)\\&\quad-g^2\mathbf{A}(\varphi_1^2+\varphi_2^2)+\xi_3(\mathbf{r},t).\end{aligned}\tag{12}$$

It is assumed that all field fluctuate independently, so that

$$\langle\xi_j(\mathbf{r},t)\rangle=0,\quad\langle\xi_j(\mathbf{r},t)\xi_k(\mathbf{r}',t)\rangle=\delta_{jk}\delta(\mathbf{r}-\mathbf{r}')\delta(t-t').\tag{13}$$

In the discrete version of the TDGLM equations the interactions between only a few nearest neighbors are taken into account. This coarsening of the description reduces the number of necessary computational operations (makes it proportional to the number of array elements) and allows one to reproduce the ordering of a system with a large number of vortices fairly rapidly. At the same time the coarsening wipes out all information about long-range interaction in the system, which if taken into account leads, at the least, to an essentially nonlocal addition to the quadratic part of the generating TDGLM functional,

$$\delta\mathscr{F}[\varphi]=\sum_j\int d\mathbf{r}'d\mathbf{r}''\varphi_j(\mathbf{r}')\Lambda(\mathbf{r}'-\mathbf{r}'')\varphi_j(\mathbf{r}'')\tag{14}$$

with the logarithmic kernel

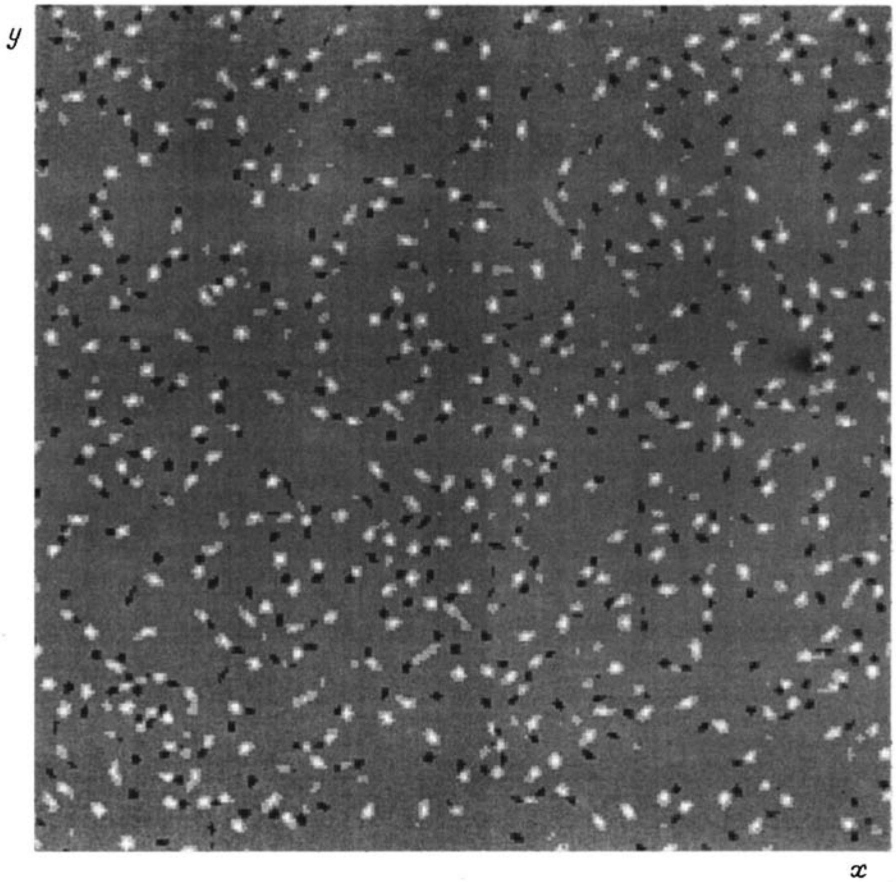

FIG. 4. Vortex structure in TDGLM. The current density distribution (18) is indicated by different shades of gray for a typical stage in the evolution of a fluctuating two-component system.

$$\Lambda(\mathbf{r}'-\mathbf{r})\propto\ln|\mathbf{r}'-\mathbf{r}|. \tag{15}$$

If this additional term is taken into account, we must allow for the interaction of all points of the array with each other, which makes all the computational merits of the method worthless.

However, if one has in mind a comparison of the results obtained by the methods of molecular dynamics and molecular kinetics, it would be interesting to find some proof of the existence of the chains mentioned earlier at least within the local approach. As noted in Refs. 36, 38, and 39, the simplest topological reason for such vortices to emerge within TDGLM is the intersection of the zero curves for different components of the order parameter. The generation of a gauge magnetic field by the current

$$\frac{1}{\gamma_3}\frac{\partial\mathbf{A}}{\partial t}=-g(\varphi_1\nabla\varphi_2-\varphi_2\nabla\varphi_1)+\dots$$

manifests itself only at the later stages in the kinetics as a contribution to the vortex interaction. This means that in the kinetic approach the vortex chains must appear even in the simplest nontrivial version of the model:

$$\frac{1}{\gamma_1}\frac{\partial\varphi_1}{\partial t}=\Delta\varphi_1-\varphi_1[\tau+\beta(\varphi_1^2+\varphi_2^2)]+\xi_1(\mathbf{r},t),$$

$$\frac{1}{\gamma_2}\frac{\partial\varphi_2}{\partial t}=\Delta\varphi_2-\varphi_2[\tau+\beta(\varphi_1^2+\varphi_2^2)]+\xi_2(\mathbf{r},t). \tag{16}$$

Formally we are dealing with two order parameters, whose interaction

$$\delta\mathscr{F}_{\text{int}}[\varphi]=\beta\int d\mathbf{r}\,\frac{\varphi_1^2(\mathbf{r})\varphi_2^2(\mathbf{r})}{2} \tag{17}$$

is such that a large fluctuation of one of the fields at the given point in space interferes with the ordering of the other field. Their ordered domains grow along the boundary separating them, and the smallest (fluctuation) local symmetry breaking in the given mesoscopic region is enough to form a chain of domains of one field along the long boundary of the other field.

The vortex structure of such ordering can be described by the curl of the current $\mathbf{J}=g(\varphi_1\nabla\varphi_2-\varphi_2\nabla\varphi_1)$, which in the two-dimensional case amounts to the following combination of components of the order parameter:

$$\text{curl }\mathbf{J}=2g\left(\frac{\partial\varphi_1}{\partial y}\frac{\partial\varphi_2}{\partial x}-\frac{\partial\varphi_2}{\partial y}\frac{\partial\varphi_1}{\partial x}\right). \tag{18}$$

In Fig. 4 this combination is indicated by different shades of gray for a typical stage in the evolution of a fluctuating two-component system. One can clearly see chains of vortices and antivortices.

Figure 5 shows how the vortex chains of Fig. 4 are related to the quantity $M=|\varphi_2\varphi_1|$, which is a reflection of both the intersection of the zero curves and the localization of the regions where these components are both nonzero and hence where their contribution to the current is not small.

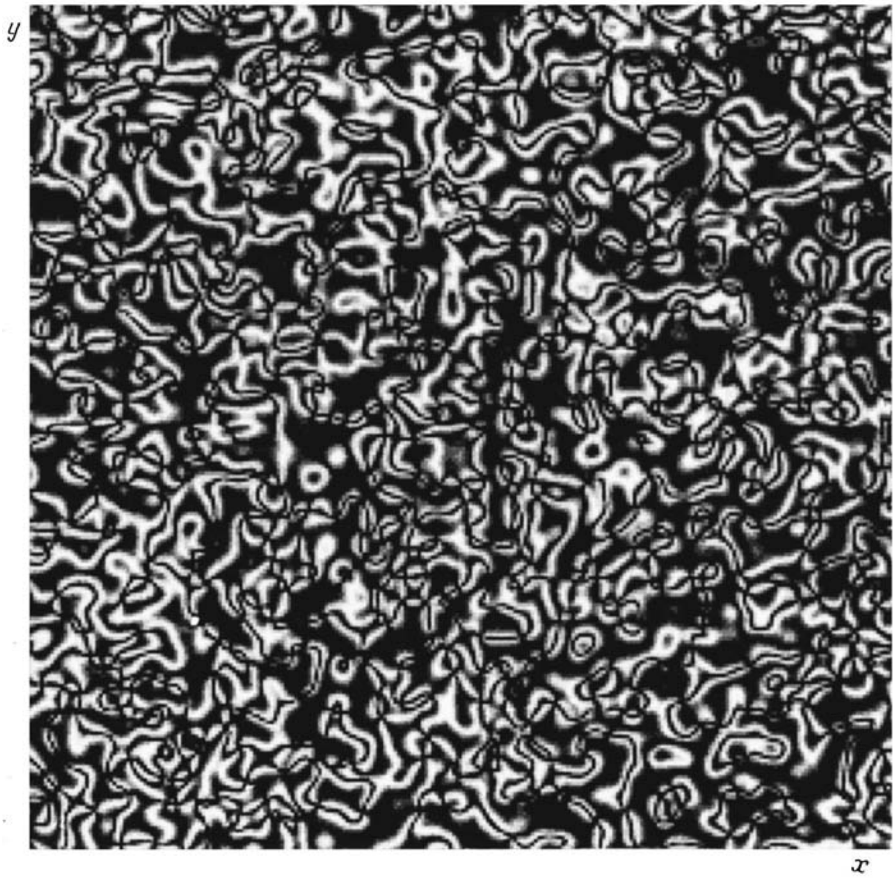

FIG. 5. Relationship between the $M=|\varphi_2\varphi_1|$ and the vortex chains in Fig. 4.

3. CHAIN MEMORIZING IN PHASE SEPARATION

Mathematically, the above problem is a particular case of phase separation. Its subsequent kinetic scenario consists of the growth of large domains and disappearance of small domains.[34,35] This process is accompanied by a merger of the points of intersection of zero curves. Vortices and antivortices ''attract'' and annihilate each other. If the net curl is nonzero, the fluctuation-generated ''antivortices'' are suppressed and there remains a system of vortices of a given density and of the same sign. This, in particular, is the case with a superconductor in an external magnetic field.[38] When there is pinning, the vortices remain localized near the points where they form in the chains.

Actually we are dealing with the mutual overlap of the large-scale properties of fluctuating fields,[37] which generate low-dimensional structures from density folds, and localized topological excitations in multicomponent system of various nature (see Ref. 40 and the literature cited therein). Hence, the kinetic memory of low-dimensional structures, including vortex chains, is a fairly universal feature of systems of this kind. For instance, recently Bogdanov and Hubert[40,41] found that, in addition to one-dimensional order-parameter structures, two-dimensional vortices can form in systems with the Dzyaloshinskiĭ–Morya interaction

$$W_D=\mathbf{J}_j\cdot\frac{\partial\mathbf{J}_k}{\partial\mathbf{r}}-\mathbf{J}_k\cdot\frac{\partial\mathbf{J}_j}{\partial\mathbf{r}}. \qquad (19)$$

However, Bogdanov and Hubert[40,41] assumed that the magnetic vortices form a regular hexagonal lattice. In Ref. 42 it was shown that such a structure does not emerge spontaneously from the paraphase; rather, its formation can be stimulated by a specially organized kinetic scenario. Here the continuum can be described in terms of the equation

$$\frac{\partial\mathbf{m}}{\partial t}=\alpha\Delta\mathbf{m}-\beta\ \mathrm{curl}\ \mathbf{m}+\mathbf{h}-\frac{\delta\Phi[\mathbf{m}]}{\delta\mathbf{m}}+\xi(\mathbf{r},t), \qquad (20)$$

where the three-component vector $\mathbf{m}=\{m_x,m_y,m_z\}$ can assume arbitrary values in the ordering process, and the fixation of the absolute value at $m^2=1$ is guaranteed by the appropriate choice of the local part of the free-energy functional, $\delta\Phi[\mathbf{m}]$. In numerical experiments involving such a system it is indeed possible to obtain fragments of a close-packed hexagonal vortex structure and a correlation function with a sixth-order axis.[42] However, the large-scale structure that is formed by the system usually contains a large number of chains. Figure 6 depicts a fragment of a typical vortex structure that the mechanism described in Ref. 42 is able to produce. Clearly visible are fragments of a compact structure close to the hexagonal one and many vortex chains separated by voids that emerge as a result of ''memorizing'' the kinetic stage in the evolution. Several stages of the memorizing process are depicted in Fig. 7. It is evident that at the fluctuation stage (when the energy regions with opposite values of m_z are close to each other) the regions with positive m_z, which precede cylindrical vortices of the given sign, are captured along the domain boundaries of the space with negative m_z. The energy of the vortex structure that emerges later differs

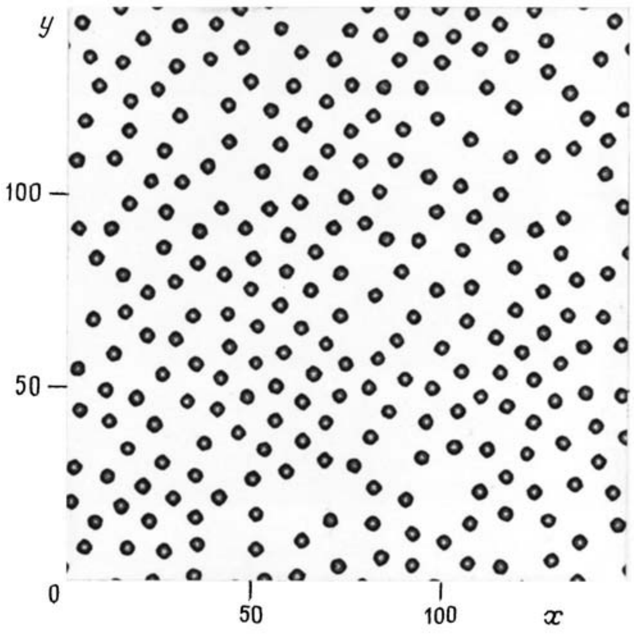

FIG. 6. Fragment of a typical vortex structure obtained by the method described in Ref. 42 on the basis of the equation $\partial \mathbf{m}/\partial t = \alpha \Delta \mathbf{m} - \beta \operatorname{curl} \mathbf{m} + \mathbf{h} - \delta\Phi[\mathbf{m}]/\delta\mathbf{m} + \xi(\mathbf{r},t)$.

little from the energy of the regular lattice, while adding new topological excitations requires surmounting a high barrier.

This scenario of chain freezing coincides with the mechanism of virtual-phase formation described in Refs. 43 and 44. At an early stage the system rapidly equalizes the various nonlocal contributions to the energy. Here the time-increasing correlation radius, $\zeta(t)\rightarrow\infty$, successively reaches the scales at which each interaction drops off, and this determines the spatial structures. In the given case these scales are the domain surface energy $\Xi = \alpha(\nabla\cdot\mathbf{m})^2/2$ and the long-range Dzyaloshinskiĭ–Morya energy $W_D = \beta \mathbf{m}\cdot\operatorname{curl}\mathbf{m}$. The subsequent process is logarithmically slow and is terminated by any manifestation of nonideal behavior (in numerical calculations the boundary conditions are sufficient).

The competition of interactions with different radii may be enough to generate an effectively multicomponent structure (as, for instance, in a system of competing ferro- and antiferromagnetic interactions[45]), so that chains of one type of domains at the boundaries of domains of another type can be observed for any number of fluctuating fields, even for a single scalar field. For the scalar density $\phi(\mathbf{r})$ the essence of the process manifests itself in a purer form. As an example, Figs. 8a and b depict two stages of memorizing such structures in a scalar magnetic field, with the nonlocal part

$$\begin{aligned}\delta\mathscr{F}[\phi(\mathbf{r})] &= \int d\mathbf{r} \int d\mathbf{r}' \, \frac{\phi(\mathbf{r})\Lambda(\mathbf{r}'-\mathbf{r}'')\phi(\mathbf{r}')}{2} \\ &= \int d\mathbf{r} \int d\mathbf{r}' \, \frac{\phi(\mathbf{r})\Lambda_a(\mathbf{r}'-\mathbf{r}'')\phi(\mathbf{r}')}{2} \\ &\quad + \int d\mathbf{r} \, \frac{(\nabla\phi(\mathbf{r}))^2}{2} \end{aligned} \tag{21}$$

of the free-energy functional

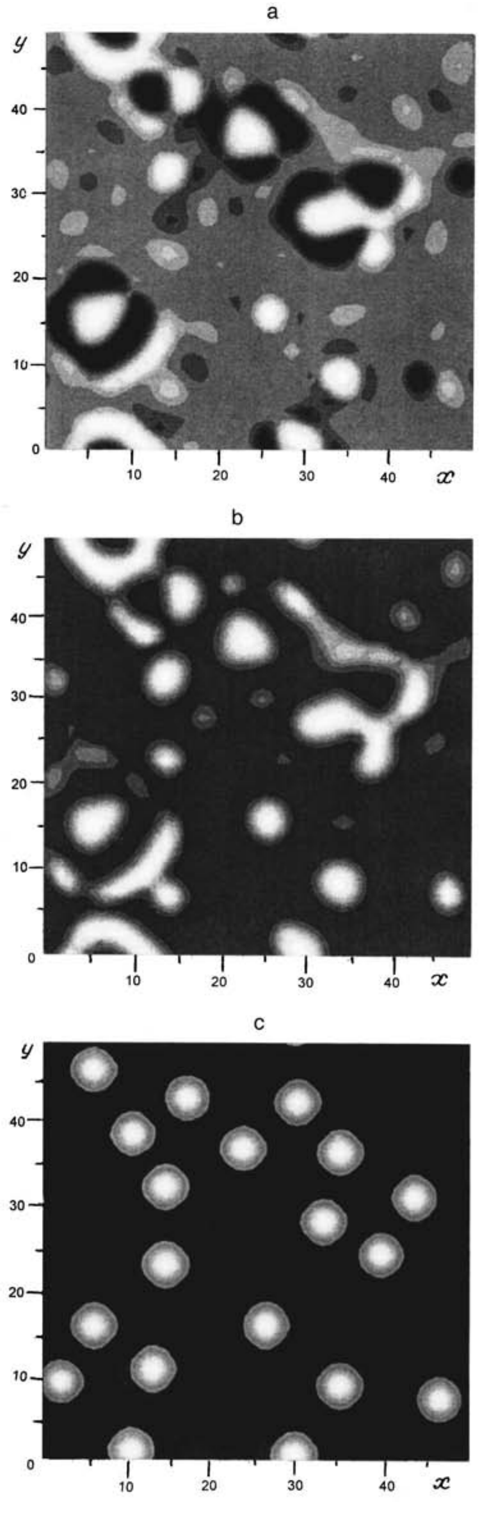

FIG. 7. Generation of a vortex chain in the structure depicted in Fig. 6.

$$\mathscr{F}[\phi(\mathbf{r})] = \int d\,\mathbf{r}\left[\int d\mathbf{r}' \, \frac{\phi(\mathbf{r})\Lambda(\mathbf{r}'-\mathbf{r}'')\phi(\mathbf{r}')}{2} + \frac{\tau\phi^2(\mathbf{r})}{2} + \frac{b\phi^4(\mathbf{r})}{4}\right] \tag{22}$$

containing ferromagnetic,

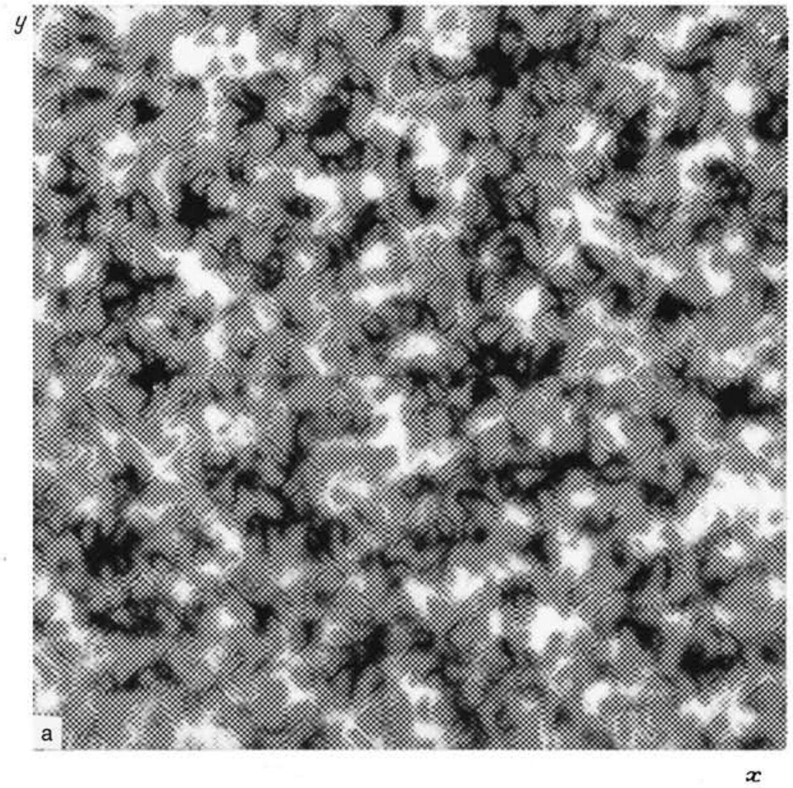

FIG. 8. (a) First stage in memorizing a virtual phase in a scalar system. (b) Second stage in memorizing a virtual phase in a scalar system.

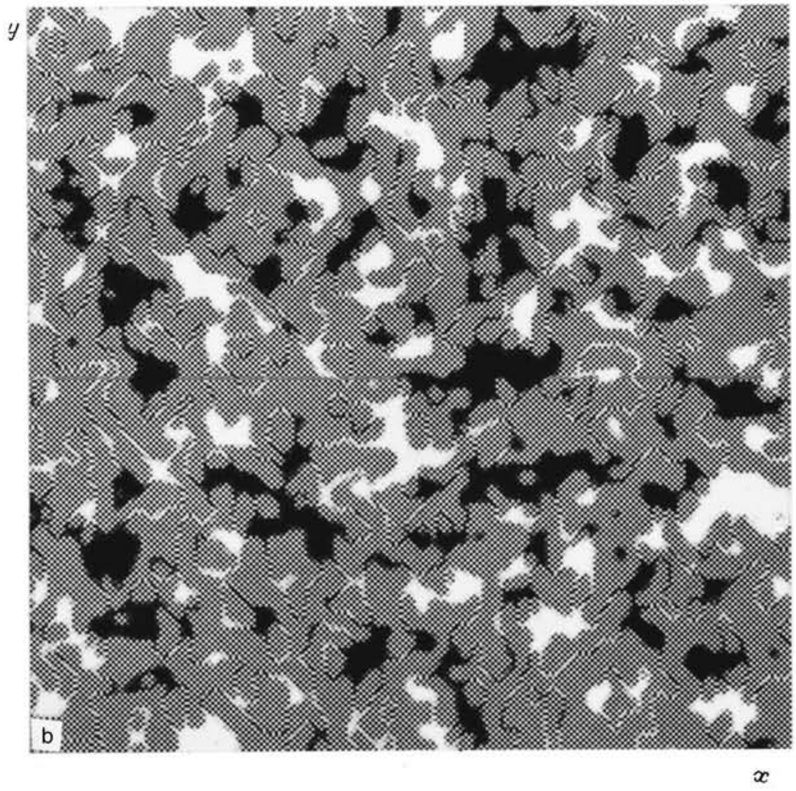

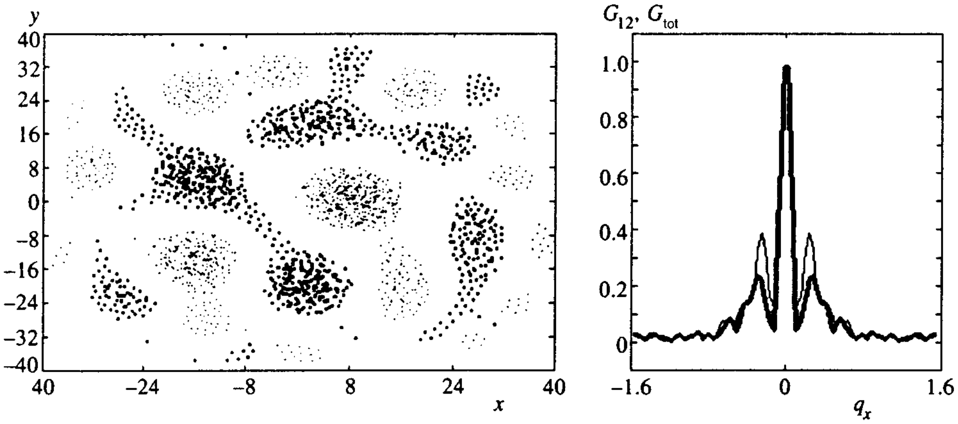

FIG. 9. Intermediate stage of phase separation in molecular dynamics. Particles belonging to different species are depicted by dots of different sizes.

$$\delta\mathscr{F}_{\rm ferro}[\phi(\mathbf{r})]=\int d\mathbf{r}\,\frac{(\nabla\phi(\mathbf{r}))^2}{2},$$

and antiferromagnetic,

$$\delta\mathscr{F}_{\rm anti}[\phi(\mathbf{r})]=\int d\mathbf{r}\int d\mathbf{r}'\,\frac{\phi(\mathbf{r})\Lambda_a(\mathbf{r}'-\mathbf{r}'')\phi(\mathbf{r}')}{2},$$

contributions ($\delta\mathscr{F}_{\rm ferro}[\phi(\mathbf{r})]\geqslant\delta\mathscr{F}_{\rm anti}[\phi(\mathbf{r})]$). As $\zeta(t)\rightarrow\infty$, antiferromagnetic domains appear earlier in the kinetics and localize the more advantageous homogeneous domains at the boundaries. When $\delta\mathscr{F}_{\rm ferro}[\phi(\mathbf{r})]\simeq\delta\mathscr{F}_{\rm anti}[\phi(\mathbf{r})]$ (the case depicted in Figs. 8a and b), this virtual phase[43,44] becomes stable.

Similar processes have been observed in molecular dynamics in the presence of phase separation.[1–3] This approach is even more suitable when the average densities are conserved, since it does not require special measures to ensure flux balancing. The main goal of these researchers was to reproduce the scaling (known from analytical approaches) of the growth of the average radius ($\langle R(t)\rangle\rightarrow\infty$ as $t\rightarrow\infty$) of the domains during phase separation. At the same time, the method made it possible to detect more subtle effects.

Here we will mention only one such effect that is of interest in the context of the present study, i.e., the ordering of subsystems in each others' self-consistent field, accompanied by formation of a crystal lattice. Figure 9 depicts the intermediate stage in phase separation (for more details see Refs. 1–3). Clearly visible are the ''whiskers'' that connect domains of one type near the boundaries of the domains of the other subsystem. Also clearly visible inside such domains are lattice fragments that have already formed. The inset to Fig. 9 depicts the Fourier transforms of the total correlation function calculated over all particles, $G_{\rm tot}(\mathbf{q})=\int d\mathbf{r}d\mathbf{r}'\times\exp(i\mathbf{r}\cdot\mathbf{q})\langle\rho(\mathbf{r})\rho(\mathbf{r}+\mathbf{r}')\rangle$, and of the correlation function of one of the subsystems, $G_1(\mathbf{q})$ (the light and heavy curves, respectively). In addition to the maxima at small $\mathbf{q}=\mathbf{q}_{0j}\neq 0$, which are the same for both functions and correspond to large-scale domains in real space, the curve representing $G_1(\mathbf{q})$ also exhibits peaks at large $\mathbf{q}=\mathbf{q}_{1j}\neq 0$, which correspond to the fine structure forming inside the domains. With a short-range interaction, the two subsystems can be interpreted as boundary conditions imposed on each other. Strictly speaking, however, the crystallization of each subsystem takes place in the mean field of the other subsystem, as it does in the ordering of the (anti)vortex system described above.

One promising application of direct modeling of phase separation in dynamical systems is the effect of giant magnetoresistance in lanthanum manganites and other magnetic conductors, an effect that is being actively discussed by the scientific community. Experimental data[46] suggest that the state of these materials with an unsaturated spontaneous magnetic moment is of the two-phase ferro–antiferromagnetic type, and the possible phase-separation mechanism is of the electron type. The more advantageous ferromagnetic state is realized only when the carrier concentration becomes high. If the concentration is insufficient, all carriers may coalesce into localized ''ferromagnetic drops.'' A magnetic field facilitates the transition of the entire crystal into a ferromagnetic state, so that percolation of regions with such ordering becomes possible. Nagaev[46] believes that giant magnetoresistance is responsible for this process.

In 1996 Krivoruchko[47] discussed a phenomenological model of a magnetic non-single-phase state and found, among other things, that a macroscopic description can be used if the fraction of the ferromagnetic phase in the antiferromagnetic matrix is small. In the general case there is no way in which one can obtain an expression for the conductivity, although the physics of the phenomenon is retained and hence the effect of electron flow in a magnetic field can be reproduced by direct numerical modeling.

[1] E. Velasco and S. Toxyaerd, Phys. Rev. Lett. **71**, 388 (1993).
[2] F. J. Alexander, S. Chen, and D. W. Grunau, Phys. Rev. B **48**, 634 (1993).
[3] G. Leptoukh, B. Strickland, and C. Roland, Phys. Rev. Lett. **74**, 3636 (1995).
[4] S. Bastea and J. L. Lebowitz, Phys. Rev. Lett. **75**, 3776 (1995).
[5] D. Wei and G. N. Patey, Phys. Rev. Lett. **68**, 2043 (1992).
[6] J. J. Weis and D. Levesque, Phys. Rev. Lett. **71**, 2729 (1993).
[7] J. Ayton, M. I. P. Gingras, and G. N. Patey, Phys. Rev. Lett. **75**, 2360 (1995).
[8] I. M. Svishchev and P. G. Kusalik, Phys. Rev. Lett. **73**, 975 (1994).
[9] I. M. Svishchev and P. G. Kusalik, Phys. Rev. Lett. **75**, 3289 (1995).
[10] N. Kukharkin, S. A. Orszag, Y. Yakhot, Phys. Rev. Lett. **75**, 2486 (1995).
[11] L. M. Smith and V. Yakhot, Phys. Rev. Lett. **71**, 352 (1993).
[12] K. S. Fine, A. C. Cass, W. G. Flynn, and C. F. Driscoll, Phys. Rev. Lett. **75**, 3277 (1995).
[13] V. L. Berezinskiĭ, Zh. Éksp. Teor. Fiz. **59**, 907 (1970) [Sov. Phys. JETP

32, 493 (1971)]; Zh. Éksp. Teor. Fiz. **61**, 1144 (1971) [Sov. Phys. JETP **34**, 610 (1972)].

[14] J. M. Kosterlitz and D. J. Thouless, J. Phys. C **6**, 1181 (1973).

[15] J. M. Kosterlitz, J. Phys. C **7**, 1046 (1974).

[16] P. Minnhagen, Rev. Mod. Phys. **59**, 1001 (1987).

[17] N. D. Mermin and H. Wagner, Phys. Rev. Lett. **17**, 1133 (1966).

[18] P. C. Hohenberg, **158**, 383 (1967).

[19] V. Ambegaokar, B. I. Halperin, D. R. Nelson, and E. D. Siggia, Phys. Rev. B **19**, 1806 (1980).

[20] S. A. Trugman and S. Doniach, Phys. Rev. B **26**, 3682 (1982).

[21] B. Groh and S. Dietrich, Phys. Rev. Lett. **72**, 2422 (1994).

[22] D. Schechtman *et al.*, Phys. Rev. Lett. **53**, 1951 (1984).

[23] P. A. Kalugin, A. Yu. Kitaev, and L. S. Levitov, JETP Lett. **41**, 145 (1985).

[24] D. V. Olenev and Yu. Kh. Vekilov, JETP Lett. **64**, 612 (1996).

[25] V. E. Fortov, A. P. Nefedov, V. M. Torchinskiĭ, V. N. Molotkov, A. G. Khrapak, O. F. Petrov, and K. F. Volykhin, JETP Lett. **64**, 92 (1996).

[26] A. M. Grishin, A. Yu. Martynovich, and S. V. Yampol'skiĭ, Zh. Éksp. Teor. Fiz. **101**, 649 (1992) [Sov. Phys. JETP **74**, 345 (1992)].

[27] L. A. Gurevich *et al.*, Physica C **195**, 323 (1992).

[28] I. V. Grigorieva, L. A. Gurevich, and L. A. Vannikov, Physica C **195**, 327 (1992).

[29] Ü. Parts, E. V. Thuneberg, G. E. Volovik, J. H. Koivuniemi, V. M. H. Ruutu, M. Heinilä, J. M. Karimäki, and M. Krusius, Phys. Rev. Lett. **72**, 3839 (1994).

[30] M. Heinila and G. E. Volovik, Physica B **210**, 300 (1995).

[31] T. Sh. Misirpashaev and G. E. Volovik, Physica B **210**, 338 (1995).

[32] A. E. Filippov, A. V. Radievsky, and A. S. Zeltser, Phys. Rev. B **54**, 3504 (1996).

[33] L. D. Landau and E. M. Lifshitz, *Statistical Physics*, Pergamon Press, Oxford (1989).

[34] T. M. Rogers, K. R. Elder, and R. C. Desai, Phys. Rev. B **37**, 9638 (1988).

[35] K. R. Elder and R. C. Desai, Phys. Rev. B **40**, 243 (1989).

[36] A. S. Zel'tser and A. É. Filippov, Zh. Éksp. Teor. Fiz. **106**, 1117 (1994) [JETP **79**, 605 (1994)].

[37] A. S. Zel'tser and A. É. Filippov, JETP Lett. **62**, 627 (1995).

[38] A. E. Filippov, A. V. Radievsky, and A. S. Zeltser, Phys. Lett. A **192**, 131 (1994).

[39] N. Shvartsman and I. Freud, Phys. Rev. Lett. **72**, 1008 (1994).

[40] A. Bogdanov, JETP Lett. **62**, 247 (1995).

[41] A. N. Bogdanov and A. Hubert, J. Magn. Magn. Mater. **138**, 255 (1996).

[42] A. É. Filippov, Zh. Éksp. Teor. Fiz. **111**, 1775 (1997) [JETP **84**, 971 (1997)].

[43] S. Semenovskaya and A. G. Khachaturyan, Phys. Rev. Lett. **67**, 2223 (1991).

[44] Long-Qing Chen and A. G. Khachaturyan, Phys. Rev. B **46**, 5889 (1992).

[45] Yu. M. Ivanchenko, A. A. Lisyanskiĭ, and A. É. Filippov, Zh. Éksp. Teor. Fiz. **87**, 1019 (1984) [Sov. Phys. JETP **60**, 582 (1984)].

[46] É. L. Nagaev, Usp. Fiz. Nauk **166**, 833 (1996) [Phys. Usp. **39**, 781 (1996].

[47] V. N. Krivoruchko, Fiz. Nizk. Temp. **22**, 1047 (1996) [Low Temp. Phys. **22**, 798 (1996)].

Translated by Eugene Yankovsky

Scattering of electrons by a potential step in a magnetic field

V. M. Zhilin and S. V. Iordanskiĭ

Institute of Solid State Physics, Russian National Academy of Sciences, 142432 Chernogolovka, Moscow Region, Russia

(Submitted 24 April 1997)
Zh. Éksp. Teor. Fiz. **112**, 1756–1762 (November 1997)

The scattering of two-dimensional electrons drifting in crossed electric and magnetic fields by an abrupt step in the external potential is discussed. The problem is reduced to solving a system of ordinary differential equations. It is shown that for moderate electric fields scattering with a change of Landau level numbers becomes appreciable. © *1997 American Institute of Physics.* [S1063-7761(97)01611-9]

1. INTRODUCTION

Two-dimensional electrons in a strong magnetic field have been the subject of a multitude of theoretical and experimental studies. Due to the discreteness of the spectrum and macroscopic degeneracy of the Landau levels, the actual physical properties of these systems are determined by the mechanism that lifts the degeneracy, because otherwise the electron velocity vanishes and charge transport is impossible. In particular, the quantum Hall effect is closely related to the existence of a random potential caused by impurities.

For the same reason, the problem of electron scattering also cannot be formulated for free electrons, because the velocity of the electrons again equals zero. However, in the presence of an external potential a drift velocity of the electrons appears in crossed electric and magnetic fields, and a scattering problem can be formulated. The most studied problem is one in which electrons are scattered by a saddle point potential (near the intersection of two potential contours), which can be solved exactly in the quadratic approximation.[1]

In this paper we investigate scattering of electrons by an abrupt step in the external potential of the form

$$U=-U_0\theta(y),\quad \theta(y)=\begin{cases}1, & y>0,\\ 0, & y<0,\end{cases}\tag{1}$$

which is an idealization of the edge of an abrupt nonuniformity with dimensions that greatly exceed the magnetic length $l_H^2=c\hbar/eH$, where H is the external magnetic field directed along the normal to the two-dimensional xy plane.

Such a nonuniformity can be created artificially by applying control electrodes, or it can arise for internal reasons that cause an abrupt varying distribution of localized electrons, as is postulated in a number of explanations for the destruction of the dissipationless state in the quantum Hall effect.[2,3] Far from the step we will assume that a uniform electric field exists along the x direction, which leads to a finite velocity $v_y>0$ for electron drift in the direction towards the step. This field can either be an idealization of a smooth random potential or may be created intentionally. Then the problem that arises is one where an electron in a magnetic field is scattered by the potential

$$U=-\epsilon x-U_0\theta(y),\tag{2}$$

where $\epsilon<0$ is the electric field.

Note that all the electrons, both incident and scattered, move in the same direction ($v_y>0$), which is provided by the corresponding direction of the magnetic field. The scattering results in a change of the Landau level number and a shift of the position of the wave along the x axis subject to the law of conservation of energy (elastic scattering), as shown schematically in Fig. 1. This type of scattering can be of interest as a way to create nonequilibrium populations of Landau levels and generate monochromatic cyclotron radiation.

In what follows we will use a system of units where $l_H=1$, $\hbar\omega_c=e\hbar H/mc=1$.

2. REDUCTION OF THE PROBLEM TO A SYSTEM OF ORDINARY DIFFERENTIAL EQUATIONS

The Schrödinger equation for this problem takes the form

$$\left\{\frac{1}{2}\left(i\frac{\partial}{\partial x}\right)^2+\frac{1}{2}\left(i\frac{\partial}{\partial y}+x\right)^2+[-\epsilon x-U_0\theta(y)]\right\}\psi=E\psi,\tag{3}$$

where ψ is the wave function of an electron and the Landau gauge is chosen. The energy of the electron E is determined by the incident wave as $y\to-\infty$, where

$$\psi\approx A_s e^{ik_s y}\Phi_s(x-k_s-\epsilon),$$
$$E=s+\frac{1}{2}-k_s\epsilon-\frac{\epsilon^2}{2},\tag{4}$$

s labels the Landau level, and $\Phi_s(x)$ are normalized oscillator functions. Here we have used the solution to Eq. (3) for $U_0=0$; the quantities k_s, A_s are given by the incident wave.

Without loss of generality we can set $k_s=0$, $A_s=1$. The case $k_s\neq 0$ is reduced to the case $k_s=0$ by a corresponding shift along the x axis. We limit ourselves to the case $s=0$, where the incident wave is in the lowest Landau level, although the problem can be solved without any particular changes for any s.

Equation (3) does not allow separation of variables. In order to solve it we Fourier-transform Eq. (3) with respect to the variable y:

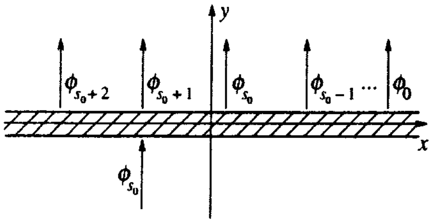

FIG. 1. Schematic illustration of the scattering process. The arrows show the positions of waves with different Landau numbers, accurate to within a magnetic length. The direction of the arrows corresponds to the direction of motion at the waves. The scattering zone is cross hatched.

$$\left(i\frac{\partial}{\partial x}\right)^2\psi_k+(x-k)^2\psi_k-2\epsilon x\psi_k-2E\psi_k=2U_0\psi_k^-, \tag{5}$$

where $\psi_k=\psi_k^+ + \psi_k^-$ and

$$\psi_k^-=\int_0^\infty e^{-iky}\psi(x,y)dy,\quad \psi_k^+=\int_{-\infty}^0 e^{-iky}\psi(x,y)dy.$$

According to the well-known properties of the Fourier transform, the function ψ_k^- is an analytic function in the lower half of the complex k plane, and can be written as the integral

$$\psi_k^-=-\frac{1}{2\pi i}\int\frac{1}{k'-k+i\delta}\psi_{k'}dk', \tag{6}$$

where the integral runs along the real axis, and $\delta\to+0$. The left side of Eq. (5) can be transformed using the Green's function for the oscillator equation:

$$G_k(x,x')=\sum_s\frac{1}{E_s(k)-E}\Phi_s(x-k-\epsilon)\Phi_s(x'-k-\epsilon), \tag{7}$$

where

$$\Phi_s(x)=e^{-x^2/2}H_s(x)\frac{1}{\sqrt{\sqrt{\pi}2^s s!}}, \tag{8}$$

and H_s is a Hermite polynomial:

$$H_s(x)=e^{x^2}\left(-\frac{d}{dx}\right)^s e^{-x^2}. \tag{9}$$

The energy E contains a positive and small imaginary part in accordance with the Sommerfeld conditions.

As a result we obtain an integral equation for the function $\psi_k(x)$:

$$\psi_k(x)=-\frac{U_0}{2\pi i}\int G_k(x,x')\frac{1}{k'-k+i\delta}\psi_{k'}(x')dx'dk'+\psi_0, \tag{10}$$

where ψ_0 describes the incident wave. If we use the expansion

$$\psi_k(x)=\sum_s c_s(k)\Phi_s(x-k-\epsilon),$$

which follows from the completeness of the system of functions Φ_s, then Eq. (10) is converted to a system of equations for the coefficients $c_s(k)$:

$$[E_s(k)-E]c_s(k)=-\frac{U_0}{2\pi i}\int\frac{\Gamma_{ss'}(k-k')}{k'-k+i\delta}c_{s'}(k')dk', \tag{11}$$

where

$$\Gamma_{ss'}(k)=\int\Phi_s(x-k)\Phi_{s'}(x)dx. \tag{12}$$

Because according to Eq. (4) $E_s(k)$ is a linear function of k, these equations can be converted to a system of differential equations for the quantities

$$\phi_s(y)=\int c_s(k)e^{iky}\frac{dk}{2\pi}, \tag{13}$$

which have the form

$$\left(i\epsilon\frac{\partial}{\partial y}+s+\frac{1}{2}-E\right)\phi_s(y)=\sum_{s'}V_{ss'}(y)\phi_{s'}(y). \tag{14}$$

The coefficients $V_{ss'}$ are determined by the functions $\Gamma_{ss'}(k)$:

$$V_{ss'}(y)=U_0\int_{-\infty}^y dy\int\Gamma_{ss'}(k)e^{iky}\frac{dk}{2\pi}. \tag{15}$$

In what follows we will assume that $U_0>0$. The incident wave should correspond to a current of electrons from $y\to-\infty$ up to the step at $y=0$. The magnitude of this current

$$j_y=\int e^{-iky}\left(-i\frac{\partial}{\partial y}-x\right)e^{iky}\Phi_s^2(x-k-\epsilon)dx=-\epsilon>0$$

requires that $\epsilon<0$. This result can be obtained from the Sommerfeld condition as well.

The behavior of $\phi_s(y)$ as $y\to-\infty$ is determined by prescribing the incident wave in the form $\phi_s=\exp(ik_sy)\delta_{s,s_0}$, while the asymptotic behavior as $y\to+\infty$ gives the amplitude of the scattered wave:

$$\phi_s|_{y\to+\infty}=A_{ss_0}e^{ik_sy},$$

where A_{s,s_0} is the scattering amplitude for a transition $s\to s_0$. As for the oscillator functions, they enter as factors into the asymptotic behavior of the total wave function

$$\psi(x,y\to+\infty)=\sum_s A_{ss_0}e^{ik_sy}\Phi_s(x-k_s-\epsilon),$$

and also, according to Eqs. (12)–(15) determine the coefficients $V_{ss'}(y)$.

The integral (15) can be expressed in terms of Hermite polynomials, because

$$\int e^{iky}\Phi_s(x-k)\Phi_{s'}(x)dx\,dk=\frac{1}{2\pi}\tilde{\Phi}_s^*(y)\tilde{\Phi}_{s'}(y),$$

where $\tilde{\Phi}_s^*(y)=\sqrt{2\pi}i^{-s}\Phi_s(y)$ and $\tilde{\Phi}_{s'}(y)=\sqrt{2\pi}i^{s'}\Phi_s(y)$. Thus, we obtain according to Eq. (15)

$$V_{ss'}(y)=U_0 i^{s'-s}\int_{-\infty}^y\Phi_s(y)\Phi_{s'}(y)dy. \tag{16}$$

This expression for $s=s'$ has the form

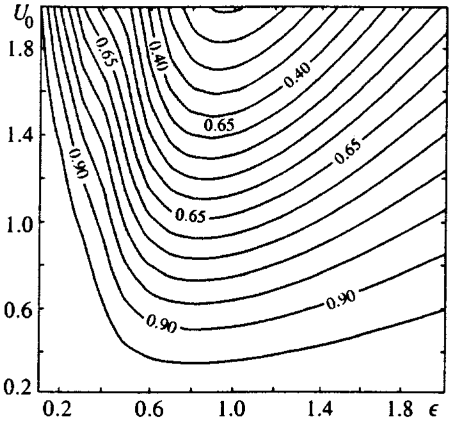

FIG. 2. Level lines for the probability $|\phi_0|^2$ of a transition without change in the Landau level for $s_0=0$ in the (ϵ,U_0) plane.

$$V_{ss'}=U_0\left[\sum_{l=0}^{l=s-1}\frac{e^{-y^2}}{2^s s!\sqrt{\pi}}H_{s-l}(y)\left(\frac{d}{dy}\right)^l H_s(y)\right.$$

$$\left.+\frac{1}{\sqrt{\pi}}\int_{-\infty}^{y}e^{-y^2}dy\right], \tag{17}$$

while for $s>s'$

$$V_{ss'}=U_0\,\frac{i^{s'-s}}{\sqrt{2^s s!2^{s'}s'!\pi}}\sum_{l=0}^{l=s'}e^{-y^2}H_{s-l-1}(y)$$

$$\times\left(\frac{d}{dy}\right)^l H_{s'}(y). \tag{18}$$

For $s<s'$,

$$V_{ss'}=V^{*}_{s's}. \tag{19}$$

Equations (14) combined with Eqs. (17)–(19) give an infinite system of ordinary differential equations for the functions $\phi_s(y)$ in accordance with the specified asymptotic behavior as $y\rightarrow-\infty$. By finding these functions we solve the scattering problem.

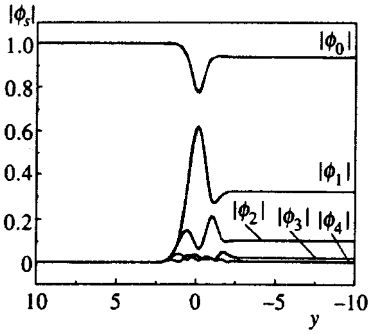

FIG. 3. Amplitude for a transition $|\phi_s(y)|$ for five values $s=$ 1, 2, 3, 4, 5 as a function of y when $U_0=1$ and $\epsilon=0.4$.

3. DETERMINING THE SCATTERING AMPLITUDE

Equations (14) contain the electric field ϵ as a coefficient in front of the derivatives. Therefore, in the case of small electric fields and finite U_0 the quasiclassical approximation can be used. We can show that the matrix of coefficients does not have multiple roots. Therefore, in this case there is only the diagonal scattering $s_0\rightarrow s_0$ to exponential accuracy with respect to $1/\epsilon$, and the probability of other processes is small, which corresponds to above-barrier reflection or the adiabatic approximation. Electrons sense this step at large distances from it and are slowly turned in the direction of the step, gradually intersecting it. In the opposite limiting case $U_0\ll\epsilon$, the step may be treated as a perturbation, and the principal term in the scattering amplitude corresponds to the diagonal process $s_0\rightarrow s_0$. Between these two limiting cases there is a maximum for nondiagonal scattering. The corresponding scattering amplitude can be determined numerically by finding the solution $\phi_s(y)$ to the system (14). It is found that the amplitudes A_{ss_0} fall off rapidly as s deviates from s_0, which allows us to replace the infinite system of equations by a finite system with high accuracy.

The system of differential equations was solved numerically by the Runge–Kutta and Berlitz–Steuner methods. Subprograms from the ''Numerical Recipes'' package were used. The maximum number of waves was chosen to equal five, which is enough to ensure sufficient accuracy. A length

TABLE I. Probability for scattering of various waves for $U_0=1$.

U_0	ϵ	$\lvert\phi_0\rvert^2$	$\lvert\phi_1\rvert^2$	$\lvert\phi_2\rvert^2$	$\lvert\phi_3\rvert^2$	$\lvert\phi_4\rvert^2$
1.0000	0.1000	0.9997	0.0003	0.0000	0.0000	0.0000
1.0000	0.2000	0.9844	0.0154	0.0002	0.0000	0.0000
1.0000	0.3000	0.9397	0.0572	0.0030	0.0001	0.0000
1.0000	0.4000	0.8823	0.1039	0.0127	0.0010	0.0001
1.0000	0.5000	0.7922	0.1790	0.0241	0.0044	0.0004
1.0000	0.6000	0.7199	0.2297	0.0406	0.0083	0.0015
1.0000	0.7000	0.6789	0.2360	0.0696	0.0124	0.0031
1.0000	0.8000	0.6621	0.2163	0.0943	0.0230	0.0043
1.0000	0.9000	0.6617	0.1892	0.1036	0.0400	0.0056
1.0000	1.0000	0.6718	0.1637	0.0997	0.0550	0.0097

of 10 for the y interval on which the system of equations was solved ensured a good approximation. The scattering amplitude was calculated for an incident wave with $s_0=0$ as a function of electric field ϵ and height of the step U_0. Figure 2 shows contours for the probability of diagonal scattering in the (ϵ, U_0) plane. Figure 3 shows the magnitude of $\phi_s(y)$ for various s when $U_0=1$, $\epsilon=0.4$. The good convergence with respect to s is evident. In these tables we show the probability of scattering for various waves when $U_0=1$ and for different ϵ. We see that the diagonal amplitude A_{00} and the amplitude A_{01} have the largest values; the others are much smaller. The transition probability $|A_{01}|$ for a moderate field $\epsilon=0.4$ and $U_0=1$ is quite appreciable, and comes to around 0.1 of the probability for the diagonal transition. This implies a fairly high efficiency for obtaining population inversion after scattering. Possibly this mechanism can explain the appearance of cylotron radiation when the dissipationless regime of the quantum Hall effect is disrupted.[4]

The authors are grateful to S. V. Manakov for discussing the mathematical questions connected with this problem. The work was supported by the Russian Fund for Fundamental Research (Grant 95-02-883) and INTAS (Grant No. 95-I/Ru-675).

[1] H. A. Fertig and B. I. Halperin, Phys. Rev. B **33**, 8447 (1986).
[2] M. Djakonov and F. Pikus, Solid State Commun. **83**, 413 (1992).
[3] S. V. Iordanskiĭ, JETP Lett. **58**, 316 (1993).
[4] *The Quantum Hall Effect*, R. E. Prange and S. M. Girvin eds. (Springer-Verlag, New York, 1987) [Russ. transl. Mir, Moscow, 1989].

Translated by Frank J. Crowne

Theory of the electronic structure and spin susceptibility of $La_{2-x}Sr_xCuO_4$

M. V. Eremin,*) S. G. Solov'yanov, and S. V. Varlamov

Kazan State University, 420008 Kazan, Russia

(Submitted 19 February 1997)
Zh. Éksp. Teor. Fiz. **112**, 1763–1777 (November 1997)

We solve the problem of the effect of strong electron correlations on the homogeneous spin susceptibility of current carriers in CuO_2 planes. We show that the dependence of the spin susceptibility $\chi(T)$ of high-T_c superconductors of the $La_{2-x}Sr_xCuO_4$ type on temperature and the doping index x can be explained fairly well by the two-band model suggested earlier (the singlet-correlated oxygen band plus the lower Hubbard band of copper). The model has features in common with the phenomenological $t-J$ model but cannot be reduced to the latter completely. In contrast to the $t-J$ model, the density of states of the oxygen holes has a peak near the bottom of the band. It is the presence of this peak together with the non-Fermi-liquid properties that explain the unusual behavior of the spin susceptibility of $La_{2-x}Sr_xCuO_4$. © *1997 American Institute of Physics.* [S1063-7761(97)01711-3]

1. INTRODUCTION

The temperature dependence of the spin susceptibility of $La_{2-x}Sr_xCuO_4$ has been analyzed by a number of researchers (see, e.g., Refs. 1–7). The interest in this dependence is great because it carries information about the specific features of the spectrum of elementary excitations in the superconducting CuO_2 planes. Immediately after the first studies it became evident that the strong dependence of the spin susceptibility of $La_{2-x}Sr_xCuO_4$ on temperature and composition can be explained by the ordinary Fermi-liquid theory, provided that the following assumption is true: the energy spectrum of elementary excitations of the CuO_2 plane has a peak in the density of states of an unknown origin, with the chemical potential being, for some reason, independent of temperature.[8] Generally speaking, geometry considerations for two-dimensional systems lead quite naturally to the following dispersion law for the quasiparticles: $\varepsilon_k = 2t[\cos(k_x a)+\cos(k_y a)]$, which has a peak in the density of states (the Van Hove peak) at the center of the energy band. Some researchers[9–11] who adopted this hypothesis calculated the magnetic susceptibility and found that it explains many magnetic properties of the normal phase of cuprates. However, this scenario (the Van Hove scenario; a detailed review can be found in Ref. 12) meets with serious problems in the ordinary Fermi-liquid theory: (1) for a half-filled band the number of current carriers per copper site must be of order unity ($x\approx 1$), which completely disagrees with the chemical composition of $La_{2-x}Sr_xCuO_4$; (2) it is not known why the chemical potential close to the extremely sharp peak in the density of states is independent or almost independent of temperature, although by rights this dependence should be exponential; (3) the scenario is unable to describe a metal–insulator transition at low doping levels; and other problems.

According to photoemission data,[13,14] the Fermi level in $La_{2-x}Sr_xCuO_{4+\delta}$ with $0<x<0.3$ is at the bottom of the band rather than at its center. In this connection, to explain the behavior of spin susceptibility, Ruvalds *et al.*[15,16] phenomenologically introduced a peak in the density of states precisely near the bottom of the hole band of CuO_2. To get rid of the strong temperature dependence of the chemical potential, the existence of another broad band near the Fermi level, in addition to the CuO_2 band, is allowed. The assumption that such an additional band can exist seems to be quite natural, since the CuO_2 plane is not the only fragment of the unit cell of $La_{2-x}Sr_xCuO_4$. Levin and Quader[17,18] used a similar phenomenological model of a step in the density of states near the Fermi level to explain the scaling of the temperature dependence of the magnetic susceptibility, the specific heat, the Hall coefficient, and other characteristics of double-layer cuprates.

The goal of the present research is to show that many problems of the above Fermi-liquid description of the magnetic susceptibility in the normal phase of $La_{2-x}Sr_xCuO_4$ are solved if we allow for strong electron correlations. In a brief communication (Ref. 19) we remarked that the peak in the density of states near the bottom of the conduction band of CuO_2 can appear quite naturally as a result of hybridization of singlet-correlated oxygen holes and copper states. As noted in Ref. 19, this hybridization peak will be the first to be populated by holes in $La_{2-x}Sr_xCuO_4$. The numerical calculations in Ref. 19 were done with the four-band approximation (the lower Hubbard copper band, two oxygen bands, and the copper–oxygen singlet band). Since the occurrence of a hybridization peak is due primarily to the mixing of only the two lowest bands, in this paper we develop and augment the more simple (but still equivalent to that used in Ref. 19) two-band model proposed in Ref. 20 and independently in Ref. 21. As in Ref. 20, we describe the singlet state by a linear combination of Zhang–Rice singlets, neutral oxygen, and Cu^{3+} $(S=0)$ states. To make the calculation model as close to reality as possible, we allow for hole hopping from copper to oxygen and in the oxygen sublattices. In Ref. 21, the Cu^{3+} $(S=0)$ states and the holes hopping between positions in the oxygen sublattice were not taken into account. In contrast to Ref. 20, however, we employ a variant of the method used in decoupling the equations that is better than the Hubbard-I variant, as was done in Ref. 21 (see a similar method of decoupling equations in the Hubbard model in Refs. 22 and 23).

1063-7761/97/110963-08$10.00

We relate the results of our calculations to the data on real $La_{2-x}Sr_xCuO_4$ by comparing calculated and measured homogeneous spin susceptibilities for different temperatures and doping indices x. As in Ref. 24, we calculate the effect of strong electron correlations (non-Fermi-liquid effects) on the spin susceptibility in the rapid spin fluctuation mode, i.e., when the average value of the spin projection on a copper site, $\langle S_z \rangle$, is much smaller than 1/2.

2. THE MODEL HAMILTONIAN

To describe the electronic structure of the CuO_2 plane we use the hole representation. In La_2CuO_4 there is one hole to each copper ion. In $La_{2-x}Sr_xCuO_4$ there are additional holes in the oxygen positions. We select the hole state within a single unit cell of CuO_2 in the form

$$|\sigma_d\rangle = d_\sigma^\dagger|0\rangle, \quad |dd\rangle = d_\uparrow^\dagger d_\downarrow^\dagger|0\rangle,$$

$$|\sigma_p\rangle = p_\sigma^\dagger|0\rangle, \quad |pp\rangle = p_\uparrow^\dagger p_\downarrow^\dagger|0\rangle,$$

$$|pd\rangle = \frac{1}{\sqrt{2}}(p_\uparrow^\dagger d_\downarrow^\dagger - p_\downarrow^\dagger d_\uparrow^\dagger)|0\rangle, \tag{1}$$

where $|0\rangle$ is the vacuum state, which corresponds to $Cu^+(d^{10})$, and $d_\sigma^\dagger$ and $p_\sigma^\dagger$ are the creation operators for holes in the copper and oxygen positions, respectively. As in Ref. 25, from the atomic σ-orbitals of oxygen holes we construct the Wannier functions

$$|p_{i\sigma}\rangle = \frac{1}{N}\sum_{k,j} \beta_k P_{j\sigma}^s \exp(i\mathbf{k}\cdot\mathbf{R}_{ij}), \tag{2}$$

where $P_{j\sigma}^s$ is an antisymmetric combination of oxygen σ-orbitals.[25] In the Zhang–Rice approximation we have

$$\beta_k = \{1 - 0.5[\cos(k_x a) + \cos(k_y a)]\}^{-1/2}.$$

The Hamiltonian for a separate plane has the form

$$H = \sum_i H_{0i} + H_1, \tag{3}$$

where the operator

$$\begin{aligned} H_{0i} &= \varepsilon_d \sum_\sigma d_{i\sigma}^\dagger d_{i\sigma} + \varepsilon_p \sum_\sigma p_{i\sigma}^\dagger p_{i\sigma} \\ &+ \frac{I_{dd}}{2}\sum_\sigma d_{i\sigma}^\dagger d_{i\bar{\sigma}}^\dagger d_{i\bar{\sigma}} d_{i\sigma} + \frac{I_{pp}}{2}\sum_\sigma p_{i\sigma}^\dagger p_{i\bar{\sigma}}^\dagger p_{i\bar{\sigma}} p_{i\sigma} \\ &+ V_{pd}\sum_{\sigma\sigma'} d_{i\sigma}^\dagger d_{i\sigma} p_{i\sigma'}^\dagger p_{i\sigma'} + t_0 \sum_\sigma (d_{i\sigma}^\dagger p_{i\sigma} + p_{i\sigma}^\dagger d_{i\sigma}) \end{aligned} \tag{4}$$

refers to one cell in the CuO_2 plane, and the operator H_1 in (3) describes the hopping of holes in the plane. In accordance with the data from the literature, we select a standard set of parameters. The energy difference between the states $|d_{i\sigma}\rangle$ and $|p_{i\sigma}\rangle$ is $\varepsilon_p - \varepsilon_d = 1$ eV. The Coulomb repulsions of holes in copper and oxygen positions are, respectively, $I_{dd} = 5$ eV and $I_{pp} = 1$ eV. The parameter V_{pd} of the Coulomb repulsion of copper and oxygen holes is zero. The hopping integrals are $t_{pd} = 1$ eV, $t^{(xx)} = t^{(yy)} = 0.1$ eV, and $t^{(xy)} = 0.25$ eV. The hopping parameter t_0 is expressed in terms of the hybridization parameter t_{pd} by $t_0 = 1.9164 t_{pd}$.

Using the well-known expansion

$$f = \sum_{p,q} \langle p|f|q\rangle X^{p,q}, \tag{5}$$

where $X^{p,q}$ are Hubbard operators constructed using the basis functions (1), and f is an arbitrary operator, we find that

$$d_\sigma^\dagger = X^{\sigma_d,0} + (-1)^{1/2-\sigma_d}\left(X^{dd,\overline{\sigma}_d} + \frac{1}{\sqrt{2}} X^{pd,\overline{\sigma}_p} \right),$$

$$p_\sigma^\dagger = X^{\sigma_p,0} + (-1)^{1/2-\sigma_p}\left(X^{pp,\overline{\sigma}_p} + \frac{1}{\sqrt{2}} X^{pd,\overline{\sigma}_d} \right), \tag{6}$$

with the result that the Hamiltonian H_{0i} can be written as follows:

$$\begin{aligned} H_{0i} &= \varepsilon_d \sum X_i^{\sigma_d,\sigma_d} + \varepsilon_p \sum X_i^{\sigma_p,\sigma_p} + (I_{dd} + 2\varepsilon_d) X_i^{dd,dd} \\ &+ (I_{pp} + 2\varepsilon_p) X_i^{pp,pp} + (V_{pd} + \varepsilon_d + \varepsilon_p) X_i^{pd,pd} \\ &+ H_{\text{hop}}. \end{aligned} \tag{7}$$

Let us now study the structure of H_{hop} within one cell. After carrying out the transformations (6), we get

$$\begin{aligned} H_{\text{hop}} &= t_0 \sum (d_\sigma^\dagger p_\sigma + p_\sigma^\dagger d_\sigma) = t_0 \sum (X^{\sigma_d,0} X^{0,\sigma_p} \\ &+ X^{\sigma_p,0} X^{0,\sigma_d}) + \sqrt{2} t_0 (X^{pd,pp} + X^{dd,pd} + X^{pd,dd} \\ &+ X^{pp,pd}). \end{aligned} \tag{8}$$

The right-hand side of this equation shows that there is hybridization of both one- and two-particle states. To diagonalize the Hamiltonian within a single cell we must do one more canonical transformation of the form

$$\psi^{\sigma_d,0} = c_d X^{\sigma_d,0} + c_p X^{\sigma_p,0},$$

$$\psi^{pd,0} = c_{dd} X^{dd,0} + c_{pp} X^{pp,0} + c_{pd} X^{pd,0}. \tag{9}$$

Here the relationship between the operators $d_\sigma^\dagger$ and $p_\sigma^\dagger$ and the operators $\psi^{p,q}$ is determined by expansions of the form

$$\begin{aligned} d_\sigma^\dagger &= c_{1d}\psi^{\sigma_d,0} + c_{2d}\psi^{\sigma_p,0} + (-1)^{1/2-\sigma}(c_{3d}\psi^{dd,\overline{\sigma}_d} \\ &+ c_{4d}\psi^{pp,\overline{\sigma}_d} + c_{5d}\psi^{pd,\overline{\sigma}_d} + c_{6d}\psi^{dd,\overline{\sigma}_p} + c_{7d}\psi^{pp,\overline{\sigma}_p} \\ &+ c_{8d}\psi^{pd,\overline{\sigma}_p}), \end{aligned} \tag{10}$$

$$\begin{aligned} p_\sigma^\dagger &= c_{1p}\psi^{\sigma_d,0} + c_{2p}\psi^{\sigma_p,0} + (-1)^{1/2-\sigma}(c_{3p}\psi^{dd,\overline{\sigma}_d} \\ &+ c_{4p}\psi^{pp,\overline{\sigma}_d} + c_{5p}\psi^{pd,\overline{\sigma}_d} + c_{6p}\psi^{dd,\overline{\sigma}_p} + c_{7p}\psi^{pp,\overline{\sigma}_p} \\ &+ c_{8p}\psi^{pd,\overline{\sigma}_p}), \end{aligned}$$

The Hamiltonian (7) diagonalized in this way becomes

$$\begin{aligned} H_{0i} &= E_d \sum \psi_i^{\sigma_d,\sigma_d} + E_p \sum \psi_i^{\sigma_p,\sigma_p} + E_{dd}\psi_i^{dd,dd} \\ &+ E_{pp}\psi_i^{pp,pp} + E_{pd}\psi_i^{pd,pd} \end{aligned} \tag{11}$$

and has eigenvalues

$$E_d=\frac{\varepsilon_d+\varepsilon_p}{2}-\frac{1}{2}\sqrt{(\varepsilon_p-\varepsilon_d)^2+4t_0^2},$$

$$E_p=\frac{\varepsilon_d+\varepsilon_p}{2}+\frac{1}{2}\sqrt{(\varepsilon_p-\varepsilon_d)^2+4t_0^2}, \tag{12}$$

while E_{dd}, E_{pp}, and E_{pd} can be found by solving the equation

$$\det\begin{vmatrix} I_{dd}+2\varepsilon_d-E & 0 & \sqrt{2}t_0 \\ 0 & I_{pp}+2\varepsilon_p-E & \sqrt{2}t_0 \\ \sqrt{2}t_0 & \sqrt{2}t_0 & V_{pd}+\varepsilon_d+\varepsilon_p-E \end{vmatrix}=0. \tag{13}$$

From (11)–(13) we see that the lowest quasiparticle excitation energies are $E_{pd}-E_p$, $\varepsilon_d=E_d$, and $\varepsilon_{pd}=E_{pd}-E_d$. The energy ε_d corresponds to the lower Hubbard band of copper, while ε_{pd} corresponds to the singlet-correlated oxygen band filled in the process of doping. The quasiparticle band with the energy $E_{pd}-E_p$ lies below ε_d. It is always filled and is not considered in our discussion.

In our treatment the singlet states of the hole band ε_{pd} are linear combinations of the Zhang–Rice singlet, the Cu^{3+} $(S=0)$ state, and the neutral-oxygen state. These states are mixed, and the proper combination is determined by the secular equation (13). In particular, with the above choice of the set of parameters we arrive at an expression for the singlet creation operator:

$$\psi^{pd,0}=0.9X^{pd,0}+0.35X^{pp,0}+0.28X^{dd,0}. \tag{14}$$

Clearly, the ground singlet state is 80% Zhang–Rice singlet, 12% neutral oxygen, and 8% Cu^{3+} $(S=0)$. At first glance the fraction of the Cu^{3+} $(S=0)$ state seems to be much smaller than the value found from cluster calculations.[26] The explanation lies in the different definitions of the Cu^{3+} state. To be able to compare our results with those of Moskvin *et al.*,[26] we must transform the basis (1) and write the state (14) as a molecular-orbital (MO) expansion. The procedure of such a transformation has been discussed by Martin.[27] With it we can easily see that the MO method[26] is equivalent to the above description.

The adopted model with two bands near the Fermi surface has much in common with the well-known Hubbard model.[28] In particular, the equation for the number of holes per cell can be written as

$$n=1+\delta=\sum d_\sigma^\dagger d_\sigma+\sum p_\sigma^\dagger p_\sigma=\sum \psi^{\sigma_d,\sigma_d}+2\psi^{pd,pd}, \tag{15}$$

where δ is the number of additional holes. The anticommutator relations are similar to the Hubbard relations:

$$\{\psi^{pd,\sigma_p},\psi^{\sigma_p,pd}\}=\psi^{pd,pd},$$

$$\{\psi^{pd,\sigma_d},\psi^{\sigma_d,pd}\}=\psi^{pd,pd}+\psi^{\sigma_d,\sigma_d}=\frac{1}{2}+\frac{\delta}{2}=P_{pd},$$

$$\{\psi^{\sigma_d,0},\psi^{0,\sigma_d}\}=\psi^{00}+\psi^{\sigma_d,\sigma_d}=P_d. \tag{16}$$

If we take into account the completeness condition

$$\psi^{00}+\psi^{\uparrow,\uparrow}+\psi^{\downarrow,\downarrow}+\psi^{pd,pd}=1 \tag{17}$$

(for now this condition is approximate), we find that

$$P_d=\frac{1}{2}-\frac{\delta}{2} \tag{18}$$

in the absence of magnetization. At $\delta=0$ we have an insulator state (just as we do in the Hubbard theory). The singlet correlated band is similar to the upper Hubbard band. For instance, with an increasing hole concentration δ the statistical weight of the band grows as $2\delta/(1+\delta)$. But there is also an important difference. The subband splitting energy is roughly ten times smaller than it is in the Hubbard model. In the two-band representation of the Hubbard model there is no spin–spin coupling of the form $J_{ij}[2(S_iS_j)-n_in_j/2]$. Such coupling appears only in the one-band representation as a result of allowing for the effect of the upper subband (in our case the E_{pd} subband) in second-order perturbation theory. In our case the superexchange interaction of copper spins is present in the two-band variant, too. It allows for the effect of the high-lying singlet states E_{dd} and E_{pp} on the lower subbands ε_d and ε_{pd}, resulting from the virtual hopping of holes to neighboring lattice sites. However, we will see that the effect is much weaker than in the one-band variant. This fact is important to the theory because it becomes possible to properly account for the superexchange interaction of copper spins even at low doping levels, when the width of the singlet band E_{pd} is relatively small.

3. THE HOPPING OPERATOR AND THE SUPEREXCHANGE INTERACTION

The operator representing the hopping of holes from site to site in the CuO_2 plane in the representation of the Wannier functions $p_{j\sigma}$ is

$$H_1=-t^{(pd)}\sum_{i\neq j} C_{ij}(d_{i\sigma}^\dagger p_{j\sigma}+p_{j\sigma}^\dagger d_{i\sigma})+\sum_{i\neq j}(t^{(xy)}S_{ij}$$
$$-t^{(xx)}D_{ij})p_{i\sigma}^\dagger p_{j\sigma}, \tag{19}$$

where the coefficients C_{ij}, S_{ij}, and D_{ij} are given by the expressions

$$C_{ij}=\frac{2}{N}\sum \beta_k^{-1}\exp(i\mathbf{k}\cdot\mathbf{R}_{ij}),$$

$$S_{ij}=\frac{1}{N}\sum[\cos(k_xa)+\cos(k_ya)$$
$$-2\cos(k_xa)\cos(k_ya)]\beta_k^2\exp(i\mathbf{k}\cdot\mathbf{R}_{ij}),$$

$$D_{ij}=\frac{1}{2N}\sum[\cos(k_xa)+\cos(k_ya)$$
$$-\cos(2k_xa)-\cos(2k_ya)]\beta_k^2\exp(i\mathbf{k}\cdot\mathbf{R}_{ij}). \tag{20}$$

The calculated values of these coefficients are listed in Table I. Substituting (10) in (19) and leaving only the operators of the two bands closest to the Fermi level, we get

TABLE I. The values of the coefficients C_{ij}, S_{ij}, and D_{ij} calculated via (20).

$i \backslash j$	0	1	2	3	4
			C_{ij}		
0	0				
1	−0.2747	−0.0461			
2	−0.0269	−0.0134	−0.0064		
3	−0.0069	−0.0051	−0.0032	−0.0020	
4	−0.0027	−0.0023	−0.0017	−0.0012	−0.0008
			S_{ij}		
0	0				
1	0.5357	−0.2393			
2	0.1252	−0.0341	−0.0206		
3	0.0331	−0.0015	−0.0072	−0.0048	
4	0.0103	0.0022	−0.0019	−0.0023	−0.0016
			D_{ij}		
0	0				
1	0.4446	0.2393			
2	−0.1252	0.0340	0.0206		
3	−0.0332	0.0014	0.0071	0.0047	
4	−0.0104	−0.0022	0.0018	0.0023	0.0016

$$H_1=\sum_{i\neq j} t_{ij}^{(1)}\psi_i^{pd,\overline{\sigma}}\psi_j^{\overline{\sigma},pd}+\sum_{i\neq j} t_i^{(2)}\psi_i^{\sigma,0}\psi_j^{0,\sigma}$$
$$+\sum_{i\neq j} t_{ij}^{(12)}(-1)^{s-\sigma}(\psi_i^{\sigma,0}\psi_j^{\overline{\sigma},pd}+\psi_j^{pd,\overline{\sigma}}\psi_i^{0,\sigma})$$
$$-\sum_{i>j} J_{ij}(-1)^{1-\sigma-\sigma'}\psi_i^{\sigma,\sigma'}\psi_j^{\overline{\sigma},\overline{\sigma'}}. \tag{21}$$

Here and in what follows σ has the meaning of the symbol σ_d. The effective hopping integrals in (21) are related to the copper–oxygen hopping integral $t^{(pd)}$ and the oxygen–oxygen hopping integrals $t^{(xy)}$ and $t^{(xx)}$, as follows:

$$t_{ij}^{(1)}=2c_{5d}c_{5p}(-t^{(pd)}C_{ij})+c_{5p}^2(t^{(xy)}S_{ij}-t^{(xx)}D_{ij}),$$
$$t_{ij}^{(2)}=2c_{1d}c_{1p}(-t^{(pd)}C_{ij})+c_{1p}^2(t^{(xy)}S_{ij}-t^{(xx)}D_{ij}),$$
$$t_{ij}^{(12)}=(c_{1d}c_{5p}+c_{1p}c_{5d})(-t^{(pd)}C_{ij})$$
$$+c_{1p}c_{5p}(t^{(xy)}S_{ij}-t^{(xx)}D_{ij}). \tag{22}$$

Note that in contrast to the well-known $t-J$ model, the hops between second and third neighbors are effective. The importance of taking into account the hops between second and third neighbors when analyzing the band structure near the Fermi surface has recently been stressed by a number of investigators.[29–31] The reason is that the ratio of the corresponding hopping integrals affects the shape and position of the peak in the density of states that is near the Fermi level. Nevertheless, all calculated values must be interpreted as estimates. The point is that singlet copper–oxygen states are coupled with vibrational modes even more strongly than copper states.[32] This fact must lead to the appearance of polaron factors of the form[33]

$$\exp\left(-\gamma\frac{E_{\text{pol}}}{\hbar\omega}\right), \tag{23}$$

which may be several times smaller than unity. Since this problem has yet to be studied, in what follows we use only the relative values of the hopping integrals (22), while the absolute values are chosen in accordance with photoemission data,[34] i.e., the width of the band. The factor (23) estimated in this way is set equal to 1/3.

The last sum on the right-hand side of Eq. (21) represents the superexchange interaction of copper spins. It is obtained in second-order perturbation theory, as it is in the Anderson theory,[35] via the excited singlets E_{dd} and E_{pp}. The expression for J_{ij} is

$$J_{ij}=2\left\{\frac{[-(c_{1d}c_{3p}+c_{1p}c_{3d})t^{(pd)}C_{ij}+c_{1p}c_{3p}(t^{(xy)}S_{ij}-t^{(xx)}D_{ij})]^2}{E_{dd}-2E_d}\right.$$
$$\left.+\frac{[-(c_{1d}c_{7p}+c_{1p}c_{7d})t^{(pd)}C_{ij}+c_{1p}c_{7p}(t^{(xy)}S_{ij}-t^{(xx)}D_{ij})]^2}{E_{pp}-2E_d}\right\}. \tag{24}$$

Numerical estimates for the nearest copper sites show that $J=2J_{i,i+1}\approx 0.03$ eV. Note that in the one-band representation the expression (24) would have an additional term of the form

$$\frac{2(t_{i,i+1}^{(12)})^2}{E_{pd}-2E_d}\approx 0.05\ \text{eV}. \tag{25}$$

The sum of the contributions (24) and (25) must be compared with the value of the superexchange integral, $2J_{i,i+1}=0.13$ eV, determined from neutron-scattering experiments.[36]

4. SPIN SUSCEPTIBILITY

The energy operator of the spin system in an external magnetic field directed along the z axis is

$$H_z=-g_d\beta H\sum d_{i\sigma}^{\dagger}\langle\sigma|S_d^z|\sigma\rangle d_{i\sigma}$$

$$-g_p\beta H\sum p_{i\sigma}^{\dagger}\langle\sigma|S_p^z|\sigma\rangle p_{i\sigma}, \tag{26}$$

where S_d^z and S_p^z are spin operators of holes distributed over copper and oxygen positions, respectively. Using (10), we obtain

$$H_z=-g\beta H\sum S_{zi}. \tag{27}$$

Here the g factor is given by the expression

$$g=g_d|c_{1d}|^2+g_p|c_{1p}|^2 \tag{28}$$

and we have introduced the notation

$$S_{zi}=\frac{1}{2}(\psi_i^{\uparrow,\uparrow}-\psi_i^{\downarrow,\downarrow}). \tag{29}$$

The value of the g factor does not depend on the doping level. Hence we can assume $g_{\parallel}=2.3\pm 0.1$ and $g_{\perp}=2.1\pm 0.05$, as in the case of lightly doped cuprates. To calculate the average value $\langle S_{zi}\rangle$ we use a method proposed in Ref. 24. However, in contrast to Ref. 24, we employ a variant of the method for the decoupling of Green's equations that is better than the Hubbard-I variant, as was done in Refs. 21–23.

The elementary excitations spectrum with allowance for the energy of spins in an external field has the form

$$\varepsilon_{1k\uparrow,2k\uparrow}=\frac{E_{k\uparrow}^{(dd)}+E_{k\downarrow}^{(pp)}}{2}$$

$$\pm\frac{1}{2}\sqrt{(E_{k\uparrow}^{(dd)}-E_{k\downarrow}^{(pp)})^2+4E_{k\downarrow}^{(dp)}E_{k\uparrow}^{(pd)}}, \tag{30}$$

where $E_{k\uparrow}^{(dd)}$, $E_{k\downarrow}^{(pp)}$, $E_{k\uparrow}^{(pd)}$ and $E_{k\downarrow}^{(dp)}$ are the Fourier transforms of the corresponding coefficients $E_{ij\uparrow}^{(dd)}$, $E_{ij\downarrow}^{(pp)}$, $E_{ij\uparrow}^{(pd)}$, and $E_{ij\downarrow}^{(dp)}$ determined by the equations

$$\langle\psi_j^{0,0}+\psi_j^{\uparrow,\uparrow}\rangle E_{ij\uparrow}^{(dd)}=\langle\{[\psi_i^{0,\uparrow},H],\psi_j^{\uparrow,0}\}\rangle,$$

$$\langle\psi_j^{\downarrow,\downarrow}+\psi_j^{pd,pd}\rangle E_{ij\downarrow}^{(pp)}=\langle\{[\psi_i^{\downarrow,pd},H],\psi_j^{pd,\downarrow}\}\rangle,$$

$$\langle\psi_j^{0,0}+\psi_j^{\uparrow,\uparrow}\rangle E_{ij\uparrow}^{(pd)}=\langle\{[\psi_i^{\downarrow,pd},H],\psi_j^{\uparrow,0}\}\rangle,$$

$$\langle\psi_j^{\downarrow,\downarrow}+\psi_j^{pd,pd}\rangle E_{ij\downarrow}^{(dp)}=\langle\{[\psi_i^{0,\uparrow},H],\psi_j^{pd,\downarrow}\}\rangle. \tag{31}$$

The square brackets on the right-hand sides of (31) denote commutators with the Hamiltonian

$$H=H_0+H_1+H_z \tag{32}$$

(see (11), (21), and (27)), and the braces denote anticommutators.

Using the equation for the chemical potential (15), the completeness condition (17), and the definition of $\langle S_{zi}\rangle$, for the site averages we have

$$\langle\psi_i^{pd,pd}+\psi_i^{\uparrow,\uparrow}\rangle=\frac{1+\delta}{2}+\langle S_{zi}\rangle,$$

$$\langle\psi_i^{pd,pd}+\psi_i^{\downarrow,\downarrow}\rangle=\frac{1+\delta}{2}-\langle S_{zi}\rangle,$$

$$\langle\psi_i^{\uparrow,\uparrow}+\psi_i^{0,0}\rangle=\frac{1-\delta}{2}+\langle S_{zi}\rangle,$$

$$\langle\psi_i^{\downarrow,\downarrow}+\psi_i^{0,0}\rangle=\frac{1-\delta}{2}-\langle S_{zi}\rangle. \tag{33}$$

The interstitial averages on the right-hand sides of (31) can easily be expressed in terms of the number of doped holes, δ, the average value $\langle S_{zi}\rangle$, and the spin correlation functions $\langle S_iS_j\rangle$; in particular,

$$\langle(\psi_i^{\downarrow,\downarrow}+\psi_i^{pd,pd})(\psi_j^{\downarrow,\downarrow}+\psi_j^{pd,pd})+\psi_i^{\downarrow,\uparrow}\psi_j^{\uparrow,\downarrow}\rangle=\left(\frac{1+\delta}{2}\right)^2$$

$$+\langle S_iS_j\rangle-\left(\frac{1+\delta}{2}\right)(\langle S_{zi}\rangle+\langle S_{zj}\rangle), \tag{34}$$

etc. Substituting (33) and (34) in (31) and (30), we see that the quasiparticle excitation energies depend on the average values $\langle S_{zi}\rangle$. In the rapid spin fluctuations mode, i.e., when $\langle S_{zi}\rangle$ is independent of i and is much smaller than 1/2, we have

$$\varepsilon_{1k\uparrow}=\varepsilon_k^{(1)}-\frac{1}{2}g\beta H-F_{1k}\frac{\langle S_z\rangle}{2},$$

$$\varepsilon_{2k\uparrow}=\varepsilon_k^{(2)}-\frac{1}{2}g\beta H-F_{2k}\frac{\langle S_z\rangle}{2}, \tag{35}$$

where ε_{1k} and ε_{2k} are the quasiparticle energies in the absence of a magnetic field:

$$\varepsilon_{1k,2k}=\frac{E_k^{(dd)}+E_k^{(pp)}}{2}$$

$$\pm\frac{1}{2}\sqrt{(E_k^{(dd)}-E_k^{(pp)})^2+4E_k^{(dp)}E_k^{(pd)}}. \tag{36}$$

Here we have used the following notation:

$$E_k^{(dd)}=\varepsilon_d+t_k^{dd}+\frac{2J_k^{dd}}{1-\delta},\quad E_k^{(pp)}=\varepsilon_{pd}+t_k^{pp}+\frac{2J_k^{pp}}{1+\delta},$$

$$E_k^{(pd)}=\sum_l\left[\frac{1-\delta}{2}-\frac{2}{1+\delta}\langle S_iS_l\rangle\right]t_{il}^{(12)}\exp(i\mathbf{k}\cdot\mathbf{R}_{il}),$$

$$E_k^{(dp)}=\sum_l \left[\frac{1+\delta}{2}-\frac{2}{1-\delta}\langle S_iS_l\rangle\right]t_{il}^{(12)}\ \exp(i\mathbf{k}\cdot\mathbf{R}_{il}),$$

$$t_k^{dd}=\sum_l \left[\frac{1-\delta}{2}+\frac{2}{1-\delta}\langle S_iS_l\rangle\right]t_{il}^{(2)}\ \exp(i\mathbf{k}\cdot\mathbf{R}_{il}),$$

$$t_k^{pp}=\sum_l \left[\frac{1+\delta}{2}+\frac{2}{1+\delta}\langle S_iS_l\rangle\right]t_{il}^{(1)}\ \exp(i\mathbf{k}\cdot\mathbf{R}_{il}),$$

$$J_k^{dd}=\frac{1}{2}J[4\langle S_iS_j\rangle^{(1)}-1]-J\langle \psi_i^{\downarrow,0}\psi_{i+1}^{0,\downarrow}\rangle[\cos(k_xa) \\ +\cos(k_ya)],$$

$$J_k^{pp}=\frac{1}{2}J[1+2\delta-4\langle S_iS_j\rangle^{(1)}]-J\langle \psi_i^{pd,\uparrow}\psi_{i+1}^{\uparrow,pd}\rangle[\cos(k_xa) \\ +\cos(k_ya)], \tag{37}$$

with $\langle S_iS_j\rangle^{(1)}$ the spin correlation function for the nearest copper spins. The functions F_{1k} and F_{2k} are given by the expressions

$$\frac{1}{2}F_{1k,2k}=t_k^p-t_k^d-T_k^p+T_k^d \\ \pm\frac{1}{\varepsilon_{1k}-\varepsilon_{2k}}\left\{(E_k^{(pp)}-E_k^{(dd)})[t_k^p+t_k^d-T_k^p-T_k^d] \\ -2\delta\frac{E_k^{(pd)}E_k^{(dp)}}{1-\delta^2}\right\}, \tag{38}$$

where

$$T_k^p=\frac{E_k^{pp}+2\delta J-\varepsilon_{pd}}{1+\delta},\quad T_k^d=\frac{E_k^{dd}-\varepsilon_d}{1-\delta},$$

$$t_k^p=\sum_l t_{il}^{(1)}\exp(i\mathbf{k}\cdot\mathbf{R}_{il}),\quad t_k^d=\sum_l t_{il}^{(2)}\ \exp(i\mathbf{k}\cdot\mathbf{R}_{il}). \tag{39}$$

Equations (35) show that the energy of quasiparticles in a magnetic field differs considerably from the Fermi energy, at which both F_{1k} and F_{2k} would vanish. This is one of the most important reasons for the non-Fermi-liquid nature of the spin susceptibility. Each quasiparticle is in a kind of effective magnetic field generated by the other particles, and this field does not vanish when spin–spin coupling is switched off, i.e., when $J=0$. Another reason for the non-Fermi-liquid behavior is related to the special behavior of the spectral weight. For instance, the spectral weight of the singlet band varies under doping not as δ (the case of a Fermi liquid) but as $2\delta/(1+\delta)$, i.e., the band is completely filled at $\delta=1$ and is half-filled already at $\delta=1/3$.

There are different calculational techniques that lead to the same self-consistent equation for $\langle S_z\rangle$. Since from the viewpoint of applications the most interesting case is $\delta>0$, i.e., when the chemical potential is in the band ε_{1k}, it is convenient to use the following chain of equalities:

$$\delta=\frac{1}{N}\sum\ \langle\psi_k^{pd,\uparrow}\psi_k^{\uparrow,pd}\rangle \\ =\frac{1}{N}\sum\ \langle\psi_k^{pd,\downarrow}\psi_k^{\downarrow,pd}\rangle=\frac{1}{N}\left(\frac{1+\delta}{2}-\langle S_z\rangle\right) \\ \times\sum_k\left[\frac{\varepsilon_{1k\uparrow}-E_{k\uparrow}^{(dd)}}{\varepsilon_{1k\uparrow}-\varepsilon_{2k\uparrow}}f(\varepsilon_{1k\uparrow}-\mu) \\ +\frac{E_{k\uparrow}^{dd}-\varepsilon_{2k\uparrow}}{\varepsilon_{1k\uparrow}-\varepsilon_{2k\uparrow}}f(\varepsilon_{2k\uparrow}-\mu)\right], \tag{40}$$

where

$$f(\varepsilon_{1k\uparrow}-\mu)=\left[1+\exp\frac{\varepsilon_{1k\uparrow}-\mu}{\Theta}\right]^{-1}$$

is the Fermi function, μ is the chemical potential, and $\Theta=kT$.

Expanding the right-hand side of Eq. (40) in $\langle S_z\rangle$ and allowing for (35), we arrive at an expression for $\langle S_z\rangle$ as a function of the magnetic field and hence at an expression for the magnetic susceptibility $\chi(\Theta,\delta)$ per copper site:

$$\chi(\Theta,\delta)=\frac{(1+\delta)^2}{[4\delta+\Lambda(\Theta,\delta)+Z(\Theta,\delta)]}\chi_p(\Theta,\delta). \tag{41}$$

This is the typical expression for the Pauli–Lindhard susceptibility in the two-band model:

$$\chi_p(\Theta,\delta)=-\frac{1}{2N}(g\beta)^2\sum_k\left[\frac{\varepsilon_{1k}-E_k^{(dd)}}{\varepsilon_{1k}-\varepsilon_{2k}}\frac{\partial f(\varepsilon_{1k})}{\partial\varepsilon_{1k}} \\ +\frac{E_k^{(dd)}-\varepsilon_{2k}}{\varepsilon_{1k}-\varepsilon_{2k}}\frac{\partial f(\varepsilon_{2k})}{\partial\varepsilon_{2k}}\right]. \tag{42}$$

The functions $Z(\Theta,\delta)$ and $\Lambda(\Theta,\delta)$ are

$$Z(\Theta,\delta)=\frac{(1+\delta)^2}{2N}\sum\left[\frac{\varepsilon_{1k}-E_k^{(dd)}}{\varepsilon_{1k}-\varepsilon_{2k}}F_{1k}\frac{\partial f(\varepsilon_{1k})}{\partial\varepsilon_{1k}} \\ +\frac{E_k^{(dd)}-\varepsilon_{2k}}{\varepsilon_{1k}-\varepsilon_{2k}}F_{2k}\frac{\partial f(\varepsilon_{2k})}{\partial\varepsilon_{2k}}\right],$$

$$\Lambda(\Theta,\delta)=\frac{(1+\delta)^2}{2N}\sum\ \Phi_k[f(\varepsilon_{1k})-f(\varepsilon_{2k})]. \tag{43}$$

The origin of the function Φ_k is related to the dependence of the coefficients of the Fermi functions in (40) on the spin direction. This function is given by the formula

$$\Phi_k=\frac{2}{\varepsilon_{1k}-\varepsilon_{2k}}(t_k^p+t_k^d-T_k^p-T_k^d) \\ +\frac{2(E_k^{(pp)}-E_k^{(dd)})}{(\varepsilon_{1k}-\varepsilon_{2k})^3}\left[\frac{4\delta E_k^{(dp)}E_k^{(pd)}}{1-\delta^2}-(E_k^{(pp)}-E_k^{(dd)}) \\ \times(t_k^p+t_k^d-T_k^p-T_k^d)\right]. \tag{44}$$

Since both (43) and (44) contain the difference in energies and the difference in the Fermi functions of different bands, the contribution to susceptibility represented in (41) by the

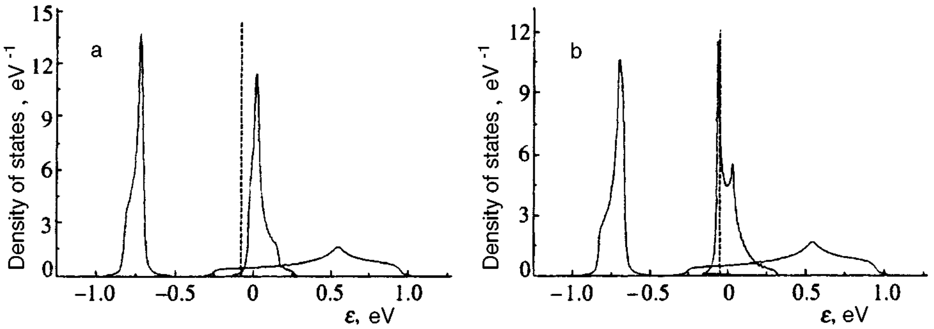

FIG. 1. Density of states at $T=300$ K: (a) at $x=0.15$, and (b) at $x=0.25$. The vertical dashed lines indicate the position of the chemical potential.

function $\Lambda(\Theta,\delta)$ resembles the mixed susceptibility in Fermi −liquid theory. Thus, the occurance of such a correction is quite natural. Our numerical estimates show that the function $\Lambda(\Theta,\delta)$ is relatively unimportant and that for a detailed comparison with the mixed susceptibility it is sufficient to write this correction to susceptibility in additive form after expanding the denominator in (41) in a Taylor series. We also note that at $t_k^{(12)}=0$ the function $\Lambda(\Theta,\delta)$ vanishes.

As noted in the Introduction, the behavior of $\chi_p(\Theta,\delta)$ has been thoroughly studied for different variants of the density of states (see, e.g., Refs. 8, 16, and 17). The implicit dependence of this function on the degree of doping δ is related to the different density of states on the Fermi level for different values of δ.

The denominator in (41) shares features with the well known Stoner factor in Fermi-liquid theory. In particular, if we temporarily drop the second band and put $\langle S_iS_j\rangle^{(1)}=-3/4$ (the maximum value of antiferromagnetic correlations) in (37), we find that

$$Z(\Theta,\delta)=2(1+\delta)^2[-t_k^p(\mu)+4J]\chi_p(\Theta,\delta), \qquad (45)$$

where $t_k^p(\mu)$ is the value of t_k^p at the Fermi level. Depending on the nature of band filling, $t_k^p(\mu)$ can be either positive or negative. Generally, the temperature dependences $Z(\Theta,\delta)$ and $\chi_p(\Theta,\delta)$ are the same when $F_{1k}(\mu)$ is negative and are opposite when $F_{1k}(\mu)$ is positive. The latter case is realized in the limit of strong doping, since $t_k^p(\mu)>0$. Here, however, the denominator in (41) does not change its sign, always remaining positive. The function $\chi(\Theta,\delta)$ is the paramagnetic spin susceptibility (for all positive values of δ).

5. NUMERICAL RESULTS AND DISCUSSION

The density of states of the bands ε_{1k} and ε_{2k} is depicted in Fig. 1 for two values of x, 0.15 and 0.25 (at $T=300$ K this corresponds to $\delta=0.02$ and 0.09, respectively). The position of the chemical potential at $T=300$ K is depicted by a dashed vertical line. The lower Hubbard copper band corresponds to the ε_{1k} band (in the range from -1.0 to -0.5 eV). It is completely filled. The holes that form as a result of doping populate the singlet band ε_{2k} (in the range from -0.15 to 0.3 eV). Since the unit cell of $La_{2-x}Sr_xCuO_4$ does not only contain a CuO_2 fragment, as in Refs. 15–18, we allow also for the existence of an additional relatively broad band near the Fermi level. This band is introduced phenomenologically in the form of a background band about 1.25 eV wide. As Fig. 1b shows, there are two peaks in the density of states of the singlet band. The peak at the bottom of the band is due to the hybridization of the states ε_d and ε_{pd}, and for $0.15<x<0.25$ the chemical potential is near this peak. The second peak in the high-energy region is due to the geometrical features of the two-dimensional lattice. This is the Van Hove peak, which at $t^{(12)}=0$ (see (21)) is approximately at the band's center. The dependence of the spin correlation functions $\langle S_iS_j\rangle$ on the doping index was specified in the same way as in Ref. 21. At $\delta=0$, 0.2, and 0.4 the functions for the first neighbors were $\langle S_iS_j\rangle^{(1)}=-0.25$, -0.10, and 0, respectively; for the second neighbors they were $\langle S_iS_j\rangle^{(2)}=0.15$, 0.06, and 0. Note that at $\delta=0$ the factors that determine the dependence of the effective hopping integrals on the spin correlation functions $\langle S_iS_j\rangle$ in the expressions for t_k^{dd} and t_k^{pp} can be reduced to the form $\frac{1}{2}+2\langle S_iS_j\rangle$, found in Ref. 37, via an exact calculation of the spectrum of one-particle excitations of a hole in the Ising lattice. At $\langle S_iS_j\rangle=-0.25$ the widths of the bands vanish, which is known (see, e.g., Ref. 28) to be needed for a meaningful description of the boundary region in insulator–metal transitions. In this sense our variant of describing a singlet band is equivalent to the variant in Ref. 38 but does not require auxiliary bosons.

The temperature curves of the spin susceptibility calculated via formula (41) for $x=0.15$, 0.18, 0.22, and 0.25 are depicted in Fig. 2. The corresponding values of δ were calculated in accordance with the density-of-states pattern (Fig.

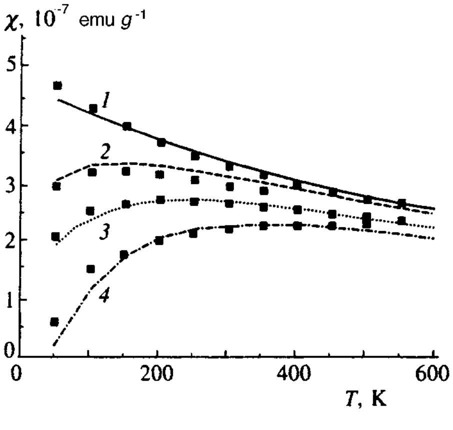

FIG. 2. The temperature curves of the spin susceptibility calculated via formula (41): filled square ■ correspond to the experimental data of Ref. 39. Curve *1* corresponds to $x=0.25$, curve *2* to $x=0.22$, curve *3* to $x=0.18$, and curve *4* to $x=0.15$.

1), and at $T=300$ K were found to be $\delta=0.02$, 0.04, 0.06, and 0.09. Figure 2 shows that formula (41) is a good representation of the strong dependence of the spin susceptibility on temperature and doping level observed in experiments.[1–6,39] The spin susceptibility of the broad background band, as suggested by the density of states, is low and depends neither on T nor on δ. At low doping levels the chemical potential is just in front of the hybridization peak in the density of states of the singlet band (Fig. 1a). The energy interval between the chemical potential and the position of the peak in the density of states acts as a ''pseudogap.'' As the temperature increases, the quasiparticles are ''flung'' into the region of high densities of states, with the result that susceptibility increases. As the degree of doping δ increases, the Fermi level enters the peak in the density of states, the pseudogap narrows, and spin susceptibility increases. Finally, as the chemical potential passes the peak in the density of states, the system finds itself in the narrow-band mode or in the local-level mode, which naturally leads to a decrease in spin susceptibility with increasing temperature, which resembles the Curie law.

The denominator in (41) plays an interesting role. At small values of δ the function $Z(T,\delta)$ decreases both as a function of δ and as a function of temperature. As a result, this denominator facilitates a better description of absolute values and the asymptotic behavior of spin susceptibility at high temperatures than the classical Pauli–Lindhard theory with the same density-of-states pattern.[40]

In conclusion, here is one more argument in favor of the density-of-states pattern used in this paper. From neutron scattering studies it is known (see, e.g., Ref. 41) that the $La_{2-x}Sr_xCuO_4$ compounds have spatial dynamic spin correlations that are incommensurable with the lattice period. This is quite natural from the viewpoint of the density-of-states pattern of Fig. 1, since the chemical potential is near the peak in the density of states, which means that the system is indeed unstable with respect to formation of charge- and spin-density waves. In this connection the results of our calculations exceed the limits of this paper and, in particular, may serve as a real basis for studies of the instability and fluctuations in such (and related) compounds.

The authors are grateful to K. A. Kikoin and R. Hayn for the useful remarks. This work was partially supported by the Russian ''High-temperature Superconductivity'' Program (Project No. 94029) and the Soros Graduate Student International Program.

*)E-mail: Mikhail.Eremin@ksu.ru

---

[1] D. C. Johnston, Phys. Rev. Lett. **62**, 957 (1989).
[2] J. B. Torrance, A. Bezinge, A. I. Nazzal *et al.*, Phys. Rev. B **40**, 8872 (1989).
[3] R. Yoshizaki, N. Ishikawa, H. Sawada *et al.*, Physica C **166**, 417 (1990).
[4] M. Oda, T. Nakano, Y. Kamada *et al.*, Physica C **183**, 234 (1991).
[5] Y.-Q. Song, M. A. Kennard, K. R. Poeppelmeier *et al.*, Phys. Rev. Lett. **70**, 3131 (1993).
[6] H. Y. Hwang, B. Batlogg, H. Takagi *et al.*, Phys. Rev. Lett. **72**, 2636 (1994).
[7] V. Barzykin, D. Pines, and D. Thelen, Phys. Rev. B **50**, 16 052 (1994).
[8] V. V. Moshalkov, Physica B **163**, 59 (1990).
[9] P. Benard, L. Chen, and A.-M. S. Tremblay, Phys. Rev. B **47**, 15 217 (1993).
[10] K. Levin, Q. Si, and Y. Zha, Physica C **235–240**, 71 (1994).
[11] J. Bok and J. Bouvier, Physica C **244**, 357 (1995).
[12] R. S. Markiewicz, cond-mat/9611238, submitted to J. Phys. Chem. Solids.
[13] H. Romberg, M. Alexander, N. Nucker *et al.*, Phys. Rev. B **42**, 8768 (1990).
[14] Z.-X. Shen, Physica B **197**, 632 (1994).
[15] J. Thoma, S. Tewari, J. Ruvalds *et al.*, Phys. Rev. B **51**, 15 393 (1995).
[16] J. Ruvalds, Supercond. Sci. Technol. **9**, 1 (1996).
[17] G. A. Levin and K. F. Quader, Physica C **258**, 261 (1996).
[18] K. F. Quader and G. A. Levin, Philos. Mag. B **74**, 609 (1996).
[19] M. V. Eremin, S. G. Solov'yanov, S. V. Varlamov, D. Brinkman, M. Mali, R. Markendorf, and J. Roos, JETP Lett. **60**, 125 (1994).
[20] M. V. Eremin, S. G. Solovjanov, and S. V. Varlamov, J. Phys. Chem. Solids **56**, 1713 (1995).
[21] N. M. Plakida, R. Hayn, and J.-L. Richard, Phys. Rev. B **51**, 16 599 (1995).
[22] L. M. Roth, Phys. Rev. **184**, 451 (1969).
[23] J. Beenen and D. M. Edwards, Phys. Rev. B **52**, 13 636 (1995).
[24] M. Eremin, S. Solovjanov, S. Varlamov *et al.*, in *Proc. 10th Anniv. Workshop on Physics, Material, and Applications of HTS* (Houston, TX, March 1996), World Scientific, River Edge, N.J. (1996), p/ 517.
[25] F. C. Zhang and T. M. Rice, Phys. Rev. B **37**, 3759 (1988).
[26] A. S. Moskvin, N. N. Lozhkareva, Yu. P. Sukhorukov, M. A. Sidorov, A. A. Samokhvalov, Zh. Éksp. Teor. Fiz. **105**, 967 (1994) [JETP **78**, 518 (1994)].
[27] R. Martin, Phys. Rev. B **53**, 15 501 (1996).
[28] E. V. Kuz'min, G. A. Petrakovskiĭ, Z. A. Zavadskiĭ, *Physics of Magnetically Ordered Substances* [in Russian], Nauka, Moscow (1976), p. 97.
[29] R. Hayn, A. F. Barabanov, J. Schulenberg *et al.*, Phys. Rev. B **53**, 11 714 (1996).
[30] V. I. Belinicher, A. L. Chernyshev, and V. A. Shubin, Phys. Rev. B **53**, 335 (1996).
[31] L. F. Feiner, J. H. Jefferson, and R. Raimondi, Phys. Rev. Lett. **76**, 4939 (1996).
[32] M. V. Eremin, Z. Naturforsch. **49a**, 385 (1994).
[33] K. I. Kugel' and D. I. Khomskiĭ, Zh. Éksp. Teor. Fiz. **79**, 987 (1980) [Sov. Phys. JETP **52**, 501 (1980)].
[34] Z.-X. Shen and D. S. Dessau, Phys. Rep. **253**, 1 (1995).
[35] P. W. Anderson, Phys. Rev. **115**, 2 (1959).
[36] S. M. Hayden, G. Aeppli, T. G. Perring *et al.*, Phys. Rev. B **54**, 6905 (1996).
[37] D. I. Khomskiĭ, Fiz. Met. Metalloved. **29**, 31 (1970).
[38] T. Tanamoto, H. Kohno, and H. Fukujama, J. Phys. Soc. Jpn. **62**, 1445 (1993); J. Phys. Soc. Jpn. **63**, 2741 (1994).
[39] T. Nakano, Phys. Rev. B **49**, 16 000 (1994).
[40] M. V. Eremin, E. Sigmund, S. G. Solovjanov *et al.*, J. Supercon. **9**, 299 (1996).
[41] K. Yamada, S. Wakimoto, G. Shirane *et al.*, Phys. Rev. Lett. **75**, 1626 (1995); K. Yamada, J. Wada, K. Kurahashi *et al.*, submitted to Phys. Rev. Lett. .

Translated by Eugene Yankovsky

Nonlinear time-independent and time-dependent propagation of light in direct-gap semiconductors with paired excitons bound into biexcitons

A. Kh. Rotaru

State University of Moldova, 277000 Kishinev, Moldova

V. Z. Tronchu

Institute of Applied Physics, Academy of Sciences of Moldova, 277028 Kishinev, Moldova

(Submitted 3 March 1997)
Zh. Éksp. Teor. Fiz. **112**, 1778–1790 (November 1997)

We study a new class of nonlinear cooperative phenomena that occur when light propagates in direct-gap semiconductors. The nonlinearity here is due to a process, first discussed by A. L. Ivanov, L. V. Keldysh, and V. V. Panashchenko, in which two excitons are bound into a biexciton by virtue of their Coulomb interaction. For the geometry of a ring cavity, we derive a system of nonlinear differential equations describing the dynamical evolution of coherent excitons, photons, and biexcitons. For the time-independent case we arrive at the equation of state of optical bistability theory, and this equation is found to differ considerably from the equations of state in the two-level atom model and in the exciton region of the spectrum. We examine the stability of the steady states and determine the switchover times between the optical bistability branches. We also show that in the unstable sections of the equation of state, nonlinear periodic and chaotic self-pulsations may arise, with limit cycles and strange attractors being created in the phase space of the system. The scenario for the transition to the dynamical chaos mode is found. A computer experiment is used to study the dynamic optical bistability. Finally, we discuss the possibility of detecting these phenomena in experiments.

1. INTRODUCTION

The paper written by Elesin and Kopaev,[1] on the optical hysteresis of excitons was followed by numerous theoretical and experimental investigations.[2–9]

The interest in optical bistability caused by excitons and biexcitons in condensed media is due the interest in the giant optical nonlinearities at the long-wave intrinsic absorption edge of the crystal spectrum, short relaxation times, and low switchover energies and short switchover times between the optical bistability branches.

More than that, in the unstable sections of the optical bistability curve, regular and chaotic self-pulsations may arise in the system of excitons, photons and biexcitons. All of this opens possibilities for studying essentially new optical phenomena that involve excitons and biexcitons and in using these phenomena for practical purposes, primarily for optical processing of data and for building new-generation computers with optical logical circuits.

In Refs. 10–22 we constructed a theory of optical bistability, optical switchover, and regular and stochastic oscillations accompanied by the formation of classical and strange attractors in the phase space of excitons, photons, and biexcitons.

The possibility of optical multistability in a system of coherent excitons and biexcitons being induced by noise was predicted in Refs. 23 and 24.

It must be noted, however, that in Refs. 5, 6, 18 and 19 optical bistability was studied only with allowance for the huge oscillator strength of the exciton–biexciton transition,[25–27] i.e., only the process of creation of a biexciton **p** through the absorption by an exciton **q** of a photon **p**−**q** was taken into account. Ivanov *et al.*[28,29] were the first to show that there is also another process, determined by the term

$$\frac{1}{\sqrt{V}}M(p,q)b_p^\dagger a_{\mathbf{q}}a_{\mathbf{p}-\mathbf{q}},$$

which describes direct binding of two excitons, **p**−**q** and **q**, into a biexciton by virtue of the Coulomb attraction of the excitons. Actually, in Refs. 28 and 29 an essentially new mechanism of the exciton–biexciton transformation of the semiconductor spectrum was proposed, i.e., the formation of a biexciton through direct Coulomb binding of two excitons. In particular, it was found that this mechanism effectively shifts both exciton and biexciton levels toward the long-wave part of the spectrum.

The present paper studies time-independent and time-dependent optical bistability, the phenomena of optical self-oscillations and switchover when the exciton–photon interaction and the Coulomb binding of two excitons into a single biexciton introduced in Refs. 28 and 29 are taken into account. The Heisenberg equations of motion for excitons and biexcitons and a wave equation for the field are used to derive a system of nonlinear differential equations describing the dynamical evolution of the system. In the time-independent (stationary) case we derive an equation of state of the optical bistability theory. We also study the stability of time-independent solutions and predict the formation of regular and chaotic self-pulsations. The scenario of the transition to dynamic optical chaos is established, and we discuss the possibility of optical turbulence. Finally, we examine the switchover times between the optical bistability branches and the phenomenon of dynamic optical bistability for the case where external pumping is a function of time having parabolic form.

2. THE HAMILTONIAN AND THE BASIC EQUATIONS OF THE PROBLEM

A distinctive feature of the present stage in studying optical bistability is that the geometry of the experiment is a decisive factor. Suppose that a monochromatic coherent electromagnetic wave is incident on a ring cavity with a semiconductor specimen of length L and that the wave generates excitons that are Bogolyubov-coherent. Owing to the Coulomb interaction,[28,29] the excitons may form biexcitons. This process, which ensures that the problem is nonlinear, is determined by the term $(1/\sqrt{V})Db^{\dagger}aa$.

The system Hamiltonian is the sum of three Hamiltonians (the Hamiltonian of the free excitons, the Hamiltonian of the free biexcitons, and the field Hamiltonian) and the interaction Hamiltonian, which consists of a term responsible for the interaction of coherent excitons and the electromagnetic field and a term responsible for the interaction of coherent excitons and coherent biexcitons. In our model the interaction Hamiltonian can be written as follows:

$$H_{\text{int}}=i\hbar g(aE^{+}-a^{\dagger}E)+i\hbar D(ba^{\dagger}a^{\dagger}-b^{\dagger}aa), \tag{1}$$

where $a^{\dagger}$ and $b^{\dagger}$ are the exciton and biexciton creation operators, g is the exciton–photon coupling constant, D is the constant of direct binding of two excitons into a biexciton, and E^{+} is the positive-frequency part of the electric field in the electromagnetic wave. Here and in what follows we assume that the system has unit volume and drop the wave vector labels.

The equations of motion for the exciton amplitude a and the biexciton amplitude b are

$$\frac{da}{dt}=-i\omega_{\text{ex}}a-gE+2Dba^{\dagger}-\gamma_{\text{ex}}a, \tag{2}$$

$$\frac{db}{dt}=-i\omega_{\text{biex}}b-Daa-\gamma_{\text{biex}}b, \tag{3}$$

where $\hbar\omega_{\text{ex}}$ and $\hbar\omega_{\text{biex}}$ are the energy of exciton and biexciton formation, and γ_{ex} and γ_{biex} are the decay constants for excitons and biexcitons, respectively, which determine the rate at which the quasiparticles leave the coherent modes for the incoherent. These constants were introduced into the equations phenomenologically. Note that the equations were obtained strictly within the quantum theory of fluctuations and dissipation from the flux part of the respective Fokker–Planck equation.[30]

The equation of motion of the component E of the electromagnetic field is equivalent to the wave equation

$$c_1^2\frac{\partial^2 E}{\partial z^2}-\frac{\partial^2 E}{\partial t^2}=-4i\pi\hbar g\frac{\partial^2 a}{\partial t^2}, \tag{4}$$

where c_1 is the speed with which the field propagates in the semiconductor.

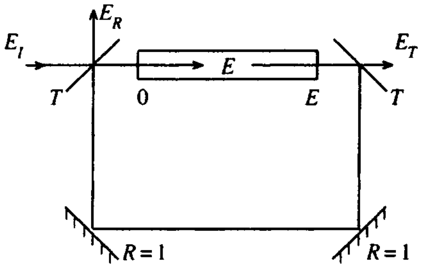

FIG. 1. Ring cavity diagram: E_I, E_R, and E_T are the amplitudes of the incident, reflected, and transmitted fields, respectively; and T is the transmission coefficient of the cavity mirrors.

We write the exciton, biexciton, and field amplitudes in the form of modulated plane waves:

$$\begin{aligned} a(z,t)&=A'(z,t)e^{i(kz-\omega t)},\\ b(z,t)&=B'(z,t)e^{2i(kz-\omega t)},\\ E(z,t)&=E'(z,t)e^{i(kz-\omega t)}, \end{aligned} \tag{5}$$

where ω and k are the carrier frequency and the wave vector, and $A'(z,t)$, $B'(z,t)$, and $E'(z,t)$ are slowly varying amplitudes.

Below in our calculations we use the truncated equation approximation, which is valid if

$$\left|\frac{\partial E'}{\partial t}\right|\ll\omega|E'|, \quad \left|\frac{\partial E'}{\partial z}\right|\ll k|E'|,\dots .$$

Substituting (5) in (2)–(4), using the approximation of slowly varying amplitudes, and ignoring the effects of spatial dispersion of excitons and biexcitons (which are unimportant in the region of the spectrum of interested to us), we get

$$\frac{dA'}{dt}=i(\omega-\omega_{\text{ex}})A'-gE'+2DB'A'^{\dagger}-\gamma_{\text{ex}}A', \tag{6}$$

$$\frac{dB'}{dt}=i(2\omega-\omega_{\text{biex}})B'-DA'A'-\gamma_{\text{biex}}B', \tag{7}$$

$$\frac{\partial E'}{\partial t}+\frac{kc_1^2}{\omega}\frac{\partial E'}{\partial z}=2\pi\hbar\omega gA'+\frac{\omega^2-c_1^2k^2}{2\omega}E'. \tag{8}$$

In what follows it is convenient to introduce dimensionless variables:

$$X=\frac{E'}{E_s}, \quad B=\frac{B'}{B_s}, \quad A=\frac{A'}{A_s},$$

$$E_s=\frac{\gamma_{\text{biex}}^2}{gD}, \quad A_s=B_s=\frac{\gamma_{\text{biex}}}{D},$$

and $C=\alpha L/4T$ is the optical bistability constant, with

$$\alpha=\frac{4\pi\hbar g^2\omega^2}{c_1k\gamma_{\text{ex}}},$$

and T the transmission coefficient of the cavity mirrors (Fig. 1); $d=\gamma_{\text{ex}}/\gamma_{\text{biex}}$ is the relative decay of an exciton in comparison to a biexciton; $\delta_0=(2\omega_{\text{ex}}-\omega_{\text{biex}})/\gamma_{\text{biex}}$ is the reduced biexciton energy; $\delta_1=(\omega-\omega_{\text{ex}})/\gamma_{\text{biex}}$ is the dimensionless detuning from an exciton level; $\sigma=C_1^2kT/K\gamma_{\text{biex}}\omega$

is the damping of the electric field amplitude in the cavity (the cavity's Q-factor); $\tau=\gamma_{\text{biex}}t$ is the dimensionless time variable; and

$$\Delta_1=\frac{\omega^2-c_1^2k^2}{2\omega\gamma_{\text{biex}}}.$$

With allowance for the normalized quantities, the system of equations (6)–(8) becomes

$$\frac{dX}{d\tau}=i\Delta_1X-\frac{\sigma L}{T}\frac{\partial X}{\partial z}+2C\sigma A, \tag{9}$$

$$\frac{dA}{d\tau}=i\delta_1A+iX-2iBA^*-dA, \tag{10}$$

$$\frac{dB}{d\tau}=i(2\delta_1+\delta_0)B-iAA-B. \tag{11}$$

As noted earlier, the semiconductor is placed inside a ring cavity between two mirrors with a transmission coefficient T. The other two mirrors are assumed ideal. The boundary conditions for the ring cavity are

$$E(0,t)=\sqrt{T}E_I+RE(L,t-\Delta t)e^{iF},$$

$$E_T=\sqrt{T}E(L,t),$$

where E_I is the amplitude of the pump field (at the entrance to the cavity), E_T is the field amplitude at the the cavity's exit, $R=1-T$ is the reflection coefficient of the cavity mirrors, $\Delta t=(L+2l)/c_0$ is the time lag introduced by feedback, with c_0 the speed of light in vacuum, and $F=kL+k_0(2l+L)$ is the phase increment of the field in the cavity, with k_0 the wave vector of the field in vacuum.

Introducing the dimensionless input and output field amplitudes,

$$E_I=\frac{Y}{E_s}\sqrt{T},\quad E_T=\frac{X}{E_s}\sqrt{T},$$

we arrive at the boundary conditions for the normalized amplitudes:

$$\begin{gathered}TY+R[X_1(L,\tau-\Delta\tau)\\ \times\cos F-X_2(L,\tau-\Delta\tau)\sin F]=X_1(0,\tau),\\ R[X_1(L,\tau-\Delta\tau)\sin F+X_2(L,\tau-\Delta\tau)\cos F]=X_2(0,\tau),\end{gathered} \tag{12}$$

where X_1 and X_2 are the real and imaginary parts of the field strength.

Below we employ the widely used mean-field approximation.[2] Meystre was the first to propose this model[31] in studying optical bistability in a system of two-level atoms inside a ring cavity. We assume that all functions describing optical bistability are weakly dependent on the spatial variable, so that for the entire space within the cavity they are assumed constant, i.e., independent of position. The validity of the mean-field approximation for a Fabry–Perot cavity was discussed by Bischoferger and Shen.[32] In particular, it was found that at large values of the optical bistability constant and small values of the transmission coefficient the results of the mean field theory are equivalent to the exact numerical solution of the Maxwell–Bloch equations. The mean-field method was employed in Refs. 5, 6, and 15–19 to study optical bistability in a system of excitons and biexcitons.

Using the mean-field approximation

$$\int_0^L E'(z)dz\approx[E'(L)-E'(0)]L \tag{13}$$

and the boundary conditions (12), from Eqs. (9)–(11) we obtain a system of nonlinear differential equations describing the temporal evolution of coherent photons, excitons, and biexcitons:

$$\begin{aligned}\frac{dX_1}{d\tau}=&-\Delta_1X_2-\frac{\sigma(1-R\cos F)}{T}X_1-\frac{\sigma R\sin F}{T}X_2\\ &+2C\sigma A_1+\sigma Y,\end{aligned} \tag{14}$$

$$\begin{aligned}\frac{dX_2}{d\tau}=&\Delta_1X_1-\frac{\sigma(1-R\cos F)}{T}X_2+\frac{\sigma R\sin F}{T}X_1\\ &+2C\sigma A_2,\end{aligned} \tag{15}$$

$$\frac{dA_1}{d\tau}=-dA_1-\delta_1A_2-X_1+2(B_1A_1+B_2A_2), \tag{16}$$

$$\frac{dA_2}{d\tau}=-dA_2+\delta_1A_1+X_2+2(B_2A_1-B_1A_2), \tag{17}$$

$$\frac{dB_1}{d\tau}=-(2\delta_1+\delta_0)B_2-B_1-A_1^2+A_2^2, \tag{18}$$

$$\frac{dB_2}{d\tau}=(2\delta_1+\delta_0)B_1-B_2-2A_1A_2, \tag{19}$$

where we have allowed for the fact that X, A, and B are complex-valued quantities: $X_1=\operatorname{Re}X$, $X_2=\operatorname{Im}X$, $A_1=\operatorname{Re}A$, $A_2=\operatorname{Im}A$, $B_1=\operatorname{Re}B$, and $B_2=\operatorname{Im}B$.

At present there is no standard algorithm for solving general nonlinear differential equations, so that obtaining analytic solutions of the system of equations (14)–(19) is an extremely difficult (if not impossible) problem. In this connection we did a numerical experiment and analyzed the stability of time-independent states.

Note that our system of equations (14)–(19) is a particular case of the theory of evolution of a system of type $\dot{\mathbf{X}}=\mathbf{F}(\mathbf{X})$, where $\mathbf{X}$ is a vector in the R^n space ($n>1$), with each component of $\mathbf{X}$ describing a single mode, and $\mathbf{F}(\mathbf{X})$ is the vector field of the system.

For dissipative systems the volume of the phase space decreases, since the divergence of $\dot{\mathbf{X}}$ is negative:

$$\operatorname{div}\dot{\mathbf{X}}=\operatorname{div}\mathbf{F}=\sum_{i=1}^{n}\frac{\partial\mathbf{F}_i}{\partial\mathbf{X}_i}<0.$$

The evolution of the system of equations (14)–(19) largely depends on the evolution of a small volume of the phase space of this system. If we consider the motion of points in the phase space as that of a liquid with a divergence

$$\frac{\partial\dot{X}_1}{\partial X_1}+\frac{\partial\dot{X}_2}{\partial X_2}+\frac{\partial\dot{A}_1}{\partial A_1}+\frac{\partial\dot{A}_2}{\partial A_2}+\frac{\partial\dot{B}_1}{\partial B_1}+\frac{\partial\dot{B}_2}{\partial B_2}$$

$$= -2\left[1+d+\frac{\sigma(1-R\cos F)}{T}\right],$$

we conclude that any small volume of the phase space of the system of equations (14)–(19) tends to zero as $\tau\rightarrow\infty$ at a rate equal to $[2+2d+2\sigma(1-R\cos F)/T]^{-1}$. If the stationary states of the system are unstable, the attractors in the phase space can be a limit cycle, a torus, and a strange attractor. They correspond, respectively, to nonlinear periodic, quasiperiodic, and stochastic self-oscillations in the system.

In the stationary case, from Eqs. (14)–(19) we obtain equations that relate the densities of the coherent excitons and biexcitons to the field intensity,

$$Z_e\left[\left(d+\frac{2Z_e}{1+\delta_2^2}\right)^2+\left(\frac{2\delta_2 Z_e}{1+\delta_2^2}-\delta_1\right)^2\right]=X_{st}^2, \qquad (20)$$

$$Z_b=\frac{Z_e^2}{1+\delta_2^2}, \qquad (21)$$

and the equation of state of optical bistability theory, which relates the field intensities at the entrance to, and exit from, the cavity,

$$Y_{st}^2=X_{st}^2\left\{\left[\frac{1-R\cos F}{T}+\frac{2CQ_1}{Q}\right]^2+\left[\frac{\Delta_1}{\sigma}+\frac{R}{T}\sin F-\frac{2CQ_2}{Q}\right]^2\right\}, \qquad (22)$$

where $Z_e=A_1^2+A_2^2$ is the exciton density, $Z_b=B_1^2+B_2^2$ is the biexciton density, $X_{st}=\sqrt{X_1^2+X_2^2}$ is the field amplitude inside the crystal, $\delta_2=2\delta_1+\delta_0$, and

$$Q_1=d+\frac{2Z_e}{1+\delta_2^2},\quad Q_2=\delta_1-\frac{2\delta_2 Z_e}{1+\delta_2^2},\quad Q^2=Q_1^2+Q_2^2.$$

Equation (22) is the equation of state of optical bistability theory in a system of coherent excitons and biexcitons with paired excitons bound into biexcitons due to the Coulomb interaction. It is an analog of the equations of state in the theory of two-level media and the exciton region of the spectrum,[6,15,33] but differs considerably from the latter. In contrast to Eqs. (20) and (21), which determine the nonlinear dependence between the densities of coherent excitons and excitons and the electromagnetic field and lead to bistabilities of the density–light type, Eq. (22) describes the dependence of the light intensity at the exit from the cavity on the light intensity and the entrance. Under certain conditions this equation leads to a bistability of the light–light type.

3. COMPUTER EXPERIMENT: STATIONARY AND NONSTATIONARY OPTICAL BISTABILITY AND SELF-PULSATIONS

It is interesting to study the stability of stationary states in connection with the possibility of optical nonlinear self-pulsations emerging in a system of coherent quasiparticles.

The characteristic equation for the Jacobian of the system is

$$|\lambda E-J|=\begin{vmatrix} -\lambda-P_1 & -P_2 & 2C\sigma & 0 & 0 & 0\\ P_2 & -\lambda-P_1 & 0 & 2C\sigma & 0 & 0\\ -1 & 0 & -\lambda-d+2B_1 & -\delta_1+2B_2 & 2A_1 & 2A_2\\ 0 & -1 & \delta_1+2B_2 & -\lambda-d-2B_1 & -2A_2 & 2A_1\\ 0 & 0 & -2A_1 & 2A_2 & -\lambda-1 & -\delta_2\\ 0 & 0 & -2A_2 & 2A_1 & \delta_2 & -\lambda-1 \end{vmatrix},$$

where

$$P_1=\frac{\sigma(1-R\cos F)}{T},\quad P_2=\Delta_1+\frac{\sigma R\sin F}{T},$$

and E is the identity matrix. If the real parts of all the roots of the characteristic equation are negative, the corresponding stationary states are stable with respect to small perturbations. If we use the Routh–Hurwitz criterion, we can show that a section of the X_{st} vs. Y_{st} curve is unstable. Figure 2 depicts the stationary nonlinear dependence of the amplitude X_{st} of the transmitted field on the amplitude Y_{st} of the incident field at $\delta_0=5$, $C=5$, $F=2\pi n$, $\Delta_1=0$, and $\delta_1=10$. The figure shows that at such values of the parameters there is no optical bistability of the light–light type. The resulting instability window is depicted by a dashed curve. At point A, corresponding to the beginning of the instability region in a system of coherent quasiparticles, periodic self-pulsations emerge, and the phase trajectory becomes a limit cycle (Fig.

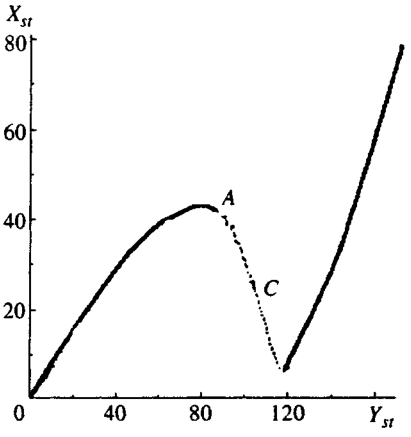

FIG. 2. Stationary dependence of the amplitude X_{st} of the transmitted field on the amplitude Y_{st} of the incident field for the following values of the parameters: $\delta_0=5$, $C=5$, $F=2\pi n$, $\Delta_1=0$, and $\delta_1=10$ (both X_{st} and Y_{st} are measured in volts per centimeter).

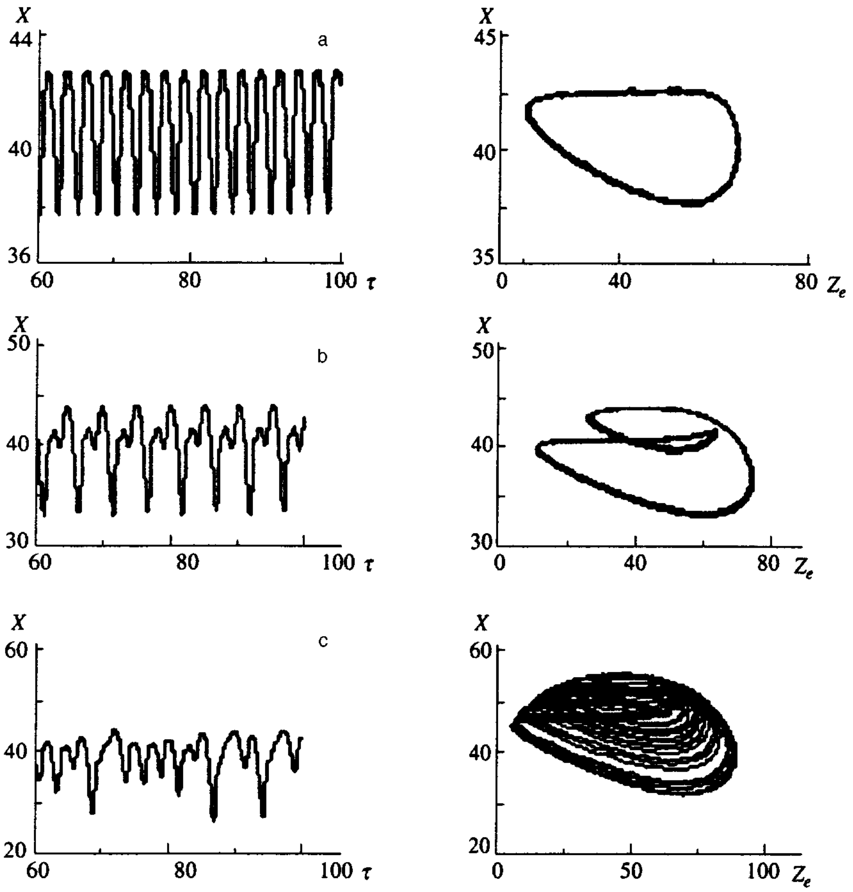

FIG. 3. Oscillations in a ring cavity (left) and their phase portraits in the $X-Z_e$ plane(right) at $\delta_0=5$, $C=5$, $F=2\pi n$, $\Delta_1=0$, $\delta_1=10$, $\sigma=1$, $d=0.1$, $T=0.01$ for different values of the pump field: (a) $Y=82.5$, (b) $Y=83$, and (c) $Y=85$ (X is measured in volts per centimeter, τ in 10^{-12} s, and Z_e in 10^{14} cm^{-3}.

3a). As the representative point moves closer to the center, the oscillation instability windows become more complicated. One can observe a cascade of bifurcations of oscillation-period doubling (Fig. 3b), as a result of which a stochastic self-oscillation mode emerges in the middle section of the instability window. This leads to optical turbulence in the system of coherent excitons, photons, and biexcitons. Figure 3c depicts a stochastic self-modulating process and the corresponding projections of the phase trajectories onto the $X-Z_e$ plane at a pump amplitude $Y=85$. The surface in the phase space to which the phase trajectories converge varies with pump intensity. In contrast to the famous Lorentz dynamic chaos, where stochastic oscillations and the creation of a strange attractor are related to hops between the corresponding equilibrium states, in the present case the stochasticity is related to the creation of a strange attractor in a six-dimensional phase space, which is filled in a complicated manner by nonintersecting phase trajectories.

As the pump intensity is increased, the strange attractor finally becomes unstable and transforms into a stable limit cycle, with nonlinear regular periodic self-pulsations setting in in the system.

As the detuning δ_1 from resonance between the frequency of the external electromagnetic field and the exciton frequency increases, the stationary dependence between the amplitude of the transmitted field on the amplitude of the incident (pump) field, $X_{st}(Y_{st})$, changes substantially. For small values of Y_{st} the dependence is linear and unique. As Y_{st} grows, the dependence becomes nonlinear and at certain values of the parameters, multivalued.

Figure 4a depicts the stationary dependence of the amplitude X_{st} of the transmitted field on the amplitude Y_{st} of the incident field at $\cos F=1$, $C=5$, $\Delta_1=0$, $\delta_1=30$, $\delta_0=5$, and $\sigma=10$. Clearly, at such values of the parameters a three-valued region develops, in which for one value of Y_{st} there are three values of X_{st}. When Y_{st} is low, the amplitude if the transmitted field increases with Y_{st} along the upper branch of the hysteresis curve. At a certain value of Y_{st} the systems jumps to the lower branch of the curve along which X_{st} increases with Y_{st}. If we decrease the amplitude of the incident field, the representative point moves along the lower branch of the hysteresis curve and then jumps to the upper branch, along which X_{st} decreases further as Y_{st} decreases. The dashed section of the curve depicts the unstable part of the X_{st} vs. Y_{st} dependence. Thus, stationary optical bistability emerges in the system of coherent excitons, photons, and biexcitons. In contrast to the model of two-level atoms, where optical bistability is realized in counterclockwise movement, here optical bistability is realized in clockwise movement. Research has shown that at such values of the parameters both optical bistability branches are stable. Hence it is interesting to study the switchover time between the two branches. Such a study is based on the system of equations (14)–(19). We have done a computer experiment in which the initial conditions are chosen so that they correspond to the value of the pump field amplitude Y_{st} near the downward

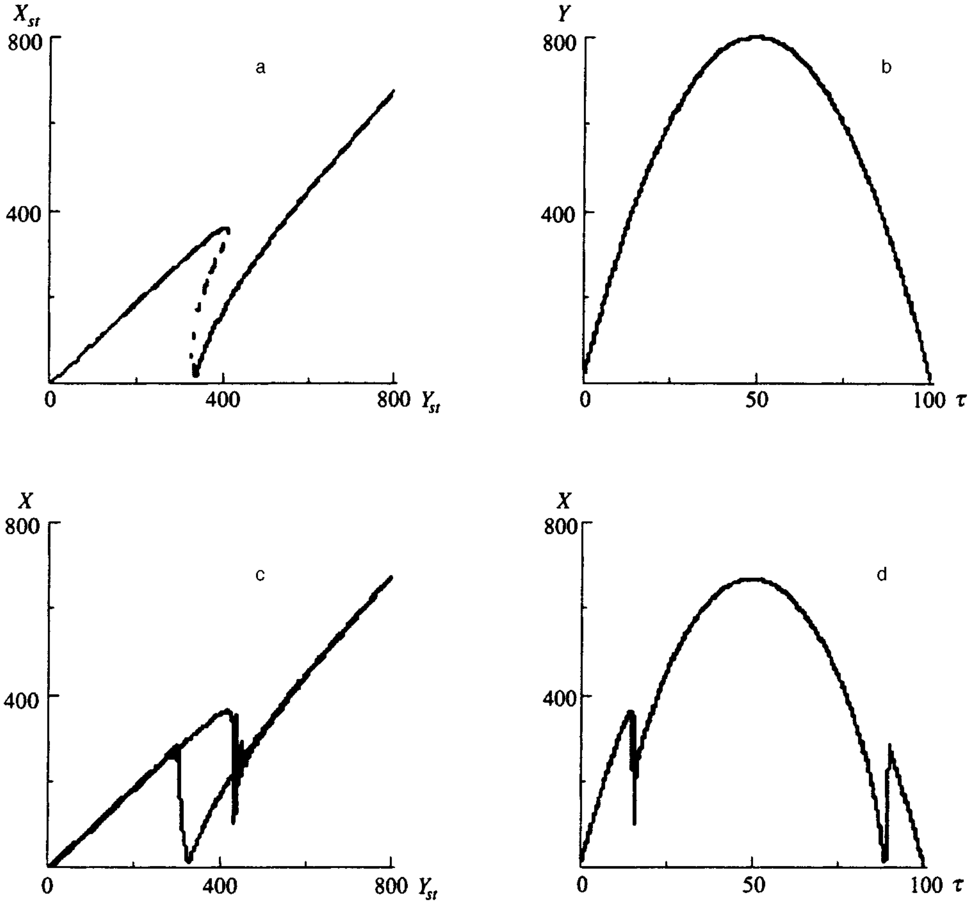

FIG. 4. (a) Stationary dependence of the amplitude X_{st} of the transmitted field on the amplitude Y_{st} of the incident field at $\delta_0=5$, $C=5$, $F=2\pi n$, $\Delta_1=0$, $\delta_1=30$, $\sigma=1$, $d=0.1$, and $T=0.01$; (b) shape of incident pulse; (c) dynamic optical bistability; and (d) shape of pulse at the exit from the cavity.

switchover threshold. At time $\tau=0$ we specify the jump in Y_{st} so that $Y_{st}+\Delta Y$ decreases on the other side of the corresponding switchover threshold. Figure 5 depicts both switchover modes: (a) from the upper branch of the optical bistability curve to the lower, and (b) from the lower branch to the upper. We see that the switchover times are of the same order of magnitude and amount to $4\gamma_{\mathrm{biex}}$. Since the relaxation times t of excitons and biexcitons are approximately 10^{-10}–10^{-12} s, optical switchover times in the system of coherent excitons and biexcitons are in the picosecond range, which makes it possible to use this optical bistability mechanism for designing high-speed optical memory cells.

When the Q-factor of the cavity is lowered, switchover becomes accompanied by oscillations, which reduces the effectiveness of operation of the bistable element.

At $F=\pi/2+2\pi n$, $C=5$, $\Delta_1=0$, $\delta_1=-30$, $\delta_0=5$, and $\sigma=1$, a hysteresis in the form a figure-eight develops in the system (Fig. 6a). For this to happen the strength of the incident field must be high.

In optical bistability experiments one often observes not stationary optical bistability but dynamic optical bistability,

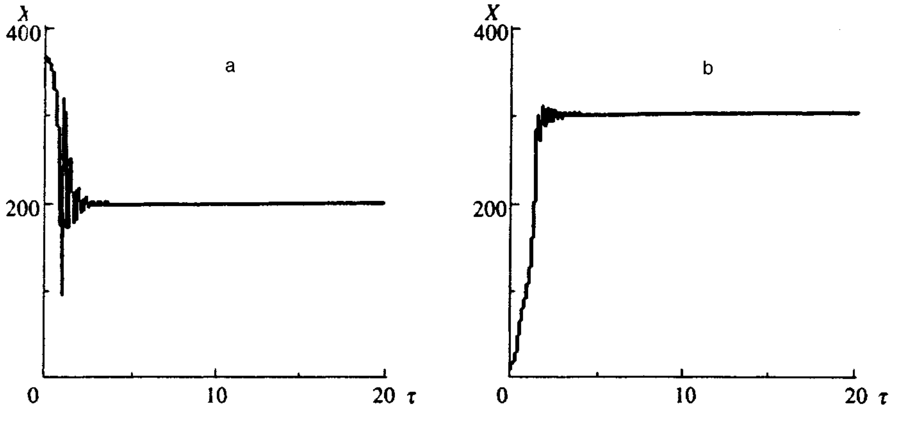

FIG. 5. Optical switchover from the upper branch of the optical bistability curve to the lower branch (a), and vice versa (b).

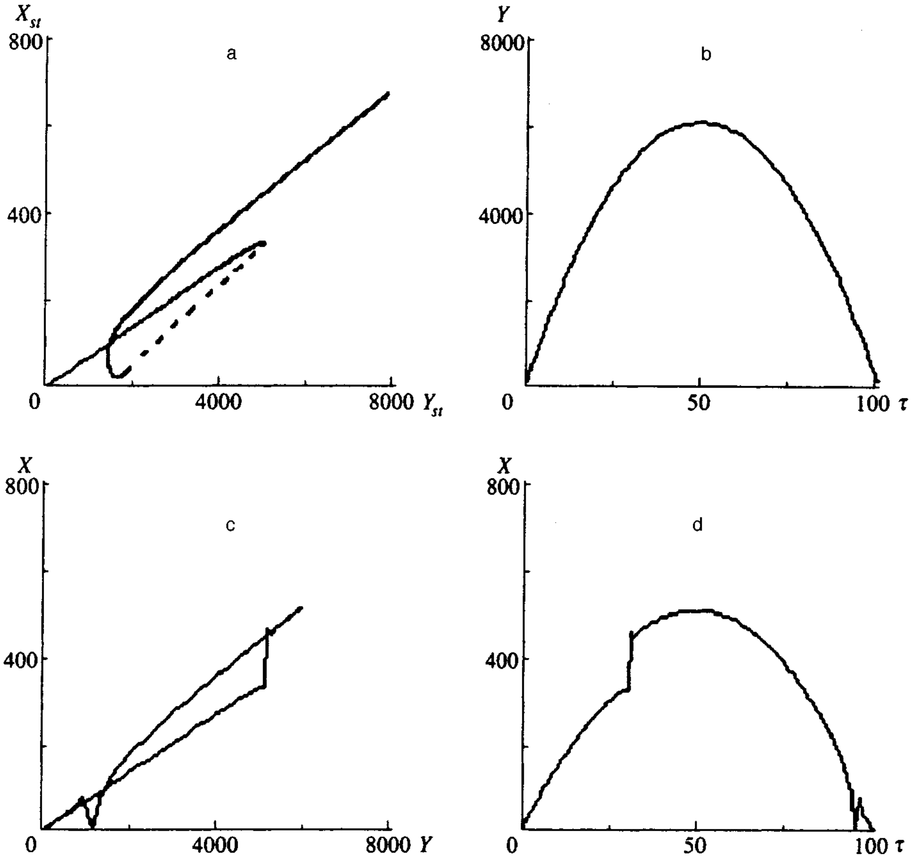

FIG. 6. (a) Stationary dependence of the amplitude X_{st} of the transmitted field on the amplitude Y_{st} of the incident field at $\delta_0=5$, $C=5$, $F=\pi/2+2n\pi$, $\Delta_1=0$, $\delta_1=-30$, $\sigma=1$, $d=0.1$, and $T=0.01$; (b) shape of incident pulse; (c) dynamic optical bistability; and (d) shape of pulse at the exit from the cavity.

obtained as a result of comparing the time-dependent pump field with the corresponding response of the system. Bischofberger and Shen[32] were the first to study optical bistability of this type. They studied both theoretically and experimentally the behavior of a nonlinear Fabry–Perot interferometer filled with a Kerr medium to which pulses of different shape were applied. The agreement between theoretical and experimental data was perfect.

We solved the system of nonlinear differential equations (14)–(19) numerically with allowance for the boundary conditions for a ring cavity where $Y(\tau)$ is parabolic function of time. The results of the computer experiment are depicted in Figs. 4b–4d for $F=2\pi n$, $C=5$, $\Delta_1=0$, $\delta_1=30$, $\delta_0=5$, $\sigma=10$, $d=0.1$, and $T=0.01$ and in Figs. 6b–6d for $F=\pi/2+2n\pi$, $C=5$, $\Delta_1=0$, $\delta_1=-30$, $\delta_0=5$, $\sigma=1$, $d=0.1$, and $T=0.01$. Figures 4b and 6d display, respectively, the temporal shape of the incident and transmitted electromagnetic fields, with the pulse length τ being equal to 100 ($t=100\times10^{-12}$ s). Figure 4d shows that the pulse is deformed after it has travelled through the cavity. Figure 4c displays the dependence of the amplitude of the transmitted field on the amplitude of the incident field. We see that in this case dynamic optical bistability emerges in the system of coherent excitons, photons, and biexcitons, with the direction of bistability being clockwise. If the pulses are made shorter, the system is unable to react to their passage, with the result that they are not deformed.

In conclusion we discuss the possibility of observing these effects in experiments. Here are numerical estimates of crystals of the CdS type, in which $\hbar D=10^{-9}$ eV cm$^{3/2}$, $\hbar g=0.1$ eV cm$^{-1/2}$ V^{-1}, $\hbar\omega=2$ eV, $\hbar c_0k_0\approx2$ eV, $\hbar\gamma_{\text{ex}}=10^{-5}$ eV, $\hbar\gamma_{\text{biex}}=10^{-4}$ eV, $T=0.01$, $L=10^{-6}$ m, and $\hbar(2\omega-\omega_{\text{biex}})=-0.0.4$ eV. The critical power at which it is possible to observe these nonlinear phenomena is $P\sim40\times10^3$ W cm^{-2}. Here the exciton and biexciton densities are of order 10^{16} cm^{-3} and 10^{14} cm^{-3}, respectively. The upward switchover time $t_\uparrow$ is approximately 2×10^{-12} s, the downward switchover time $t_\downarrow$ is approximately 4×10^{-12} s, and the switchover energy is of order 50×10^{-12} J.

Thus, our numerical estimates suggest that optical hysteresis loops, switchover, and self-pulsations in the system of excitons and biexcitons in semiconductors with paired excitons bound into biexcitons can indeed be observed.

Note that these chaotic self-oscillations, which occur because of the instability of the stationary states, are one more example of the formation of temporal structures in nonlinear dynamical systems. At the same time, the initial equations are nonlinear partial differential equations describing the space–time evolution of coherent quasiparticles in condensed media. As is known, equations of this type allow for the development of spatial turbulence.[34] Aranson *et al.*[34] discovered a new class of transitions of the ''order–chaos'' type in the form of moving transition fronts. Similar phenomena can occur in a system of coherent excitons, photons, and biexcitons. In addition to dynamic optical turbulence, spatial turbulence can develop and ''order–chaos'' and ''chaos–order'' structures can emerge.

[1] V. F. Elesin and Yu. V. Kopaev, Zh. Éksp. Teor. Fiz. **62**, 1447 (1972) [Sov. Phys. JETP **35**, 760 (1972)].

[2] H. Gibbs, *Optical Bistability: Controlling Light with Light*, Academic Press, New York (1985).

[3] V. A. Kochelap, L. Yu. Melnikov, and V. N. Sokolov, Fiz. Tekh. Poluprovodn. **16**, 1167 (1982) [Sov. Phys. Semicond. **10**, 746 (1982)].

[4] V. A. Kochelap, L. Yu. Melnikov, and V. N. Sokolov, Kvant. Elektron. (Kiev) No. 24, 42 (1987).

[5] A. Kh. Rotaru and V. A. Zalozh, *Optical Self-organization of Excitons and Biexcitons in Semiconductors* [in Russian], Shtiintsa, Kishinev (1990).

[6] P. I. Khadzhi, G. D. Shibarshina, and A. Kh. Rotaru, *Optical Bistability in a System of Excitons and Biexcitons in Semiconductors* [in Russian], Shtiintsa, Kishinev (1988).

[7] A. M. Bakiev, V. S. Dneprovskiĭ, Z. D. Kovalyuk, and V. A. Stadnik, JETP Lett. **38**, 596 (1983).

[8] V. S. Dneprovskiĭ, Usp. Fiz. Nauk **145**, 149 (1985) [Sov. Phys. Usp. **28**, 93 (1985)].

[9] V. S. Dneprovskiĭ, Izv. Akad. Nauk SSSR, Ser. Fiz. **50**, 661 (1986).

[10] A. H. Rotaru and G. D. Shibarshina, Phys. Lett. **109**, 292 (1985).

[11] A. Kh. Rotaru, Fiz. Tverd. Tela (Leningrad) **29**, 3282 (1987) [Sov. Phys. Solid State **29**, 1883 (1987)].

[12] A. Kh. Rotaru, Fiz. Tverd. Tela (Leningrad) **28**, 2492 (1986) [Sov. Phys. Solid State **28**, 1393 (1986)].

[13] A. U. Bobrysheva, V. A. Zalozh, and A. Kh. Rotaru, Fiz. Tverd. Tela (Leningrad) **33**, 915 (1991) [Sov. Phys. Solid State **33**, 518 (1991)].

[14] V. A. Zalozh, S. A. Moskalenko, and A. Kh. Rotaru, Zh. Éksp. Teor. Fiz. **95**, 601 (1989) [Sov. Phys. JETP **68**, 338 (1989)].

[15] B. Sh. Parkanskiĭ and A. Kh. Rotaru, Zh. Éksp. Teor. Fiz. **99**, 899 (1991) [Sov. Phys. JETP **72**, 499 (1991)].

[16] B. Sh. Parkanskiĭ and A. Kh. Rotaru, Fiz. Tverd. Tela (Leningrad) **33**, 2250 (1991) [Sov. Phys. Solid State **33**, 1268 (1991)].

[17] B. Sh. Parkanskiĭ and A. Kh. Rotaru, Fiz. Tverd. Tela (Leningrad) **33**, 3378 (1991) [Sov. Phys. Solid State **33**, 1905 (1991)].

[18] V. A. Zalozh, A. Kh. Rotaru, and V. Z. Tronchu, Zh. Éksp. Teor. Fiz. **103**, 994 (1993) [JETP **76**, 487 (1993)].

[19] V. A. Zalozh, A. Kh. Rotaru, and V. Z. Tronchu, Zh. Éksp. Teor. Fiz. **105**, 260 (1994) [JETP **78**, 138 (1994)].

[20] A. Kh. Rotaru and S. V. Shura, Zh. Éksp. Teor. Fiz. **104**, 2374 (1993) [JETP **77**, 60 (1993)].

[21] A. Kh. Rotaru and S. V. Shura, Zh. Éksp. Teor. Fiz. **107**, 450 (1995) [JETP **80**, 240 (1995)].

[22] V. P. Mis'ko, S. A. Moskalenko, A. Kh. Rotaru, and Yu. M. Shvera, Zh. Éksp. Teor. Fiz. **99**, 1215 (1991) [Sov. Phys. JETP **72**, 676 (1991)].

[23] A. E. Barbéroshie, I. I. Gontsya, Yu. N. Nika, and A. Kh. Rotaru, Zh. Éksp. Teor. Fiz. **104**, 2655 (1993) [JETP **77**, 211 (1993)].

[24] A. Kh. Rotaru and K. V. Shura, Fiz. Tverd. Tela (Leningrad) **33**, 1973 (1991) [Sov. Phys. Solid State **33**, 1111 (1991)].

[25] A. A. Gogolin and É. I. Rashba, JETP Lett. **17**, 478 (1973).

[26] É. I. Rashba, Fiz. Tekh. Poluprovodn. **8**, 1241 (1974) [Sov. Phys. Semicond. **8**, 807 (1974)].

[27] E. Hanamura, Solid State Commun. **12**, 951 (1973).

[28] A. L. Ivanov and V. V. Panashchenko, JETP Lett. **49**, 39 (1989).

[29] A. L. Ivanov, L. V. Keldysh, and V. V. Panashchenko, Zh. Éksp. Teor. Fiz. **99**, 641 (1991) [Sov. Phys. JETP **72**, 359 (1991)].

[30] S. A. Moskalenko, A. Kh. Rotaru, and Yu. M. Shvera, Teor. Mat. Fiz. **75**, 295 (1988).

[31] P. Meystre, Opt. Commun. **26**, 277 (1978).

[32] T. Bischoferger and Y. Shen, Phys. Rev. A **19**, 1169 (1979).

[33] R. Bonifacio and L. Lugiato, Lett. Nuovo Cimento **21**, 510 (1978).

[34] I. S. Aranson, A. V. Gaponov-Grekhov, M. I. Rabinovich, and N. M. Starobinets, Zh. Éksp. Teor. Fiz. **90**, 1707 (1986) [Sov. Phys. JETP **63**, 1000 (1986)].

Translated by Eugene Yankovsky

Magnetoexciton absorption in coupled quantum wells

Yu. E. Lozovik*)

Institute of Spectroscopy, Russian Academy of Sciences, 142092 Troitsk, Moscow Region, Russia

A. M. Ruvinskiĭ

Moscow Institute of Steel and Alloys, 117936 Moscow, Russia

(Submitted 2 April 1997)
Zh. Éksp. Teor. Fiz. **112**, 1791–1808 (November 1997)

A Mott exciton in coupled quantum wells in a transverse magnetic field H is considered. An expression for the exciton spectrum in an arbitrary magnetic field for large separations D between quantum wells containing an electron (e) and a hole (h) is given. The exciton spectrum in a strong magnetic field for different Landau levels at arbitrary D has been calculated. Changes in the parameter D/l, where $l=\sqrt{\hbar c/eH}$ is the magnetic length, cause rearrangement of the magnetoexciton dispersion curves $\mathscr{E}(P)$, where $\mathbf{P}$ is the conserved ''magnetic'' momentum, which is a function of the separation between the electron and hole in the plane of the quantum wells. Off-center (''roton'') extrema occur only for $D/l<(D/l)_{\rm cr}$, where $(D/l)_{\rm cr}$ is a function of the exciton quantum numbers n and m. The magnetoexciton effective mass in states with magnetic quantum number $m=0$ monotonically increases with H and D, while in states with $m\neq 0$ it is a nonmonotonic function of D/l. The probability of generating an exciton in coupled quantum wells increases with H. Absorption of electromagnetic radiation due to transitions between excitonic levels in coupled quantum wells is discussed. For an exciton containing a heavy hole the oscillator strengths $f_{n_1 m}^{n_2 m+1}$ increase with H and the oscillator strengths $f_{n_1 m}^{n_2 m-1}$ decrease.
[S1063-7761(97)01911-2]

1. INTRODUCTION

Exciton systems containing electrons (e) and holes (h) in different quantum wells in a structure with coupled wells have attracted considerable attention recently,[1–7] in particular, owing to predictions of superfluidity of $e-h$ pairs that should manifest itself as persistent electric currents.[8–10] Interesting Josephson-like effects have also been predicted (see Refs. 11–14 and references therein).

Very interesting properties have been displayed by two-dimensional exciton systems in strong magnetic fields.[15–21] Theoretical studies[15,17–20] have shown, in particular, that the ground state of such systems is an ideal gas of excitons at any density. This result is in good agreement with experimental data (see Refs. 22 and 23 and references therein). Moreover, exact solutions for the ground state (which corresponds to a Bose condensate of nonbosons) and for some excited states of planar $e-h$ systems on one Landau level[17] have been obtained using the supersymmetry of the studied system.[17,19,20] In the case of spatially separated $e-h$ systems, the supersymmetry is broken, and an interesting question of the system phase diagram arises (see Refs. 10, 24–27 and references therein).

Pairs composed of spatially separated electrons and holes (indirect excitons) can condense in a liquid phase and for other phases,[10,24–27] some of which are similar to phases of three-dimensional exciton systems.[28–31] These phases can exists only under the condition that the exciton lifetime is much longer than the thermalization time. This condition can be satisfied in excitons containing electrons and holes in different quantum wells, since recombination of electrons and holes is slower due to the small overlap of the electron and hole wave functions. An electric field perpendicular to the semiconducting layers also leads to a smaller overlap between electron and hole wave functions, and hence a slower recombination rate. Recent experimental studies of exciton spectra in double and coupled quantum wells[6,7] have also stimulated investigation of properties of an isolated exciton composed of spatially separated electron and hole as a first step in developing the theory of such systems.

In Sec. 2 an exciton spectrum in an arbitrary magnetic field at large separations between quantum wells (when the size of the $e-h$ bound state in the quantum well plane is smaller than the separation D between the wells) is derived analytically. The exciton energy in a strong magnetic field at arbitrary D as a function of the magnetic momentum, $\mathscr{E}(P)$, is also calculated. It turns out that sideband (''roton'') minima at nonzero momenta, $P\neq 0$, previously detected in the case of a two-dimensional magnetoexciton,[16] occur only at separations between quantum wells smaller than a critical value. The critical parameters $(D/l)_{\rm cr}$, where $l=\sqrt{\hbar c/eH}$ is the magnetic length, are calculated. In Sec. 3 the exciton spectrum in degenerate states is calculated. A change in D leads to a similar rearrangement of dispersion curves. The effect of the quantum well width on the magnetoexciton spectrum is also discussed (Sec. 4). In Sec. 5 the probabilities of magnetoexciton creation and transitions between magnetoexciton levels with absorption (or emission) of a photon are discussed. The results of our work and proposed experiments for studying the magnetoexciton dispersion are discussed in the Conclusion.

2. TWO-DIMENSIONAL EXCITON COMPOSED OF A SPATIALLY SEPARATED ELECTRON AND HOLE IN MAGNETIC FIELD

Consider an exciton containing a spatially separated electron and hole in coupled quantum wells in transverse magnetic fields. Suppose that the separation between exciton levels is considerably smaller than the characteristic energy of size quantization ($\sim\pi^2\hbar^2/2m_{e,h}^{\perp}d_{e,h}^2$) in the quantum well, where $m_{e,h}^{\perp}$ are the electron and hole effective masses in the magnetic field direction and $d_{e,h}$ is the quantum well width. Then we can take into account only the motion of the electron and hole in the plane of the quantum wells:

$$\hat{H}=\frac{1}{2m_e}\left(\frac{\hbar}{i}\boldsymbol{\nabla}_e+\frac{e}{c}\mathbf{A}_e\right)^2+\frac{1}{2m_h}\left(\frac{\hbar}{i}\boldsymbol{\nabla}_h-\frac{e}{c}\mathbf{A}_h\right)^2 -\frac{e^2}{\epsilon\sqrt{D^2+(\mathbf{r}_e-\mathbf{r}_h)^2}}, \tag{1}$$

where $\mathbf{r}_{e,h}$ are the two-dimensional vectors of the electron and hole positions in the well plane, $m_{e,h}$ are the electron and hole effective masses in the plane of the wells, and $\epsilon=(\epsilon_1+\epsilon_2)/2$, and $\epsilon_{1,2}$ are background permittivities of materials surrounding the quantum wells.

The Schrödinger equation for an exciton in a magnetic field $\mathbf{H}$ is invariant with respect to a translation of the electron and hole through the same vector in the plane of the wells and a simultaneous gauge transformation of $\mathbf{A}(\mathbf{r})$. This invariance leads to conservation of the exciton magnetic momentum $\mathbf{P}$, which is identical to the usual center-of-mass momentum at $H=0$. The existence of an integral of motion in a magnetic field makes the theoretical analysis of three-[32] and two-dimensional[16] magnetoexcitons considerably easier. Below we use magnetic momentum conservation in calculating the spectrum of an indirect two-dimensional magnetoexciton.

The operator of the exciton magnetic momentum is expressed as

$$\hat{\mathbf{P}}=\frac{\hbar}{i}\boldsymbol{\nabla}_e+\frac{e}{c}\mathbf{A}_e+\frac{\hbar}{i}\boldsymbol{\nabla}_h-\frac{e}{c}\mathbf{A}_h-\frac{e}{c}\mathbf{H}\times(\mathbf{r}_e-\mathbf{r}_h). \tag{2}$$

Here we use the symmetrical gauge of the vector potential: $\mathbf{A}=(1/2)\mathbf{H}\times\mathbf{r}$.

Using the commutative property $[\hat{H},\hat{\mathbf{P}}]=0$, we seek the exciton wave functions in the form of eigenfunctions of the operator $\hat{\mathbf{P}}$:

$$\Psi(\mathbf{r}_e,\mathbf{r}_h)=\exp\left\{i\frac{\mathbf{R}}{\hbar}\cdot\left(\mathbf{P}+\frac{e}{2c}\mathbf{H}\times\mathbf{r}\right)\right\}\Phi_p(\mathbf{r}), \tag{3}$$

where $\mathbf{P}$ is an eigenvalue of $\hat{\mathbf{P}}$, $\mathbf{R}=(m_e\mathbf{r}_e+m_h\mathbf{r}_h)/M$, $M=m_e+m_h$, and $\mathbf{r}=\mathbf{r}_e-\mathbf{r}_h$.

The wave functions $\Phi_p(\mathbf{r})$ of the relative motion are solutions of the equation

$$\left(-\frac{\hbar^2}{2\mu}\Delta+\frac{e\hbar}{2i\mu c}\gamma\mathbf{H}\times\mathbf{r}\cdot\boldsymbol{\nabla}+\frac{e^2}{8\mu c^2}H^2r^2+\frac{e}{cM}\mathbf{H}\times\mathbf{r}\cdot\mathbf{P} +\frac{P^2}{2M}-\frac{e^2}{\epsilon\sqrt{D^2+r^2}}\right)\Phi_p(\mathbf{r})=E\Phi_p(\mathbf{r}), \tag{4}$$

where $\mu=m_em_h/M$ is the exciton reduced mass in the plane of the quantum wells and $l=\sqrt{\hbar c/eH}$ is the magnetic length.

1. First let us consider the case when the separation D between the quantum wells is considerably larger than the exciton dimension $|\langle\mathbf{r}_e-\mathbf{r}_h\rangle|$ in the plane of the wells. Then the operator of the Coulomb interaction between the electron and hole can be approximately expressed by the formula

$$-\frac{e^2}{\epsilon D}+\frac{e^2(\mathbf{r}_e-\mathbf{r}_h)^2}{2D^3\epsilon}. \tag{5}$$

Let us seek the wave function $\Phi_p(\mathbf{r})$ in the form

$$\Phi_p(\mathbf{r})=\Phi(\mathbf{r}-\alpha\boldsymbol{\rho}_0)\exp\left(i\frac{\mathbf{r}\cdot\mathbf{P}}{2\hbar}\gamma\alpha\right), \tag{6}$$

where $\boldsymbol{\rho}_0=c\mathbf{H}\times\mathbf{P}/eH^2$, $\gamma=(m_h-m_e)/M$, and α is a function of H and D defined in order to eliminate the terms linear in $\mathbf{P}\times\mathbf{r}$ and containing $\mathbf{P}\cdot\nabla$ in Eq. (4) [with due account of Eq. (5)].

Using ansatz (6) and

$$\alpha(H,D)=\frac{4\mu}{M}\frac{1}{\beta^2-\gamma^2} \tag{7}$$

we transform Eq. (4) to

$$\left(-\frac{\hbar^2}{2\mu}\Delta+\frac{e\hbar}{2i\mu c}\gamma\mathbf{H}\cdot\mathbf{r}\times\boldsymbol{\nabla} +\frac{e^2}{8\mu c^2}H^2r^2\beta^2\right)\Phi(\mathbf{r})=\mathscr{E}\Phi(\mathbf{r}), \tag{8}$$

where

$$E=\mathscr{E}+\frac{P^2}{2M}(1-\alpha)-\frac{e^2}{\epsilon D}, \tag{9}$$

$\beta=\sqrt{1+l^4/aD^3}$, and $a=\epsilon\hbar^2/e^2\mu$ is the effective Bohr radius of the exciton. Thus, we obtain for $\Phi(\mathbf{r})$

$$\Phi_{nm}(\mathbf{r})=\sqrt{\frac{n!\beta}{2\pi(n+|m|)!}}\frac{\exp(im\phi)}{l} \times\left(\sqrt{\frac{\beta}{2}}\frac{r}{l}\right)^{|m|}L_n^{|m|}\left(\frac{\beta r^2}{2l^2}\right)\exp\left(-\frac{\beta r^2}{4l^2}\right), \tag{10}$$

where L_n^m are Laguerre polynomials. The spectrum of Eq. (8) is fully quantized:

$$\mathscr{E}_{nm}=\hbar\omega_c\beta\left[n+\frac{1}{2}(|m|+1)\right]+\frac{m}{2}\gamma\hbar\omega_c, \tag{11}$$

where $\omega_c=eH/\mu c$ is the cyclotron frequency.

For $\gamma=0$ the levels defined by Eq. (11) are degenerate in the quantum number $N=2n+|m|$. Each state except (0,0) is $(N+1)$-fold degenerate. The states $(n\neq0,0)$ and $(0,m\neq0)$, in which $\gamma/\beta=(2n-|m|)/m$, are also degenerate.

The approximate expression (5) applies in the limit $D^2\gg\langle(\mathbf{r}+\alpha\boldsymbol{\rho}_0)^2\rangle$, i.e., when

$$\left(\frac{D}{l}\right)^4+4\frac{D}{a}\gg 1, \tag{12}$$

$$\frac{D}{l}+\frac{l^3}{aD^2}\frac{M}{\mu}\gg\frac{Pl}{\hbar}. \tag{13}$$

Condition (12) applies to the case of small and intermediate fields for $D\gg a$, and in the case of strong magnetic fields ($l\ll a$) under the weaker condition $D\gg l$. Condition (13) holds for small magnetic momentum P.

At $H=0$ we derive from Eqs. (9) and (11)

$$E_{nm}=-\frac{e^2}{\epsilon D}\left[1-\sqrt{\frac{a}{D}}(2n+|m|+1)\right]+\frac{P^2}{2M} \tag{14}$$

in accordance with the result of Ref. 33. In the case of a strong magnetic field, when $l^4\ll aD^3$ holds, we obtain the spectrum of an indirect magnetoexciton:

$$E_{nm}=\hbar\omega_c\left[n+\frac{1}{2}(|m|+\gamma m+1)\right]-\frac{e^2}{\epsilon D}\left[1-\frac{l^2}{D^2}(2n+|m|+1)\right]+\left(1-\frac{l^4}{aD^3}\frac{M}{\mu}\right)\frac{P^2}{2}\frac{c^2}{\epsilon D^3H^2}. \tag{15}$$

The spectrum (9) yields an exciton effective mass in the form

$$M_{\text{exc}}=\left(\frac{\partial^2E_{nm}}{\partial P^2}\right)^{-1}=M+H^2\frac{\epsilon D^3}{c^2}. \tag{16}$$

2. Now let us consider a magnetoexciton composed of a spatially separated electron and hole in coupled quantum wells in strong magnetic fields at arbitrary D. We assume that the spacing $eH/\mu c$ between excitonic levels with adjacent Landau quantum numbers (see below) and between size-quantized levels are much larger than the mean energy of the Coulomb interaction between the electron and hole, i.e., the magnetoexciton energy. Then we will show that for $D\ll l$ the characteristic Coulomb energy of an $e-h$ pair (or the magnetoexciton band width) is $\sim e^2/l\epsilon$, and for $D\gg l$ it is $\sim e^2l^2/D^3\epsilon$. Hence, the conditions formulated above lead to the inequalities

$$l\ll a_{e,h},\quad d_{e,h}^2\ll a_{e,h}^{\perp}l \tag{17}$$

for the barrier width between the quantum wells with $D\ll l$ and

$$l^4\ll a_{e,h}D^3,\quad d_{e,h}^2l^2\ll a_{e,h}^{\perp}D^3 \tag{18}$$

for $D\gg l$, where $a_{e,h}=\epsilon\hbar^2/m_{e,h}e^2$ are the effective Bohr radii for electrons and holes in the plane of the quantum wells and $a_{e,h}^{\perp}=\epsilon\hbar^2/m_{e,h}^{\perp}e^2$ are the effective Bohr radii in the magnetic field direction.

In this case, it is more convenient to seek exciton wave functions in the form

$$\Psi(\mathbf{r}_e,\mathbf{r}_h)=\exp\left\{\frac{i}{\hbar}\mathbf{R}\cdot\left(\mathbf{P}+\frac{e}{2c}\mathbf{H}\times\mathbf{r}\right)\right\}\times\exp\left(\frac{1}{2}i\gamma\mathbf{r}\cdot\mathbf{P}\right)\Phi(\mathbf{r}-\boldsymbol{\rho}_0). \tag{19}$$

The wave functions of the relative motion, $\Phi(\mathbf{r}-\boldsymbol{\rho}_0)$, are solutions of the equation

$$\left(-\frac{\hbar^2}{2\mu}\Delta+\frac{e\hbar}{2i\mu c}\gamma\mathbf{H}\cdot\mathbf{r}\times\boldsymbol{\nabla}+\frac{e^2}{8\mu c^2}H^2r^2-\frac{e^2}{\epsilon\sqrt{D^2+(\mathbf{r}+\boldsymbol{\rho}_0)^2}}\right)\Phi(\mathbf{r})=E\Phi(\mathbf{r}). \tag{20}$$

In accordance with conditions (17) and (18), let us calculate the exciton energy by treating the Coulomb interaction as a perturbation. In the first order of perturbation theory in the parameter $l/a_{e,h}$ in the case of $D\ll l$ or the parameter $l^4/a_{e,h}D^3$ in the case of $D\gg l$, one can ignore transitions to other Landau levels. Thus, $\Phi(\mathbf{r})$ can be described by Eq. (10) at $\beta=1$. The spectrum unperturbed by the Coulomb interaction is independent of P:

$$E_{nm}^0=\hbar\omega_c\left[n+\frac{1}{2}(|m|+\gamma m+1)\right], \tag{21}$$

where $n=\min(n_1,n_2)$, $m=|n_1-n_2|$, and $n_{1,2}$ are the electron and hole quantum numbers.

For $\gamma=\pm1$ the spectrum is degenerate in the angular momentum $m<0$ ($m>0$). In real quantum wells, the quasiparticle effective masses are finite, so we have $|\gamma|<1$, and there is no degeneracy in the angular momentum of the relative motion.

For some values of the ratio m_e/m_h the excitonic levels defined by Eq. (21) can also be degenerate. For example, if $m_e=m_h$, the levels with quantum numbers $n=0$, $m=1$ and $n=0$, $m=-1$ coincide. When $\gamma=(2-|m|)/m$, the level $n=1$, $m=0$ coincides with the levels $n=0$, $|m|\geq 2$ (we will discuss this case in detail in Sec. 3).

The unperturbed spectrum E_{nm}^0 is independent of the magnetic momentum $\mathbf{P}$. The operator of the $e-h$ interaction

$$\hat{V}(r)=-\frac{e^2}{\epsilon\sqrt{D^2+r^2}} \tag{22}$$

commutes with $\hat{\mathbf{P}}$, so it can be made diagonal with respect to $\mathbf{P}$. Thus, in the nondegenerate case, the magnetoexciton spectrum $E_{nm}(P)$ can be expressed in the first order of perturbation theory as

$$E_{nm}(P)=E_{nm}^0+\mathscr{E}_{nm}(P),$$

where

$$\mathscr{E}_{nm}(P)=-\left\langle nmP\left|\frac{e^2}{\epsilon\sqrt{D^2+r^2}}\right|nmP\right\rangle, \tag{23}$$

and E_{nm}^0 is the unperturbed spectrum given by Eq. (21).

The dispersion of a two-dimensional magnetoexciton at $D=0$ (i.e., the spectrum of a direct exciton) was analyzed in Ref. 16. Below we will show that the exciton spectrum consists of bands whose width monotonically decreases with D (the bandwidth of the direct exciton is $\sim e^2/l$). At small D (see below) the dispersion curves are nonmonotonic in all states except $n=m=0$. In states (n,m) the dispersion curves have $n+1$ minima, and in the case $m=0$ the first and deepest minimum corresponds to zero momentum. In states with $m \neq 0$ the dispersion curves have a maximum at $P=0$.

Using the method of Ref. 16, we transform Eq. (23) to

$$\mathscr{E}_{nm}(P,D) = -\frac{e^2}{2\pi l^2}\frac{n!}{(n+|m|)!}$$

$$\times \int \Phi^*_{nm}(\mathbf{r}-\boldsymbol{\rho}_0)\Phi_{nm}(\mathbf{r}-\boldsymbol{\rho}_0)\frac{d^2\mathbf{r}}{\sqrt{D^2+r^2}}$$

$$= -\text{const}\cdot \int N_{nm}(\mathbf{r})\frac{d^2\mathbf{r}}{\sqrt{(\mathbf{r}+\boldsymbol{\rho}_0)^2+D^2}}. \qquad (24)$$

This expression can be interpreted as an energy of interaction between a two-dimensional charge distribution with density $-eN_{nm}(\mathbf{r})$ and a point charge e with coordinates $(-\boldsymbol{\rho}_0,D)$. The function $N_{nm}(r)$ is symmetrical about the center and has $N_{\text{max}}=n+1$ maxima with width $\sim l$ and $N_{\text{min}}=n+1-\delta_{0,m}$ minima. The first maximum has the largest amplitude at arbitrary quantum numbers n and m. There is a maximum of $N_{nm}(r)$ at the center (0,0) for $m=0$ and a minimum for $m \neq 0$. The main contribution to the integral in Eq. (24) is, obviously, due to the overlap region of the disk of radius D (with the point charge at its center) and the rings corresponding to the maxima of the function $N_{nm}(r)$.

Using the electrostatic analogue described above, let us analyze qualitatively the dispersion of the magnetoexciton in states with quantum numbers $n=0$ and $m \neq 0$. The function $N_{0m}(r)$ has the only maximum with the radius $r_{\text{max}}=\sqrt{2|m|}l$ and a minimum at $r_{\text{min}}=0$. By varying $\boldsymbol{\rho}_0$ we simultaneously move the point charge and change the overlap region of the disk and ring corresponding to the maximum in $N_{0m}(r)$. When $Pl \ll \hbar$ and $D \ll l$ hold, this region is small and, by virtue of the central symmetry of the charge distribution, the integral has a minimum at $P=0$. Therefore the momentum $P=0$ for $D \ll l$ corresponds to the maximum on the dispersion curve. The overlap region in largest for $P \approx r_{\text{max}}\hbar/l^2$ and $D \ll l$ so the momentum $P=r_{\text{max}}\hbar/l^2$ corresponds to a minimum on the dispersion curve (the ''roton'' minimum). Further increase in the momentum leads to a decrease in the overlap region, which means that the exciton energy drops.

Now let us consider the effect of changes in D on $\mathscr{E}_{nm}(P,D)$. At $P=0$ the overlap region increases with D from zero at $D=0$ to $S_{\text{cr}}=2\pi l r_{\text{max}}$ for $D \geqslant r_{\text{max}}+l/2$, i.e., at $D_{\text{cr}} \sim r_{\text{max}}$ the extremum type changes from a maximum to minimum, and the roton minimum disappears at the same time. A further increase in D leads to a larger separation between the point-like charge and the ring center, hence a smaller minimum amplitude.

Similar considerations apply to a magnetoexciton in an arbitrary state (n,m). The dispersion curves always have extrema at $P=0$ shaped as minima at arbitrary D if $m=0$. For $m \neq 0$ the extremum at $P=0$ is a maximum in the case $D \ll l$ and a minimum for $D \gg l$. For $D \ll l$ the dispersion curve has $n+1$ minima, and for $D \gg l$ [to be exact, for $D \gg r^{n+1}_{\text{max}}$, where r^{n+1}_{max} is the largest radius of the maximum of function $N_{nm}(r)$] the only minimum is located at $P=0$. There is a certain order in which roton extrema disappear, and this order depends on their amplitudes and the separations between neighboring rings.

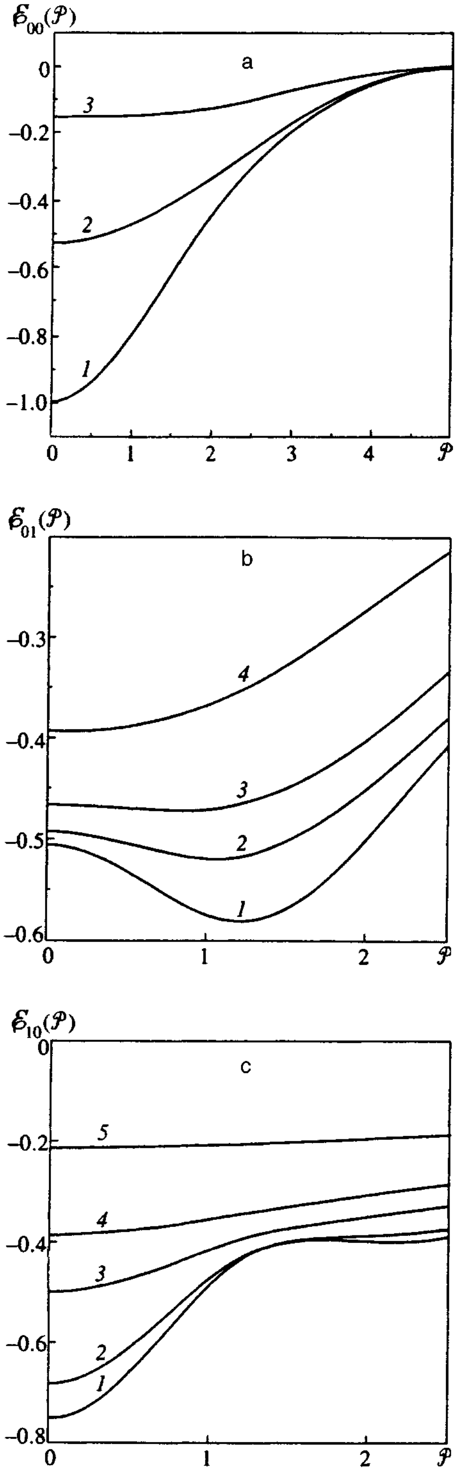

FIG. 1. Dispersion curves $\mathscr{E}(\mathscr{P},\mathscr{D})$ of a magnetoexciton: (a) in state $n=m=0$ at $\mathscr{D}=0$, 1, and 5 (curves *1, 2,* and *3,* respectively); (b) in states $n=0$, $m=\pm 1$ at $\mathscr{D}=0$, 0.25, 0.5, and *1* (curves *1, 2, 3,* and *4*); (c) in states $n=1$, $m=0$ at $\mathscr{D}=0$, 0.1, 0.3, 0.5, and 1 (curves *1, 2, 3, 4,* and *5*).

The dispersion of an indirect magnetoexciton is determined by the two dimensionless parameters $\mathscr{P}=Pl/\hbar$ and $\mathscr{D}=D/l$. Our calculations indicate that the width of the indirect exciton bands ($\mathscr{D} \neq 0$) decreases with $\mathscr{D}$ (Fig. 1). The

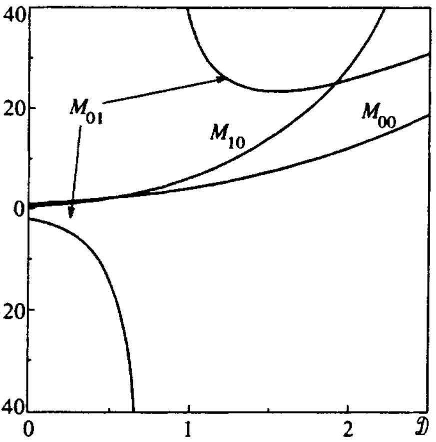

FIG. 2. Effective masses M of a magnetoexciton in states $(n,m)=(0,0)$, $(0,\pm1)$, (1,0) as functions of $\mathscr{D}$. The effective masses are measured in units of $M_0=2^{3/2}\hbar^2/e^2l\sqrt{\pi}$, which is the direct magnetoexciton mass on level (0,0).

shapes of the extrema on the dispersion curves in the limit $\mathscr{D}\ll1$ are the same as in the case of a direct exciton. One can derive from Eq. (24) expressions for the exciton energy with momentum $\mathscr{P}=0$ in an arbitrary state (n,m), for example,

$$\mathscr{E}_{00}(\mathscr{D})=-E^0\exp\left(\frac{\mathscr{D}^2}{2}\right)\operatorname{erfc}\left(\frac{\mathscr{D}}{\sqrt{2}}\right),$$

$$\mathscr{E}_{0,\pm1}(\mathscr{D})=-E^0\left[\left(\frac{1}{2}-\frac{\mathscr{D}^2}{2}\right)\exp\left(\frac{\mathscr{D}^2}{2}\right)\times\operatorname{erfc}\left(\frac{\mathscr{D}}{\sqrt{2}}\right)+\frac{\mathscr{D}}{\sqrt{2\pi}}\right],$$

$$\mathscr{E}_{10}(\mathscr{D})=-E^0\left[\left(\frac{3}{4}+\frac{\mathscr{D}^2}{2}+\frac{\mathscr{D}^4}{4}\right)\exp\left(\frac{\mathscr{D}^2}{2}\right)\operatorname{erfc}\left(\frac{\mathscr{D}}{\sqrt{2}}\right)-\frac{\mathscr{D}}{2\sqrt{2\pi}}-\left(\frac{\mathscr{D}}{\sqrt{2}}\right)^3\frac{1}{\sqrt{\pi}}\right], \tag{25}$$

where $E^0=(e^2/\epsilon l)\sqrt{\pi/2}$, and erfc is the complementary error function. The absolute values of the functions $\mathscr{E}_{00}(\mathscr{D})$, $\mathscr{E}_{0,\pm1}(\mathscr{D})$, and $\mathscr{E}_{10}(\mathscr{D})$ decrease monotonically with $\mathscr{D}$.

The dispersion curves always have extrema at $P=0$, so a magnetoexciton effective mass can be defined as usual:

$$\frac{1}{M_{nm}}=\left.\frac{\partial^2\mathscr{E}_{nm}(P)}{\partial P^2}\right|_{P=0}.$$

For states with quantum numbers (0,0), $(0,\pm1)$, and (1,0) we obtain (Fig. 2)

$$M_{00}(\mathscr{D})=M_0\left[(1+\mathscr{D}^2)\exp\left(\frac{\mathscr{D}^2}{2}\right)\operatorname{erfc}\left(\frac{\mathscr{D}}{\sqrt{2}}\right)-\mathscr{D}\sqrt{\frac{2}{\pi}}\right]^{-1},$$

$$M_{0,\pm1}(\mathscr{D})=M_0\left[(3+\mathscr{D}^2)\frac{\mathscr{D}}{\sqrt{2\pi}}-\left(\frac{1}{2}+2\mathscr{D}^2+\frac{\mathscr{D}^4}{2}\right)\exp\left(\frac{\mathscr{D}^2}{2}\right)\operatorname{erfc}\left(\frac{\mathscr{D}}{\sqrt{2}}\right)\right]^{-1},$$

$$M_{10}(\mathscr{D})=M_0\left[\left(\frac{7}{4}+\frac{25\mathscr{D}^2}{4}+\frac{11\mathscr{D}^4}{4}+\frac{\mathscr{D}^6}{4}\right)\exp\left(\frac{\mathscr{D}^2}{2}\right)\operatorname{erfc}\left(\frac{\mathscr{D}}{\sqrt{2}}\right)-\left(\frac{17}{2}+5\mathscr{D}^2+\frac{\mathscr{D}^4}{2}\right)\mathscr{D}\frac{1}{\sqrt{2\pi}}\right]^{-1}. \tag{26}$$

Here $M_0=2^{3/2}\epsilon\hbar^2/e^2l\sqrt{\pi}$ is the direct exciton mass in the lowest level $(n=m=0)$. The magnetoexciton effective mass in high magnetic fields depends only on the magnetic field and parameter D/l (it is independent of the bare effective masses of electrons and holes). Note also that the defined effective mass is determined by the effective interaction between electrons and holes, so that $M(H)\to\infty$ as $e/\epsilon\to0$.

Below we will calculate the dispersion curves $\mathscr{E}_{nm}(\mathscr{P},\mathscr{D})$ and effective masses $M_{nm}(\mathscr{D})$ of a magnetoexciton as functions of the parameter $\mathscr{D}$. We will show that the magnetoexciton effective mass in the state $m=0$ increases with the magnetic field and separation D between quantum wells, whereas in states with $m\neq0$ the magnetoexciton effective mass (at the central minimum) is a nonmonotonic function of $\mathscr{D}$.

In the limit of small momenta, $\mathscr{P}\ll1$, and $\mathscr{D}\ll1$, the dispersion curves are described by the formula

$$\mathscr{E}_{n|m|\geq1}(\mathscr{P},\mathscr{D})=-\frac{e^2}{\epsilon}\left\langle\frac{1}{r}\right\rangle_{n,|m|\geq1,P=0}+\frac{P^2}{2M_{n|m|\geq1}(\mathscr{D})}+E^0\frac{\mathscr{D}^2}{4\sqrt{\pi}}\frac{(n+|m|)!}{n!}\times\sum_{s_1s_2=0}^{n}Q^{nm}_{s_1s_2}\Gamma\left(|m|+s_1+s_2-\frac{1}{2}\right), \tag{27}$$

where

$$Q^{nm}_{s_1s_2}=\frac{C_n^{s_1}C_n^{s_2}(-1)^{s_1+s_2}}{(|m|+s_1)!(|m|+s_2)!},$$

C_n^s is the number of combinations of n elements s at a time, and $\langle r^{-1}\rangle_{nm,P=0}=\langle nm,0|r^{-1}|nm,0\rangle$.

It is remarkable that at $m=0$ the changes in all dispersion functions are linear in $\mathscr{D}$, i.e., they are not analytical functions of $\mathscr{D}^2$, which is included in the interaction Hamiltonian:

$$\mathcal{E}_{n0}(\mathcal{P},\mathcal{D})=-\frac{e^2}{\epsilon}\left\langle\frac{1}{r}\right\rangle_{n0,P=0}+E^0\frac{2}{\sqrt{\pi}}\mathcal{D}+E^0\frac{\mathcal{D}^2}{4\sqrt{\pi}}\sum_{s_1s_2=0}^{n}Q^{n0}_{s_1s_2}\Gamma\left(s_1+s_2-\frac{1}{2}\right)+\frac{P^2}{2M_{n0}(\mathcal{D})}. \tag{28}$$

The effective mass of an indirect magnetoexciton in the limit $\mathcal{D}\ll 1$ increases with $\mathcal{D}$ in accordance with the formulas

$$\frac{1}{M_{nm}(\mathcal{D})}=\begin{cases}\dfrac{1}{M_{n0}}-\mathcal{D}\dfrac{(2n+1)2^{3/2}}{\sqrt{\pi}M_0}+\dfrac{9}{8}\mathcal{D}^2\dfrac{1}{\sqrt{\pi}M_0}\\ \quad\times\displaystyle\sum_{s_1s_2=0}^{n}Q^{n0}_{s_1s_2}\Gamma(s_1+s_2-3/2), \quad m=0,\\ \dfrac{1}{M_{n,\pm1}}+\mathcal{D}\dfrac{(n+1)2^{3/2}}{\sqrt{\pi}M_0}+\dfrac{9}{8}\mathcal{D}^2\dfrac{(n+1)}{\sqrt{\pi}M_0}\\ \quad\times\displaystyle\sum_{s_1s_2=0}^{n}Q^{n1}_{s_1s_2}\Gamma(s_1+s_2-1/2), \quad |m|=1,\\ \dfrac{1}{M_{n|m|\geqslant2}}+\dfrac{9}{8}\mathcal{D}^2\dfrac{1}{\sqrt{\pi}M_0}\dfrac{(n+|m|)!}{n!}\\ \quad\times\displaystyle\sum_{s_1s_2=0}^{n}Q^{nm}_{s_1s_2}\Gamma(|m|+s_1+s_2-3/2), \quad |m|\geqslant2,\end{cases}$$

where M_{nm} is the direct magnetoexciton mass (when the electron and hole are in the same layer):

$$\frac{1}{M_{nm}}=-\frac{1}{2\sqrt{\pi}M_0}\frac{(n+|m|)!}{n!}\times\sum_{s_1s_2=0}^{n}Q^{nm}_{s_1s_2}\Gamma\left(|m|+s_1+s_2-\frac{1}{2}\right). \tag{29}$$

At $m=0$ and arbitrary n the effective masses of direct and indirect excitons are positive (the dispersion curves have minima), and for $m\neq0$ the effective masses are negative (correspond to dispersion maxima). The effective mass of an indirect exciton in the state $n=0$, $|m|\gg1$ is expressed as

$$M_{0m}=-2\sqrt{\pi}M_0\left(|m|-\frac{1}{2}\right)^{3/2}\left(1-\frac{9}{4}\frac{\mathcal{D}^2}{|m|-1/2}\right)^{-1}.$$

At small separations $\mathcal{D}$ between quantum wells containing electrons and holes, the dispersion curves (including those in the state $n=m=0$) are nonmonotonic and have $n+1$ minima. Our calculations indicate that all off-center roton minima on the dispersion curves $\mathcal{E}_{nm}(\mathcal{P},\mathcal{D})$ gradually disappear as $\mathcal{D}$ increases, in conformity with the qualitative analysis given above (see Fig. 1a,b), and for $\mathcal{D}>\mathcal{D}_{\mathrm{cr}}$ there is only one minimum at zero momentum. The type of extremum at $\mathcal{P}=0$ changes if $M^{-1}_{nm}(\mathcal{D}_{\mathrm{cr}})\to0$. The electrostatic analogue of our model clearly indicates that, for example, $\mathcal{D}_{\mathrm{cr}}\sim r_{\max}$ for $n=0$. At $m=1$ and $m=2$ we have $\mathcal{D}^{01}_{\mathrm{cr}}=0.756$ and $\mathcal{D}^{02}_{\mathrm{cr}}=1.233$.

For $\mathcal{D}\gg1$ and $\mathcal{P}\ll1$ the dispersion is described by the formula

$$\mathcal{E}_{nm}(\mathcal{P},\mathcal{D})=-\frac{e^2}{\mathcal{D}\epsilon}\left(1-\frac{\langle r^2\rangle_{nm,P=0}}{2D^2}\right)+\frac{P^2}{2M_{nm}(\mathcal{D})}. \tag{30}$$

On the three lowest levels (at $P=0$) we have $\langle r^2\rangle_{00}=2l^2$, $\langle r^2\rangle_{0,\pm1}=4l^2$, and $\langle r^2\rangle_{10}=6l^2$.

The magnetoexciton effective mass increases in the range $\mathcal{D}\gg1$:

$$M_{nm}(\mathcal{D})=\mathcal{D}^3\frac{\sqrt{\pi}}{2^{3/2}}M_0\left(1-\frac{3\langle r^2\rangle_{nm,P=0}}{2D^2}\right)^{-1}.$$

For $n=0$ and $|m|\gg1$ we derive from the latter expression

$$M_{0m}(\mathcal{D})=\mathcal{D}^3\frac{\sqrt{\pi}}{2^{3/2}}M_0\left(1-\frac{3}{\mathcal{D}^2}(|m|+1)\right)^{-1}.$$

For $\mathcal{P}\gg1$ and $\mathcal{P}\gg\mathcal{D}$ the dispersion functions have the following asymptotic forms:

$$\mathcal{E}_{nm}(\mathcal{P},\mathcal{D})=-\frac{e^2}{\epsilon\mathcal{P}l}\left(1-\frac{\mathcal{D}^2}{2\mathcal{P}^2}+\frac{\langle r^2\rangle_{nm,P=0}}{4\mathcal{P}^2l^2}\right). \tag{31}$$

The mean separation between the electron and hole in the plane of the quantum wells, $\langle r\rangle_{nmP}=l^2\mathbf{H}\times\mathbf{P}/\hbar H$, increases with the magnetic momentum, and the energy of Coulomb interaction between electrons and holes, $\mathcal{E}_{nm}(\mathcal{P},\mathcal{D})$, decreases. Therefore, at sufficiently large separations $\mathcal{D}$ between coupled quantum wells, the magnetoexcitonic effect can be suppressed owing to the strong interaction with impurities and terraces in quantum wells compared to the Coulomb interaction between electrons and holes. Interaction with a random field may cause localization of the magnetoexciton,[34] and in highly disordered system disappearance of magnetoexcitonic effects.

3. SPECTRUM OF AN INDIRECT MAGNETOEXCITON: EFFECTS OF DEGENERACY

In some cases, the unperturbed spectrum is quasi-degenerate, i.e., the spacing between unperturbed levels is smaller than the characteristic energy $\mathcal{E}_{nm}(P)$ of the interaction between electrons and holes.[16] For example, in the case $\gamma=0$ the levels with quantum numbers $(n,m\neq0)$ and $(n,-m)$ are degenerate. When $\gamma=(2n-|m|)/m$ holds, the levels $(n\neq0,0)$ and $(0,m)$ coincide if $|m|>n$. Hence, owing to the possible quasi-degeneracy, the applicability of the formulas derived in the previous section is limited by the conditions

$$\gamma\gg\frac{l}{a_{e,h}}, \quad \left|-\frac{\gamma m+|m|}{2}+n\right|\gg\frac{l}{a_{e,h}}$$

for $D/l\ll1$ and

$$\gamma\gg\frac{l^4}{a_{e,h}D^3}, \quad \left|-\frac{\gamma m+|m|}{2}+n\right|\gg\frac{l^4}{a_{e,h}D^3}$$

for $D/l\gg1$.

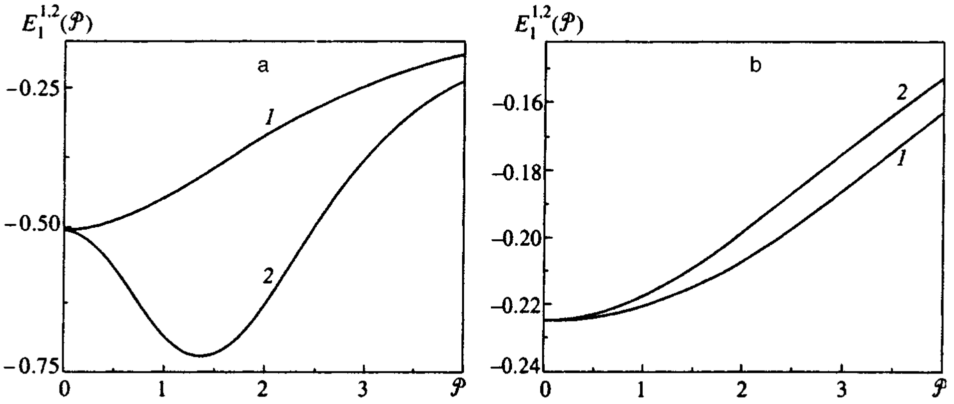

FIG. 3. Dispersion curves of a magnetoexciton in a degenerate state $N=1$; $N=2\min(n_1,n_2)+|n_1-n_2|$, where n_1 and n_2 are Landau quantum numbers of electrons and holes: (a) $\mathcal{D}=0$, curve *2* has a roton minimum; (b) $\mathcal{D}=3$.

At $m_e=m_h$ the energy given by Eq. (21) is a function of the quantum number $N=2n+|m|$, and all levels are $(N+1)$-fold degenerate (the ground state with $N=0$ is nondegenerate).

In the first order of perturbation theory, we have the dispersion functions of level $N=1$:

$$E_1^{1,2}(\mathbf{P},\mathcal{D})=\hbar\omega_c+\mathcal{E}_{01}(\mathcal{P},\mathcal{D}) \pm\left|\left\langle 0-1P\left|\frac{e^2}{\epsilon\sqrt{D^2+r^2}}\right|01P\right\rangle\right|. \tag{32}$$

At $P=0$ the level is still degenerate since $\langle 0-10|e^2/(\epsilon\sqrt{D^2+r^2})|010\rangle=0$. At $P\neq 0$ the magnetoexciton energy splits into two branches with effective masses (Fig. 3)

$$\frac{1}{M_{1,2}(\mathcal{D})}=\frac{1}{M_{01}(\mathcal{D})}\pm\alpha(\mathcal{D}), \tag{33}$$

$$\frac{1}{\alpha(\mathcal{D})}=M_0\left[-(5+\mathcal{D}^2)\,\frac{\mathcal{D}}{2}\,\frac{1}{\sqrt{2\pi}}+\left(\frac{3}{4}+\frac{3}{2}\,\mathcal{D}^2+\frac{\mathcal{D}^4}{4}\right)\exp\left(\frac{\mathcal{D}^2}{2}\right)\operatorname{erfc}\left(\frac{\mathcal{D}}{\sqrt{2}}\right)\right]^{-1}. \tag{34}$$

In the limit $\mathcal{D}\ll 1$ and $\mathcal{P}\ll 1$ we have

$$E_1^{1,2}(\mathcal{P},\mathcal{D})=\hbar\omega_c-\frac{1}{2}E^0\left(1-\frac{\mathcal{D}^2}{2}\right)-\frac{P^2}{2M_{1,2}(\mathcal{D})}, \tag{35}$$

where

$$M_1(\mathcal{D})=4M_0\left(1+\frac{3}{2}\,\mathcal{D}^2\right),$$

$$M_2(\mathcal{D})=-\frac{4}{5}M_0\left(1+\frac{16}{5}\,\sqrt{\frac{2}{\pi}}\,\mathcal{D}-\frac{33}{10}\,\mathcal{D}^2\right).$$

An increase in $\mathcal{D}$ results in the disappearance of the roton minimum in E_1^2. For $\mathcal{D}\gg 1$ we obtain

$$E_1^{1,2}(\mathcal{P},\mathcal{D})=\hbar\omega_c-\frac{e^2}{D\epsilon}\left(1-\frac{2}{\mathcal{D}^2}\right)+\frac{P^2}{2M_{1,2}(\mathcal{D})} \tag{36}$$

and effective masses

$$M_1(\mathcal{D})=\mathcal{D}^3\sqrt{\frac{\pi}{2}\frac{M_0}{2}}\left(1-\frac{33}{8\mathcal{D}^2}\right),$$

$$M_2(\mathcal{D})=\mathcal{D}^3\sqrt{\frac{\pi}{2}\frac{M_0}{2}}\left(1+\frac{129}{8\mathcal{D}^2}\right).$$

For $\mathcal{P}\gg 1$ we have

$$E_1^{1,2}(\mathcal{P},\mathcal{D})\sim -E^0\sqrt{\frac{2}{\pi}\frac{1}{\mathcal{P}}}.$$

Similarly, level $N=2$ splits into three branches with quantum numbers $n=1$, $m=0$, and $n=0$, $m=\pm 2$:

$$E_2^{1,2}(\mathcal{P},\mathcal{D}) =\frac{3}{2}\hbar\omega_c+\frac{1}{2}\{\mathcal{E}_{10}(\mathcal{P},\mathcal{D})+\mathcal{E}_{02}(\mathcal{P},\mathcal{D})+\Delta_2(\mathcal{P},\mathcal{D}) \pm\sqrt{[\mathcal{E}_{10}(\mathcal{P},\mathcal{D})-\mathcal{E}_{02}(\mathcal{P},\mathcal{D})-\Delta_2(\mathcal{P},\mathcal{D})]^2+8\Delta_1(\mathcal{P},\mathcal{D})^2}\}, \tag{37}$$

$$E_2^3(\mathcal{P},\mathcal{D})=\frac{3}{2}\hbar\omega_c+\mathcal{E}_{02}(\mathcal{P},\mathcal{D})-\Delta_2(\mathcal{P},\mathcal{D}), \tag{38}$$

where

$$\left\langle 10\left|\frac{e^2}{\epsilon\sqrt{D^2+(\mathbf{r}+\boldsymbol{\rho}_0)^2}}\right|0\pm 2\right\rangle=e^{\pm 2i\phi_0}\Delta_1(\mathcal{P},\mathcal{D}),$$

$$\left\langle 0-2\left|\frac{e^2}{\epsilon\sqrt{D^2+(\mathbf{r}+\boldsymbol{\rho}_0)^2}}\right|02\right\rangle=e^{4i\phi_0}\Delta_2(\mathcal{P},\mathcal{D}), \tag{39}$$

and ϕ_0 is the polar angle of vector $\boldsymbol{\rho}_0$. At $\mathcal{P}=0$ we obtain $\Delta_1(0,\mathcal{D})=\Delta_2(0,\mathcal{D})=0$, so the levels E_2^2 and E_2^3 are still degenerate at $\mathcal{P}=0$. The off-center extrema gradually disappear as $\mathcal{D}$ increases, and for $\mathcal{D}\gg 1$ we only have the minimum at $\mathcal{P}=0$.

4. EFFECT OF QUANTUM WELL WIDTH

Now let us consider a more realistic model with a small but finite width of the quantum wells containing electrons and holes. We assume, as in the previous sections, that the well width is the smallest characteristic dimension of the system. Given the inequalities (17) and (18), we can apply the adiabatic approximation. The transverse motion in the quantum well is the fastest, so the electron–hole potential can be averaged over the wave functions

$$\sqrt{\frac{2}{d}}\sin\left(\frac{\pi k_1}{d}z_1\right),\qquad \sqrt{\frac{2}{d}}\sin\left[\frac{\pi k_2}{d}(z_2-d)\right]$$

describing size quantization of electrons and holes in the quantum wells.

The resulting changes in the dispersion curves do not qualitatively modify the exciton spectrum. For $D\ll l$ and $\mathscr{P}=0$ we have

$$\begin{aligned}\delta\mathscr{E}_{n|m|\geqslant 1}(0,\mathscr{D}) &= E^0\frac{1}{4\sqrt{\pi}}\left[\mathscr{D}^2+2\mathscr{D}\frac{d}{l}\right.\\ &\quad\left.+\frac{7d^2}{6l^2}-\frac{d^2}{2\pi^2 l^2}\left(\frac{1}{k_1^2}+\frac{1}{k_2^2}\right)\right]\frac{(n+|m|)!}{n!}\\ &\quad\times\sum_{s_1s_2=0}^{n}Q^{nm}_{s_1s_2}\Gamma\left(|m|+s_1+s_2-\frac{1}{2}\right)\end{aligned}\qquad(40)$$

(k_1 and k_2 are quantum numbers of quantization of electrons and holes) and

$$\begin{aligned}\delta\mathscr{E}_{n0}(0,\mathscr{D}) &= E^0\sqrt{\frac{2}{\pi}}\left(\mathscr{D}+\frac{d}{l}\right)+E^0\frac{1}{4\sqrt{\pi}}\\ &\quad\times\left[\mathscr{D}^2+2\mathscr{D}\frac{d}{l}+\frac{7d^2}{6l^2}-\frac{d^2}{2\pi^2l^2}\left(\frac{1}{k_1^2}+\frac{1}{k_2^2}\right)\right]\\ &\quad\times\sum_{s_1s_2=0}^{n}Q^{n0}_{s_1s_2}\Gamma\left(s_1+s_2-\frac{1}{2}\right)\end{aligned}$$

at $m=0$. In the case $\mathscr{D}\gg 1$ we obtain

$$\delta\mathscr{E}_{nm}(0,\mathscr{D})\sim E^0\frac{dl}{D^2}\frac{1}{\sqrt{2\pi}}.$$

As an illustration, we have plotted dispersion curves of an exciton composed of an electron and a hole localized in neighboring quantum wells with a width of $d=0.5l$ each. Figure 4 shows calculations for states (00), $(0,\pm 1)$, and (10) compared to the dispersion functions of magnetoexcitons composed of an electron and hole in two different planes at a distance $\mathscr{D}=0.5$ from one another. As can be seen in Fig. 4, the dispersion curves are different, but the difference is not great. The discrepancy between the dispersion curves corresponding to these two cases decreases with the exciton momentum. This is quite natural because the magnetoexciton momentum is proportional to the separation between electrons and holes measured in the plane of the quantum wells.

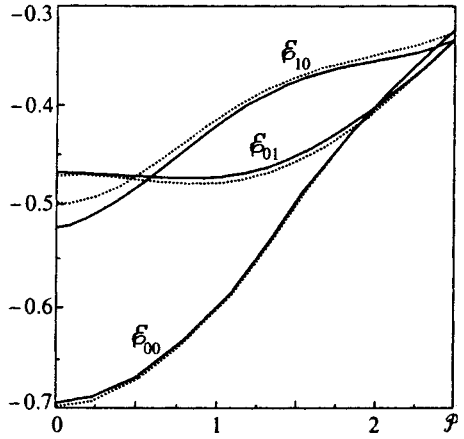

FIG. 4. Dispersion curves of magnetoexcitons in coupled quantum wells with widths $d_e=d_h=0.5l$ (solid lines). The wells with electrons and holes have a common surface; for comparison the case of two separated quantum wells of small thickness at $D=0.5l$ (dashed lines) is also presented.

5. MAGNETOEXCITON PHOTOABSORPTION AND TRANSITIONS BETWEEN EXCITONIC LEVELS

As is well known,[35,32] the probability of generating an exciton is proportional to the factor $|\Psi(0)|^2$. In order to obtain simple analytical expressions we limit our analysis to the case of large D. According to Eqs. (3), (6), and (10), the probability of creating an exciton in coupled quantum wells in the state $n=m=0$ when Eqs. (12) and (13) hold is proportional to

$$|\Psi(0)|^2=\frac{\beta}{2\pi l^2}\exp\left(-\frac{\beta\alpha^2\rho_0^2}{2l^2}\right).\qquad(41)$$

The probability of magnetoexciton generation increases with magnetic field H in accordance with the formula

$$\begin{aligned}|\Psi(0)|^2&=\frac{e}{2\pi\hbar c}\sqrt{H^2+4H_0^2\frac{\mu}{M}}\\ &\quad\times\exp\left(-\frac{2\pi^2\hbar c}{e\lambda^2}\frac{H^2\sqrt{H^2+4H_0^2\mu/M}}{(H^2+H_0^2)^2}\right),\end{aligned}\qquad(42)$$

where $H_0=\sqrt{Mc^2/\epsilon D^3}$, and λ is the photon wavelength.

Now let us consider the problem of the long-wave photon absorption due to a transition between levels of an indirect magnetoexciton in coupled quantum wells. The probability of interexcitonic transitions with absorption (or emission) of a photon is

$$W=2\pi|\langle 2|\hat{F}|1\rangle|^2\delta(E_2-E_1\mp\hbar\omega),\qquad(43)$$

where $E_{1,2}$ are excitonic levels determined by Eqs. (9) and (11),

$$\hat{F}=\frac{e}{c}[\tilde{\mathbf{A}}(\mathbf{r}_e)\cdot\hat{\mathbf{v}}_e-\tilde{\mathbf{A}}(\mathbf{r}_h)\cdot\hat{\mathbf{v}}_h],\qquad(44)$$

$$\tilde{\mathbf{A}}(\mathbf{r},t)=\sum_{k\alpha}\sqrt{\frac{2\pi\hbar c}{Vk}}\,\mathbf{e}_{\alpha k\alpha}e^{i(\mathbf{k}\cdot\mathbf{r}-\omega t)}+\text{H.c.},$$

$\mathbf{e}_\alpha$ are vectors of the photon circular polarization in the plane of the quantum wells,

$$\hat{\mathbf{v}}_{e,h}=\frac{1}{m_{e,h}}\left(\frac{\hbar}{i}\nabla_{e,h}\pm\frac{e}{2c}\mathbf{H}\times\mathbf{r}_{e,h}\right)$$

are the operators of the electron and hole velocities in magnetic field. The matrix element of the transition operator $\hat{F}$ in terms of the center-of-mass coordinates $\mathbf{R}$ and relative electron–hole coordinates $\mathbf{r}$ has the form

$$\frac{e}{c}\left\langle n_2m_2\mathbf{P}_2;1\left|\frac{\widetilde{\mathbf{A}}_e-\widetilde{\mathbf{A}}_h}{M}\frac{\hbar}{i}\frac{\partial}{\partial\mathbf{R}}+\left(\frac{\widetilde{\mathbf{A}}_e}{m_e}+\frac{\widetilde{\mathbf{A}}_h}{m_h}\right)\left(\frac{\hbar}{i}\nabla_r+\frac{e}{2c}\mathbf{H}\times\mathbf{R}\right)+\frac{e}{2Mc}\mathbf{H}\times\mathbf{r}\left(\frac{m_h}{m_e}\widetilde{\mathbf{A}}_e-\frac{m_e}{m_h}\widetilde{\mathbf{A}}_h\right)\right|0;n_1m_1\mathbf{P}_1\right\rangle, \tag{45}$$

where $|nm\mathbf{P}\rangle$ is the exciton state ket-vector, and $|l\rangle$ and $|0\rangle$ are the states of electromagnetic field with population numbers 1 and 0. In what follows, we will discuss only direct transitions between magnetoexciton states with momentum $P=0$. After integration with respect to $\mathbf{R}$, we have

$$\langle n_2m_2\mathbf{P};1|\hat{F}|0;n_1m_1\mathbf{P}\rangle=\left\langle n_2m_2;1\left|\frac{e}{\mu c}\widetilde{\mathbf{A}}(0)\left(\frac{e}{2c}\gamma\mathbf{H}\times\mathbf{r}+\frac{\hbar}{i}\frac{\partial}{\partial\mathbf{r}}\right)\right|0;n_1m_1\right\rangle. \tag{46}$$

Given this expression, we can calculate the oscillator strength of a transition between the levels determined by Eq. (21), which is defined by the formula[36]

$$f_{1\to2}=\frac{2\mu}{\hbar^2}(E_2-E_1)|\langle2|r_\pm|1\rangle|^2, \tag{47}$$

where $r_\pm=(x\pm iy)/2$. Integration of Eq. (47) over the angular variable yields the standard set of magnetic moment selection rules: $m\to m\pm1$. The transition $m\to m+1$ corresponds to absorption of a photon with right-hand polarization ($\mathbf{e}^+=-i/\sqrt{2}(\mathbf{e}_x+i\mathbf{e}_y)$), and the transition $m\to m-1$ corresponds to absorption of a photon with left-hand polarization $[\mathbf{e}^-=(\mathbf{e}^+)^*]$. The oscillator strength defined by Eq. (47) of the transition $(n_1,m)\to(n_2,m\pm1)$ is expressed as

$$f_{n_1m}^{n_2m\pm1}=\left(n_2-n_1+\frac{|m\pm1|-|m|}{2}\pm\frac{\gamma}{2\beta}\right)(D_{n_1m}^{n_2m\pm1})^2, \tag{48}$$

where

$$D_{n_1m}^{n_2m\pm1}=\sqrt{\frac{n_1!n_2!}{(n_1+|m|)!(n_2+|m\pm1|)!}}\times\int e^{-x}x^{(|m|+|m\pm1|+1)/2}L_{n_1}^{|m|}(x)L_{n_2}^{|m\pm1|}(x)dx. \tag{49}$$

For $m\geqslant0$, $n_1=n_2=0$ the oscillator strength is

$$f_{0m}^{0m+1}=\frac{(m+1)}{2}\left(1+\frac{\gamma}{\beta}\right), \tag{50}$$

and for $m\leqslant-1$ the transition $(0,m)\to(0,m-1)$ has the oscillator strength

$$f_{0m}^{0m-1}=\frac{(-m+1)}{2}\left(1-\frac{\gamma}{\beta}\right). \tag{51}$$

Let us consider the transitions from the ground state (0,0). The transitions $(0,0)\to(n\neq0,\pm1)$ are forbidden since $D_{00}^{n,\pm1}=0$. The oscillator strengths of the transitions between the lowest levels are given below:

$$f_{00}^{01}=\frac{1}{2}f_{10}^{11}=\frac{1}{2}+\frac{\gamma}{2\beta}, \tag{52}$$

$$f_{00}^{0-1}=f_{01}^{10}=\frac{1}{2}f_{10}^{1-1}=\frac{1}{2}-\frac{\gamma}{2\beta}. \tag{53}$$

The oscillator strength given by Eq. (48) is a monotonic function of H:

$$f_{n_1m}^{n_2m\pm1}=(D_{n_1m}^{n_2m\pm1})^2\left(n_2-n_1+\frac{|m\pm1|-|m|}{2}\pm\frac{\gamma H}{2\sqrt{H^2+4H_0^2\mu/M}}\right), \tag{54}$$

$f_{n_1m}^{n_2m+1}$ increases (decreases) with H for an exciton with a heavy (light) hole, and $f_{n_1m}^{n_2m-1}$ decreases (increases) in this case.

6. CONCLUSIONS

We have investigated the spectrum of a two-dimensional magnetoexciton in coupled quantum wells. The spectrum consists of separate bands, whose widths decrease when the separation D between the quantum wells increases. The shapes of the dispersion curves $\mathscr{E}(\mathscr{P},\mathscr{D})$, where $\mathscr{P}$ is the conserved magnetic momentum, proportional to the exciton size in the quantum well plane, depend sensitively on the separation $\mathscr{D}$ between the quantum wells. In the limit $\mathscr{D}\ll1$ the dispersion curves are nonmonotonic in all nondegenerate states, except the ground state $(n=m=0)$. In states (n,m) the dispersion curves have $n+1$ minima. At $m=0$ and all n, zero momentum $\mathscr{P}=0$ corresponds to a minimum in $\mathscr{E}_{nm}(\mathscr{P},\mathscr{D})$, and for $m\neq0$ to a maximum. Side-band extrema corresponding to momenta $\mathscr{P}\neq0$ gradually disappear as $\mathscr{D}$ increases, and for $\mathscr{D}>\mathscr{D}_{\mathrm{cr}}$ only one extremum (i.e., a minimum at $\mathscr{P}=0$) survives. For large $\mathscr{D}$ and small $\mathscr{P}$ dispersion functions have been calculated analytically in an arbitrary magnetic field.

The spectra of magnetoexcitons in degenerate states have been calculated. At $\gamma=0$ $(m_e=m_h)$ the spectrum depends on the quantum number $N=2n+|m|$, and each level is $(N+1)$-fold degenerate (the state $N=0$ is nondegenerate). Off-center extrema corresponding to momentum $\mathscr{P}\neq0$ gradually disappear with an increase in $\mathscr{D}$, and for $\mathscr{D}\gg1$ there is only one minimum at $\mathscr{P}=0$ in states with $N=1$ and $N=2$.

Note that it would interesting to detect roton exciton states with momenta $\mathscr{P}\neq0$. They could be detected using layers with high Miller indices or artificial superlattices applied to the surface of samples with quantum wells by means of nanotechniques. Roton magnetoexcitons can also result from relaxation of a magnetoexciton from maxima with momentum $\mathscr{P}=0$ to an off-center minimum on a dispersion curve. Since the momentum of such a minimum satisfies $\mathscr{P}_r \propto \sqrt{H}$, this state can be metastable in strong magnetic fields. In this connection, it would be interesting to investigate collective properties of roton excitons.

We have also calculated the probability of magnetoexciton photogeneration in coupled quantum wells and the oscillator strengths of the transition between magnetoexciton levels in coupled quantum wells with absorption (or emission) of electromagnetic radiation.

The work was supported by the Russian Fund for Fundamental Research, the *Physics of Solid-State Nanostructures* and *Surface Atomic Structures* programs, and INTAS.

One of the authors (Yu.E.L.) acknowledges helpful discussions of results of this work with M. Bayer, A. Forchel, and V. B. Timofeev during his stay at Würzburg University.

*)e-mail: lozovik@alpha.isan.troitsk.ru

---

[1] T. Fukuzawa, E. E. Mendez, and J. M. Hong, Phys. Rev. Lett. **64**, 3066 (1990).

[2] L. V. Butov, V. D. Kulakovskii, G. E. W. Bauer, A. Forchel, and D. Grützmacher, Phys. Rev. B **46**, 12765 (1992).

[3] L. V. Butov, A. Zrenner, G. Abstreiter, G. Böhm, and G. Weigmann, Phys. Rev. Lett. **73**, 304 (1994).

[4] J.-P. Cheng, J. Kono, B. D. McCombe, I. Lo, W. C. Mitchel, and C. E. Stutz, Phys. Rev. Lett. **74**, 450 (1995).

[5] U. Sivan, P. M. Solomon, and H. Strikman, Phys. Rev. Lett. **74**, 450 (1995).

[6] L. V. Butov, A. Zrenner, G. Abstreiter, A. V. Petinova, and K. Eberl, Phys. Rev. B **52**, 12153 (1995).

[7] M. Bayer, V. B. Timofeev, F. Faller, T. Gutbrod, and A. Forchel, Phys. Rev. B **54**, 8799 (1996).

[8] Yu. E. Lozovik and V. I. Yudson, JETP Lett. **22**, 274 (1975); Yu. E. Lozovik and V. I. Yudson, Solid State Commun. **18**, 628 (1976); Solid State Commun. **21**, 211 (1977); Yu. E. Lozovik, in Proceedings of the 1st All-Union Conference on Dielectric Electronics, Tashkent (1973), p. 53.

[9] Yu. E. Lozovik and V. I. Yudson, Zh. Éksp. Teor. Fiz. **71**, 738 (1976) [Sov. Phys. JETP **44**, 389 (1976)].

[10] Yu. E. Lozovik and O. L. Berman, JETP Lett. **64**, 573 (1996); Zh. Éksp. Teor. Fiz. **111**, 1879 (1997) [JETP **84**, 1027 (1997)]; Yu. E. Lozovik and O. L. Berman, Phys. Scr. **55**, 491 (1997).

[11] Yu. E. Lozovik and V. I. Yudson, JETP Lett. **25**, 11 (1977).

[12] Yu. E. Lozovik and A. V. Klyuchnik, J. Phys. C **11**, L483 (1978); A. V. Klyuchnik and Yu. E. Lozovik, Zh. Éksp. Teor. Fiz. **76**, 670 (1979) [Sov. Phys. JETP **49**, 335 (1979)]; Yu. E. Lozovik and A. V. Klyuchnik, Low Temp. Phys. **38**, 761 (1980).

[13] S. I. Shevchenko, Phys. Rev. Lett. **72**, 3242 (1994).

[14] Yu. E. Lozovik and A. V. Poushnov, Phys. Lett. A **228**, 399 (1997).

[15] I. V. Lerner and Yu. E. Lozovik, Zh. Éksp. Teor. Fiz. **80**, 1488 (1981) [Sov. Phys. JETP **53**, 763 (1981)]; Zh. Éksp. Teor. Fiz. **82**, 1188 (1982) [Sov. Phys. JETP **55**, 691 (1982)].

[16] I. V. Lerner and Yu. E. Lozovik, Zh. Éksp. Teor. Fiz. **78**, 1167 (1980) [Sov. Phys. JETP **51**, 588 (1980)].

[17] A. B. Dzyubenko and Yu. E. Lozovik, Fiz. Tverd. Tela (Leningrad) **25**, 874 (1983) [Sov. Phys. Solid State **25**, 500 (1983)]; Fiz. Tverd. Tela (Leningrad) **26**, 1540 (1984) [Sov. Phys. Solid State **26**, 938 (1984)].

[18] D. Paquet, T. M. Rice, and K. Ueda, Phys. Rev. B **32**, 5208 (1985).

[19] A. B. Dzuybenko and Yu. E. Lozovik, J. Phys. A **24**, 415 (1991).

[20] A. H. MacDonald and E. H. Rezayi, Phys. Rev. B **42**, 3224 (1990).

[21] S. M. Dikman and S. V. Iordanskiĭ, JETP Lett. **63**, 50 (1996).

[22] D. S. Chemla, J. B. Stark, and W. H. Knox, in *Ultrafast Phenomena VIII*, ed. by J.-L. Martin *et al.*, Springer (1993), p. 21.

[23] G. Finkelstein, H. Strikman, and I. Bar-Joseph, Preprint of Weizmann Institute of Science, Rehovot, Israel.

[24] D. Yoshioka and H. Fukuyama, J. Phys. Soc. Jpn. **45**, 137 (1978).

[25] Yu. A. Bychkov and E. I. Rashba, Solid State Commun. **48**, 399 (1983).

[26] X. M. Chen and J. J. Quinn, Phys. Rev. Lett. **67**, 895 (1991).

[27] Xuejun Zhy, P. B. Littlewood, Mark S. Hybertsen, and T. M. Rice, Phys. Rev. Lett. **74**, 1633 (1995).

[28] L. V. Keldysh and Yu. V. Kopaev, Fiz. Tverd. Tela (Leningrad) **6**, 2791 (1964) [Sov. Phys. Solid State **6**, 2219 (1964)]; A. N. Kozlov and L. A. Maksimov, Zh. Éksp. Teor. Fiz. **48**, 1184 (1965) [Sov. Phys. JETP **21**, 790 (1965)]; L. V. Keldysh and A. N. Kozlov, Zh. Éksp. Teor. Fiz. **54**, 978 (1968) [Sov. Phys. JETP **27**, 521 (1968)]; B. I. Halperin and T. M. Rice, Solid State Phys. **21**, 115 (1968); L. V. Keldysh and A. P. Silin, Kratk. Soobshch. Fiz. **No 8**, 33 (1975); Yu. E. Lozovik and V. I. Yudson, Fiz. Tverd. Tela (Leningrad) **17**, 1613 (1975) [Sov. Phys. Solid State **17**, 1054 (1975)]; A. V. Klyuchnik and Yu. E. Lozovik, Fiz. Tverd. Tela (Leningrad) **20**, 625 (1978) [Sov. Phys. Solid State **20**, 364 (1978)].

[29] Yu. Kagan, B. V. Svistunov, and G. V. Shlyapnikov, Zh. Éksp. Teor. Fiz. **93**, 552 (1987) [Sov. Phys. JETP **66**, 314 (1987)].

[30] A. A. Gorbatsevich and I. V. Tokatly, Zh. Éksp. Teor. Fiz. **108**, 1723 (1995) [JETP **81**, 945 (1995)].

[31] V. S. Babichenko and M. N. Kiselev, JETP Lett. **57**, 179 (1993).

[32] L. P. Gor'kov and I. E. Dzyaloshinskiĭ, Zh. Éksp. Teor. Fiz. **53**, 717 (1967) [Sov. Phys. JETP **26**, 449 (1968)].

[33] Yu. E. Lozovik and V. N. Nishanov, Fiz. Tverd. Tela (Leningrad) **18**, 3267 (1976) [Sov. Phys. Solid State **18**, 1905 (1976)].

[34] Zh. S. Gevorkyan and Yu. E. Lozovik, Fiz. Tverd. Tela (Leningrad) **27**, 1800 (1985) [Sov. Phys. Solid State **27**, 1079 (1985)].

[35] R. J. Elliott and R. Loudon, J. Phys. Chem. Solids **15**, 196 (1960).

[36] H. Hasegawa and R. E. Howard, J. Phys. Chem. Solids **21**, 179 (1961).

Translation provided by the Russian Editorial office.

Galvanomagnetic properties of $Hg_{1-x}Mn_xTe_{1-y}Se_y$ semimagnetic semiconductors

V. A. Kul'bachinskiĭ, I. A. Churilov, P. D. Mar'yanchuk, and R. A. Lunin

M. V. Lomonosov Moscow State University, 119899 Moscow, Russia

(Submitted 2 April 1997)
Zh. Éksp. Teor. Fiz. **112**, 1809–1815 (November 1997)

The galvanomagnetic properties of single crystals of the semimagnetic semiconductors $Hg_{1-x}Mn_xTe_{1-y}Se_y$ with $0.01<y<0.1$ and $x=0.05$ and 0.14 in the temperature range 4.2–300 K are investigated. The features of the temperature dependence of the Hall coefficient R_H and the complicated behavior of R_H in a magnetic field are attributed quantitatively to the existence of three groups of current carriers, viz., electrons and two types of holes, for which the temperature dependences of the densities and mobilities are obtained. A transition from p-type to n-type conductivity is observed as the Se content is increased, and the negative magnetoresistance simultaneously gives way to positive magnetoresistance. [S1063-7761(97)02011-8]

1. INTRODUCTION

Semimagnetic semiconductors, or magnetically dilute semiconductors, are solid solutions in which one of the components is replaced by an atom of a transition element M with an uncompensated magnetic moment. Among the compounds $A^{II}_{1-x}M_xB^{VI}$ (A^{II} and B^{VI} are group-II and group-VI elements, respectively, and M is a metal), the $Hg_{1-x}Mn_xTe$ and $Hg_{1-x}Mn_xSe$ semimagnetic semiconductors have been studied quite thoroughly.[1–3] It has been established that $Hg_{1-x}Mn_xTe$ has p-type conduction,[4] while $Hg_{1-x}Mn_xSe$ always has n-type conduction with a high electron density.[5] The type of conduction is related to the appearance of charged defects in the crystals: in $Hg_{1-x}Mn_xTe$ the acceptor defects are vacancies in the mercury sublattice, and in $Hg_{1-x}Mn_xSe$ the donors are mercury atoms in interstitial positions and vacancies in the selenium sublattice. It would be of interest to investigate $Hg_{1-x}Mn_xTe_{1-y}Se_y$ semimagnetic semiconductors. It can be theorized that specific compensation of the different defects occurs as the concentration is varied, making it possible to regulate the type and density of charge carriers in the quaternary compound. The galvanomagnetic properties of $Hg_{1-x}Mn_xTe_{1-y}Se_y$ were previously studied as a function of the Mn content in Refs. 6–8, and, in addition, transitions to a spin-glass state were investigated in Refs. 7 and 8.

In the present work the galvanomagnetic properties (in the temperature range 4.2–300 K) of single crystals of the solid solutions $Hg_{1-x}Mn_xTe_{1-y}Se_y$ with $x=0.05$ and 0.14 are investigated as the selenium concentration is varied from $y=0.01$ to $y=0.10$.

2. SAMPLES

Single crystals of $Hg_{1-x}Mn_xTe_{1-y}Se_y$ were grown by the Bridgman method from chemically pure components. Samples with the characteristic dimensions $0.6\times0.6\times5\ mm^3$ were cut from the ingots by electroerosion for the measurements. The manganese content was precisely determined using x-ray probe microanalysis and measurements of the absolute value of the magnetic susceptibility at room temperature, which gave identical results to within the measurement error. The Se content in the samples is indicated according to these data. The absence of inclusions of other phases in the samples and their homogeneity were established as a result of electron probe microanalysis and magnetic measurements. The homogeneity of the samples was also monitored by measuring the Hall coefficient R_H at different points along the samples. (The differences between the values of R_H was less than a few percent, attesting to the high homogeneity of the samples investigated.)

The electrical measurements were carried out on freshly prepared samples at a constant current by the four-point probe technique. Samples of $Hg_{1-x}Mn_xTe_{1-y}Se_y$ with $x=0.05$, 0.14 and $y=0.01$, 0.05, 0.075, 0.10 were investigated. Several parameters of the single crystals investigated at $T=4.2$ K are presented in Tables I and II. In the tables n, p_1, and p_2 are the electron and hole densities, respectively,

TABLE I. Parameters of the samples of $Hg_{0.86}Mn_{0.14}Te_{1-y}Se_y$ investigated at 4.2 K.

N	y	n, 10^{14} cm^{-3}	μ_e, 10^4 $cm^2/V\cdot s$	p_1, 10^{17} cm−3	μ_{p1}, $cm^2/V\cdot s$	p_2, 10^{15} cm^{-3}	μ_{p2}, $cm^2/V\cdot s$
1	0.01	0.3	−6.0	2.7	820	9.0	3000
2	0.05	0.003	−6.0	0.9	130	0.46	4800
3	0.075	2.5	−3.0	7.8	850	25.0	5300
4	0.10	1.1	−1.2	42.0	60	0.52	4100

TABLE II. Parameters of the samples of $Hg_{0.95}Mn_{0.05}Te_{1-y}Se_y$ investigated at 4.2 K.

N	y	n, 10^{14} cm^{-3}	μ_e, 10^4 $cm^2/V\cdot s$	p_1, 10^{17} cm^{-3}	μ_{p1}, $cm^2/V\cdot s$	p_2, 10^{15} cm^{-3}	μ_{p2}, $cm^2/V\cdot s$
1	0.01	5.3	−1.5	2.8	715	7.2	2000
2	0.10	72.0	−0.56	8.2	80	4.8	5700

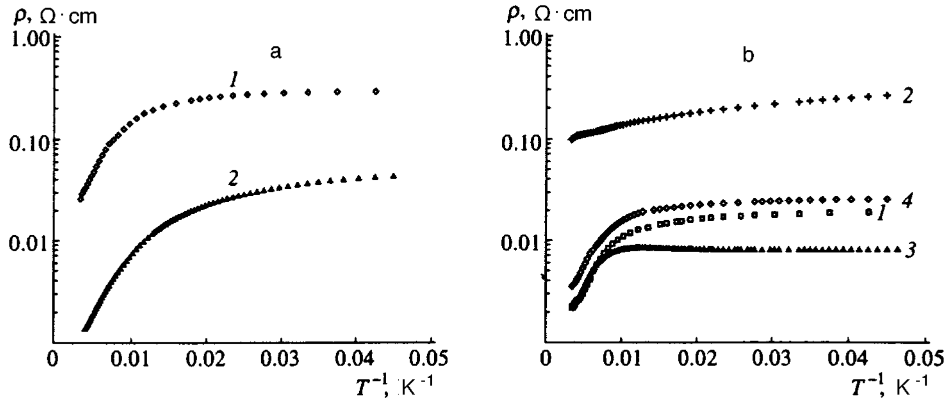

FIG. 1. Dependence of the resistivity on the reciprocal temperature for samples of $Hg_{1-x}Mn_xTe_{1-y}Se_y$ with different Mn and Se contents: a—$x=0.05$, *1*—$y=0.01$, *2*—$y=0.10$; b—$x=0.14$, *1*—$y=0.01$, *2*—$y=0.05$, *3*—$y=0.075$, *4*—$y=0.10$.

μ_e, μ_{p1}, and μ_{p2} are the electron and hole mobilities, and y is the Se concentration in the samples.

It has been reported that the near-surface region has a significant influence on the electric and galvanomagnetic properties of semiconductor solid solutions based on mercury telluride.[9] To eliminate this effect, the samples were etched immediately before the measurements. Special investigations showed that holding the etched samples in air for several days does not alter their electrophysical properties, particularly the complicated behavior of the Hall coefficient in a magnetic field at different temperatures, i.e., the near-surface region does not influence the results obtained.

3. RESULTS OF MEASUREMENTS OF THE GALVANOMAGNETIC PROPERTIES AND DISCUSSION

As the temperature is lowered, the resistivity of all the samples increases, demonstrating activation behavior with an activation energy of about 30 meV at temperatures above $\simeq 100$ K (Fig. 1). The samples with the smallest selenium content exhibit negative magnetoresistance at temperatures below $T=30$ K, which increases with decreasing temperature. As the selenium content increases, the negative magnetoresistance decreases, and at the Se concentration $y=0.10$ the magnetoresistance becomes positive even at liquid-helium temperatures. As an example, Fig. 2 presents the dependence $\rho(B)$ of the resistivity for samples of $Hg_{0.95}Mn_{0.05}Te_{1-y}Se_y$ with $y=0.01$ (Fig. 2a) and $y=0.10$ (Fig. 2b). Figure 3 presents the relative variation of the resistivity $[\rho(B)-\rho(0)]/\rho(0)$ in a magnetic field B for the five samples investigated. The negative magnetoresistance in large magnetic fields can be attributed to the increase in conductivity within an impurity band, which is typical of $Hg_{1-x}Mn_xTe$,[1–3] due to overlap of the wave functions on the acceptors in a magnetic field, i.e., the so-called magnetic boil-off of holes.[10–14] As the Se concentration increases, the role of conduction within the acceptor impurity band decreases, and the samples even change their type of conduction from p to n; therefore, the negative magnetoresistance gives way to positive magnetoresistance.

3.1. Determination of the mobilities of different groups of carriers from Hall measurements

The behavior of the Hall coefficient R_H at different temperatures as a function of the magnetic field is very complicated (Fig. 4). The samples of $Hg_{0.86}Mn_{0.14}Te_{1-y}Se_y$ with a direct band gap at 4.2 K have a positive Hall coefficient $R_H>0$ (see Figs. 4a and 4b). As the temperature increases, the sign of R_H in weak fields becomes negative. An increase in the selenium concentration leads to an increase in the electron density and to reversal of the sign of the Hall coefficient in weak magnetic fields. This effect is more pronounced in the gapless samples. As an example, Figs. 4c and 4d present plots of the dependence of R_H on the magnetic field at different temperatures for the samples of $Hg_{0.95}Mn_{0.05}Te_{1-y}Se_y$ with $y=0.01$ (c) and $y=0.10$ (d).

A satisfactory quantitative description of the $R_H(B)$

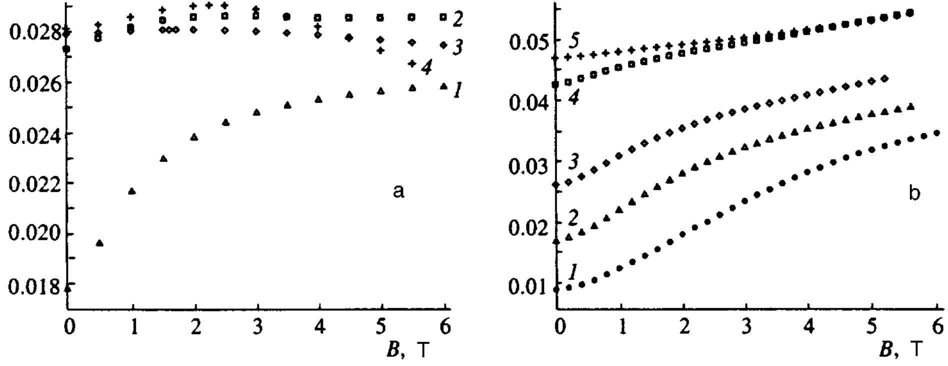

FIG. 2. Dependence of the resistivity on the magnetic field for the samples of $Hg_{0.95}Mn_{0.05}Te_{1-y}Se_y$ with $y=0.01$ (a) and $y=0.10$ (b) at various temperatures T, K: a) *1*—83, *2*—40, *3*—16, *4*—4.2; b) *1*—88, *2*—61, *3*—42, *4*—21, *5*—4.2.

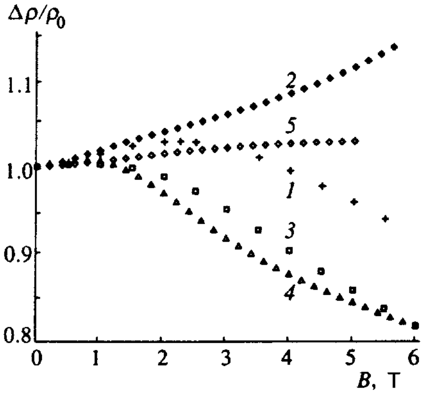

FIG. 3. Relative magnetoresistance at $T=4.2$ K in samples of $Hg_{1-x}Mn_xTe_{1-y}Se_y$ with various compositions: *1*—$x=0.05$, $y=0.01$, *2*—$x=0.05$, $y=0.1$; *3*—$x=0.14$, $y=0.01$; *4*—$x=0.14$, $y=0.075$; *5*—$x=0.14$, $y=0.10$.

curves in Fig. 4 can be obtained only if we take into account three types of carriers: band electrons and two types of holes with different densities and mobilities, of which some are intrinsic while others correspond to an acceptor impurity band.[7,8] The Hall coefficient depends on the magnetic field in the following manner (the Hall factor for all the groups being equal to unity):

$$R_H(B)=N(A^2+N^2B^2)^{-1}, \tag{1}$$

where we have introduced the notation

$$N=\frac{en\mu_e^2}{1+\mu_e^2B^2}+\frac{ep_1\mu_{p1}^2}{1+\mu_{p1}^2B^2}+\frac{ep_2\mu_{p2}^2}{1+\mu_{p2}^2B^2}, \tag{2}$$

$$A=\frac{en\mu_e}{1+\mu_e^2B^2}+\frac{ep_1\mu_{p1}}{1+\mu_{p1}^2B^2}+\frac{ep_2\mu_{p2}}{1+\mu_{p2}^2B^2}. \tag{3}$$

In Fig. 4 the lines are $R_H(B)$ curves calculated with consideration of the three groups of carriers cited. Tables I and II present the electron and hole densities and mobilities at 4.2 K obtained from fitting the $R_H(B)$ curves. Fitting the experimental $R_H(B)$ curves for different temperatures permitted the determination of the mobilities and densities of the three groups of carriers, which are presented in Tables I–III. All the mobilities decrease with increasing temperature. The values of the electron mobility are highest, as is typical of $Hg_{1-x}Mn_xTe$. In addition, the electron density increases as the selenium content in the samples is increased until the type of conduction changes from p to n (the samples with $x=0.05$). The mobilities increase with decreasing temperature in all three groups, while the carrier densities decrease.

3.2. Determination of the mobilities of different groups of carriers from the positive magnetoresistance

The classical magnetoresistance was also utilized to find the mobilities of the different groups of carriers in the samples investigated. Beck and Anderson[15] proposed a method which transforms the dependence of the resistivity on the magnetic field into a so-called mobility spectrum,

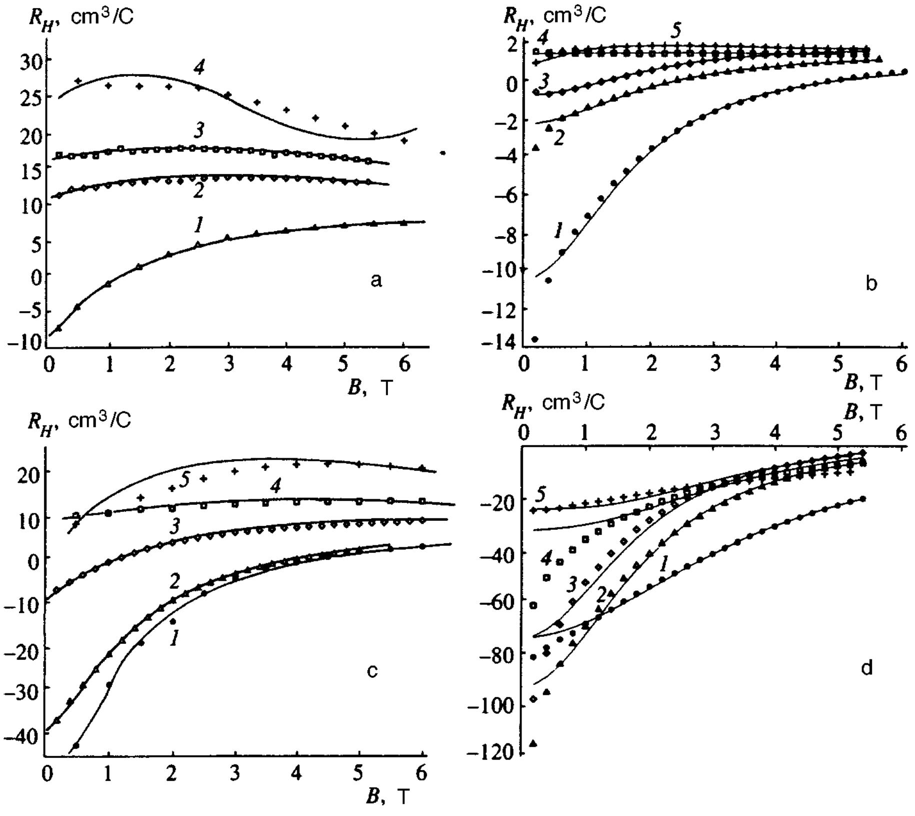

FIG. 4. Dependence of the Hall coefficient on the magnetic field for samples of $Hg_{1-x}Mn_xTe_{1-y}Se_y$ with $x=0.14$ and $y=0.01$ (a), $x=0.14$ and $y=0.10$ (b), $x=0.05$ and $y=0.01$ (c), and $x=0.05$ and $y=0.10$ (d) at various temperatures T, K: a) *1*—42, *2*—17, *3*—8.5, *4*—4.2; b) *1*—79, *2*—53, *3*—42, *4*—21, *5*—4.2; c) *1*—81, *2*—59, *3*—36, *4*—15, *5*—4.2; d) *1*—95, *2*—61, *3*—39, *4*—20, *5*—4.2. Points—experimental data; lines—results of calculations for three types of carriers using Eq. (1) (see text).

TABLE III. Mobilities of the charge carriers in samples of $Hg_{1-x}Mn_xTe_{1-y}Se_y$ determined from mobility spectra (column 1) and from Hall measurements (column 2) at various temperatures.

		μ_e, $cm^2/V\cdot s$		μ_{p1}, $cm^2/V\cdot s$		μ_{p2}, $cm^2/V\cdot s$	
Sample	T, K	1	2	1	2	1	2
$Hg_{0.86}Mn_{0.14}Te_{0.90}Se_{0.10}$	79	−5700	−6500	70	60	2400	-
$Hg_{0.86}Mn_{0.14}Te_{0.90}Se_{0.10}$	42	−6600	−5000	75	50	-	800
$Hg_{0.86}Mn_{0.14}Te_{0.90}Se_{0.10}$	4.2	−10 000	−12 000	50	60	3100	4100
$Hg_{0.95}Mn_{0.05}Te_{0.90}Se_{0.10}$	4.2	−4500	−5700	60	80	3400	5700

which gives the maximum conductivity as a function of the mobility. It is assumed in this method that the carrier density n is a continuous function $n(\mu)$ of the mobility μ, so that the transverse conductivity tensor elements can be written in the form of integrals, which sum the contributions of each of the groups of carriers to the conductivity:

$$\sigma_{xx}(B)=\int_{-\infty}^{\infty}\frac{s(\mu)d\mu}{1+(\mu B)^2},$$

$$\sigma_{xy}(B)=\int_{-\infty}^{\infty}\frac{s(\mu)\mu B d\mu}{1+(\mu B)^2}, \tag{4}$$

where $s(\mu)d\mu=en(\mu)d\mu$ is the contribution of the carriers having a mobility from μ to $\mu+d\mu$ to the mobility when $B=0$. It is assumed in these equations that the electrons have negative mobility and the holes have positive mobility. If there are N types of carriers with discrete densities n_i and mobilities μ_i $(i=1,\dots,N)$, the mobility spectrum will display N peaks, whose centers are located at μ_i and whose amplitudes equal $en_i\mu_i$. The mobility-spectrum method is applicable, if 1) there is no quantization of the energy spectrum in the magnetic fields,[16] i.e., the magnetic fields are weak; 2) the magnetic fields do not significantly bend the trajectories of carriers in the region where they interact with scattering centers (vacancies in the mercury sublattice, interstitial mercury atoms, vacancies in the selenium sublattice, etc.).

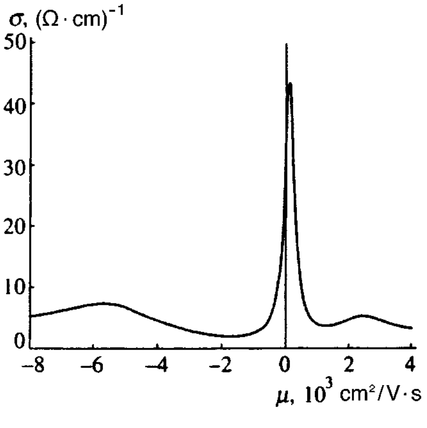

FIG. 5. Mobility spectrum of $Hg_{0.86}Mn_{0.14}Te_{0.90}Se_{0.10}$ at 79 K. The three maxima correspond to three groups of carriers (the mobility is negative for electrons).

The values of the positive magnetoresistance in the range from 0.2 T to 5 T for different samples were transformed into mobility spectra. Figure 5 presents the mobility spectrum of $Hg_{0.86}Mn_{0.14}Te_{0.90}Se_{0.10}$ at 79 K. This figure shows that there are three groups of carriers with different mobilities: two groups of holes and a group of electrons. The mobility values obtained from the mobility spectra agree well with the values calculated from the magnetic-field dependences of the Hall coefficient in all the samples. The electron densities and mobilities determined from the maxima in the mobility spectrum are presented in Table III.

4. CONCLUSIONS

Thus, in $Hg_{1-x}Mn_xTe_{1-y}Se_y$ semimagnetic semiconductors the transport properties, reversal of the sign of the Hall coefficient as the temperature increases, and its complicated behavior in a magnetic field are determined by the electrons and two groups of holes. As the selenium concentration is increased, the electron density rises, and the type of conduction changes from p to n. At 4.2 K the samples of $Hg_{1-x}Mn_xTe_{1-y}Se_y$ with $y<0.1$ exhibit negative magnetoresistance, which is attributed to alteration of the overlap of the wave functions of the acceptors in a magnetic field and goes over to positive magnetoresistance at a high Se content. The temperature dependence of the mobilities and densities as a function of the selenium content has been obtained for the three groups of carriers, viz., electrons and two types of holes.

[1] J. K. Furdyna, J. Appl. Phys. **64**, R29 (1988).
[2] N. B. Brandt and V. V. Moshchalkov, Adv. Phys. **33**, 194 (1984).
[3] I. I. Lyapilin and I. M. Tsidil'kovskiĭ, Usp. Fiz. Nauk **146**, 35 (1985) [Sov. Phys. Usp. **28**, 349 (1985)].
[4] N. B. Brandt, V. V. Moshchalkov, A. O. Orlov *et al.*, Zh. Éksp. Teor. Fiz. **84**, 1059 (1983) [Sov. Phys. JETP **57**, 614 (1983)].
[5] Zh. T. Ismailov, V. A. Kul'bachinskiĭ, S. M. Chudinov *et al.*, Fiz. Tekh. Poluprovodn. **22**, 375 (1988) [Sov. Phys. Semicond. **22**, 231 (1988)].
[6] K. R. Krylov, N. K. Lerinman, A. I. Ponomarev *et al.*, Fiz. Tekh. Poluprovodn. **28**, 1382 (1994) [Semiconductors **28**, 779 (1994)].
[7] V. A. Kul'bachinskiĭ, P. D. Mar'yanchuk, and I. A. Churilov, Fiz. Tekh. Poluprovodn. **29**, 2007 (1995) [Semiconductors **29**, 1047 (1995)].
[8] V. A. Kulbachinskii, P. D. Maryanchuk, I. A. Churilov *et al.*, Semicond. Sci. Technol. **10**, 463 (1995).
[9] V. I. Ivanov-Omskii, N. N. Berchenko, and A. I. Elizarov, Phys. Status Solidi A **103**, 11 (1987).
[10] J. Mycielski, in *Recent Development in Condensed Matter Physics*, J. T. DeVreese (ed.), Plenum, New York (1981), Vol. 1, p. 725.
[11] L. R. Gawron and J. Trylski, in *Lecture Notes in Physics 152. Physics of*

Narrow Gap Semiconductors, Proceedings of the Lintz Conference, 1981, F. Gornik, H. Heinrich, and L. Palmetshofer (eds.), Springer, Berlin (1982), p. 294.
[12] A. Mycielski and J. Mycielski, J. Phys. Soc. Jpn. Suppl. A **49**, 807 (1980).
[13] W. B. Johnson, J. R. Anderson, and D. R. Stone, Phys. Rev. B **29**, 6679 (1984).
[14] A. B. Davydov, B. B. Ponikarov, and I. M. Tsidilkovskii, Phys. Status Solidi B **101**, 127 (1980).
[15] W. A. Beck and J. R. Anderson, J. Appl. Phys. **62**, 541 (1987).
[16] I. A. Panaev, S. A. Studenikin, D. I. Lubyshev, and V. P. Migal, Semicond. Sci. Technol. **8**, 1822 (1993).

Translated by P. Shelnitz

Spin diffusion and relaxation in three-dimensional isotropic Heisenberg antiferromagnets

K. A. Kikoin

Kurchatov Institute Russian Scientific Center, 123182 Moscow, Russia

M. N. Kiselev

Kurchatov Institute Russian Scientific Center, 123182 Moscow, Russia; Laboratoire Léon Brillouin, CEA-CNRS, CE Saclay, 91191 Gif-sur-Yvette Cedex, France

(Submitted 3 April 1997)
Zh. Éksp. Teor. Fiz. **112**, 1816–1829 (November 1997)

A theory is proposed for kinetic effects in isotropic Heisenberg antiferromagnets at temperatures above the Néel point. The scaling behavior of the generalized coefficient of spin diffusion and relaxation constant in the paramagnetic phase is studied in terms of the approximation of interacting modes. It is shown that the kinetic coefficients in an antiferromagnetic system are singular in the fluctuation region. The corresponding critical indices for diffusion and relaxation processes are calculated. The scaling dimensionality of the kinetic coefficients agrees with the predictions of dynamic similarity theory and a renormalization group analysis. The proposed theory can be used to study the momentum and frequency dependence of the kinetic parameters, and to determine the form of the scaling functions. The role of nonlocal correlations and spin-fluid effects in magnetic systems is discussed. © *1997 American Institute of Physics.* [S1063-7761(97)02111-2]

1. INTRODUCTION

Recent heightened interest in the critical dynamics of antiferromagnetic materials[1–6] has been stimulated by active experimental and theoretical research on quasi-two-dimensional magnetic correlations in high-temperature superconductors, and on the anomalous magnetic properties of heavy-fermion compounds.[6–8] In particular, critical spin fluctuations have been invoked to explain the non-Fermi fluid behavior of the specific heat and resistance at low temperatures in the compounds[7,8] $\mathrm{CeCu}_{6-x}\mathrm{Au}_x$ and $\mathrm{Ce}_{1-x}\mathrm{La}_x\mathrm{Ru}_2\mathrm{Si}_2$ near the concentration critical point. In addition, a proposed[9,10] spin-fluid approach to the Heisenberg model, based on introducing resonating valence bonds with Fermi statistics for excitations in the magnetic sublattice (spinons), may, in turn, also serve as a scenario for describing the behavior of cerium compounds with heavy fermions.[11,12] Here it turns out that critical spin fluctuations play an important role in the formation mechanism of a spin fluid. The behavior of the kinetic coefficients in this case can deviate substantially from that predicted by dynamic similarity theory.[13]

In this paper we develop a microscopic approach for studying the scaling behavior of the spin diffusion coefficient and the relaxation constant of an isotropic Heisenberg antiferromagnet in the fluctuation region above the Néel temperature. The scaling dimensionality of the kinetic coefficients in magnets was predicted by Halperin and Hohenberg,[14,15] who developed a hypothesis of scale invariance based on the idea that the values of the dynamic critical indices are conserved on both sides of the phase transition. Maleev then made a microscopic study of spin diffusion in the paramagnetic phase of ferromagnets.[16,17] He, in particular, established the approximations required to satisfy the requirements of the hypothesis of scale invariance, and studied the momentum and frequency dependence of the spin diffusion coefficient. The analogous problem for antiferromagnets will be examined in the present paper.

It is known[14] that in the neighborhood of a phase transition, two regions can be distinguished in the momentum-temperature plane: a hydrodynamic region determined by long-wavelength fluctuations in the ordering parameter $\mathbf{N}=\mathbf{N}_1-\mathbf{N}_2$, the difference in the moments of the sublattices, with characteristic wave vectors $q\xi\ll 1$, where $q=|\mathbf{k}-\mathbf{Q}|$ describes the deviation of the moment from the antiferromagnetic vector $\mathbf{Q}$ and ξ is the correlation length, and a critical region, with wave vectors $q\xi\gg 1$. Here the concept of a correlation length is related to the characteristic behavior of the ordering parameter $\mathbf{N}$. In an antiferromagnet, however, there is an additional conserved quantity, the vector $\mathbf{M}=\mathbf{M}_1+\mathbf{M}_2$, the sum of the moments of the sublattices. Nevertheless, we shall also refer to the long-wavelength fluctuation region for the vector $\mathbf{M}$, $k\xi\ll 1$, as hydrodynamic. In this paper we examine the behavior of the spin correlation functions in the paramagnetic phase and establish the relationship between the kinetic coefficients in the fluctuation region of the phase diagram.

In the hydrodynamic regime, the dynamics of the fluctuations in the magnetization have a diffusive character, i.e., the variation in the magnetic moment with time obeys the macroscopic van Hove diffusion equation:

$$\frac{\partial\mathbf{M}}{\partial t}=D_0\nabla^2\mathbf{M}, \tag{1}$$

where D_0 is the spin diffusion coefficient. This behavior of the fluctuations is related to the conservation of the magnetic moment; the operator corresponding to it commutes with the Hamiltonian.

A different pattern is observed in the critical region. The nonconservation of the ordering parameter determines the

1063-7761/97/110994-07$10.00

relaxation character of the time variation in the vector **N**, i.e., the dynamics of this vector obey the relaxation equation:

$$\frac{\partial \mathbf{N}}{\partial t}=-\frac{\Gamma_0}{\chi}\mathbf{N}, \tag{2}$$

where χ is the susceptibility and the kinetic coefficient $\Gamma_0>0$. We note also that, in contrast to the diffusion equation (1), relaxation (2) can be uniform; the gradient corrections omitted from Eq. (2) are proportional to q^2 in this case. Although the average value of the magnetization vector **M** is zero on both sides of the phase transition point, fluctuations occur in the magnetization vector near the zero value. Unlike in a ferromagnet, however, the diffusion mode is not critical.

In the following we shall be interested in the dynamic susceptibility of a cubic Heisenberg antiferromagnet located in zero magnetic field above the Néel temperature:

$$H=-\sum_{\langle i,j\rangle} V_{ij}\mathbf{S}_i\cdot\mathbf{S}_j\,. \tag{3}$$

We also neglect dipole forces.[17]

The susceptibility is known to be related to the retarded spin Green function by the equation

$$\lambda(\mathbf{k},\omega)=(g\mu_0)^2K^R_{SS}(\mathbf{k},\omega), \tag{4}$$

where g is the Landé g factor, μ_0 is the Bohr magneton, and

$$K^R_{SS}(\mathbf{k},\omega)=i\int_0^\infty dt\; e^{i\omega t}\langle[S^z_{\mathbf{k}}(t),S^z_{-\mathbf{k}}(0)]\rangle,$$

$$\mathbf{S}_{\mathbf{k}}=\frac{1}{\sqrt{N}}\sum_i e^{-i\mathbf{k}\cdot\mathbf{R}_i}\mathbf{S}_i\,,$$

$$\mathbf{M}=\langle\mathbf{S}_0\rangle,\quad \mathbf{N}=\langle\mathbf{S}_{\mathbf{Q}_{\mathbf{AFM}}}\rangle. \tag{5}$$

Proceeding from Eqs. (1) and (2), we can obtain the form of the correlation functions K^R in the diffusion

$$K^R_{SS}(\mathbf{k}\to\mathbf{0},\omega)=\mathscr{K}(\mathbf{k},\omega)=G_0(k)\,\frac{iDk^2}{\omega+iDk^2} \tag{6}$$

and relaxation regions

$$K^R_{SS}(\mathbf{q}=(\mathbf{k}-\mathbf{Q})\to 0,\omega)=\mathscr{L}(\mathbf{q},\omega)=\frac{1}{-i\omega/\Gamma+G_0^{-1}(q)}. \tag{7}$$

Here G_0 is the static susceptibility.

In the fluctuation region $\tau=|T-T_c|/T_c\ll Gi$ (Gi is the Ginzburg number, which characterizes the limits of applicability of the Landau theory), when the fluctuations become large, the fluctuation dynamics obey the Halperin–Hohenberg similarity law, according to which the dynamic susceptibility χ and, therefore, the function K^R_{SS} can be expressed in terms of the scaling function F:

$$K^R_{SS}(\mathbf{k},\omega)=G_0(\mathbf{k})F\left(k\xi,\,\frac{\omega}{T_c\tau^{\nu z}}\right), \tag{8}$$

i.e., the dynamic index z which characterizes the energy scale of the critical fluctuations, $\omega\propto k^z$, can be related to a static index $\nu\approx 2/3$ which determines the variation in the correlation length, $\xi\propto\tau^{-\nu}$. For small deviations from the antiferromagnetic vector, the static susceptibility varies as $G_0(q)\propto\xi^{2-\eta}$. In the following discussion the Fisher index η, which characterizes the so-called anomalous dimensionality,[18] will be set equal to zero. This approximation is valid for three-dimensional systems.[18] It is necessary to introduce two scaling functions $\mathscr{F}_1$ and $\mathscr{F}_2$ to describe the fluctuation regions in an antiferromagnet:

$$\mathscr{K}(\mathbf{k},\omega)=G_0(\mathbf{k})\mathscr{F}_1\left(k\xi,\,\frac{\omega}{T_c\tau^{\nu z}}\right),$$

$$\mathscr{L}(\mathbf{q},\omega)=G_0(\mathbf{q})\mathscr{F}_2\left(q\xi,\,\frac{\omega}{T_c\tau^{\nu z}}\right). \tag{9}$$

Here, however, the kinetic coefficients D_0 and Γ_0 can, in turn, themselves be correlation lengths. Furthermore, as a renormalization group analysis shows,[14,19] the kinetic coefficients are singular in the fluctuation region of an antiferromagnet.

The theory developed in this paper is a variant of the interacting mode theory of Kawasaki.[20] We have tried to generalize the theory proposed by Maleev[16] for spin diffusion in ferromagnets to antiferromagnetic systems. In many regards, we follow the style and spirit of that paper. As noted before, our problem involves a study of the form of the scaling function F (see Eqs. (8) and (9)) and a determination of the frequency and momentum dependences of the kinetic coefficients in the fluctuation region, as well as establishing those approximations which must be made in a microscopic approach in order to satisfy the requirements of scaling invariance.

2. GENERALIZED KINETIC COEFFICIENTS

We therefore study the dynamic susceptibility of a cubic Heisenberg antiferromagnet located in zero magnetic field above the Néel temperature in the fluctuation region. Equations (6) and (7) can be rewritten in the more general form

$$K^R_{SS}(\mathbf{k},\omega)=\frac{i\gamma(\mathbf{k},\omega)}{\omega+iG_0^{-1}(\mathbf{k})\gamma(\mathbf{k},\omega)}, \tag{10}$$

while in the diffusion region

$$D_0=\lim_{k\to 0}\lim_{\omega\to 0}k^{-2}\gamma(\mathbf{k},\omega)G_0^{-1}(\mathbf{k}), \tag{11}$$

and in the relaxation region the generalized kinetic coefficient $\gamma(\mathbf{k},\omega)=\Gamma(\mathbf{k},\omega)$. The limit of Eqs. (6) and (7) for $\mathbf{k}\to 0$ and $\omega\to 0$ depends strongly on the relationship between k and ω, similarly to the way it does in the theory of Fermi fluids.[21] In the following we shall be interested in the quasistatic limit, i.e. $k\to 0$ and $|\omega|/k^2\to 0$.

As Maleev shows,[16] it is possible to go beyond the linear response theory and express the kinetic coefficients in terms of the Kubo function[22] of the operators S and $\dot S$ (the dot denotes differentiation with respect to time):

$$\gamma(\mathbf{k},\omega)=\frac{\Phi_{\dot S\dot S}(\mathbf{k},\omega)}{1+G_0^{-1}(k)\Phi_{SS}(\mathbf{k},\omega)}, \tag{12}$$

where

$$\Phi_{AB}(\mathbf{k},\omega)=\frac{1}{i\omega}\,[K^R_{AB}(\mathbf{k},\omega)-K^R_{AB}(\mathbf{k},0)],$$

$$K^R_{AB}(\mathbf{k},\omega)=i\int_0^\infty dt\ e^{i\omega t}\langle[A_{\mathbf{k}}(t),B_{-\mathbf{k}}(0)]\rangle.$$

Equation (12) is exact and accounts for the nonlinear nature of the relaxation forces. In the case of a purely exchange interaction in the long wavelength limit $\dot{S}_{\mathbf{k}}\sim k$, i.e., $\gamma=\Phi_{SS}(\mathbf{k},\omega)$, the denominator equals unity and Eq. (11) is the same as the result from the linear response theory. Generally speaking, however, the functions in the denominator cannot be neglected in a study of the frequency and momentum dependence of the kinetic coefficients.

It is easy to show that the retarded Green functions $K^R_{SS}(\mathbf{k},\omega)$, $K^R_{\dot{S}S}(\mathbf{k},\omega)$, and $K^R_{\dot{S}\dot{S}}(\mathbf{k},\omega)$ are related in the paramagnetic phase by simple formulas which follow from the dispersion relations:[23]

$$\begin{aligned}
&K^R_{SS}(\mathbf{k},\omega)=-i\omega K^R_{SS}(\mathbf{k},\omega),\\
&K^R_{S\dot{S}}(\mathbf{k},\omega)=-K^R_{\dot{S}S}(\mathbf{k},\omega)=i\omega K^R_{SS}(\mathbf{k},\omega),\\
&\omega^2K^R_{SS}(\mathbf{k},\omega)=[K^R_{\dot{S}\dot{S}}(\mathbf{k},\omega)-K^R_{\dot{S}\dot{S}}(\mathbf{k},0)]. \qquad (13)
\end{aligned}$$

It is clear from these relations, in particular, that $K^R_{\dot{S}S}(\mathbf{k},\omega)$ is analogous to $K^R_{\dot{S}\dot{S}}(\mathbf{k},\omega)$ in its properties and symmetry.[16]

Combining Eqs. (11) and (13) with the equation of motion for the spin operators,

$$\dot{S}^\alpha_{\mathbf{k}}=-\frac{1}{\sqrt{N}}\sum_{\mathbf{p}}\,[V(\mathbf{p}+\mathbf{k})-V(\mathbf{p})]\epsilon_{\alpha\beta\gamma}S^\beta_{\mathbf{p}+\mathbf{k}}S^\gamma_{-\mathbf{p}} \qquad (14)$$

(here $V(\mathbf{p})$ is the Fourier transform of the exchange integral) and transforming to ''imaginary'' time, we can obtain the relation between the Kubo functions and the correlators of the spin currents at the Matsubara frequencies:

$$\begin{aligned}
K_{\dot{S}\dot{S}}(\mathbf{k},\omega_n)=\frac{(a^2T_c\alpha)^2}{6N}\int_0^{1/T}d\tau e^{i\omega_n\tau}\sum_{\mathbf{p}_1,\mathbf{p}_2}&(\nabla V(\mathbf{p}_1)\mathbf{k})\\
&\times(\nabla V(\mathbf{p}_2)\mathbf{k})\\
&\times\langle T_\tau(S^\mu_{\mathbf{p}_1+\mathbf{k}}S^\rho_{-\mathbf{p}_1})_\tau(S^\mu_{-\mathbf{p}_2-\mathbf{k}}S^\rho_{\mathbf{p}_2})_0\rangle. \qquad (15)
\end{aligned}$$

In retaining only the first gradients of the potentials, $\nabla V(\mathbf{p})\approx\mathbf{p}T_ca^2\alpha$, we limit ourselves to the lowest order terms in an expansion in ka, where a is the lattice constant; the constant $\alpha\approx1$. It will be clear from the following analysis that the corrections to the kinetic coefficients will be expressed in the form of series in powers of $k\xi$ and, since $\xi\gg a$, it is valid to neglect the higher derivatives of the exchange integral. Therefore, the problem of finding the kinetic coefficients has been reduced to calculating four-spin correlators with a current vertex. This problem can be solved by analytic continuation of the temperature diagrams with an upper semiaxis into the complex ω plane. A graphical expression for the current correlator is shown in Fig. 1.

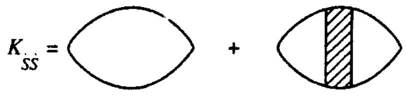

FIG. 1. Diagram series for the current correlator.

The ''seed'' poles for the spin Green functions (6) and (7) lie on the imaginary axis, i.e., if we set up some fictitious quasiparticles to correspond to these poles, their energies will be purely imaginary. Introducing quasiparticles of this sort, e.g., ''diffusons'' and ''relaxons'', allows us to obtain closed expressions for the kinetic coefficients and to determine their scaling dimensionality.

For the static susceptibility in the critical region we use the Ornstein–Zernike law:

$$G_0(\mathbf{q})=K^R_{SS}(\mathbf{q},0)=\frac{A}{T_c\tau^{2\nu}}\,\frac{1}{(q\xi)^2+1}, \qquad (16)$$

where A is a constant ($A\sim1$) and $\tau\ll1$. In the diffusion region the static susceptibility has no singularities and $G_0\approx A/2T_c$.

The following sections are devoted to analyzing the diagram series for the spin current correlator in the fluctuation regions, finding the dynamic critical indices for the kinetic coefficients, and determining the momentum and frequency dependence of the spin diffusion coefficient and relaxation constant.

3. RELATIONSHIPS AMONG THE KINETIC COEFFICIENTS

To analyze the diagram series we introduce the concept of an irreducible self-energy part as a diagram which is continuous along one interaction line. Using the definition of γ and the properties of the functions K, we rewrite the expression for the generalized kinetic coefficient in terms of irreducible self-energy parts:

$$\begin{aligned}
\gamma(\mathbf{k},\omega)=\frac{1}{i\omega}\Bigg[&\Sigma^R_{\dot{S}S}(\mathbf{k},\omega)-\Sigma^R_{\dot{S}\dot{S}}(\mathbf{k},0)\\
&+\frac{\mathscr{R}^R_{\dot{S}S}(\mathbf{k},\omega)\,\gamma(\mathbf{k},\omega)\mathscr{R}^R_{S\dot{S}}(\mathbf{k},\omega)}{-i\omega+G_0^{-1}(k)\,\gamma(\mathbf{k},\omega)}\Bigg]\\
&\times\left[1+G_0^{-1}\,\frac{\mathscr{R}^R_{\dot{S}S}(\mathbf{k},\omega)\,\gamma(\mathbf{k},\omega)}{i\omega(-i\omega+G_0^{-1}(k)\,\gamma(\mathbf{k},\omega))}\right]^{-1}.
\end{aligned} \qquad (17)$$

Equation (17) can also be obtained by analyzing the diagram series for the spin current correlator,[16] as well as directly from the Larkin equation.[12,23] In the following we use the following notation:

$$K^R_{\dot{S}S}(\mathbf{k},\omega)=\mathscr{R}^R(\mathbf{k},\omega)K^R_{SS}(\mathbf{k},\omega);$$

and Σ^R_{AB} for the irreducible self-energy parts. The graphical expression for the irreducible part $\Sigma^R_{\dot{S}\dot{S}}$ corresponds to replacing a complete vertex in Fig. 1 by an irreducible vertex. Estimating $\mathscr{R}$ in self-consistent field theory[16,24] yields

$$\mathscr{R}\sim(k\xi)(ka)\ll(k\xi)^2. \qquad (18)$$

In addition, its analytic properties imply that $\mathscr{R}^R\sim\omega$. We assume that the expression for $\mathscr{R}$ in the critical region also contains a term of order a/ξ in smallness, and for small ω we neglect this contribution. Thus, the generalized kinetic coef-

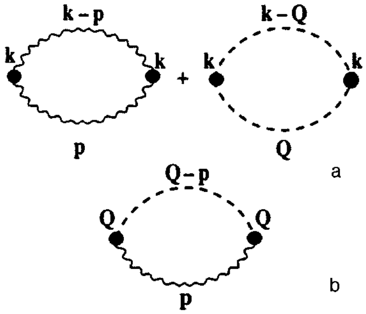

FIG. 2. Diagrams for the kinetic coefficients when two-particle intermediate states are included. A wavy line corresponds to the diffusion mode, a dashed line, to the relaxation mode. A dot denotes the vertex part of the static similarity theory.

ficient γ is defined only by the irreducible self-energy parts:

$$\gamma(\mathbf{k},\omega)=\frac{1}{i\omega}\,(\Sigma^{R}_{\dot{S}\dot{S}}(\mathbf{k},\omega)-\Sigma^{R}_{\dot{S}\dot{S}}(\mathbf{k},0)). \tag{19}$$

We now consider diagrams of a general form for the irreducible self-energy part Σ_{SS} at imaginary frequencies. These diagrams, in turn, can be classified in terms of the number of intermediate states. To begin with, we limit ourselves to diagrams with two-frequency intermediate states (Fig. 2a and b):

$$\begin{aligned}\Sigma^{(2)}_{\dot{S}\dot{S}}(\mathbf{k},i\omega)=&\frac{(T_c a^2\alpha)^2}{\sqrt{N}}\\ &\times T\sum_{\epsilon}\sum_{\mathbf{p}}\,(\mathbf{k}\Lambda^{(2)}(\mathbf{p},\mathbf{k},i\omega,i\epsilon,i(\omega-\epsilon)))\\ &\times(\mathbf{k}\Lambda^{(2)^{\dagger}}(\mathbf{p},\mathbf{k},i\epsilon,i(\omega-\epsilon),i\omega))\\ &\times K_{SS}(\mathbf{p},i\epsilon)K_{SS}(\mathbf{k}-\mathbf{p},i\omega-i\epsilon).\end{aligned} \tag{20}$$

In replacing the sum over the vectors $\mathbf{p}$ by an integral, we use $p\sim\xi^{-1}$ as an upper bound. Here the functions are integrated near the singularities (small $\mathbf{p}$ and $\mathbf{p}\sim\mathbf{q}+\mathbf{Q}$ in the neighborhood of the antiferromagnetic vector $\mathbf{Q}$).

The vertex parts Λ are analytic functions of all three frequencies, each of which has cuts along the real axis.[25] Vertex parts of this type have no other singularities in the complex ω planes.[25] Because of this property, the vertices can be resolved into a static part, which transforms into the vector vertex of static similarity theory, and a dynamic correction, which vanishes in the limit $\omega\to 0$. We now study the static part in more detail.

The static vertices in the diagrams (Fig. 2a) describe the long-wavelength processes of creating ‘‘diffuson’’–‘‘diffuson’’ and ‘‘relaxon’’–‘‘relaxon’’ pairs, i.e., identical modes interact. As we know, however, the static Green functions are independent of the direction of the momentum, i.e., diffuson and relaxon scattering processes contain the same vertex parts as do pair creation processes. This means that for these vertices, the Ward identity[18,21] holds (Fig. 3):

$$\Lambda^{(2)}(\mathbf{p},\mathbf{k},0)\sim\partial G_0^{-1}/\partial\mathbf{p}. \tag{21}$$

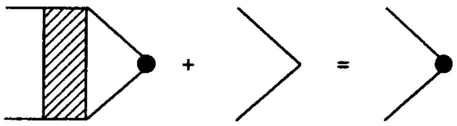

FIG. 3. The equations for a two-particle vertex part.

Here, in the second term the region of integration with respect to the momenta is concentrated near the points $\mathbf{p}\approx\mathbf{Q}$. The contribution of critical fluctuations to spin diffusion can be calculated by making the substitution $\mathbf{p}=\mathbf{q}+\mathbf{Q}$ and using the property $\partial G_0^{-1}/\partial\mathbf{p}=\partial G_0^{-1}/\partial\mathbf{q}$.

We now consider the diagram of Fig. 2b. Without loss of generality we can set the external momentum equal to the antiferromagnetic vector. In this case, we must consider two interacting modes of different kinds: a diffusion mode with short wave vectors and a relaxation mode with small deviations from the antiferromagnetism vector. Thus, the diagram of Fig. 2b describes ‘‘diffuson’’–‘‘relaxon’’ pair production. Thus, we cannot use the Ward identities for this vertex. However, the seed vertex (Fig. 3) has the scaling dimensionality

$$\Lambda_0^{(2)}(\mathbf{p},\mathbf{Q},0)\sim\partial V/\partial\mathbf{p}\sim\mathbf{p}.$$

It is also known that in the antiferromagnetic phase there is a doubling of the lattice, and the Brillouin zone of the ordered phase equals half the Brillouin zone of the disordered phase. This means that the points 0 and $\mathbf{Q}$ become equivalent in the antiferromagnetic phase. Given this fact, as well as the lack of a dependence on the direction of the momentum for the interacting modes, we may assume that rescattering by the static field does not change the scaling dimensionality of the static vertex at the antiferromagnetic vector, which can also be written in the form (21).[1)]

Continuing the diagrams shown in Fig. 2 analytically,[21] we obtain expressions for the kinetic coefficients:

$$\begin{aligned}D_0^{(2)}=&\widetilde{A}T_c\int_{-\infty}^{\infty}\frac{d\varepsilon}{2\pi}\coth\left(\frac{\varepsilon}{2T}\right)\sum_{\mathbf{p}}\,(\nabla G_0^{-1}(\mathbf{p}))^2\\ &\times\left[\operatorname{Im}\mathscr{K}(\mathbf{p},\varepsilon)\,\frac{\partial}{\partial\varepsilon}\operatorname{Im}\mathscr{K}(\mathbf{p}-\mathbf{k},\varepsilon)\right.\\ &\left.+\operatorname{Im}\mathscr{L}(\mathbf{p},\varepsilon)\,\frac{\partial}{\partial\varepsilon}\operatorname{Im}\mathscr{L}(\mathbf{p}-\mathbf{k},\varepsilon)\right],\end{aligned} \tag{22}$$

and

$$\begin{aligned}\Gamma_0^{(2)}=&\widetilde{B}\int_{-\infty}^{\infty}\frac{d\varepsilon}{2\pi}\coth\left(\frac{\varepsilon}{2T}\right)\sum_{\mathbf{p}}\,(\nabla G_0^{-1}(\mathbf{p})\mathbf{Q})^2\\ &\times\left[\operatorname{Im}\mathscr{K}(\mathbf{p},\varepsilon)\,\frac{\partial}{\partial\varepsilon}\operatorname{Im}\mathscr{L}(\mathbf{p}-\mathbf{q},\varepsilon)\right.\\ &\left.+\operatorname{Im}\mathscr{L}(\mathbf{p},\varepsilon)\,\frac{\partial}{\partial\varepsilon}\operatorname{Im}\mathscr{K}(\mathbf{p}-\mathbf{q},\varepsilon)\right].\end{aligned} \tag{23}$$

Here the index (2) indicates that only processes with two-particle intermediate states have been taken into account. For a ferromagnet it is necessary to restrict ourselves to just the first term in Eq. (22), since a single-mode regime is involved. Equations (22) and (23) can be rewritten in a somewhat different form. Setting $\mathbf{k}=0$ and $\mathbf{q}=0$ in the integrands and integrating by parts, we obtain

$$D_0^{(2)}=\frac{\widetilde{A}}{4}\int_{-\infty}^{\infty}\frac{d\varepsilon}{2\pi}\sinh^{-2}\left(\frac{\varepsilon}{2T}\right)\sum_{\mathbf{p}}(\nabla G_0^{-1}(\mathbf{p}))^2 \times[(\mathrm{Im}\,\mathscr{K}(\mathbf{p},\varepsilon))^2+(\mathrm{Im}\,\mathscr{L}(\mathbf{p},\varepsilon))^2] \qquad (24)$$

and

$$\Gamma_0^{(2)}=\frac{\widetilde{B}}{2T_c}\int_{-\infty}^{\infty}\frac{d\varepsilon}{2\pi}\sinh^{-2}\left(\frac{\varepsilon}{2T}\right)\sum_{\mathbf{p}}(\nabla G_0^{-1}(\mathbf{p})\mathbf{Q})^2 \times\mathrm{Im}\,\mathscr{K}(\mathbf{p},\varepsilon)\mathrm{Im}\,\mathscr{L}(\mathbf{p},\varepsilon). \qquad (25)$$

These expressions can be regarded as a generalization of the equations obtained by Maleev[16] from the unitarity condition for the self-energy parts to the case of two interacting modes.

The region for integrating by parts is concentrated near the singular points of the scaling functions (9). Here because of the ''critical retardation'' in the neighborhood of the phase transition points, the characteristic energies of the fluctuations satisfy the condition $\omega^*\ll T_c$, which makes it possible to retain only the first term of the expansion of the hyperbolic tangent (Eqs. (22) and (23)) or hyperbolic sine (Eqs. (24) and (25)). Evaluating the integrals with respect to the frequencies and momenta in Eqs. (22) and (24) and separating out the scaling dimensionality, we obtain a relationship between the spin diffusion coefficient and the relaxation constant:

$$D_0=b_1T_c^2a^4\left(\frac{\xi}{a}\right)^{-3}\frac{1}{D_0}+b_2T_ca^2\left(\frac{\xi}{a}\right)\frac{1}{\Gamma_0}. \qquad (26)$$

Note that in order to obtain Eq. (26), it suffices to substitute the retarded Green spin functions in the form of Eqs. (6) and (7) into Eqs. (22) and (24). After integrating with respect to the frequency, the remaining integrals over the momenta contain only the static correlator G_0. The first term is determined by a two-diffuson intermediate state, and the second by a two-relaxon intermediate state.

The integrals in Eqs. (23) and (25) can be calculated in similar fashion. The relaxation constant Γ_0 and the spin diffusion coefficient are related by the equation

$$\Gamma_0=c_1\left(\frac{\xi}{a}\right)\frac{1}{\Gamma_0}+c_2\left(\frac{\xi}{a}\right)\frac{D_0/T_ca^2}{\Gamma_0^2}. \qquad (27)$$

The coefficients $b_{1,2}$, $c_{1,2}\sim 1$ in Eqs. (26) and (27) depend on the form of the dynamic and static scaling functions, and in general cannot be calculated using this approach. Solving the closed system of algebraic equations (26) and (27) yields the following scaling dimensionality for the kinetic coefficients:[2)]

$$D_0/T_ca^2\propto\Gamma_0\propto(\xi/a)^{-1/2}. \qquad (28)$$

This sort of behavior is entirely consistent with that predicted by the dynamic scaling invariance hypothesis[14,15] and a renormalization group analysis.[15,19] Therefore, first, the kinetic coefficients for an antiferromagnet are singular in the fluctuation region, and second, spin diffusion is entirely determined by intermediate relaxation processes. The correction to the coefficient D_0 owing to self-diffusion is of smallness $\delta D_0/D_0\propto(\xi/a)^{-4}\propto\tau^{8/3}\ll 1$. That is, diffusion is not intrinsically a critical mode in an antiferromagnet. The dynamic critical index (see Eq. (8)) is $z=3/2$.

The simple physical considerations which will allow us to describe diffusion and relaxation in the fluctuation region are based on the idea that regions of size ξ with near ordering will develop as $T\to T_c$. In these regions the excitations are antiferromagnetic magnons with an acoustic dispersion character. Estimating the spin diffusion coefficient as $D_0\sim\xi^2/t_{\mathrm{diff}}$, where $t_{\mathrm{diff}}\sim\xi/c$ is the characteristic diffusion time and $c\sim\xi^{-1/2}$ is the ''sound'' speed,[14] we obtain $D_0\sim\xi^{1/2}$. Given the dynamic similarity hypothesis, according to which the dynamic critical index z, which determines the scale of the characteristic fluctuation energies, is invariant, we obtain $\Gamma_0\sim\xi^{1/2}$.

Despite the singularity of the kinetic coefficients, the relaxation time for the ordering parameter approaches infinity, which ensures the existence of macroscopic states corresponding to incomplete equilibrium.[27] The same applies to the characteristic spin diffusion times.

It should be noted that in introducing Eq. (26) we do not formally assume knowledge of the character of the excitations in the ordered phase. However, the conservation of the total moment and nonconservation of the ordering parameter actually determine the magnetic ordering properties in full.

4. FREQUENCY AND MOMENTUM DEPENDENCE OF THE KINETIC COEFFICIENTS

We shall now consider the generalized kinetic coefficients as functions of frequency and momentum. To do this we use the relationship between the retarded spin Green functions and the Kubo functions (see Eqs. (12) and (17)). Based on these equations, it is clear that the corrections associated with the frequency and momentum dependence of the kinetic coefficients are determined, first of all, by the frequency and momentum dependence of the irreducible self-energy parts, and second, by the nonlinear character of the relaxation forces. According to the estimate of Eq. (18), the momentum and frequency dependence of the kinetic coefficients can be studied in terms of the linear response theory, i.e., the nonlinearity of the relaxation forces can be neglected.

Let us first investigate the static renormalization of the kinetic coefficients. Equations (22) and (23) transform to the usual series expansion of the functions in the powers $(k\xi)^{2n}$ and $(q\xi)^{2n}$ from the static theory:

$$D^{(2)}(\mathbf{k},0)=D_0(0,0)[1+\alpha'(k\xi)^2+\dots],$$

$$\Gamma^{(2)}(\mathbf{q},0)=\Gamma_0(0,0)[1+\beta'(q\xi)^2+\dots].$$

This expansion is related to the existence of singularities in the correlators of the static theory at the points $k_i=-n^2\xi^{-2}$ (Ref. 26), where n is an integer. The coefficients α' and β' depend only on the form of the static correlation function.

We now proceed to analyze the energy dependence of the kinetic coefficients. Using Eq. (19), we obtain the following expressions for the real and imaginary parts of $\gamma(\mathbf{k},\omega)$:

$$\mathrm{Re}\ \gamma(\mathbf{k},\omega)=\frac{\mathrm{Im}\ \Sigma^{R}_{\dot{S}\dot{S}}(\mathbf{k},\omega)}{\omega},$$

$$\mathrm{Im}\ \gamma(\mathbf{k},\omega)=-\frac{\mathrm{Re}\ \Sigma^{R}_{\dot{S}\dot{S}}(\mathbf{k},\omega)-\mathrm{Re}\ \Sigma^{R}_{\dot{S}\dot{S}}(\mathbf{k},0)}{\omega}. \tag{29}$$

Since $\mathrm{Im}\ \gamma$ is an odd function of ω and $\mathrm{Re}\ \gamma$ is an even function of ω, the regular expansion of the kinetic coefficients in powers of the frequency begins with ω^2.

We introduce an effective generalized kinetic coefficient γ^* according to the definition

$$\gamma^*=\frac{\dfrac{\partial}{\partial\omega}\ \mathrm{Im}\ \Sigma^{R}_{\dot{S}\dot{S}}(\mathbf{k},\omega)|_{\omega=0}}{1+G_0^{-1}(\mathbf{k})\ \dfrac{\partial}{\partial\omega}\ \mathrm{Re}\ \Sigma^{R}_{\dot{S}\dot{S}}(\mathbf{k},\omega)|_{\omega=0}}. \tag{30}$$

This expression for the effective generalized kinetic coefficient is analogous to the definition of effective mass in the theory of quantum liquids. The role of the Z factor is played by the renormalization constant on the mass shell:

$$Z=\frac{1}{1+G_0^{-1}(\mathbf{k})\ \dfrac{\partial}{\partial\omega}\ \mathrm{Re}\ \Sigma^{R}_{\dot{S}\dot{S}}(\mathbf{k},\omega)|_{\omega=0}}.$$

Calculations of Z in the hydrodynamic and critical regions yield the following expressions for the renormalization constant:

$$Z(k\rightarrow 0)=\frac{1}{1+\epsilon'(k\xi)^2},$$

$$Z(q\rightarrow 0)=\frac{1}{1+\delta'+\delta''(q\xi)^2}, \tag{31}$$

where the constants ϵ', $\delta'\ll 1$ can also be expressed in terms of integrals of the static correlator G_0.

Extending the definition (30) to small but nonzero ω, we obtain an expansion for the real generalized spin diffusion coefficient D^* and the relaxation constant Γ^*:3)

$$D^{(2)*}(\mathbf{k},\omega)=D_0(0,0)[1+\alpha'(k\xi)^2+\alpha''_{k\xi}(\omega/\omega^*)^2+\ldots],$$

$$\Gamma^{(2)*}(\mathbf{q},\omega)=\Gamma_0(0,0)[\beta+\beta'(q\xi)^2+\beta''_{k\xi}(\omega/\omega^*)^2+\ldots]. \tag{32}$$

Here it must be noted that we do not claim to describe the behavior of the kinetic coefficients in the region $\omega\sim\omega^*$, $k,q\sim\xi^{-1}$. This range of frequencies and energies can scarcely be subject to detailed analysis at the present time. We therefore neglect the irregular corrections to the kinetic coefficients resulting from the generation in the higher orders of perturbation theory of an infinite sequence of poles in the retarded spin Green function, which contract to the real axis and cover the pole that produced them. We shall also not discuss the phenomena associated with the loss of a pole through a cut, etc.[16,17] All these corrections are small in the region of $\mathbf{k}$ and ω of interest to us and can be discarded.

We now consider the effect of the diagrams with many-particle ($m>2$) intermediate states. As noted above, we are only interested in the regular contribution:

$$\frac{\mathrm{Im}\ \Sigma^{R(m)}_{\dot{S}\dot{S}}}{\omega}\sim(ka)^2\sum_{\mathbf{p}_1}\ldots\sum_{\mathbf{p}_m}\Lambda^{(m)}(\mathbf{k},\mathbf{p}_1,\ldots,\mathbf{p}_m)$$

$$\times\Lambda^{(m)\dagger}(\mathbf{k},\mathbf{p}_1,\ldots,\mathbf{p}_m)\,\delta(\mathbf{p}_1+\ldots p_m-\mathbf{k})\ \frac{1}{\pi^{m-1}}$$

$$\times\int_{-\infty}^{\infty}\cdots\int_{-\infty}^{\infty}\frac{d\varepsilon_1\ldots d\varepsilon_m\ \mathrm{Im}\ K^R_{SS}(\mathbf{p}_1,\varepsilon_1)\ldots\mathrm{Im}\ K^R_{SS}(\mathbf{p}_m,\varepsilon_m)}{\varepsilon_1\ldots\varepsilon_m}$$

$$\times\delta(\varepsilon_1+\ldots+\varepsilon_m-\omega), \tag{33}$$

where the functions K describe both the ‘‘diffusons’’ and the ‘‘relaxons,’’ and the integrals with respect to frequency are taken near the singular points of the scaling function. For $m=2$, Eq. (33) transforms into Eqs. (24) and (25).

As $k\rightarrow 0$, there are generalizations of Ward's identity[16] for the vertex parts $\Lambda^{(m)}$ analogous to Eq. (21), as a result of which the vertex can be expressed in terms of a sum of derivatives of the ordinary m-particle vertices of the static similarity theory. Using the ‘‘dimensionality’’ estimate for static vertices,[26] according to which $\Gamma_m\propto p^{3-m/2}$, in the limit $k\rightarrow 0$ we see that replacing the diagrams with two-particle intermediate states in the creation channel for ‘‘diffusons’’ and ‘‘relaxons’’ by diagrams with m-particle intermediate states does not change the scaling dimensionality of the irreducible self-energy parts. As for the behavior of the vertex parts at the antiferromagnetic vector, here the arguments advanced for diagrams with two-particle intermediate states are also valid. Thus, considering intermediate states with more than two particles does not change the scaling dimensionality of the kinetic coefficients, but only affects the values of the constants, which in any event cannot be calculated using the approach described here. The same can be said of the corrections associated with the energy dependence of the vertex parts.[16]

In conclusion, we note that the corrections associated with the frequency and momentum dependence of the kinetic coefficients can be investigated experimentally using neutron scattering, for which the scattering cross section is determined by the quantity $\mathrm{Im}\ K^R_{SS}(\mathbf{k},\omega)/\omega$, where the imaginary part of the retarded spin Green function satisfies Eqs. (6) and (7) with the coefficients (32).

5. CONCLUSION

In this paper we have studied the scaling behavior of the generalized kinetic coefficients in a three-dimensional Heisenberg antiferromagnet. By means of an analysis based on a modified version of the interacting mode theory, we have found approximations in a microscopic approach for satisfying the requirements of the scaling invariance hypothesis. Specifically, it has been shown that in order to determine the scaling dimensionality of the kinetic coefficients, is sufficient to limit ourselves to processes with two-particle intermediate states, with the vertex parts being given by static similarity theory.

The regular frequency and momentum dependence of the spin diffusion coefficient and relaxation constant have been determined in a pole approximation. We have introduced the concept of effective kinetic coefficients, analogous to the definition of effective mass in the theory of quantum liquids. Including the renormalizations associated with multiple scattering of ''diffusons'' and ''relaxons'' has made it possible to write explicit series expressions for the scaling function in the frequency and momentum range $\omega \ll \omega^*$ and $k,q \ll \xi^{-1}$.

The static and dynamic similarity laws, as well as the assumed existence of just two modes (two singularities at low frequencies owing to the existence of the hydrodynamic and critical regimes), underlie the results obtained in this paper. The existence of diffusion and relaxation in an antiferromagnetic system is, in turn, related to the existence of a conserved quantity in the Heisenberg model and to the nonconservation of the ordering parameter in this model. Thus, all the formulas depend only to a small extent on the specific features of Heisenberg antiferromagnets and will be valid for any system with a nonconserved ordering parameter when an additional integral of the motion exists.

In more complicated physical systems, such as heavy Fermion compounds with integral filling of the f-shell (compounds based on Ce are an example of such materials) in the Kondo lattice model, for which the Heisenberg spin interaction is mediated by indirect exchange via conduction electrons, there may be a substantial deviation from the scaling behavior of Heisenberg magnets owing to the existence of additional modes that interact with paramagnons. Modes of this sort can develop, for example, as a result of spin-liquid correlations, which inhibit growth of the magnetic correlation length. In other words, a test for the existence of spin-liquid correlations may be to measure the generalized kinetic coefficients by neutron scattering. Other objects to which the methods described in this paper may be applied include systems with nearly zero or even negative temperatures of antiferromagnetic ordering,[6,28,29] anisotropic ferri-, and antiferrimagnets, and systems with dipole interactions.

The study of the kinetic coefficients near the Néel temperature carried out in this paper shows that diagram techniques for describing kinetic effects in antiferromagnets have many advantages over existing methods[14,15,20] and can be used to analyze unrenormalizable Hamiltonians, as well as for problems with nonlocal interacting modes.

In conclusion, we thank D. N. Aristov, Yu. M. Kagan, A. V. Lazuta, V. L. Pokrovskiĭ, and P. Pfeuty for valuable comments, constructive criticism, and interest in this work. We would like especially to thank S. V. Maleev for discussions which stimulated the writing of this article. This work was supported by the International Association INTAS (Projects 93-2834 and 83-285), the Netherlands Organization for the Support of Scientific Research NWO (Project 07-30-002), and the Russian Fund for Fundamental Research (Project 95-02-04250a).

[1] Recall that the anomalous dimensionality index (Fisher index) is assumed equal to zero.

[2] In a ferromagnet, the spin diffusion coefficient is not a singular function: $D_0/T_c a^2 \propto (\xi/a)^{-1/2}$.

[3] $\omega^* \sim T_c \tau^{\nu z}$ is the characteristic energy of the fluctuations, with $z=3/2$.

---

[1] S. Chakravarty, B. I. Halperin, and D. R. Nelson, Phys. Rev. B **39**, 2344 (1989).

[2] D. P. Arovas and A. Auerbach, Phys. Rev. B **38**, 316 (1988).

[3] A. Chubukov, Phys. Rev. B **44**, 392 (1991).

[4] H. Monien, D. Pines, and C. P. Slichter, Phys. Rev. B **44**, 120 (1990).

[5] D. M. Ginsberg (ed.), *Physical Properties of High-Temperature Superconductors II,* World Scientific, Singapore (1990).

[6] A. Millis, Phys. Rev. B **48**, 7183 (1993).

[7] S. Kambe *et al.*, J. Phys. Soc. Jpn. **65**, 3294 (1996).

[8] A. Rosch, A. Schröder, O. Stockert, and H. V. Löhneysen, submitted to Phys. Rev. B.

[9] P. W. Anderson, Mater. Res. Bull. **8**, 153 (1973).

[10] G. Baskaran, Z. Zou, and P. W. Anderson, Solid State Commun. **63**, 973 (1987).

[11] Yu. Kagan, K. A. Kikoin, and N. V. Prokof'ev, Physica B **182**, 201 (1992).

[12] K. A. Kikoin, M. N. Kiselev, and A. S. Mishchenko, JETP Lett. **60**, 600 (1994).

[13] K. A. Kikoin, M. N. Kiselev, and A. S. Mishchenko, Zh. Éksp. Teor. Fiz. **112**, 729 (1997) [JETP **85**, 399 (1997)].

[14] B. I. Halperin and P. C. Hohenberg, Phys. Rev. **177**, 952 (1969); Phys. Rev. **188**, 898 (1969); Rev. Mod. Phys. **49**, 435 (1977).

[15] B. I. Halperin, P. C. Hohenberg, and E. D. Siggia, Phys. Rev. B **13**, 1299 (1976).

[16] S. V. Maleev, Zh. Éksp. Teor. Fiz. **65**, 1237 (1973) [Sov. Phys. JETP **38**, 613 (1973)].

[17] S. V. Maleev, Zh. Éksp. Teor. Fiz. **66**, 889 (1974) [*sic*]; Preprints LIYaF/1038-1040 (1985); Sov. Sci. Rev. A **8**, 323 (1987).

[18] A. Z. Patashinskiĭ and V. L. Pokorovskiĭ, *Fluctuation Theory of Phase Transitions* [in Russian], Nauka, Moscow (1982).

[19] R. Freedman and G. F. Mazenko, Phys. Rev. Lett. **34**, 1571 (1975).

[20] K. Kawasaki, in *Phase Transitions and Critical Phenomena*, C. Domb and M. S. Green (eds.), Vol. 5a, Academic, New York (1976).

[21] A. A. Abrikosov, L. P. Gor'kov, and I. E. Dzyaloshinskiĭ, *Methods of Quantum Field Theory in Statistical Physics,* Dover, New York (1975).

[22] L. Kadanoff and P. Martin, Ann. Phys. **24**, 419 (1963).

[23] Yu. A. Izyumov and Yu. N. Skryabin, *Statistical Mechanics of Magnetically Ordered Systems* [in Russian], Nauka, Moscow (1987).

[24] V. G. Vaks, A. I. Larkin, and S. A. Pikin, Zh. Éksp. Teor. Fiz. **51**, 767 (1966) [*sic*]; Zh. Éksp. Teor. Fiz. **53**, 281 (1967) [Sov. Phys. JETP **26**, 188 (1967)].

[25] G. M. Eliashberg, Zh. Éksp. Teor. Fiz. **41**, 1241 (1961) [Sov. Phys. JETP **14**, 886 (1961)]; Zh. Éksp. Teor. Fiz. **42**, 1658 (1962) [Sov. Phys. JETP **15**, 1151 (1962)]; S. V. Maleev, TMF **4**, 86 (1970).

[26] A. A. Migdal, Zh. Éksp. Teor. Fiz. **55**, 1964 (1968) [Sov. Phys. JETP **28**, 1036 (1968)]; A. M. Polyakov, Zh. Éksp. Teor. Fiz. **57**, 2144 (1969) [Sov. Phys. JETP **30**, 1164 (1970)].

[27] E. M. Lifshitz and L. P. Pitaevskiĭ, *Physical Kinetics*, Pergamon Press, Oxford (1981).

[28] J. Hertz, Phys. Rev. B **14**, 1165 (1975).

[29] T. Moriya, *Spin Fluctuations in Itinerant Electron Magnetism,* Springer-Verlag, Berlin (1985).

Translated by D. H. McNeill